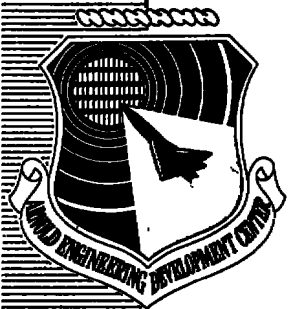


cy.1



**STRUT SUPPORT INTERFERENCE ON A CYLINDRICAL
MODEL WITH BOATTAIL AT MACH NUMBERS FROM
0.6 TO 1.4**

**PROPULSION WIND TUNNEL FACILITY
ARNOLD ENGINEERING DEVELOPMENT CENTER
AIR FORCE SYSTEMS COMMAND
ARNOLD AIR FORCE STATION, TENNESSEE 37389**

May 1976

Final Report for Period July 1, 1974 — June 30, 1975

Approved for public release; distribution unlimited.

Prepared for

**DIRECTORATE OF TECHNOLOGY (DYS)
ARNOLD ENGINEERING DEVELOPMENT CENTER
ARNOLD AIR FORCE STATION, TENNESSEE 37389**

NOTICES

When U. S. Government drawings specifications, or other data are used for any purpose other than a definitely related Government procurement operation, the Government thereby incurs no responsibility nor any obligation whatsoever, and the fact that the Government may have formulated, furnished, or in any way supplied the said drawings, specifications, or other data, is not to be regarded by implication or otherwise, or in any manner licensing the holder or any other person or corporation, or conveying any rights or permission to manufacture, use, or sell any patented invention that may in any way be related thereto.

Qualified users may obtain copies of this report from the Defense Documentation Center.

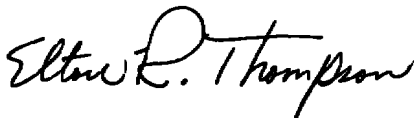
References to named commercial products in this report are not to be considered in any sense as an endorsement of the product by the United States Air Force or the Government.

This report has been reviewed by the Information Office (OI) and is releasable to the National Technical Information Service (NTIS). At NTIS, it will be available to the general public, including foreign nations.

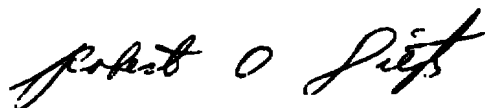
APPROVAL STATEMENT

This technical report has been reviewed and is approved for publication.

FOR THE COMMANDER



ELTON R. THOMPSON
Research & Development
Division
Directorate of Technology



ROBERT O. DIETZ
Director of Technology

UNCLASSIFIED

REPORT DOCUMENTATION PAGE		READ INSTRUCTIONS BEFORE COMPLETING FORM								
1 REPORT NUMBER AEDC-TR-76-40	2 GOVT ACCESSION NO.	3 RECIPIENT'S CATALOG NUMBER								
4 TITLE (and Subtitle) STRUT SUPPORT INTERFERENCE ON A CYLINDRICAL MODEL WITH BOATTAIL AT MACH NUMBERS FROM 0.6 TO 1.4		5 TYPE OF REPORT & PERIOD COVERED Final Report-July 1, 1974 - June 30, 1975								
		6 PERFORMING ORG REPORT NUMBER								
7 AUTHOR(s) R. C. German, ARO, Inc.		8 CONTRACT OR GRANT NUMBER(s)								
9 PERFORMING ORGANIZATION NAME AND ADDRESS Arnold Engineering Development Center(DY) Air Force Systems Command Arnold Air Force Station, Tennessee 37389		10 PROGRAM ELEMENT, PROJECT, TASK AREA & WORK UNIT NUMBERS Program Element 65807F								
11 CONTROLLING OFFICE NAME AND ADDRESS Arnold Engineering Development Center (DYFS), Air Force Systems Command Arnold Air Force Station, Tennessee 37389		12 REPORT DATE May 1976								
		13 NUMBER OF PAGES 287								
14 MONITORING AGENCY NAME & ADDRESS (if different from Controlling Office)		15 SECURITY CLASS (of this report) UNCLASSIFIED								
		15a DECLASSIFICATION/DOWNGRADING SCHEDULE N/A								
16 DISTRIBUTION STATEMENT (of this Report) Approved for public release; distribution unlimited.										
17 DISTRIBUTION STATEMENT (of the abstract entered in Block 20, if different from Report) <i>1. Struts -- Interference</i> <i>2. Mounts --</i>										
18 SUPPLEMENTARY NOTES Available in DDC										
19 KEY WORDS (Continue on reverse side if necessary and identify by block number) <table style="width: 100%; border: none;"> <tr> <td style="width: 50%;">wind tunnel</td> <td>interference</td> </tr> <tr> <td>test methods</td> <td>pressure (base)</td> </tr> <tr> <td>nozzles</td> <td>porosity</td> </tr> <tr> <td>afterbodies</td> <td>Mach numbers</td> </tr> </table>			wind tunnel	interference	test methods	pressure (base)	nozzles	porosity	afterbodies	Mach numbers
wind tunnel	interference									
test methods	pressure (base)									
nozzles	porosity									
afterbodies	Mach numbers									
20 ABSTRACT (Continue on reverse side if necessary and identify by block number) An investigation was conducted in the Aerodynamic Wind Tunnel (1T), with a sting-mounted, ogive-cylinder model and various dummy strut designs, to provide further information on sources of nozzle afterbody (NAB) interference and to determine how incremental changes in afterbody boattail and base pressures are affected by changes in support strut design and location. The investigation also included the effect of changing local wall										

UNCLASSIFIED

UNCLASSIFIED

20. ABSTRACT (Continued)

porosity on the NAB interference. An analysis of pressure data obtained on the model, boattail, base, and tunnel wall surfaces at Mach numbers from 0.6 to 1.4 indicates that interference occurs above Mach 0.99 as the result of disturbances generated by the strut leading edge which are reflected from the tunnel wall to the NAB. This interference can be minimized by using a swept strut; however, the optimum strut sweep angle and strut location is a function of Mach number and NAB geometry.

PREFACE

The work reported herein was conducted by the Arnold Engineering Development Center (AEDC), Air Force Systems Command (AFSC), and was sponsored by AEDC/DYR, AFSC, under Program Element 65807F. The results presented were obtained by ARO, Inc. (a subsidiary of Sverdrup & Parcel and Associates, Inc.), contract operator of AEDC, AFSC, Arnold Air Force Station, Tennessee. The pressure test was conducted in the Aerodynamic Wind Tunnel (1T) under ARO Project Nos. PF446 and P32P-11A. The author of this report was R. C. German, ARO, Inc. The manuscript (ARO Control No. ARO-PWT-TR-75-110) was submitted for publication on June 30, 1975.

CONTENTS

	<u>Page</u>
1.0 INTRODUCTION	7
2.0 APPARATUS	
2.1 Tunnel 1T Description	7
2.2 Acoustic Research Tunnel Description	7
2.3 Test Articles	8
2.4 Instrumentation	9
3.0 PROCEDURE AND PRECISION OF MEASUREMENTS	
3.1 Tunnel 1T Test	9
3.2 Acoustic Research Tunnel (ART) Test	10
4.0 RESULTS AND DISCUSSION	
4.1 Baseline Performance	11
4.2 Effect of Sting Flare Location	12
4.3 Effect of Strut Sweep Angle	12
4.4 Effect of Strut Location	14
4.5 Effect of Local Wall Porosity	17
4.6 Effect of Plume Simulation	18
5.0 CONCLUSIONS	18
REFERENCES	20

ILLUSTRATIONS

Figure

1. Model Installation in PWT Tunnel 1T	21
2. Model Installation in PWT Acoustic Research Tunnel	23
3. Sting-Mounted Baseline Model Showing Pressure Orifice Location	24
4. Test Configurations for Support Interference on NAB Test	25
5. Model Instrumentation Location	26
6. Photographs – Model Test in PWT Acoustic Research Tunnel	29
7. Location of Local Wall Porosity Variation	31
8. Reynolds Number Variation with Mach Number	33
9. Baseline Pressure Coefficient Data (Cylindrical Afterbody, B1)	35
10. Baseline Pressure Coefficient Data (10-deg Boattail, B2)	39
11. Wall Pressure Coefficient Distribution for Baseline Configurations, B0, B1, and B2	43

<u>Figure</u>	<u>Page</u>
12. Effect of Boattail Angle and Body Length on Base Pressure Coefficient	44
13. Baseline Pressure Coefficient Data for 10-deg Boattail with Simulated Plume	45
14. Effect of Sting Flare Location on Base Pressure Coefficient	46
15. Effect of Sting Flare Location on Interference Coefficient for Cylindrical Afterbody	48
16. Effect of Sting Flare Location on Interference Coefficient for 10-deg Boattail	50
17. Effect of Strut Sweep Angle on Base Pressure Coefficient	52
18. Effect of Strut Sweep Angle on Boattail Interference Coefficient	53
19. Effect of Strut Sweep Angle on Body Interference Coefficient	55
20. Pressure Coefficient Distribution on Model Body, Strut, and Tunnel Wall	57
21. Effect of Strut Sweep Angle on Wall Pressure Coefficient	65
22. Effect of Boattail Angle on Base Pressure Interference Coefficient for Straight and Swept Support Struts	67
23. Effect of Straight Strut Location on Base Pressure Coefficient	69
24. Effect of Straight Strut Location on Boattail Interference Coefficient	70
25. Effect of Straight Strut Location on Body Interference Coefficient	72
26. Effect of Straight Strut Location on Wall Pressure Coefficient	74
27. Schlieren Photographs for Straight Strut Located at $l/D = 0$ and 1.6	76
28. Schlieren Photograph Describing Shocks Generated by Straight Strut Configuration, B2-S2L3	77
29. Effect of Strut Location on Base Pressure Coefficient for Cylindrical Afterbody and 10-deg Boattails (with Trailing Edge at Same Station)	78
30. Effect of Strut Location on Body Pressure Interference Coefficients (with Trailing Edge at Same Station)	79
31. Effect of Strut Location on Boattail Interference Coefficients (with Strut Trailing Edge at Same Station)	81
32. Effect of Strut Position on Base Pressure Coefficient	83
33. Effect of Boattail Angle on Base Pressure Interference Coefficient for Two Swept Strut Locations	84

<u>Figure</u>	<u>Page</u>
34. Effect of Swept Strut Location on Body Interference Coefficient	86
35. Effect of Swept Strut Location with Cylindrical Afterbody	88
36. Schlieren Photographs for 45-deg Swept Strut Located at $l/D = 0$ and 1.6	89
37. Effect of Sweep Angle on Base Pressure Coefficient with Struts Located at Downstream Position, $l/D = 1.6$	90
38. Equivalent Body Shapes for Body Plus Strut Cross-Sectional Areas	91
39. Influence of Strut Trailing-Edge Design on Boattail Pressure Interference Coefficients	92
40. Effect of Swept Strut Trailing-Edge Design on Base Pressure Interference Coefficients	94
41. Effect of Swept Strut Trailing-Edge Design on Wall Pressure Coefficient Distribution ($\phi = 90$ deg)	95
42. Effect of Local Wall Porosity on Base Pressure Coefficient	96
43. Effect of Local Wall Porosity on Body Pressure Interference Coefficient	97
44. Effect of Local Wall Porosity on Boattail Pressure Interference Coefficient	99
45. Effect of Local Wall Porosity on Wall Pressure Coefficient	101
46. Effect of Local Wall Porosity on Base Pressure Coefficient for Swept Strut, S3L1	103
47. Effect of Local Wall Porosity on Boattail Pressure Interference Coefficient for Swept Strut, S3L1	104
48. Effect of Local Wall Porosity on Body Pressure Interference Coefficient for Swept Strut, S3L1	106
49. Effect of Local Wall Porosity on Wall Pressure Coefficient with Swept Strut, S3L1	108
50. Effect of Simulated Plume on Boattail Pressure Interference Coefficient	110
51. Effect of Strut Sweep Angle on Boattail and Plume Pressure Interference Coefficients	112
52. Effect of Swept Strut Location on Boattail Pressure Interference with Simulated Plume	114
53. Effect of Strut Trailing-Edge Location on Boattail Pressure Interference with Simulated Plume	116

TABLES

1. List of Test Configurations118
2. Average Base Pressure Coefficient on NAB119

APPENDIX

A. PLOTS OF TEST DATA121
NOMENCLATURE286

1.0 INTRODUCTION

A test was conducted in the transonic Aerodynamic Wind Tunnel (1T) of the Propulsion Wind Tunnel Facility (PWT) to provide basic information on the support interference on nozzle afterbody performance by measuring incremental changes in boattail and base pressures resulting from changes in sting taper location, in strut design and location, in boattail angle, and from the addition of a solid plume body to simulate jet effects. The model consisted of a sting-mounted cylindrical body with an ogive nose and boattail. Seven dummy strut configurations, two boattail configurations, one movable sting taper, one solid plume body, and two changes in local wall porosity were tested at free-stream Mach numbers from 0.60 to 1.4 with the model at zero angle of attack.

Only selected Mach numbers and those plots which adequately explain the observed results of support interference on nozzle afterbody are included in the body of the report. A complete set of data is given in Appendix A.

The characteristics of the flow around the model were also observed optically using the existing Schlieren system in the Acoustic Research Tunnel (ART) for four strut configurations at free-stream Mach numbers from 0.90 to 1.1. The results reported herein are a continuation of the work reported in Ref. 1 to investigate support interference effects.

2.0 APPARATUS

2.1 TUNNEL 1T DESCRIPTION

Tunnel 1T is a continuous flow, nonreturn wind tunnel capable of being operated at Mach numbers from 0.2 to 1.5 utilizing variable nozzle contours above $M_{\infty} = 1.10$. The tunnel is operated at a stilling chamber total pressure of about 2,850 psfa with a ± 5 -percent variation, dependent on tunnel resistance and ambient atmospheric conditions. The total temperature can be varied from 80 to 120°F above ambient temperatures as necessary to prevent visible condensation in the test section. The standard test section is 1 ft square and 37.5 in. long with six-percent porous perforated walls. The general arrangement of the tunnel and the installation of the test model are shown in Fig. 1. The tunnel wall angles were varied with Mach number in accordance with an optimum schedule given in Ref. 2.

2.2 ACOUSTIC RESEARCH TUNNEL DESCRIPTION

A 6-in. Acoustic Research Tunnel (ART) was designed and installed at the Propulsion Wind Tunnel Facility at AEDC. The ART (Fig. 2) is a continuous flow, atmospheric indraft

wind tunnel with a Mach number range capability from 0.05 to approximately 1.15 depending on the wall configuration. The ART is normally powered by the Propulsion Wind Tunnel Facility Plenum Evacuation System.

The test section is 6 in. square by 24 in. long and has solid side walls with quartz windows for the schlieren system. The top and bottom walls are ventilated and for the present test used sections of the Tunnel 1T wall (same hole size and pattern with six-percent porosity). The top and bottom wall angles were adjusted to give a 0.5-deg downstream divergence to allow for test section wall boundary-layer growth and to provide a flat Mach number distribution. The test section walls have "O" ring seals on all edges to prevent flow into or out of the plenum except through the ventilated walls. All flow into the plenum is removed through the plenum evacuation line. The flow entering the test section passes through a series of screens on either side of a honeycomb section in the stilling chamber.

2.3 TEST ARTICLES

A sketch showing the model and strut orientation in Tunnel 1T is presented in Fig. 1. The model tested in Tunnel 1T was a 1.0-in.-diam 8.1-in.-long cylindrical body with an ogive nose. The model was fabricated using the same nose and body coordinates used for the model in Ref. 1. Provisions were made to add either a cylindrical afterbody or a 10-deg conical boattail (Fig. 3). The afterbodies were designed to allow the instrumentation lines to "plug-into" the base of the cylindrical body. The instrumentation lines were then routed internally in the model body and sting. The model was sting mounted; however, each of the seven dummy strut configurations tested (Fig. 4) had a tab on the bottom of the strut which extended through a slot in the tunnel side wall for lateral support (Fig. 1). The strut instrumentation lines were routed through the bottom tab. A 0.08-in. band of No. 180 grit was placed on the nose of the model and on the strut leading edge as shown in Fig. 5 to ensure turbulent flow over the surfaces. Unfortunately, it was difficult to maintain the grit on the nose of the model.

The dummy strut configurations were scaled to be generally compatible with the model support requirements used in the PWT 16-ft wind tunnels. Each strut had a double-wedge cross section. The geometric blockage of the baseline configurations is 0.55 percent, and the geometric blockage of the strut configurations varied from 1.16 percent to 1.31 percent (see Table 1).

The model tested in ART was a 0.5-scale of the Tunnel 1T model. Four strut configurations (B2-S2L1, -S2L3, -S3L1, and -S3L3) were tested on the strut-supported model (see Fig. 6). Although the main objective of this test was to document the flow disturbances on the model in the region of strut and nozzle afterbody using a schlieren

system, the pressures on the top ($\phi = 0$) and side walls ($\phi = 90$ deg) were also recorded. A "z" axis-type schlieren system with a spark light source and 8-in.-diam quartz windows in the side walls were used for flow visualization. The flow disturbances were recorded by a 70-mm camera for five different knife edge settings. A band of No. 120 grit was also placed on the model nose and strut leading edge of the test as can be seen in Fig. 6.

The effect of local wall porosity in the region where the model and strut shock waves interact with the tunnel wall was investigated for strut Configurations S2L3 and S3L1 in Tunnel 1T and for strut Configuration S2L3 in ART (see Fig. 7). A list of the test configurations investigated is given in Table 1.

2.4 INSTRUMENTATION

The instrumentation of the Tunnel 1T model, including the cylindrical body, sting, sting taper, boattail, plume body, and struts is shown in Figs. 3 and 5. Twenty static pressure orifices were located on the axisymmetric body with four measuring base pressures which were averaged to calculate the base pressure coefficient (CPB). There were 16 static pressure orifices on the sting, eight on the sting taper at $\phi = 0$, ten on the boattail at $\phi = 0$ and 90 deg, and 16 on the solid plume body at $\phi = 0$ and 90 deg. Three strut configurations, S2L1, S3L1, and S3L3 were instrumented with 13 static pressure orifices at each the inboard and the midspan locations.

The pressures during the test in Tunnel 1T were measured by using four Scanivalves® with self-balancing precision transducers. Digitized readouts of these transducer measurements were displayed on electromanometers in the control room. The electrical signals from the transducers and tunnel-condition instrumentation were transmitted through analog-to-digital converters to a Raytheon 520 computer for final data reduction.

The wall pressures measured during the test in ART were measured using two Scanivalves and a servo-force balance precision transducer. Digitized readouts of the transducer measurements were recorded visually and on a paper tape as each pressure port was selected by the Scanivalve system.

3.0 PROCEDURE AND PRECISION OF MEASUREMENTS

3.1 TUNNEL 1T TEST

Pressure measurements were obtained at nominal Mach numbers from 0.6 to 1.4 for three baseline configurations, B1, B2, and B2-P1 for configurations with a cylindrical boattail, a 10-deg boattail, and a solid plume body, respectively. These data were recorded and entered into the computer storage. The test procedure was then repeated with the

various sting taper locations and dummy strut configurations to determine the magnitude of the interference coefficients. A list of the configurations tested and test Mach numbers is provided in Table 2, which shows the average base pressure coefficient obtained for each configuration. The model angle of attack remained zero throughout the test. The tunnel stagnation pressure range was from 2,972 to 2,789 psfa, and the total temperature was varied from 126 to 206°F. The resulting Reynolds number variation is presented in Fig. 8a.

Since the purpose of this investigation was to determine the aerodynamic interference effect induced on the model pressure distribution by the various strut support configurations, the repeatability of the data is of primary importance. A repeat test was made for some configurations to check the validity of the data over the range of test Mach numbers. A tabulation showing the repeatability of the pressure coefficients and the precision of the free-stream Mach numbers is presented as follows:

<u>M_{∞}</u>	<u>ΔM_{∞}</u>	<u>ΔCP and ΔCPB</u>	<u>$\Delta CPBT$</u>
0.600 to 0.900	± 0.003	± 0.003	± 0.009
0.900 to 0.990	± 0.003	± 0.003	± 0.004
0.990 to 1.100	± 0.003	± 0.007	± 0.027
1.100 to 1.200	± 0.003	± 0.005	± 0.033
1.200 to 1.400	± 0.003	± 0.006	± 0.034
1.400	± 0.003	± 0.005	± 0.025

3.2 ACOUSTIC RESEARCH TUNNEL (ART) TEST

The flow characteristics were obtained at nominal Mach numbers from 0.9 to 1.1 for four strut configurations with the six-percent porosity walls and for strut Configuration S2L3 at local wall porosities of three and one percent. The wall pressure distributions were recorded to measure the Mach number distribution upstream of the model and to measure the influence of model shocks on the wall pressure. The flow characteristics were then determined optically using the schlieren system at five different knife-edge settings and photographed with a 70-mm camera. The Reynolds number variation is shown in Fig. 8b.

The precision of the free-stream Mach numbers and the pressure measurements are presented as follows:

<u>M_{∞}</u>	<u>ΔM_{∞}</u>	<u>$\Delta CP(W)$</u>
0.6 to 0.9	± 0.001	± 0.002
0.9 to 0.99	± 0.001	± 0.001
0.99 to 1.10	± 0.001	± 0.001

4.0 RESULTS AND DISCUSSION

The purpose of this test was to provide basic information on the effect of support interference on nozzle afterbody performance by measuring incremental changes in model, boattail and base surface pressures resulting from changes in sting taper location, strut sweep angle, strut location, and from a simulated jet plume. The incremental changes in pressure were obtained by calculating the difference between the pressure coefficients for a given configuration and its corresponding baseline (no strut) configuration. The pressure data were obtained at nominal Mach numbers from 0.60 to 1.4 with the model maintained at zero angle of attack. To make this report more readable, only the results between $M_\infty = 0.99$ and 1.2 are shown in many cases since this is the range where the major interference occurs. A complete plot of the results for each Mach number is given in Appendix A.

4.1 BASELINE PERFORMANCE

The surface pressure coefficients on the sting-mounted cylindrical body with cylindrical afterbody and 10-deg boattail, which were used as baseline data for configurations without a jet plume simulation, are presented in Figs. 9 and 10, respectively. The cylindrical boattail surface and base pressures show the results of flow expansion around the base at subsonic and transonic speeds up to $M_\infty = 1.10$. Above $M_\infty = 1.10$ the pressure on the cylinder afterbody is approximately constant preceding the sudden expansion at the base. The pressures on the cylindrical body preceding the 10-deg boattail (Configuration B2) are approximately the same as recorded for the cylindrical afterbody above $M_\infty = 0.99$. A rapid expansion occurs at the sharp shoulder of Configuration B2 which is particularly strong at high subsonic and low supersonic Mach numbers. The expansion is followed by a recompression on the boattail surface, which is evident in the schlieren photographs referenced in a later section. It should be noted that there is a slight increase in pressure coefficient (Fig. 9a) on the B0 baseline models at $M_\infty = 1.1$ and 1.2 at a location which appears to correspond to a reflection from the tunnel wall generated by the model nose shock (see Fig. 11). This could explain the increase in base pressure noted for the shorter baseline configuration (B0) at $M_\infty = 1.10$ and 1.20 in Fig. 12, which results from a reflected shock intersecting the body closer to the base of the model. The sudden change in base pressure at Mach 1.0 reflects the sensitivity of the base drag to any aerodynamic interference in this Mach range.

The pressure distribution over the 10-deg boattail and the simulated plume without a strut, which is used as a baseline for the strut data with a simulated plume, is shown in Fig. 13. The presence of the simulated plume raises the level of the pressures on the boattail but does not change the general shape of distribution.

4.2 EFFECT OF STING FLARE LOCATION

The effect of sting flare location relative to the base of the model is most pronounced on base pressure. Comparison of the base pressure coefficient, CPB, and the base pressure interference coefficient, DCPB, for various sting flare locations shows that the beginning of the flare surface must be moved downstream 3.0 body diameters with the 10-deg boattail and 5.0 body diameters with the cylindrical boattail before the influence is minimized (see Fig. 14). Although not investigated, the size of the flare relative to the cylindrical body diameter should be an important factor in the amount of interference for a given sting flare location. The interference coefficient on the cylindrical afterbody is shown in Fig. 15 at $M_\infty = 0.99, 1.02, 1.1, \text{ and } 1.2$ for various sting flare locations. Only insignificant interferences were noted on the model body for both the cylindrical afterbody and the 10-deg boattail configurations. Interference was primarily noted on the 10-deg boattail, where separation was induced on the boattail when the sting flare was positioned 1.0 body diameter from the base of the boattail, as shown in Fig. 16. The variation of the interference coefficients on the cylindrical body for the various sting flare locations did not change appreciably at the three circumferential points of measurement ($\phi = 0, 90, \text{ and } 180 \text{ deg}$).

4.3 EFFECT OF STRUT SWEEP ANGLE

The effect on the base pressure coefficient of changing the strut sweep angle with the leading edge of the strut intersecting at the model nose is shown in Fig. 17. The strut with a sweep angle (Λ) of 45 deg (S3L1) had a smaller base pressure interference parameter, DCPB, for most Mach numbers above Mach 0.90, compared to the struts with sweep angles of $\Lambda = 0$ (S2L1) and 30 deg (S5L1). This smaller DCPB at a sweep angle of 45 deg appears to be generally accompanied by a smaller boattail interference parameter at $M_\infty = 1.02$ and 1.2, as shown in Fig. 18. There is also a definite decrease in interference on the forebody between $M_\infty = 0.99$ and 1.2 for Configuration S3L1, as shown in Fig. 19. It should be noted that the boattail interference coefficient is as large or larger than the interference on base pressure coefficient; thus, the base pressure interference coefficient is not always the best indicator of the amount of afterbody interference produced by a given strut configuration.

The effect of strut sweep angle on the pressure coefficient distribution over the 10-deg boattail body, strut, and tunnel walls at $\phi = 0$ and 90 deg is shown in Figs. 20a and b for strut Configurations S2L1 and S3L1, respectively, at $M_\infty = 0.99, 1.02, 1.1, \text{ and } 1.2$. The circumferential variation of the interference coefficient around the body is small except at the trailing edge of the straight strut. Only minor circumferential variations occur with the swept strut (S3L1). The tunnel wall pressure coefficients show some change between $\phi = 0$ and 90 deg as a result of the interaction of the two-dimensional strut

compressions from the straight strut configuration and those generated on the axisymmetric body. The effect of the bow shock generated by the model nose can be seen as a peak in CP_{wall} as the shock (SM) is reflected on the tunnel wall with both the straight strut (S2L1) and the swept strut (S3L1) configurations. The location of this reflection agrees with the B2 baseline configuration in Fig. 11. The reflection of both the leading-edge (SLE) and trailing-edge shocks (STE) from the straight strut configuration are also evident in Fig. 20a at $\phi = 90$ deg. When the strut was swept, the shocks from the strut no longer had a strong effect on the wall as they did with the straight strut. The change in shock reflections at the wall are believed to change the body pressure coefficients, $CP(B)$, upstream of the boattail as shown in Fig. 20 at $M_\infty = 1.1$ and 1.2.

A comparison of the inboard pressures on the struts for the swept and unswept configurations shows the swept strut to have a more positive value of CP (closer to CP on the body) between $M_\infty = 0.99$ and 1.2. This follows the decreased interference on the body and base pressures when the swept strut is used. It should be noted that certain values of CP near the trailing edge of the strut are not shown for some Mach numbers because of erroneous measurements. The results from tests with the cylindrical boattail are not shown since similar trends were obtained.

A comparison of the wall pressure coefficients for the three different strut sweep angles is shown in Fig. 21. The results show the wall pressure distribution for the swept struts is closer to the values obtained for the baseline configuration. The swept struts also do not have the discontinuity (at $\phi = 90$ deg) resulting from the strut trailing-edge shock that exists with the straight strut. Although the results show the wall pressure coefficients for the 30-deg swept strut (S5L1) are in closer agreement with the baseline data, the reflection of the nose and strut leading-edge shock system from the 45-deg swept strut (S3L1) gave minimum interference on the body and NAB for most Mach numbers. At Mach 1.2, the theoretical shock angle generated by the model nose is about the same angle as the leading edge of the 30-deg swept strut. This could result in a stronger interaction at the wall and thus reflect to give a stronger interference on the boattail than exists with the 45-deg swept strut. This could explain why the 30-deg swept strut gives a different trend in base pressure interference than the 45-deg swept strut for some Mach numbers (see Figs. 17 and 18).

The effect of boattail angle on base pressure interference for different strut sweep angles is shown in Fig. 22. The results show that changes in boattail angle have a much greater effect when a straight strut is used above Mach 1.0. This would indicate that a swept strut should be used when testing NAB with various boattails to minimize the interference resulting from changes in boattail angle.

Unfortunately, a single strut sweep angle cannot be selected which will give minimum interference for all NAB installations. The interference on the NAB will depend upon how the strut and nose shocks are reflected by the wall, and the location of the NAB relative to that interaction. It can only be concluded from this investigation that for this NAB model, the 45-deg swept strut gave the minimum interference for most Mach numbers above $M = 0.99$.

4.4 EFFECT OF STRUT LOCATION

The effect of support strut location and its effect on NAB interference was investigated for both a straight strut and 45-deg swept strut. Both struts were positioned at $\ell = 0$ (strut leading edge intersecting model nose at model station zero) and at $\ell = 1.6$ in. (see Fig. 4).

4.4.1 Straight Strut

The characteristics of the base pressure interference coefficient (DCPB) with changes in strut location (Fig. 23) indicate that for a straight strut the location which best matches the baseline value is a function of free-stream Mach number above $M_{\infty} = 0.99$. The interference coefficients on the boattail in Fig. 24 show trends similar to DCPB both at $\phi = 0$ and 90 deg, with the exception of $M_{\infty} = 1.20$ where only the trend at $\phi = 90$ deg is in agreement. The change in interference over the axial length of the body (Fig. 25) is also greater with the strut in the aft location (S2L3) until $M_{\infty} = 1.2$. This agrees with the trend in base pressure interference (CDPB) which indicates Configuration S2L1 gives minimum interference below $M_{\infty} = 1.2$. The interference resulting from different shock interactions at the tunnel wall can be seen in Fig. 26. The location where the model nose shock (SM) intersects the wall results in about the same value of $CP(W)$ at $\phi = 0$ as the baseline configuration with the strut (S2L3) located downstream ($\ell = 1.6$). There is an additional interaction of the conical nose shock and two-dimensional strut leading-edge shock (SLE) for the strut (S2L1) located at the nose. The interactions of the SLE and the strut trailing-edge shock (STE) with the wall and their movement with Mach number can be seen at $\phi = 90$ deg in both Figs. 26 and 27. It is interesting to note that the STE shown in the schlieren photographs occur at the same axial location on the wall as indicated by the recompressions of $CP(W)$ in Fig. 26b for similar Mach numbers. The Mach number specified on the schlieren photographs was calculated from measured wall static pressures at the NAB station. The free-stream Mach number was not high enough for the configurations shown in Fig. 27 to visually see the nose and strut leading-edge shocks whose reflection by the wall causes the major influence on the NAB. The STE can be visually seen as the shock intersects the schlieren window and would, therefore, intersect the tunnel centerline downstream of the NAB for Mach numbers much

above 1.0. One schlieren test was run with Configuration B2-S2L3 at a free-stream Mach number of 1.16 which visually shows the nose and leading-edge shocks and a recompression from their intersection on the wall (see Fig. 28). A shock can be seen at this intersection on the lower wall which reflects back to the body at about two body diameters upstream of the NAB. This corresponds to the change in body interference noted in Fig. 25. The local porosity for this data was one percent.

A comparison of straight strut Configurations S2L1 and S1L2 gives additional information on the effect of strut location. Although strut S1L2 has the leading edge at $\ell = 0.8$, the trailing edge is at the same location as the trailing edge for strut S2L1. A comparison of the base pressure coefficients in Fig. 29 for the two straight struts for both a cylindrical afterbody and 10-deg boattail shows very small differences except at $M_\infty = 1.3$ for the cylindrical (B-1) afterbody and at $M_\infty = 1.2$ for the 10-deg boattail (B-2) afterbody. Similar effects were noted on the model and boattail surfaces as shown in Figs. 30 and 31, respectively.

Strut Configuration S1L2 with $\ell = 0.8$ in. is compared in Fig. 32 with struts tested in Ref. 1 which have the same geometry as S1L2 (same chord and thickness) but are located at $\ell = 0$ and 1.6 in. The results show that the strut S1L2 in position $\ell = 0.8$ gives about the same interference on the base pressure coefficient as the C-I strut (S1L1) at $\ell = 0$ between $M_\infty = 1.0$ and 1.2. This comparison also shows that optimum strut location is a function of Mach number and the interaction of the disturbances from the model nose and strut leading edge. The interaction remained essentially the same for strut positions $\ell = 0$ and 0.8 in.

4.4.2 Swept Strut

The 45-deg swept strut was positioned at $\ell = 0$ (strut leading edge intersecting model nose at model station zero, B2-S3L1) and at $\ell = 1.6$ in. (B2-S3L3) (see Fig. 4). A comparison of the two swept strut positions and their influence on base pressure coefficient is shown in Fig. 33 for a cylindrical afterbody and a 10-deg boattail. The results show the greatest interference on base pressure coefficient, DCPB, occurs with the swept strut located at the downstream position between Mach numbers 0.99 and 1.20 for the 10-deg boattail. However, the greatest interference, DCPB, occurs with the strut located at $\ell = 0$ for the cylindrical afterbody (B1-S3L1). It is interesting to note that this trend is not always true for the interferences on the body and NAB surfaces. At $M_\infty = 1.02$, for instance, the interference on the body between the strut trailing edge and on the boattail is greater with the strut located downstream for both the 10-deg boattail configuration (B2-S3L3) and the cylindrical afterbody (B1-S3L3), as shown in Figs. 34 and 35, respectively. This interference on the boattail could be the result of disturbances which are generated by

the intersection of the strut with the wall. The schlieren photographs in Fig. 36 show the NAB to be in the region of these disturbances when the strut is in the downstream location. The interference also varies radially on the model body at $X/D = 5.5$ with the maximum interference occurring at $\phi = 180$ deg in the plane of the support strut (see Fig. 35). These trends offer additional evidence that the base pressure interference is not always the best indicator of interference characteristics of strut support systems on NAB performance. The results indicate that locating the strut closer to the NAB would tend to increase the interference on the boattail but could decrease the interference on the base pressure, depending upon the Mach number and boattail geometry.

Another significant fact arises when comparing the straight strut and 45-deg swept strut configurations for the downstream strut support location (see Fig. 37). A previous comparison of strut sweep angle effect at the forward strut location in Figs. 17 and 18 showed a significant change in interference on the base pressure and boattail pressure coefficients as a function of sweep angle at some Mach numbers (see $M_\infty = 1.2$). In Fig. 37 the difference in DCPB between the straight strut and 45-deg swept strut is not as significant with the struts located downstream of the model nose, although the swept strut still gives minimum interference. This change in trend can be explained by the fact that the struts and their accompanying shocks have been located downstream of the body nose shock at $\ell = 1.6$ to eliminate some of the complicated interactions which occur with the struts located at the model nose. This is not to say that the strut should not be located at the model nose, however, since it has been shown for some Mach numbers that the forward location may still provide minimum interference to the base pressure coefficient for some boattail geometries. Small changes (± 0.005) were also noted on the wall pressure coefficients for the two positions of the 45-deg swept strut. The interference on the wall resulting from strut shocks was also decreased compared to those observed with the straight strut. A maximum interference coefficient on the wall for the swept strut configurations was ± 0.025 at $M_\infty = 1.1$ compared to ± 0.045 for the straight strut configurations. This decrease with the swept strut configurations results from a weaker compression in the flow around the strut as the strut is swept aft. Although the pressures on the strut surface were measured for strut Configuration B2-S3L3, they are not shown since they were similar to those shown in Fig. 21b with the swept strut S3L1 located at the model nose ($\ell = 0$).

The trailing-edge design of a 45-deg swept strut was changed to Configuration B2-S4L1 (see Fig. 4) to determine how a more uniform cross-sectional area in the region near the NAB would affect the boattail and base pressures. Sketches are shown in Fig. 38 of the equivalent body shapes for four of the strut configurations tested. The equivalent body shape was calculated from the axial variation in body plus strut cross-sectional area. Although the B2-S4L1 equivalent body gave the most gradual change in cross-sectional area,

the proximity of the strut to the boattail resulted in greater interference to the boattail and base pressure coefficients as is shown in Figs. 39 and 40, respectively. The disturbance to the model base pressure was especially great for Mach numbers between 0.95 and 1.05. The disturbances for strut S4L1 are also evident on the wall pressure coefficients in Fig. 41 at $\phi = 90$ deg.

4.5 EFFECT OF LOCAL WALL POROSITY

An attempt was made to investigate the effects on NAB interference of changing the local wall porosity in the region where the various disturbances from the model interacted with the boundary layer on the tunnel wall. The two-dimensional strut leading-edge shock and its intersection on the top and bottom ($\phi = 90$ deg) walls was of particular interest. The local porosity in this region was changed from the standard six-percent (all holes open) to three- and one-percent porosity by filling a required number of the holes in a pattern shown in Fig. 7.

4.5.1 Straight Strut - S2L3

The effect of local wall porosity on the base pressure coefficient is shown in Fig. 42 for straight strut Configuration B2-S2L3. The results would indicate that above $M_\infty = 0.99$ a variable local wall porosity is desirable to minimize the interference of the disturbances generated by the straight strut. At $M_\infty = 1.1$, for instance, the effect on base pressure can be eliminated for this straight strut configuration by changing the local wall porosity to near one percent. The change in local porosity is shown in Fig. 43 to affect the pressure coefficients preceding the boattail at all radial positions around the body. The effect of porosity change on body pressure begins at $X/D = 4.5$ for $M_\infty = 0.99$ and moves to $X/D = 6.5$ for $M_\infty = 1.20$. This movement of the interference on the cylindrical body corresponds to a reflection from the wall of disturbances produced by the model nose, strut leading edge, or a combination of both. The effects of porosity on the boattail pressure coefficients in Fig. 44 have the same trend as the base pressure coefficient with the exception of $M_\infty = 1.02$. The pressure coefficients on the side walls of the tunnel ($\phi = 0$, see Fig. 45) were affected only slightly; however, the pressure coefficients on the bottom wall ($\phi = 90$ deg) showed a greater recompression (an increase $CP(W)$) as porosity was decreased. It would appear that by changing wall porosity the shocks and disturbances are reflected at a different angle and strength back to the model, thus causing a change in the interference coefficients. However, no change in the shock system was noted in the schlieren photographs when the local porosity was changed for strut Configuration B2-S2L3.

4.5.2 Swept Strut - S3L1

The effect of porosity on the 45-deg swept strut, S3L1, was not as effective as for the straight strut. Although there was a definite effect of local wall porosity on the NAB performance, the overall results indicated that a six-percent porosity gave the minimum base pressure interference at all Mach numbers except at $M_\infty = 1.1$ where one-percent porosity gave slightly less interference. These results are shown by the interferences on the base, boattail, and body pressure coefficients in Figs. 46, 47, and 48, respectively. It was noted that the effect of porosity on the body had a greater effect just upstream of the boattail at $\phi = 90$ and 180 deg for $M_\infty = 1.10$. The effect of local wall porosity on the wall pressures is shown in Fig. 49.

4.6 EFFECT OF PLUME SIMULATION

The influence of a nozzle plume on strut interference is important since nozzle afterbody tests must be accomplished with and without flow through the nozzle. In an attempt to obtain a qualitative answer, a solid plume body (see Fig. 4) was used to simulate a typical jet flow. Unfortunately, this is not an ideal method to determine jet flow effects since the entrainment and mixing characteristics of the jet cannot be simulated. A baseline plot of the pressure coefficient distribution over the boattail and the solid plume without a strut is presented in Fig. 13. The results indicate that the solid plume causes a separation over the boattail as shown in Fig. 50. The support strut interference on the boattail in the presence of a simulated plume for either a straight or swept strut in Fig. 51 would appear to be a function of Mach number. The movement of the swept strut downstream in Fig. 52 also shows the effect of strut location in the presence of a simulated plume to be a function of Mach number. If this trend holds for a real jet, then it might be said that the optimum sweep angle as well as the strut location are a function of Mach number. Further study is required to determine how representative these trends with a simulated solid plume are to a real jet. The effect of maintaining the strut trailing edge at the same station while varying the chord in the presence of a simulated plume shows only minor changes in interference on the boattail in Fig. 53, with the exception of $M_\infty = 1.02$.

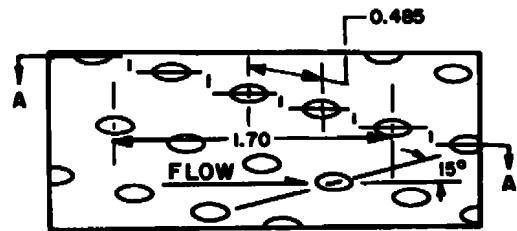
5.0 CONCLUSIONS

Experimental data were obtained for an ogive-cylindrical model in the AEDC PWT-1T Wind Tunnel. The model was sting mounted with provisions to attach dummy struts at two locations in order to assess the strut interference on the model body and afterbody pressure distribution. Two afterbody configurations (a cylindrical afterbody and a 10-deg conical boattail) were used during the experiments. Based on the analysis of the model body, afterbody, base pressure, and the tunnel wall pressure distribution the following conclusions were reached:

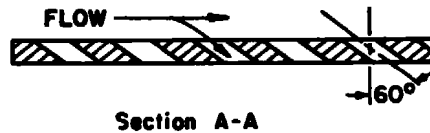
1. Caution should be exercised when analyzing NAB performance obtained with a strut-supported model. The corrections required for interference effects are not the same for all NAB installations.
2. The optimum strut sweep angle and strut location for a given NAB installation and the amount of interference produced are generally a function of free-stream Mach number and afterbody configuration.
3. The 45-deg swept strut gives the greatest decrease in base pressure interference coefficient for most Mach numbers above 0.99.
4. The disturbances generated by the model nose, the strut leading edge, or a combination of both, and their reflection from the tunnel wall to the surfaces of the NAB are important criteria in support strut design.
5. A swept strut is the best support strut to use when testing an NAB with various boattails to minimize the interference effects that occur with changes in NAB geometry.
6. The incremental changes in afterbody pressures are as large as or larger than the base pressures; thus, base pressure is not always the best indicator of the amount of afterbody interference produced by a given strut configuration.
7. The local wall porosity should be varied above Mach 0.99 to minimize the interference generated by a straight strut. However, for the swept strut a constant six-percent porosity gave minimum interference.
8. Interference was generally insignificant at Mach numbers below 0.99, although in certain cases interference was encountered around Mach 0.6.
9. Interference on NAB performance is more sensitive to strut location with a straight strut support than a swept strut.
10. A sting flare must be located a minimum 3.0 body diameters downstream of the nozzle base with a 10-deg boattail and 5.0 body diameters downstream with a cylindrical boattail to minimize base pressure interference.
11. The support strut interference on the boattail in the presence of a simulated plume is a function of Mach number.

REFERENCES

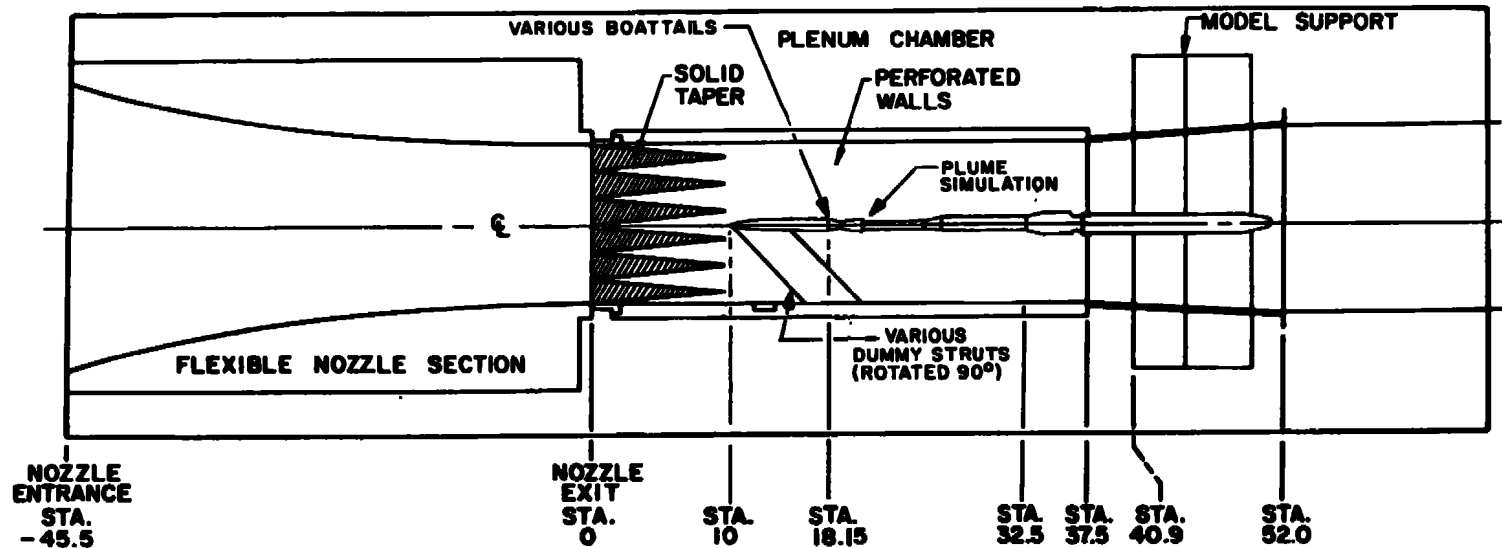
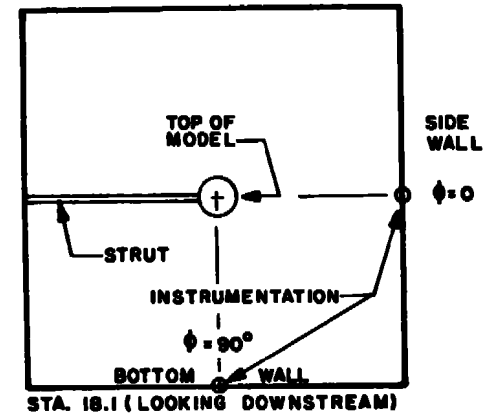
1. Reichenau, D. E. A. "Sting and Strut Support Interference Effects on a Cylindrical Model with an Ogive Nose at Mach Numbers from 0.7 to 1.4." AEDC-TR-72-175 (AD905771L), November 1972.
2. Jackson, F. M. and Sloan, E. H. "Calibration of the AEDC-PWT 1-Foot Transonic Tunnel." AEDC-TR-68-4 (AD827912), February 1968.



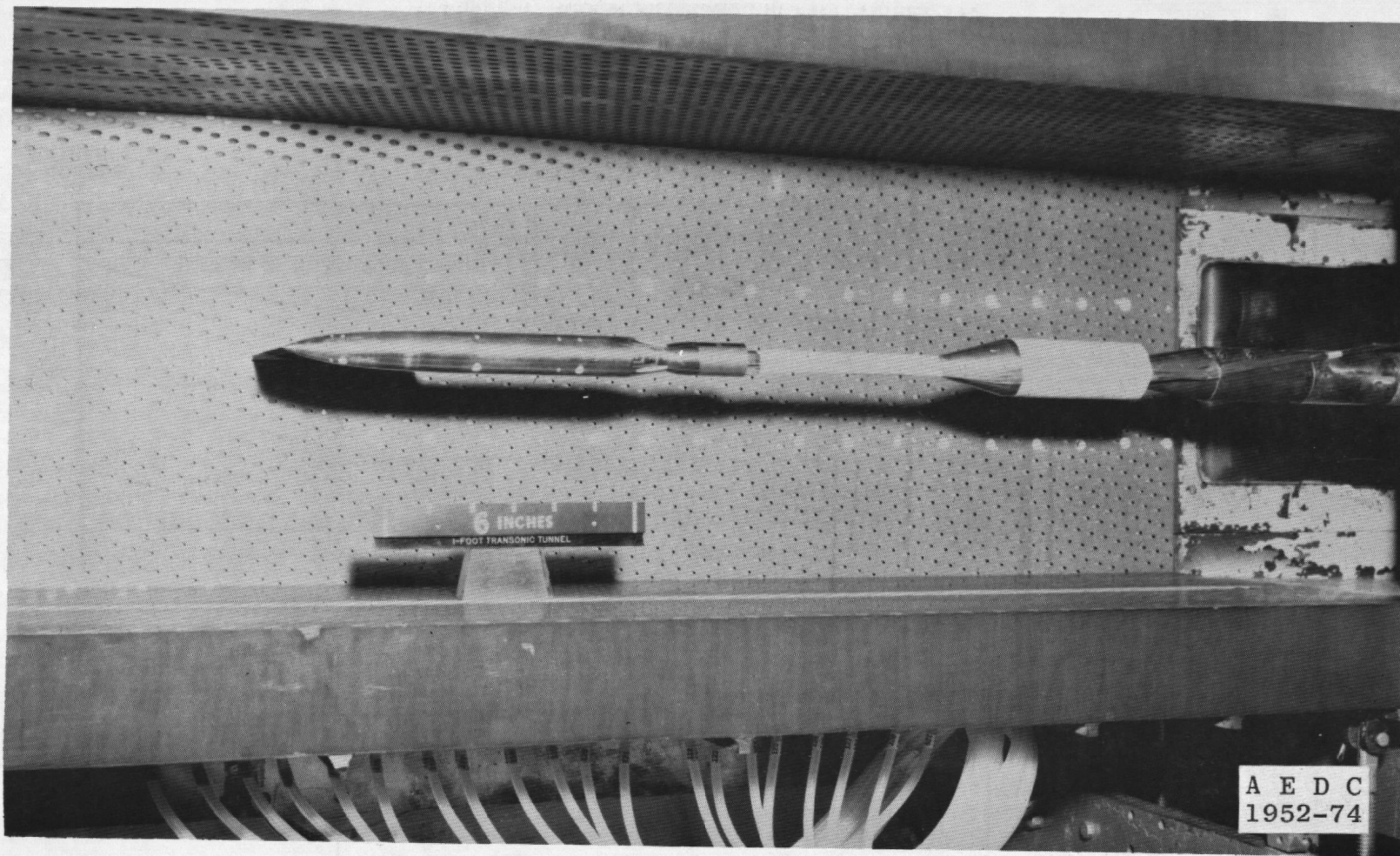
TYPICAL PERFORATED
WALL PATTERN
(ALL 4 WALLS)



6% Open Area
Hole Diameter = 0.125 in.
Plate Thickness = 0.125 in.



a. Schematic of model installation
Figure 1. Model installation in PWT Tunnel 1T.



b. Photograph of model installation
Figure 1. Concluded.

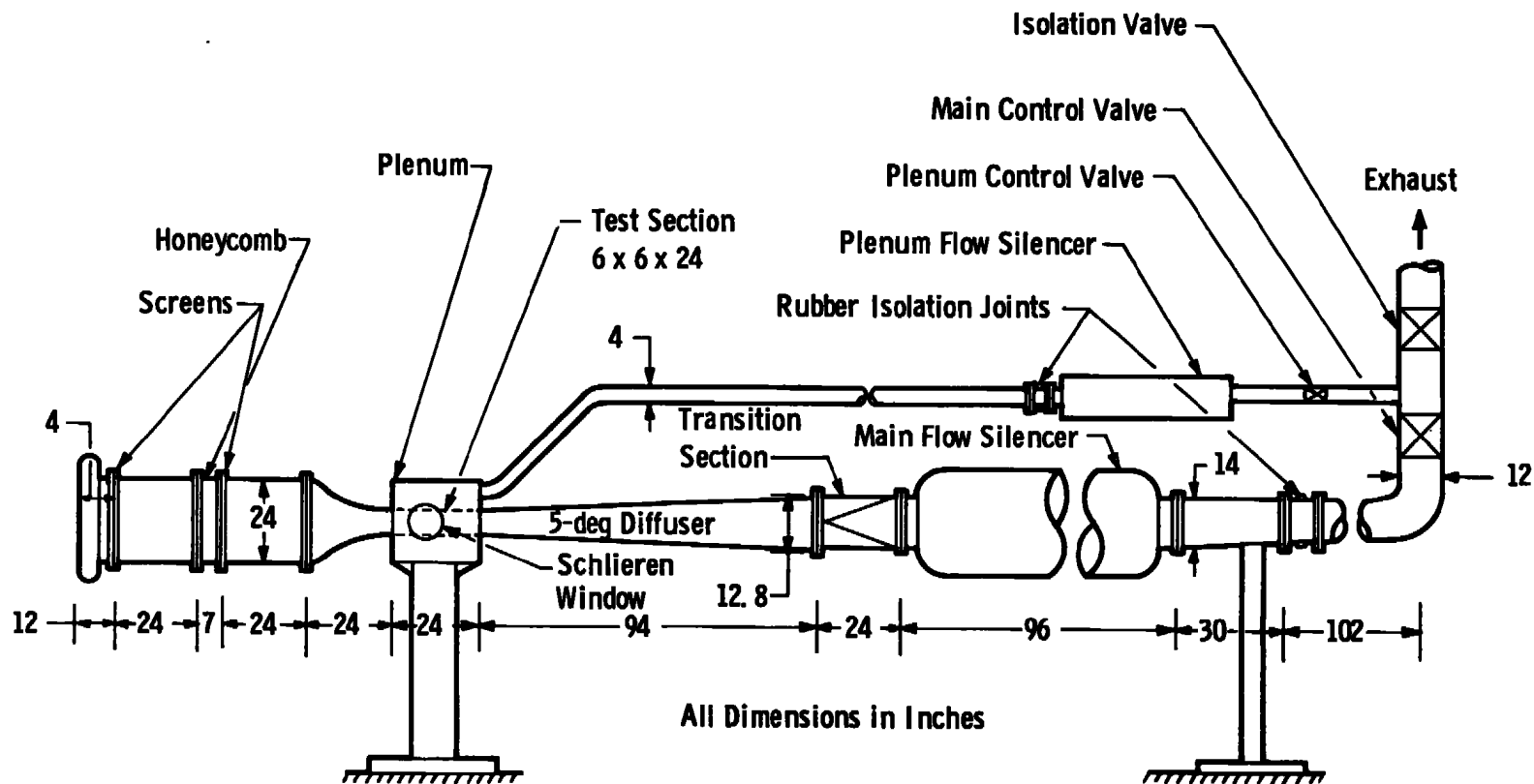
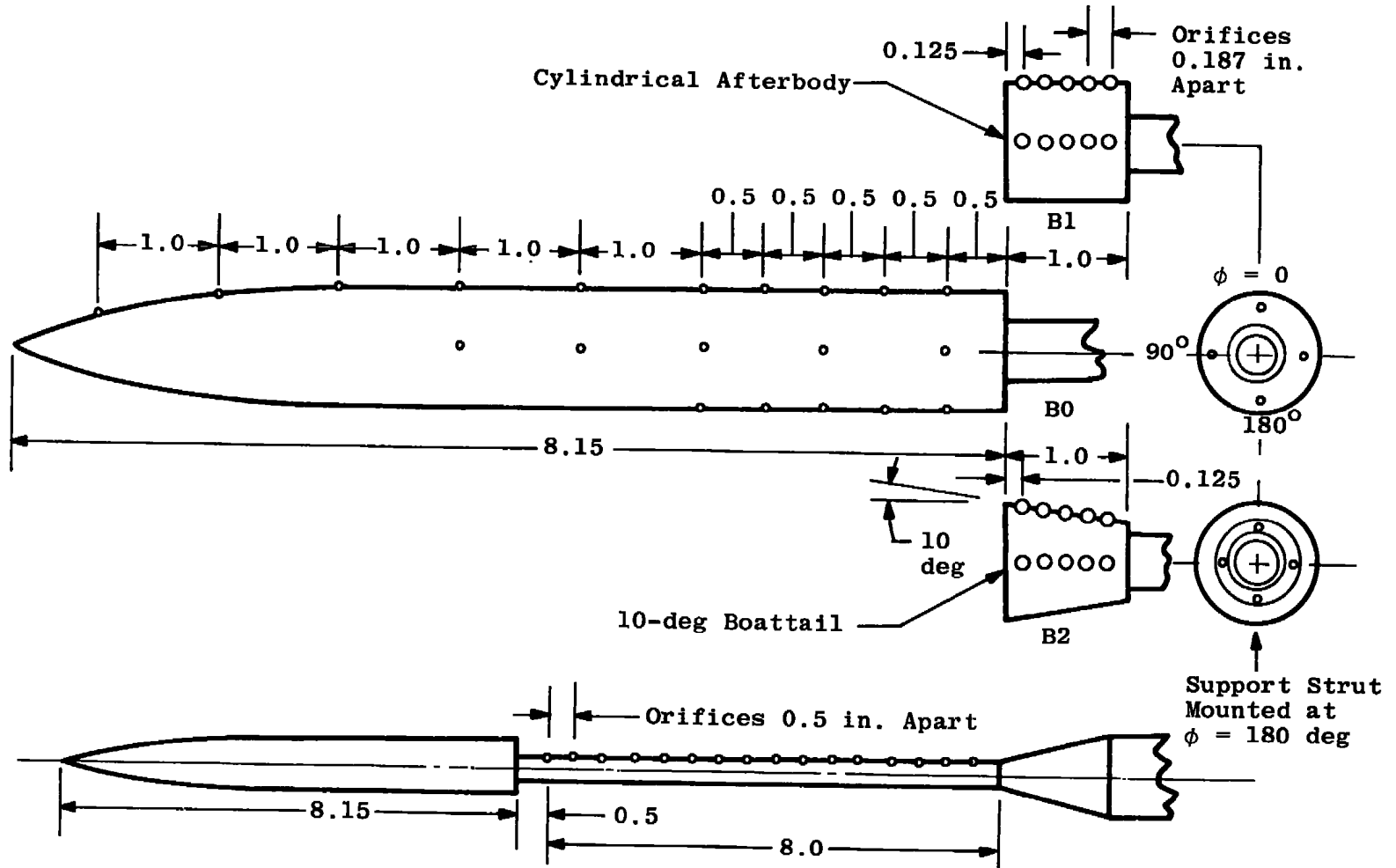


Figure 2. Model installation in PWT Acoustic Research Tunnel.



All Dimensions in Inches

Figure 3. Sting-mounted baseline model showing pressure orifice location.

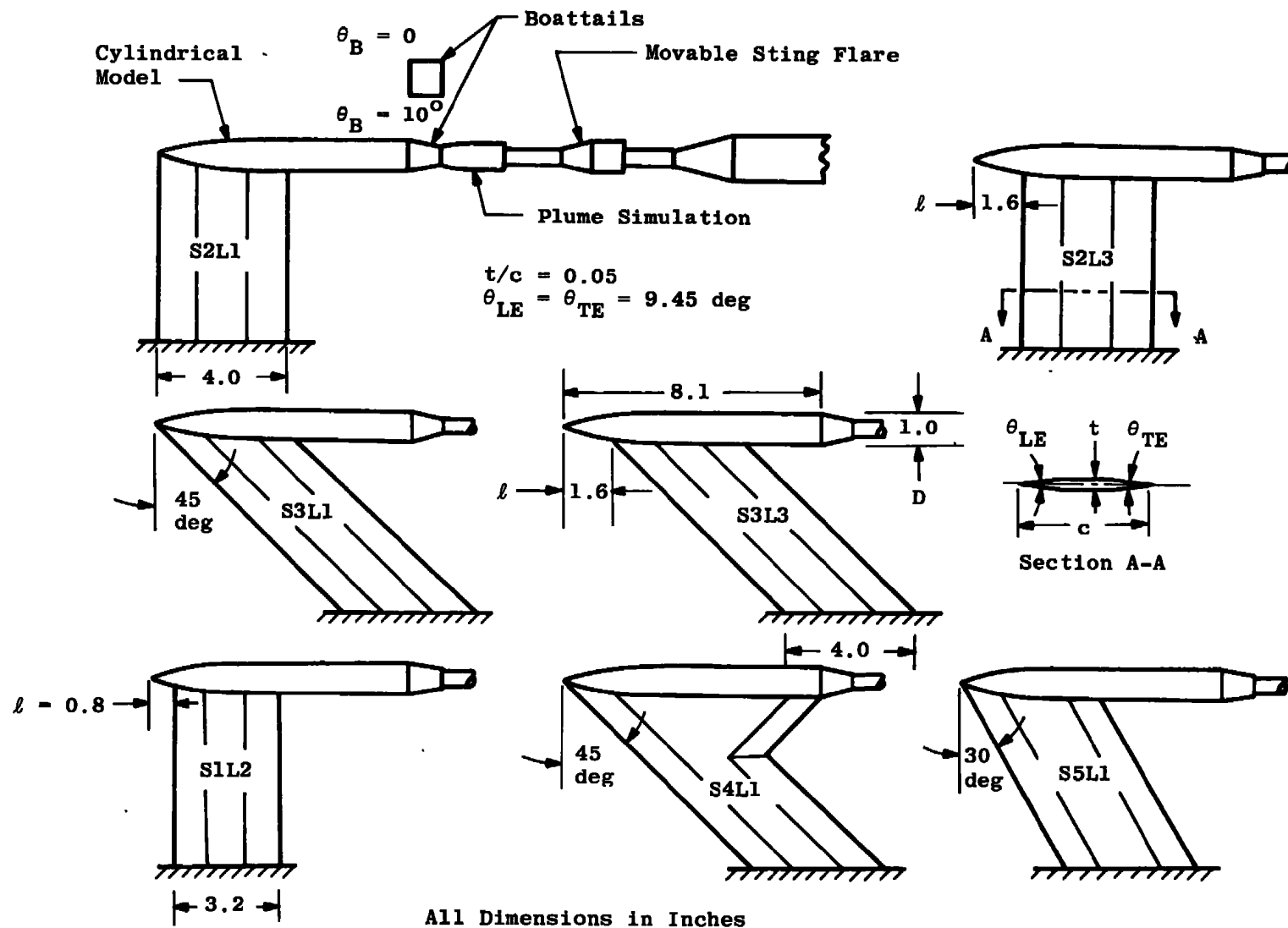
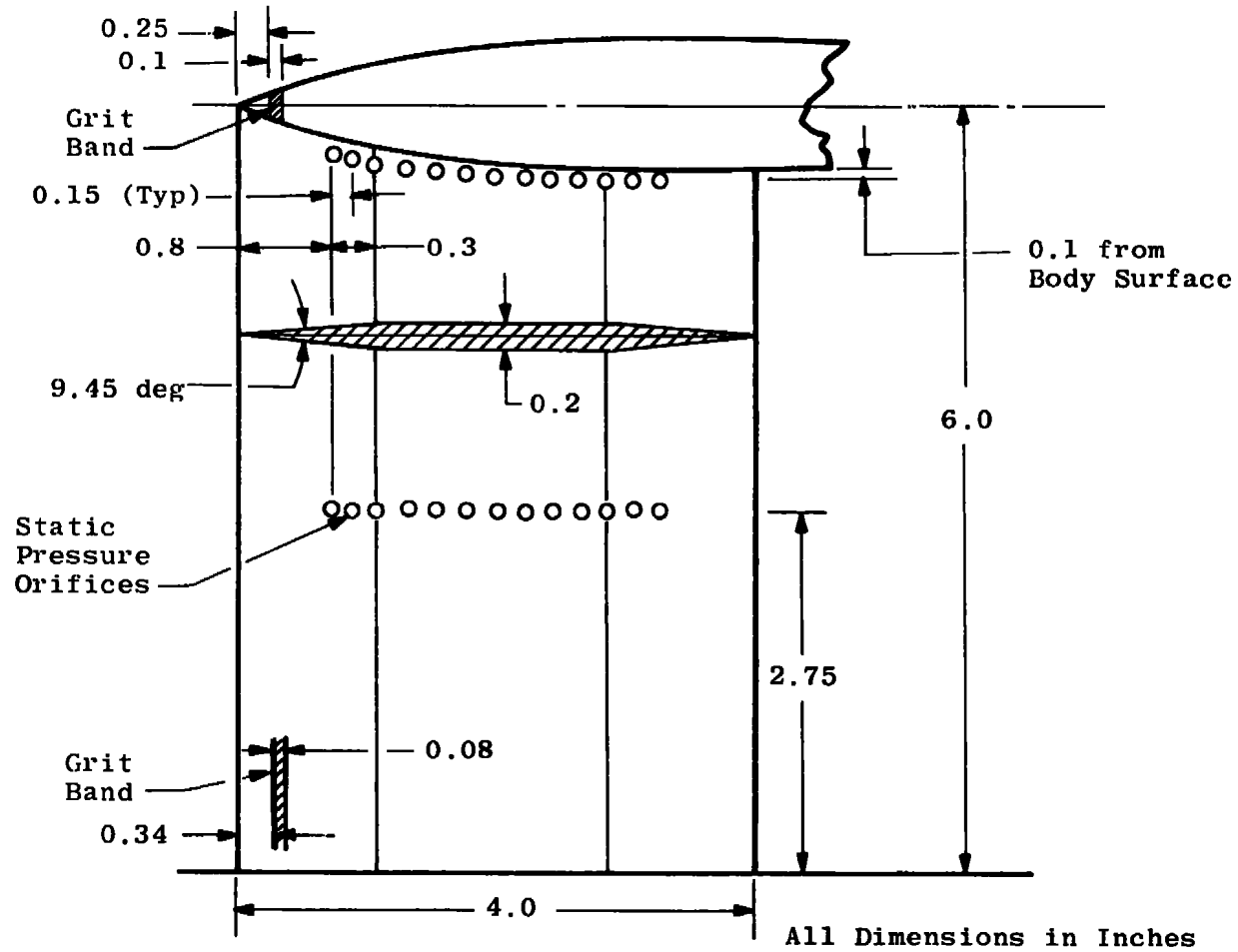
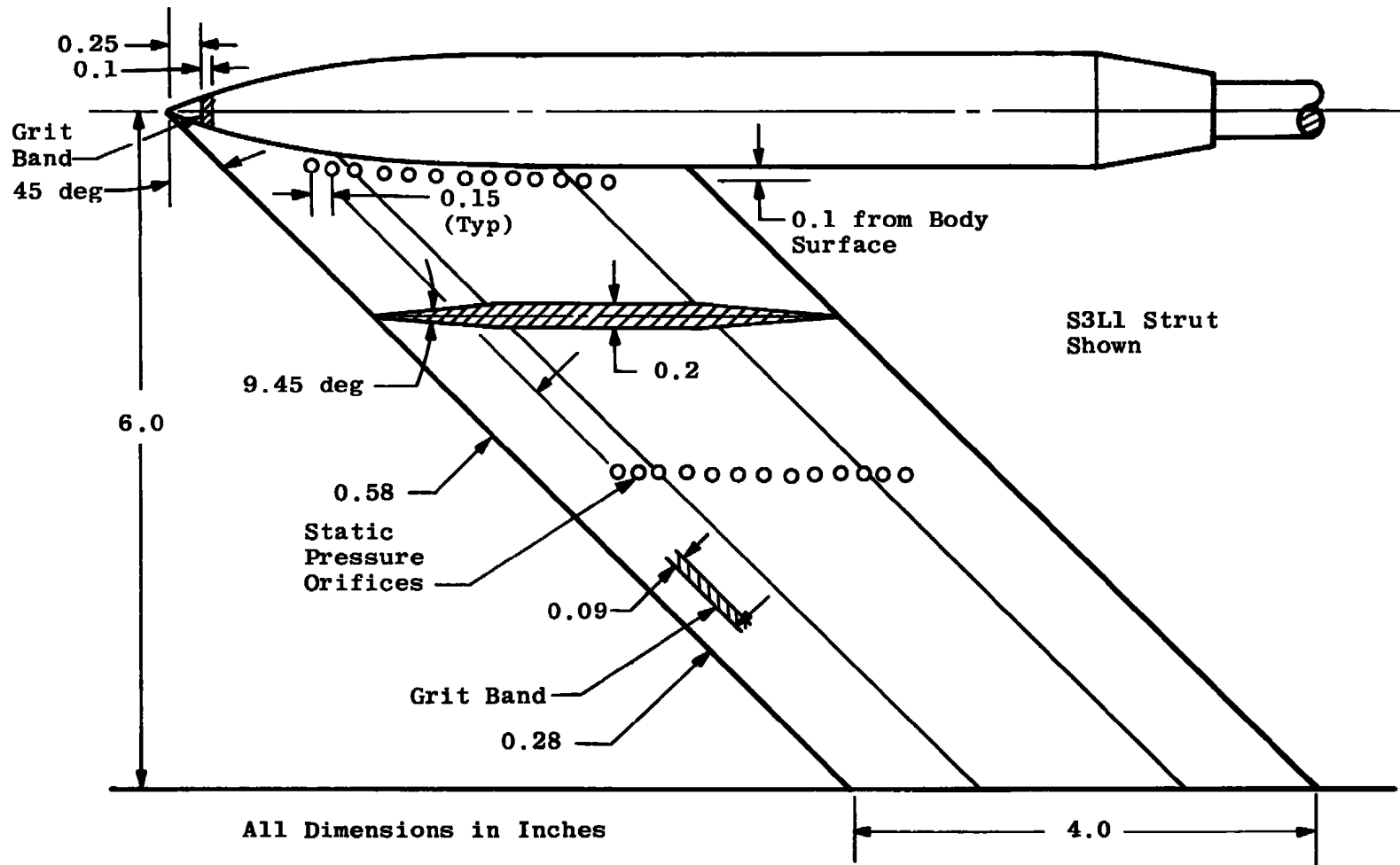


Figure 4. Test configurations for support interference on NAB test.

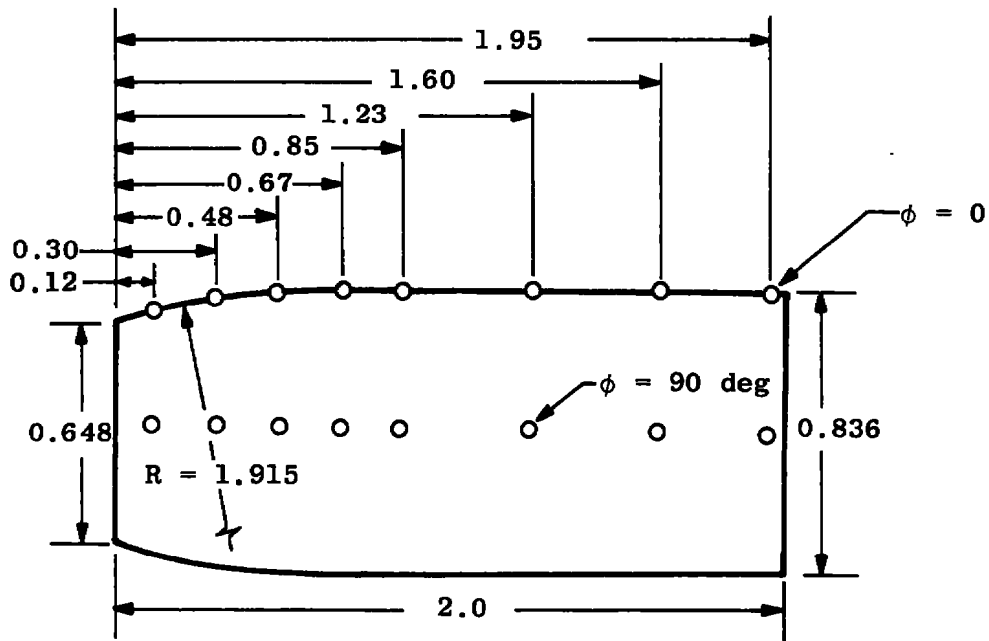


a. Straight strut (S2L1)

Figure 5. Model instrumentation location.

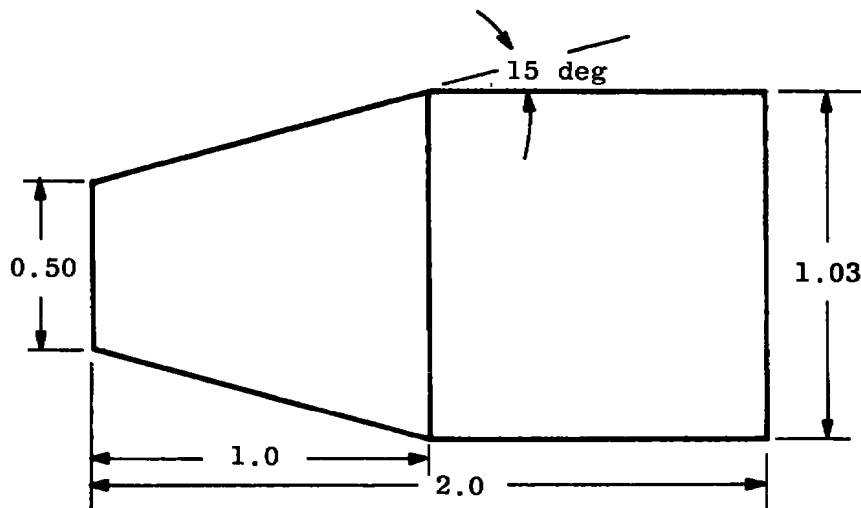


b. Swept struts (S3L1 and S3L3)
Figure 5. Continued.



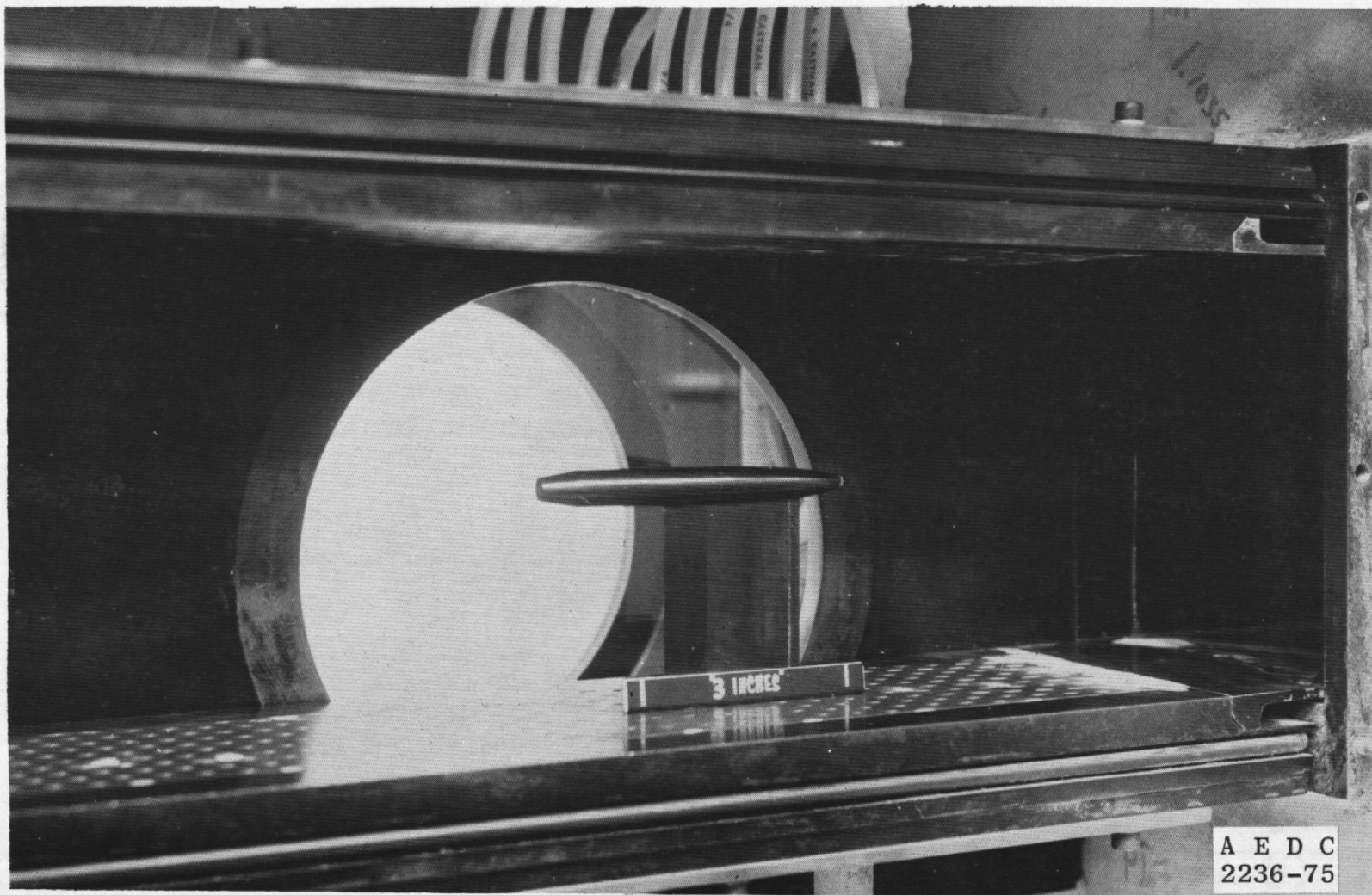
Simulated Plume (P)

All Dimensions in Inches



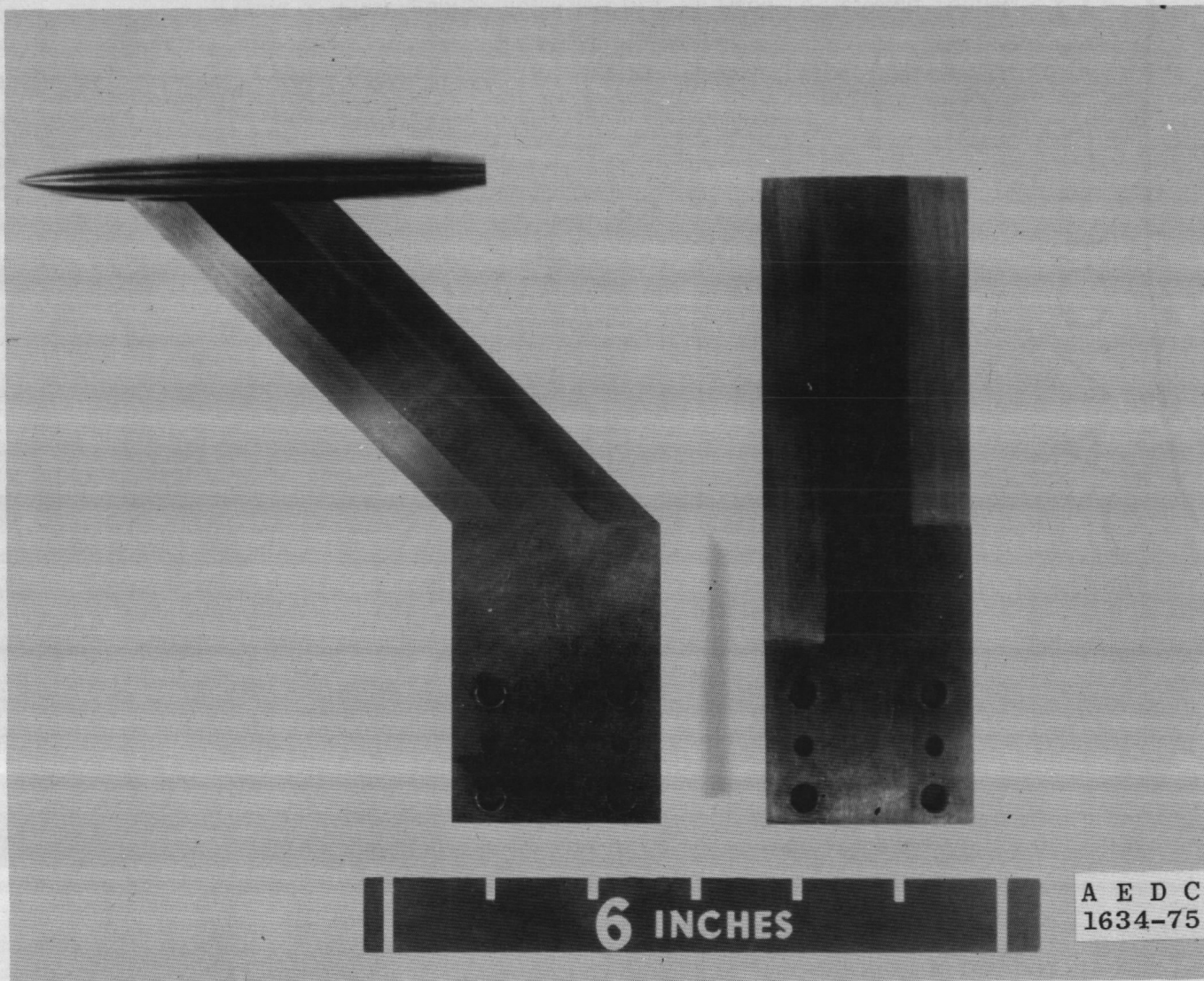
Movable Sting Flare (F)

c. Simulated plume and flare configurations
Figure 5. Concluded.

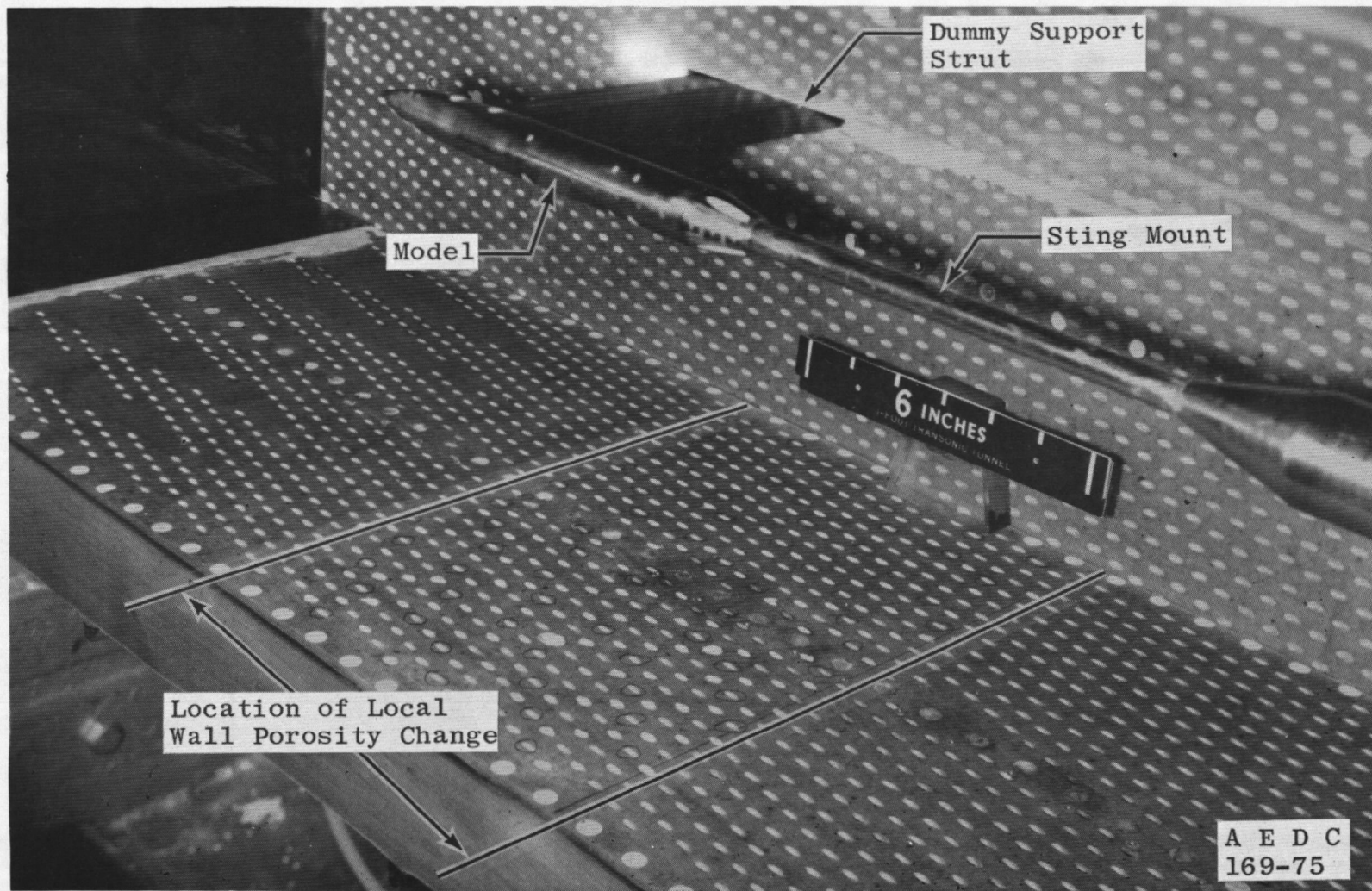


a. Model installation

Figure 6. Photographs—Model test in PWT Acoustic Research Tunnel.

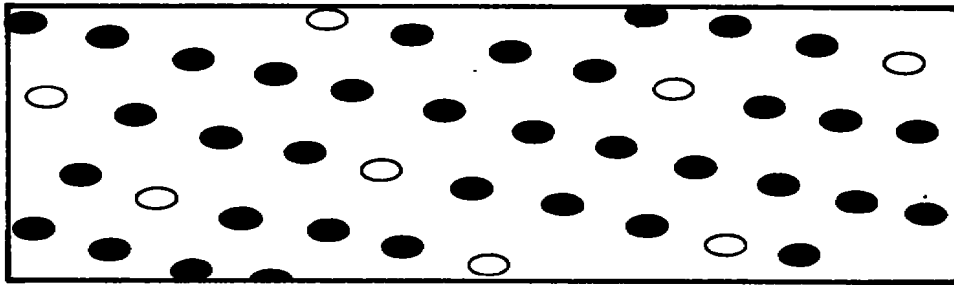


b. ART test models
Figure 6. Concluded.

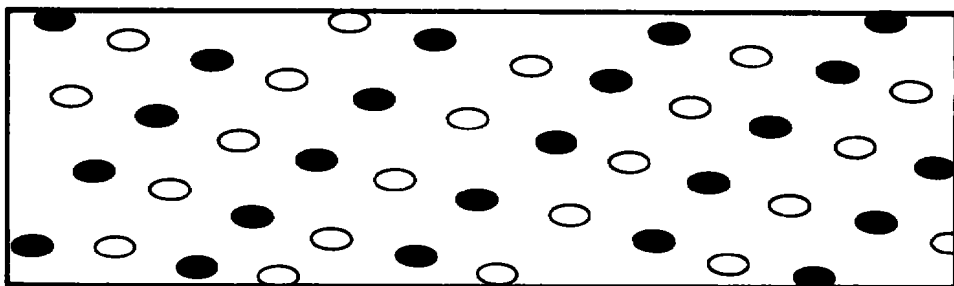


a. Tunnel 1T installation
Figure 7. Location of local wall porosity variation.

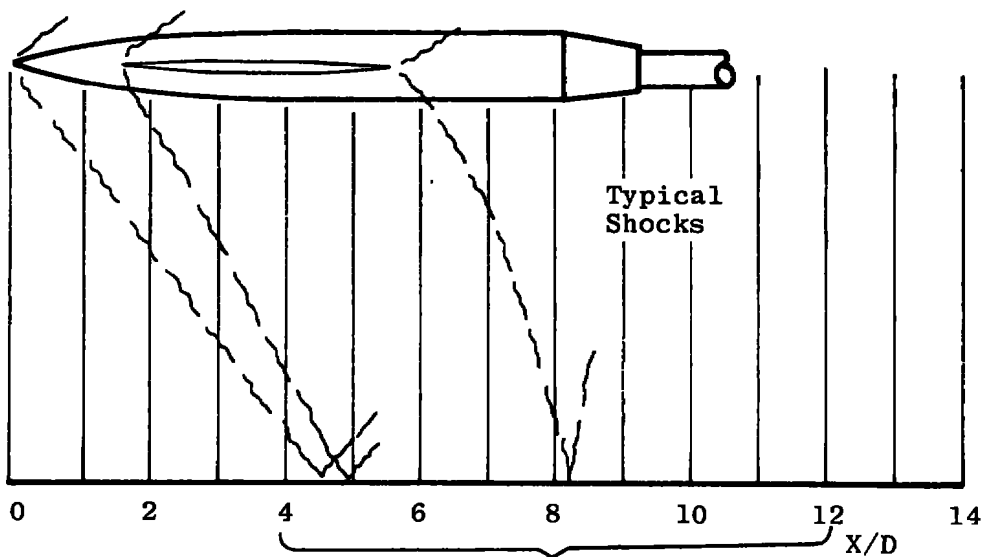
● Closed Hole
○ Open Hole



Wall Configuration W1 (1-percent Porosity)



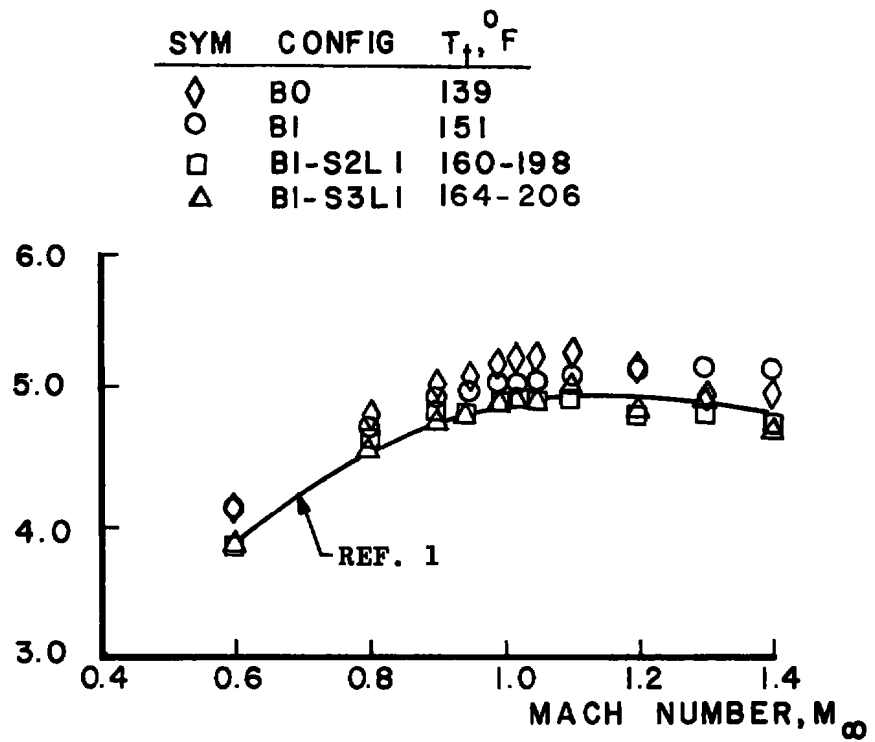
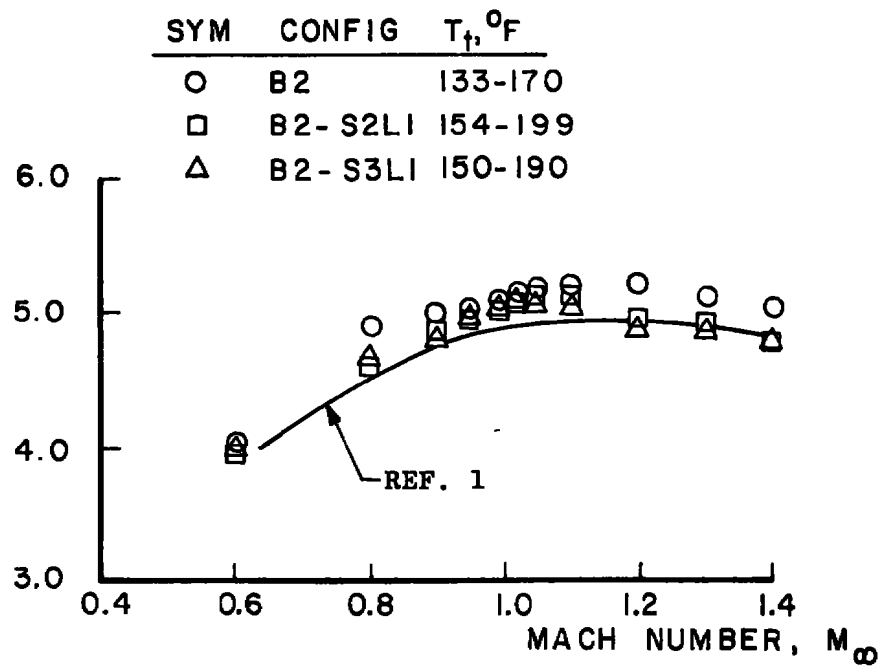
Wall Configuration W3 (3-percent Porosity)



Region of Local Porosity Change
(Top and Bottom Walls)

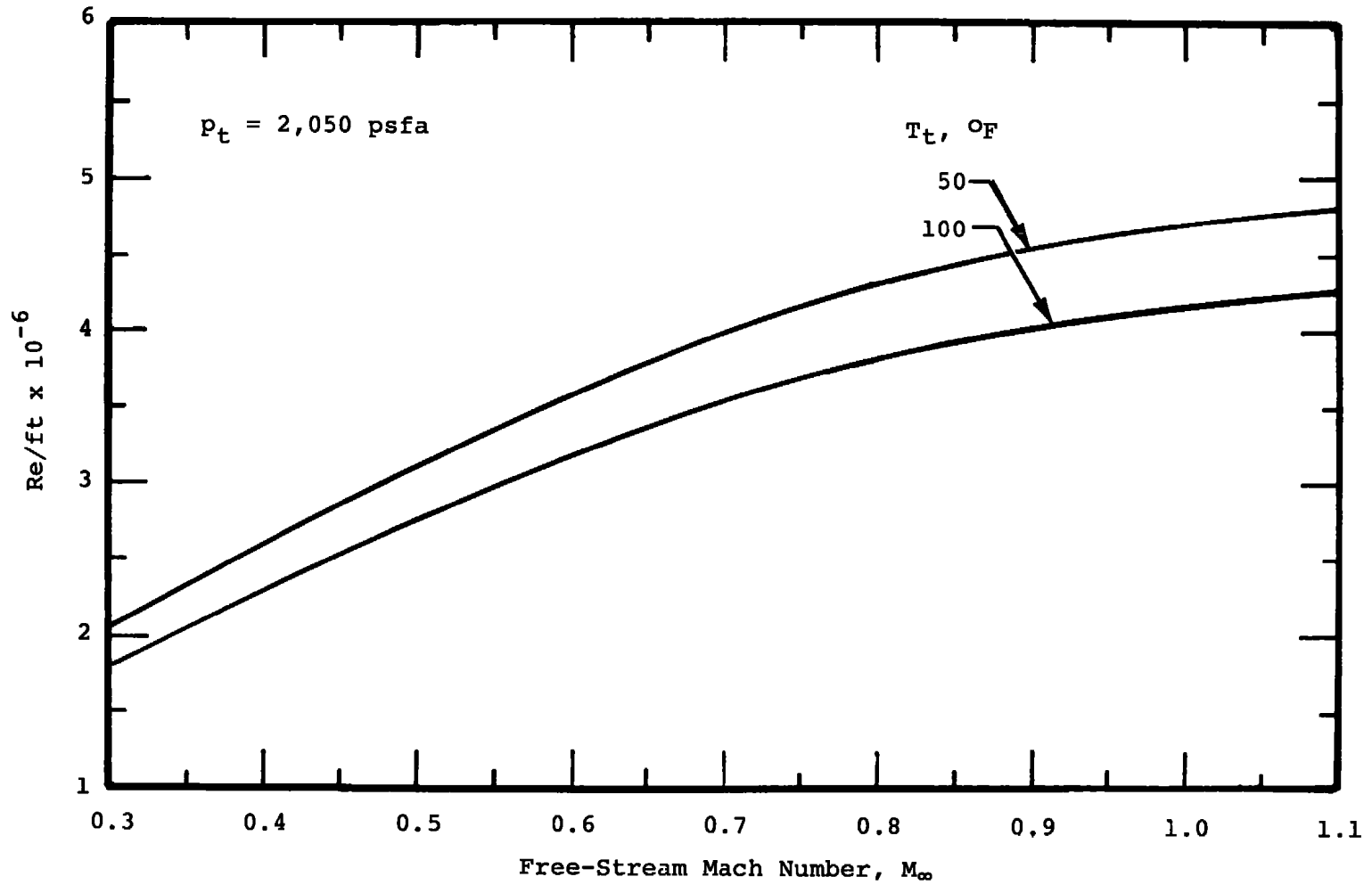
b. Sketch—porosity variation (Tunnel 1T)

Figure 7. Concluded.

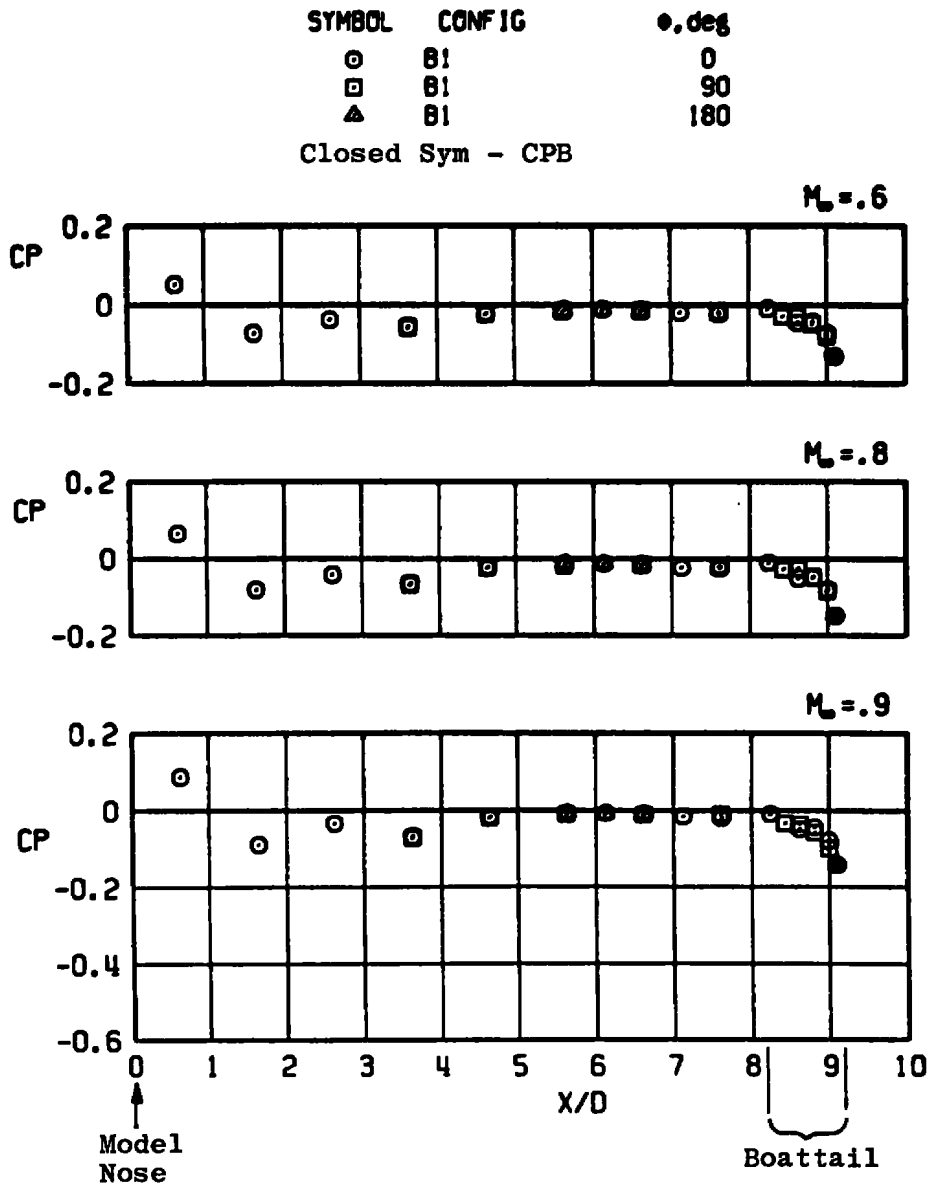
REYNOLDS NUMBER, $Re/ft \times 10^{-6}$ REYNOLDS NUMBER, $Re/ft \times 10^{-6}$ 

a. Tunnel 1T

Figure 8. Reynolds number variation with Mach number.



b. Acoustic research tunnel
Figure 8. Concluded.

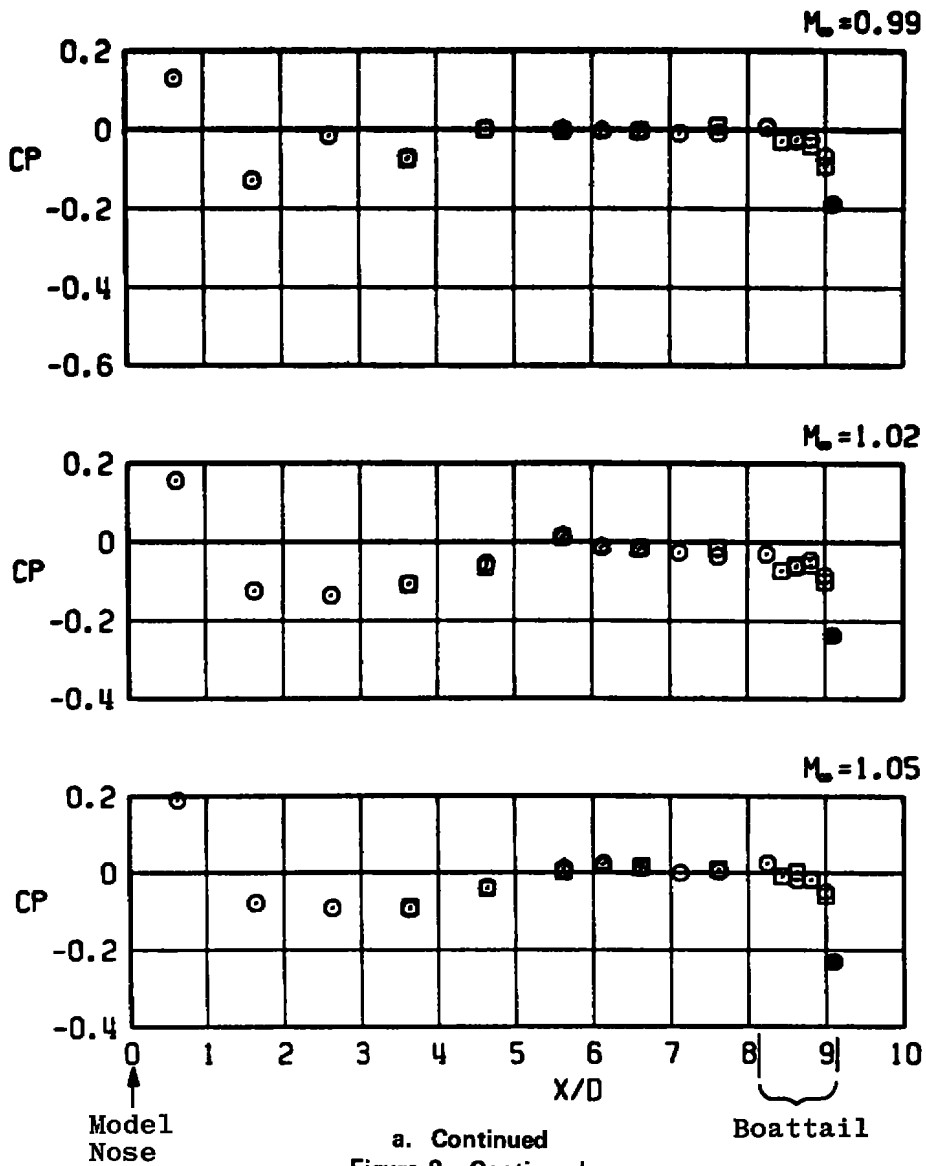


a. Model surface pressure coefficient distribution

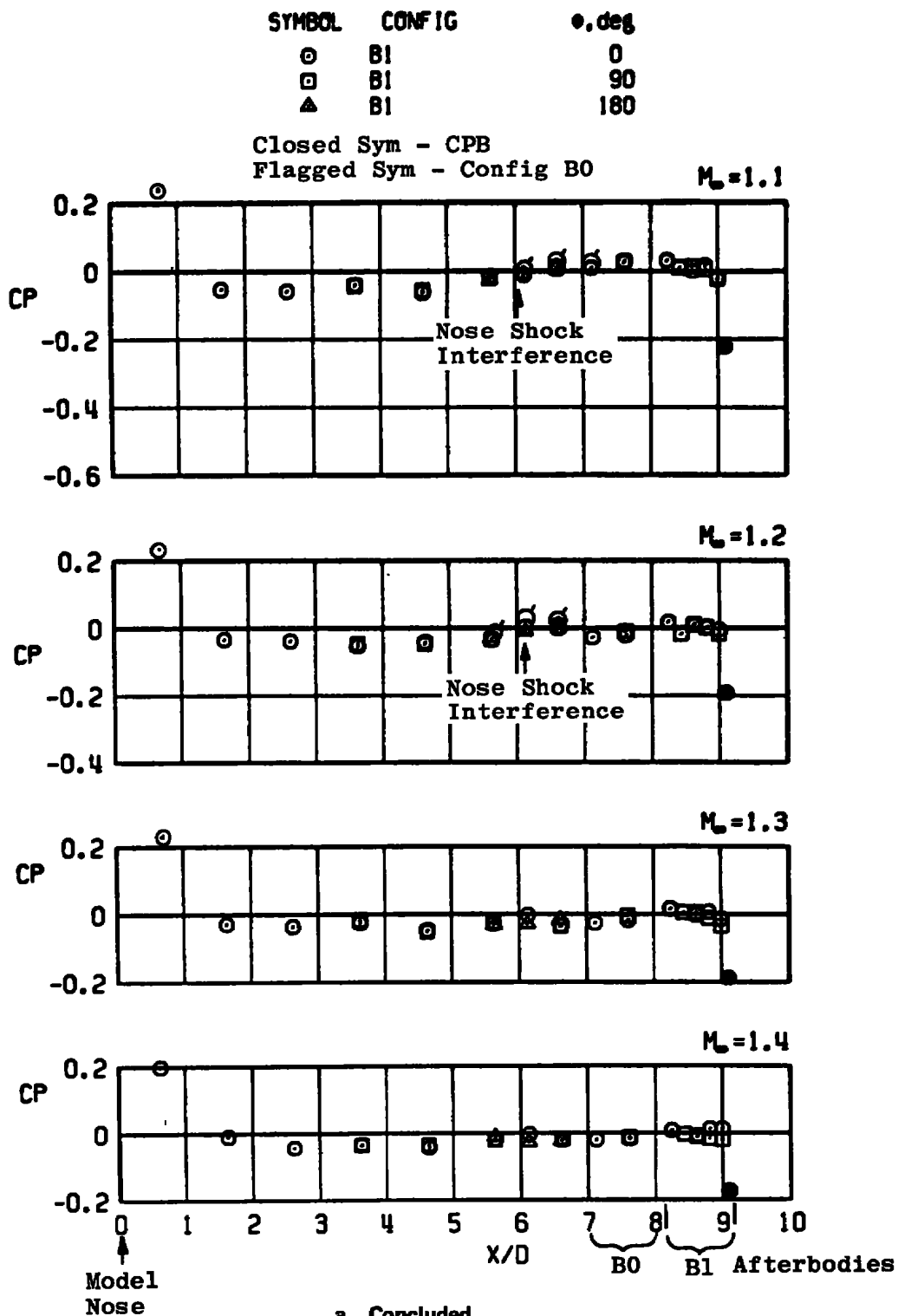
Figure 9. Baseline pressure coefficient data (cylindrical afterbody, B1).

SYMBOL	CONFIG	α , deg
○	B1	0
□	B1	90
△	B1	180

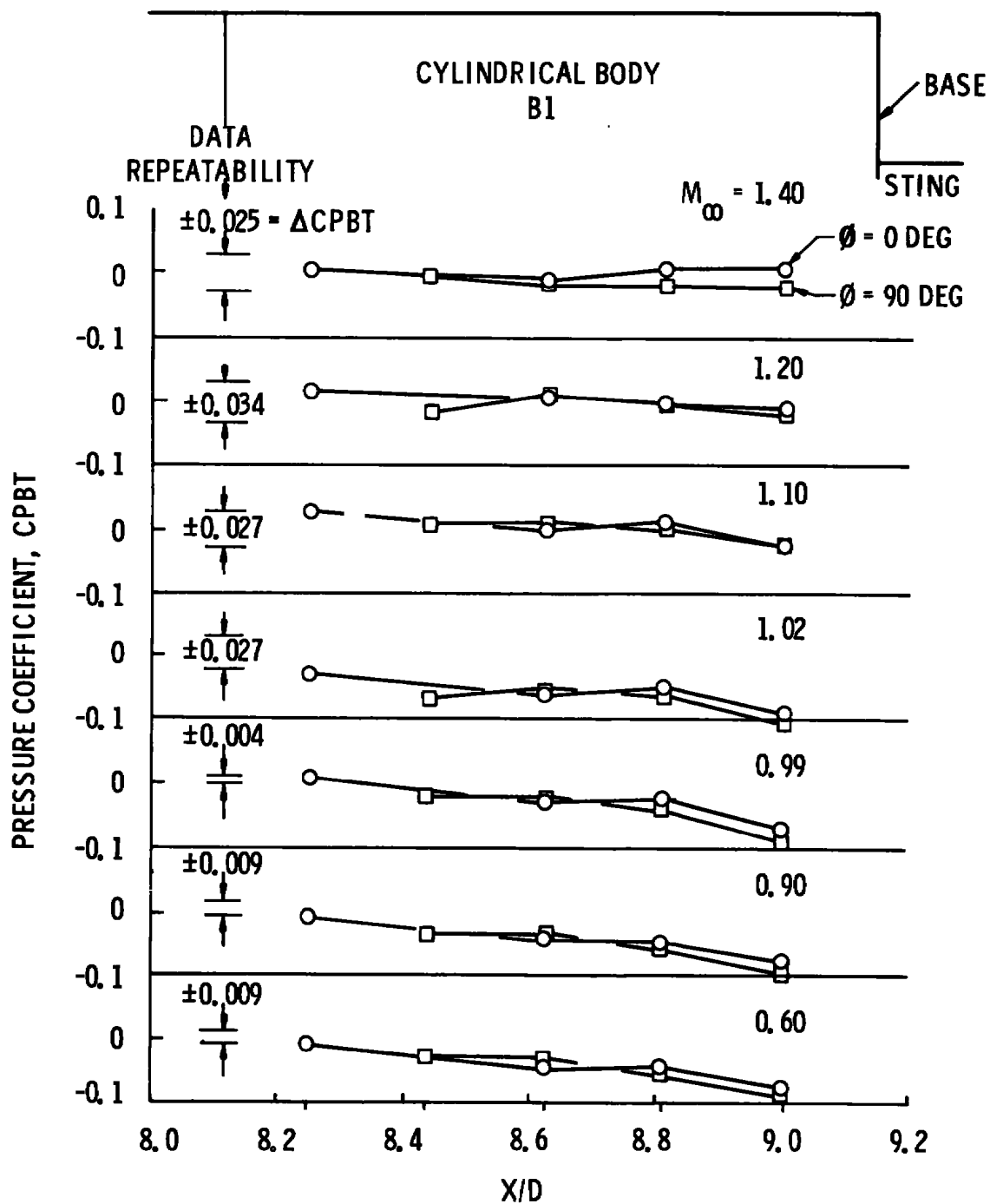
Closed Sym - CPB



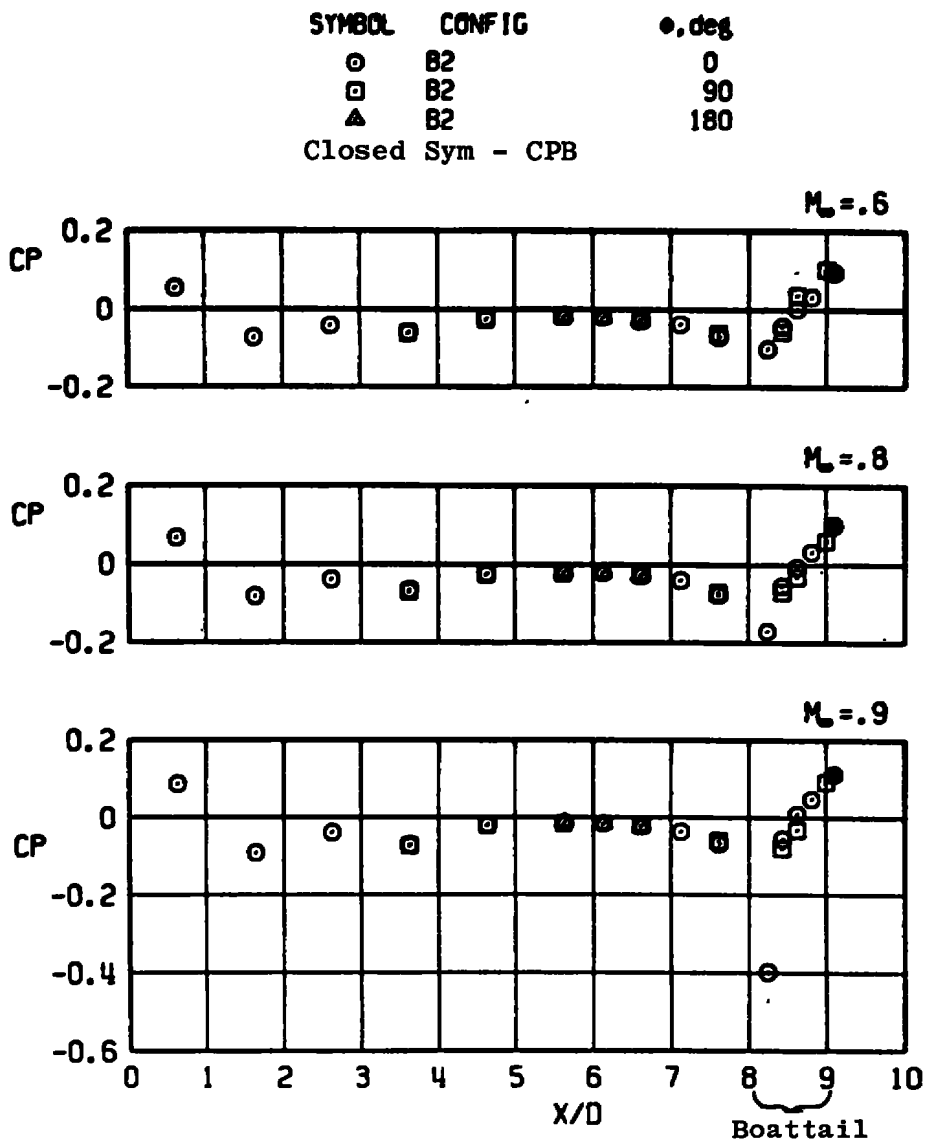
a. Continued
Figure 9. Continued.



a. Concluded
Figure 9. Continued.



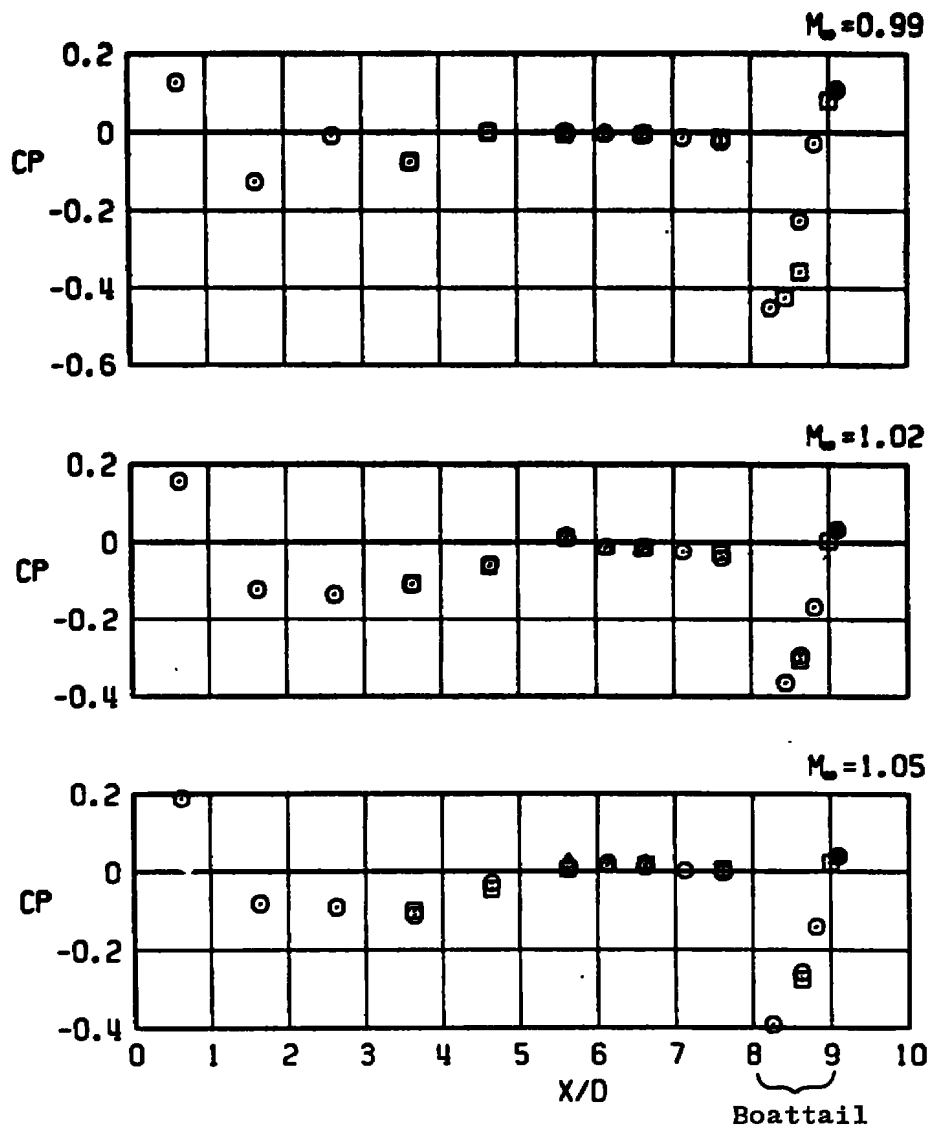
b. Boattail pressure coefficient distribution
Figure 9. Concluded.



a. Model surface pressure coefficient distribution
 Figure 10. Baseline pressure coefficient data (10-deg boattail, B2).

SYMBOL	CONFIG	α , deg
○	B2	0
□	B2	90
△	B2	180

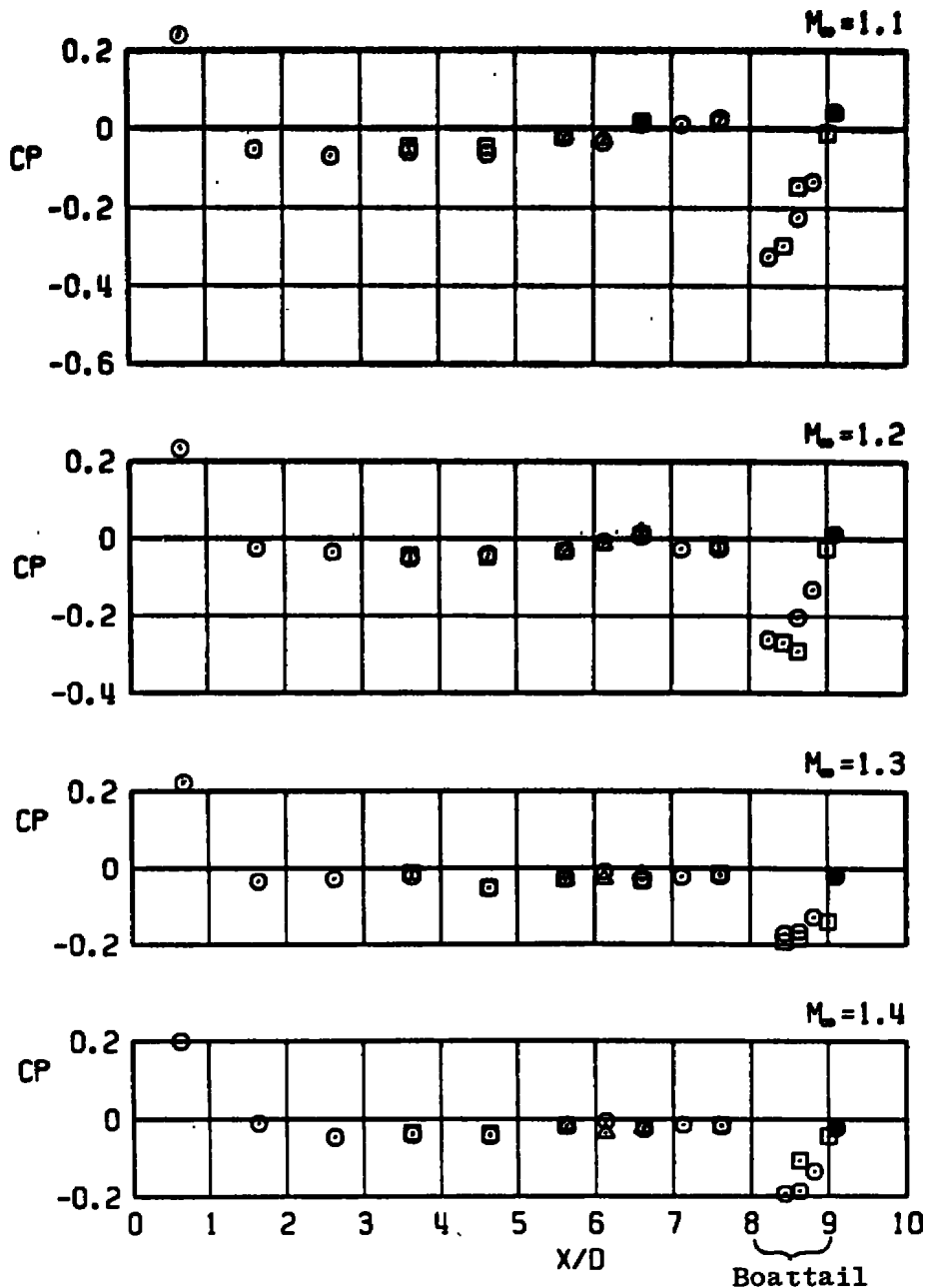
Closed Sym - CPB



a. Continued
Figure 10. Continued.

SYMBOL	CONFIG	α , deg
○	B2	0
□	B2	90
△	B2	180

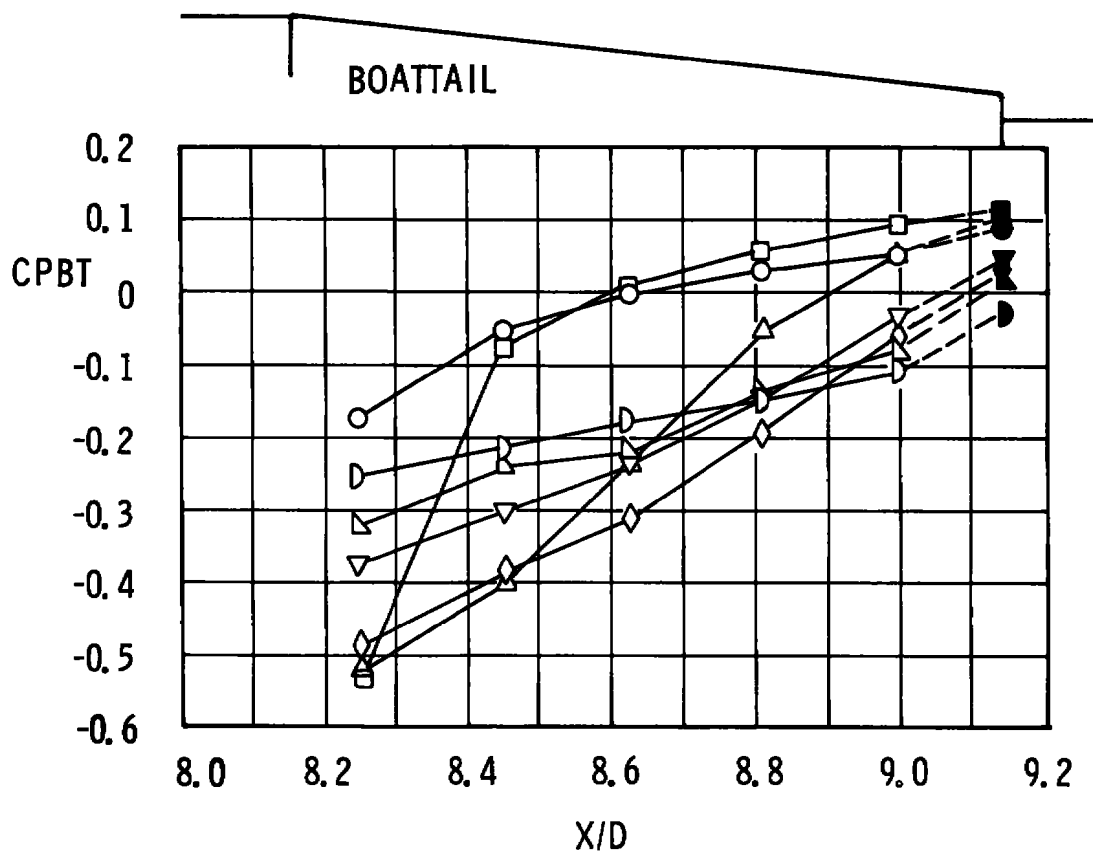
Closed Sym - CPB



a. Concluded
Figure 10. Continued.

<u>SYM</u>	<u>M_∞</u>
○	0.6
□	0.9
△	0.99
◇	1.02
▽	1.1
▲	1.2
D	1.4

SOLID SYM ~ CPB



b. Boattail pressure coefficient distribution
Figure 10. Concluded.

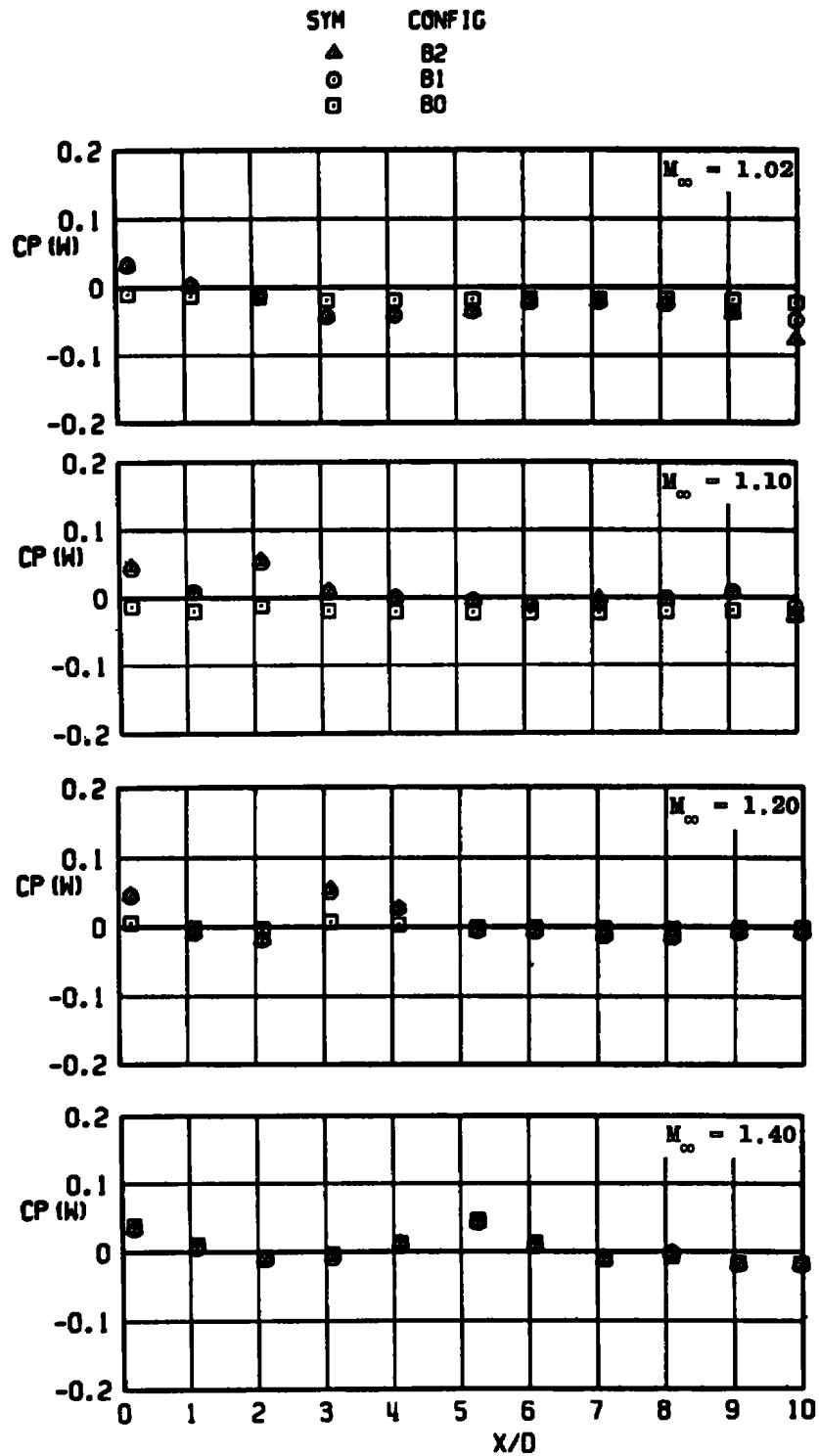


Figure 11. Wall pressure coefficient distribution for baseline configurations, B0, B1, and B2.

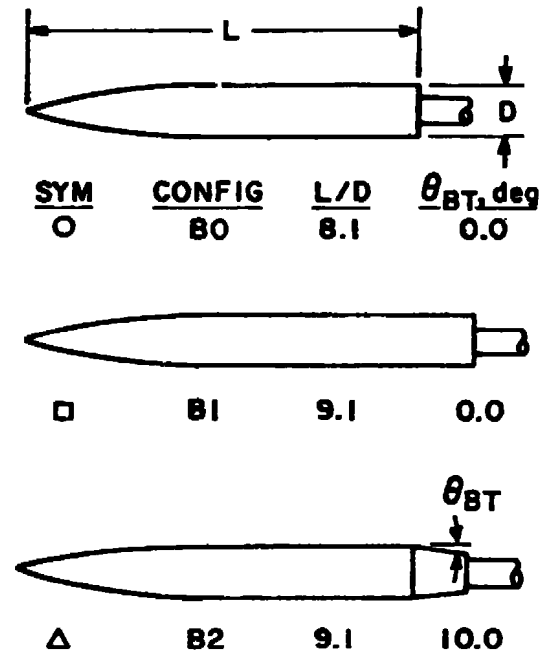
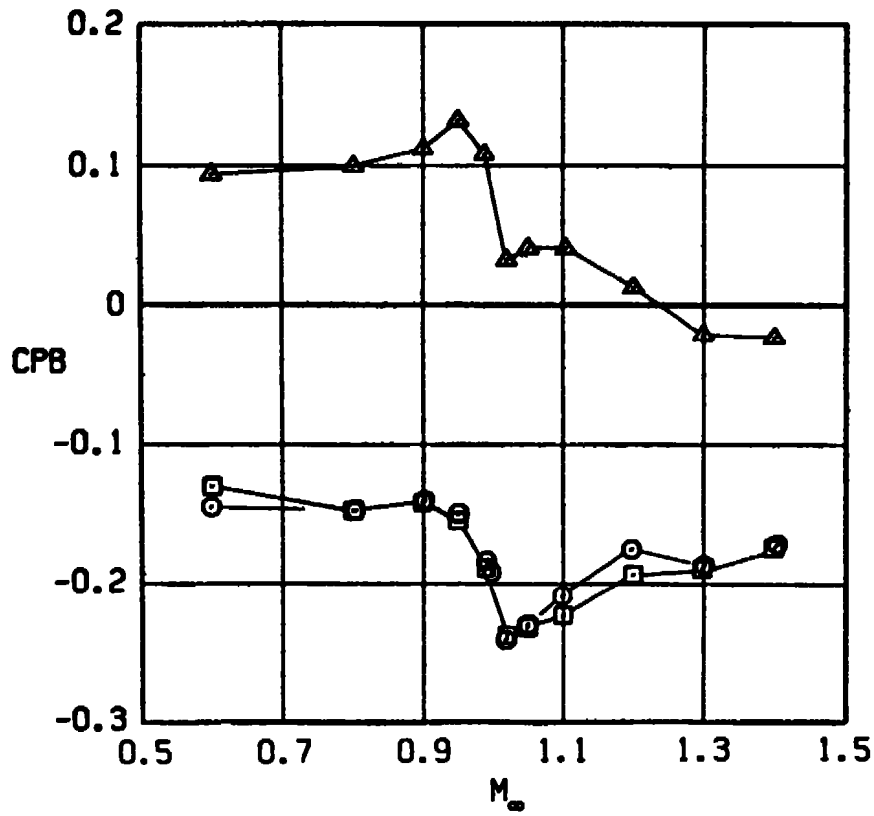


Figure 12. Effect of boattail angle and body length on base pressure coefficient.

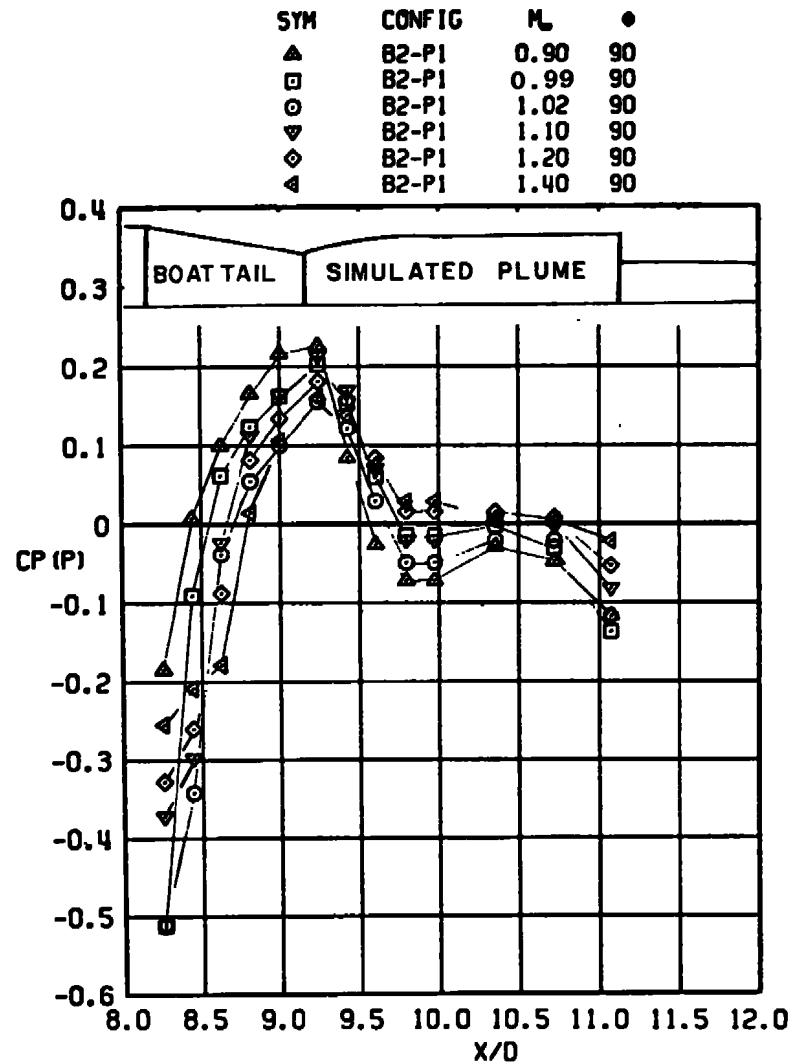
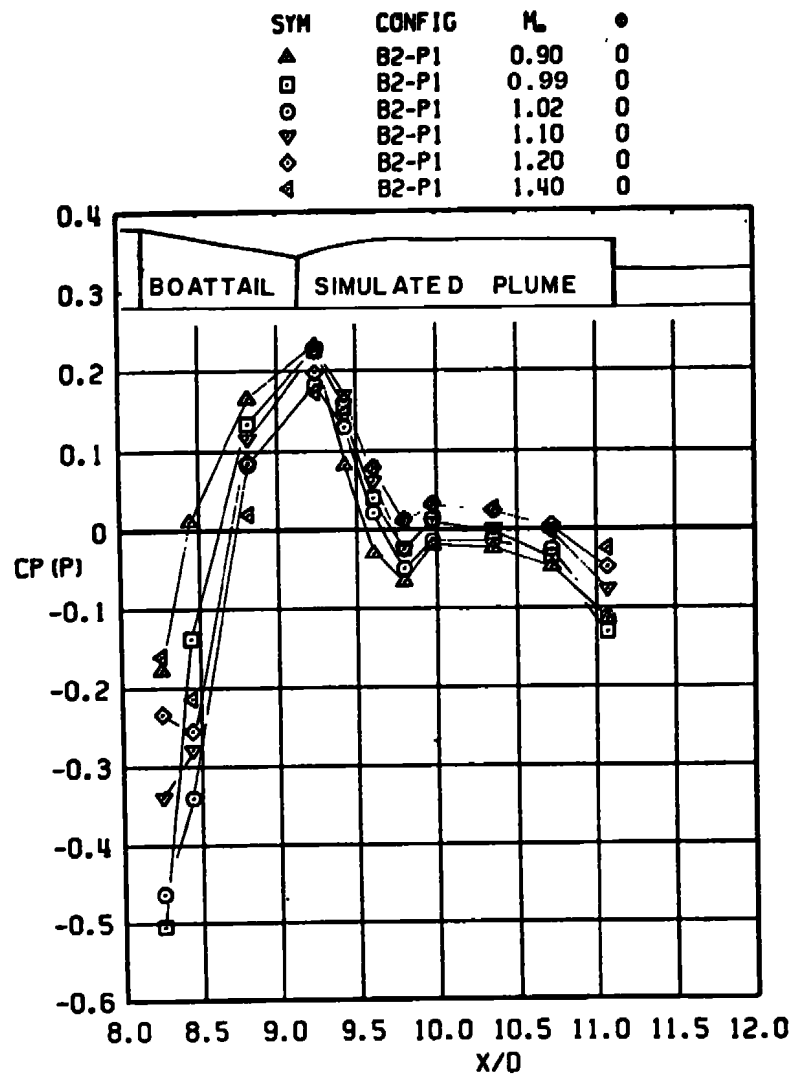
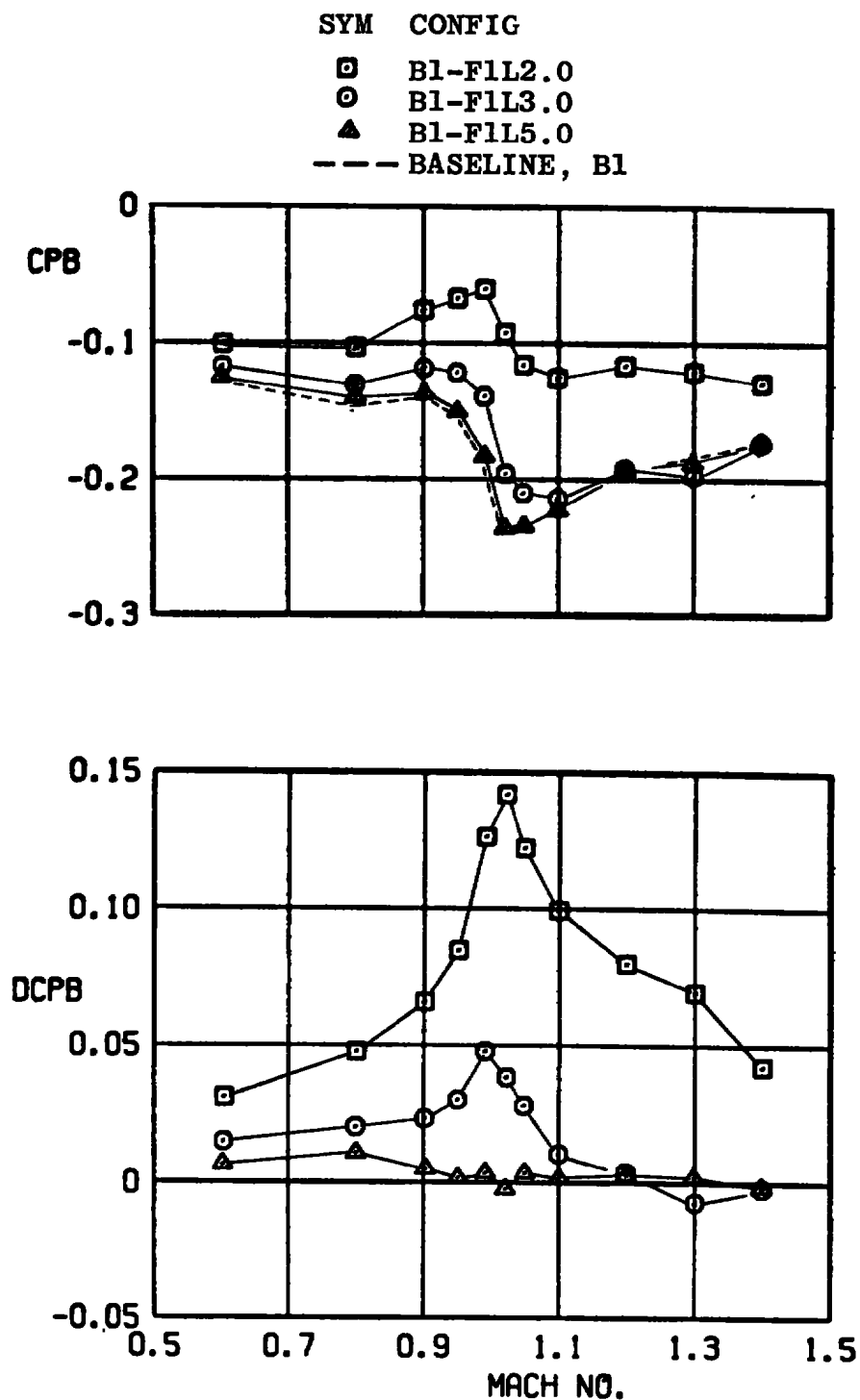
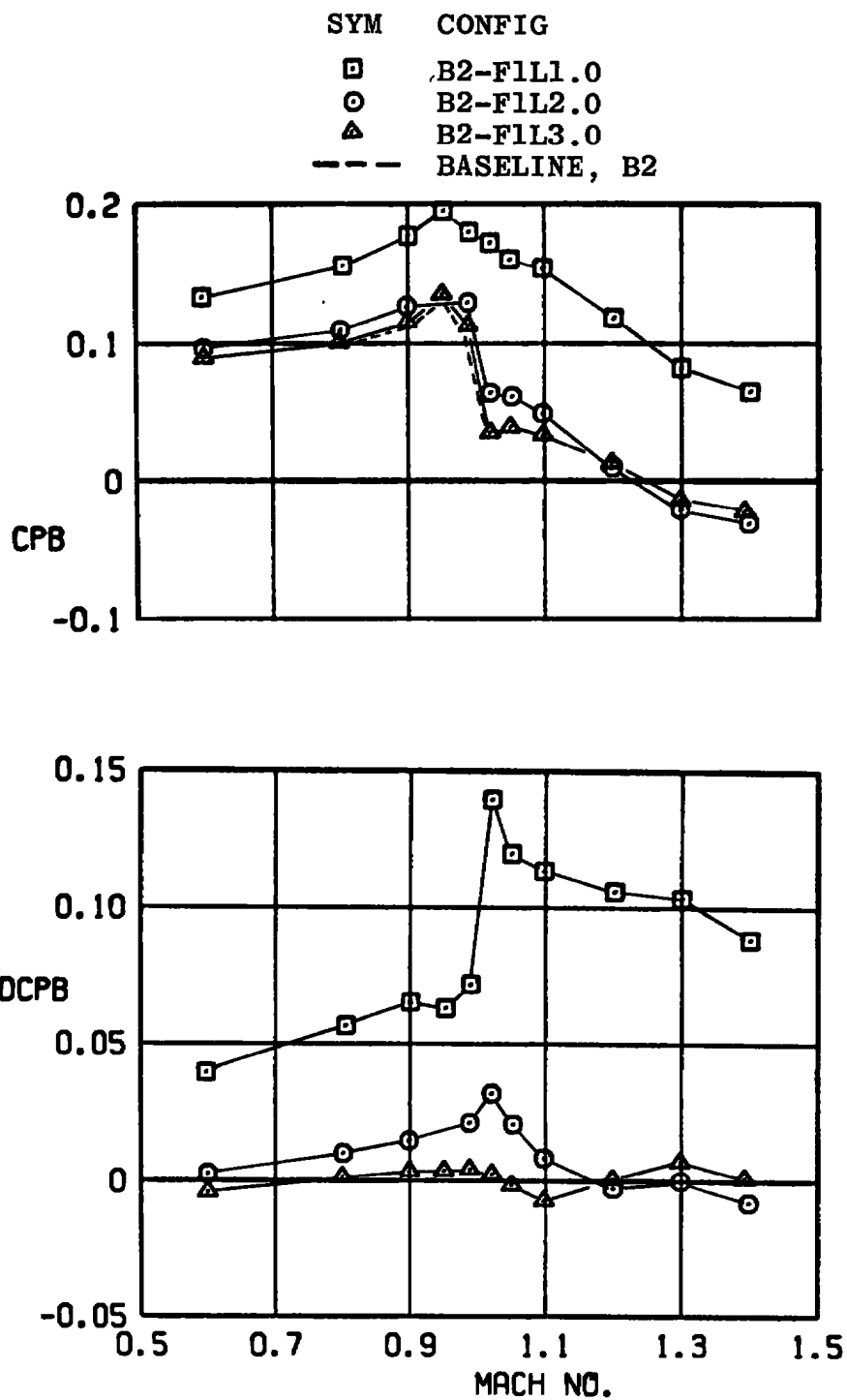


Figure 13. Baseline pressure coefficient data for 10-deg boattail with simulated plume.



a. With cylindrical afterbody, B1

Figure 14. Effect of sting flare location on base pressure coefficient.



b. With 10-deg boattail, B2
Figure 14. Concluded.

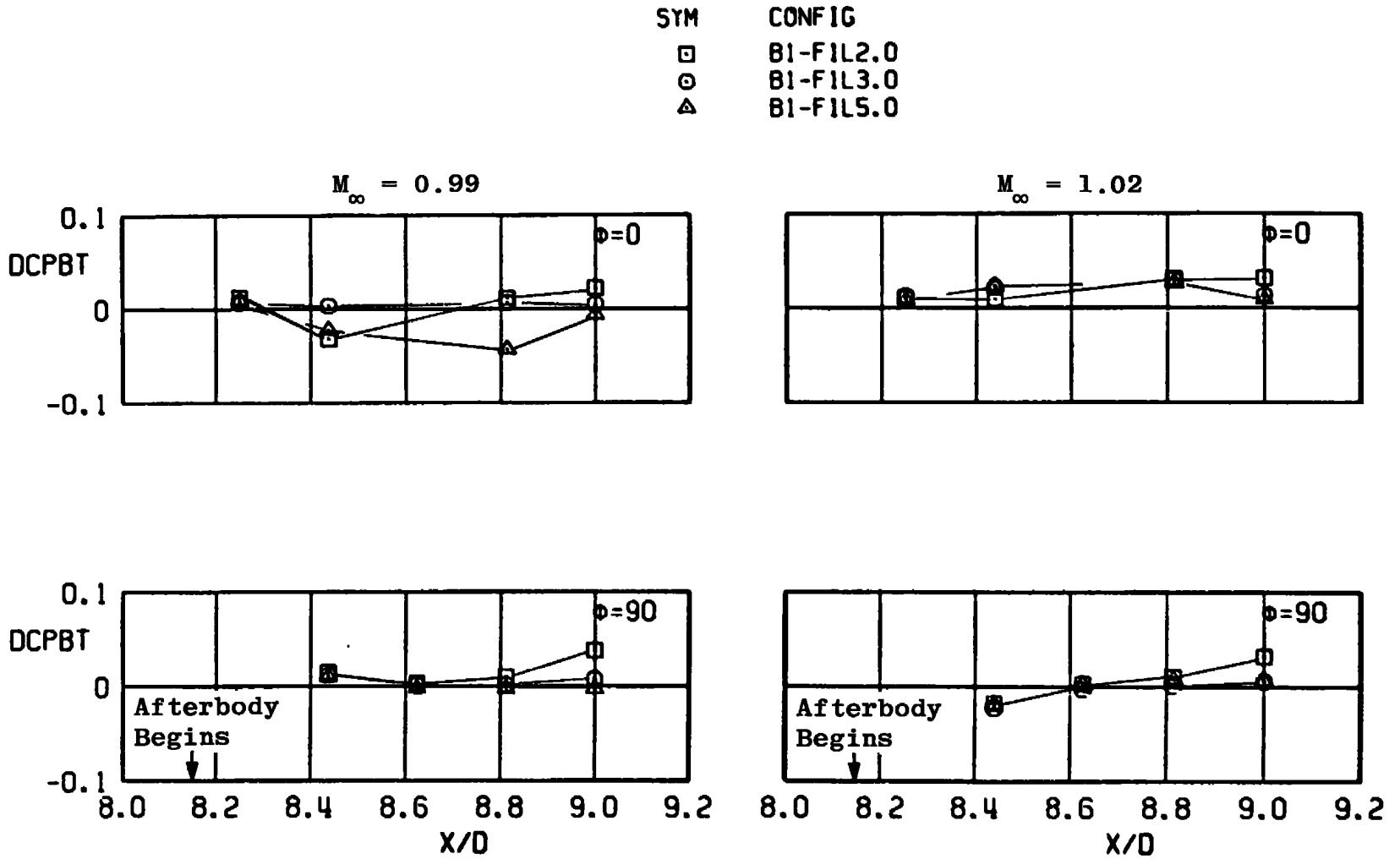


Figure 15. Effect of sting flare location on interference coefficient for cylindrical afterbody.

SYM	CONFIG
□	B1-FIL2.0
○	B1-FIL3.0
△	B1-FIL5.0

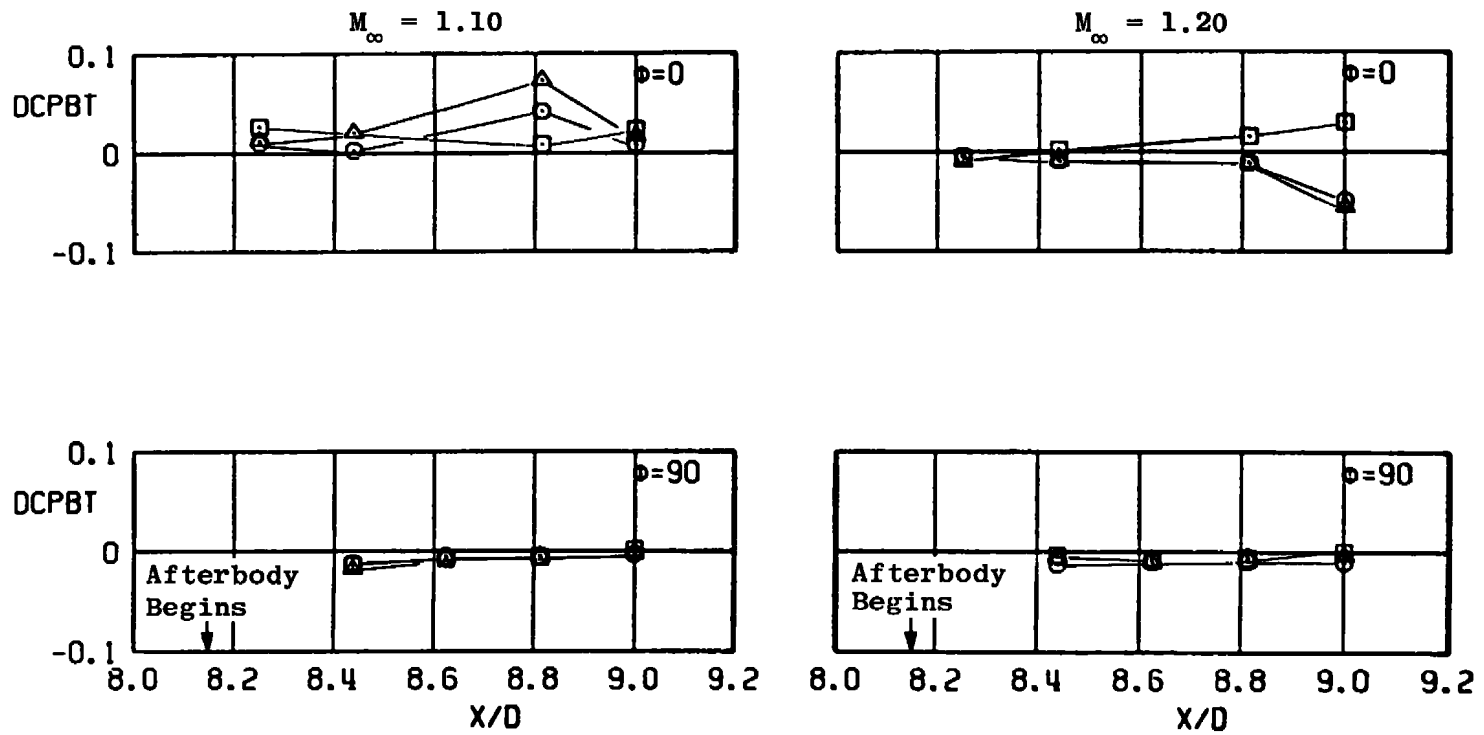


Figure 15. Concluded.

SYM	CONFIG
□	B2-FIL1.0
○	B2-FIL2.0
△	B2-FIL3.0

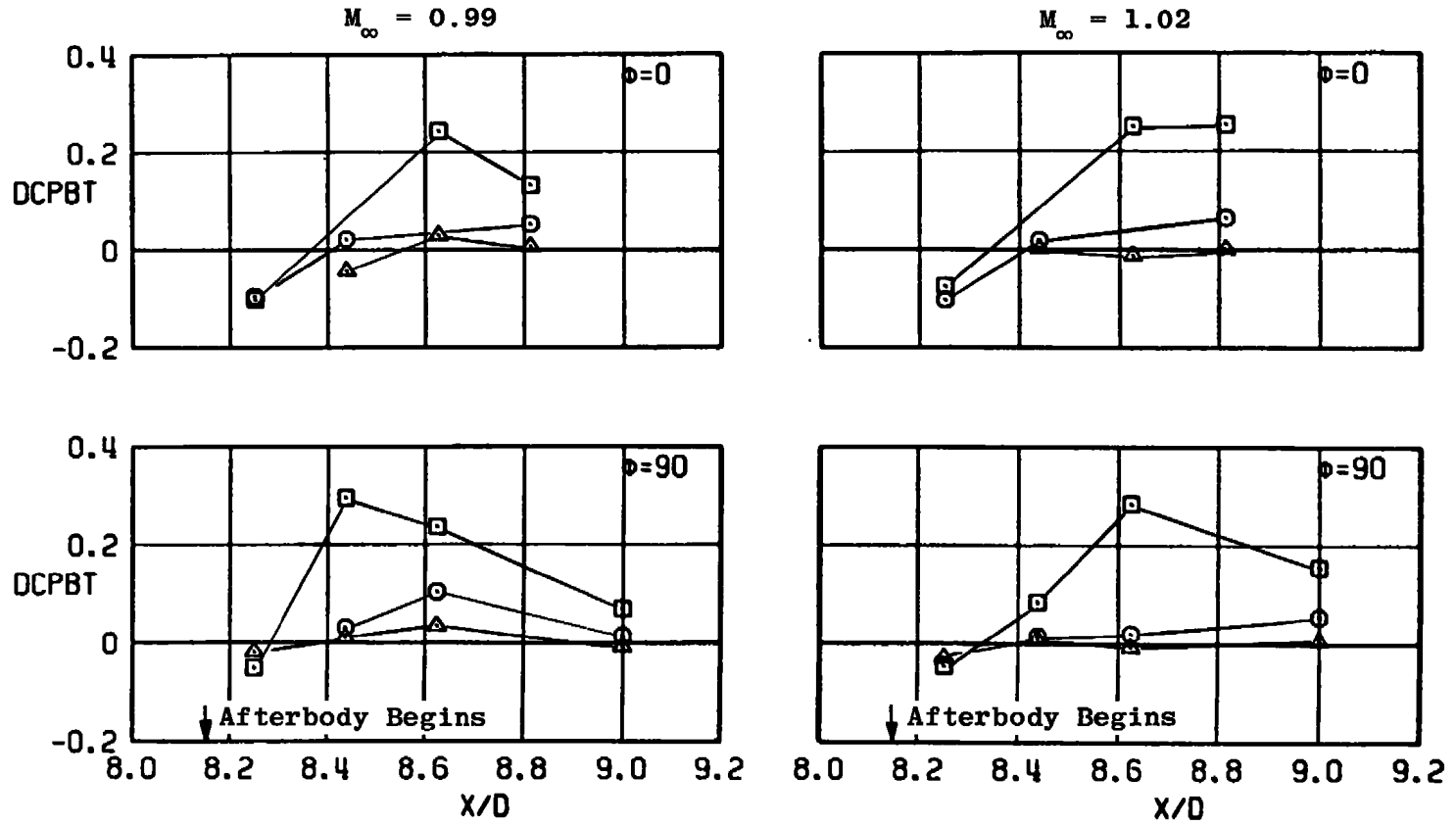


Figure 16. Effect of sting flare location on interference coefficient for 10-deg boattail.

SYM	CONFIG
□	B2-FIL1.0
○	B2-FIL2.0
△	B2-FIL3.0

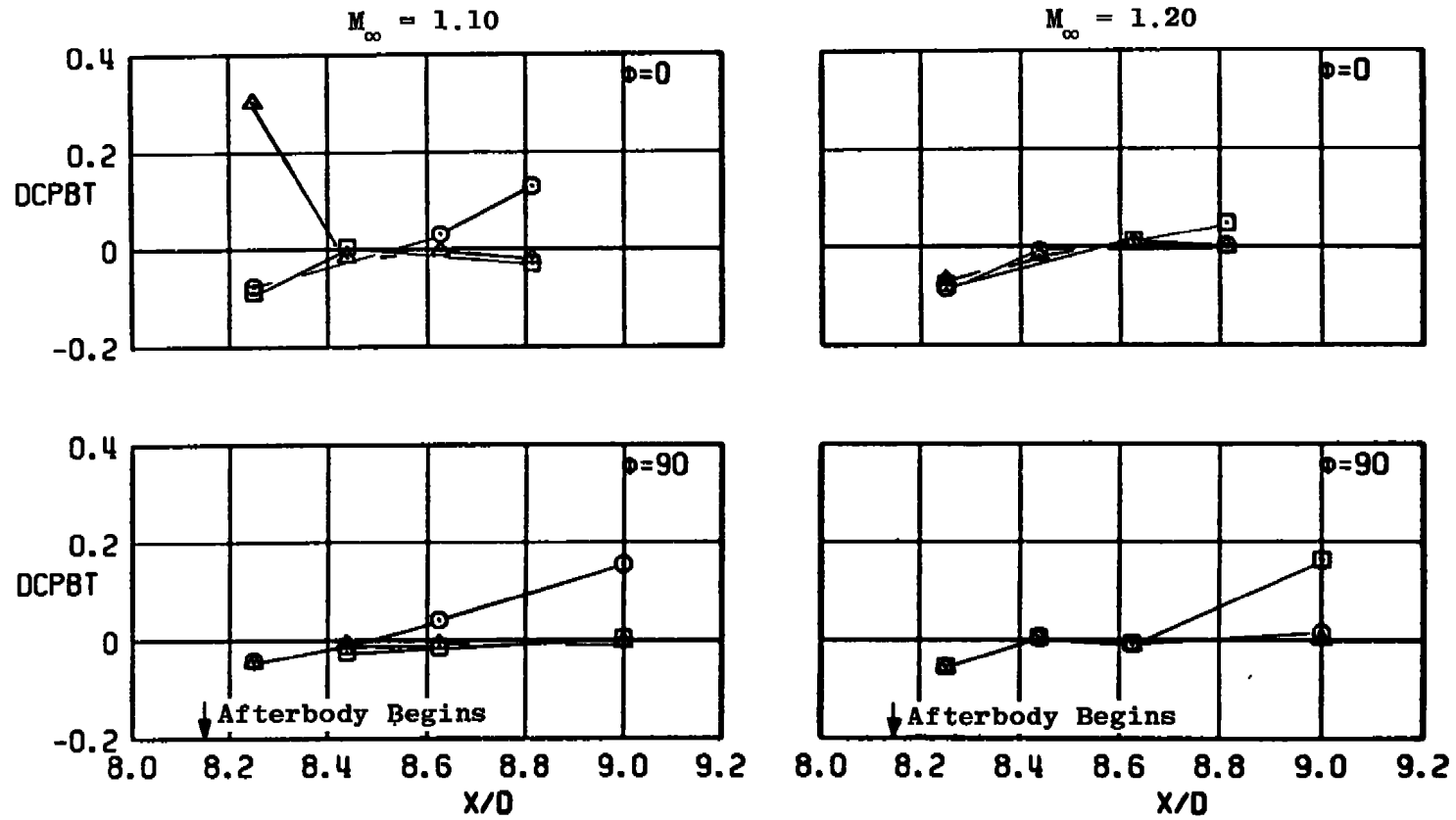


Figure 16. Concluded.

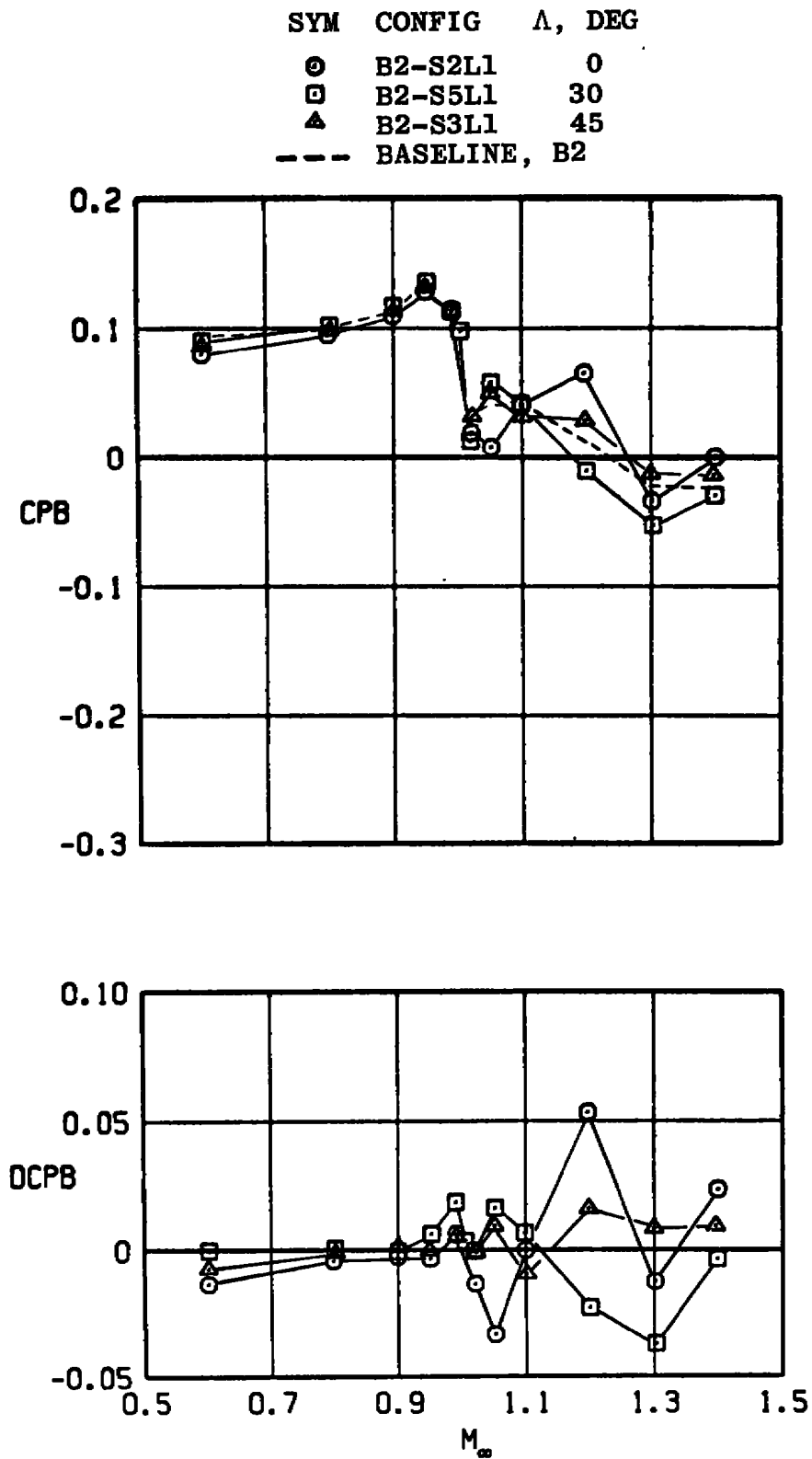


Figure 17. Effect of strut sweep angle on base pressure coefficient.

SYM	CONFIG	Λ , DEG
○	B2-S2L1	0
□	B2-S5L1	30
△	B2-S3L1	45

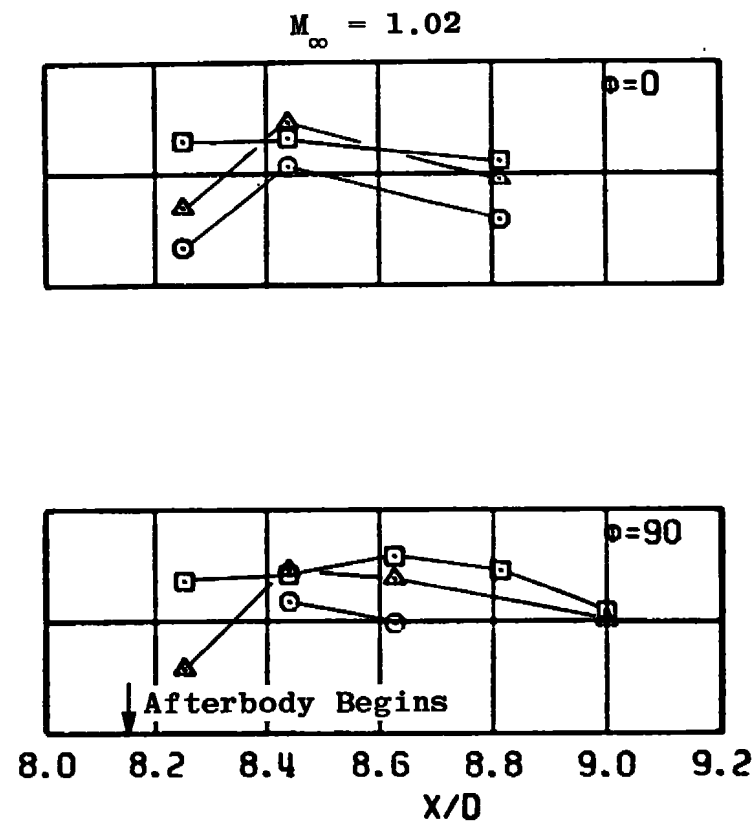
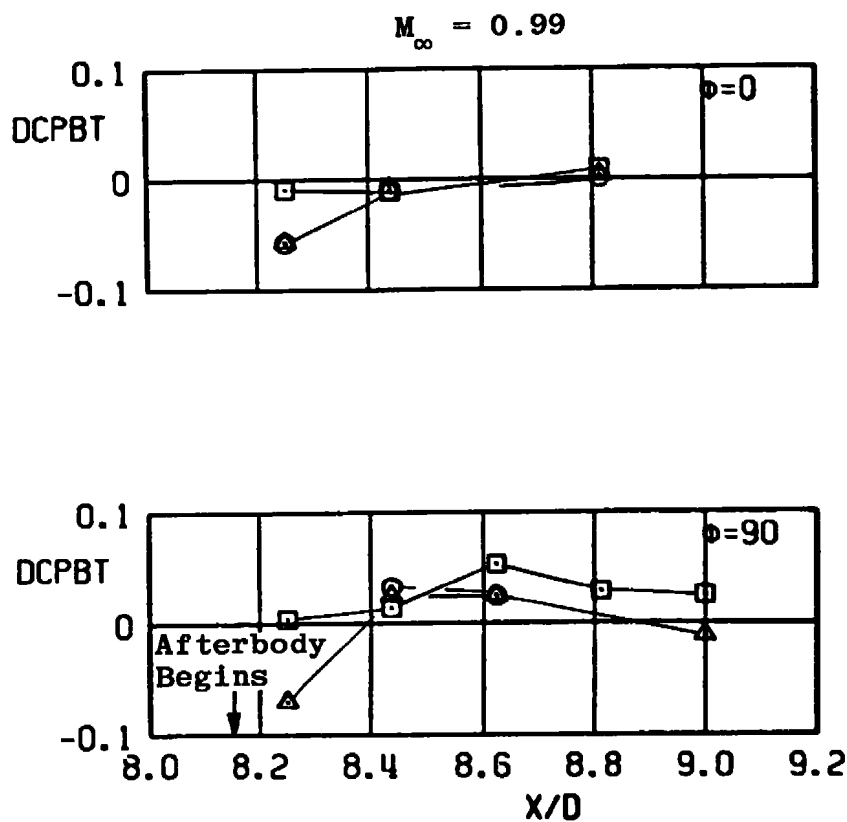


Figure 18. Effect of strut sweep angle on boattail interference coefficient.

SYM	CONFIG	Δ , DEG
○	B2-S2L1	0
□	B2-S5L1	30
△	B2-S3L1	45

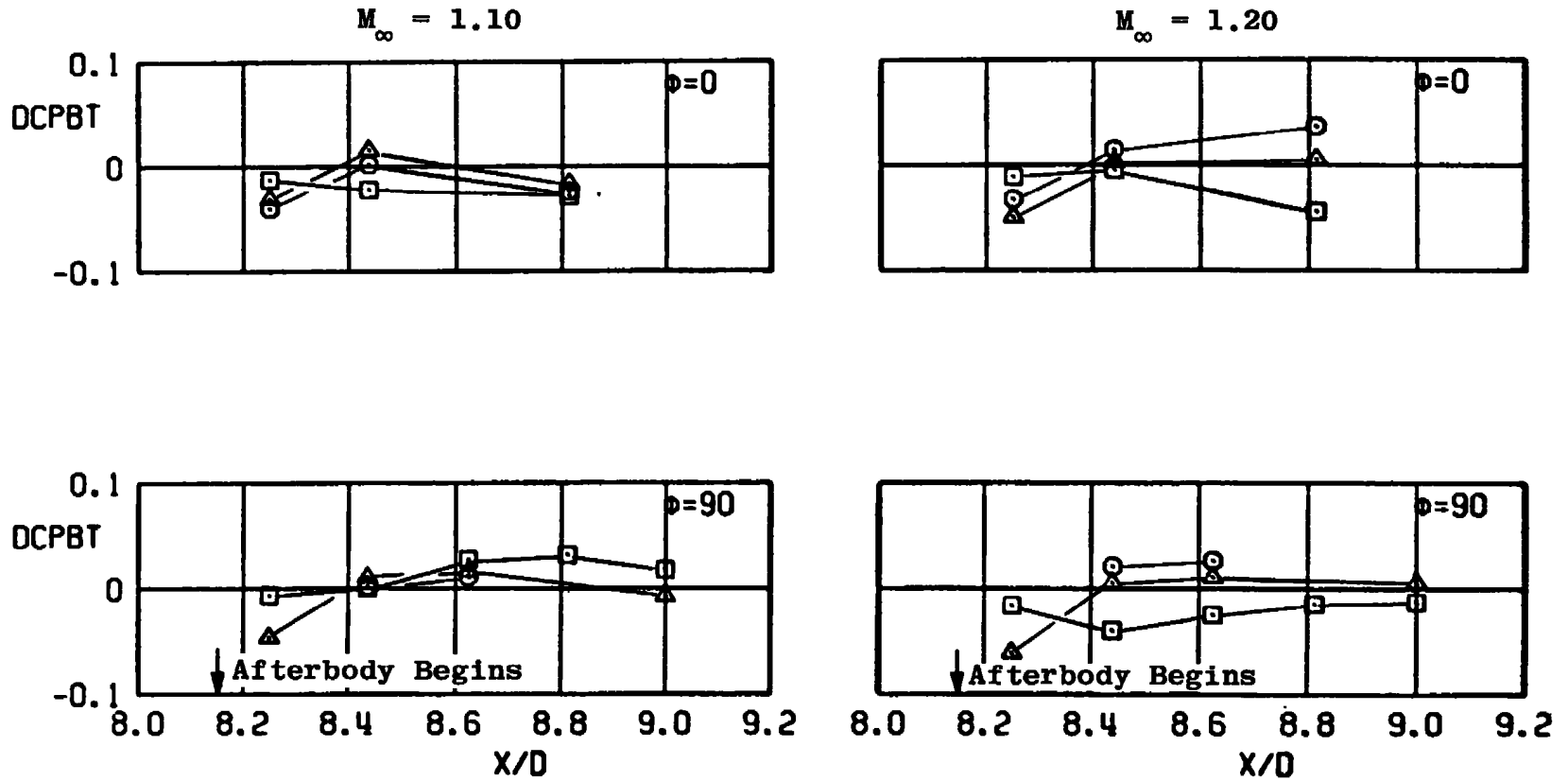


Figure 18. Concluded.

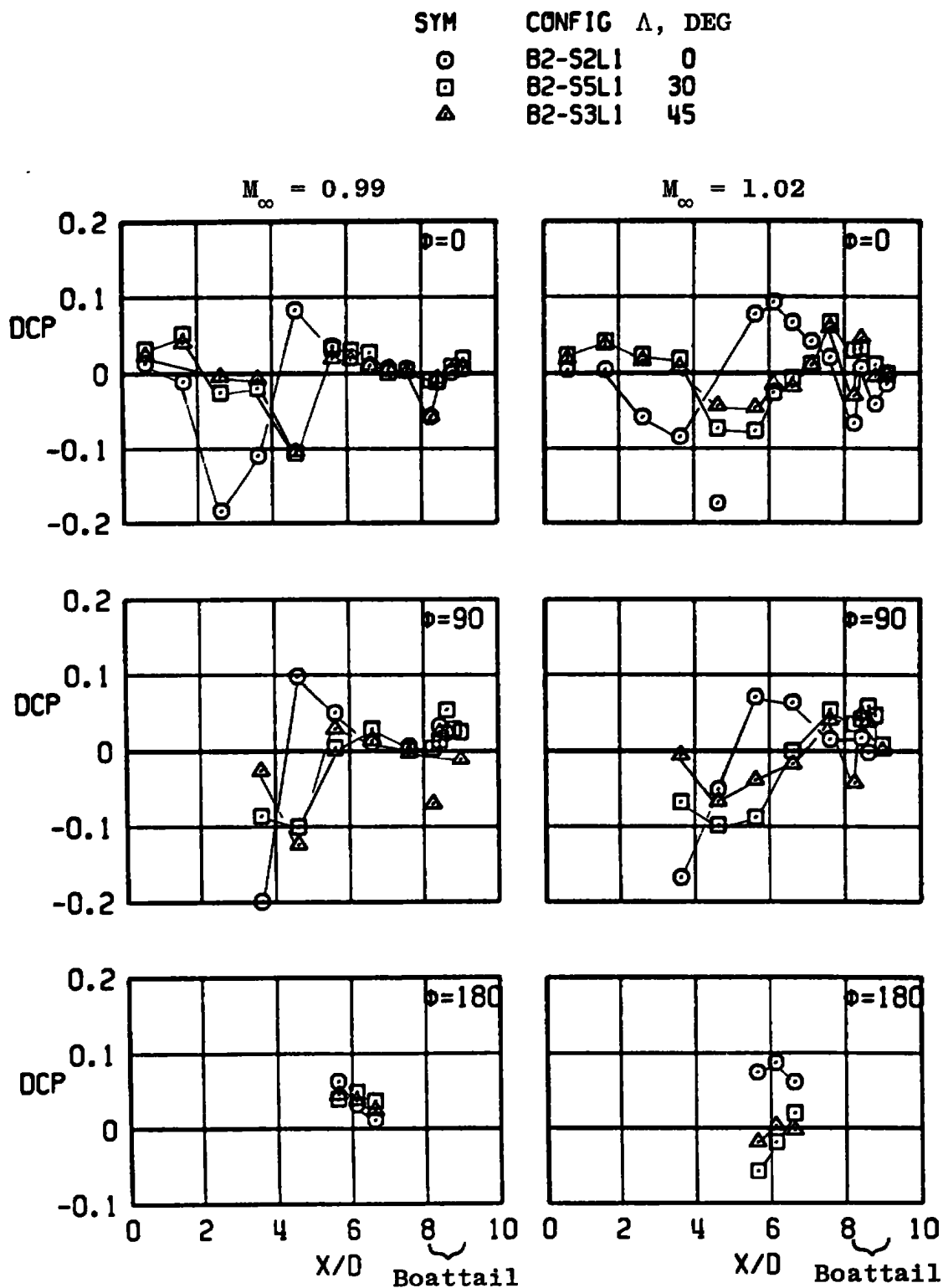


Figure 19. Effect of strut sweep angle on body interference coefficient.

SYM	CONFIG	Λ , DEG
○	B2-S2L1	0
□	B2-S5L1	30
△	B2-S3L1	45

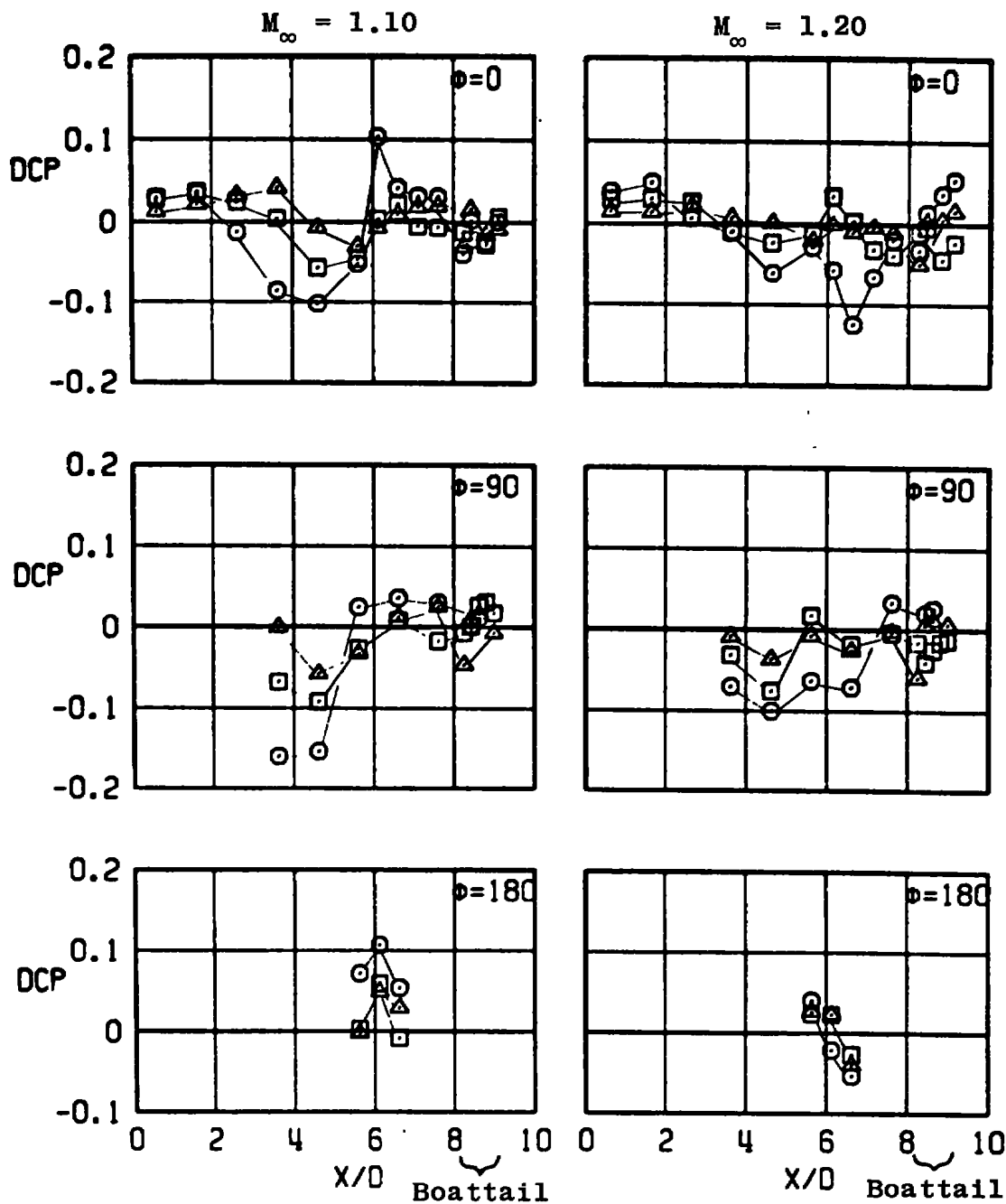
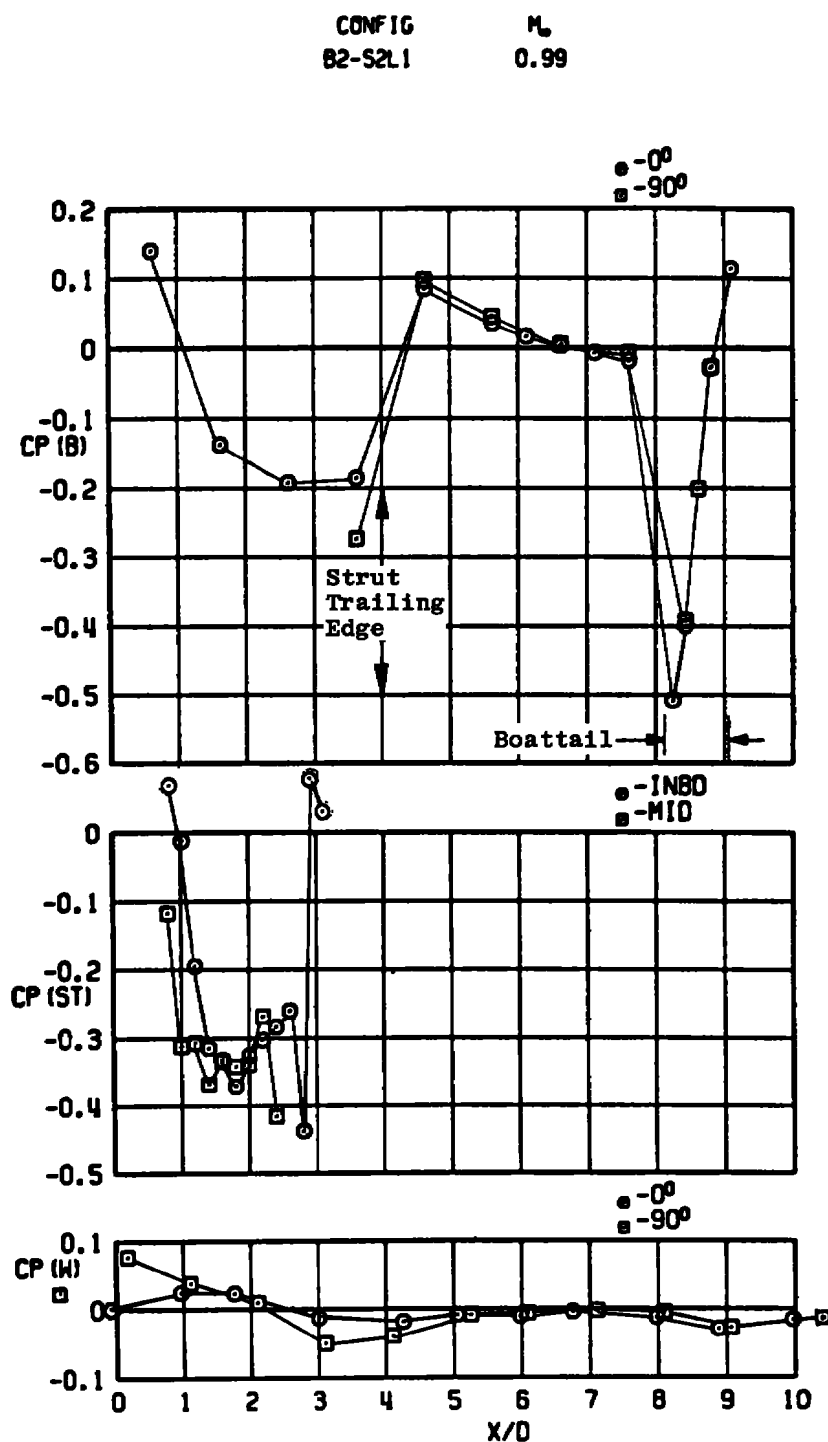


Figure 19. Concluded.

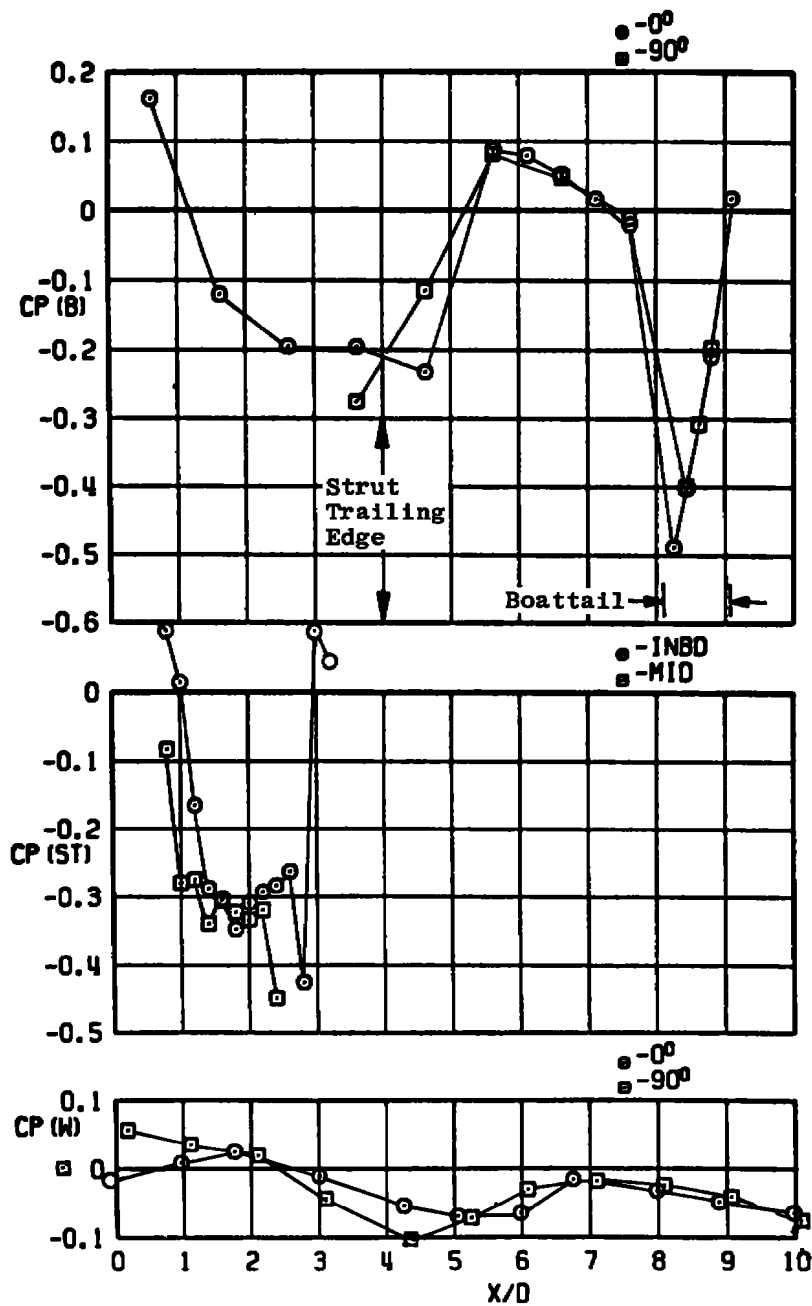


a. Straight strut configuration (B2-S2L1)

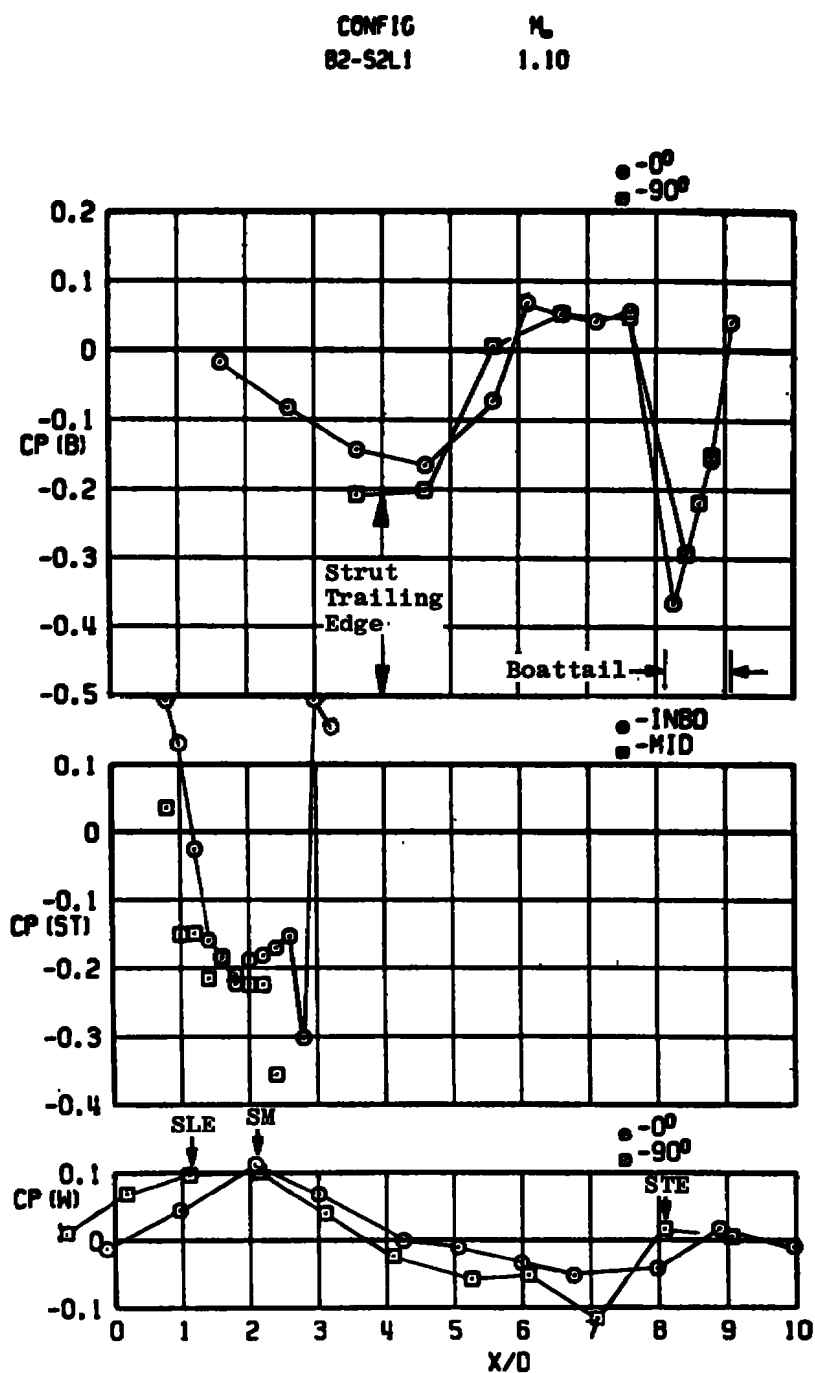
Figure 20. Pressure coefficient distribution on model body, strut, and tunnel wall.

CONFIG
B2-S2L1

M_∞
1.02



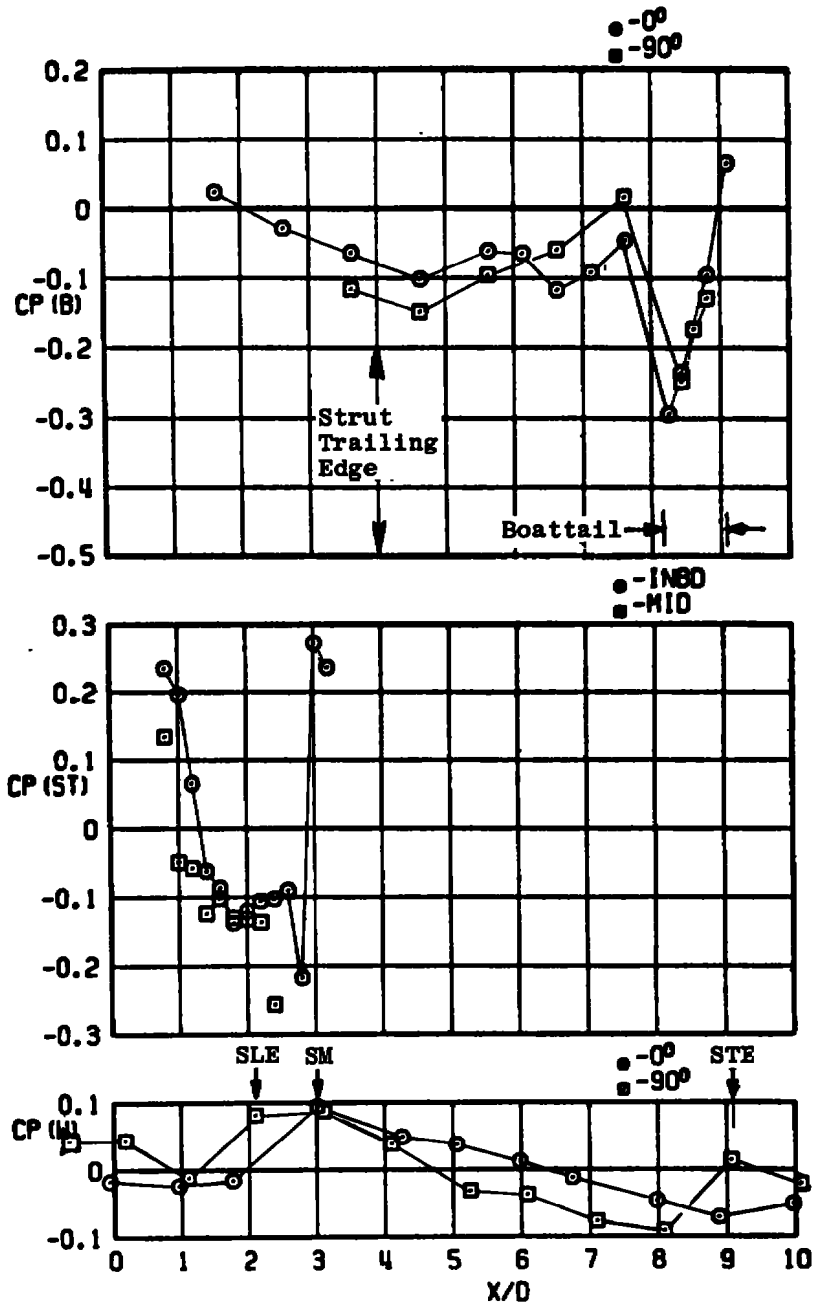
a. Continued
Figure 20. Continued.



a. Continued
Figure 20. Continued.

CONFIG
82-S2L1

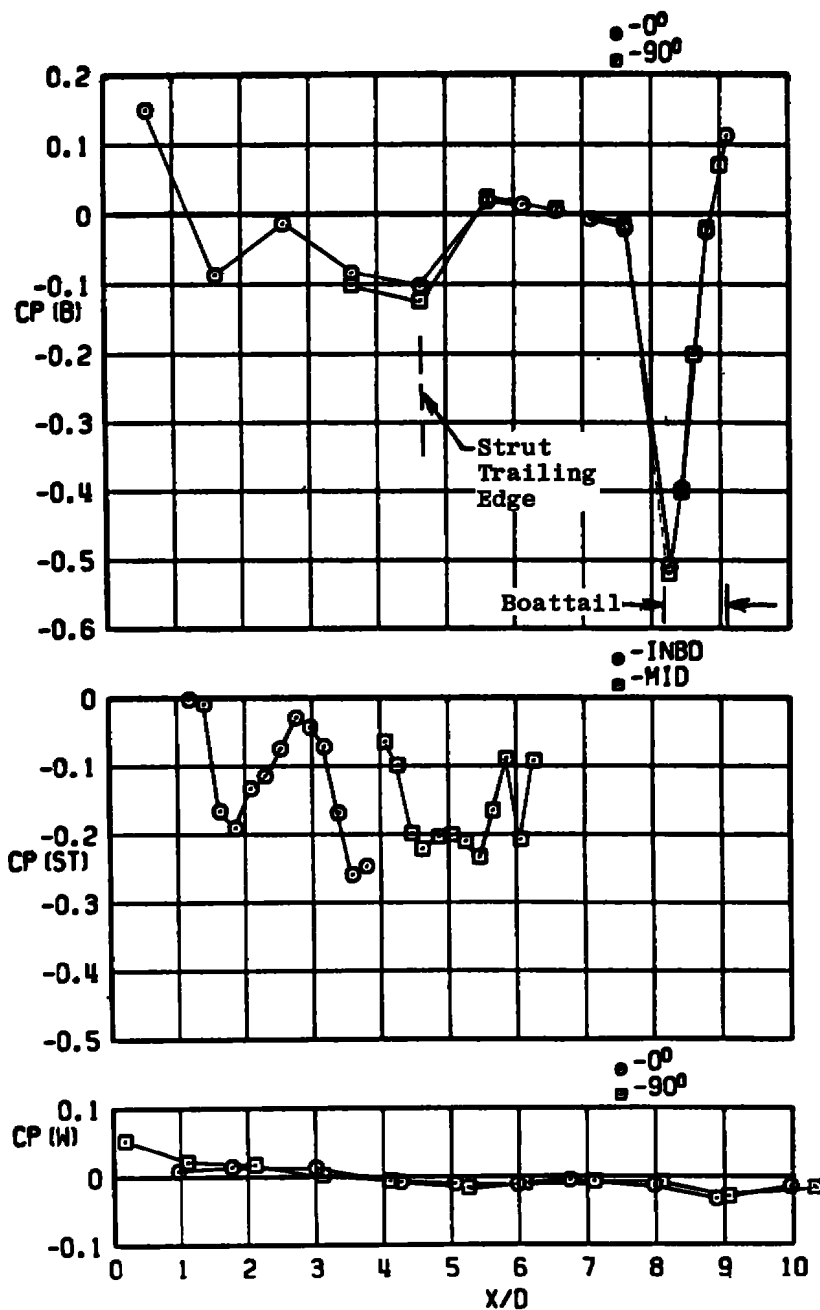
M_∞
1.20



a. Concluded
Figure 20. Continued.

CONFIG
82-S3L1

M_∞
0.99

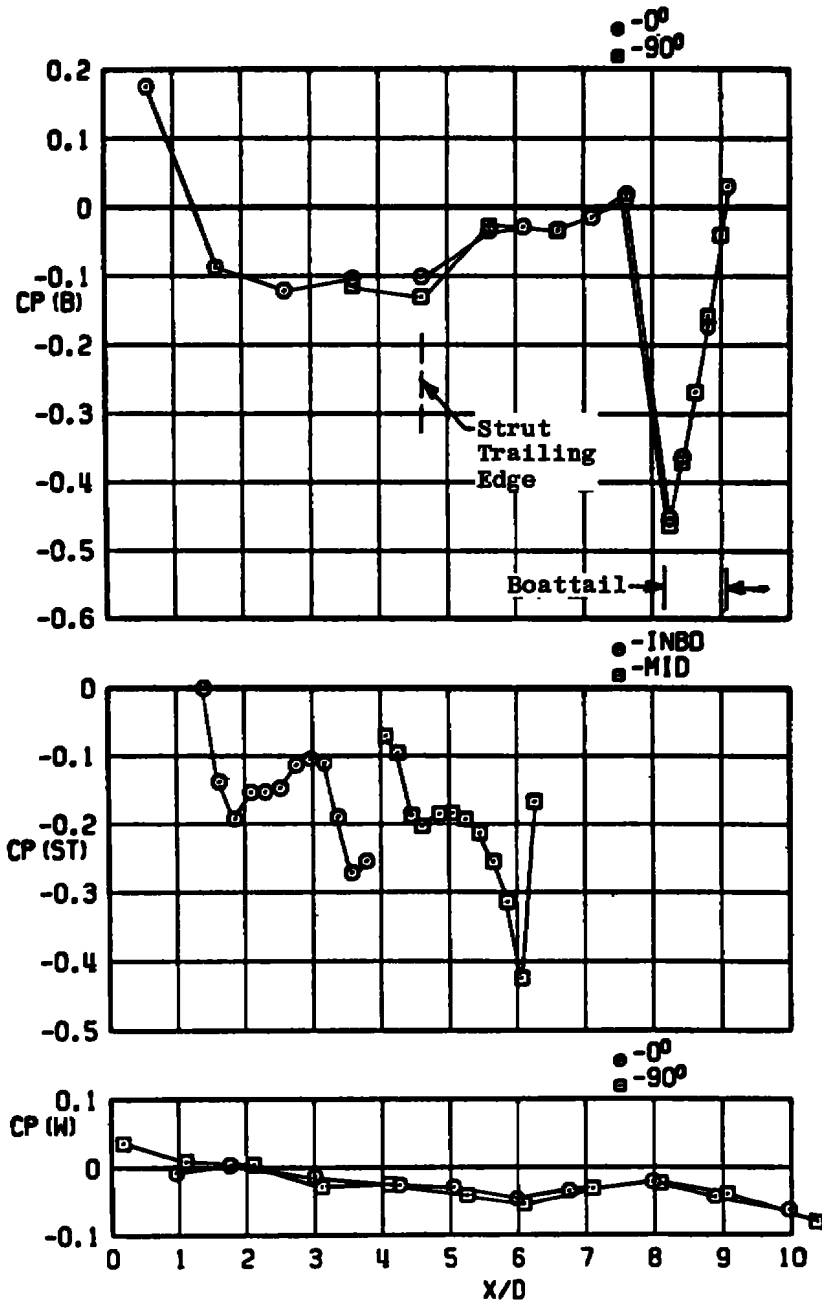


b. Swept strut configuration (B2-S3L1)

Figure 20. Continued.

CONFIG
B2-53L1

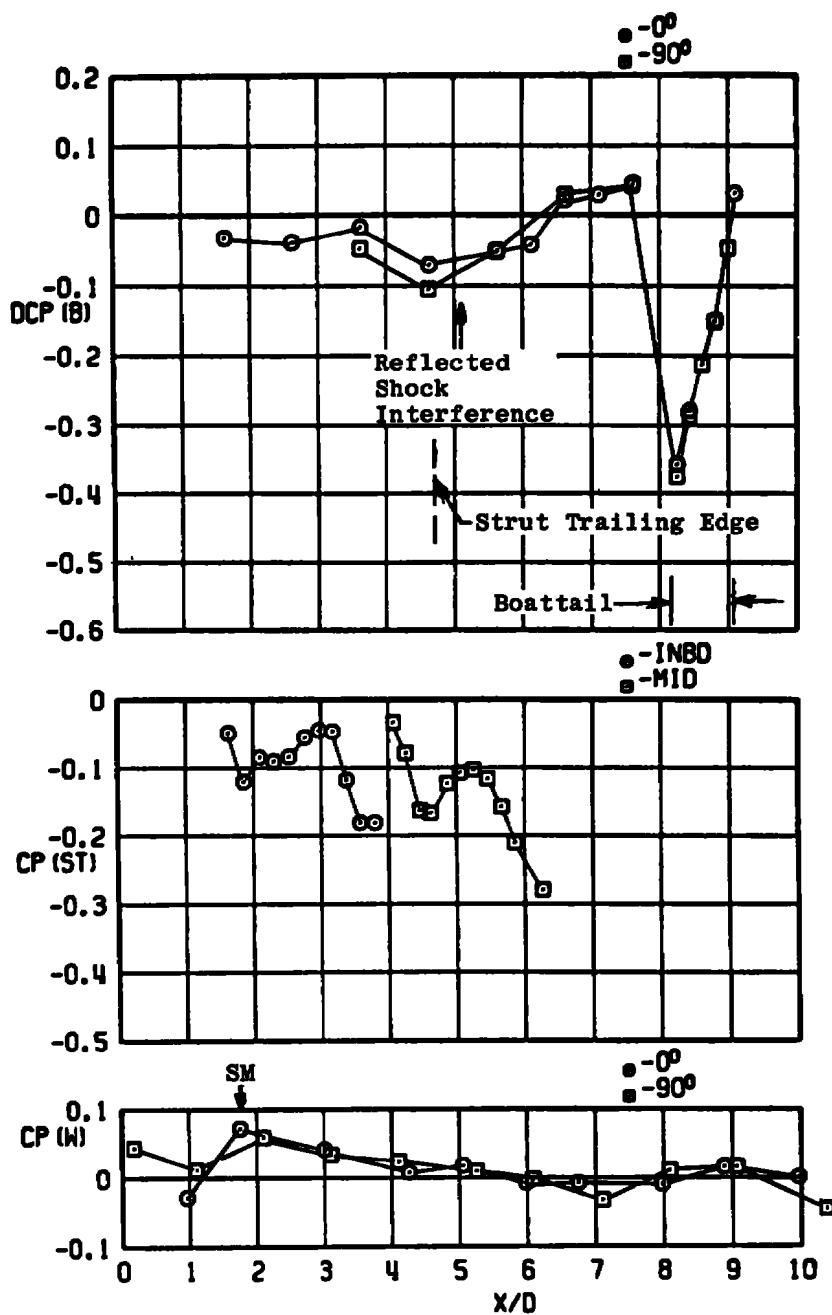
M_∞
1.02



b. Continued
Figure 20. Continued.

CONFIG
B2-S3L1

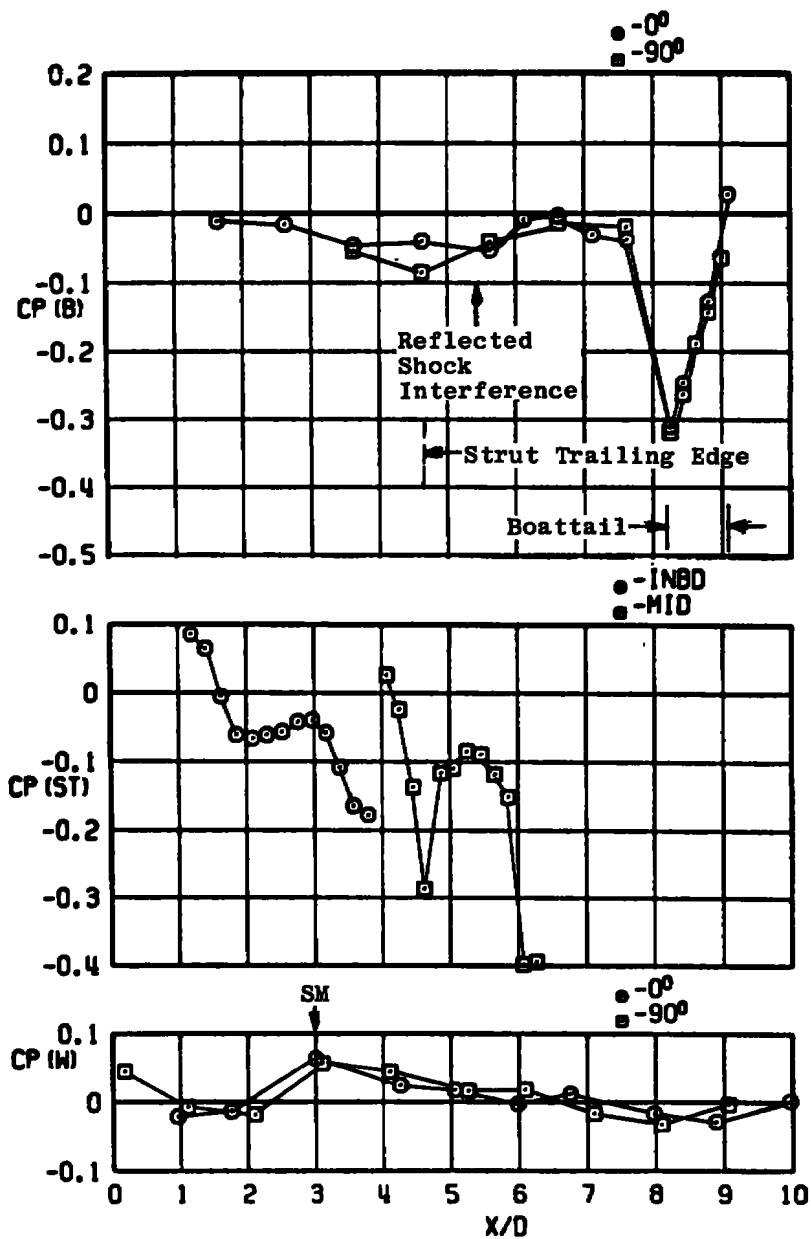
M_∞
1.10



b. Continued
Figure 20. Continued.

CONFIG
B2-S3L1

M_∞
1.20



b. Concluded
Figure 20. Concluded.

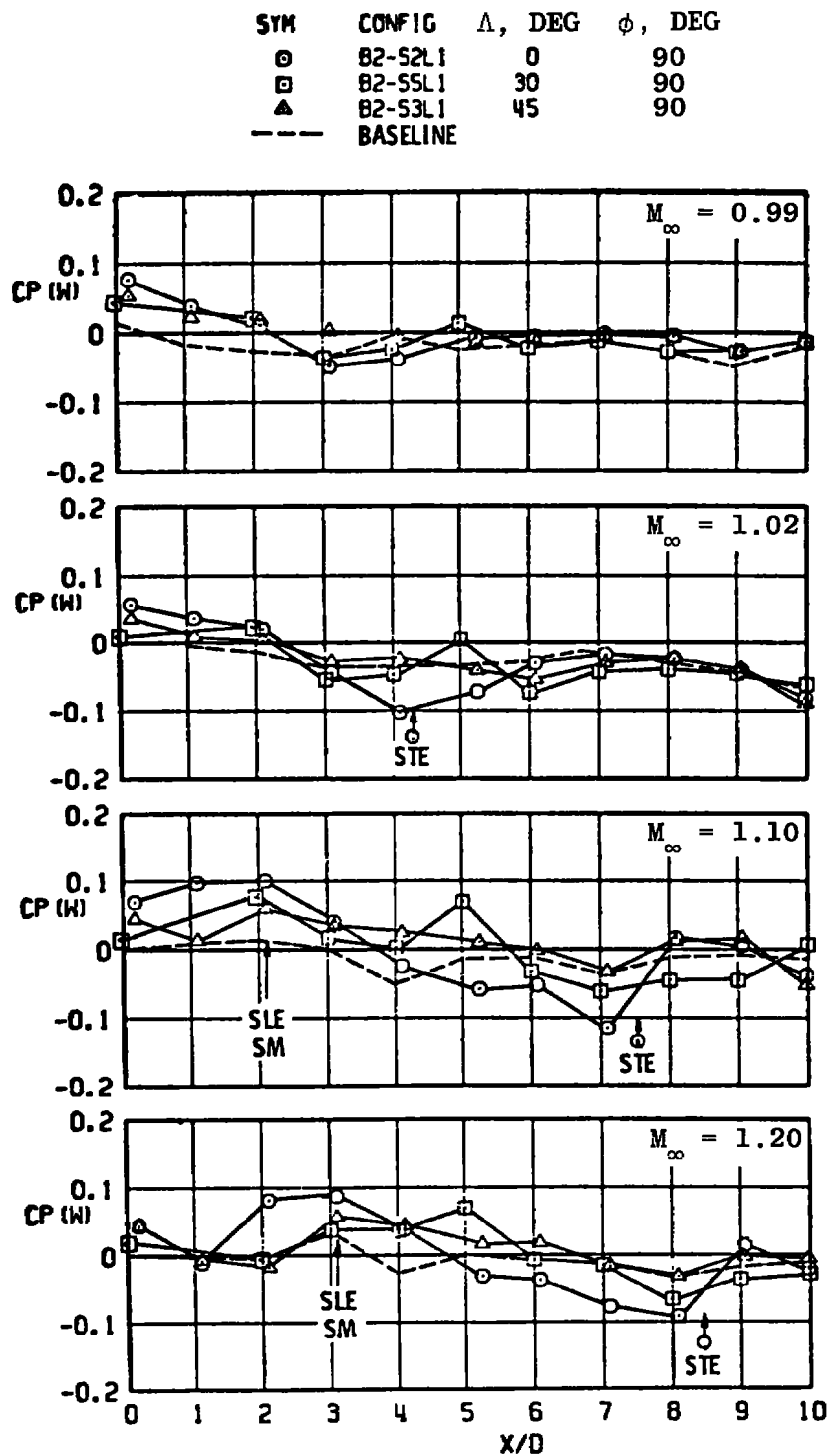


Figure 21. Effect of strut sweep angle on wall pressure coefficient.

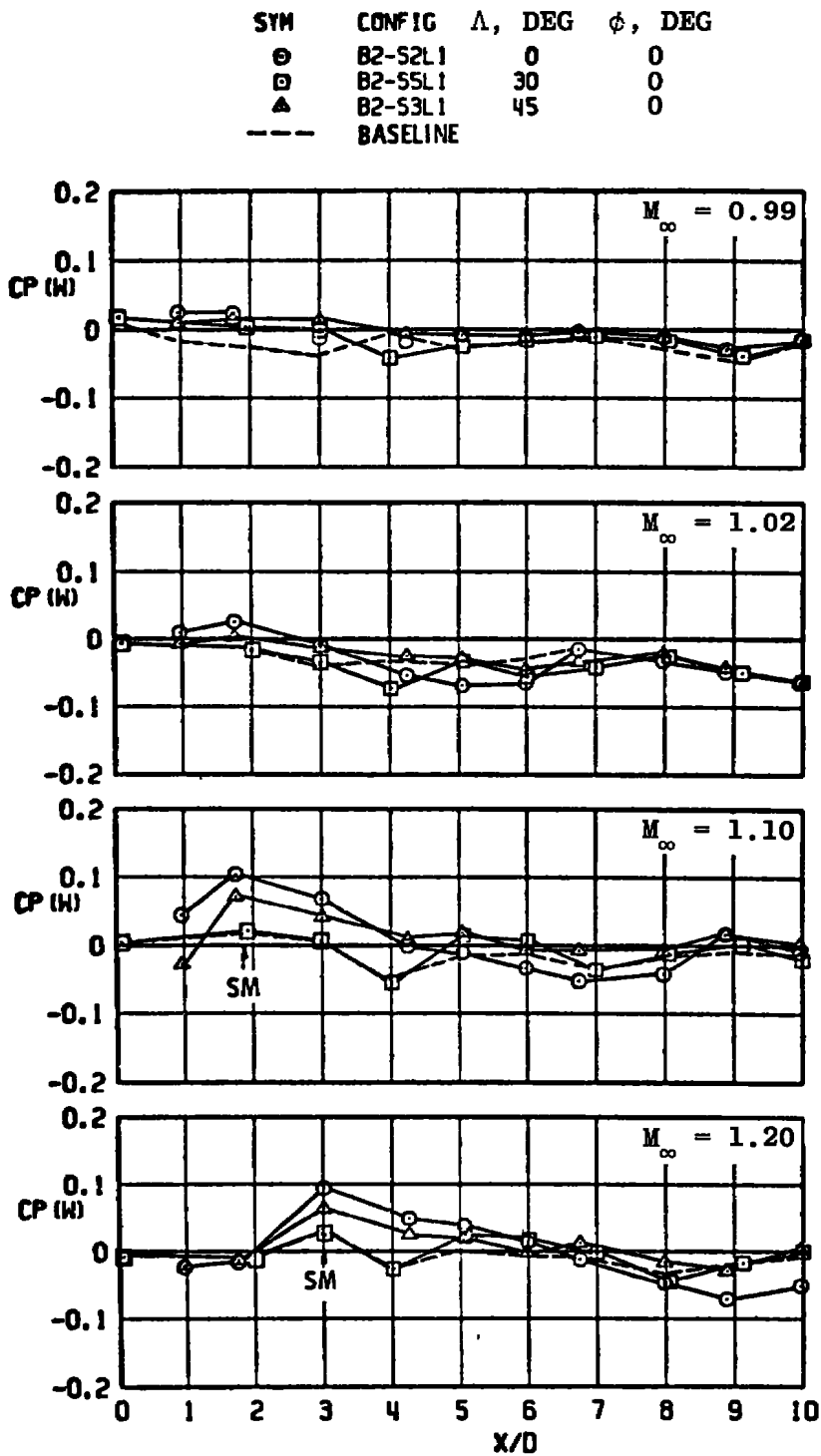


Figure 21. Concluded.

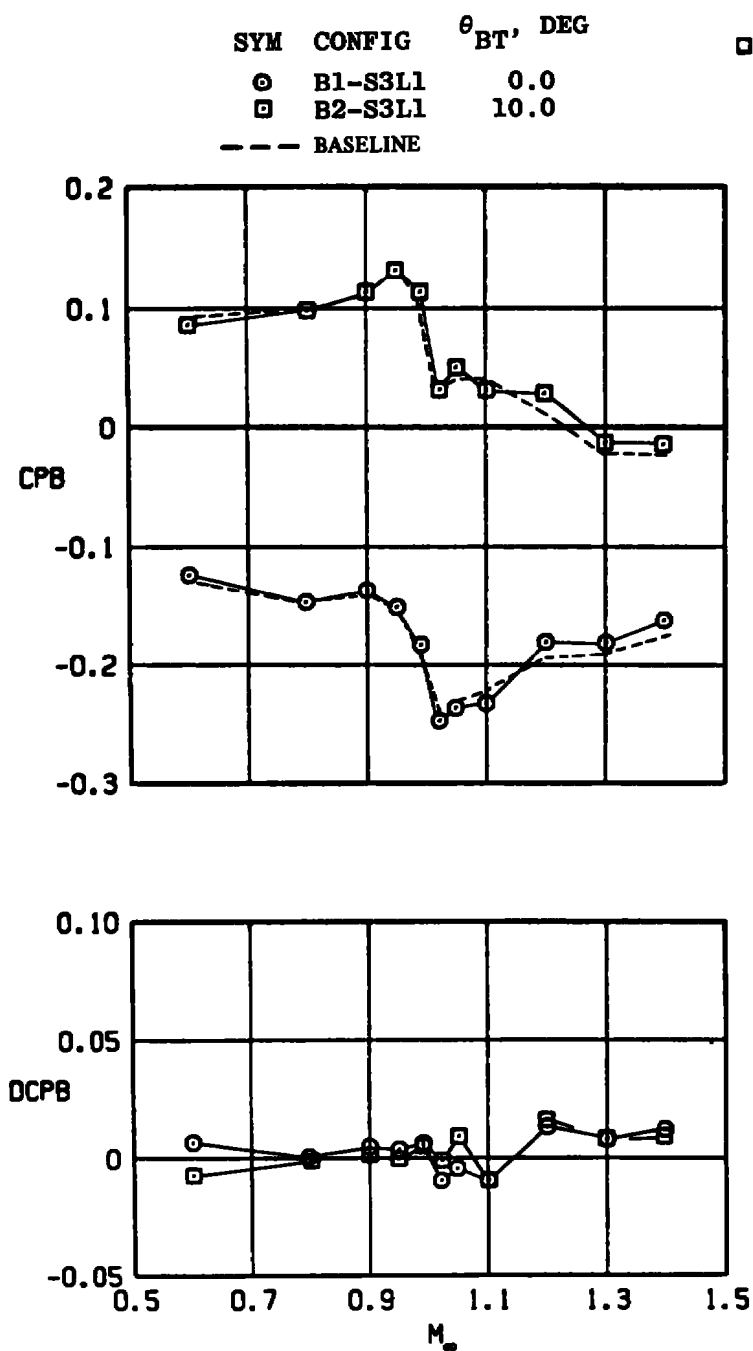
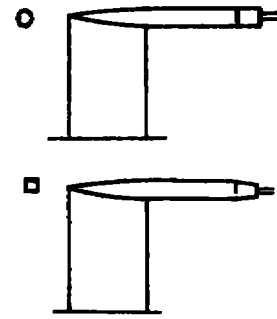


Figure 22. Effect of boattail angle on base pressure interference coefficient for straight and swept support struts.



SYM	CONFIG	θ_{BT} , DEG
○	B1-S2L1	0.0
□	B2-S2L1	10.0

--- BASELINE

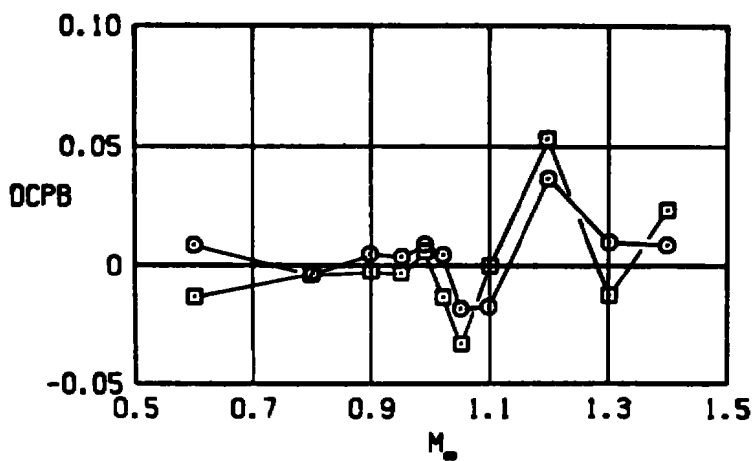
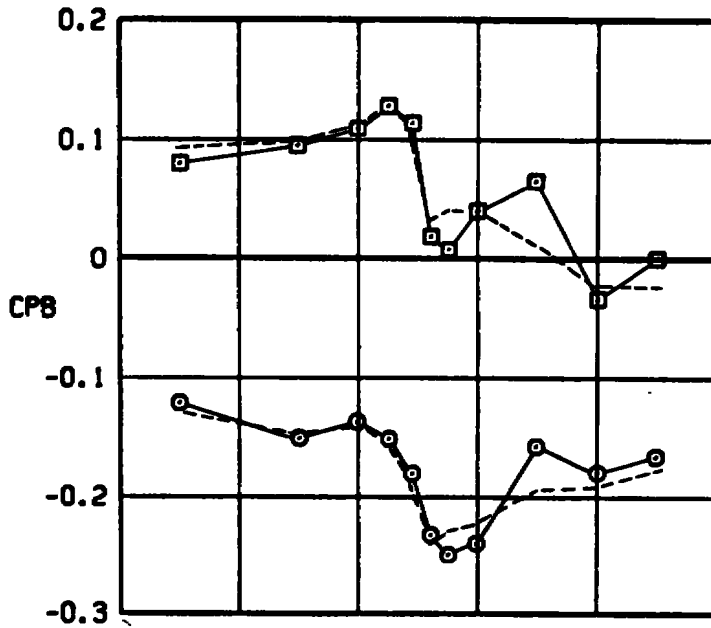


Figure 22. Concluded.

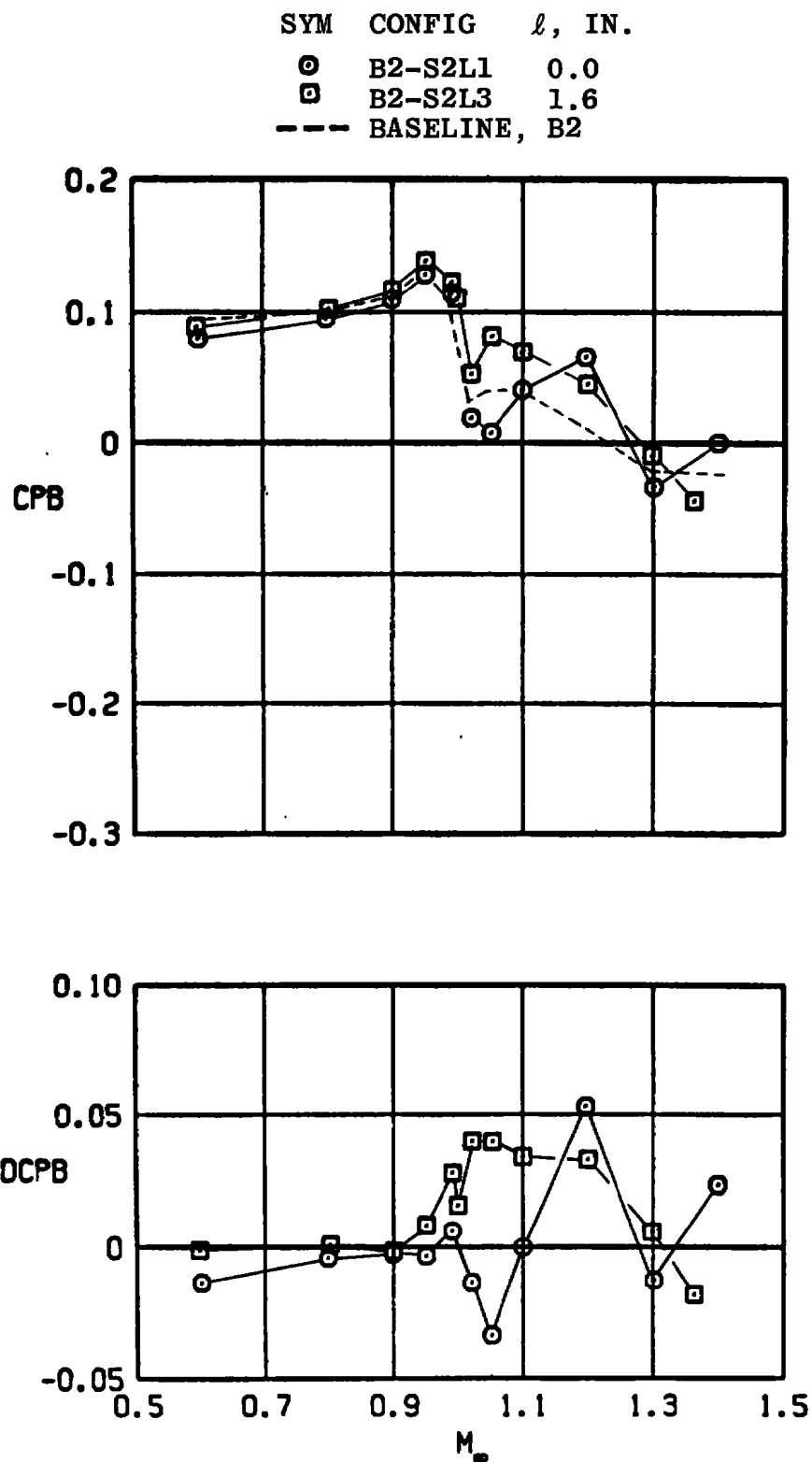


Figure 23. Effect of straight strut location on base pressure coefficient.

SYM	CONFIG	l , IN.
○	B2-S2L1	0.0
□	B2-S2L3	1.6

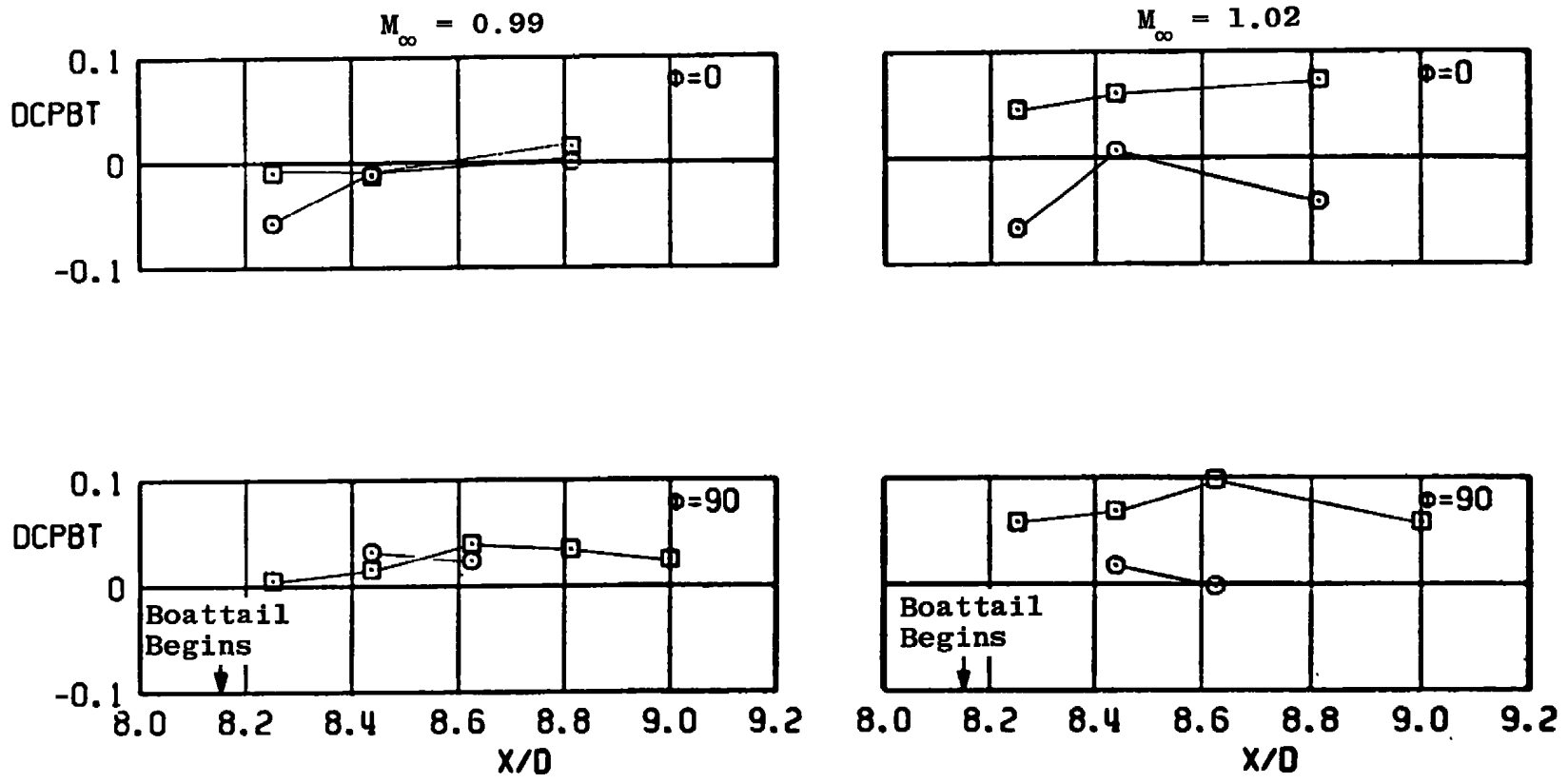


Figure 24. Effect of straight strut location on boattail interference coefficient.

SYM	CONFIG	ℓ , IN.
○	B2-S2L1	0.0
□	B2-S2L3	1.6

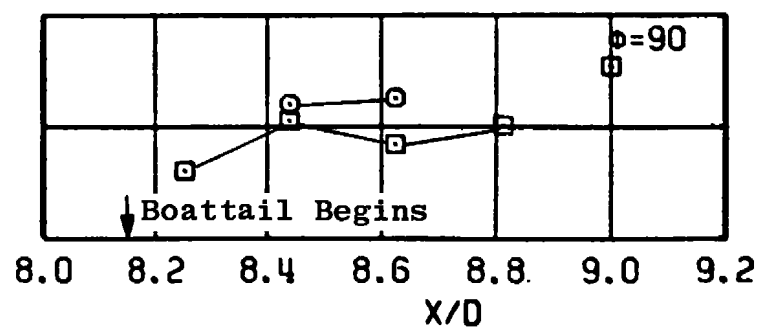
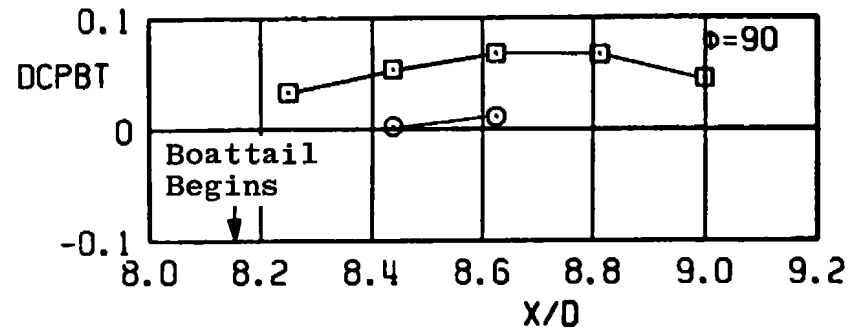
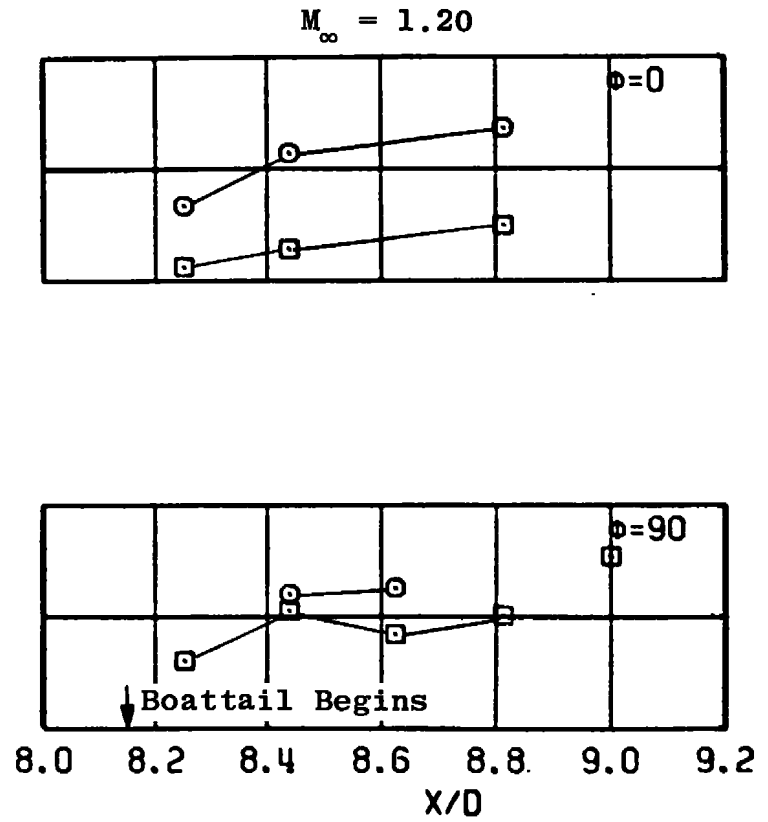
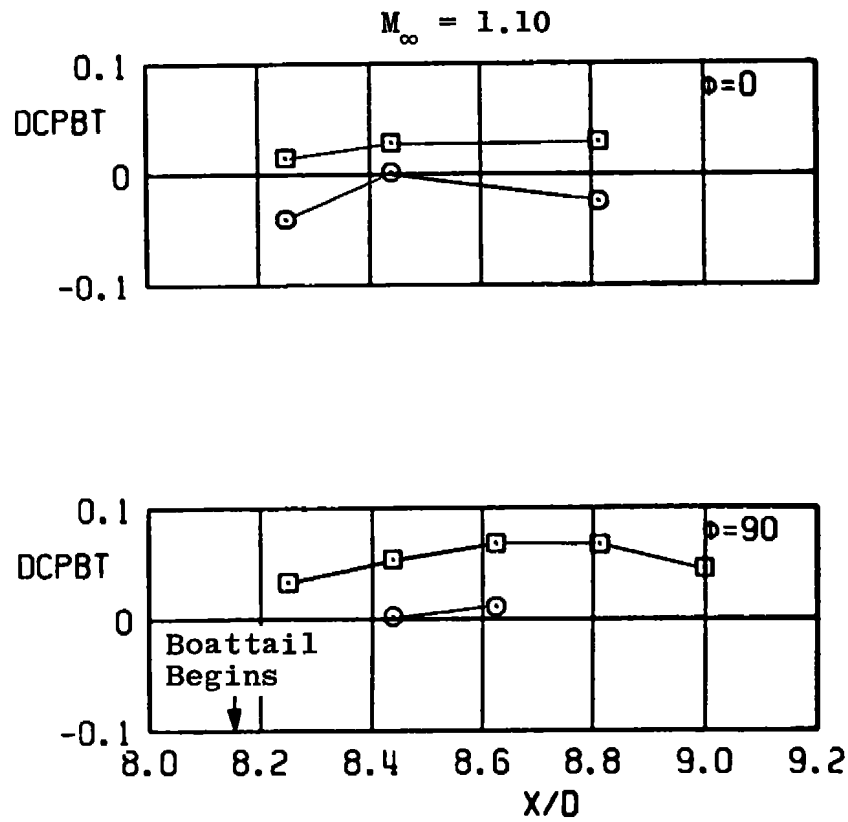


Figure 24. Concluded.

SYM	CONFIG	ℓ , IN.
○	B2-S2L1	0.0
□	B2-S2L3	1.6

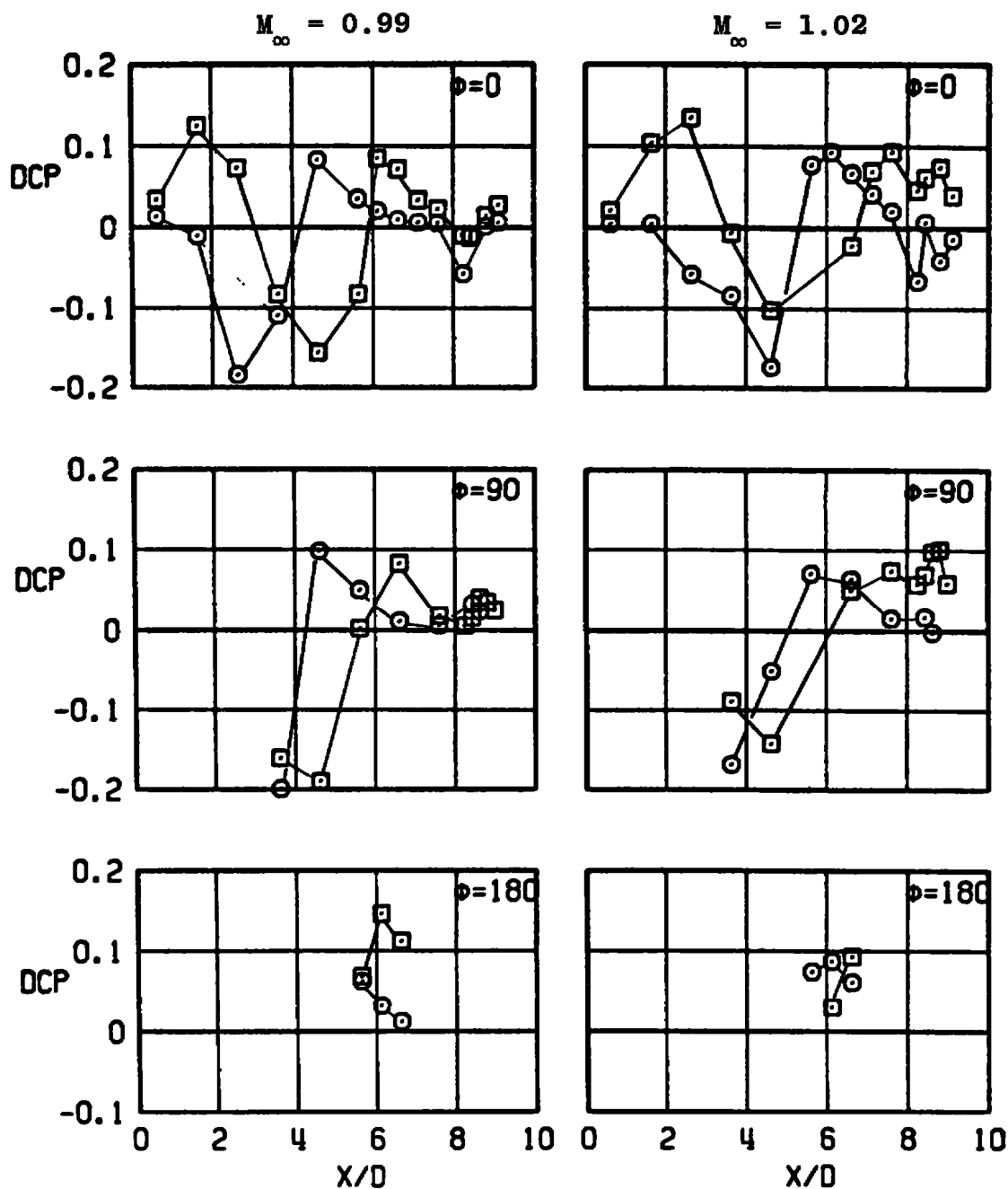


Figure 25. Effect of straight strut location on body interference coefficient.

SYM	CONFIG	ℓ , IN.
○	B2-S2L1	0.0
□	B2-S2L3	1.6

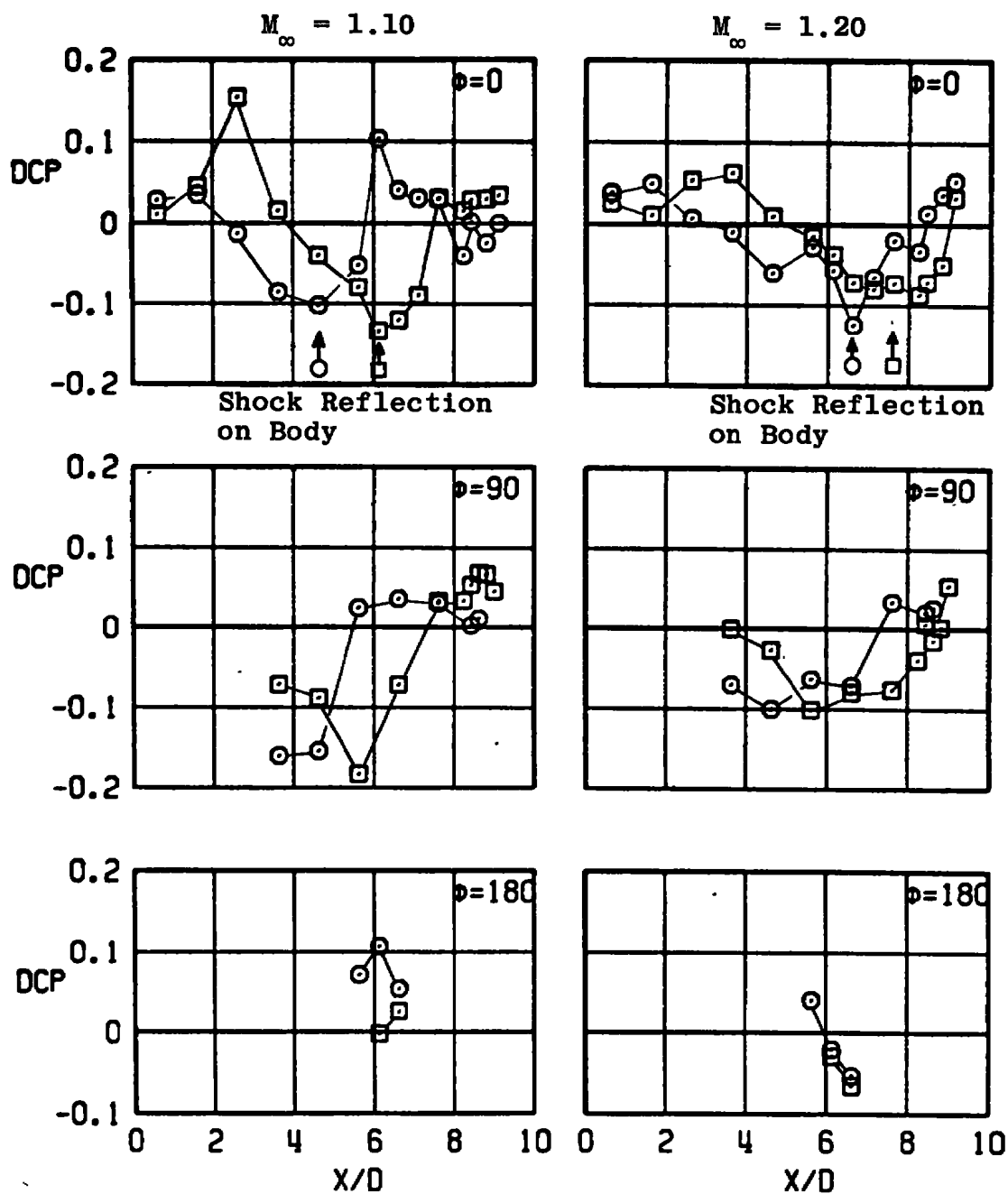


Figure 25. Concluded.

SYM	CONFIG	l , IN.	ϕ , DEG
○	B2-S2L1	0.0	0
□	B2-S2L3	1.6	0
---	BASELINE, B2		

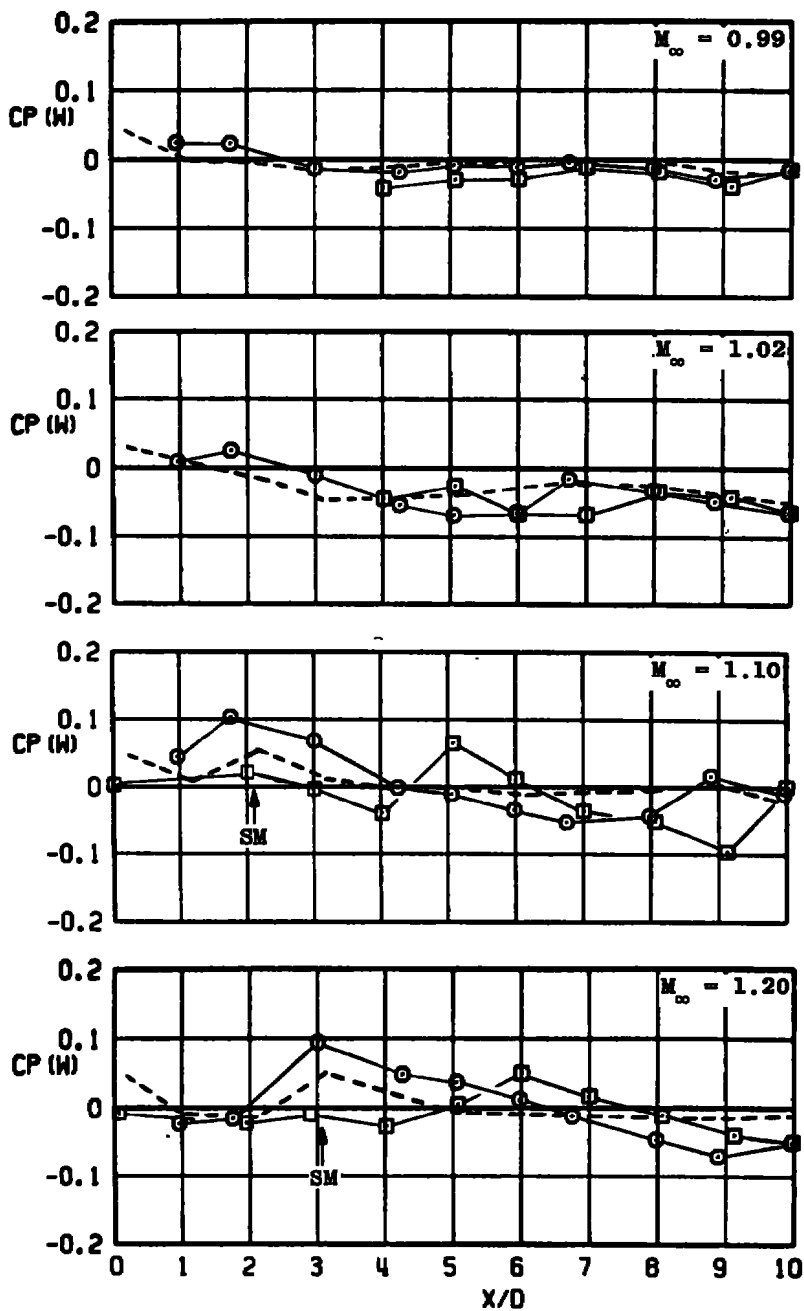


Figure 26. Effect of straight strut location on wall pressure coefficient.

SYM	CONFIG	l , IN.	ϕ , DEG
○	82-S2L1	0.0	90
□	82-S2L3	1.6	90

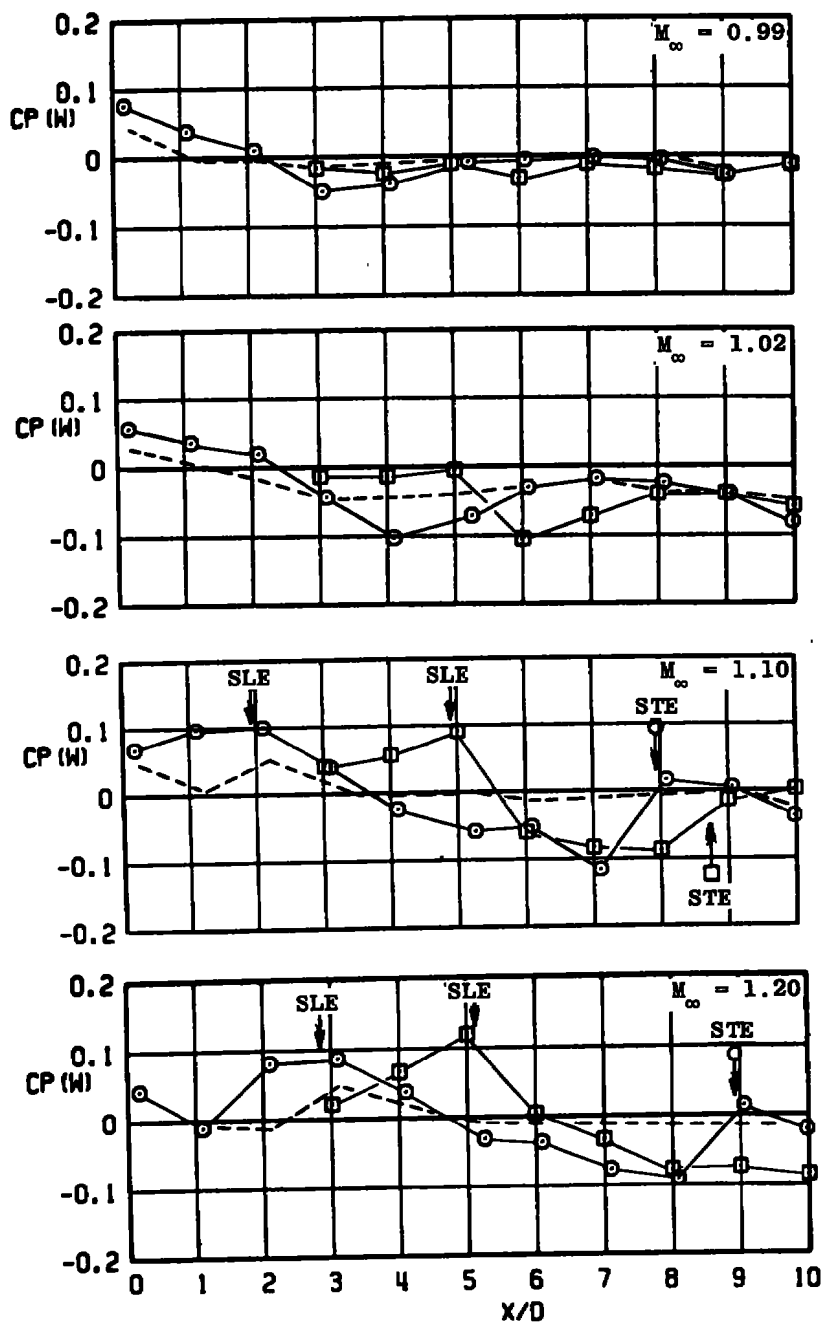
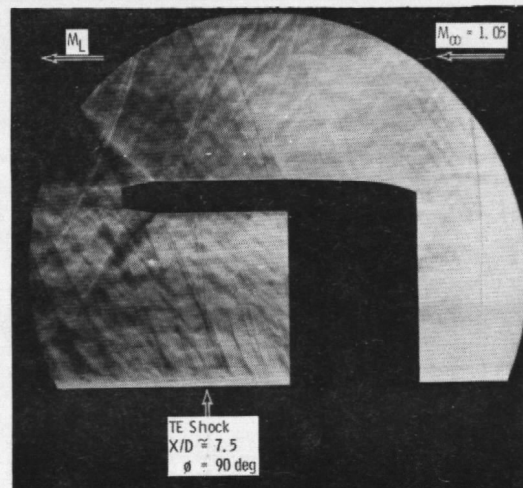
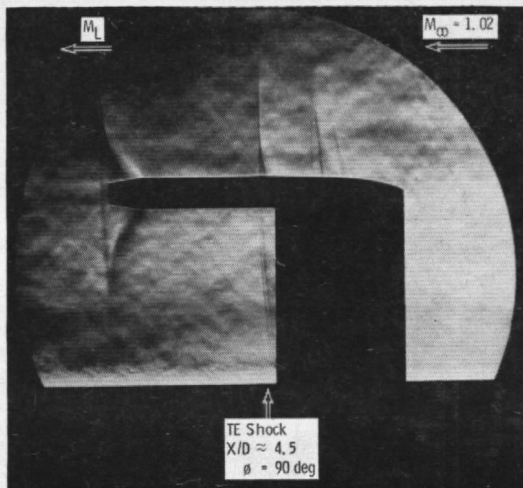
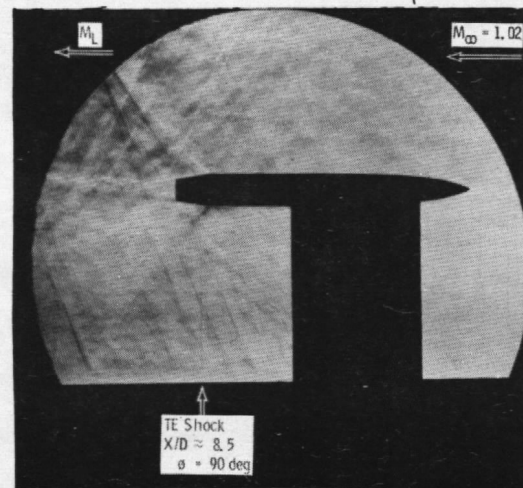
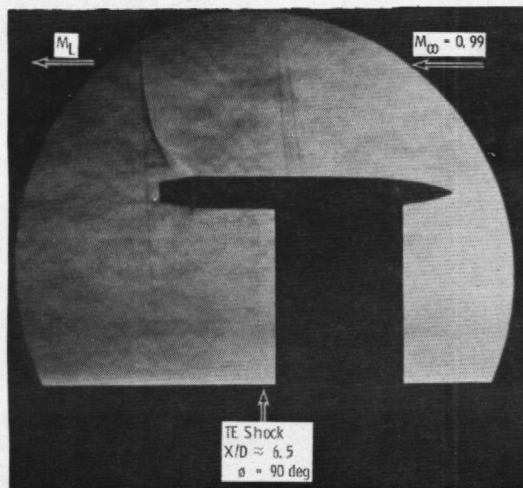


Figure 26. Concluded.



S2L1



S2L3

Figure 27. Schlieren photographs for straight strut located at $\ell/D = 0$ and 1.6.

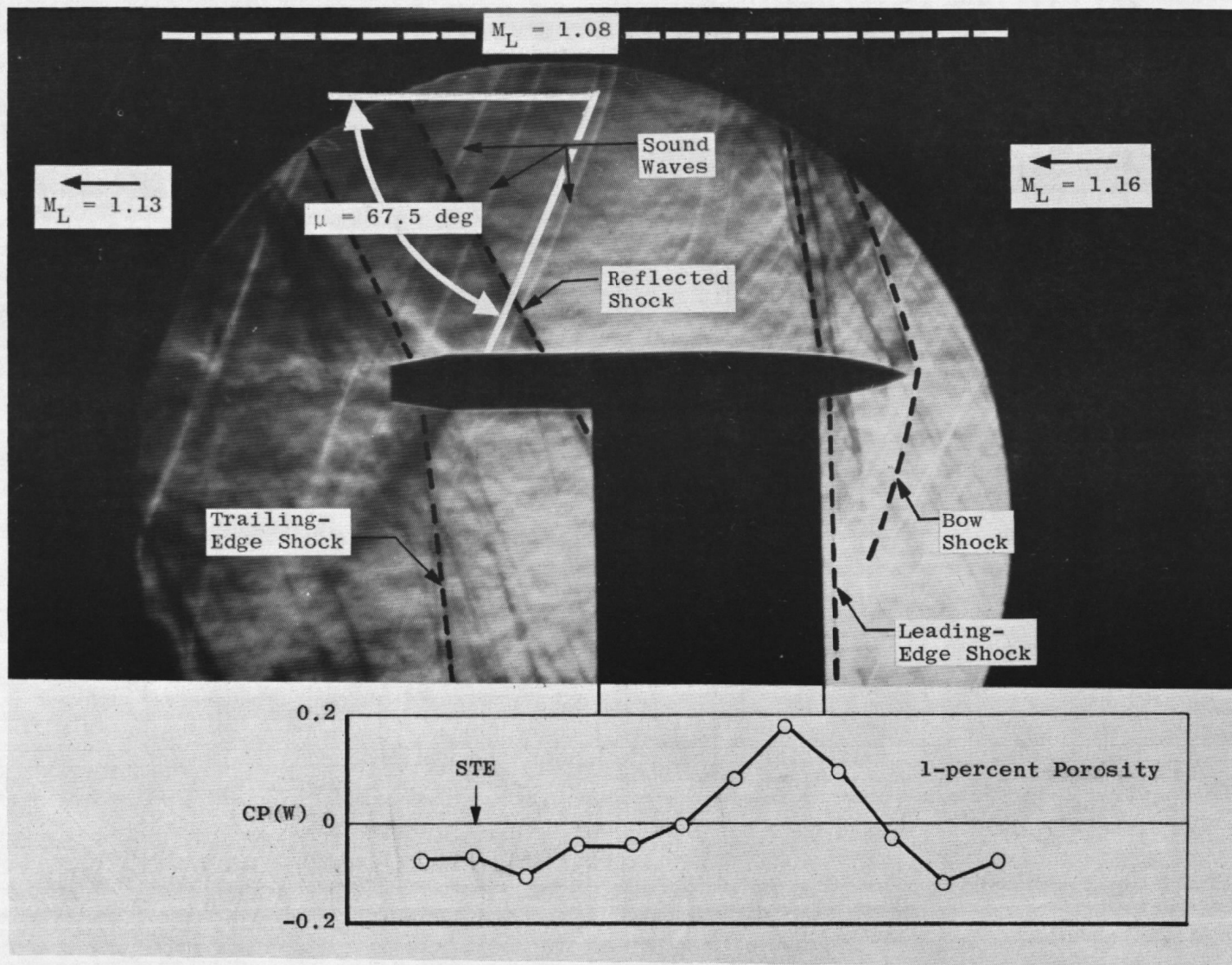


Figure 28. Schlieren photograph describing shocks generated by straight strut configuration, B2-S2L3.

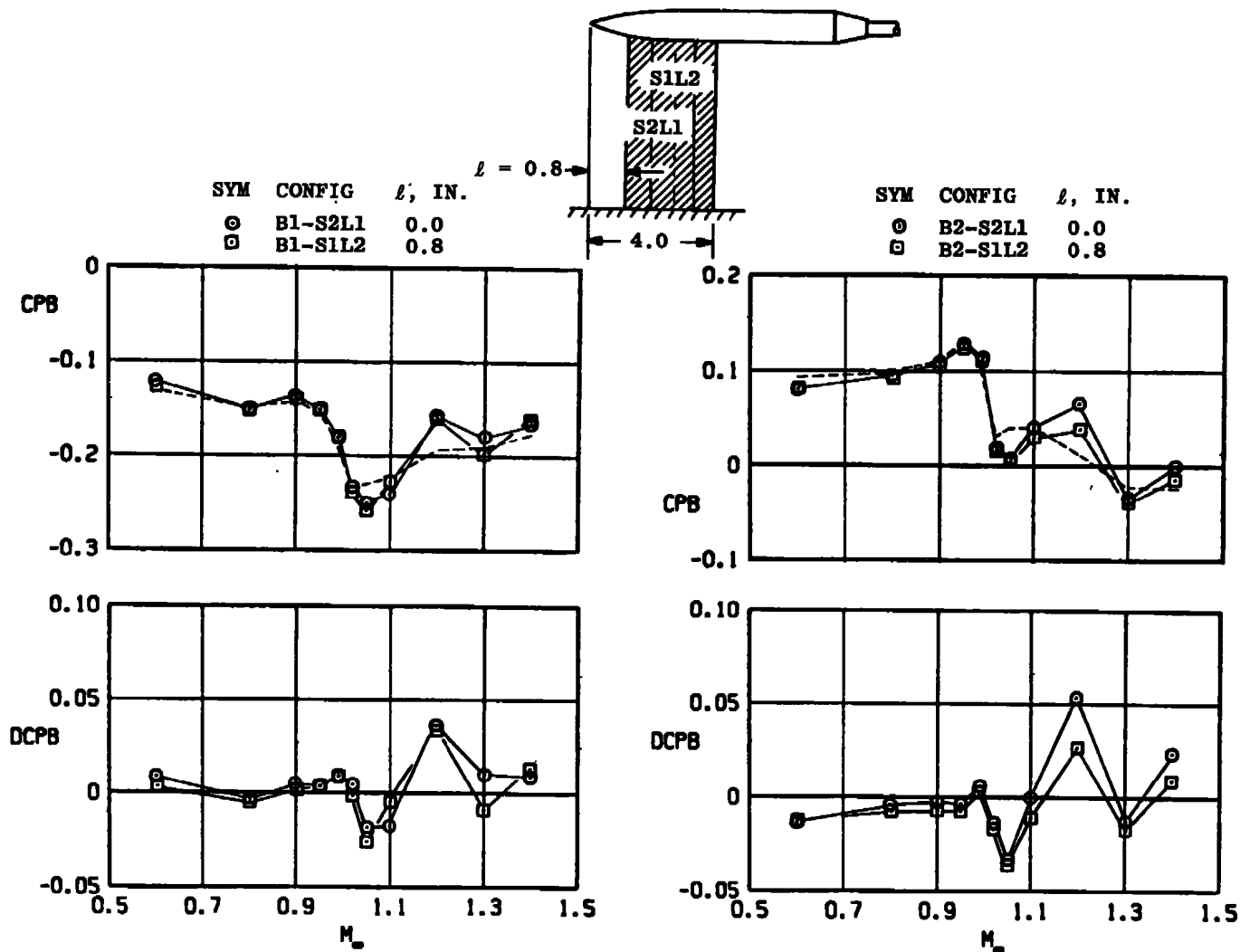


Figure 29. Effect of strut location on base pressure coefficient for cylindrical afterbody and 10-deg boattails (with trailing edge at same station).

SYM	CONFIG	l , IN.
○	B2-S2L1	0.0
□	B2-S1L2	0.8

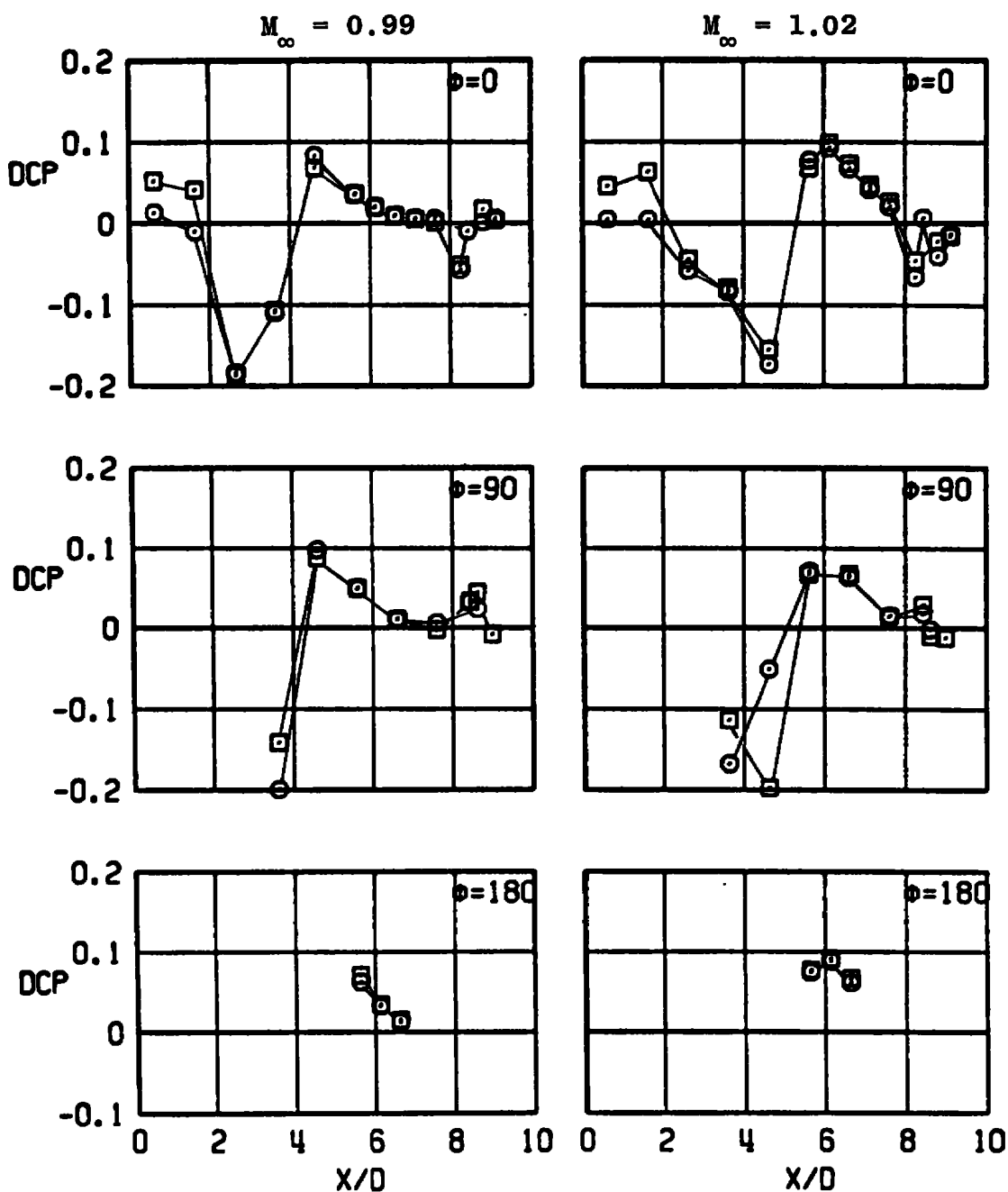


Figure 30. Effect of strut location on body pressure interference coefficients (with trailing edge at same station).

SYM	CONFIG	l , IN.
○	B2-S2L1	0.0
□	B2-S1L2	0.8

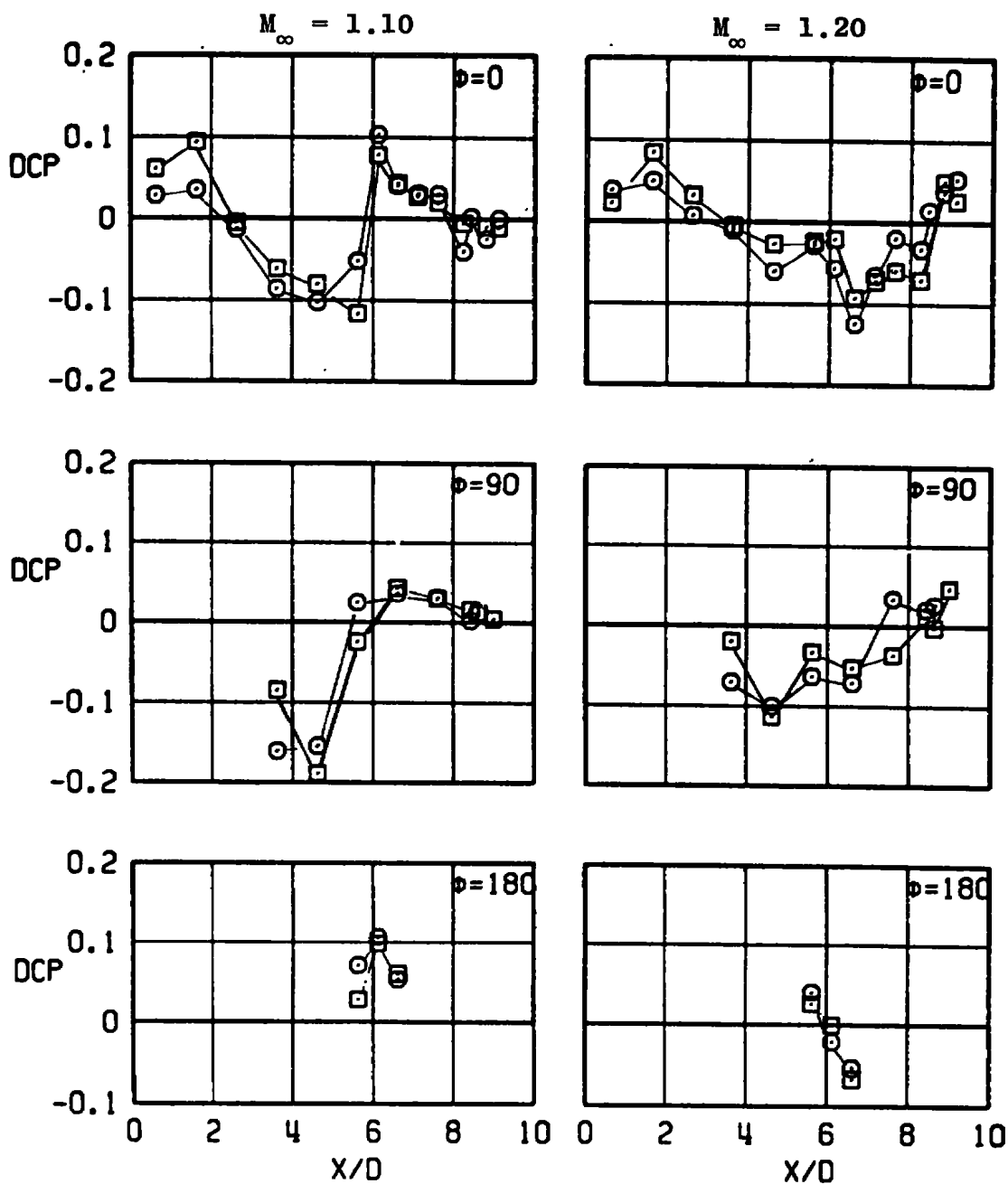


Figure 30. Concluded.

SYM	CONFIG	l , IN.
○	B2-S2L1	0.0
□	B2-S1L2	0.8

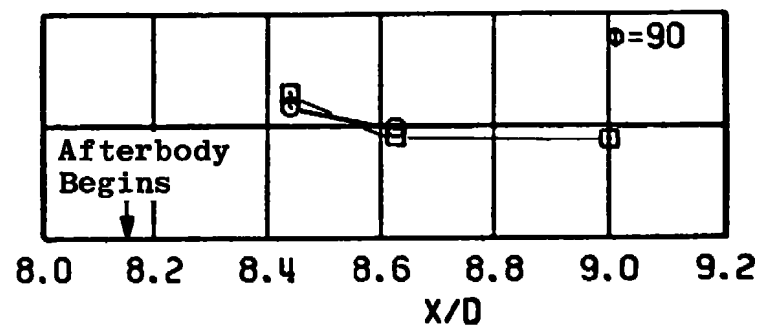
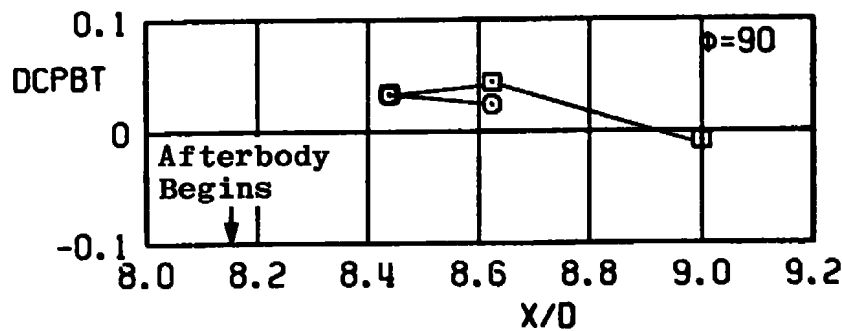
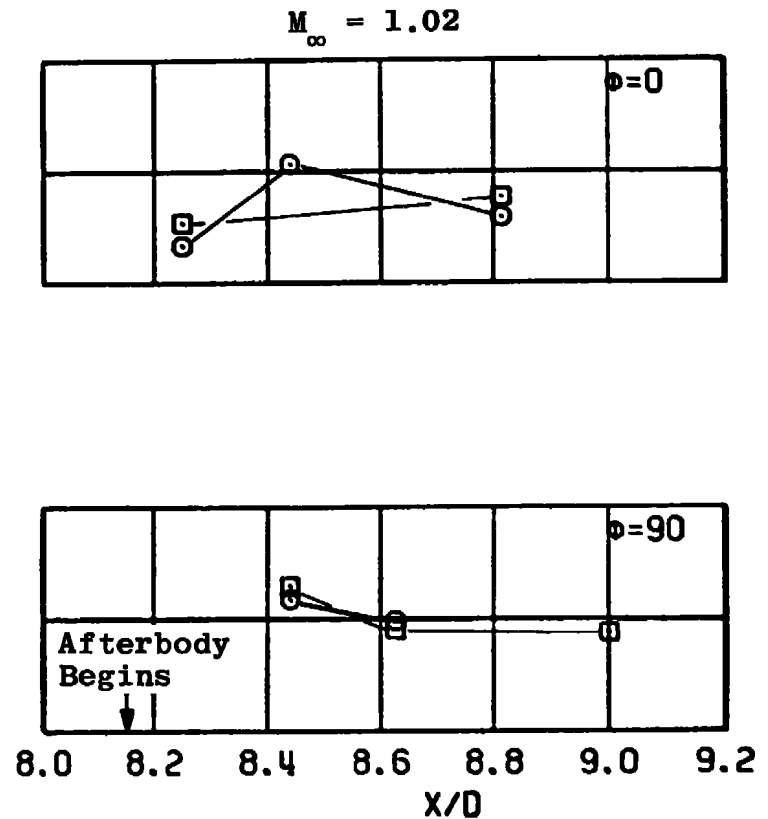
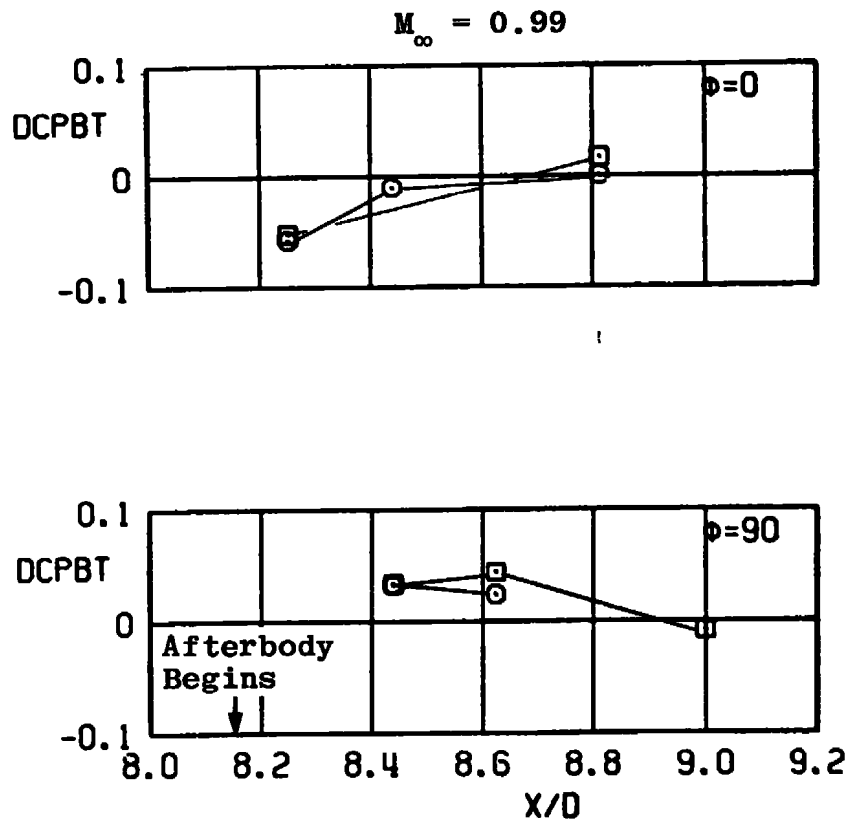


Figure 31. Effect of strut location on boattail interference coefficients (with strut trailing edge at same station).

SYM	CONFIG	l , IN.
○	B2-S2L1	0.0
□	B2-S1L2	0.8

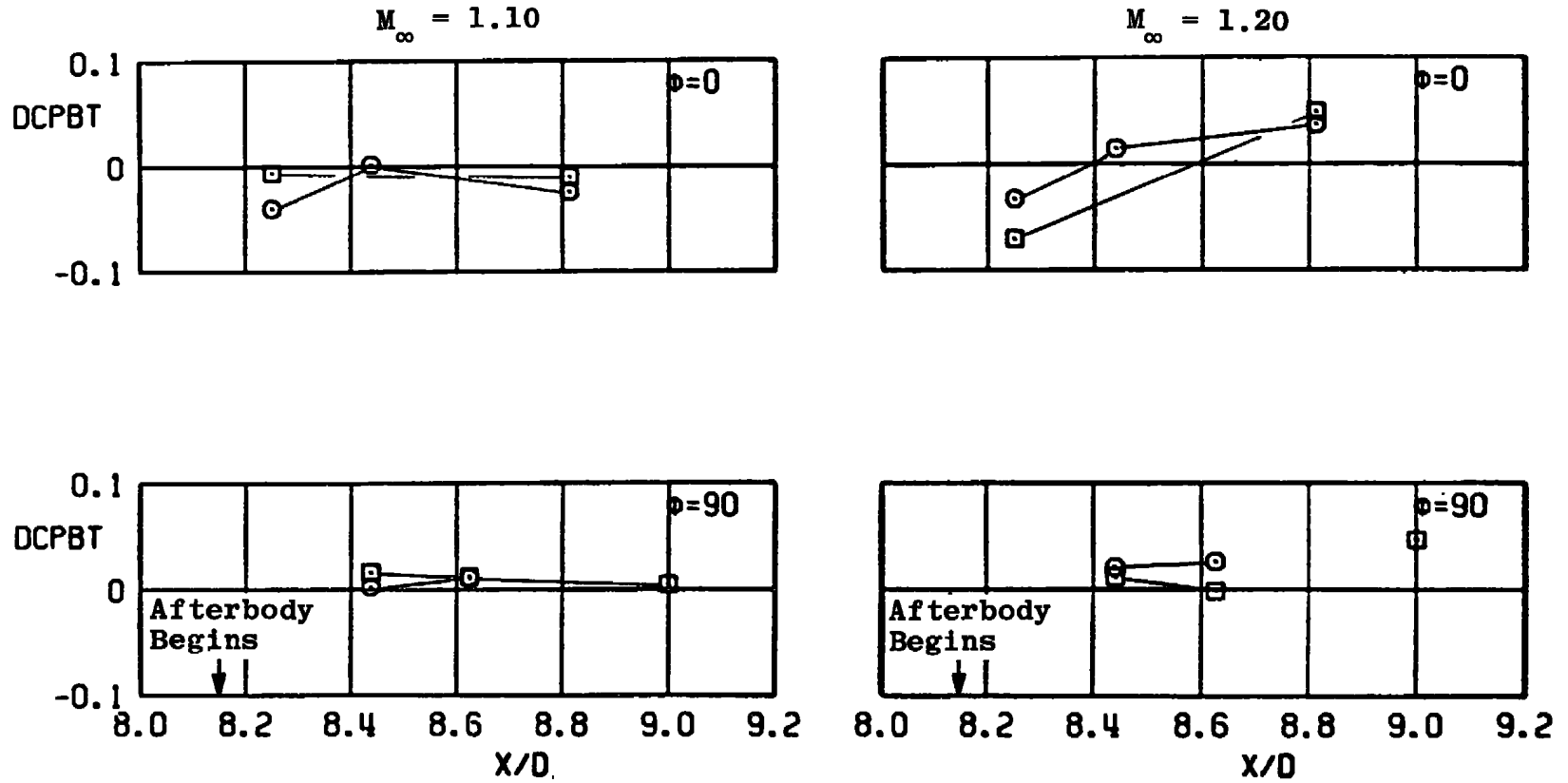


Figure 31. Concluded.

SYM	CONFIG	l , IN.	
□	B0-S1L1	0.0	Ref. 1 - Config C-I
○	B1-S1L2	0.8	
△	B0-S1L3	1.6	Ref. 1 - Config C-II

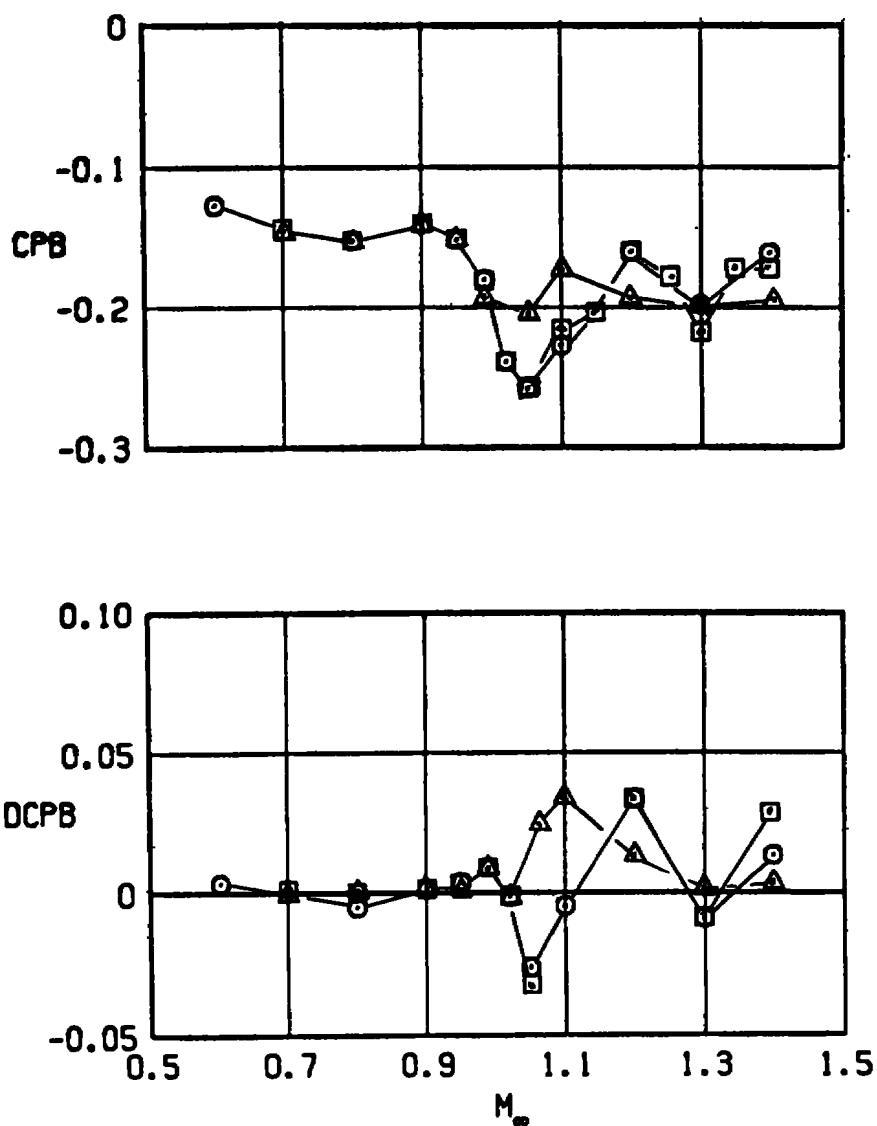


Figure 32. Effect of strut position on base pressure coefficient.

SYM	CONFIG	l , IN.	ϕ_{BT} , DEG
○	B1-S3L1	0.0	0.0
□	B2-S3L1	0.0	10.0

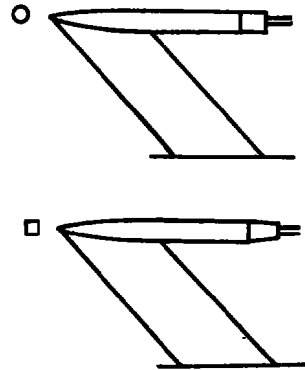
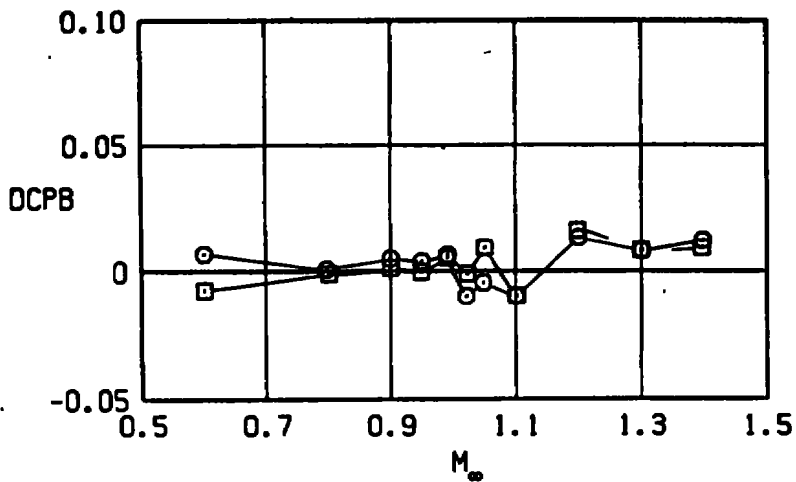
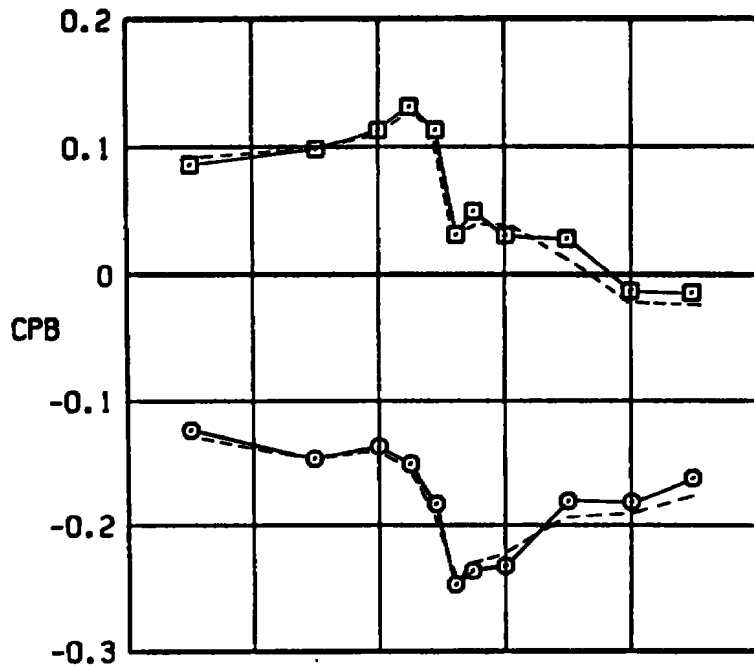


Figure 33. Effect of boattail angle on base pressure interference coefficient for two swept strut locations.

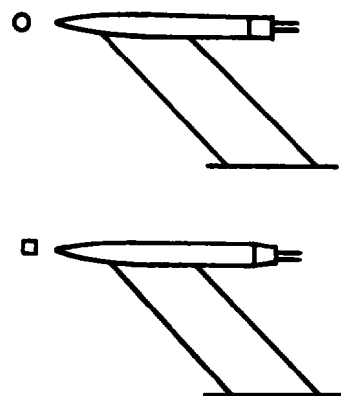
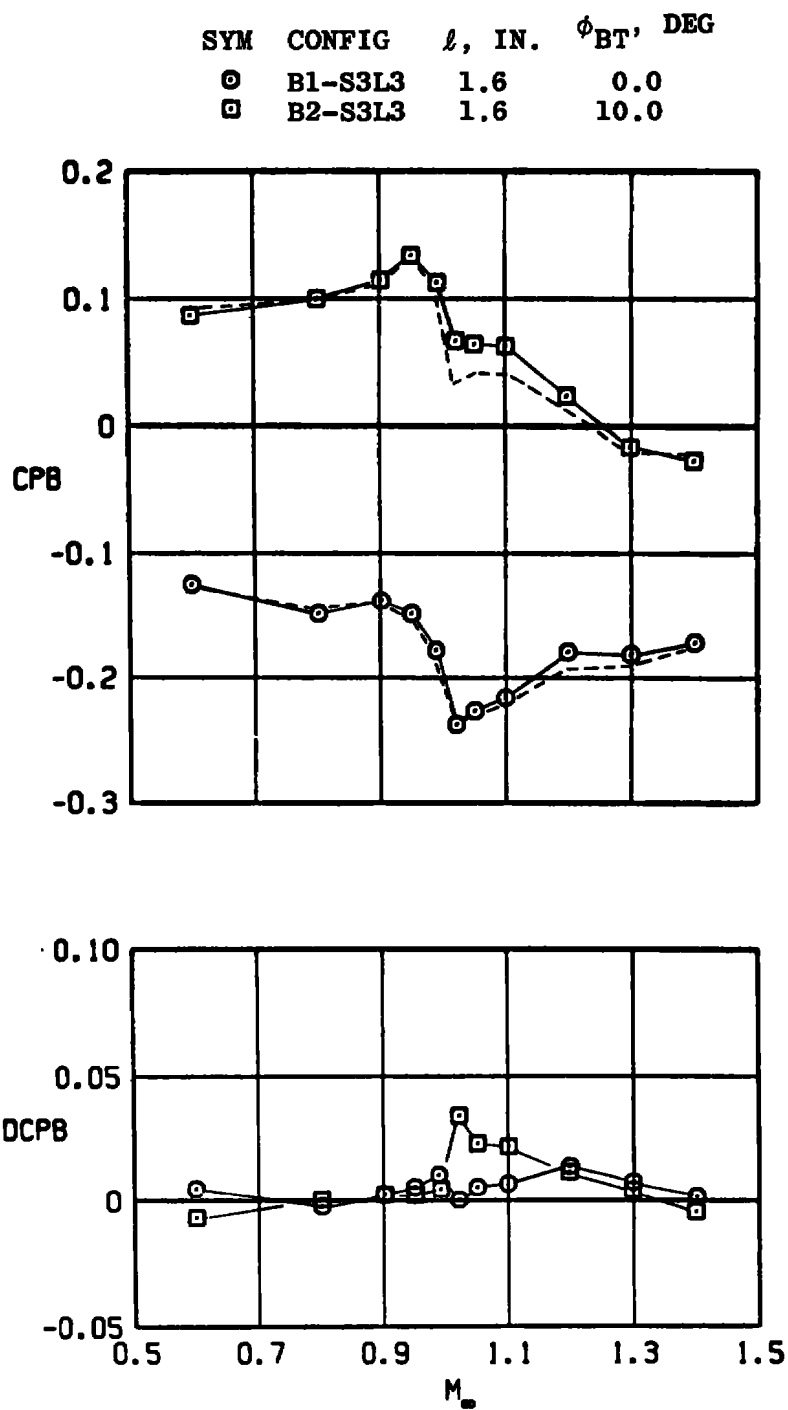


Figure 33. Concluded.

SYM	CONFIG	ℓ , IN.
○	B2-S3L1	0.0
□	B2-S3L3	1.6

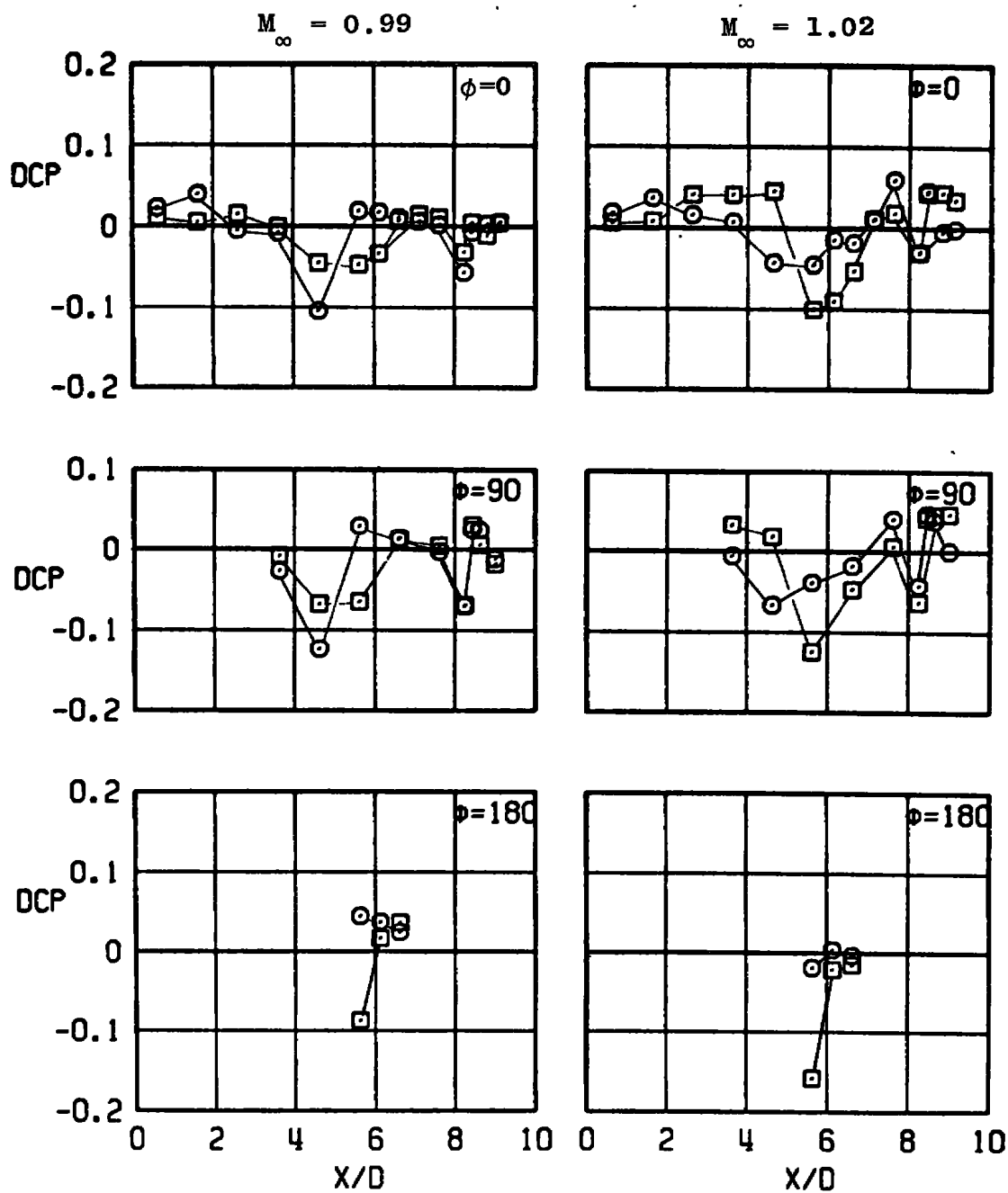


Figure 34. Effect of swept strut location on body interference coefficient.

SYM	CONFIG	ℓ , IN.
○	B2-S3L1	0.0
□	B2-S3L3	1.6

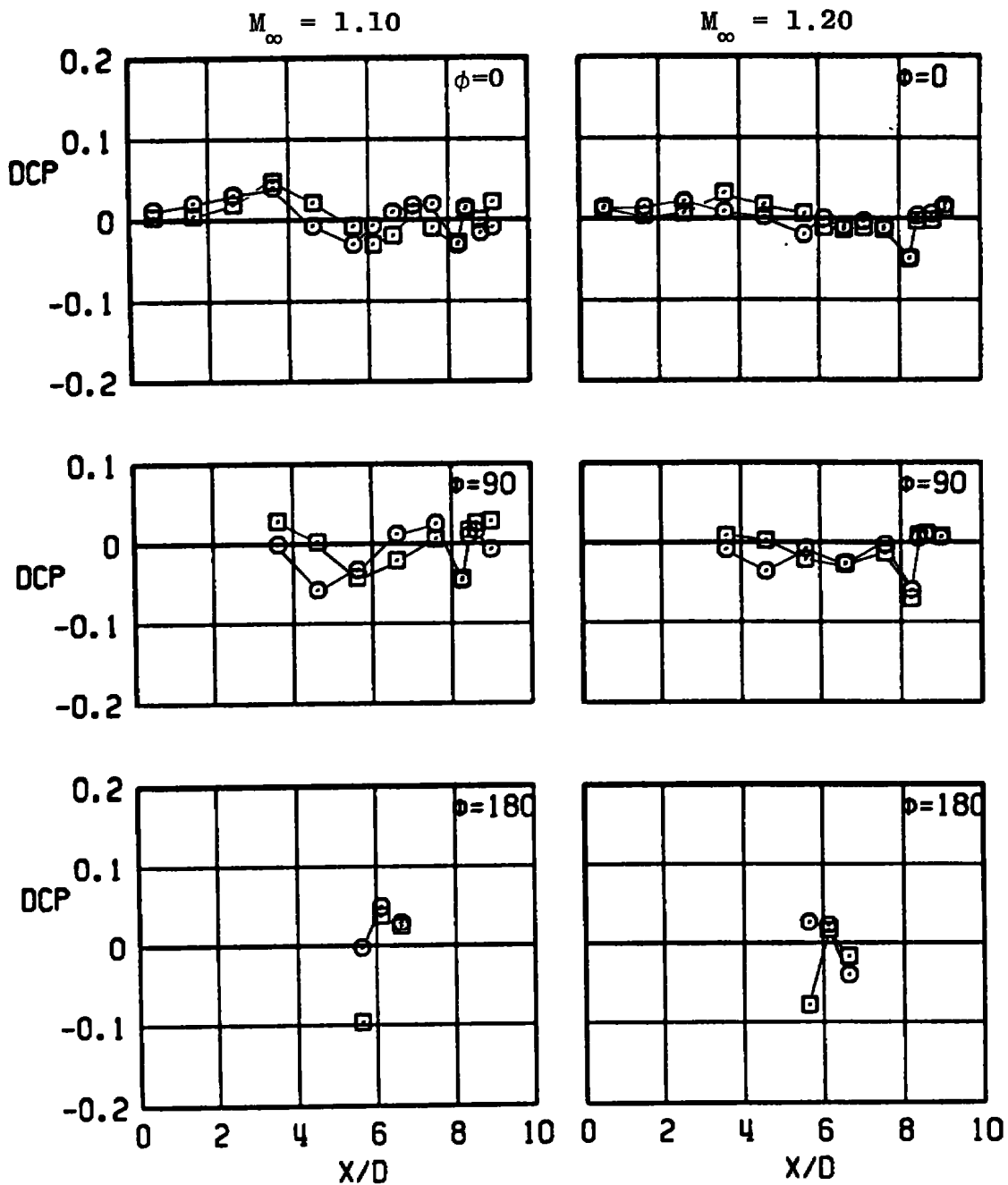


Figure 34. Concluded.

SYM	CONFIG	ℓ , IN.
○	B1-S3L1	0.0
□	B1-S3L3	1.6

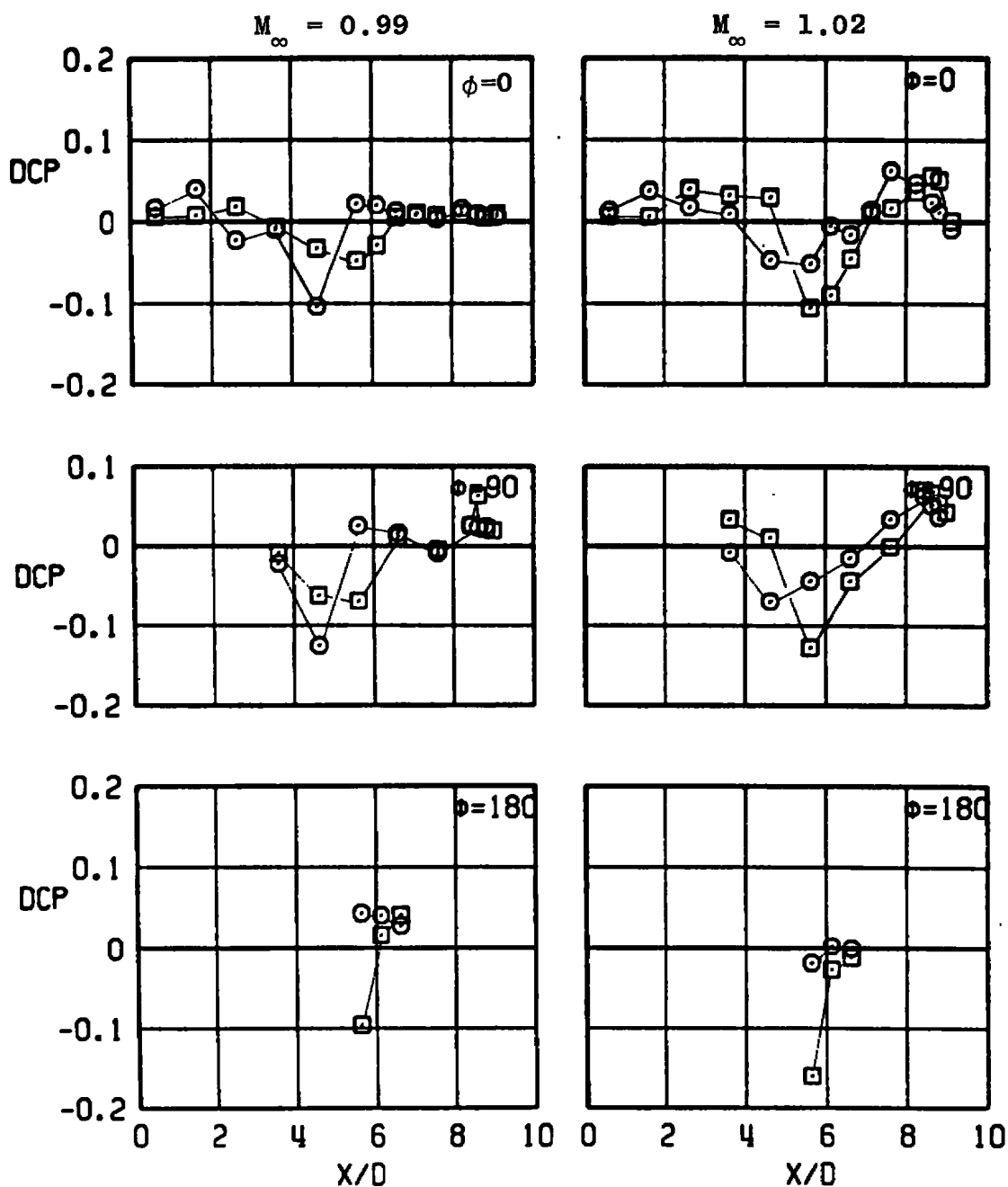
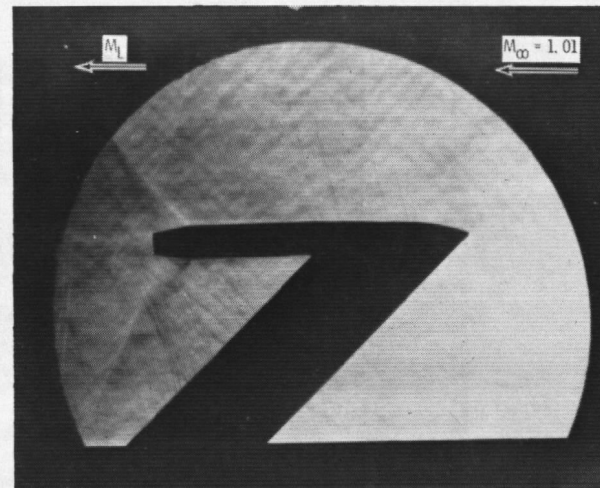
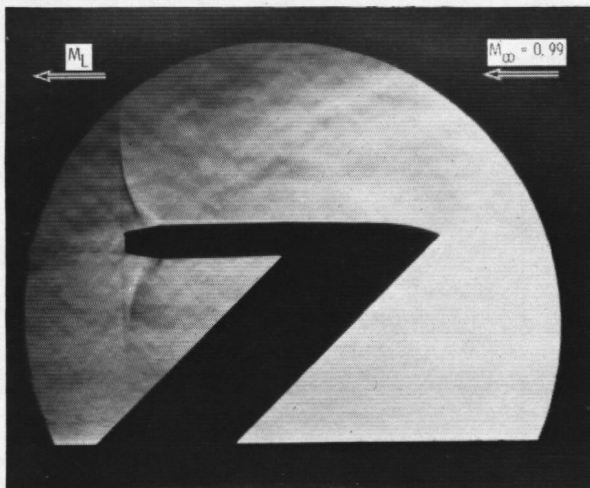
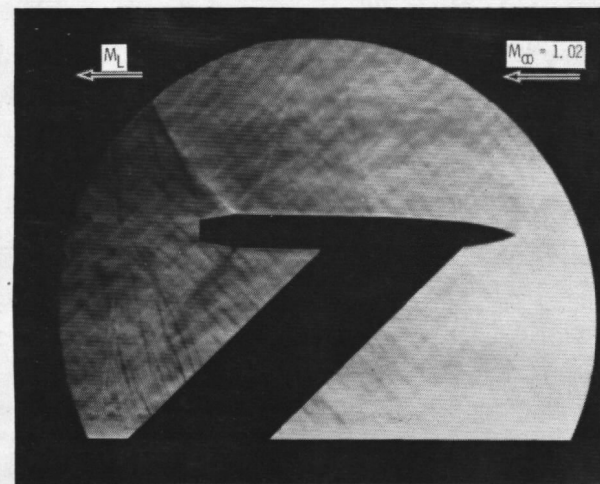
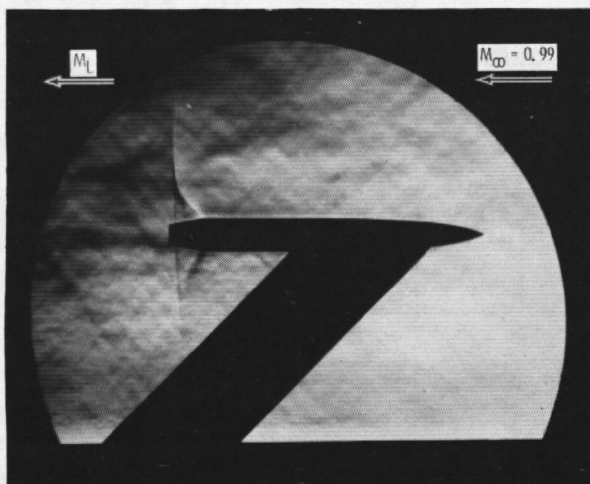


Figure 35. Effect of swept strut location with cylindrical afterbody.



S3L1



S3L3

Figure 36. Schlieren photographs for 45-deg swept strut located at $\ell/D = 0$ and 1.6.

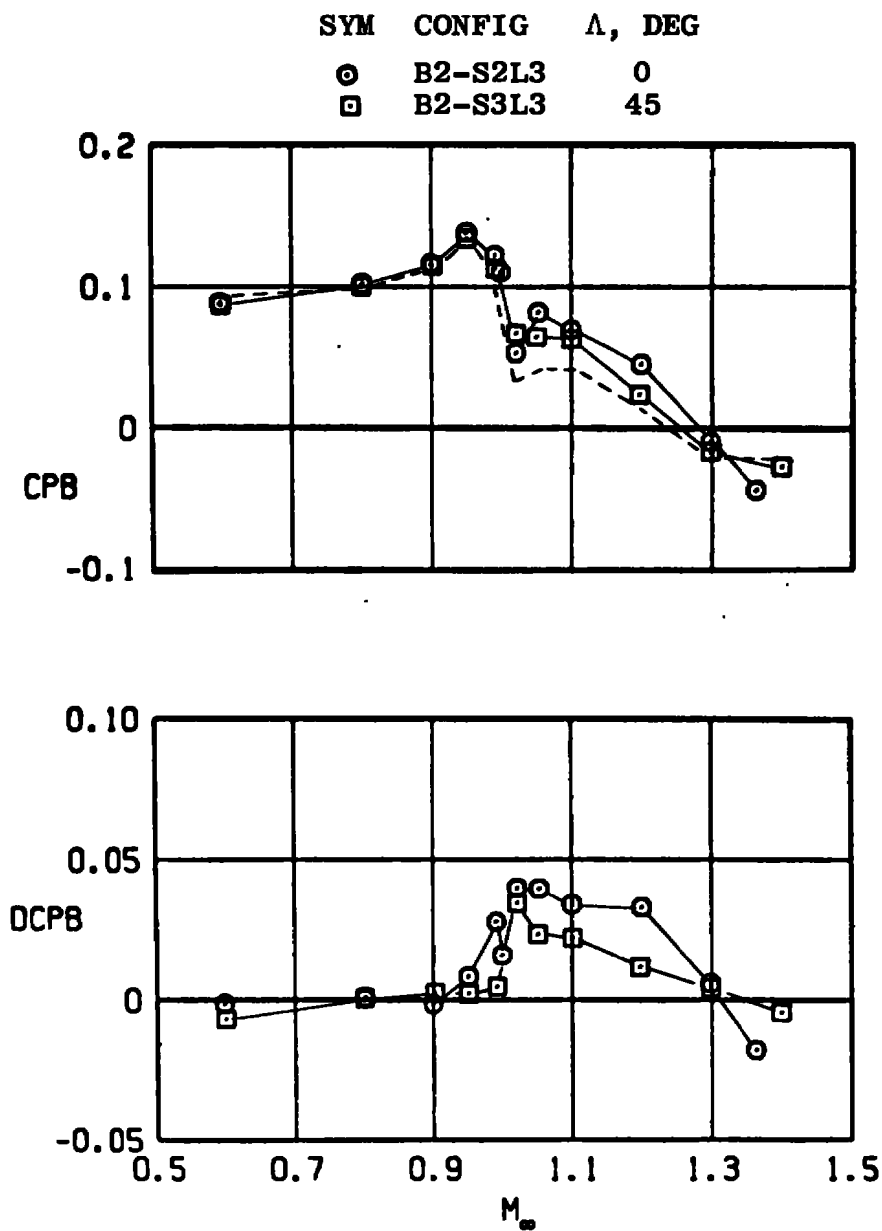


Figure 37. Effect of sweep angle on base pressure coefficient with struts located at downstream position, $l/D = 1.6$.

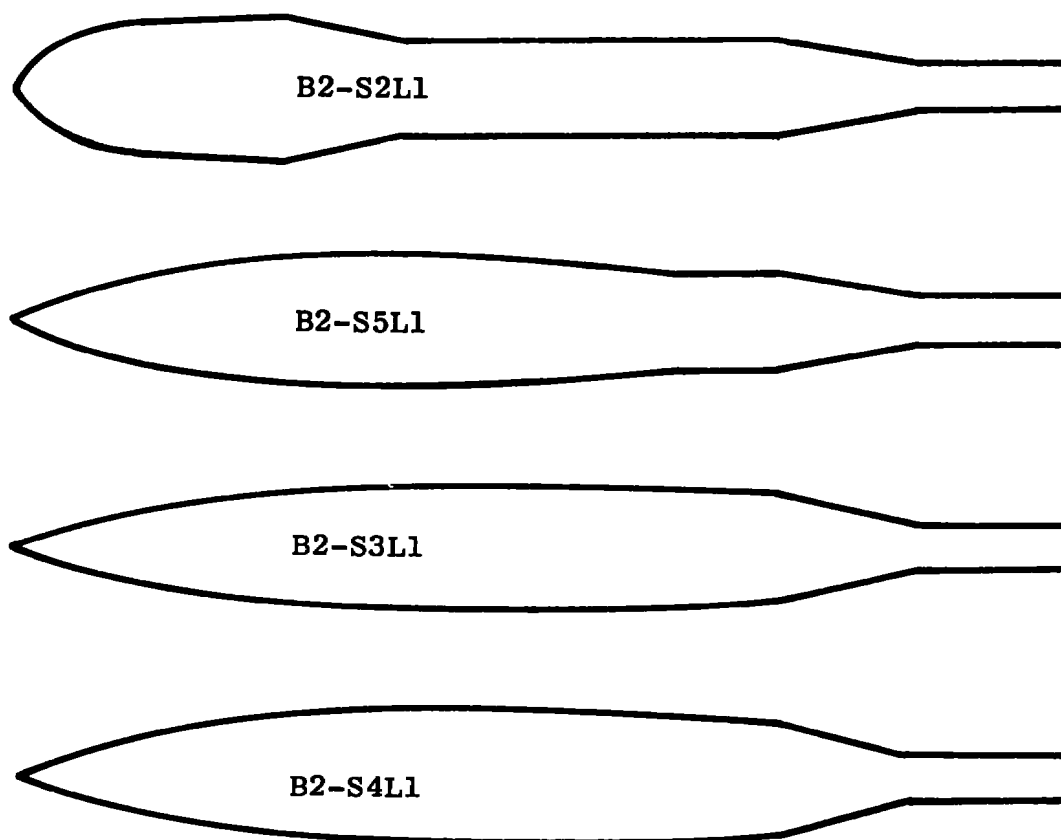


Figure 38. Equivalent body shapes for body plus strut cross-sectional areas.

SYM	CONFIG
○	B2-S3L1
□	B2-S4L1

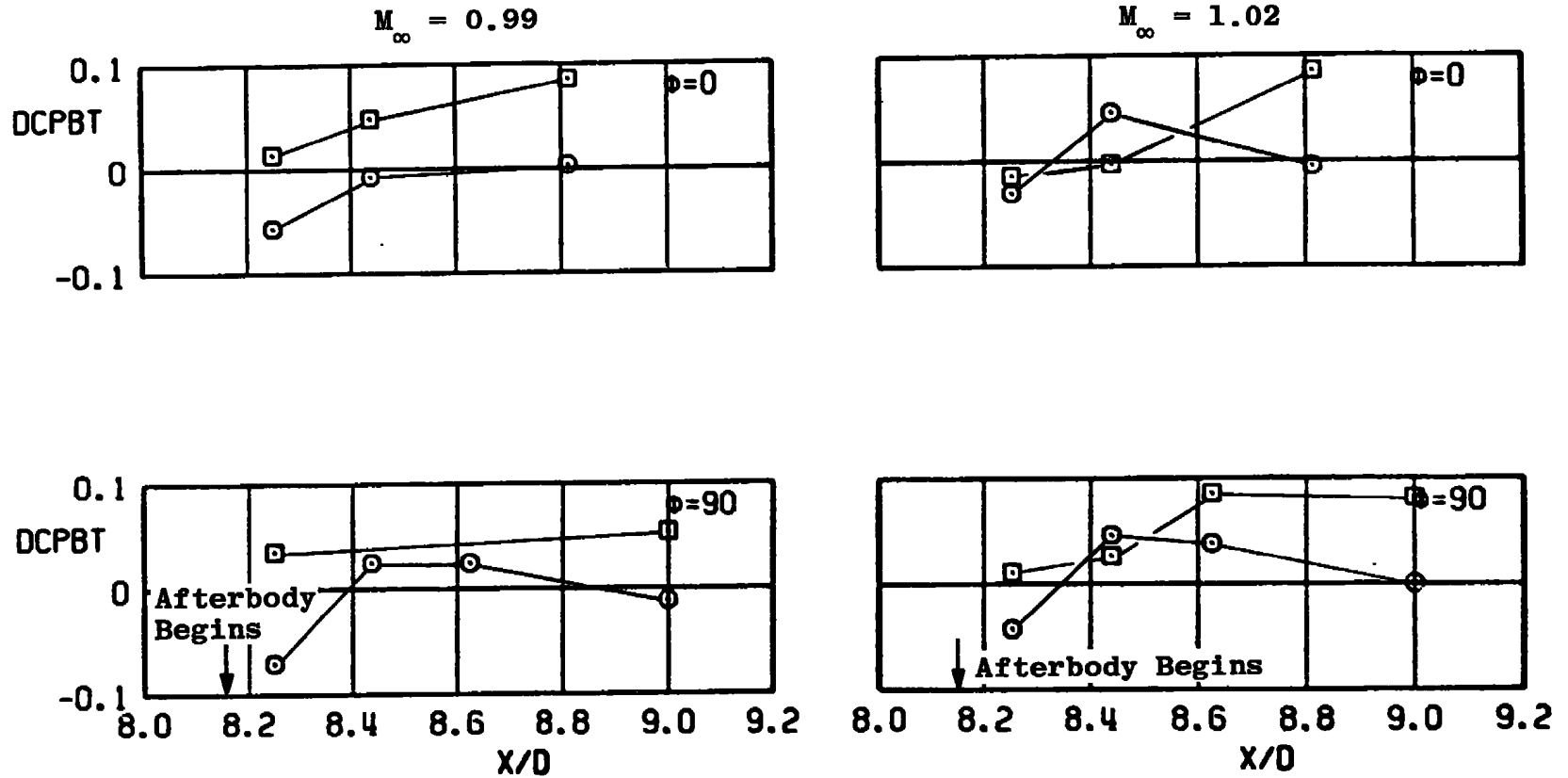


Figure 39. Influence of strut trailing-edge design on boattail pressure interference coefficients.

SYM	CONFIG
○	B2-S3L1
□	B2-S4L1

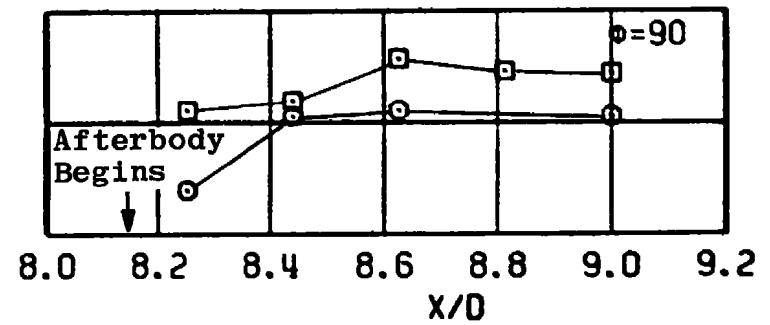
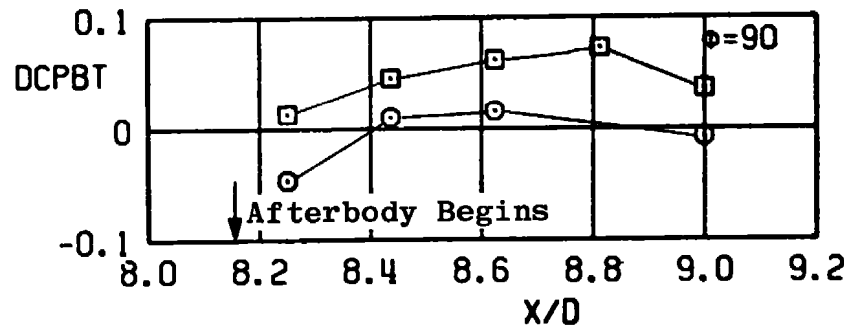
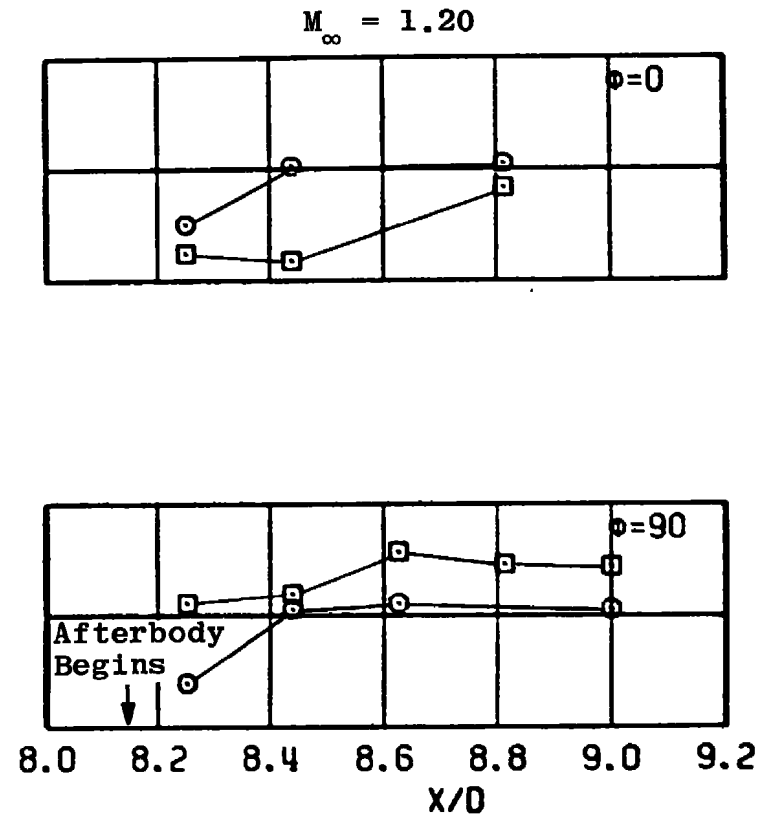
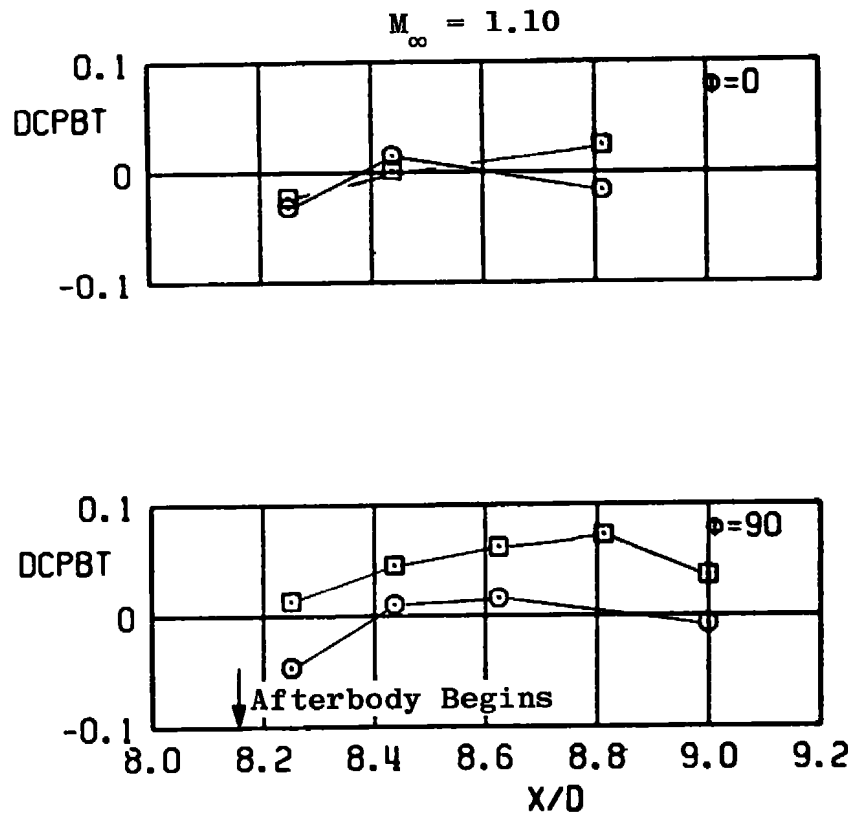


Figure 39. Concluded.

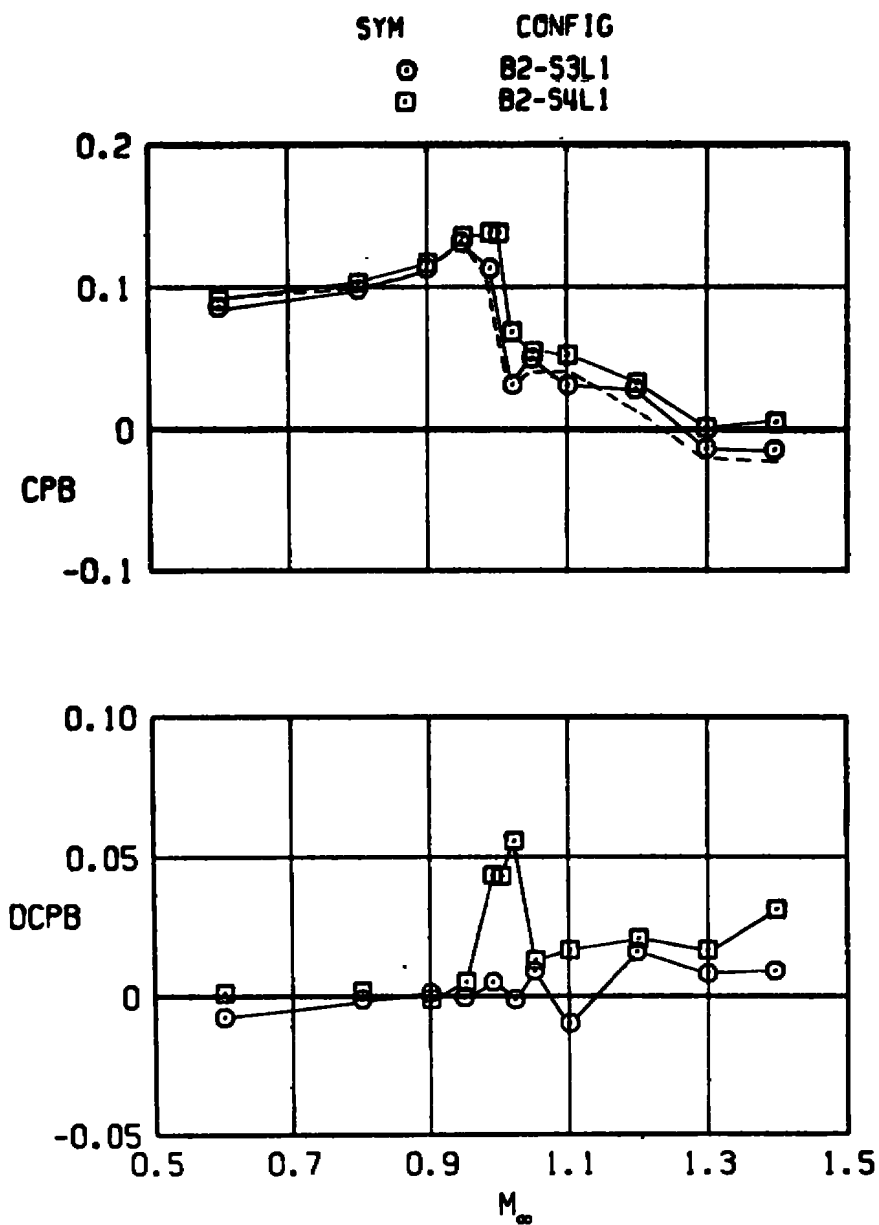


Figure 40. Effect of swept strut trailing-edge design on base pressure interference coefficients.

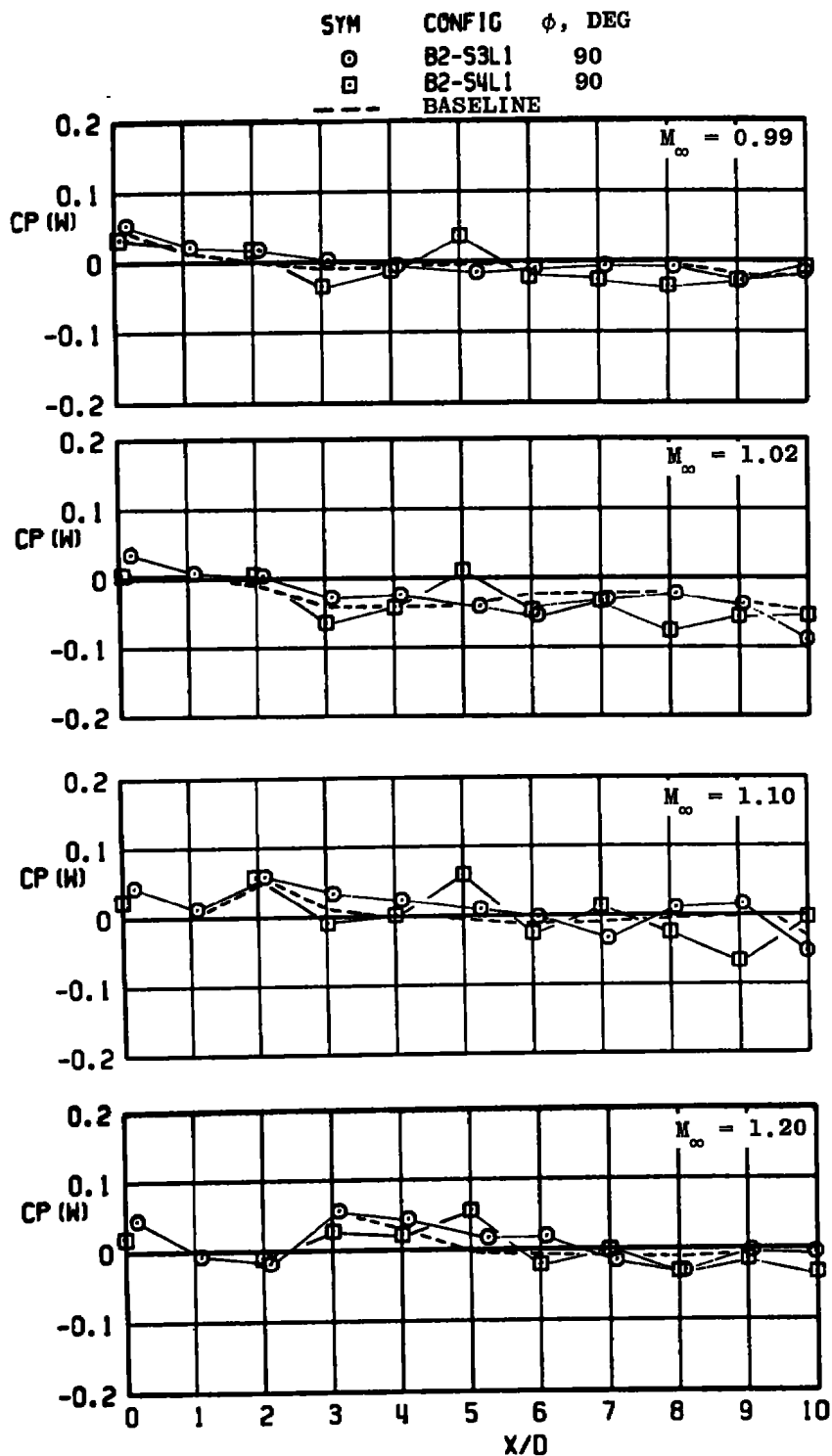


Figure 41. Effect of swept strut trailing-edge design on wall pressure coefficient distribution ($\phi = 90$ deg).

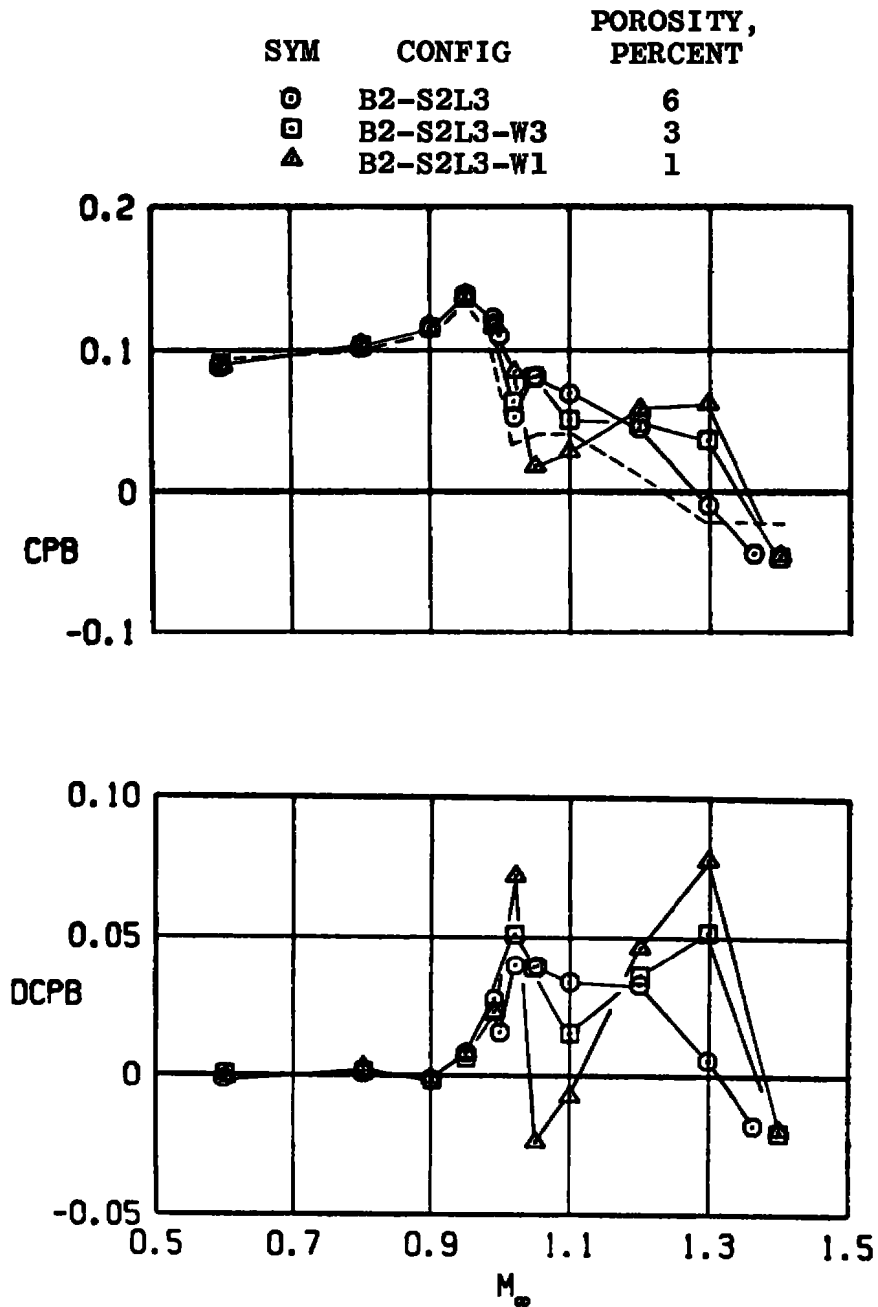


Figure 42. Effect of local wall porosity on base pressure coefficient.

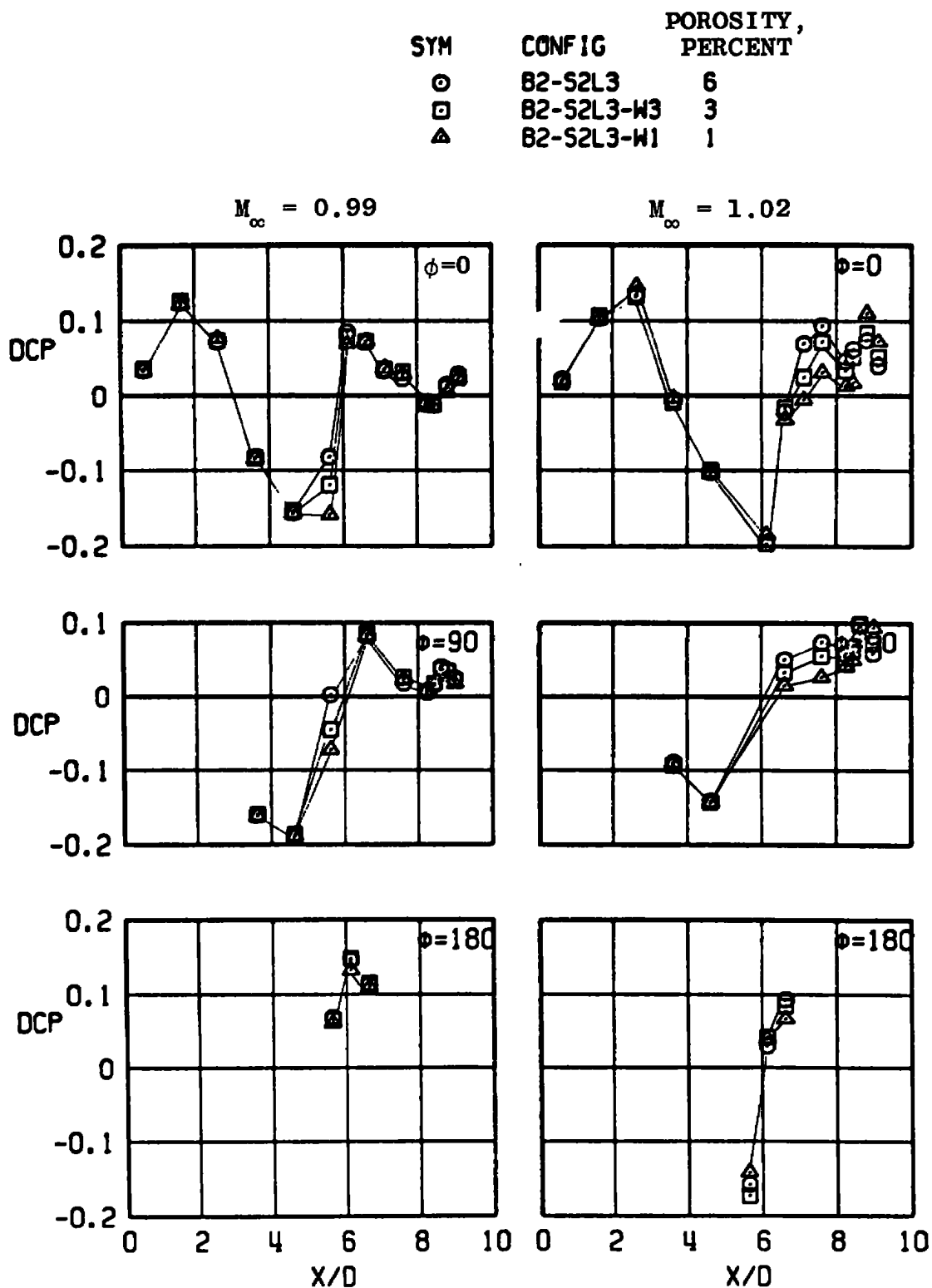


Figure 43. Effect of local wall porosity on body pressure interference coefficient.

SYM	CONFIG	POROSITY, PERCENT
○	B2-S2L3	6
□	B2-S2L3-W3	3
△	B2-S2L3-W1	1

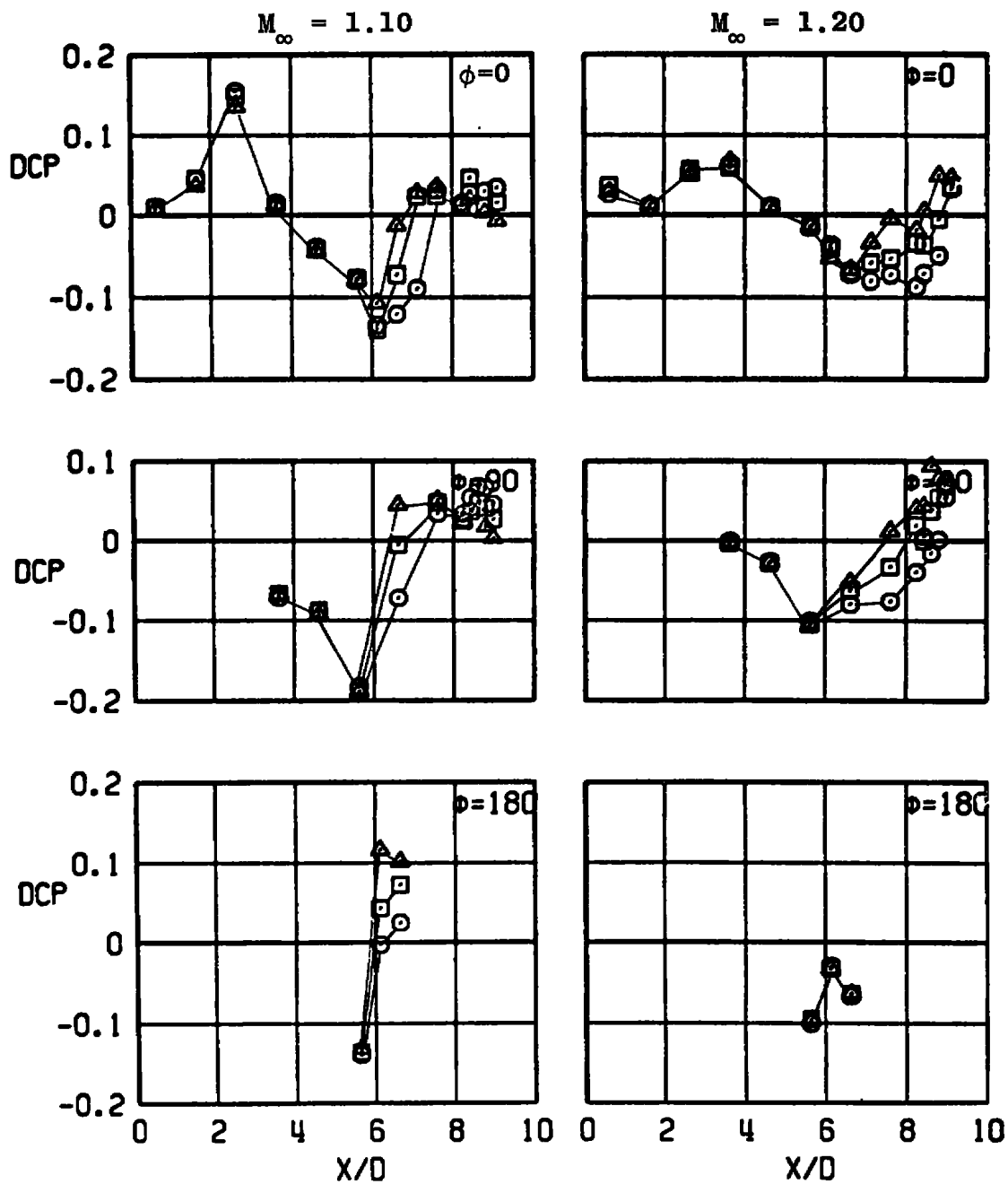


Figure 43. Concluded.

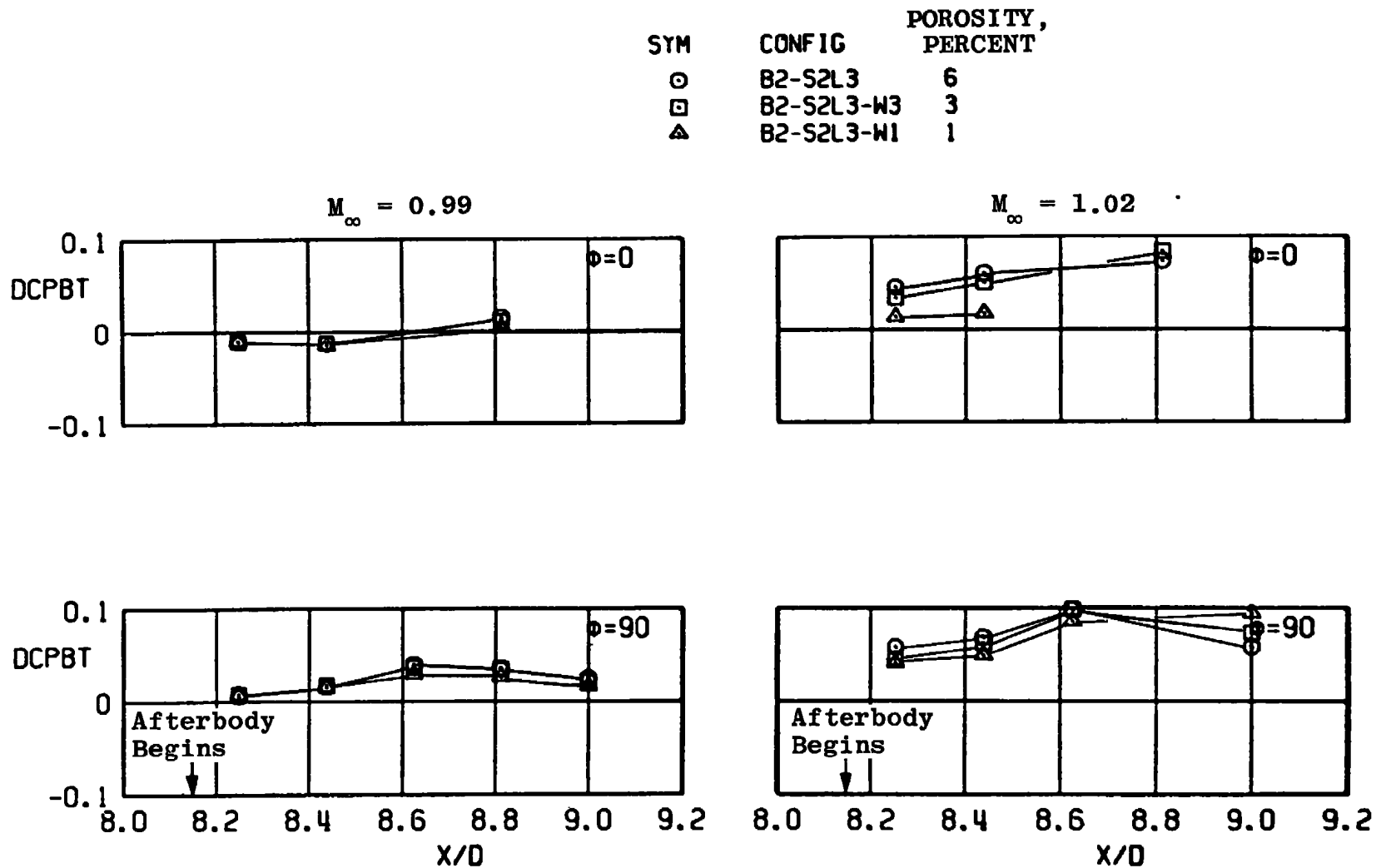


Figure 44. Effect of local wall porosity on boattail pressure interference coefficient.

SYM	CONFIG	POROSITY, PERCENT
○	B2-S2L3	6
□	B2-S2L3-W3	3
△	B2-S2L3-W1	1

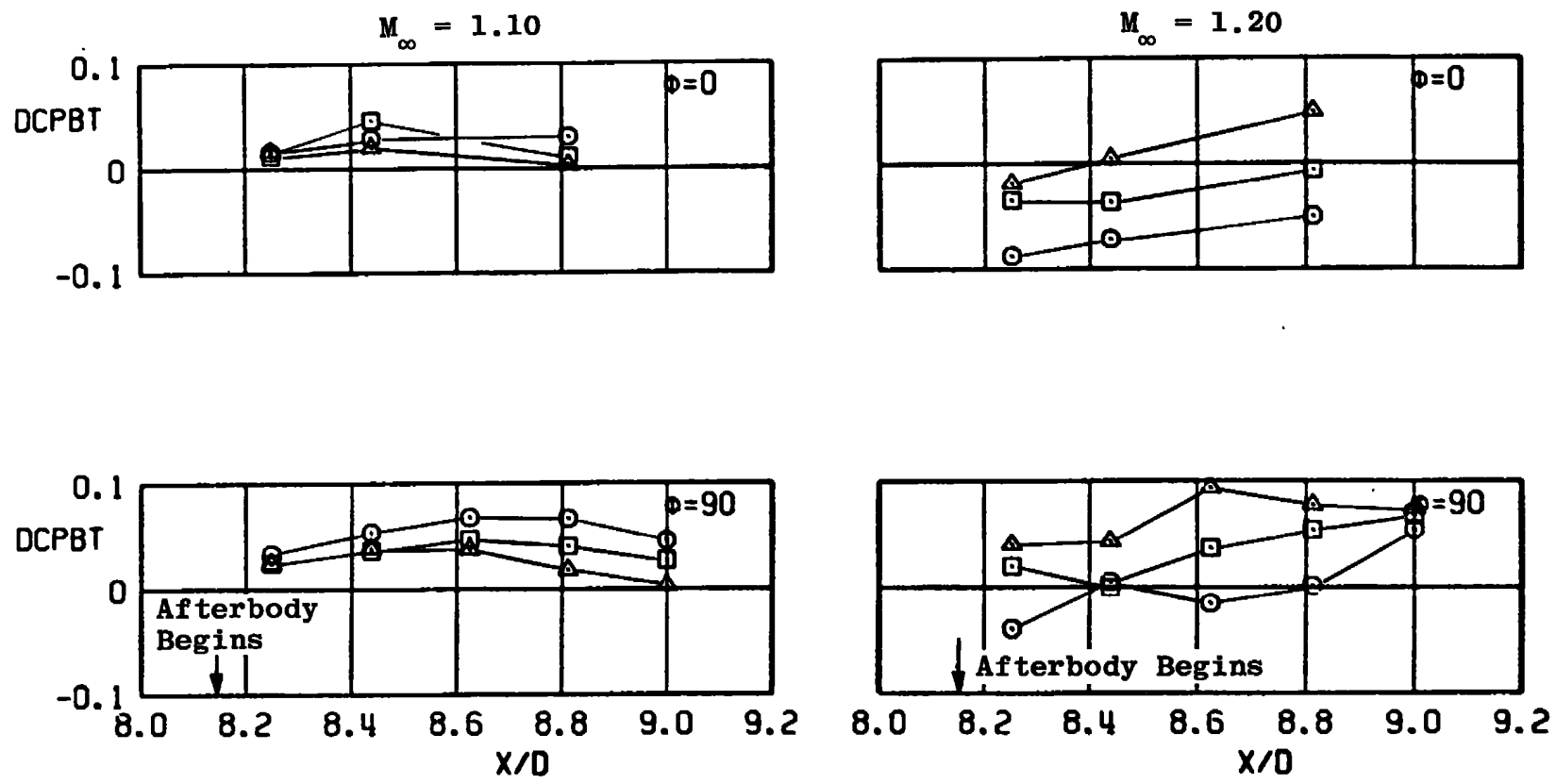


Figure 44. Concluded.

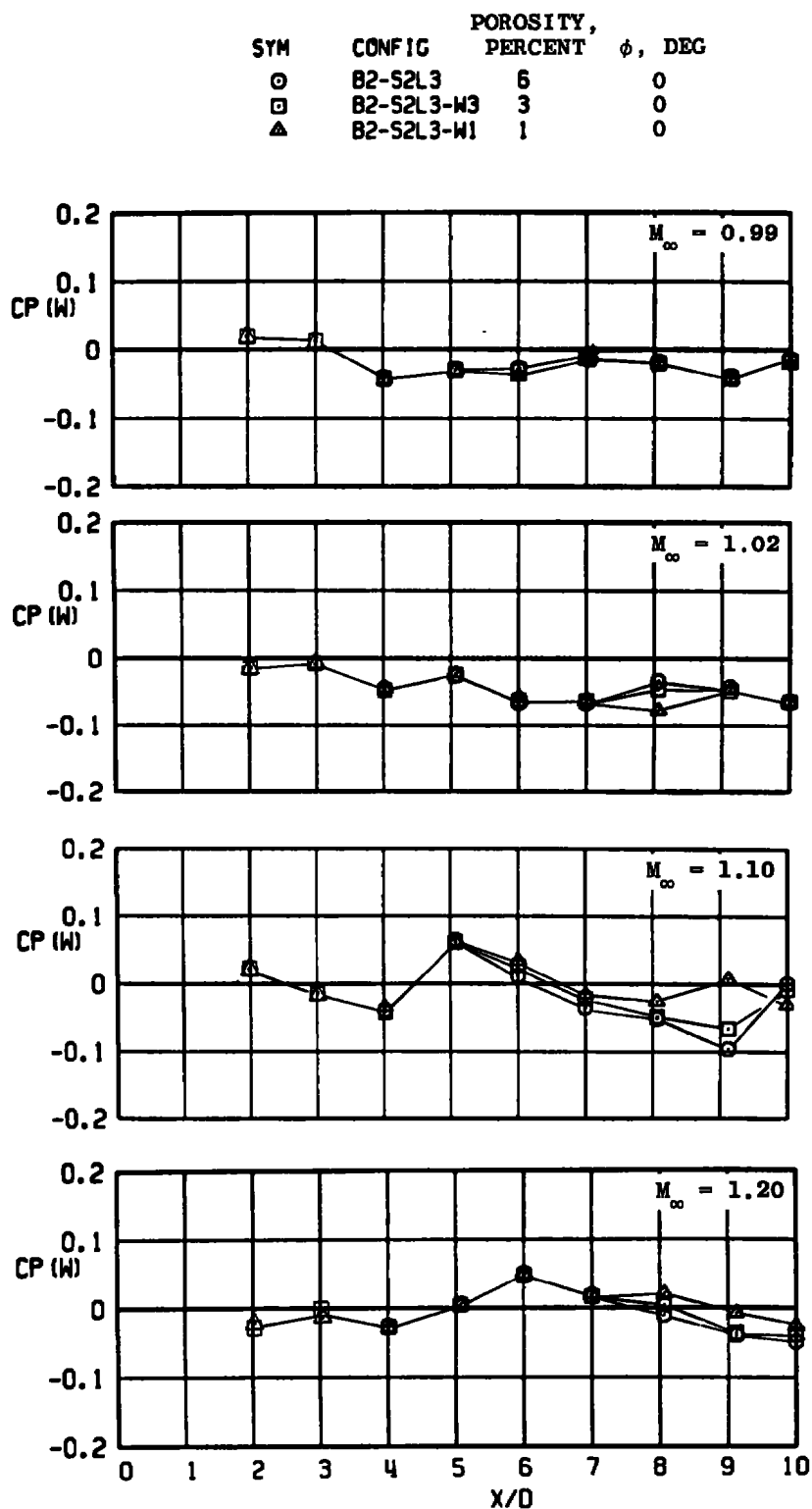


Figure 45. Effect of local wall porosity on wall pressure coefficient.

SYM	CONFIG	POROSITY, PERCENT	ϕ , DEG
○	B2-S2L3	6	90
□	B2-S2L3-W3	3	90
△	B2-S2L3-W1	1	90

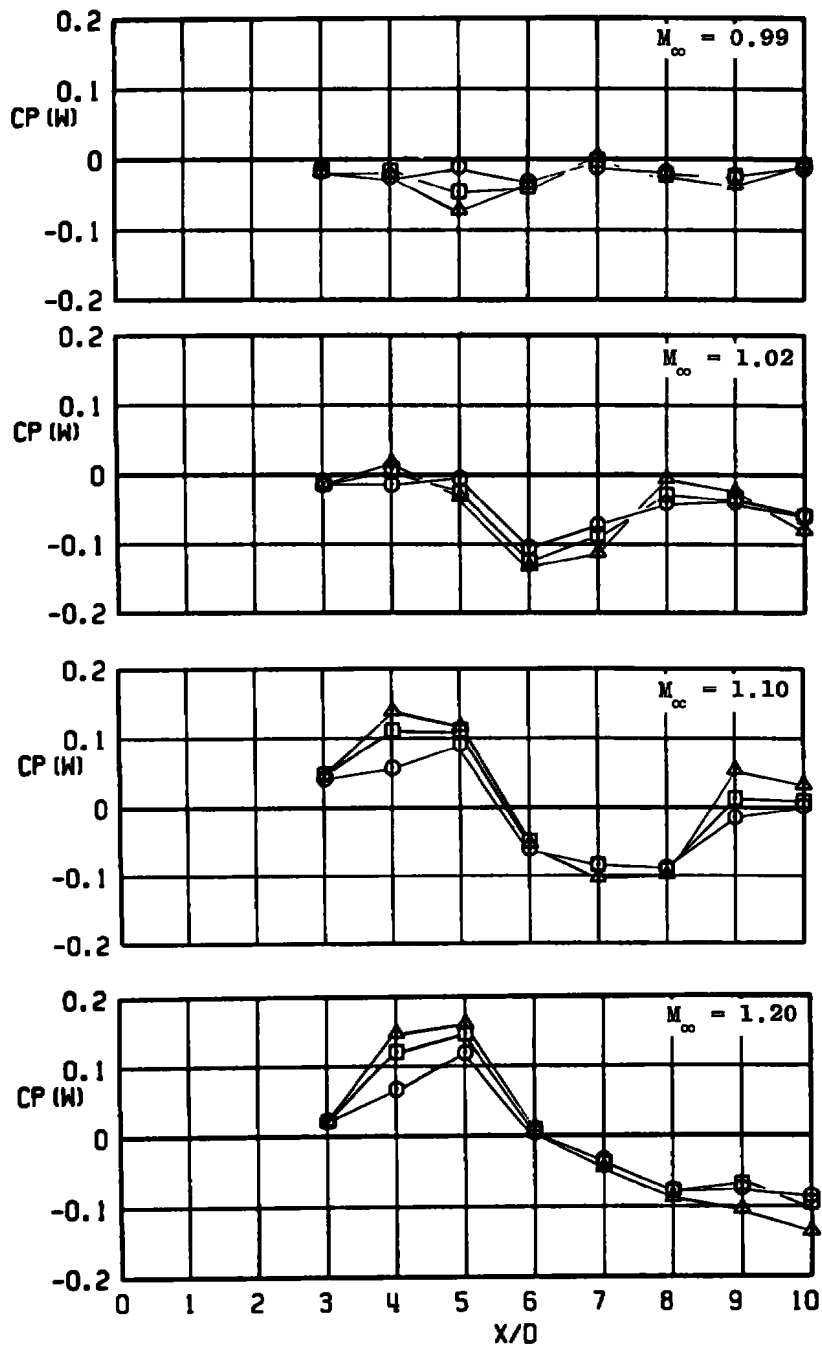


Figure 45. Concluded.

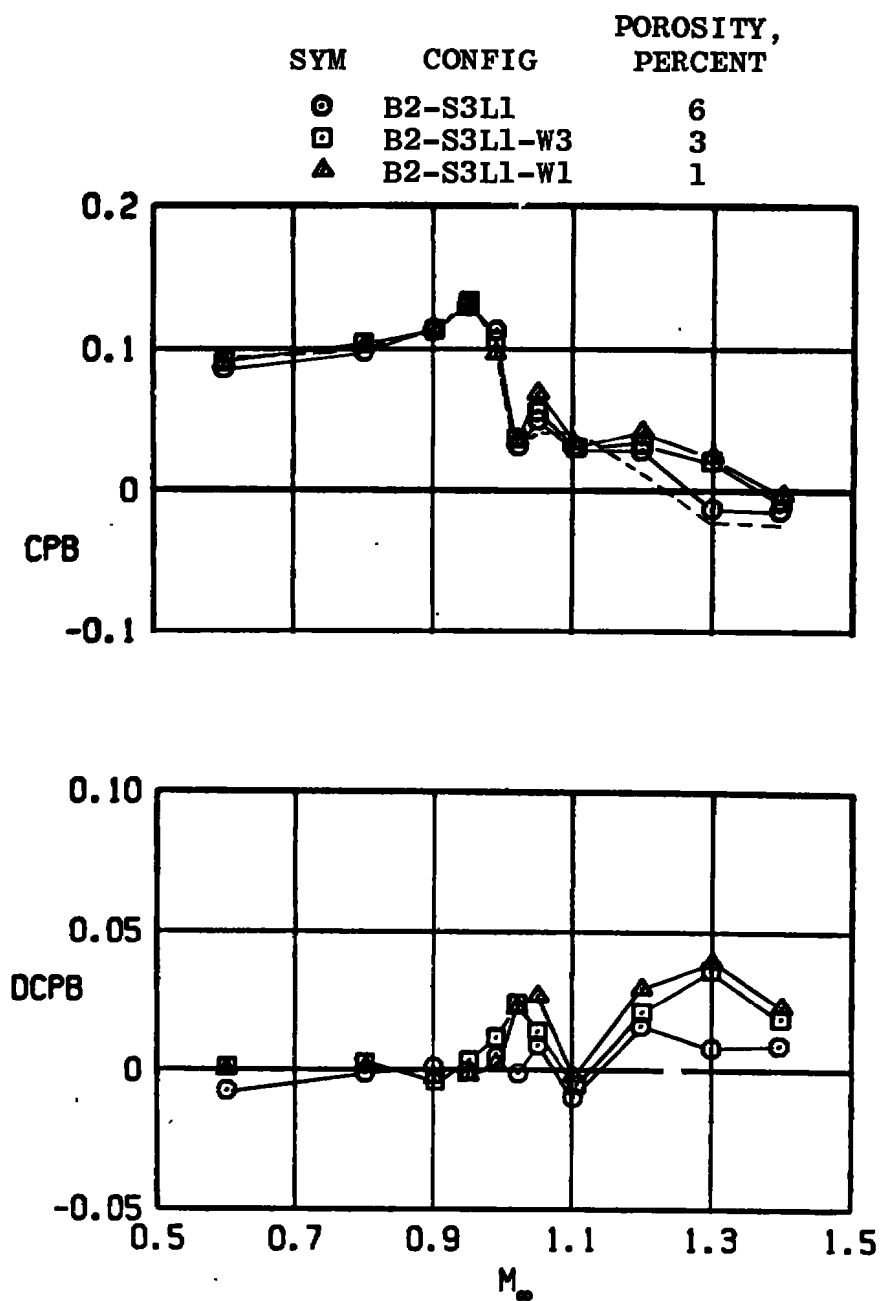


Figure 46. Effect of local wall porosity on base pressure coefficient for swept strut, S3L1.

SYM	CONFIG	POROSITY, PERCENT
○	B2-S3L1	6
□	B2-S3L1-W3	3
△	B2-S3L1-W1	1

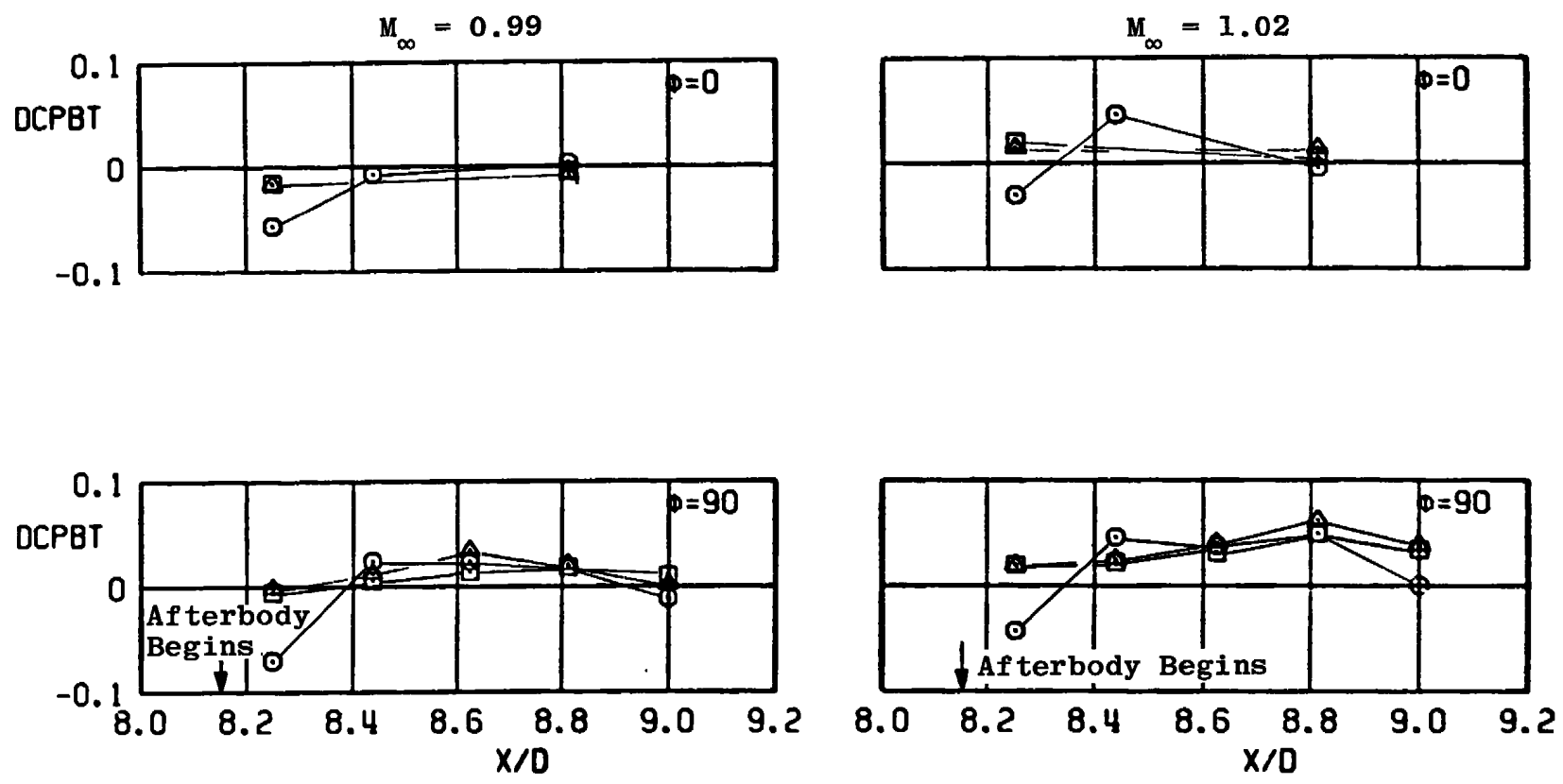


Figure 47. Effect of local wall porosity on boattail pressure interference coefficient for swept strut, S3L1.

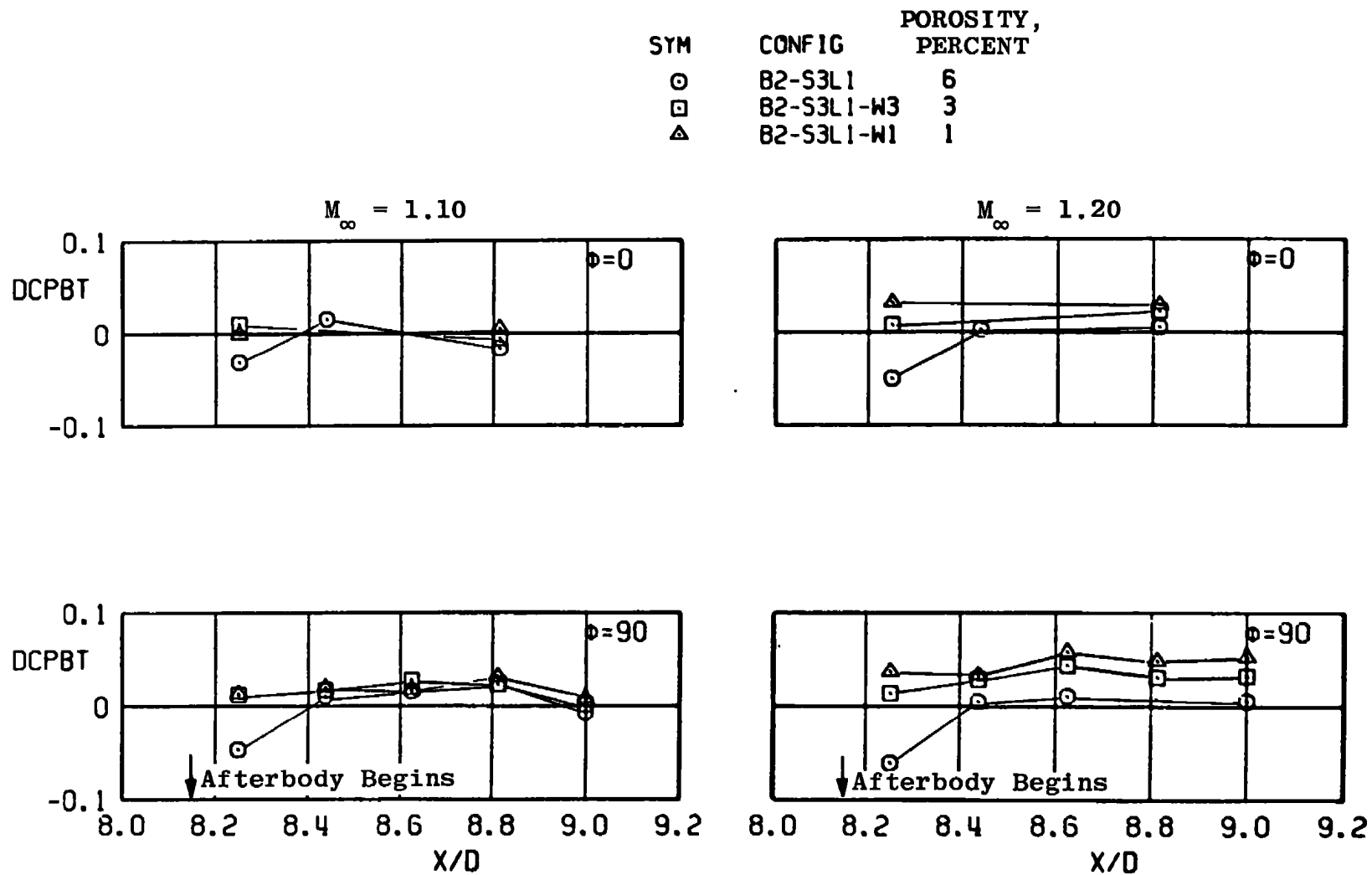


Figure 47. Concluded.

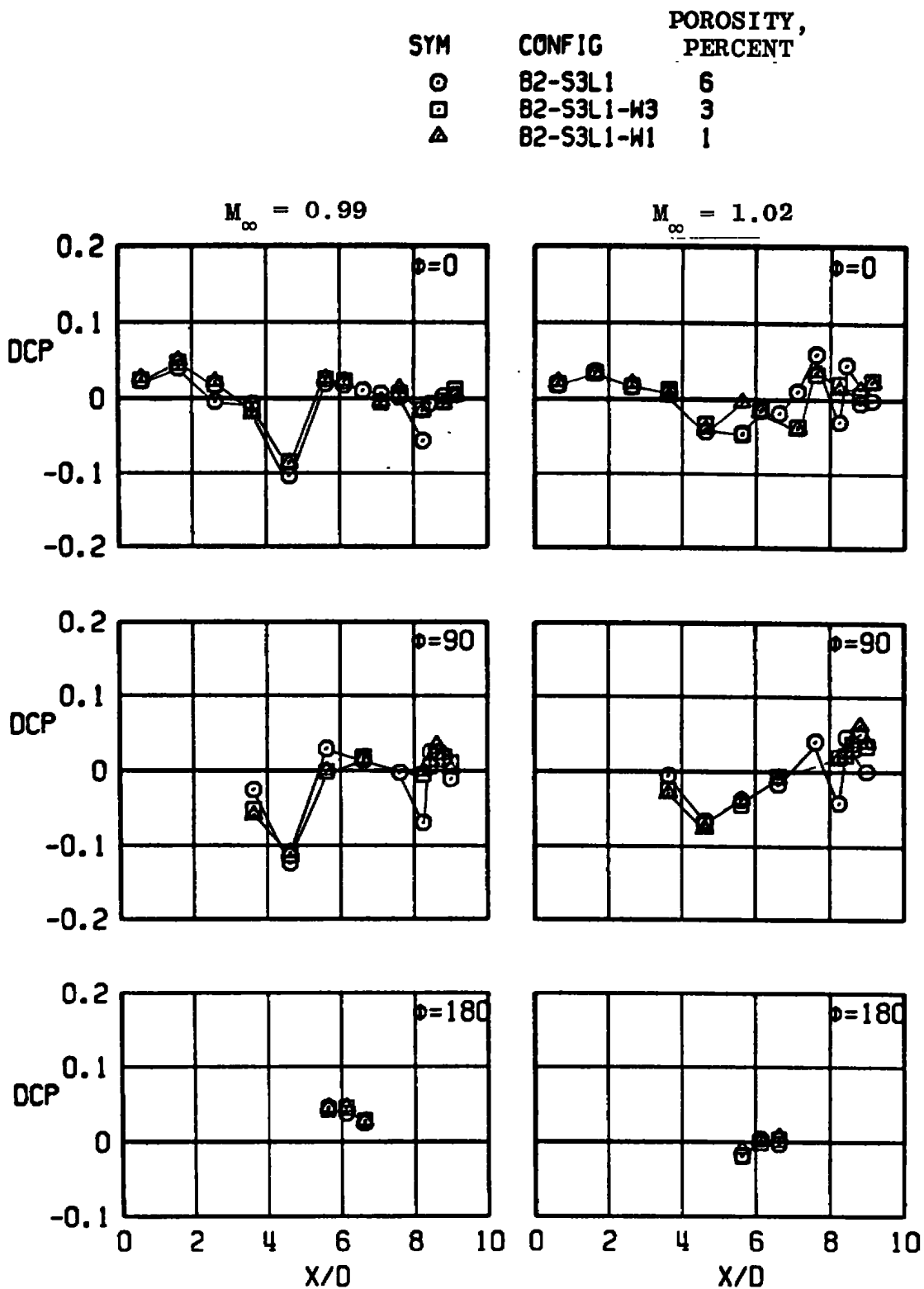


Figure 48. Effect of local wall porosity on body pressure interference coefficient for swept strut, S3L1.

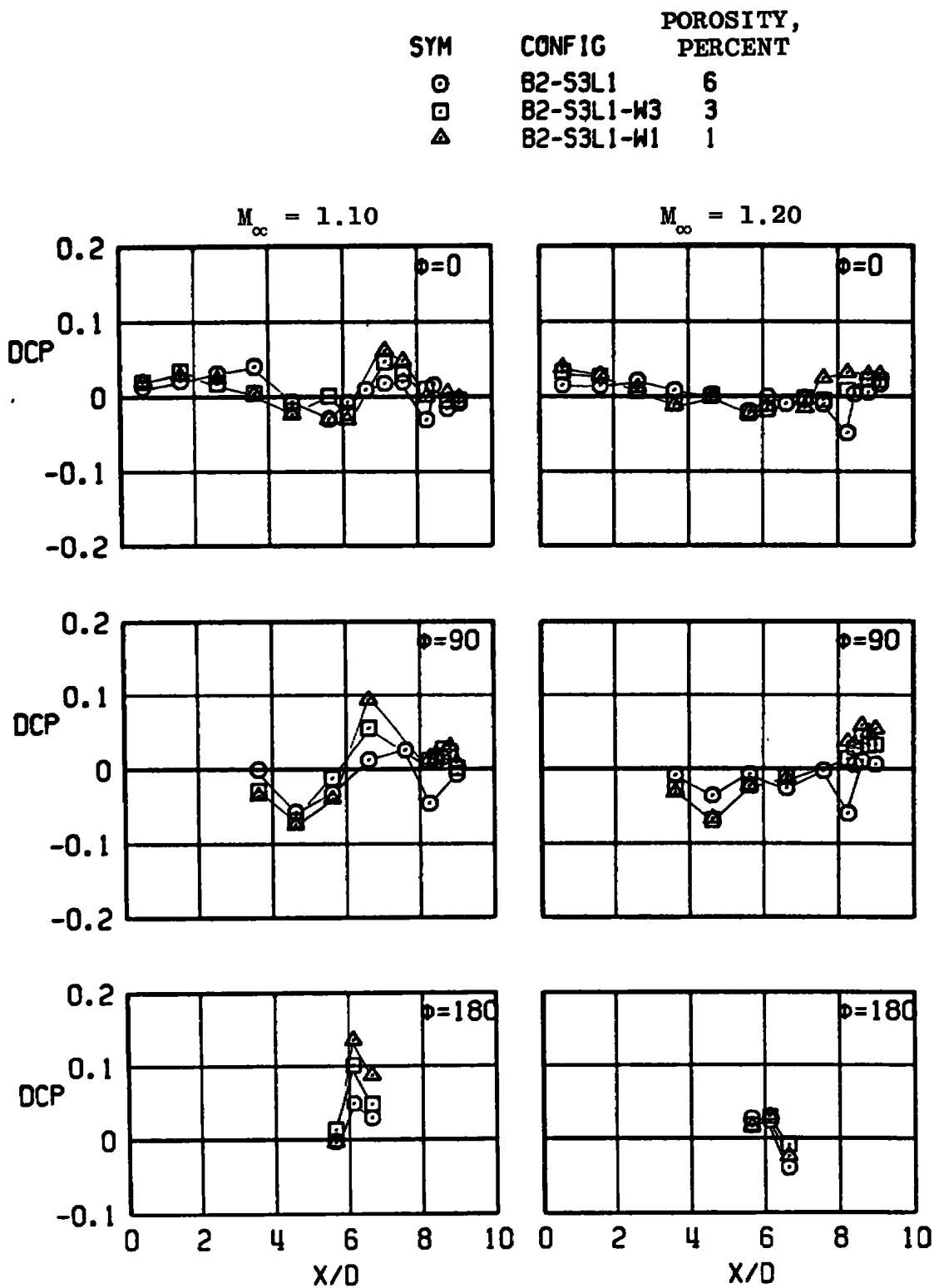


Figure 48. Concluded.

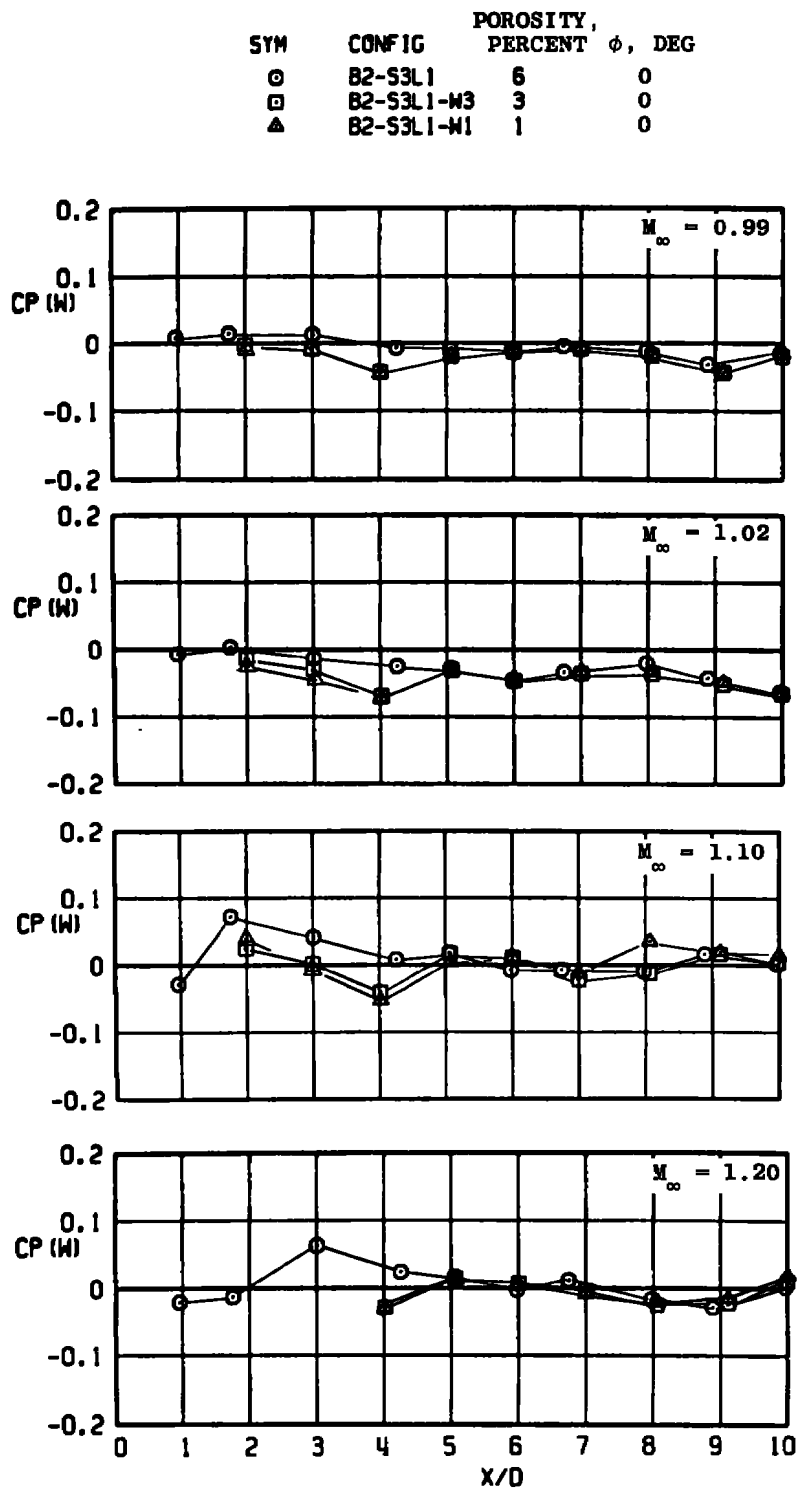


Figure 49. Effect of local wall porosity on wall pressure coefficient with swept strut, S3L1.

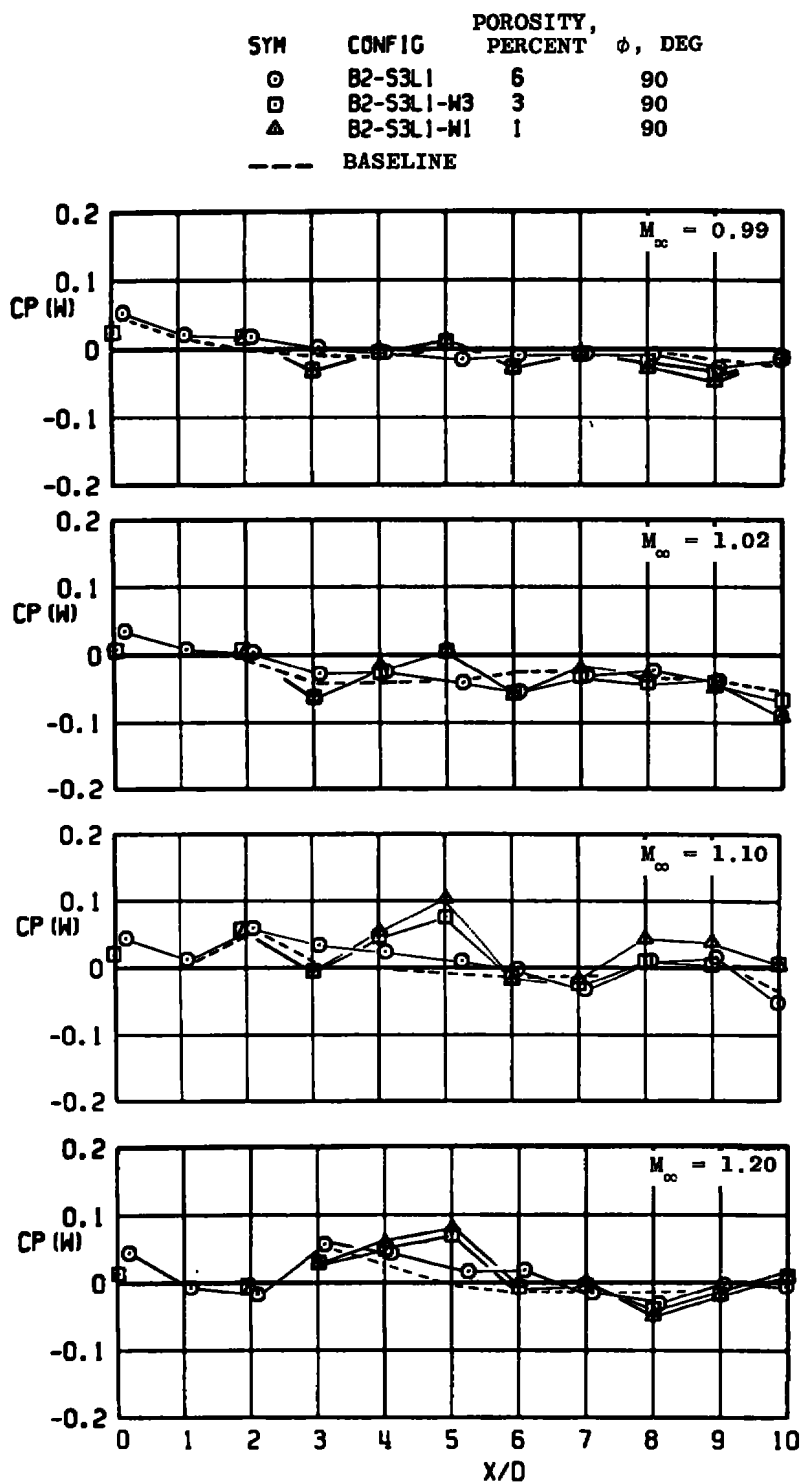


Figure 49. Concluded.

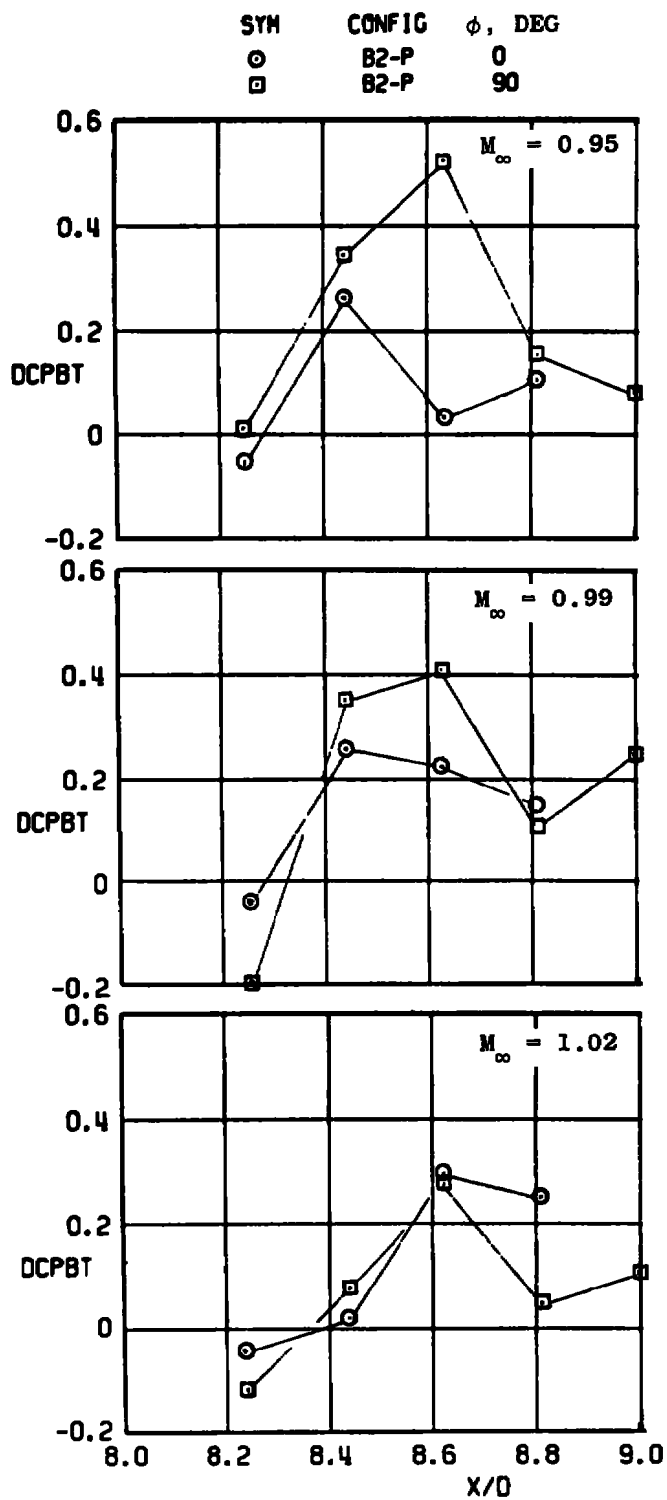


Figure 50. Effect of simulated plume on boattail pressure interference coefficient.

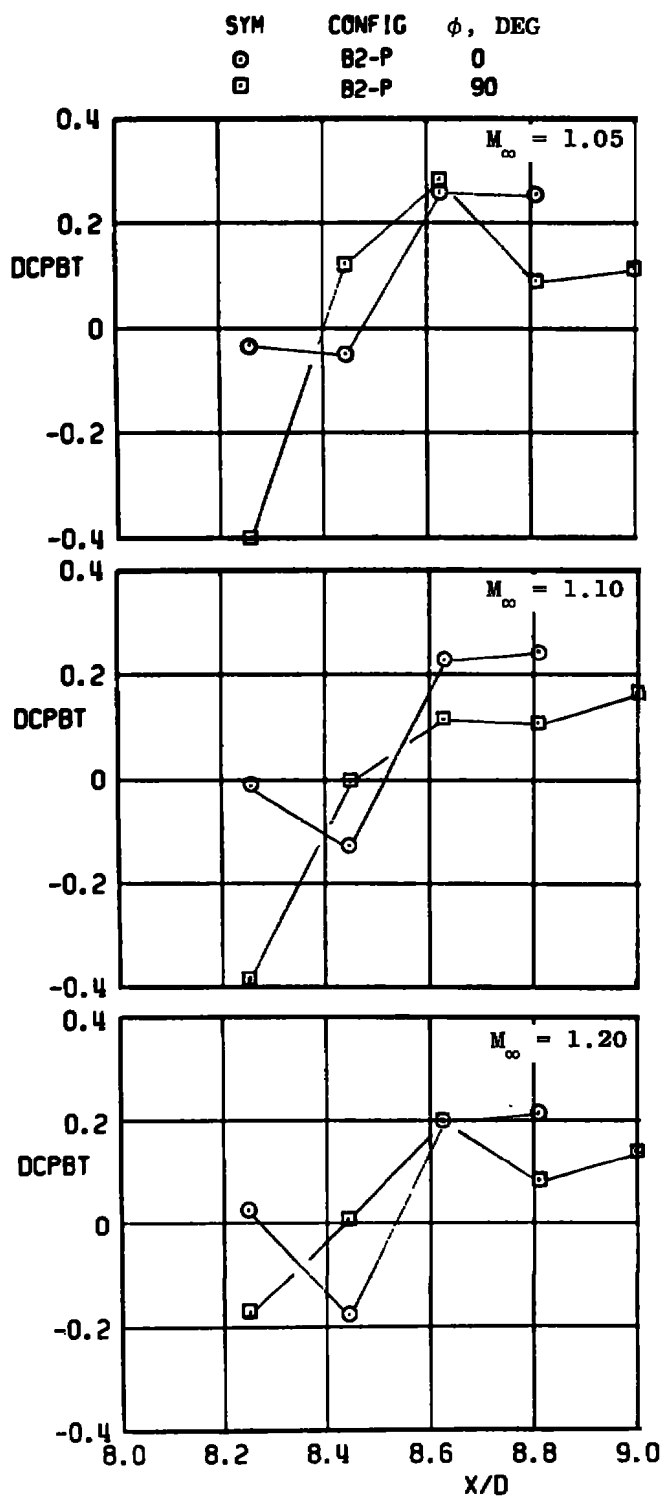


Figure 50. Concluded.

SYM	CONFIG	Λ , DEG
○	B2-S2L1-P	0
□	B2-S3L1-P	45

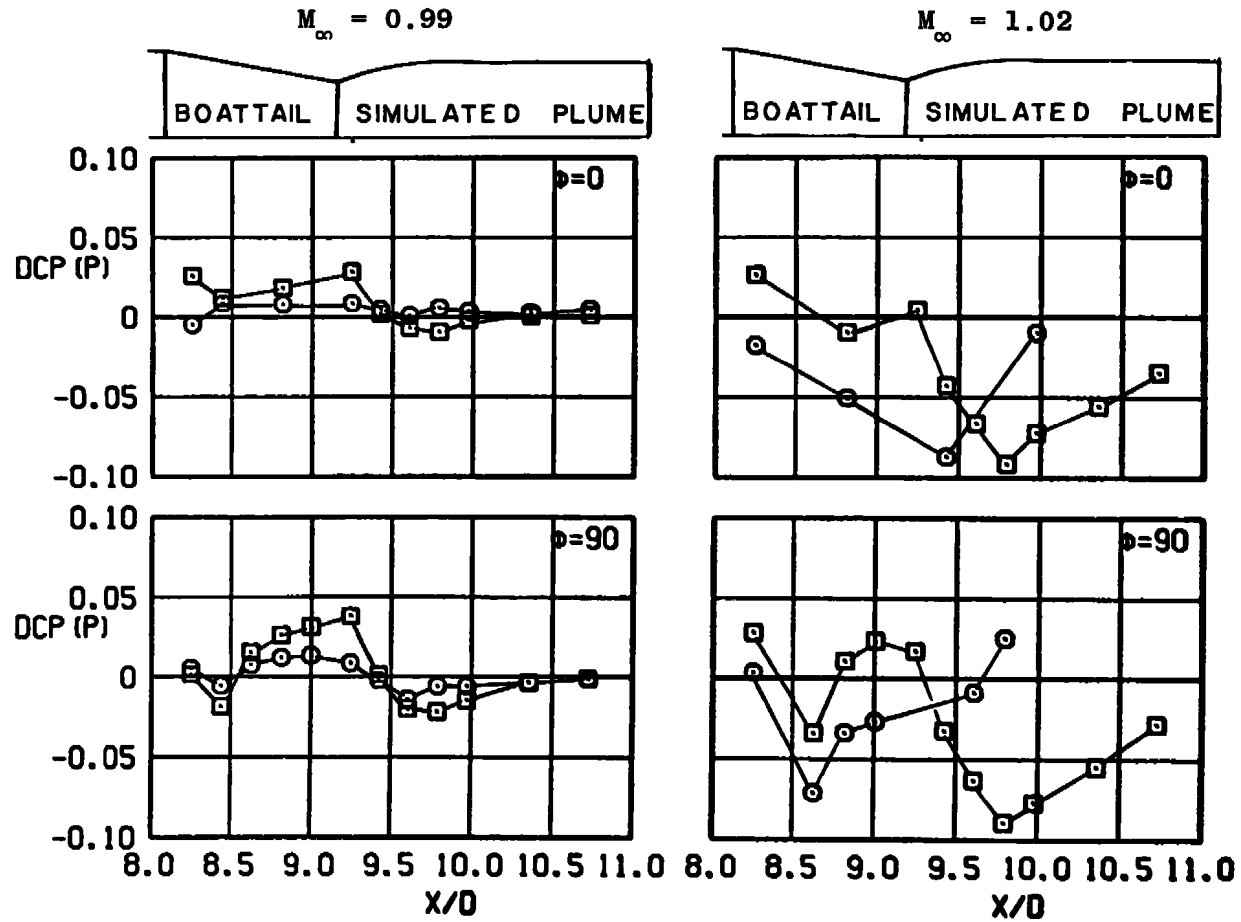


Figure 51. Effect of strut sweep angle on boattail and plume pressure interference coefficient.

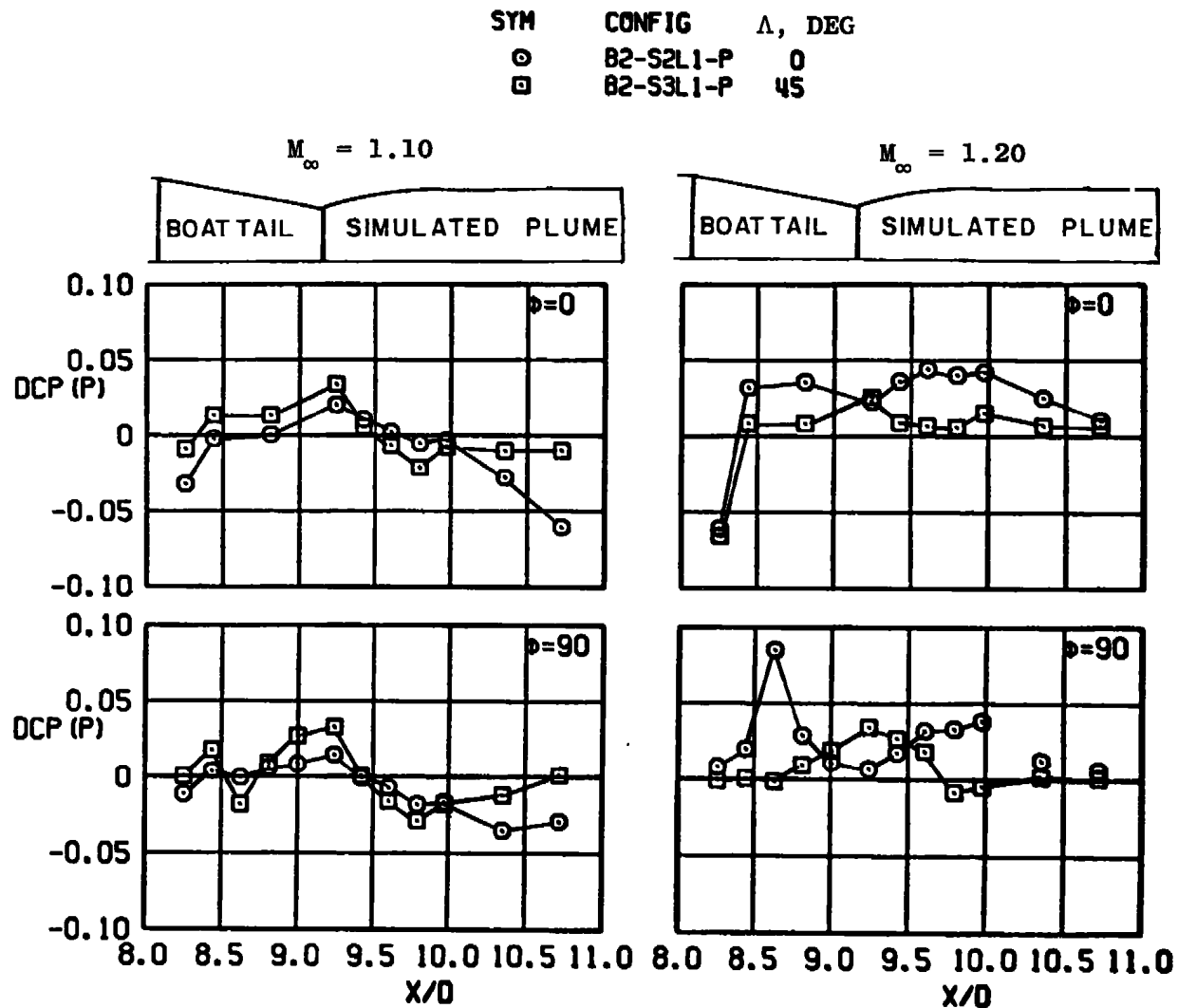


Figure 51. Concluded.

SYM	CONFIG	ℓ , IN.
○	B2-S3L1-P	0.0
□	B2-S3L3-P	1.6

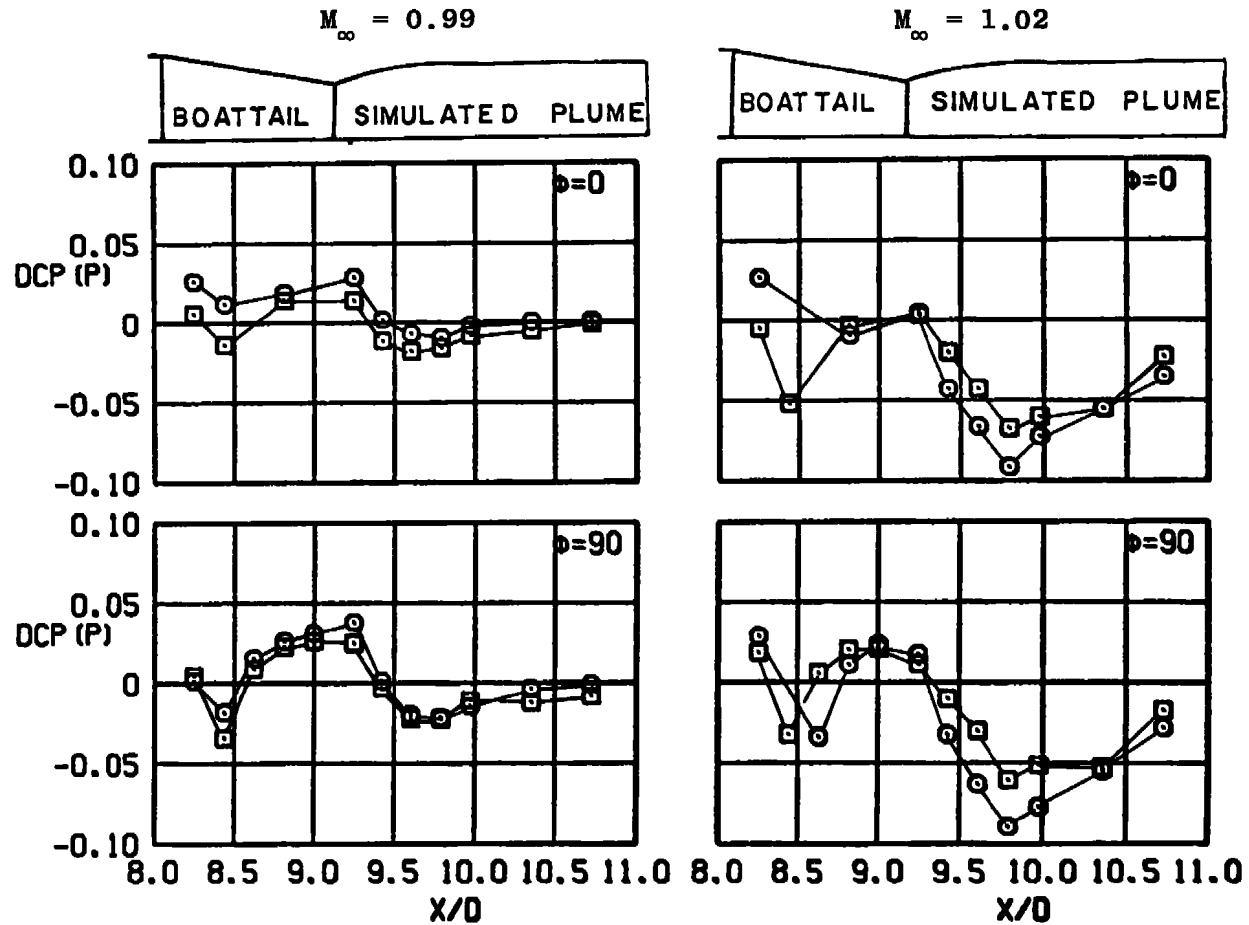


Figure 52. Effect of swept strut location on boattail pressure interference with simulated plume.

SYM	CONFIG	l , IN.
○	B2-S3L1-P	0.0
□	B2-S3L3-P	1.6

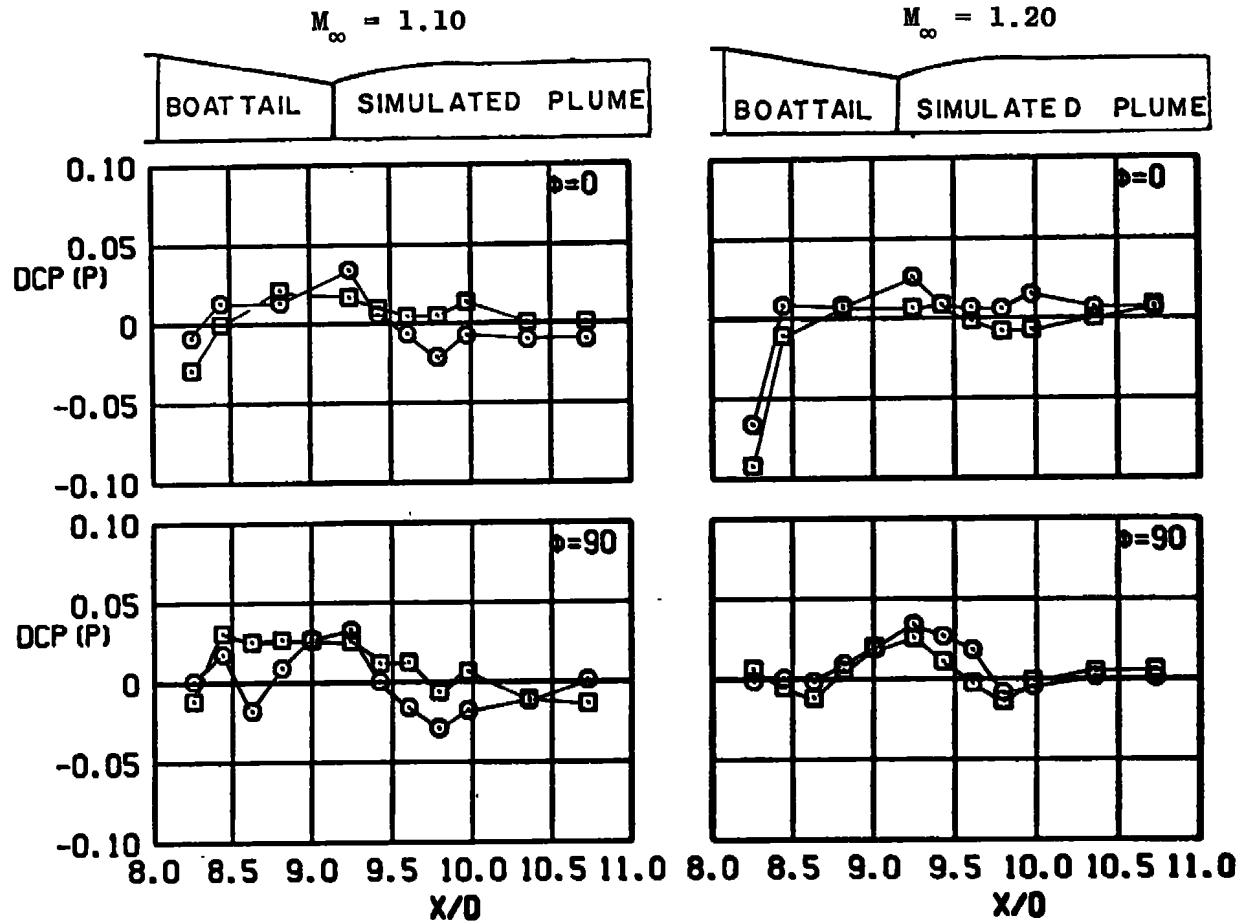


Figure 52. Concluded.

SYM	CONFIG	l , IN.
○	B2-S2L1-P	0.0
□	B2-S1L2-P	0.8

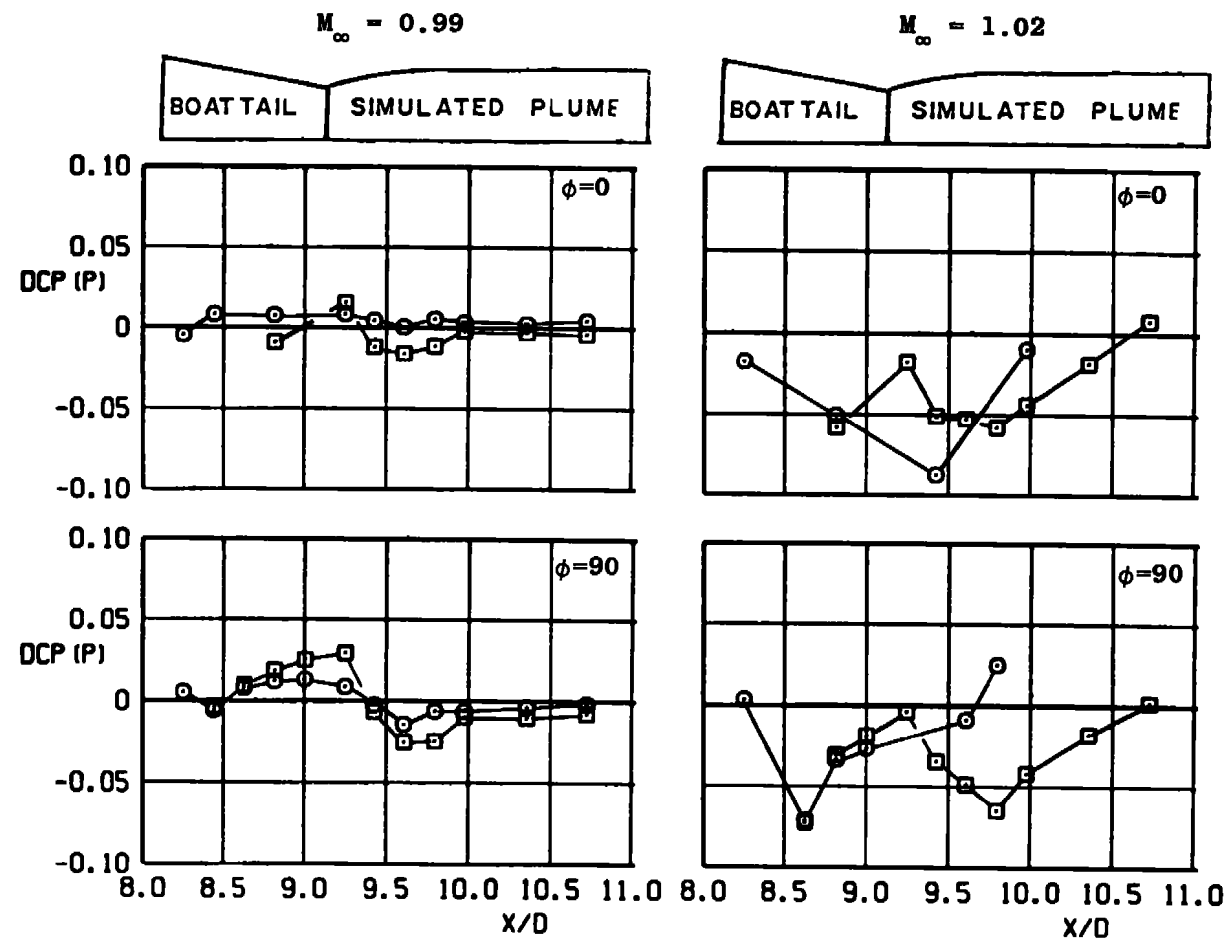


Figure 53. Effect of strut trailing-edge location on boattail pressure interference with simulated plume.

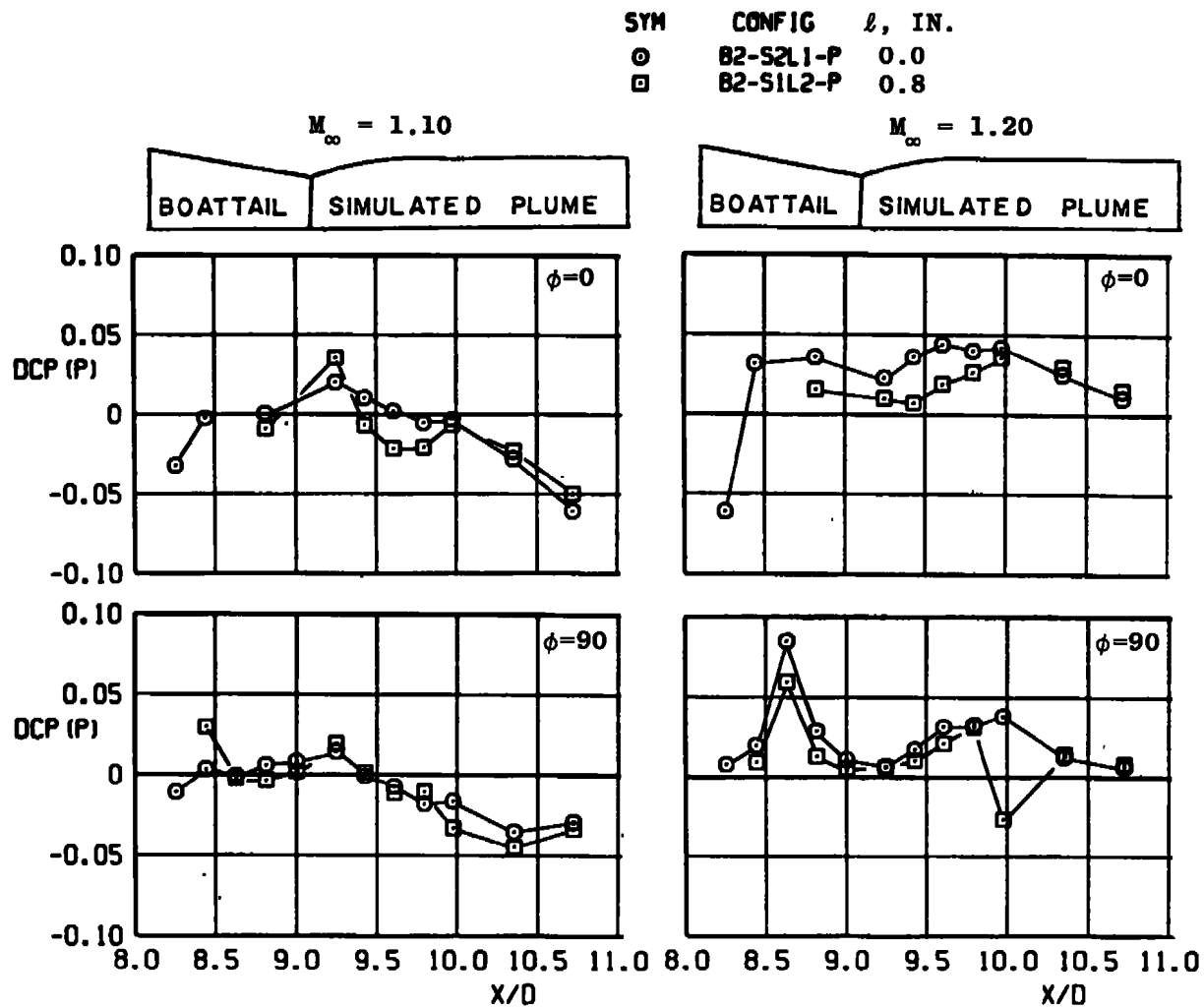


Figure 53. Concluded.

Table 1. List of Test Configurations

Body Config	L, in.	D, in.	θ_{BT} , deg	Strut Config	ℓ/D	t, in.	t/C	$\theta_{LE}=\theta_{TE}$, deg	Λ_{LE} , deg	Λ_{TE} , deg
B0	8.1	1.0	0	S1L2	0.8	0.16	0.05	9.45	0	0
B1	9.1	1.0	0	S2L1	0	0.2	0.05	9.45	0	0
B2	9.1	1.0	10	S2L3	1.6	0.2	0.05	9.45	0	0
				S3L1	0	0.2	0.05	9.45	45	45
				S3L3	1.6	0.2	0.05	9.45	45	45
				S4L1	0	0.2	0.05	9.45	45	45 (Modif.)
				S5L1	0	0.2	0.05	9.45	30	30

Flare Config	θ_F , deg	ℓ_F/D	Plume Config	Porosity Config	Porosity, percent	Test Config	Blockage, percent
F1L1.0	15.0	1.0	P	W3	3.0	B1 , B2	0.55
F1L2.0	15.0	2.0		W1	1.0	B1-, B2-S1L2	1.16
F1L3.0	15.0	3.0				B1-, B2-S2L1, -S2L3, -S3L1, -S3L3, -S4L1, -S5L1	1.31
F1L5.0	15.0	5.0					

Typical Configuration Codes

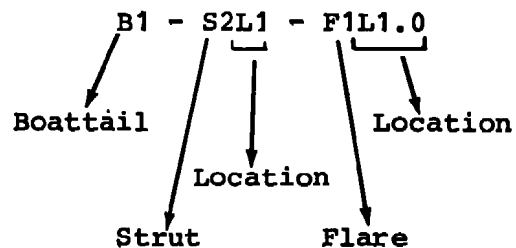


Table 2. Average Base Pressure Coefficient on NAB

Config	Avg. Base Pressure Coefficient, CPB										
	$M_\infty = 0.6$	0.8	0.9	0.95	0.99	1.02	1.05	1.10	1.20	1.30	1.40
With Cylindrical Afterbody											
B0	-0.145	-0.147	-0.140	-0.149	-0.183	-0.241	-0.227	-0.209	-0.175	-0.186	-0.171
B1	-0.132	-0.147	-0.141	-0.155	-0.190	-0.238	-0.232	-0.223	-0.194	-0.189	-0.174
B1-S2L1	-0.121	-0.150	-0.137	-0.151	-0.180	-0.233	-0.250	-0.240	-0.157	-0.180	-0.165
B1-S3L1	-0.123	-0.146	-0.137	-0.151	-0.183	-0.247	-0.236	-0.232	-0.180	-0.181	-0.162
B1-S3L3	-0.125	-0.149	-0.139	-0.149	-0.179	-0.237	-0.227	-0.216	-0.180	-0.182	-0.172
B1-S1L2	-0.127	-0.152	-0.140	-0.151	-0.180	-0.245	-0.258	-0.228	-0.160	-0.198	-0.161
With 10-deg Boattail											
B2	0.094	0.099	0.112	0.132	0.108	0.026	0.041	0.041	0.012	-0.021	-0.023
B2-WP1	0.087	0.101	0.115	0.129	0.094	0.025	0.076	0.055	0.021	0.019	-0.027
B2-S2L1	0.080	0.095	0.110	0.129	0.114	0.019	0.008	0.041	0.066	-0.034	0.234
B2-S2L3	0.089	0.102	0.117	0.139	0.122	0.053	0.082	0.070	0.045	-0.010	-0.044
B2-S2L3-W1	0.089	0.105	0.117	0.138	0.118	0.085	0.018	0.028	0.058	0.063	-0.046
B2-S2L3-W3	0.091	0.103	0.116	0.137	0.118	0.064	0.081	0.051	0.048	0.036	-0.047
B2-S3L1	0.086	0.099	0.113	0.132	0.113	0.031	0.050	0.031	0.028	-0.013	-0.014
B2-S3L1-W1	0.090	0.102	0.115	0.129	0.097	0.036	0.069	0.033	0.041	0.024	-0.003
B2-S3L1-W3	0.091	0.104	0.114	0.134	0.106	0.037	0.056	0.030	0.033	-0.007	-0.007
B2-S3L3	0.087	0.100	0.115	0.134	0.113	0.114	0.064	0.063	0.024	-0.017	-0.028
B2-S1L2	0.082	0.092	0.105	0.124	0.111	0.016	0.004	0.030	0.039	-0.039	-0.014
B2-S4L1	0.091	0.103	0.117	0.135	0.138	0.069	0.055	0.052	0.033	0.001	0.005
B2-S5L1	0.090	0.102	0.117	0.136	0.113	0.012	0.058	0.042	-0.011	-0.053	-0.030

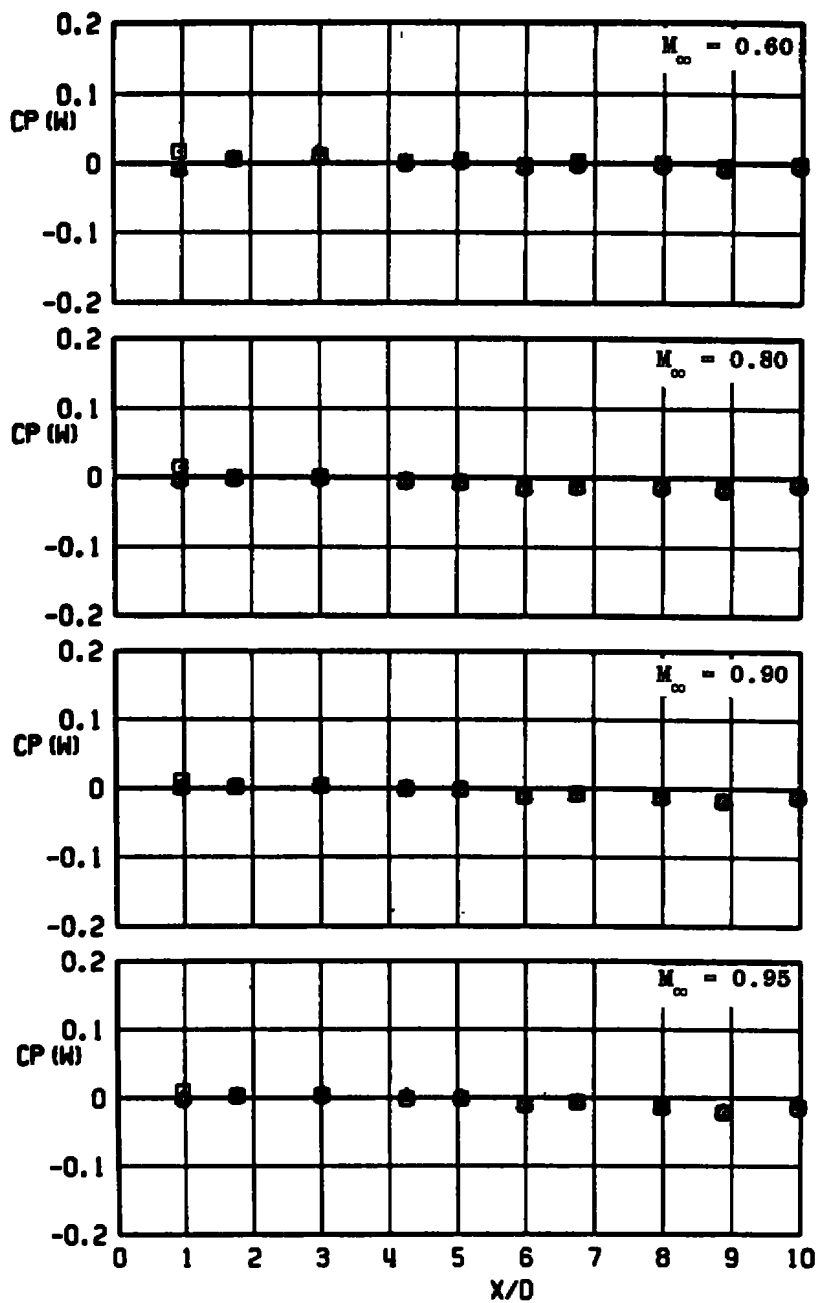
APPENDIX A

PLOTS OF TEST DATA

<u>Figure</u>	<u>Page</u>
A-1. Baseline Configurations, CP(W) versus X/D	123
A-2. Effect of Sting-Flare Position	
a. DCPBT versus X/D (Cylindrical Afterbody)	126
b. DCPBT versus X/D (10-deg Boattail)	132
A-3. Effect of Strut Sweep Angle	
a. DCP versus X/D	138
b. DCPBT versus X/D	144
c. CP(W) versus X/D, $\phi = 0$	150
d. CP(W) versus X/D, $\phi = 90$ deg	153
A-4. Effect of Strut Location	
a. DCP versus X/D (Straight Strut, 10-deg Boattail)	156
b. DCPBT versus X/D (Straight Strut, 10-deg Boattail)	162
c. CP(W) versus X/D (Straight Strut, 10-deg Boattail, $\phi = 0$)	168
d. CP(W) versus X/D (Straight Strut, 10-deg Boattail, $\phi = 90$ deg)	171
e. DCP versus X/D (30-deg Swept Strut, Cylindrical Afterbody)	174
f. DCP versus X/D (30-deg Swept Strut, 10-deg Boattail)	180
A-5. Effect of Trailing-Edge Location	
a. DCP versus X/D (Straight Strut, 10-deg Boattail)	186
b. DCPBT versus X/D (Straight Strut, 10-deg Boattail)	192
c. DCPBT versus X/D (30-deg Swept Strut, 10-deg Boattail)	198
d. CP(W) versus X/D (30-deg Swept Strut, 10-deg Boattail, $\phi = 0$)	204
e. CP(W) versus X/D (30-deg Swept Strut, 10-deg Boattail, $\phi = 90$ deg)	207
A-6. Effect of Tunnel Wall Porosity	
a. DCP versus X/D (Straight Strut, 10-deg Boattail)	210
b. DCPBT versus X/D (Straight Strut, 10-deg Boattail)	216
c. CP(W) versus X/D (Straight Strut, 10-deg Boattail, $\phi = 0$)	222
d. CP(W) versus X/D (Straight Strut, 10-deg Boattail, $\phi = 90$ deg)	225
e. DCP versus X/D (30-deg Swept Strut, 10-deg Boattail)	228
f. DCPBT versus X/D (30-deg Swept Strut, 10-deg Boattail)	234
g. CP(W) versus X/D (30-deg Swept Strut, 10-deg Boattail, $\phi = 0$)	240
h. CP(W) versus X/D (30-deg Swept Strut, 10-deg Boattail, $\phi = 90$ deg)	243

<u>Figure</u>	<u>Page</u>
A-7. Effect of Simulated Jet Plume	
a. DCP(P) versus X/D (with Varying Strut Sweep Angle	246
b. DCP(P) versus X/D (30-deg Swept Strut with Varying Position)	252
c. DCP(P) versus X/D (Straight Strut with Varying Chord)	258
A-8. Pressure Coefficient Distribution on Model Body, Strut, and Tunnel Wall	
a. Straight Strut, $\ell = 0$ (B2-S2L1)	264
b. Swept Strut Configuration, $\ell = 0$ (B2-S3L1)	270
c. Swept Strut Configuration, $\ell = 1.6$ in. (B2-S3L3)	276

SYM	CONFIG	ϕ , DEG
▲	B2	0
⊙	B1	0
□	B0	0

Figure A-1. Baseline configurations, $CP(W)$ versus X/D .

SYM	CONFIG	ϕ , DEG
▲	B2	0
○	B1	0
□	B0	0

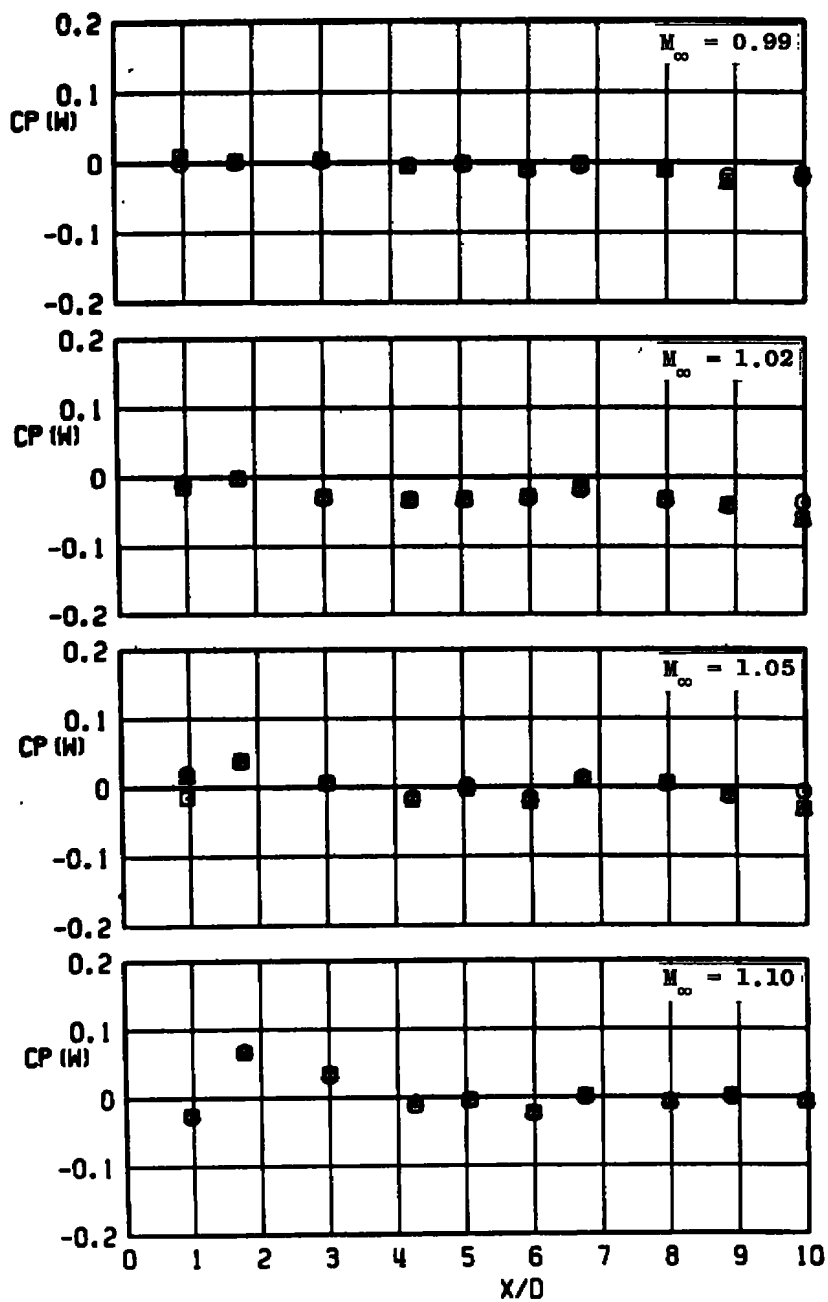


Figure A-1. Continued.

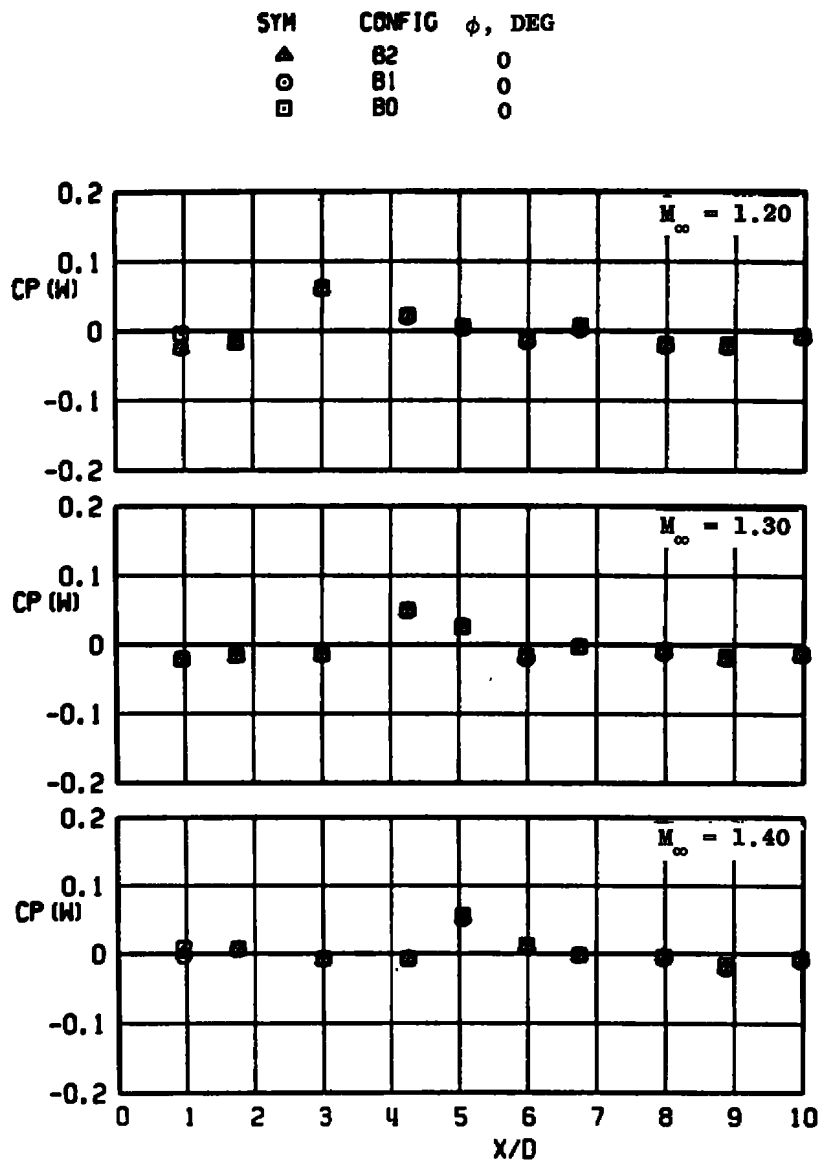
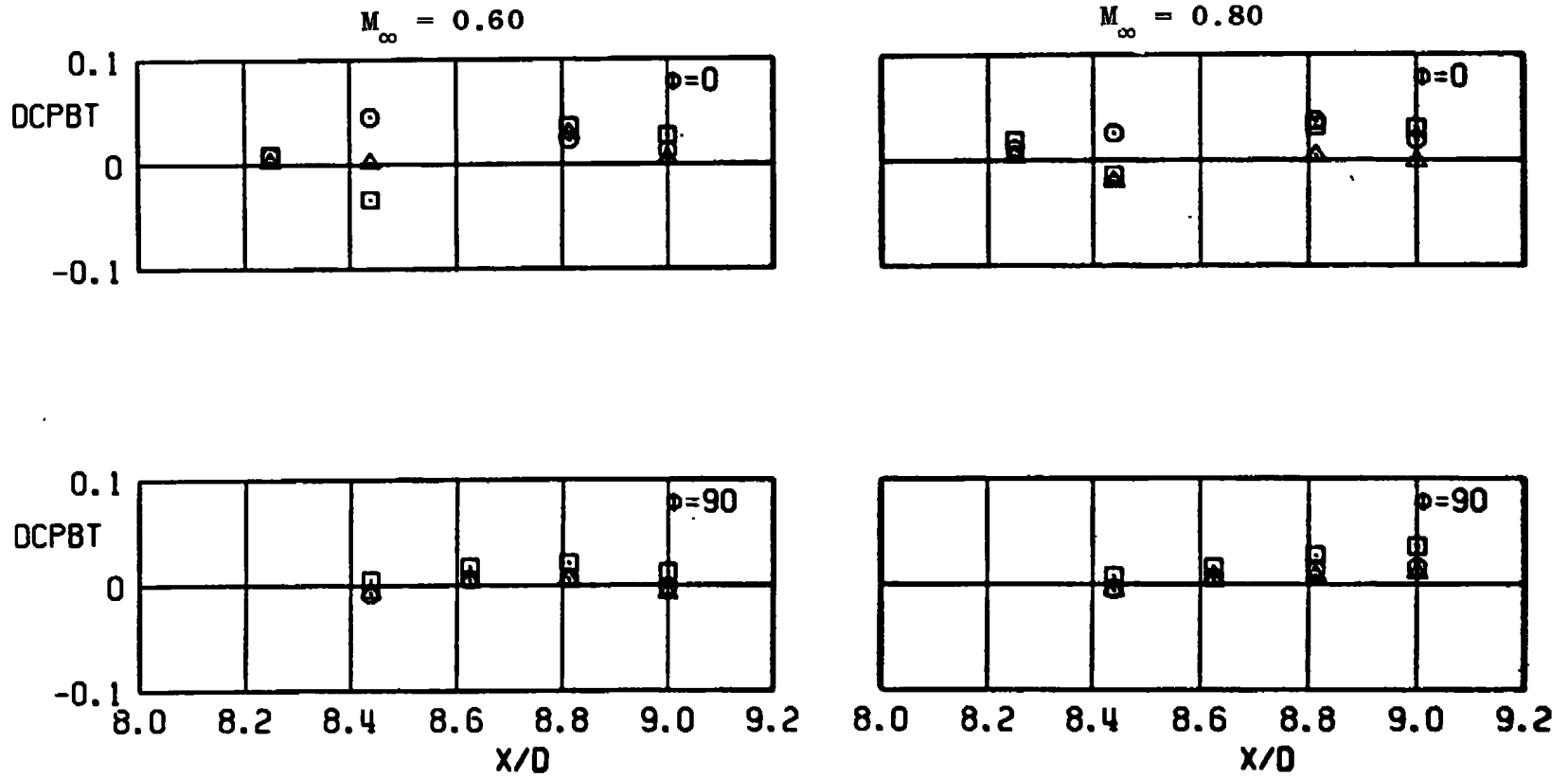


Figure A-1. Concluded.

SYM	CONFIG
□	B1-F1L2.0
○	B1-F1L3.0
△	B1-F1L5.0



a. DCPBT versus X/D (cylindrical afterbody)
Figure A-2. Effect of sting-flare position.

SYM

□

○

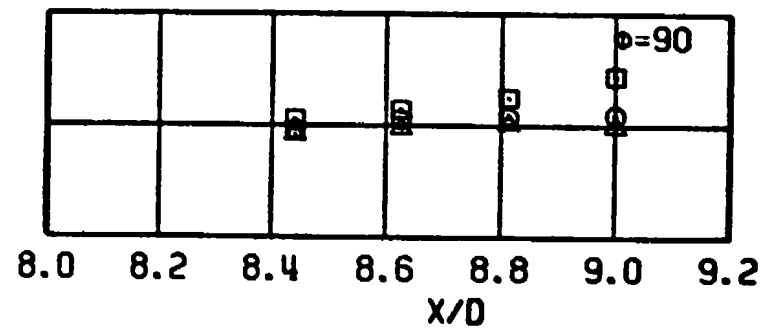
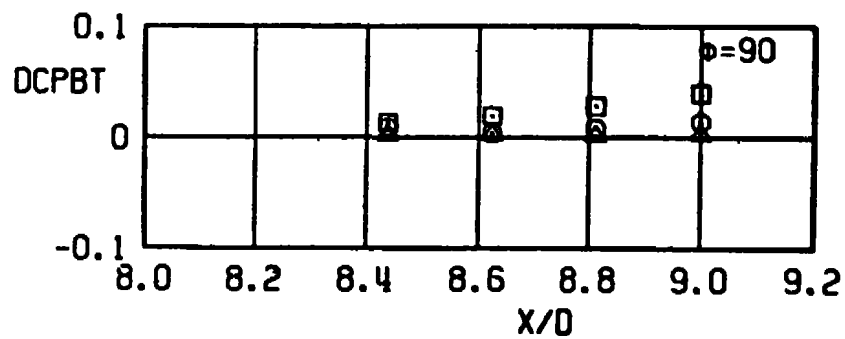
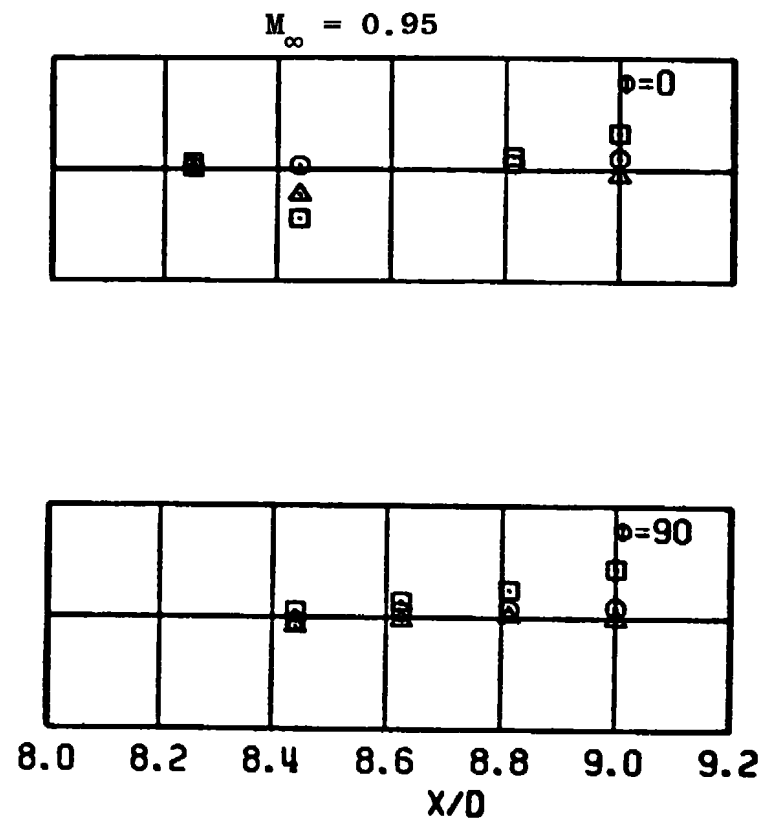
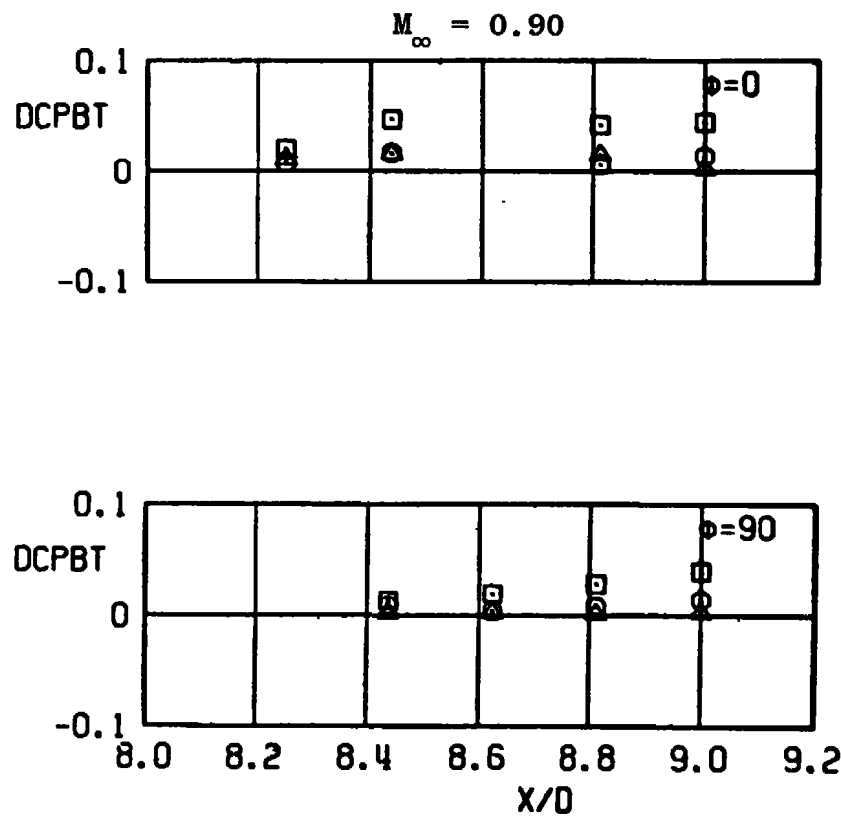
△

CONFIG

B1-FIL2.0

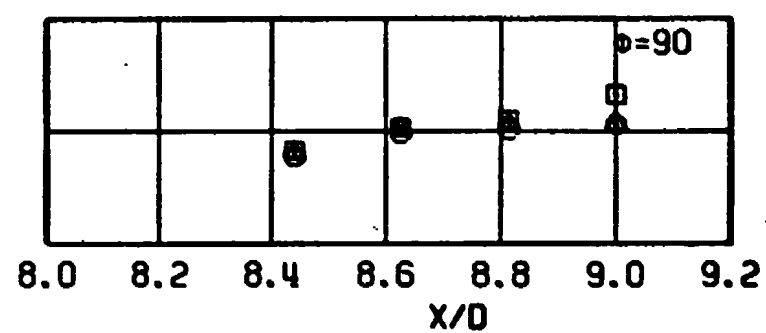
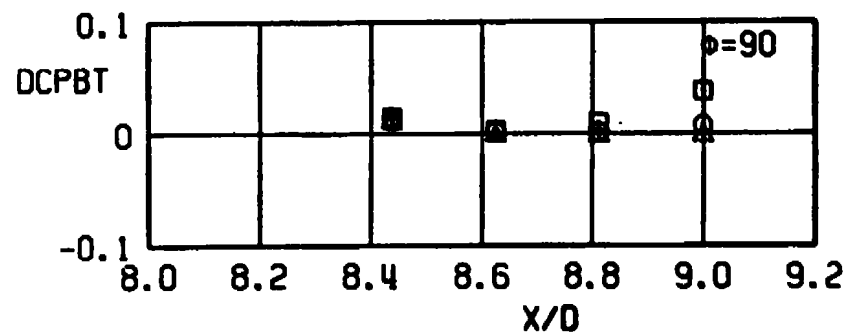
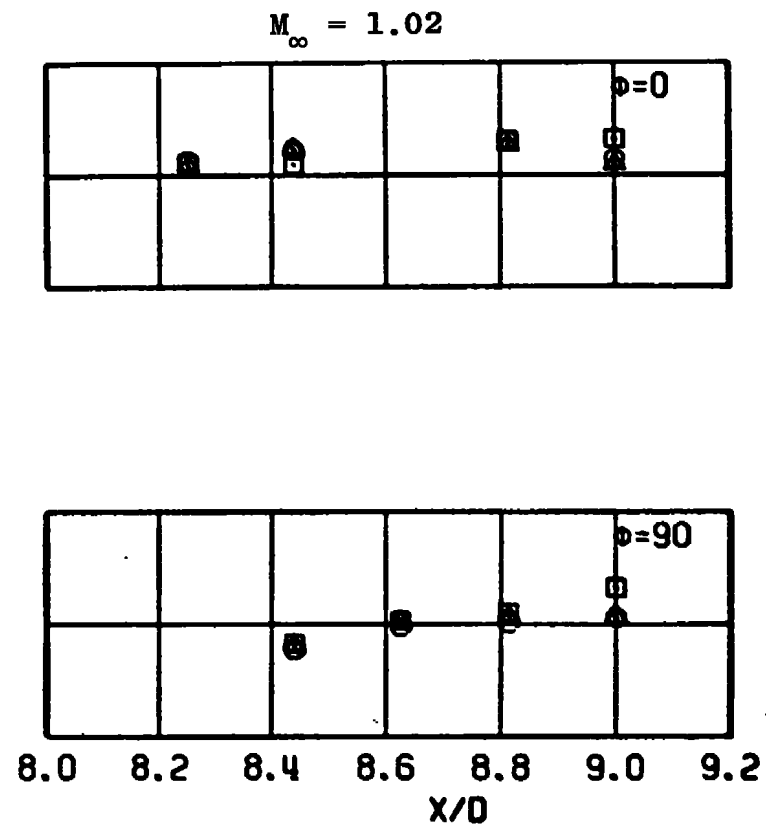
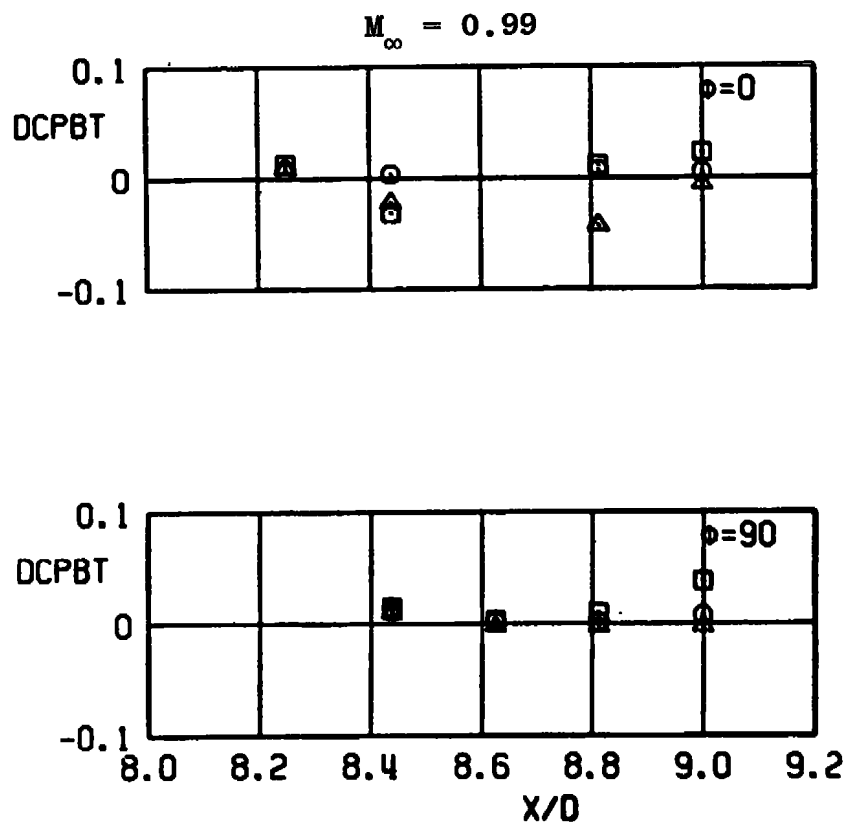
B1-FIL3.0

B1-FIL5.0



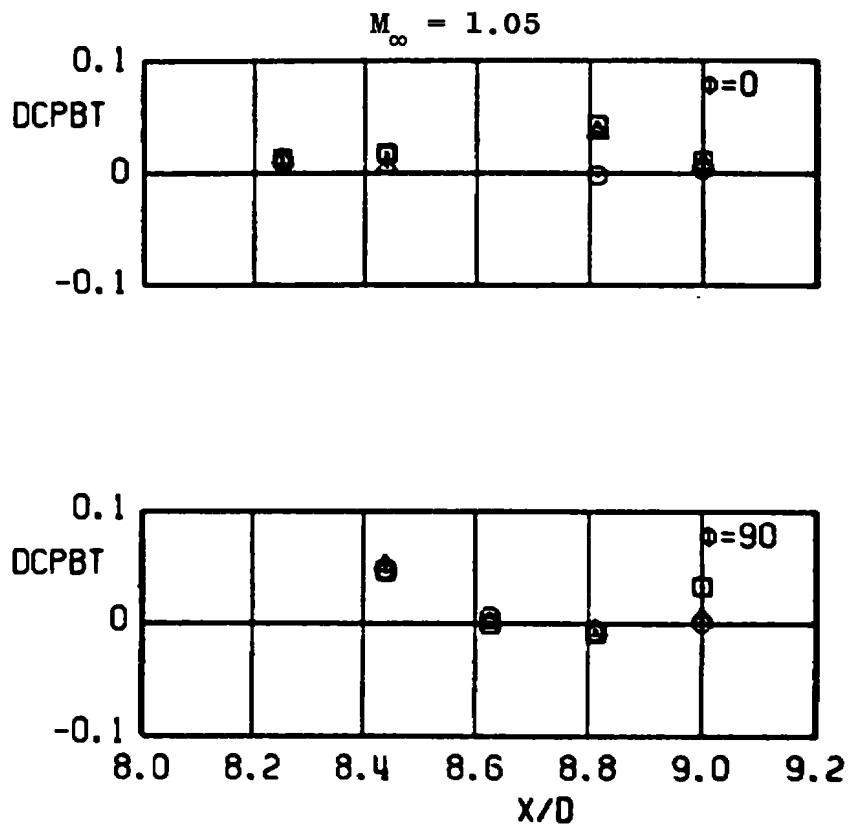
a. Continued
Figure A-2. Continued.

SYM	CONFIG
□	B1-FIL2.0
○	B1-FIL3.0
△	B1-FIL5.0



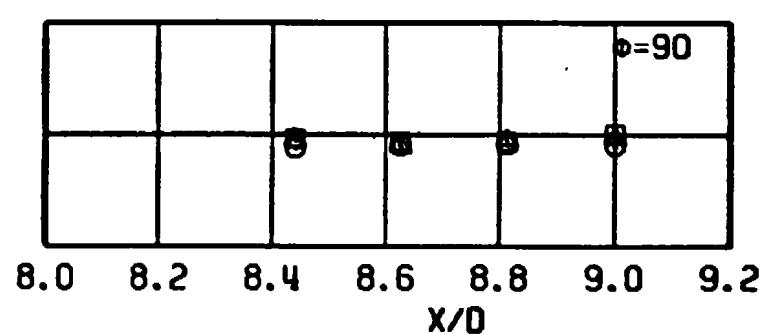
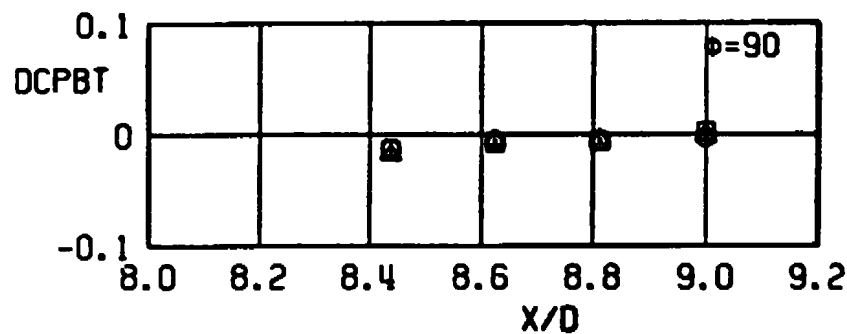
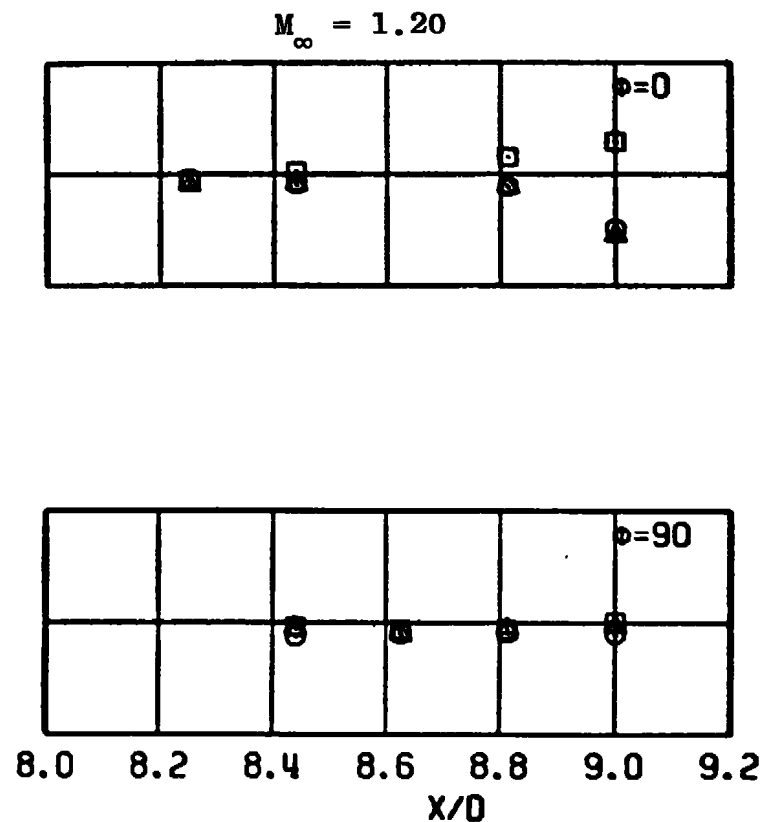
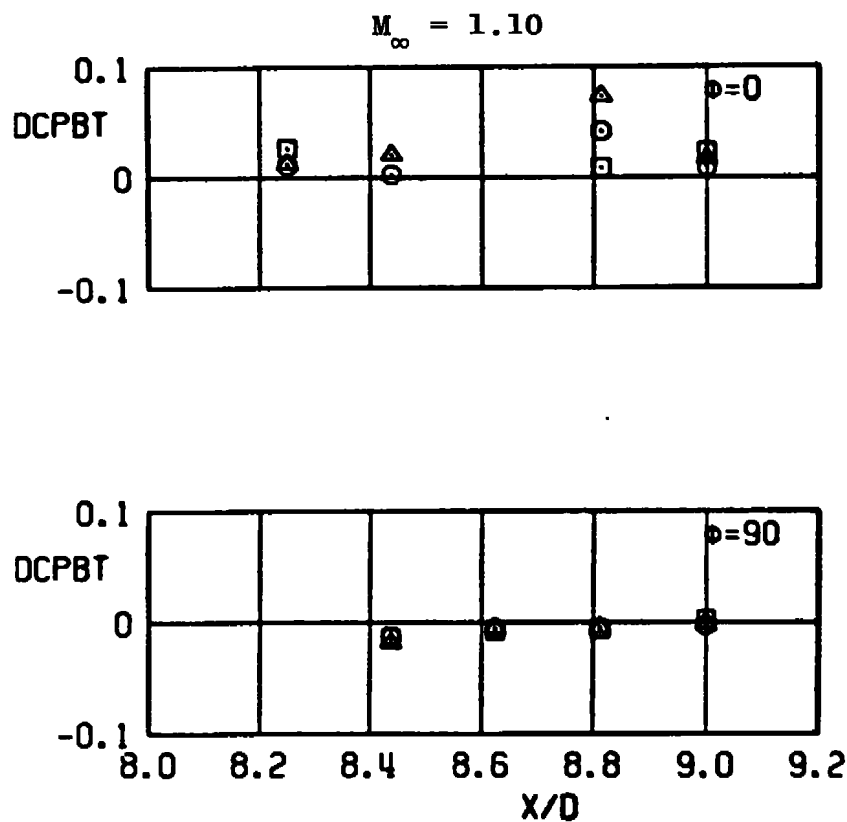
a. Continued
Figure A-2. Continued.

SYM	CONFIG
□	B1-FIL2.0
○	B1-FIL3.0
△	B1-FIL5.0



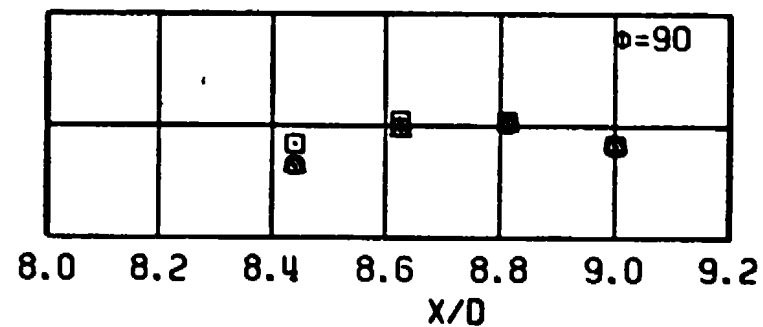
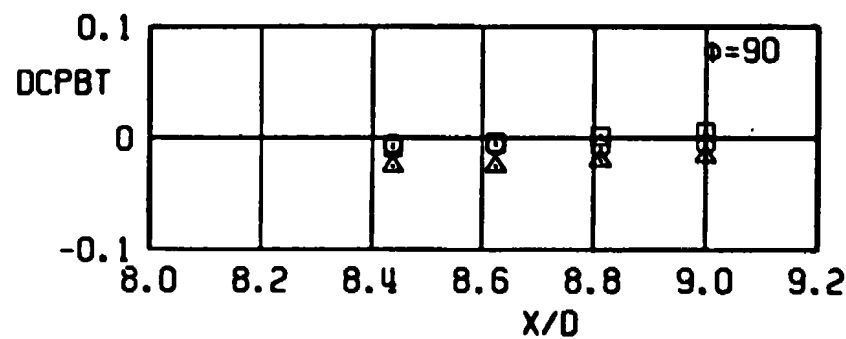
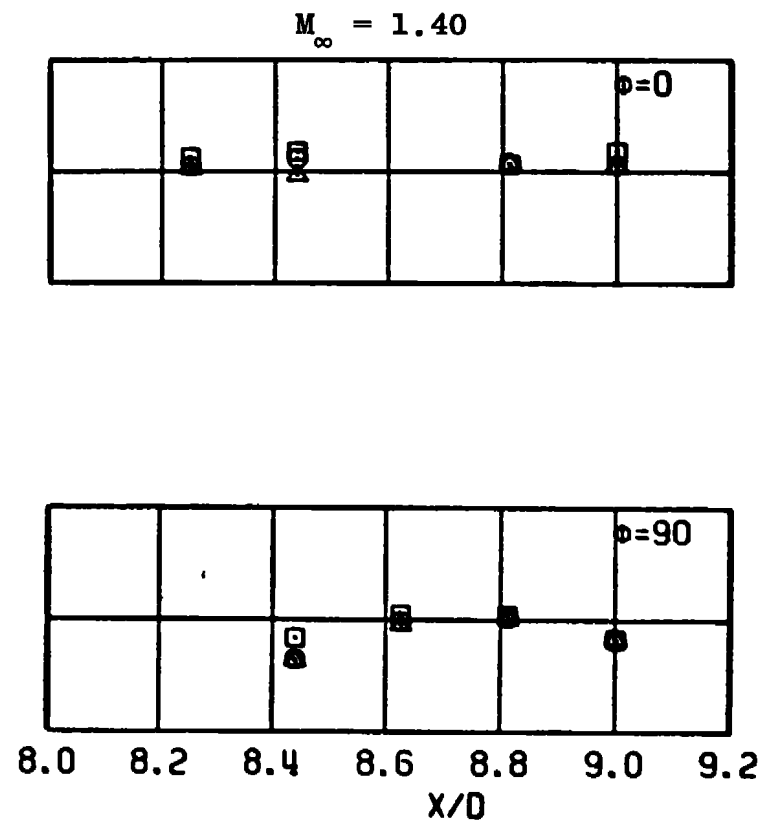
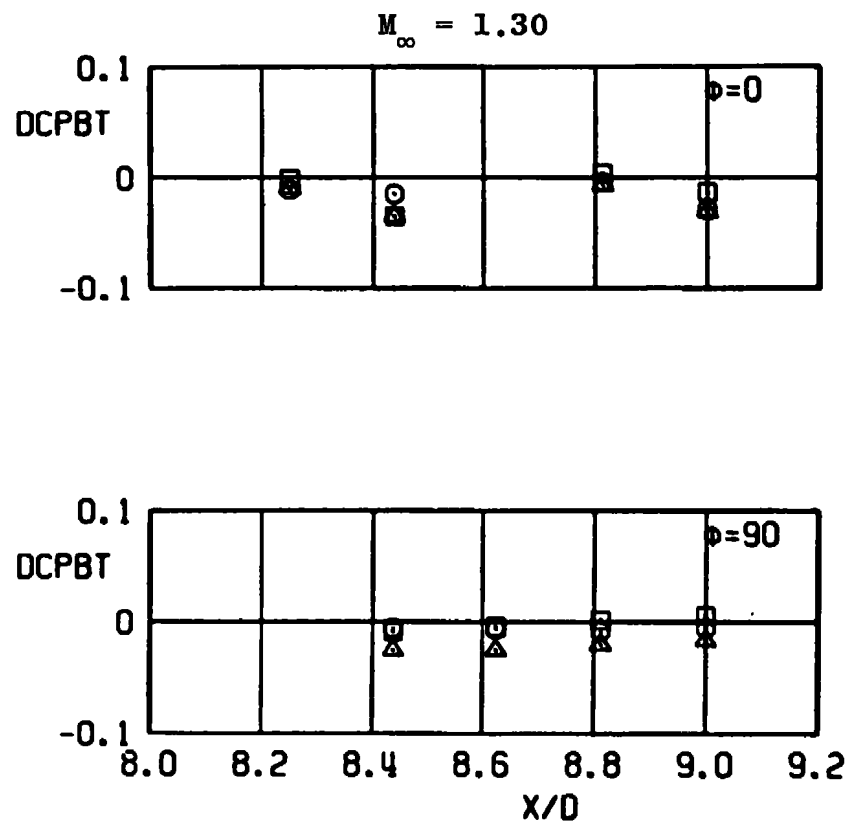
a. Continued
Figure A-2. Continued.

SYM	CONFIG
□	B1-F1L2.0
○	B1-F1L3.0
△	B1-F1L5.0



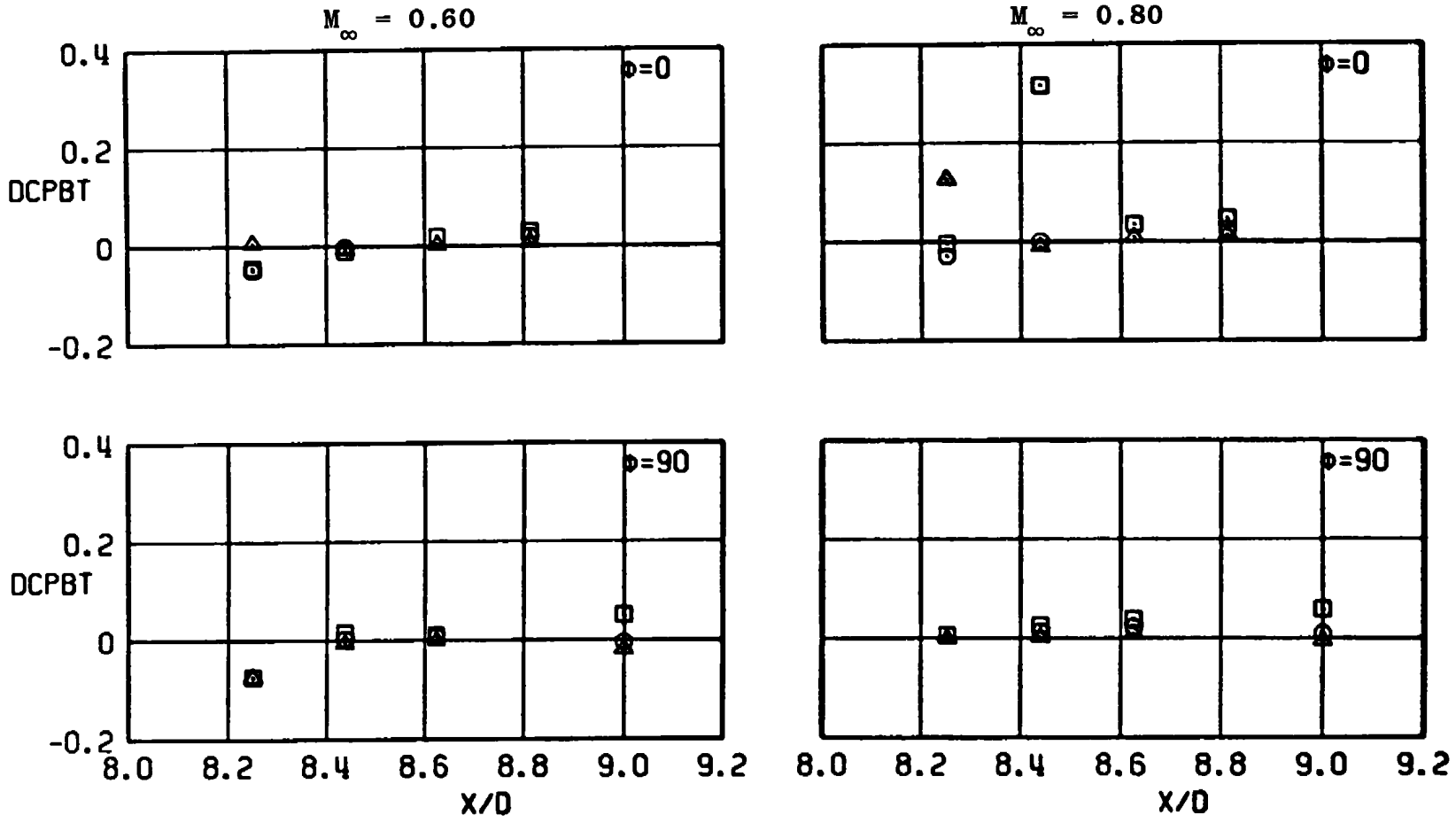
a. Continued
Figure A-2. Continued.

SYM	CONFIG
□	B1-FIL2.0
○	B1-FIL3.0
△	B1-FIL5.0



a. Concluded
Figure A-2. Continued.

SYM	CONFIG
□	B2-F1L1.0
○	B2-F1L2.0
△	B2-F1L3.0



b. DCPBT versus X/D (10-deg boattail)
Figure A-2. Continued.

SYM

□

○

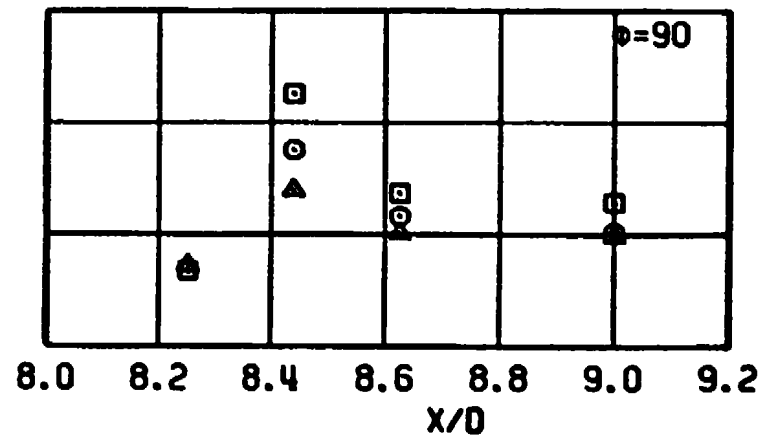
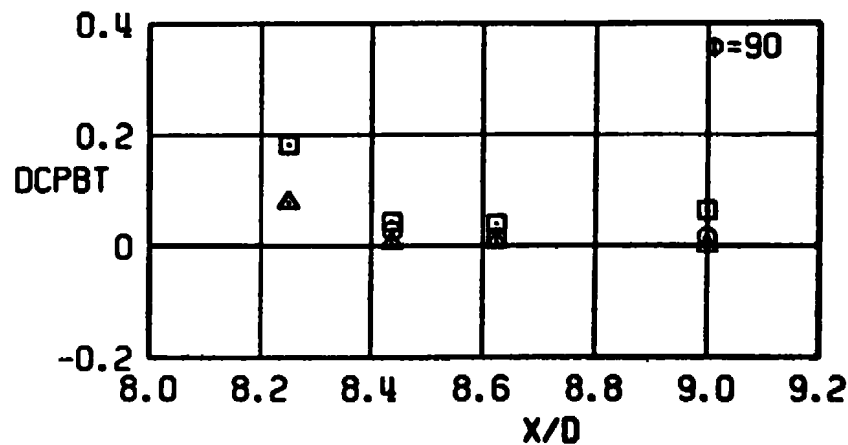
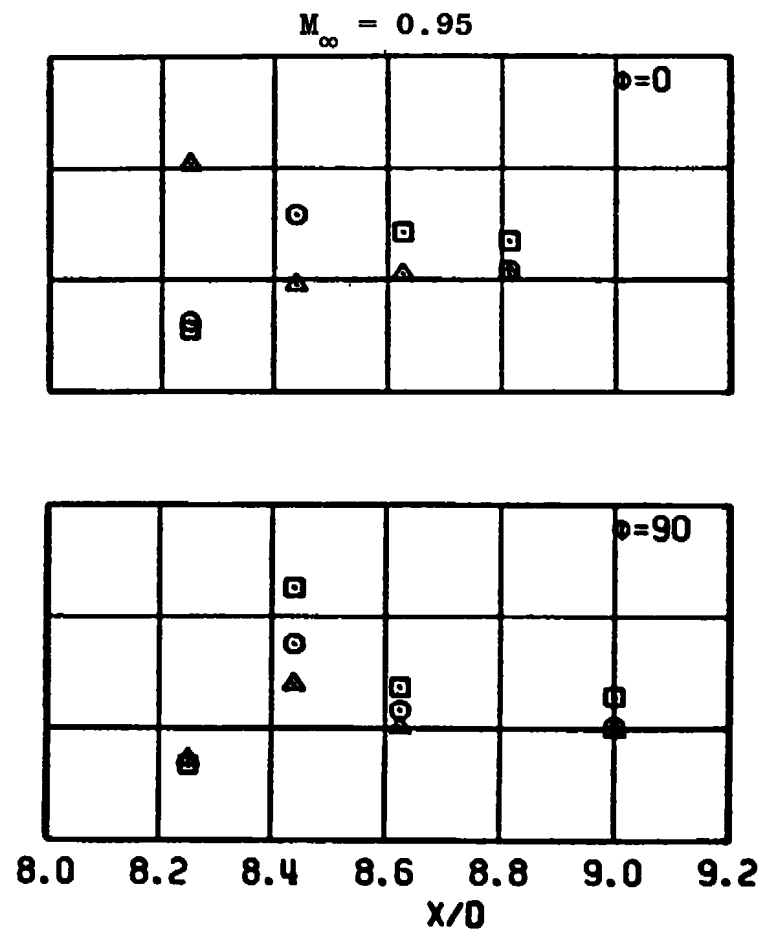
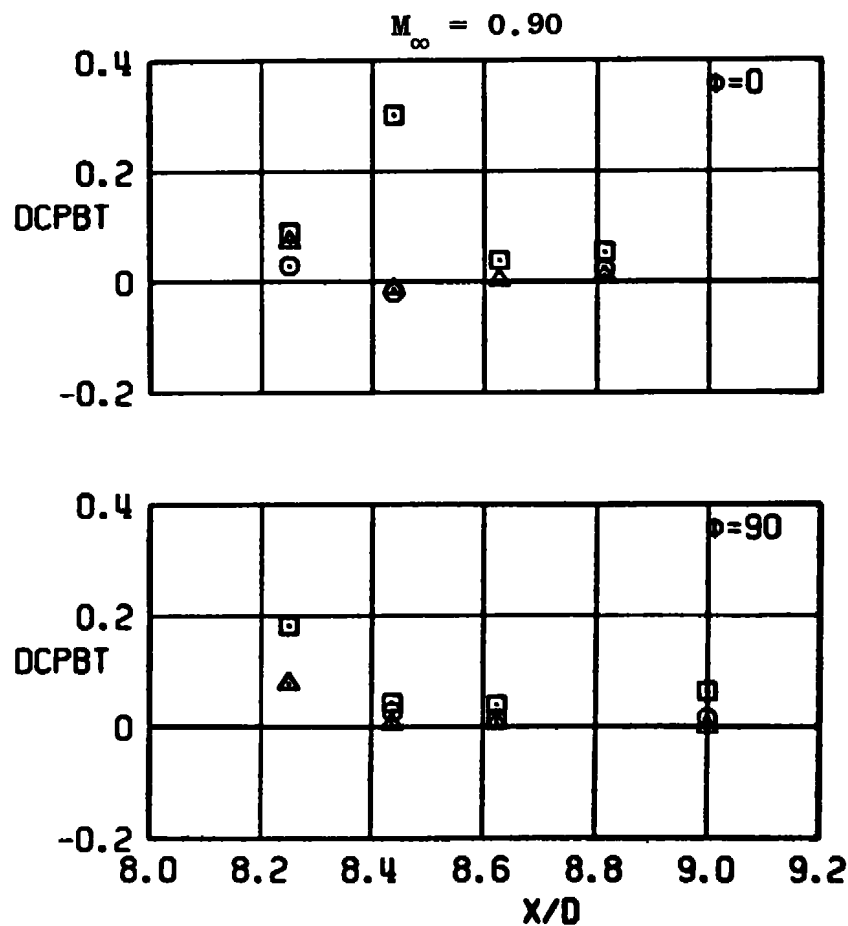
△

CONFIG

B2-F1L1.0

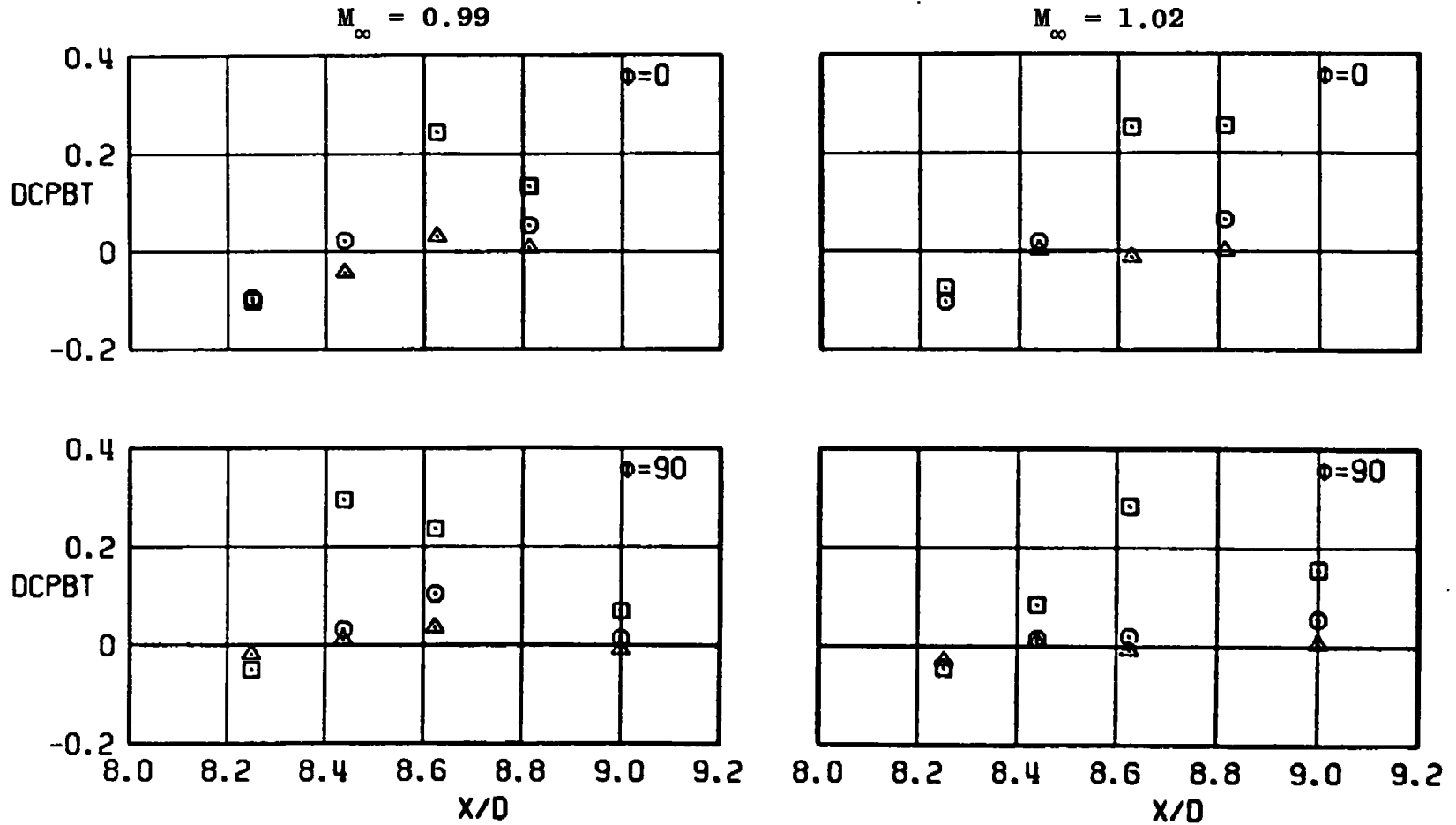
B2-F1L2.0

B2-F1L3.0

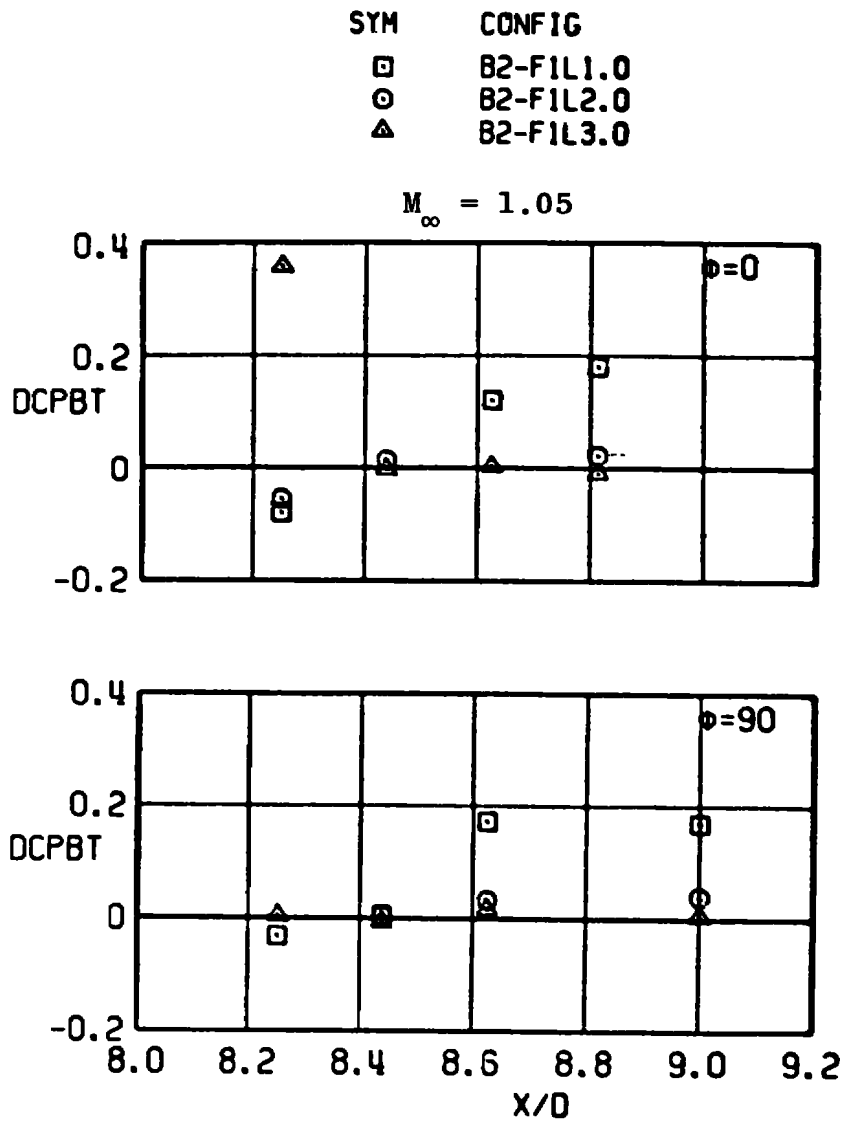


b. Continued
Figure A-2. Continued.

SYM	CONFIG
□	B2-FIL1.0
○	B2-FIL2.0
△	B2-FIL3.0

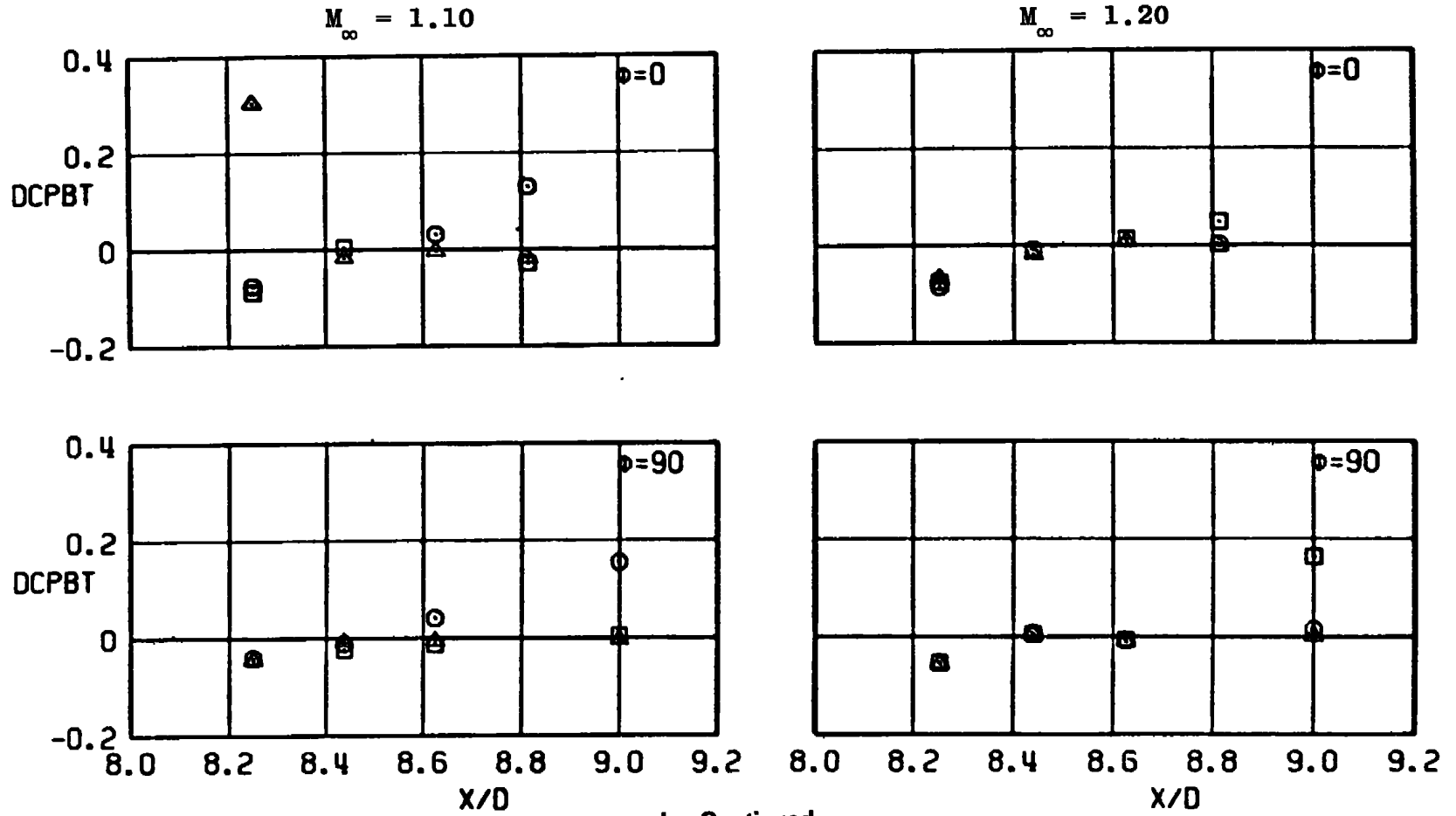


b. Continued
Figure A-2. Continued.



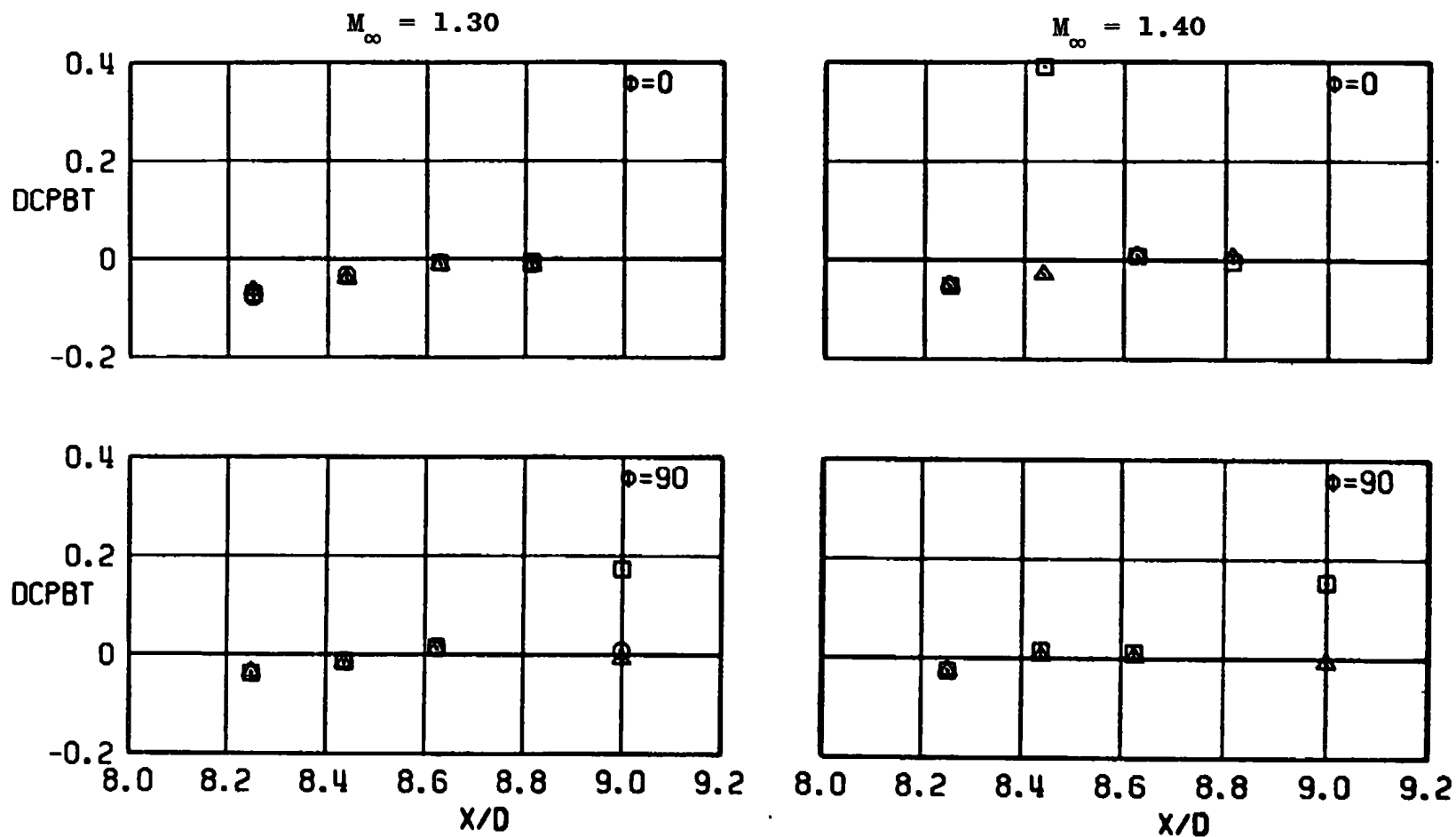
b. Continued
Figure A-2. Continued.

SYM	CONFIG
□	B2-F1L1.0
○	B2-F1L2.0
△	B2-F1L3.0



b. Continued
Figure A-2. Continued.

SYM	CONFIG
□	B2-FIL1.0
○	B2-FIL2.0
△	B2-FIL3.0



b. Concluded
Figure A-2. Concluded.

SYM	CONFIG	Λ , DEG
○	82-S2L1	0
□	82-S5L1	30
△	82-S3L1	45

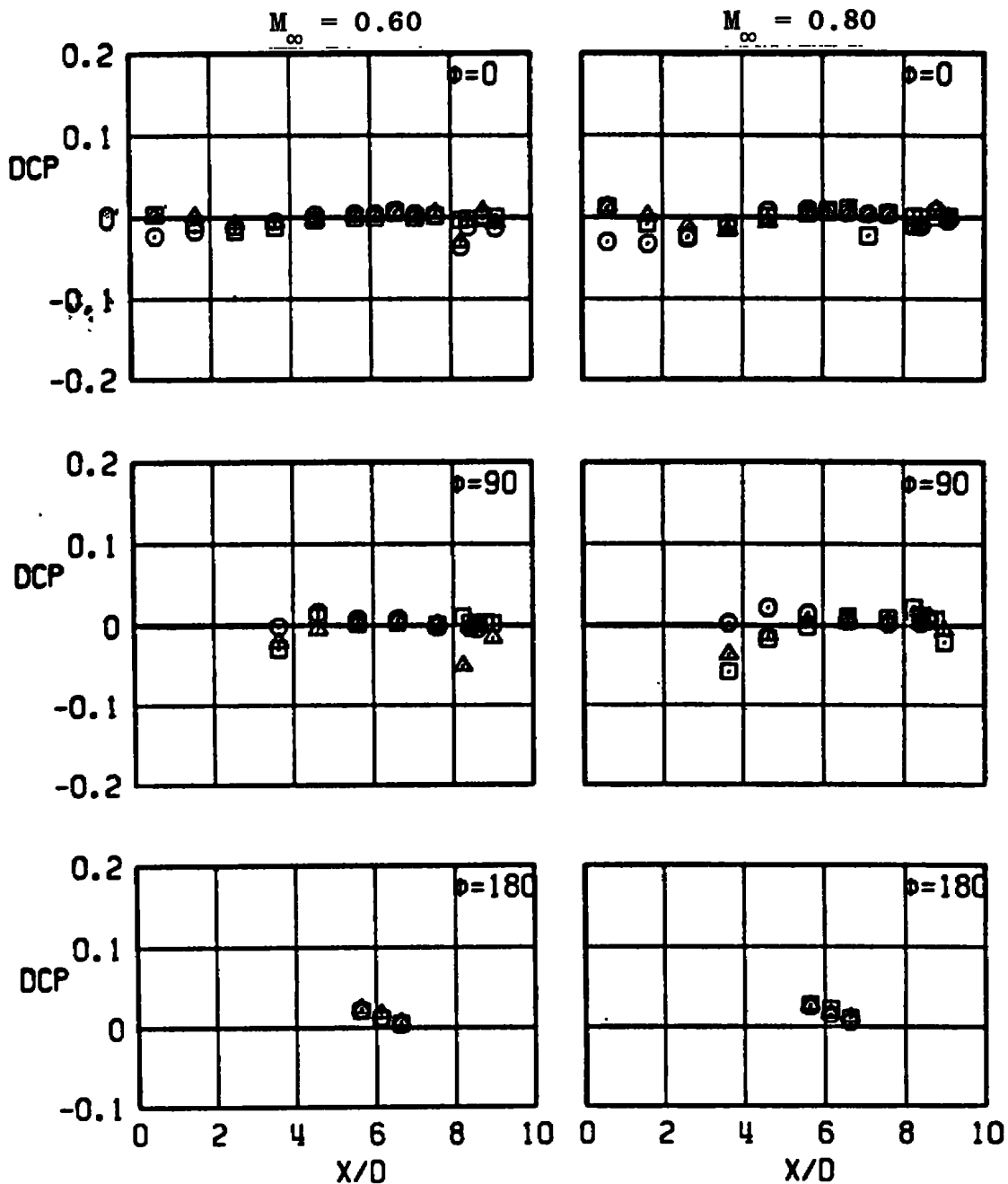
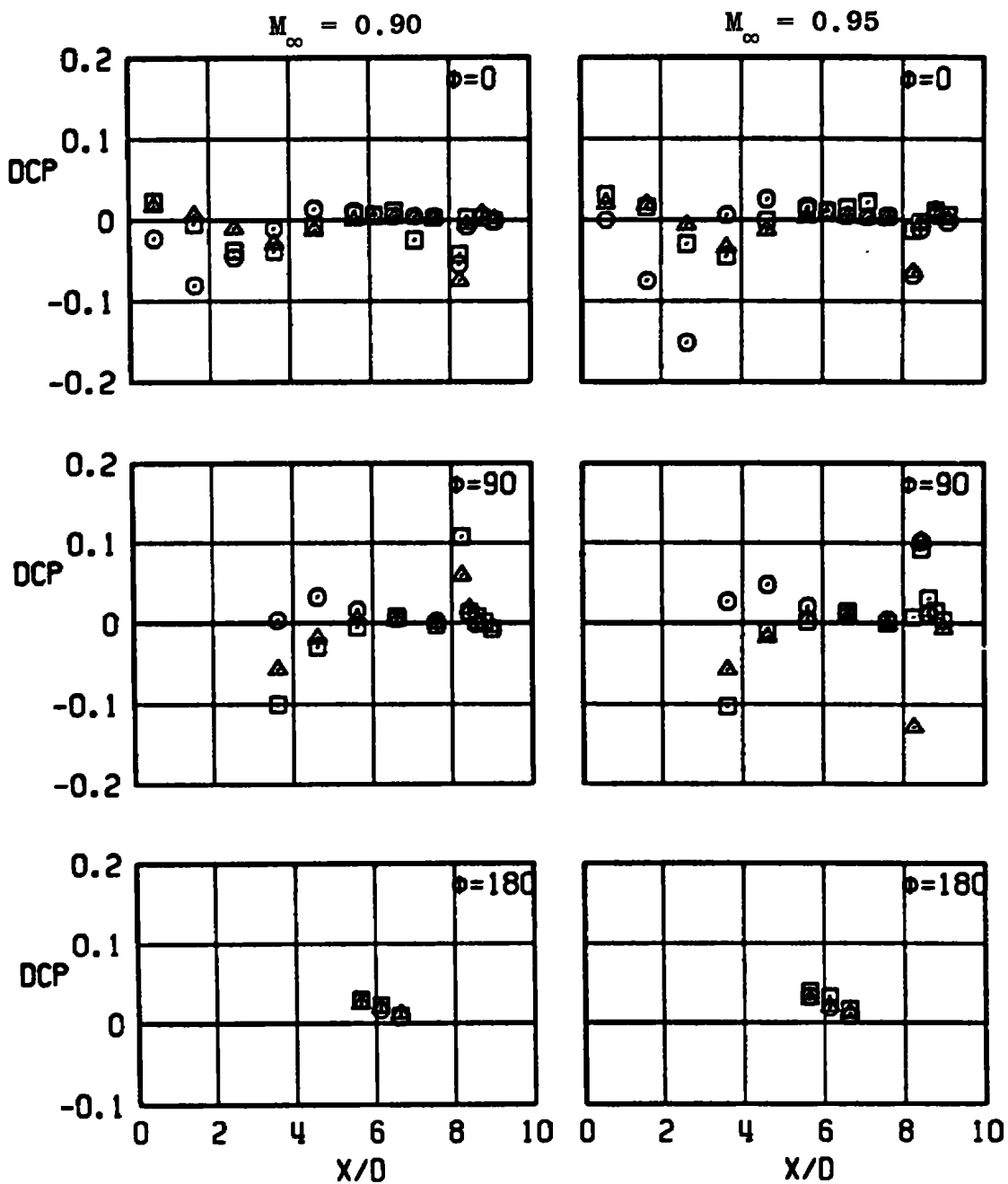
a. DCP versus X/D

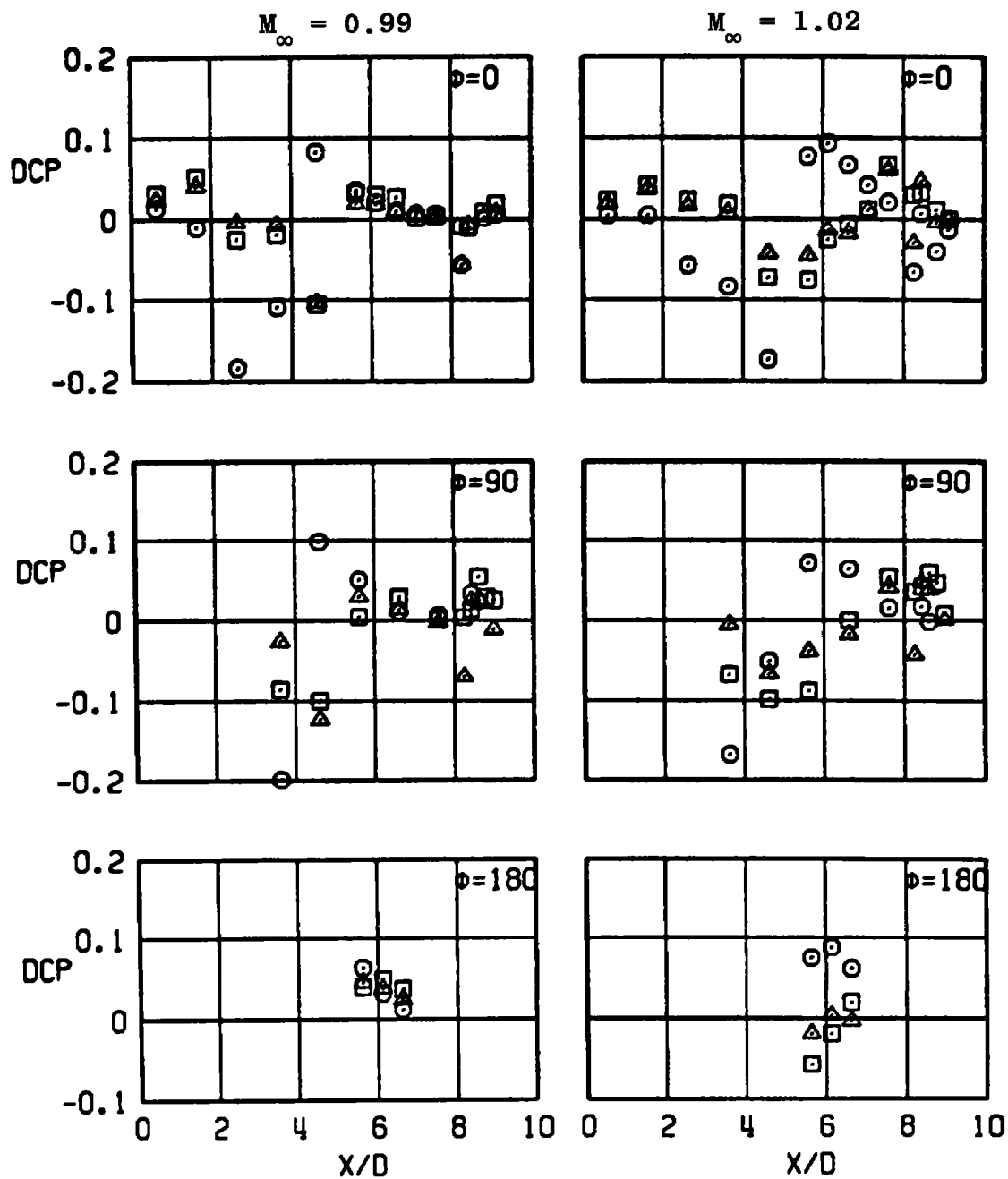
Figure A-3. Effect of strut sweep angle.

SYM	CONFIG	Λ , DEG
○	B2-S2L1	0
□	B2-S5L1	30
△	B2-S3L1	45



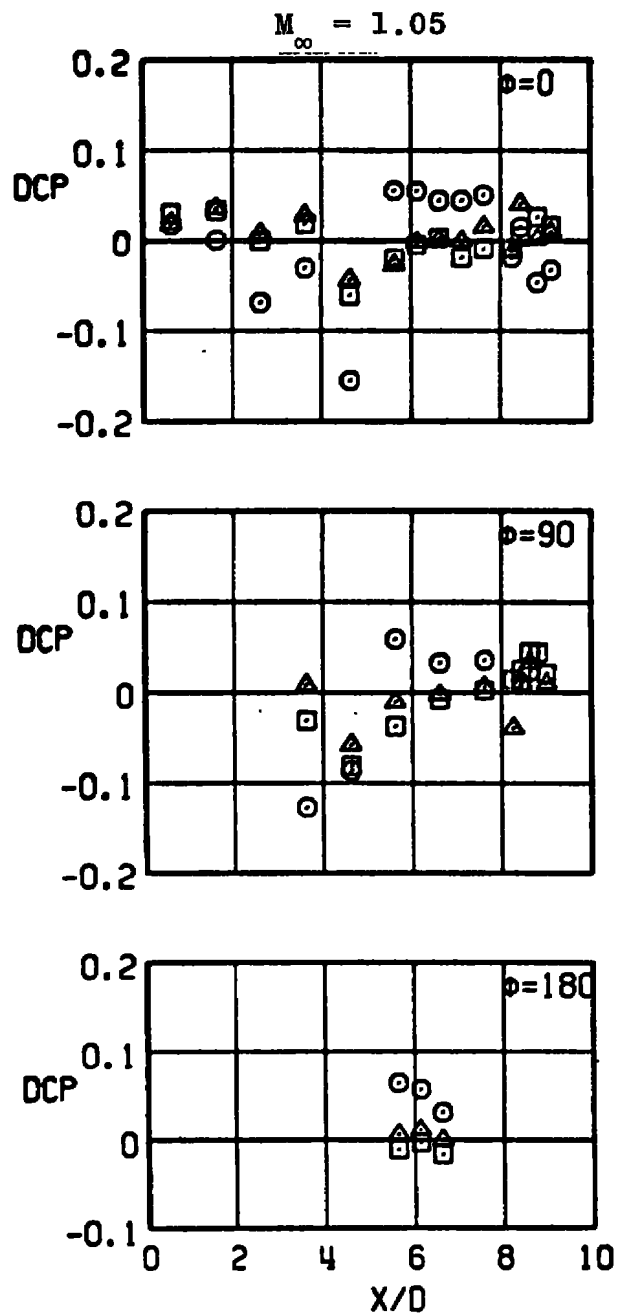
a. Continued
Figure A-3. Continued.

SYM	CONFIG	Λ , DEG
○	B2-S2L1	0
□	B2-S5L1	30
△	B2-S3L1	45



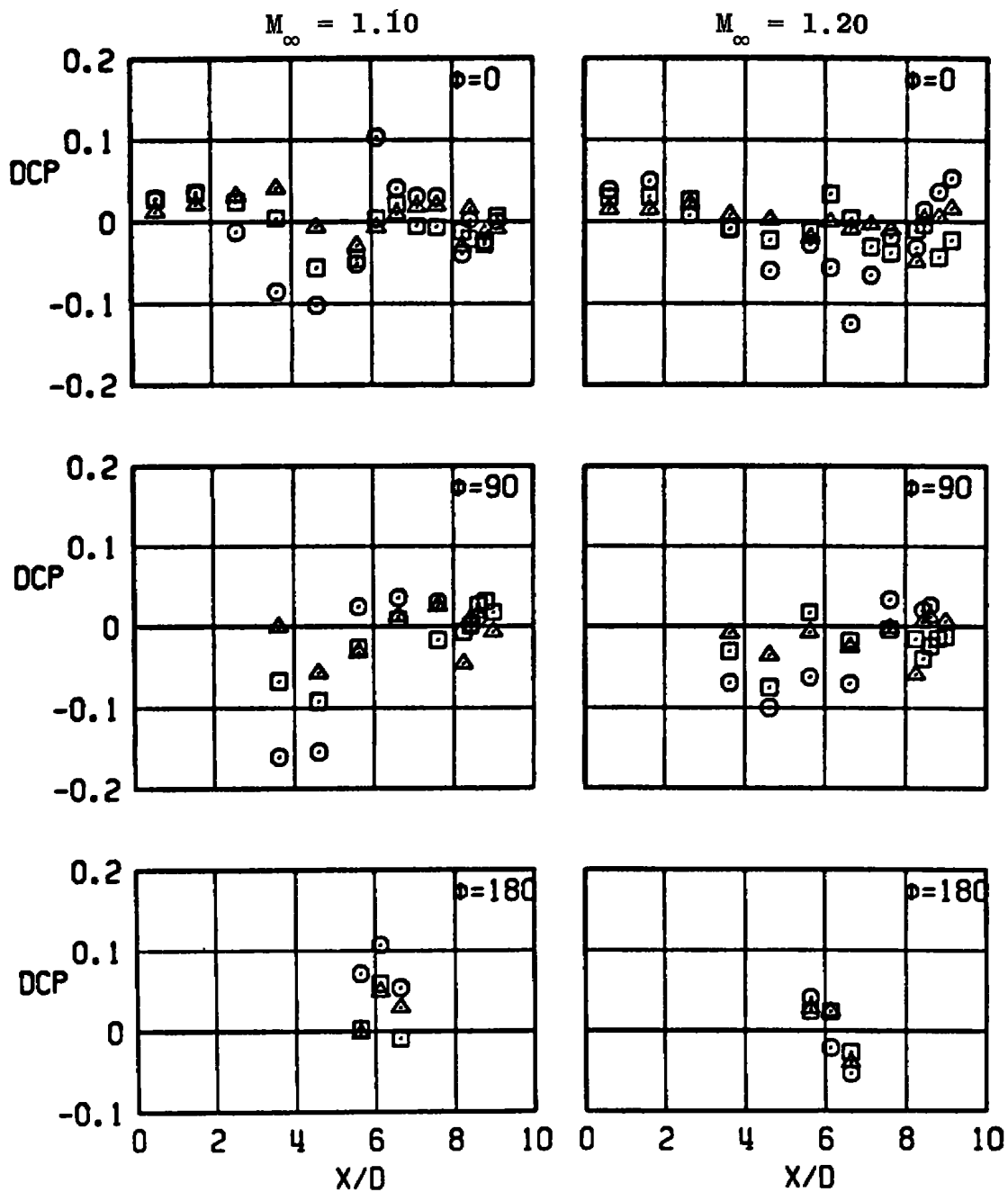
a. Continued
Figure A-3. Continued.

SYM	CONFIG	Λ , DEG
○	B2-S2L1	0
□	B2-S5L1	30
▲	B2-S3L1	45



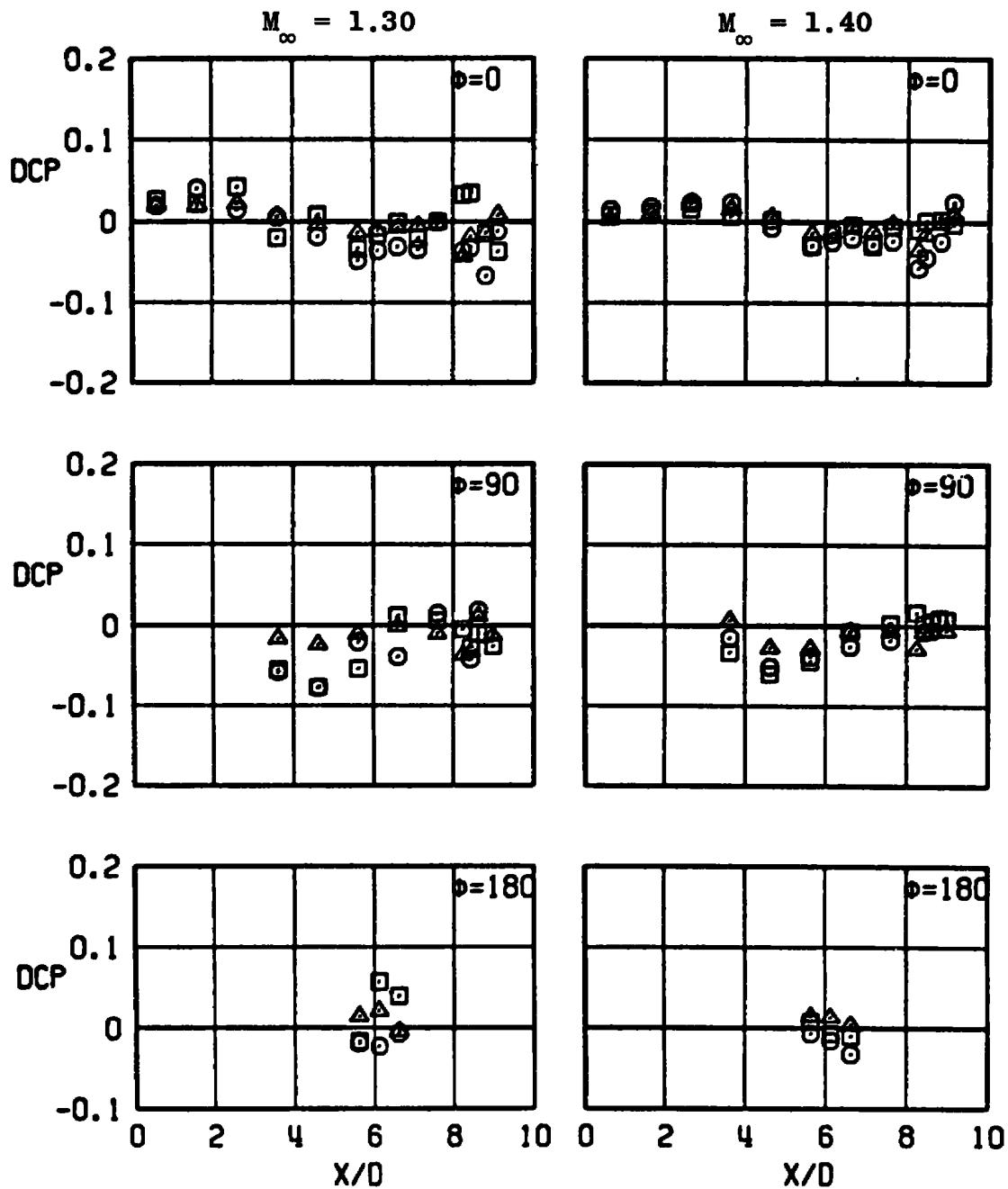
a. Continued
Figure A-3. Continued.

SYM	CONFIG	Λ , DEG
○	B2-S2L1	0
□	B2-S5L1	30
△	B2-S3L1	45



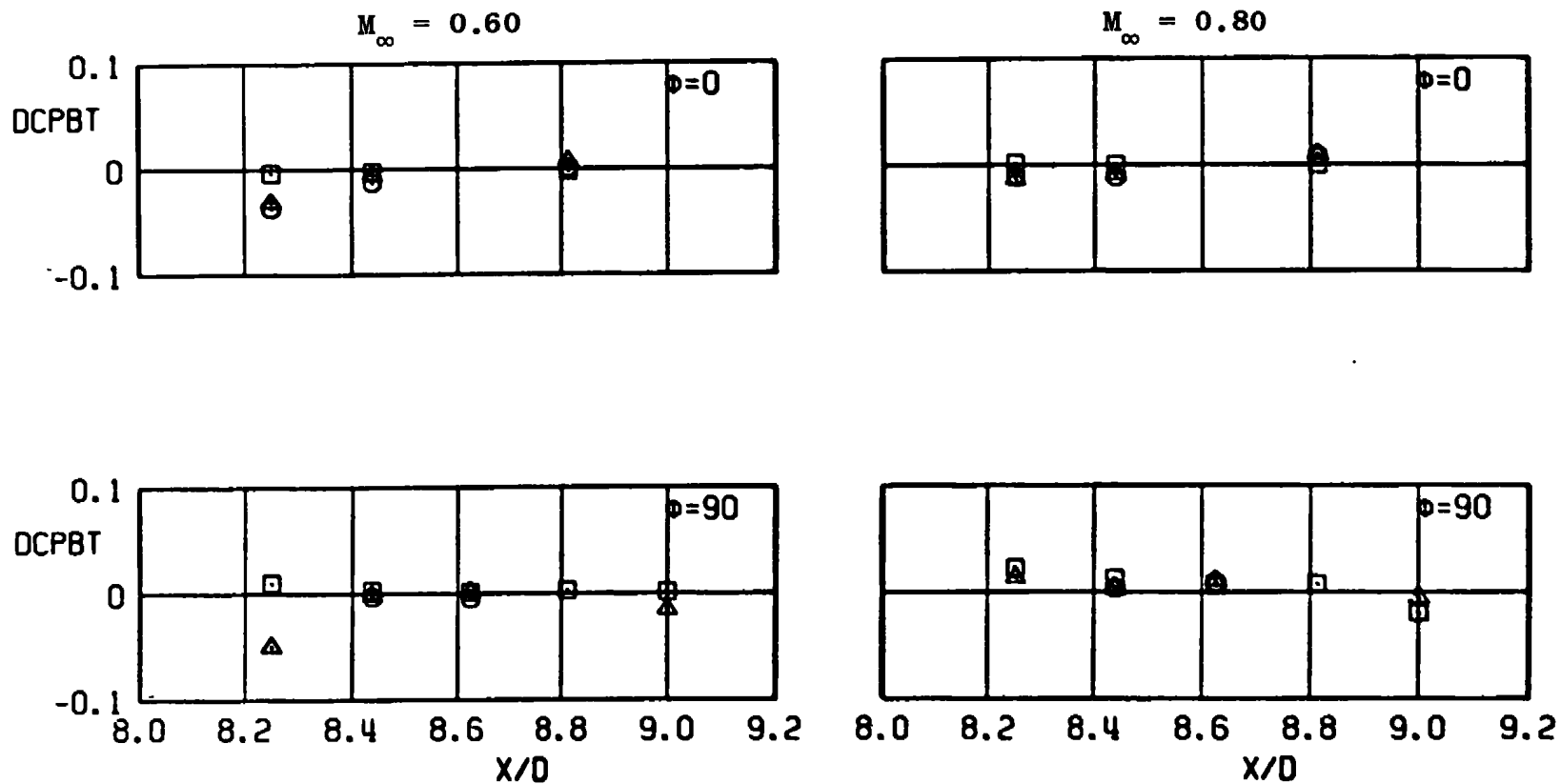
a. Continued
Figure A-3. Continued.

SYM	CONFIG	Λ , DEG
○	B2-S2L1	0
□	B2-S5L1	30
△	B2-S3L1	45



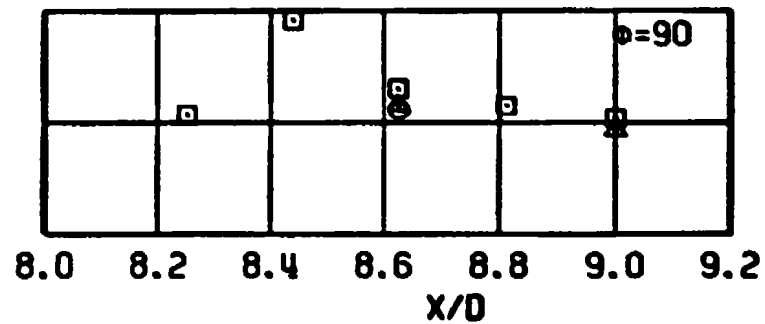
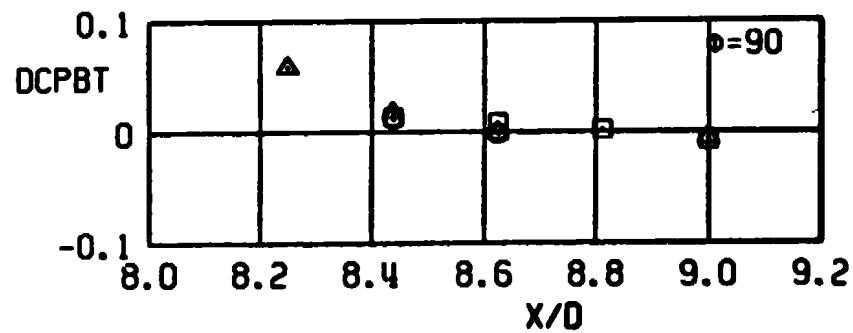
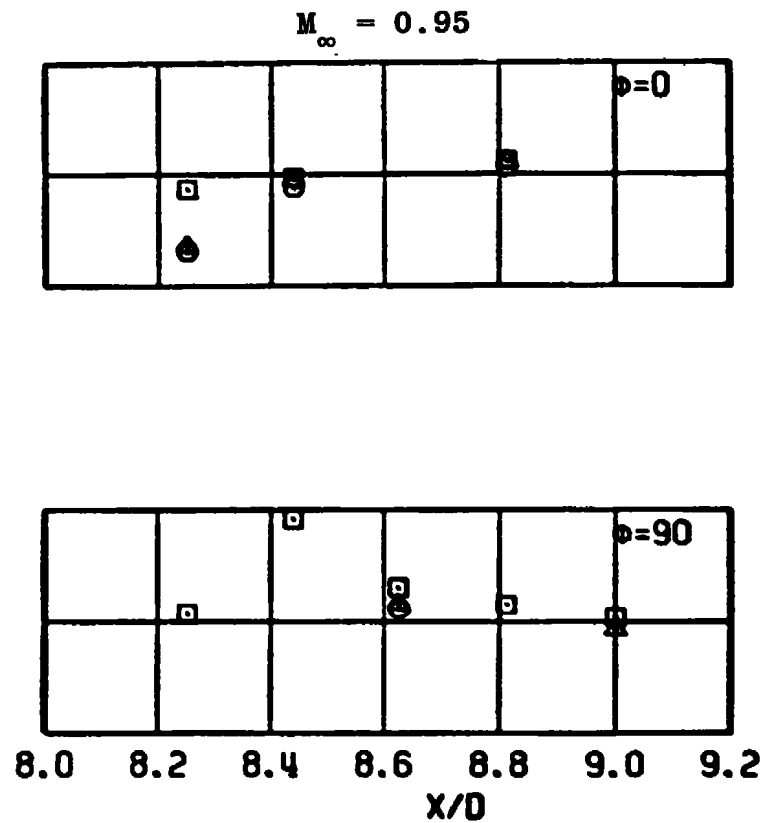
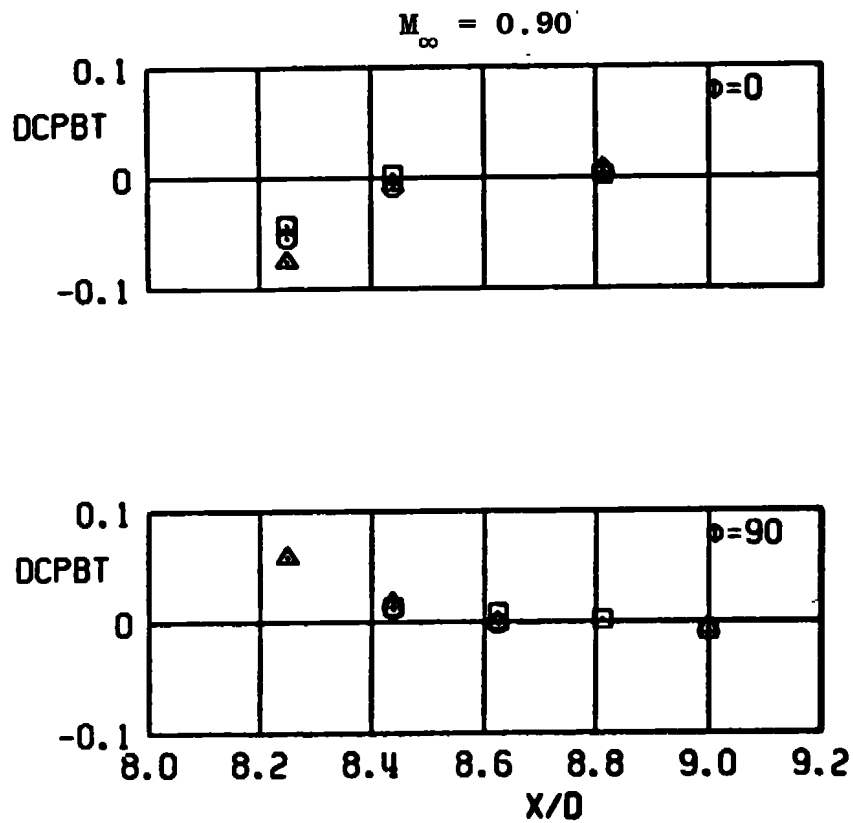
a. Concluded
Figure A-3. Continued.

SYM	CONFIG	Λ , DEG
○	B2-S2L1	0
□	B2-S5L1	30
△	B2-S3L1	45



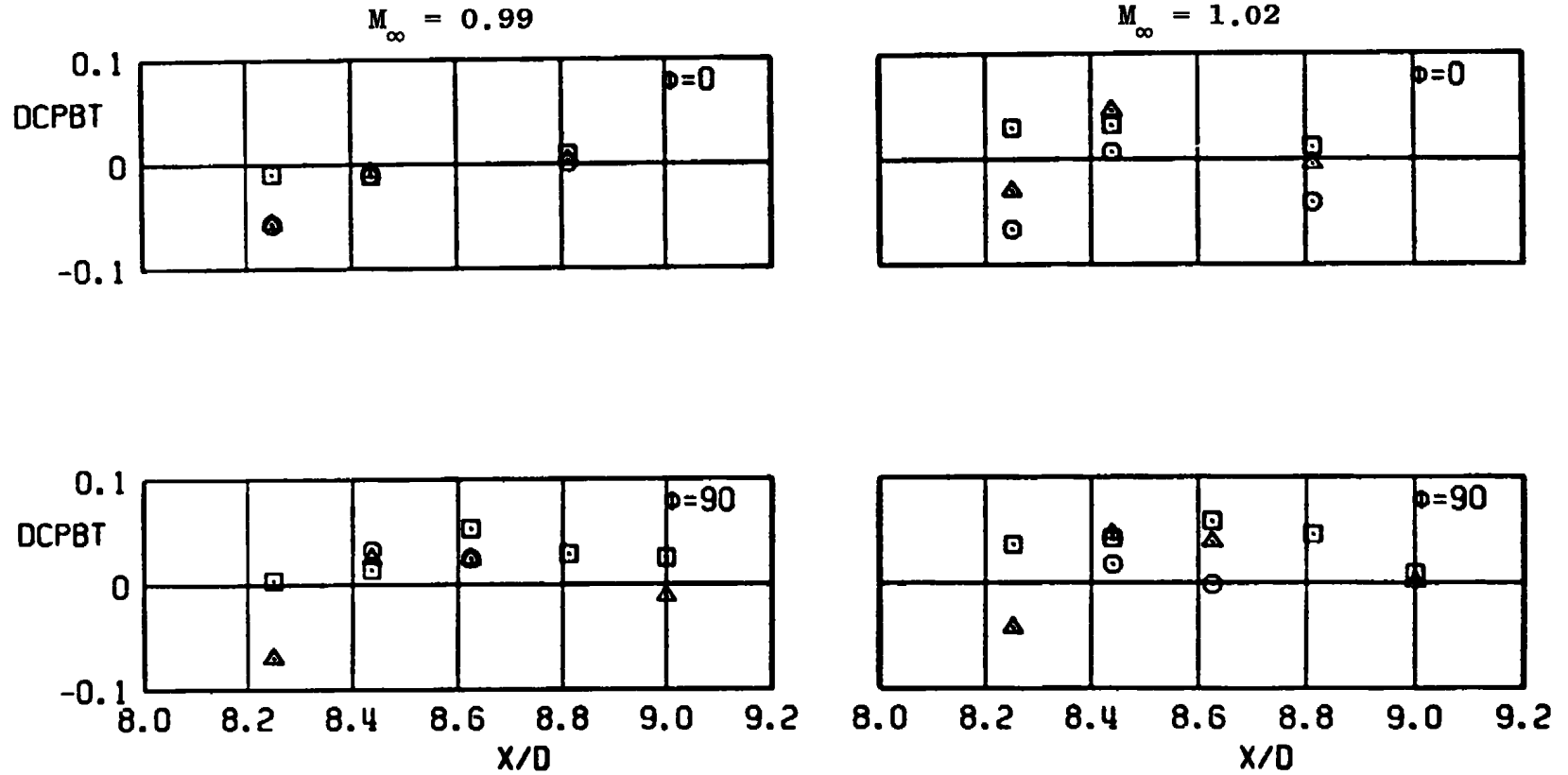
b. DCPBT versus X/D
Figure A-3. Continued.

SYM	CONFIG	Λ , DEG
○	B2-S2L1	0
□	B2-S5L1	30
△	B2-S3L1	45



b. Continued
Figure A-3. Continued.

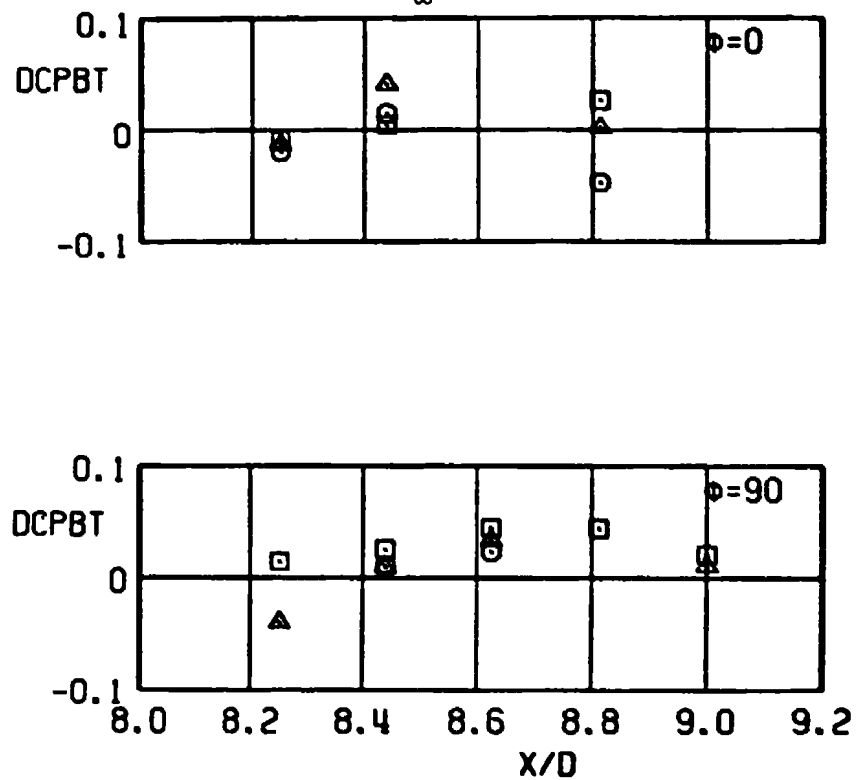
SYM	CONFIG	Λ , DEG
○	B2-S2L1	0
□	B2-S5L1	30
△	B2-S3L1	45



b. Continued
Figure A-3. Continued.

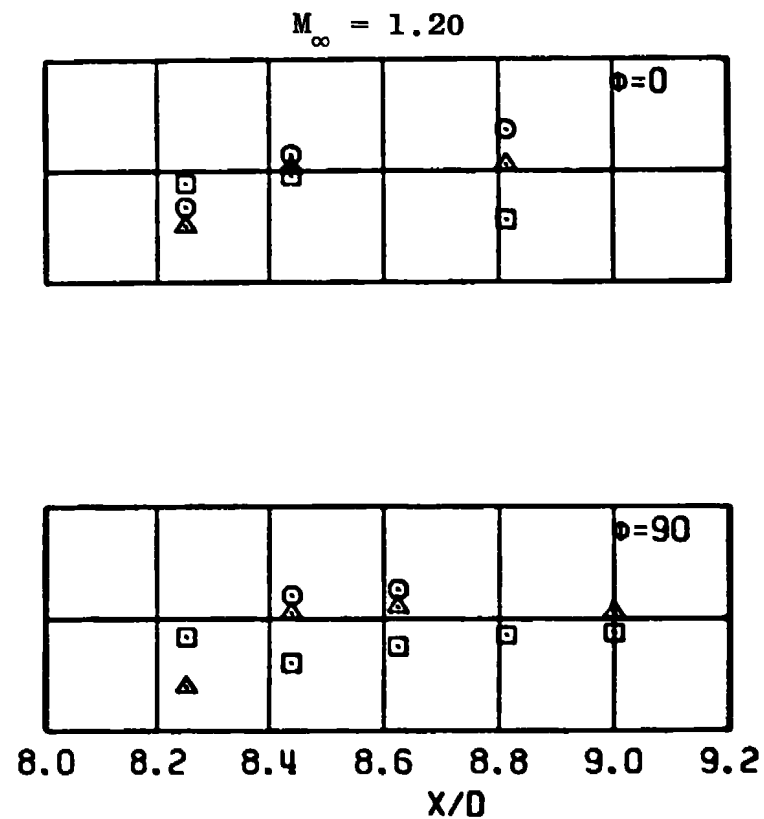
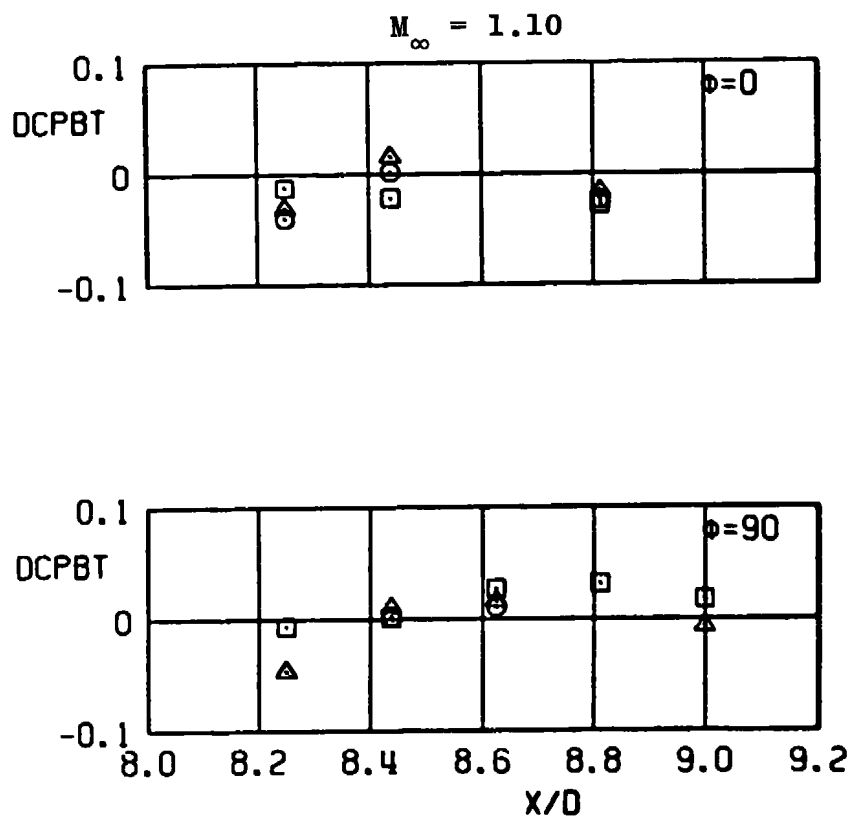
SYM	CONFIG	Λ , DEG
○	B2-S2L1	0
□	B2-S5L1	30
△	B2-S3L1	45

$$M_{\infty} = 1.05$$



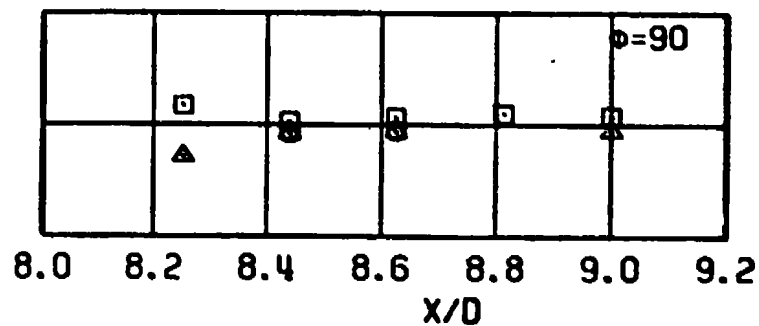
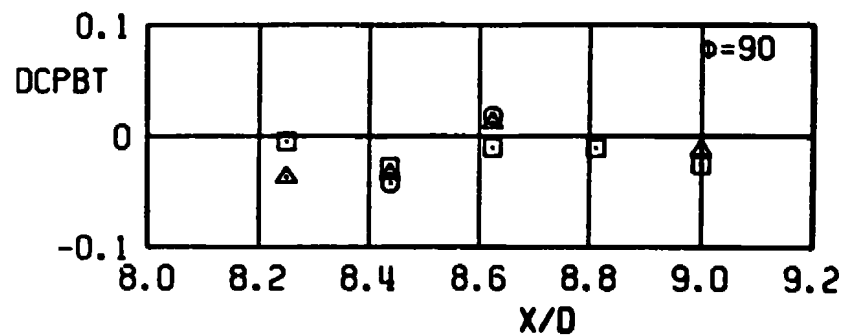
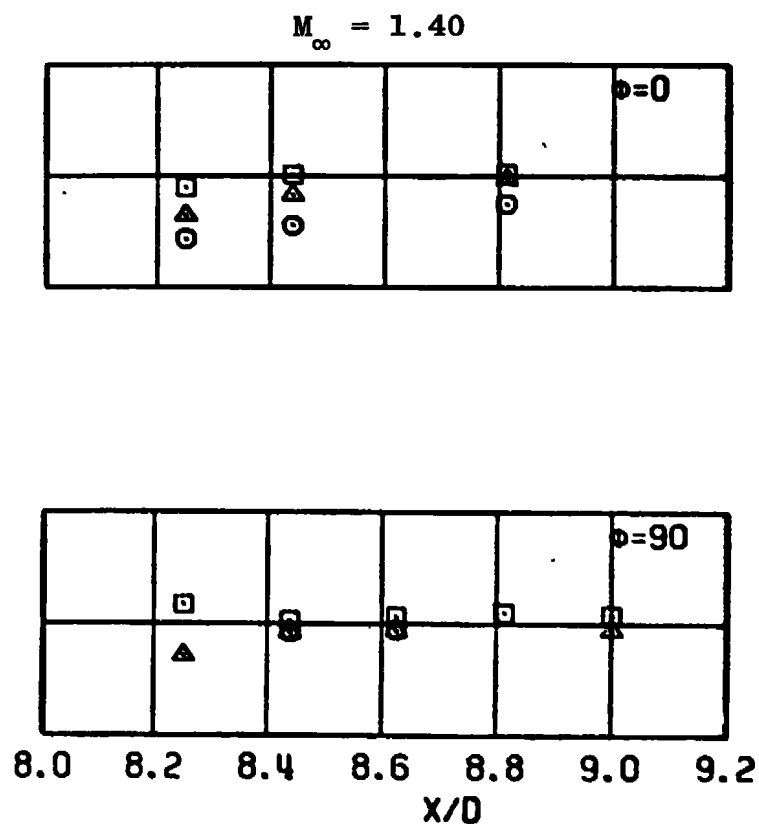
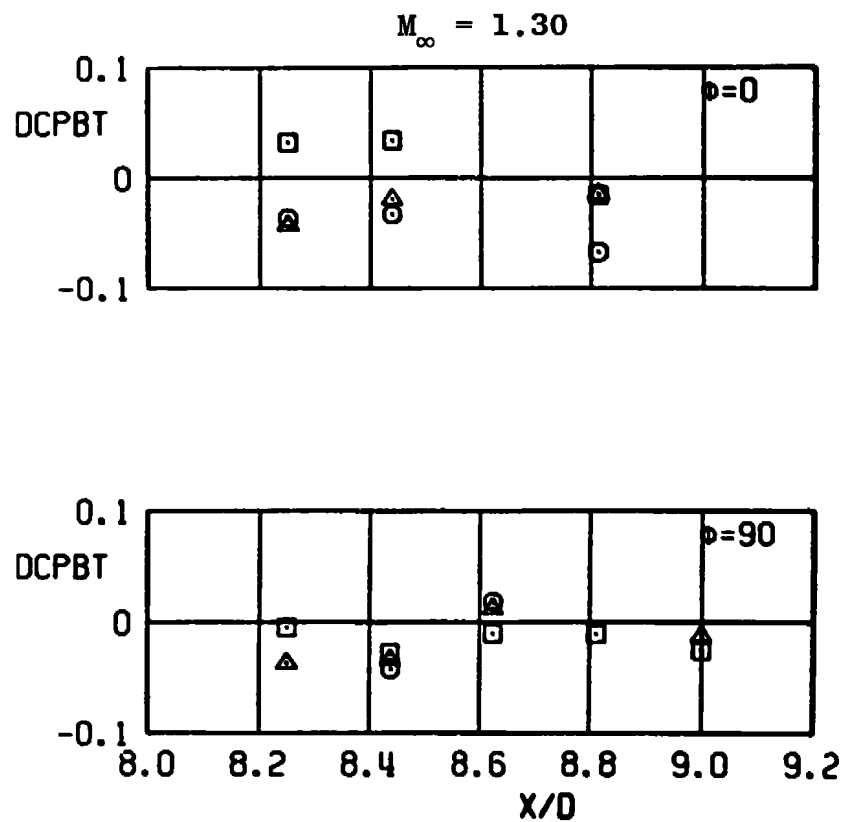
b. Continued
Figure A-3. Continued.

SYM	CONFIG	Λ , DEG
○	B2-S2L1	0
□	B2-S5L1	30
△	B2-S3L1	45



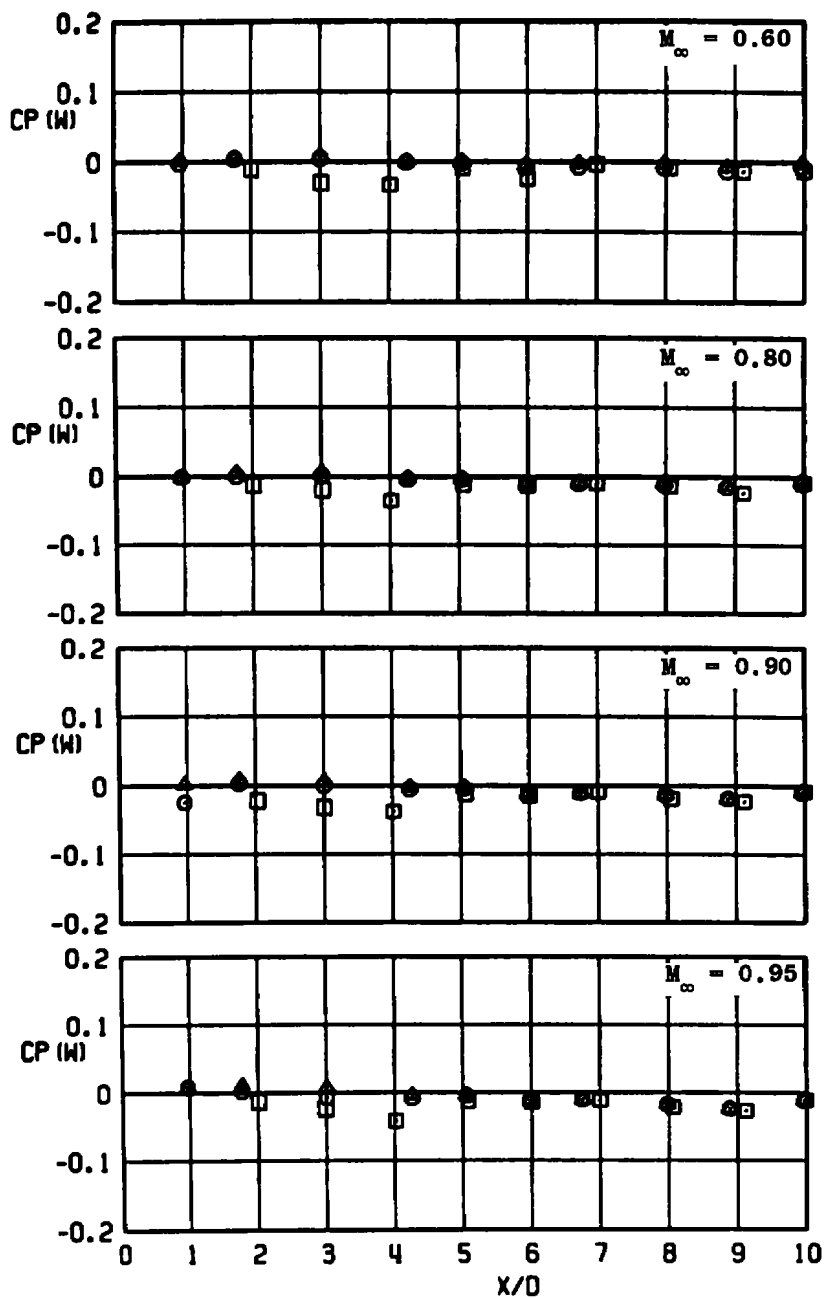
b. Continued
Figure A-3. Continued.

SYM	CONFIG	Λ , DEG
○	B2-S2L1	0
□	B2-S5L1	30
△	B2-S3L1	45



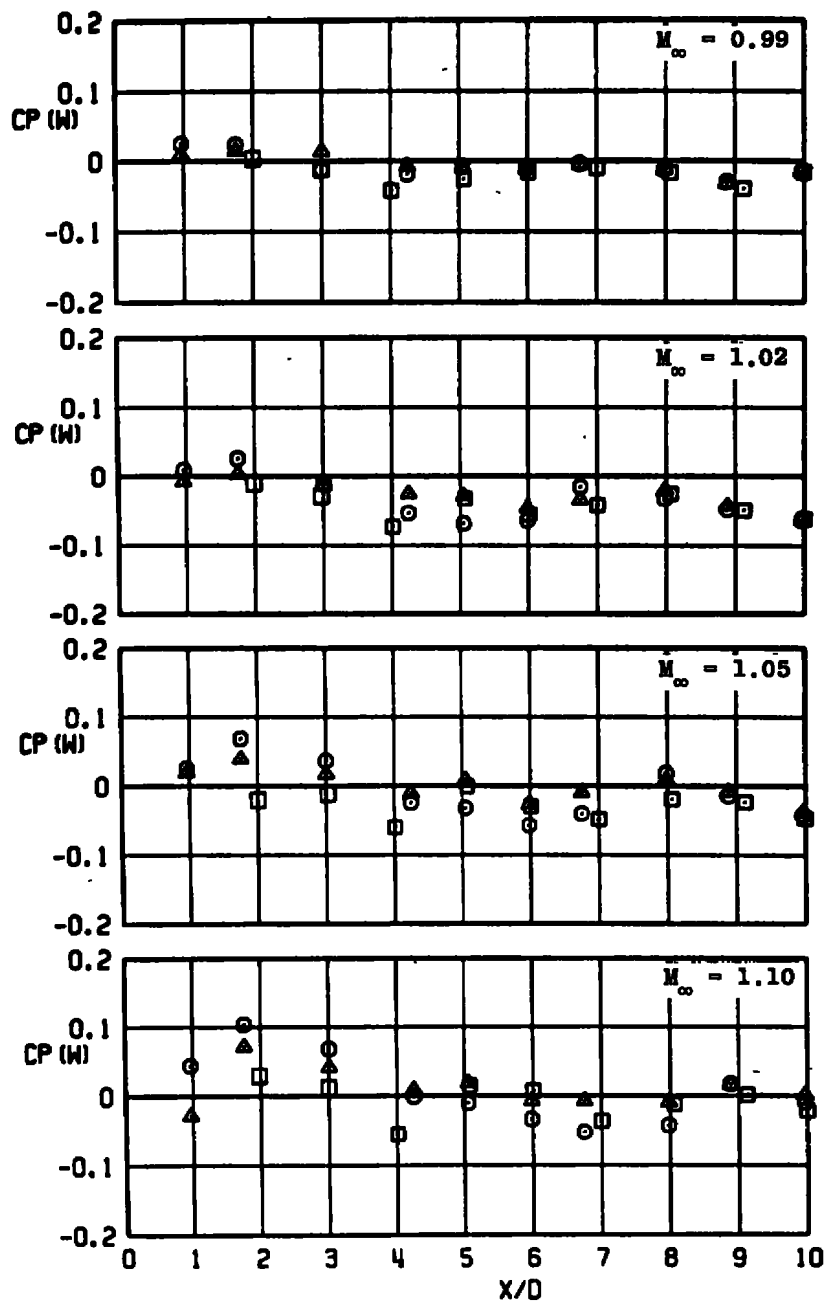
b. Concluded
Figure A-3. Continued.

SYM	CONFIG	Λ , DEG	ϕ , DEG
○	B2-S2L1	0	0
□	B2-S5L1	30	0
△	B2-S3L1	45	0



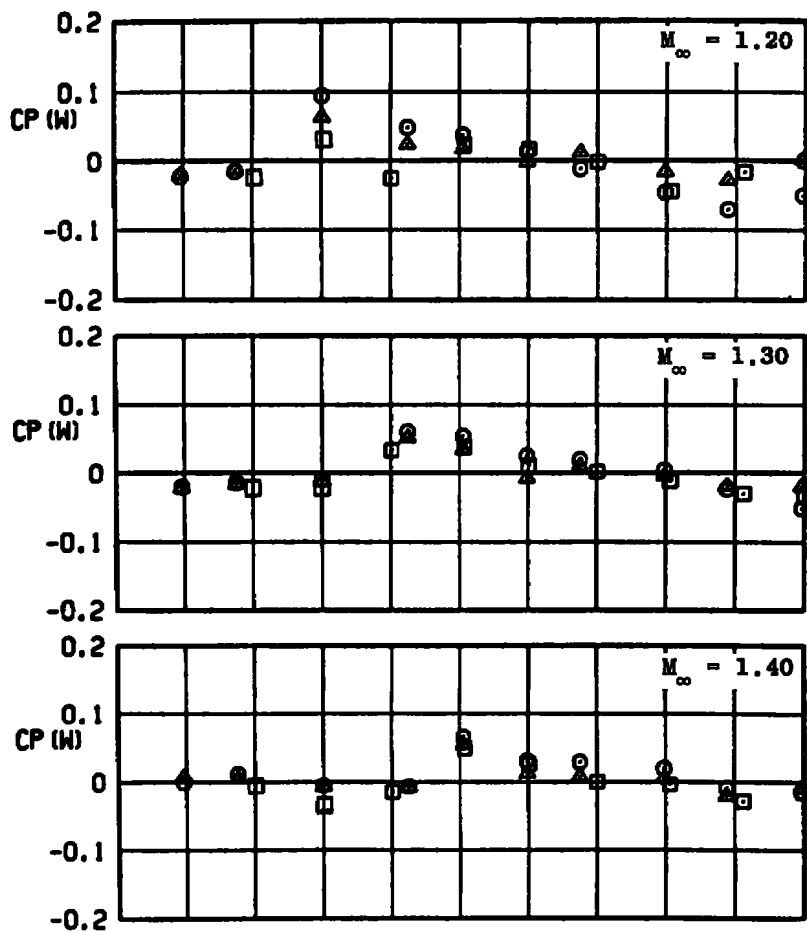
c. CP(W) versus X/D, $\phi = 0$
Figure A-3. Continued.

SYM	CONFIG	Λ , DEG	ϕ , DEG
○	B2-S2L1	0	0
□	B2-S5L1	30	0
▲	B2-S3L1	45	0



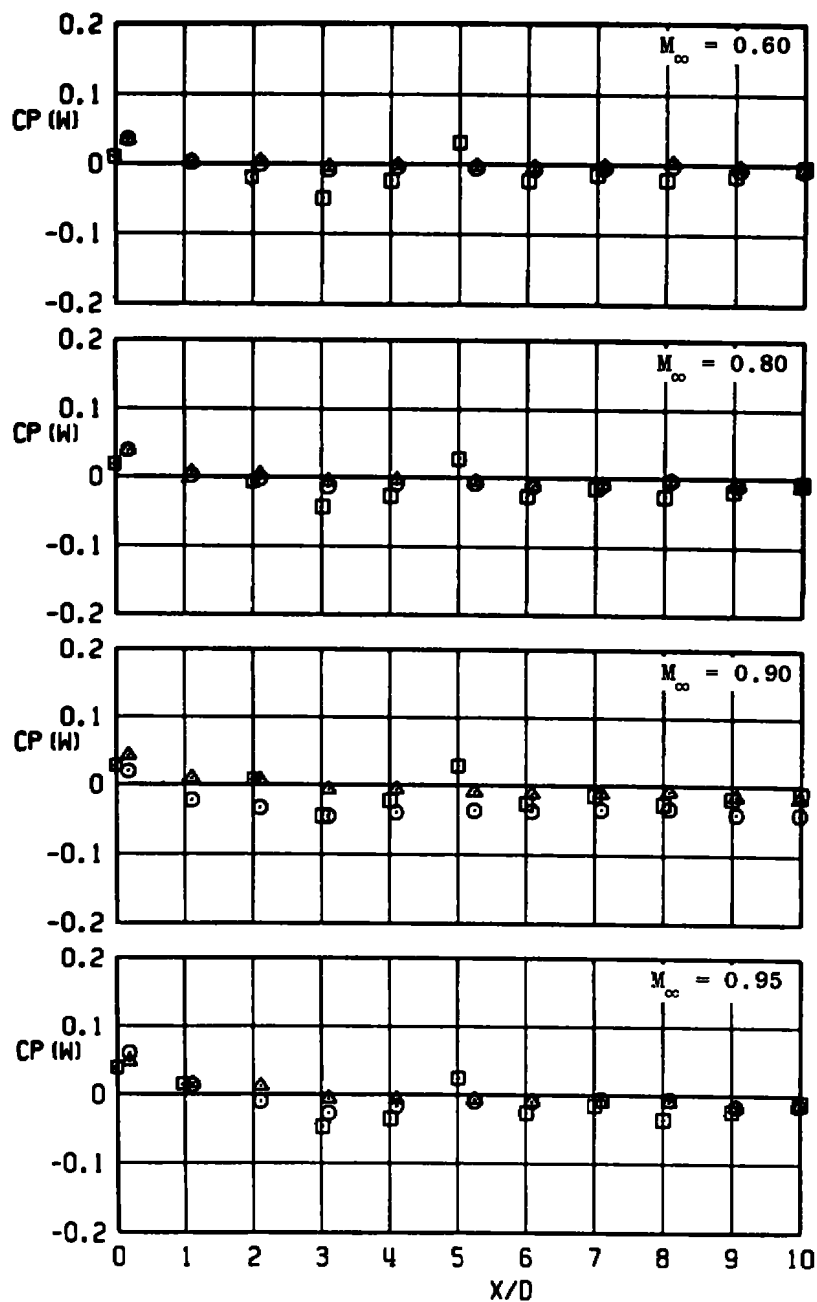
c. Continued
Figure A-3. Continued.

SYM	CONFIG	Λ , DEG	ϕ , DEG
○	B2-S2L1	0	0
□	B2-S5L1	30	0
△	B2-S3L1	45	0



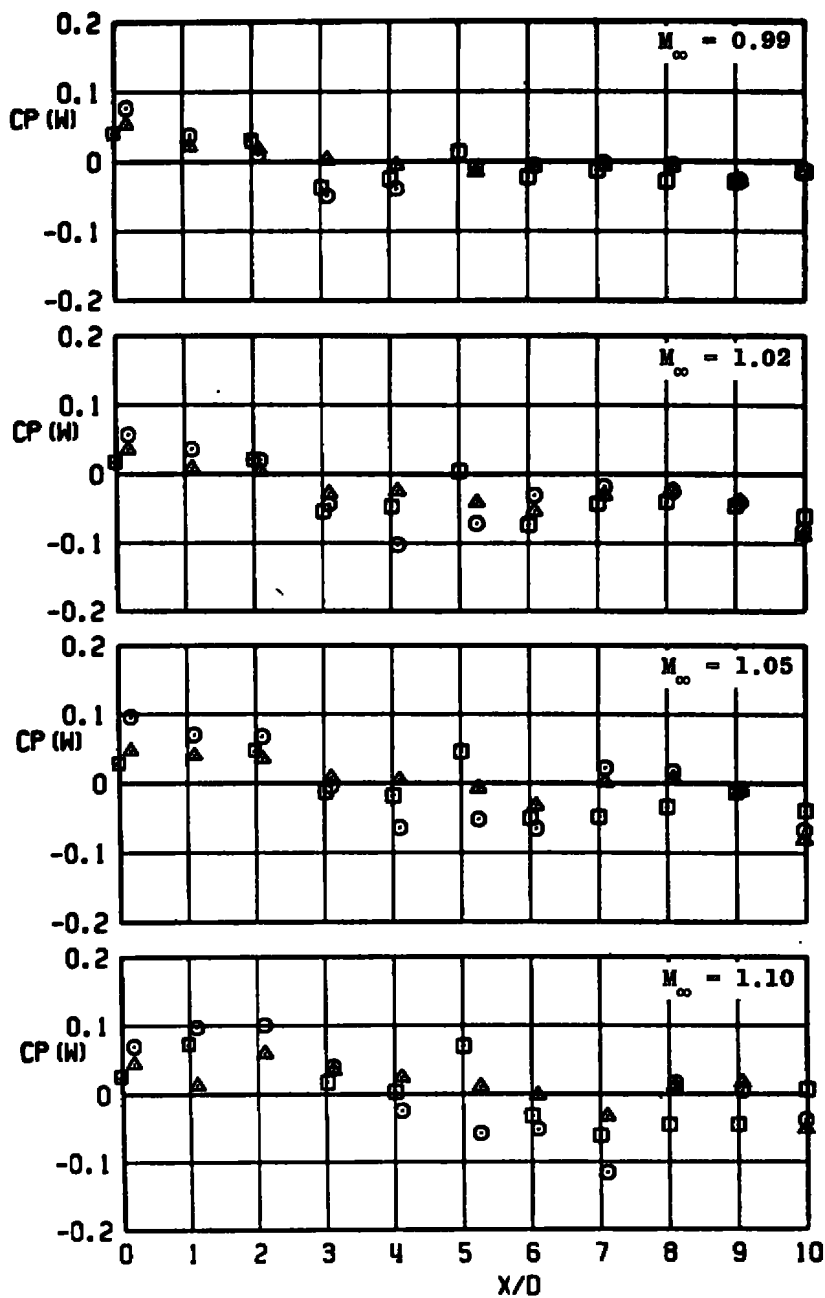
c. Concluded
Figure A-3. Continued.

SYM	CONFIG	Λ , DEG	ϕ , DEG
○	B2-S2L1	0	90
□	B2-S5L1	30	90
△	B2-S3L1	45	90



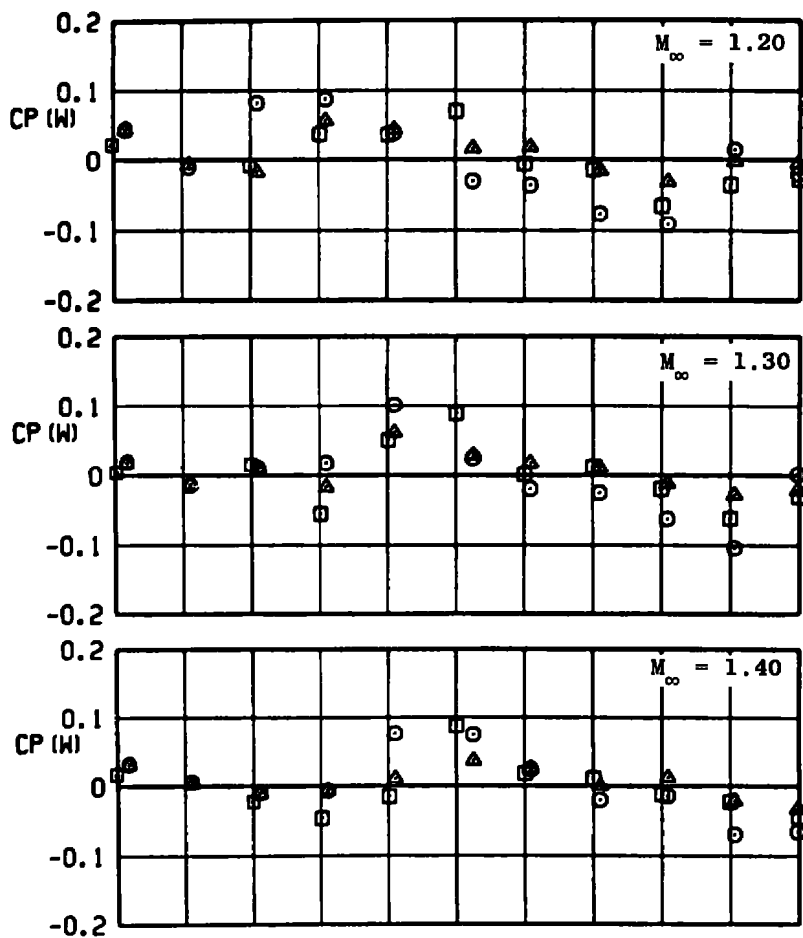
d. $CP(W)$ versus X/D , $\phi = 90$ deg
Figure A-3. Continued.

SYM	CONFIG	Λ , DEG	ϕ , DEG
○	B2-S2L1	0	90
□	B2-S5L1	30	90
▲	B2-S3L1	45	90



d. Continued
Figure A-3. Continued.

SYM	CONFIG	Λ , DEG	ϕ , DEG
○	B2-S2L1	0	90
□	B2-S5L1	30	90
△	B2-S3L1	45	90



d. Concluded
Figure A-3. Concluded.

SYM	CONFIG	l , IN.
○	B2-S2L1	0.0
□	B2-S2L3	1.6

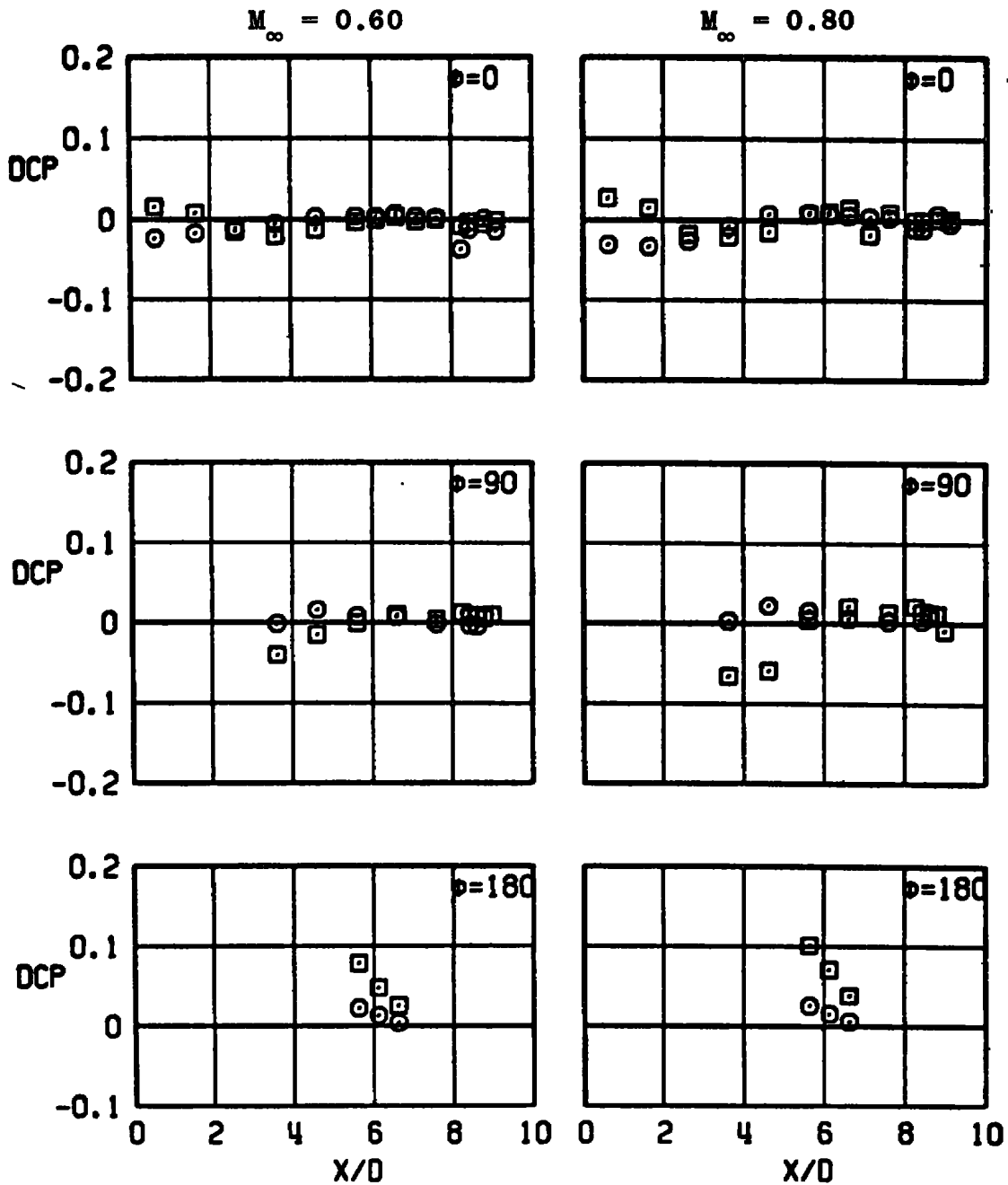
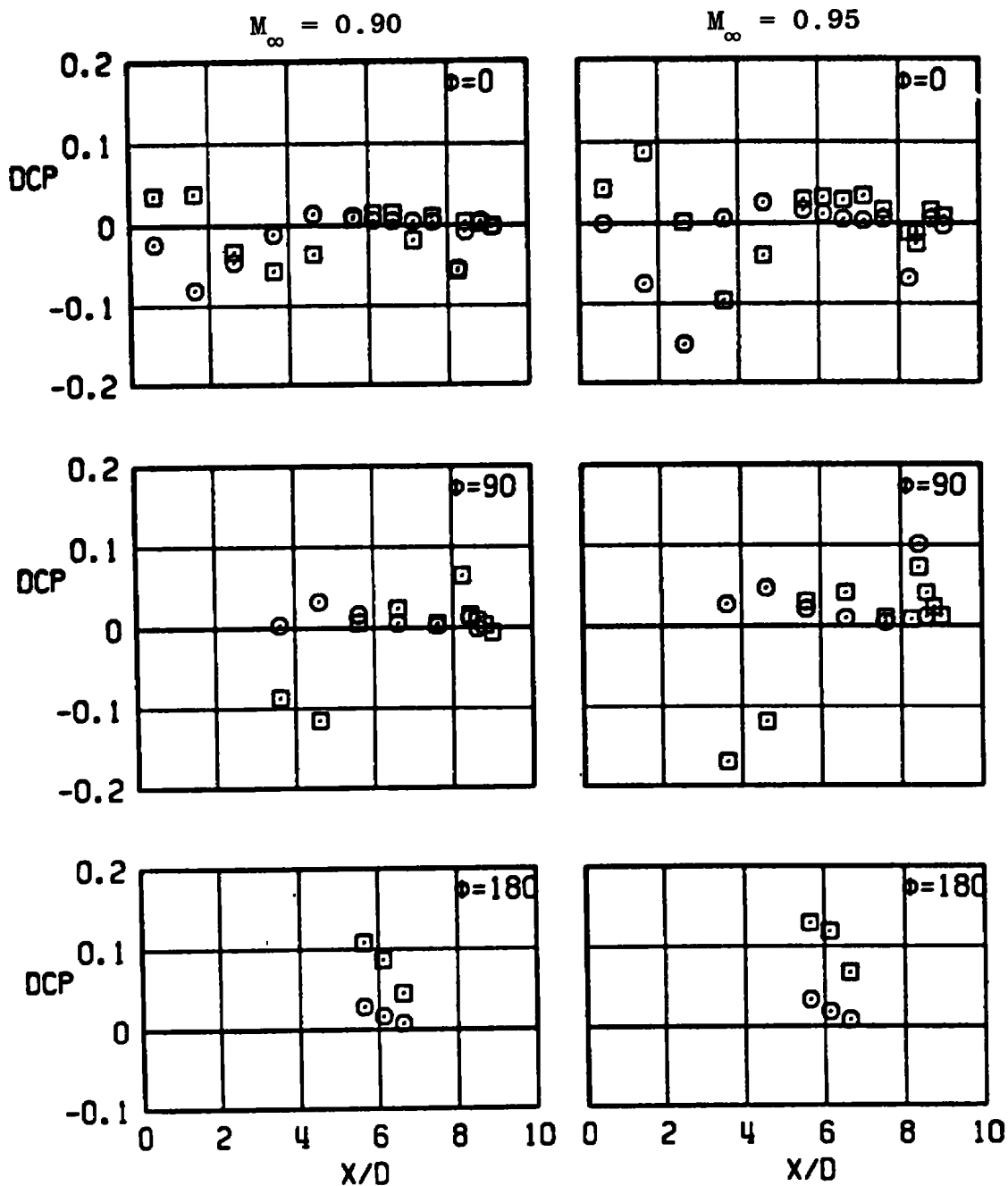
a. DCP versus X/D (straight strut, 10-deg boattail)

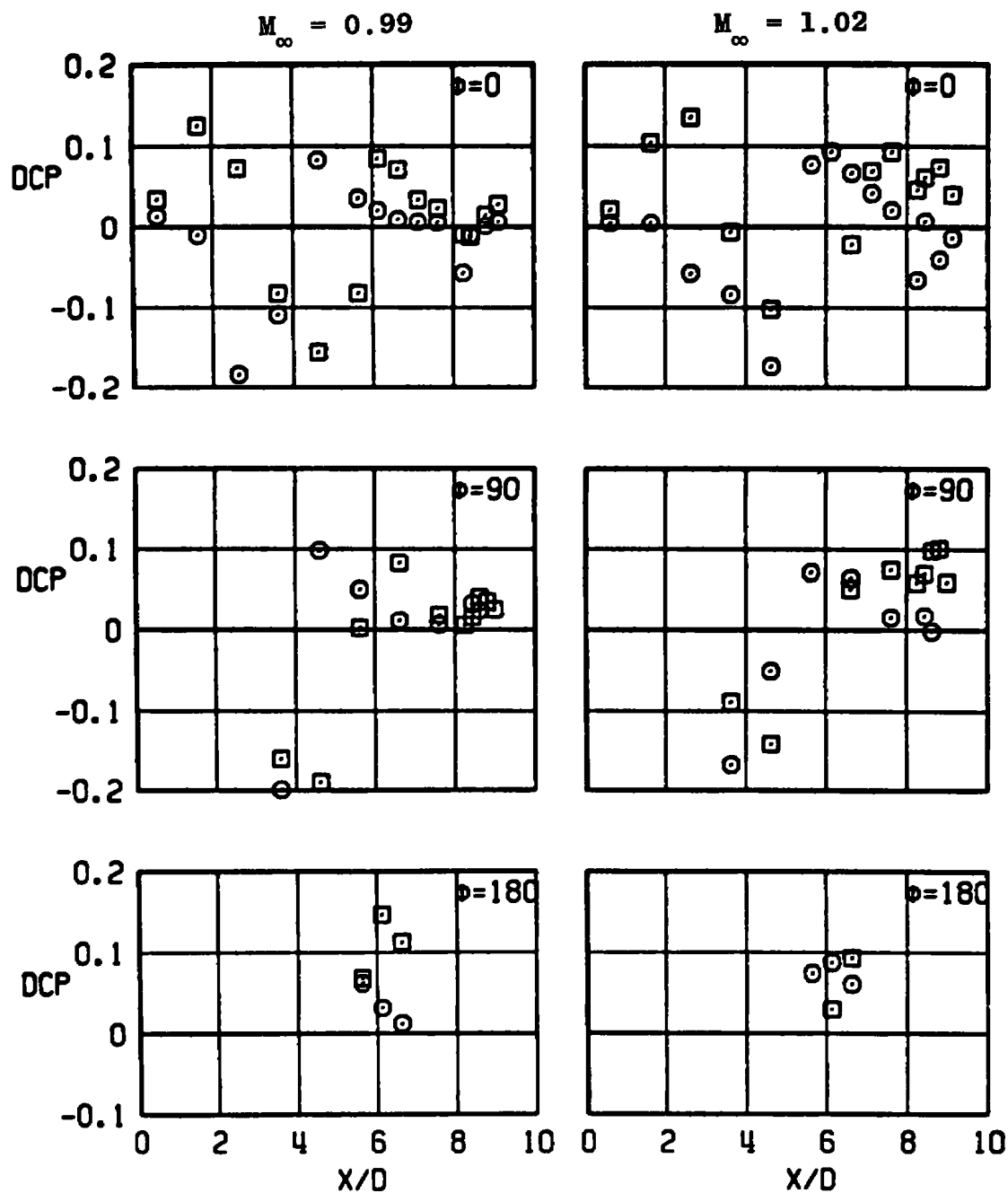
Figure A-4. Effect of strut location.

SYM	CONFIG	l , IN.
○	B2-S2L1	0.0
□	B2-S2L3	1.6



a. Continued
Figure A-4. Continued.

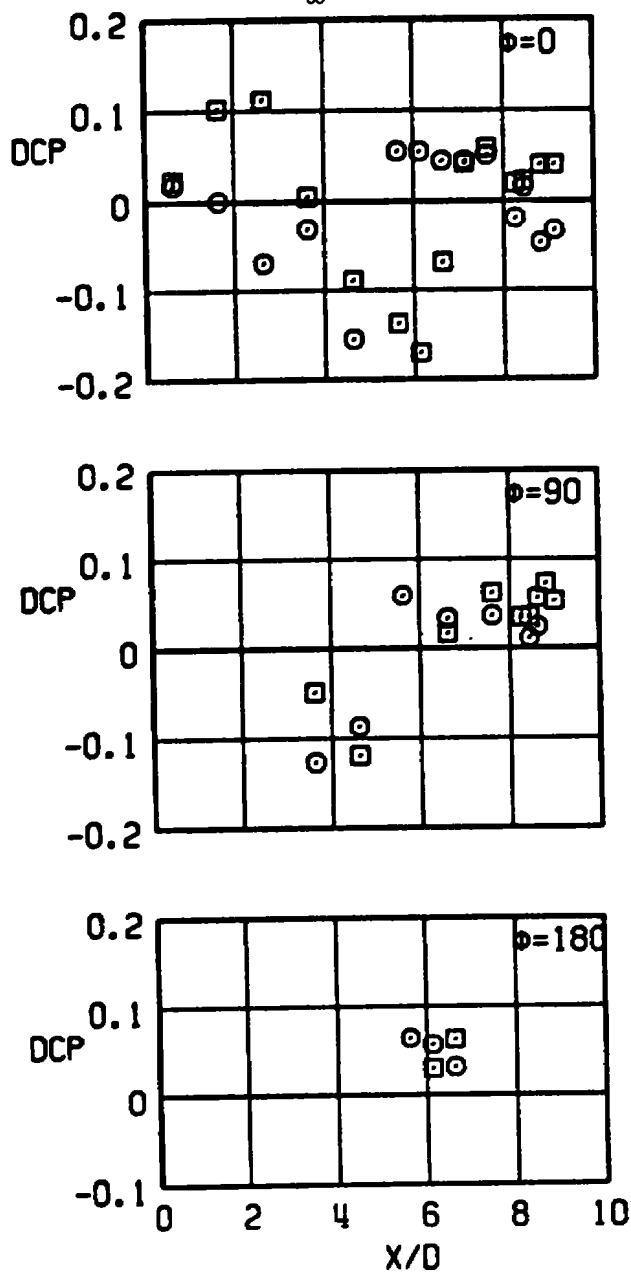
SYM	CONFIG	l , IN.
○	B2-S2L1	0.0
□	B2-S2L3	1.6



a. Continued
Figure A-4. Continued.

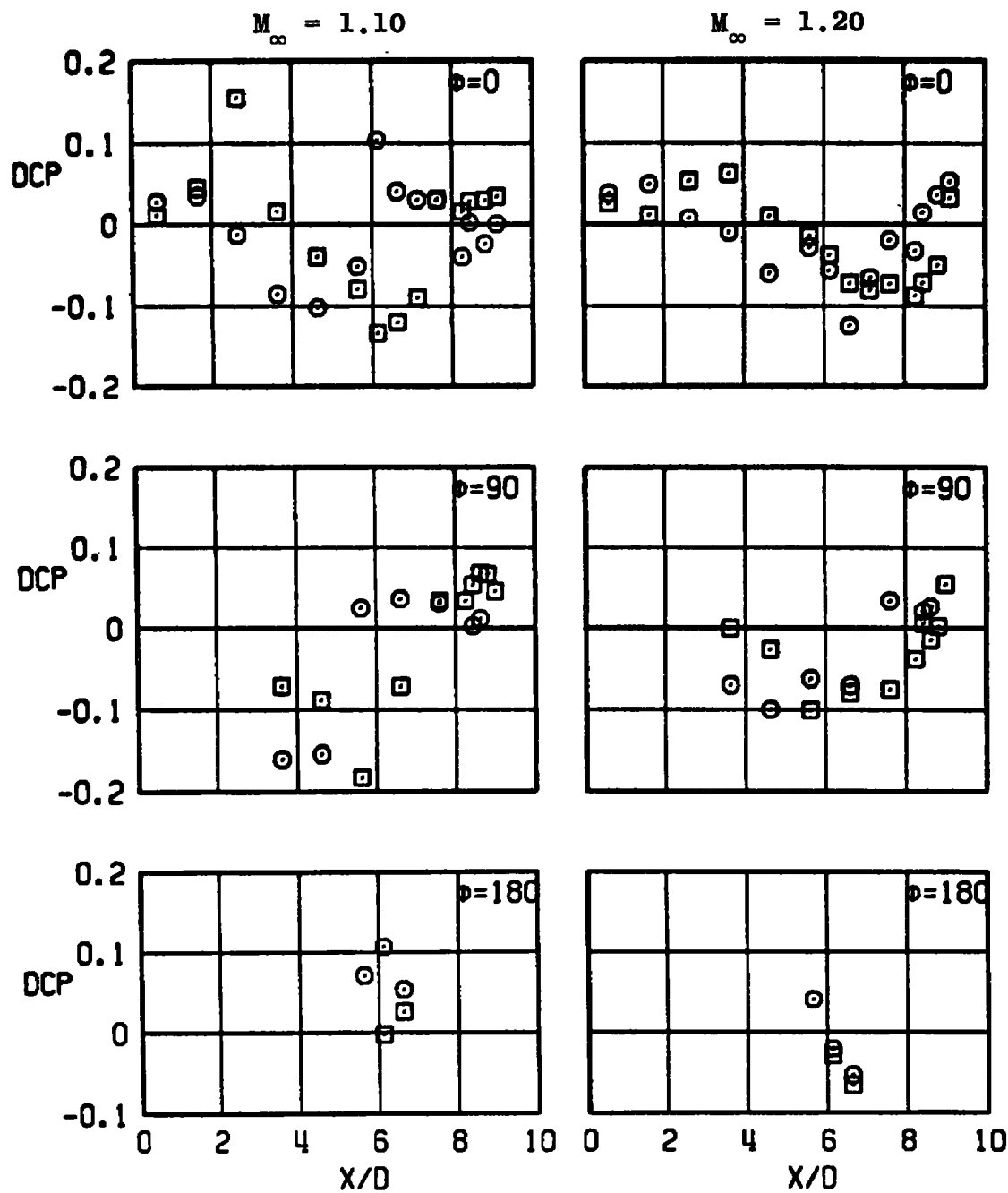
SYM	CONFIG	l , IN.
○	B2-S2L1	0.0
□	B2-S2L3	1.6

$$M_{\infty} = 1.05$$



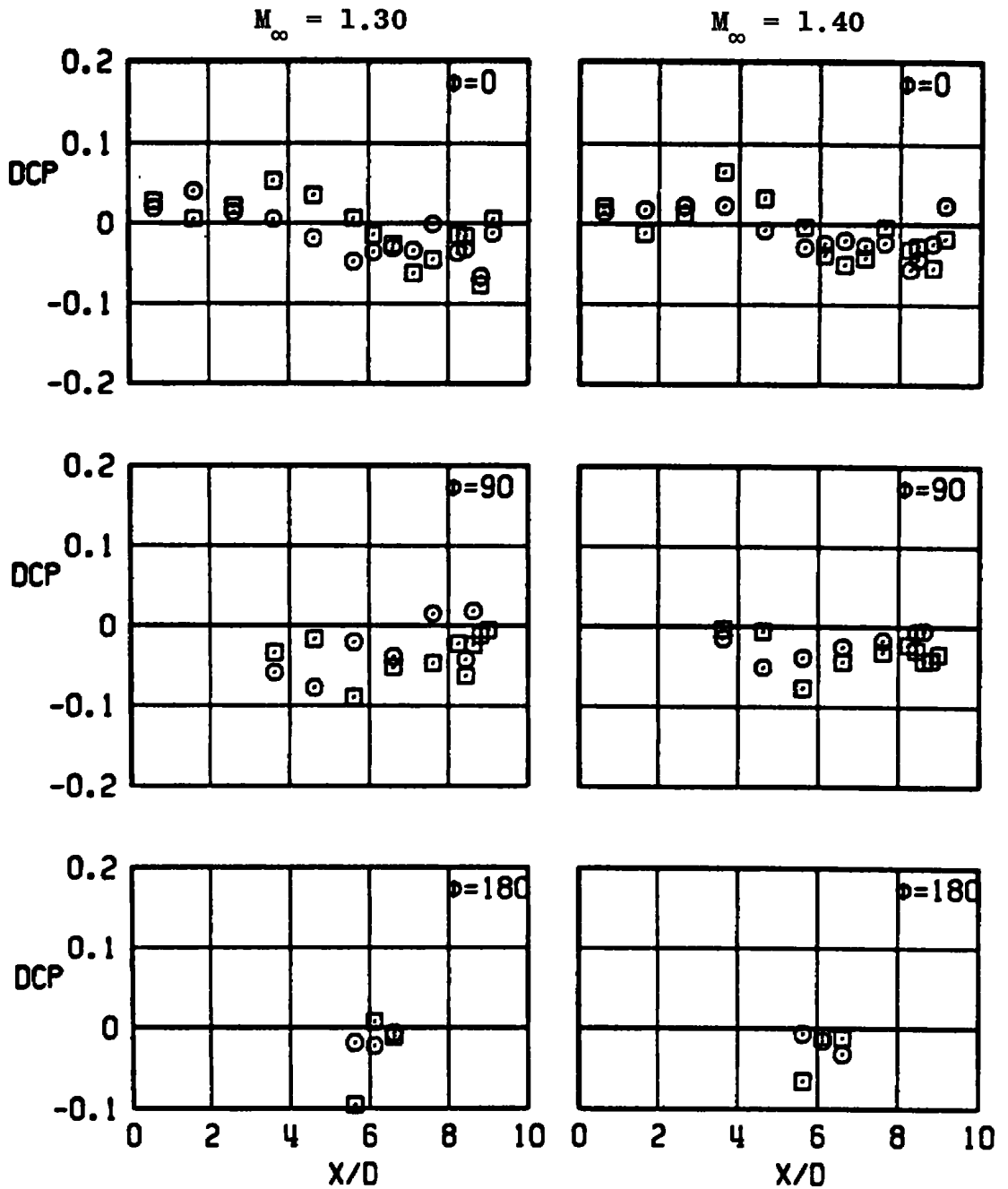
a. Continued
Figure A-4. Continued.

SYM	CONFIG	l , IN.
○	B2-S2L1	0.0
□	B2-S2L3	1.6



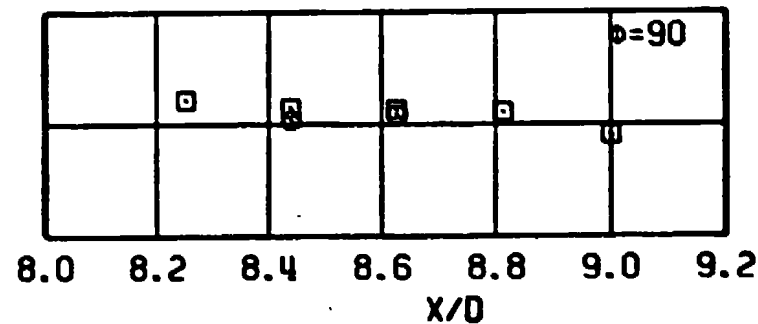
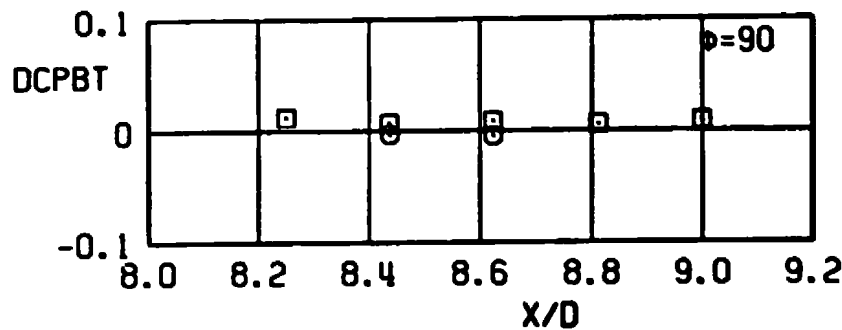
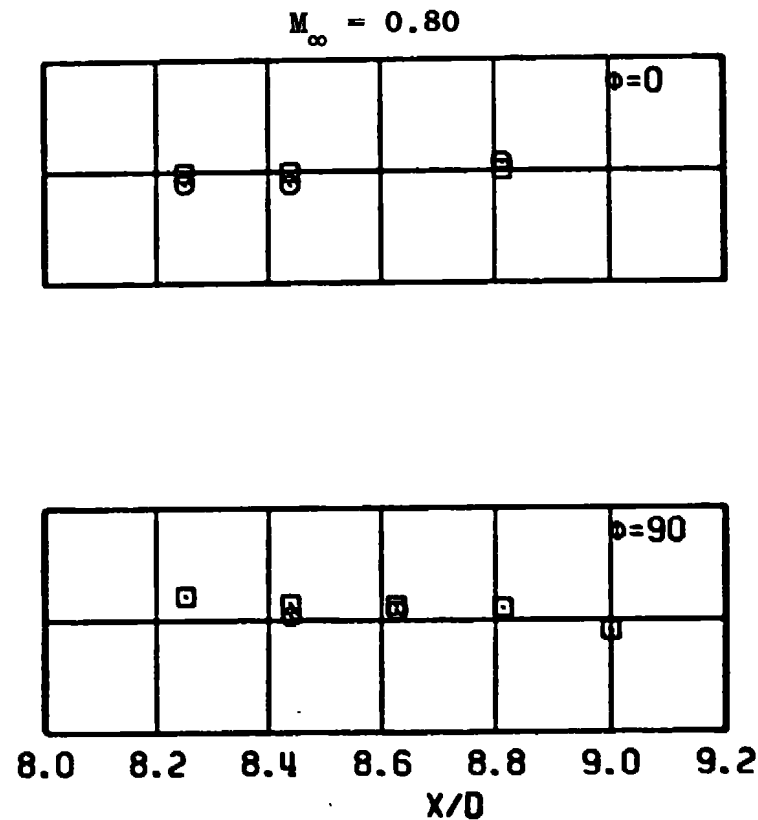
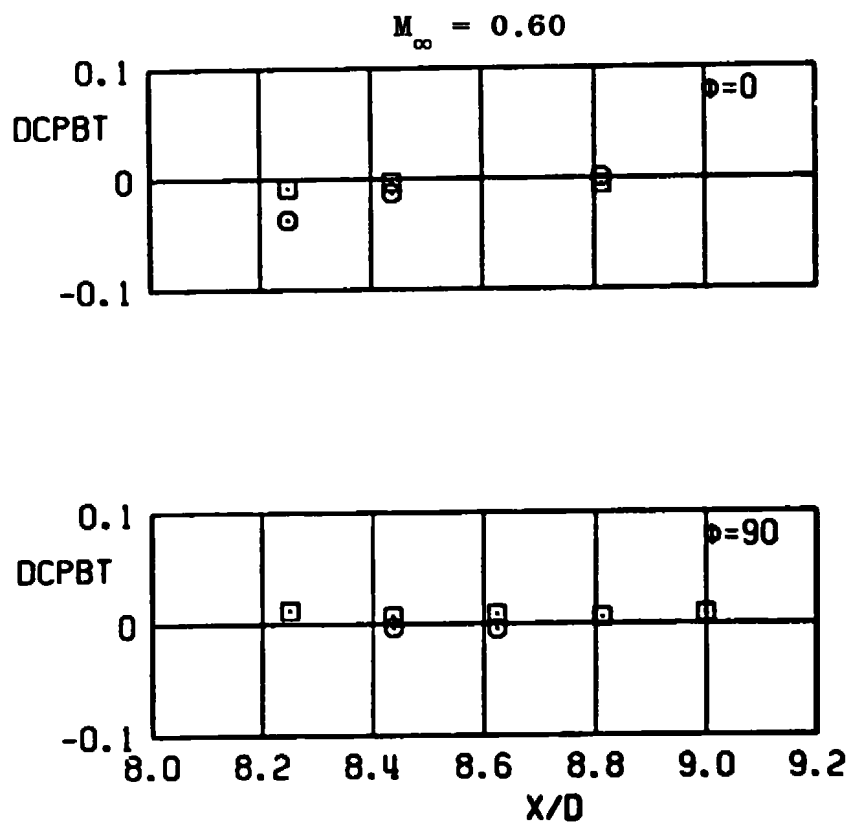
a. Continued
Figure A-4. Continued.

SYM	CONFIG	l , IN.
○	B2-S2L1	0.0
□	B2-S2L3	1.6



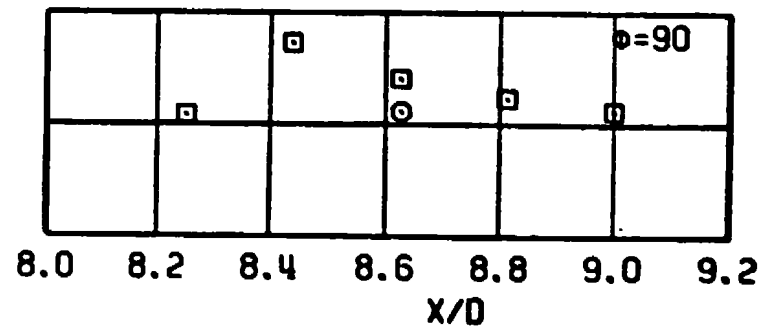
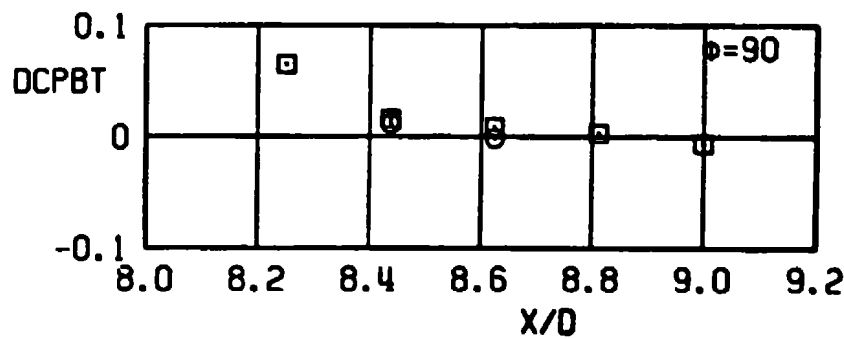
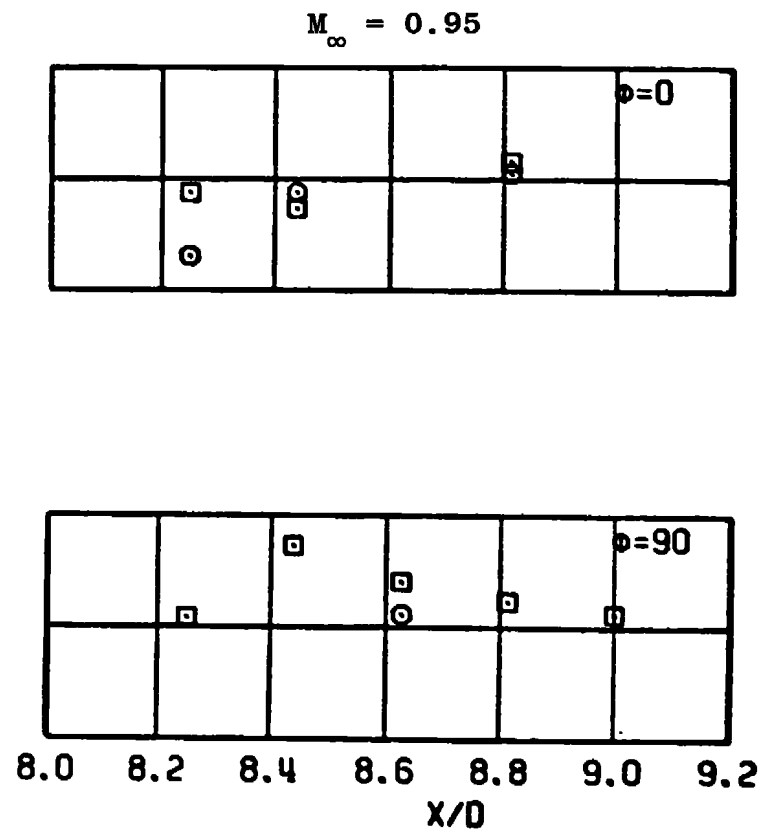
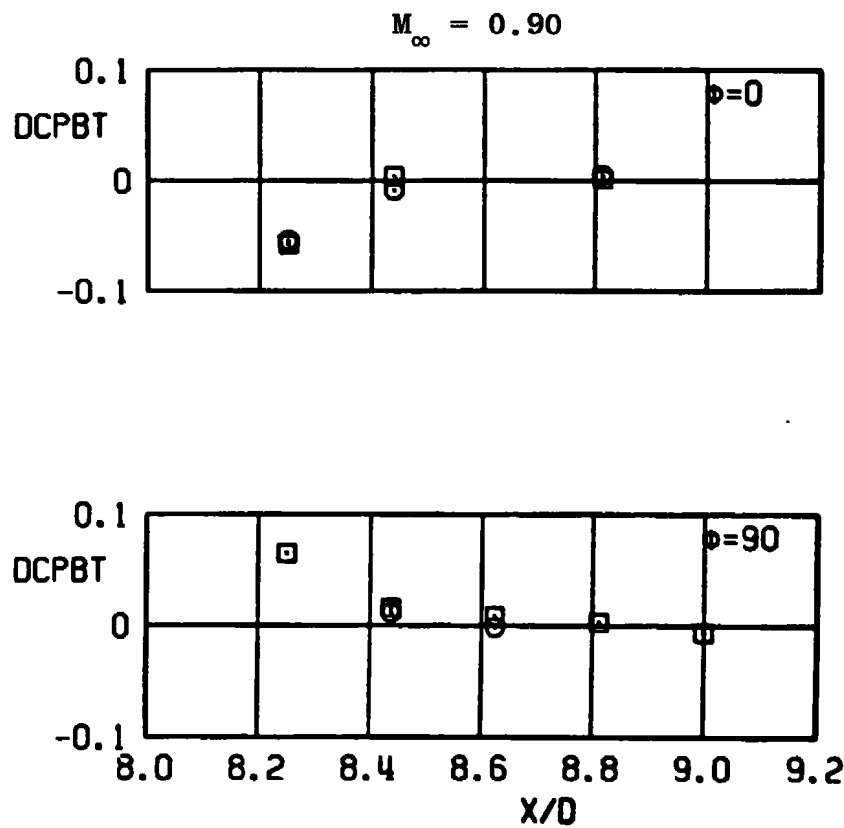
a. Concluded
Figure A-4. Continued.

SYM	CONFIG	l , IN.
○	B2-S2L1	0.0
□	B2-S2L3	1.6



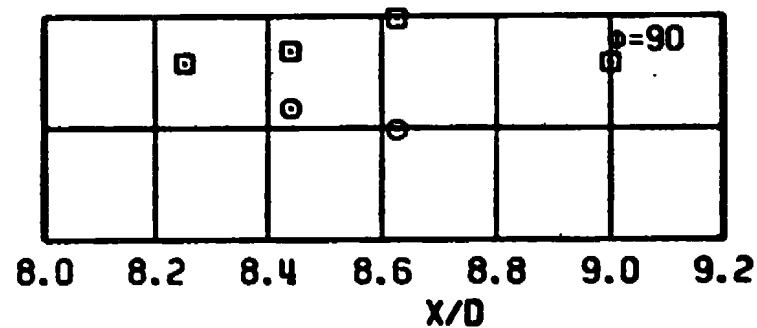
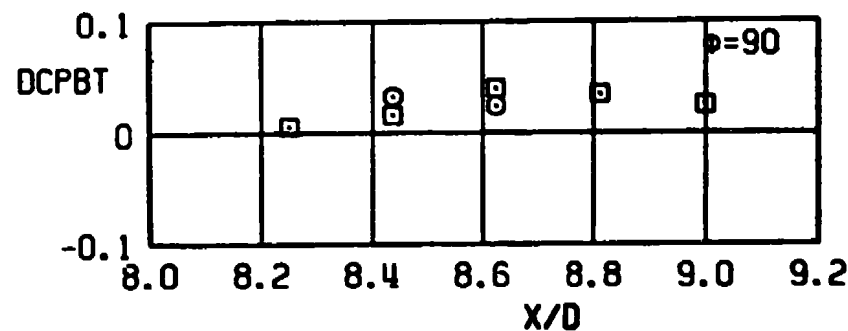
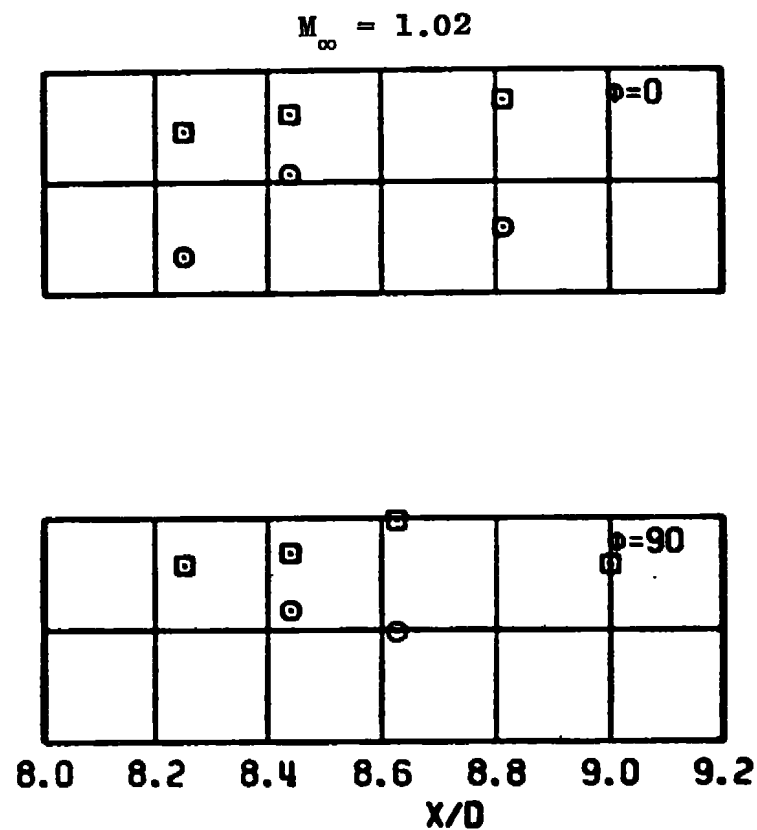
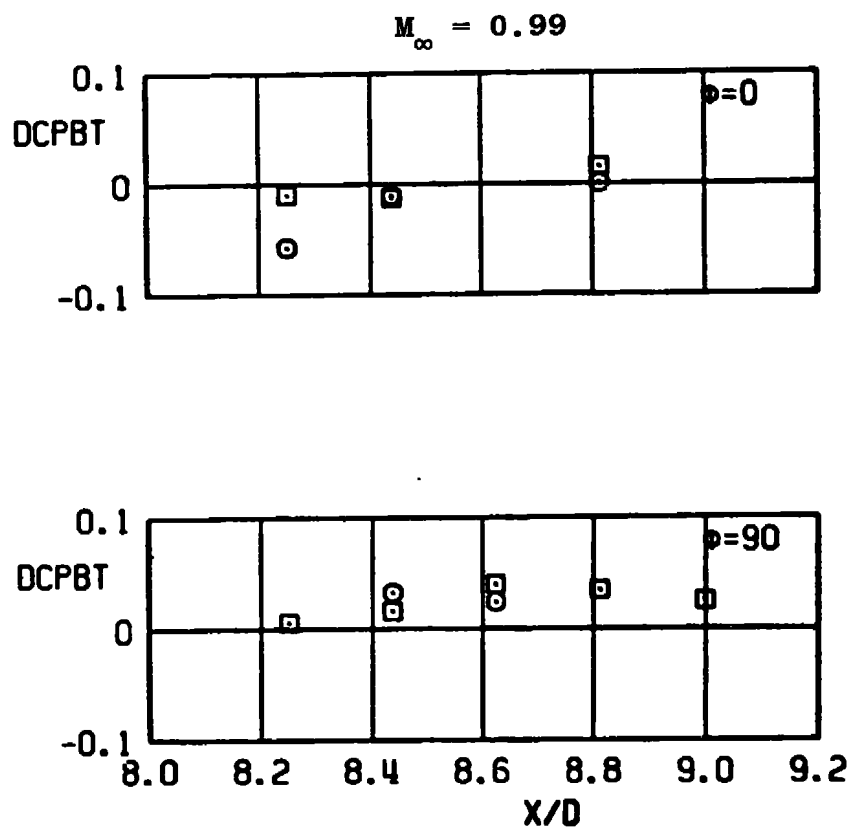
b. DCPBT versus X/D (straight strut, 10-deg boattail)
Figure A-4. Continued.

SYM	CONFIG	ℓ , IN.
○	B2-S2L1	0.0
□	B2-S2L3	1.6



b. Continued
Figure A-4. Continued.

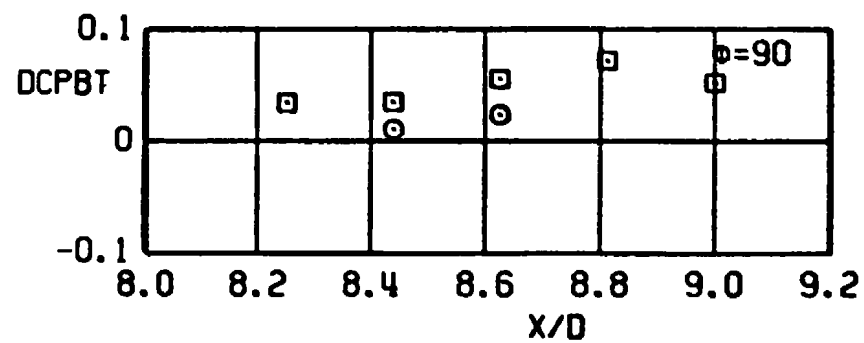
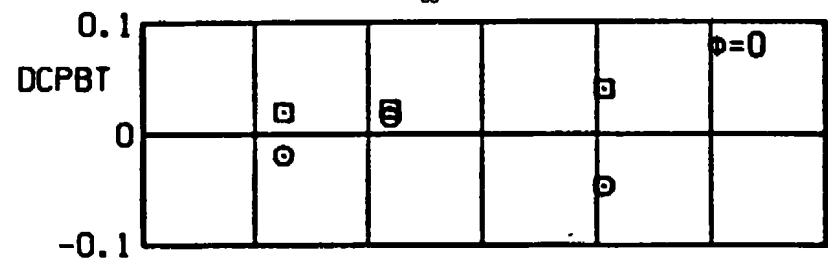
SYM	CONFIG	l , IN.
○	B2-S2L1	0.0
□	B2-S2L3	1.6



b. Continued
Figure A-4. Continued.

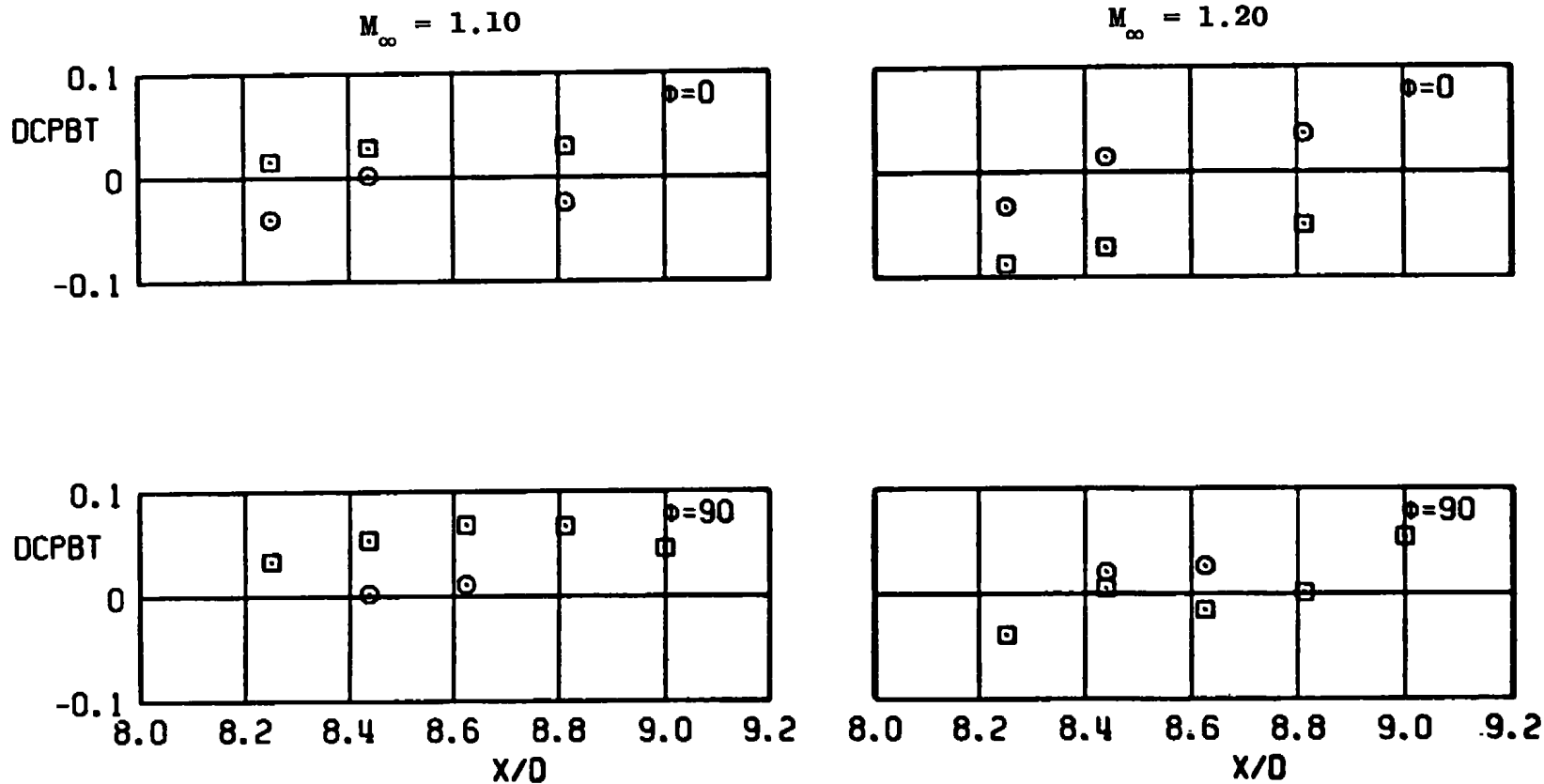
SYM	CONFIG	l , IN.
○	B2-S2L1	0.0
□	B2-S2L3	1.6

$$M_{\infty} = 1.05$$



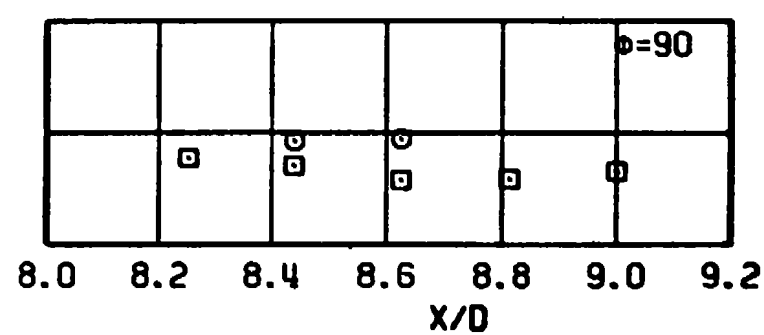
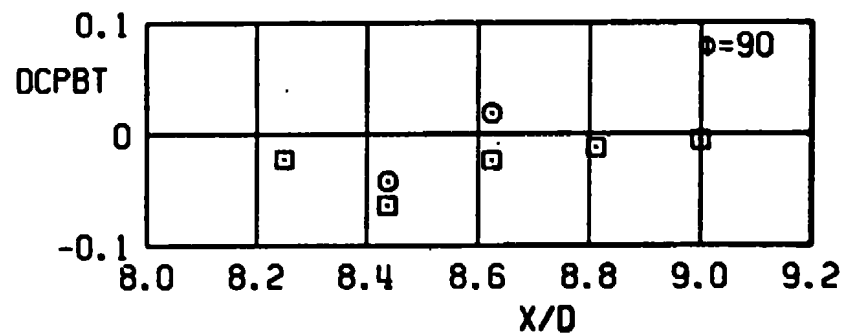
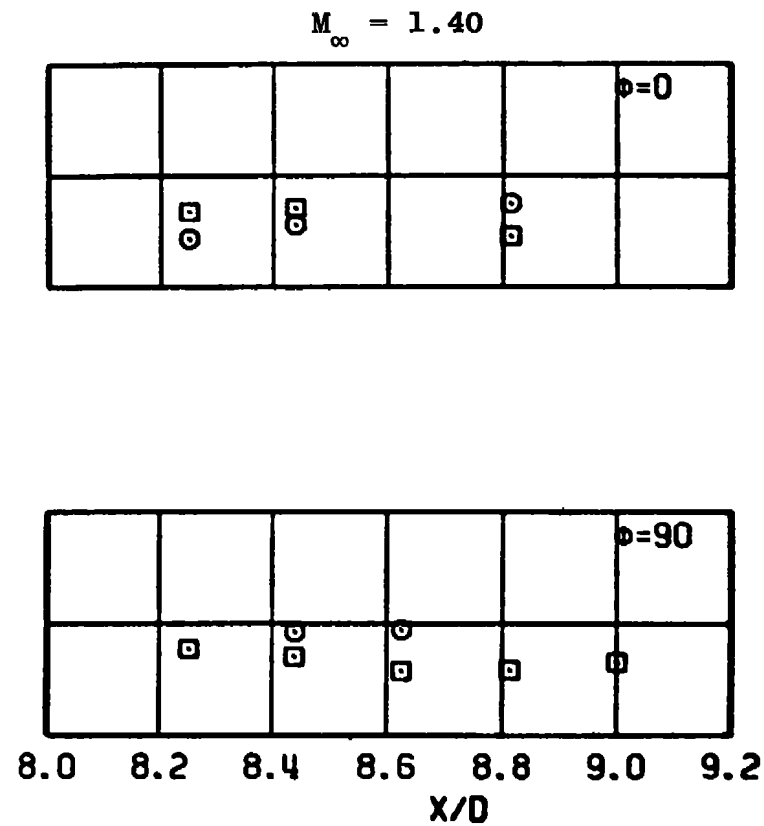
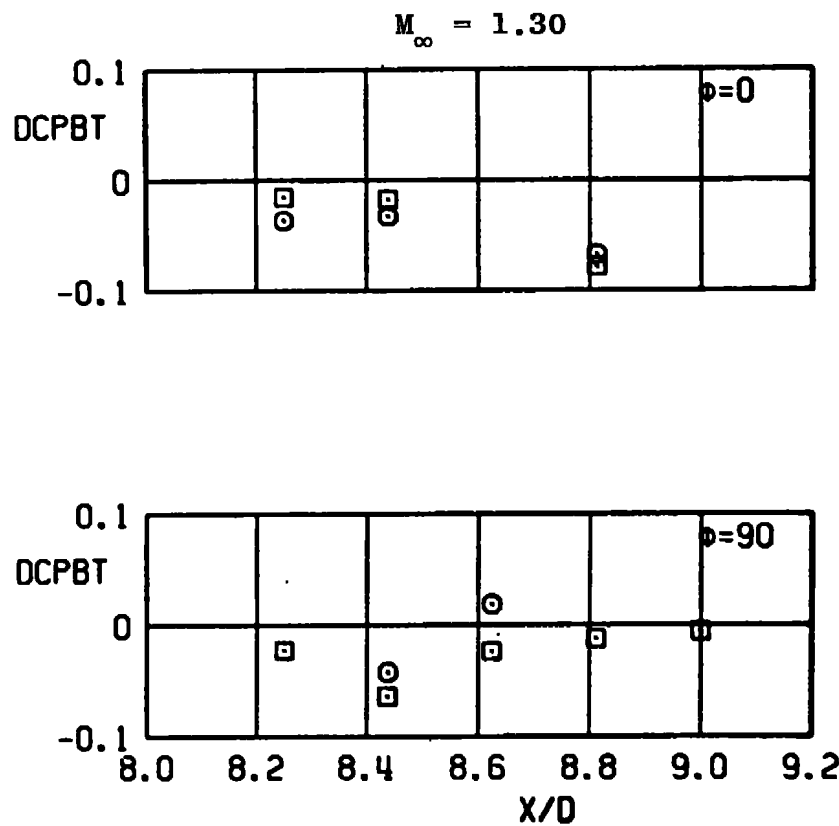
b. Continued
Figure A-4. Continued.

SYM	CONFIG	l , IN.
○	82-S2L1	0.0
□	82-S2L3	1.6



b. Continued
Figure A-4. Continued.

SYM	CONFIG	l , IN.
○	B2-S2L1	0.0
□	B2-S2L3	1.6



b. Concluded
Figure A-4. Continued.

SYM	CONFIG	l , IN.	ϕ , DEG
○	B2-S2L1	0.0	0
□	B2-S2L3	1.6	0

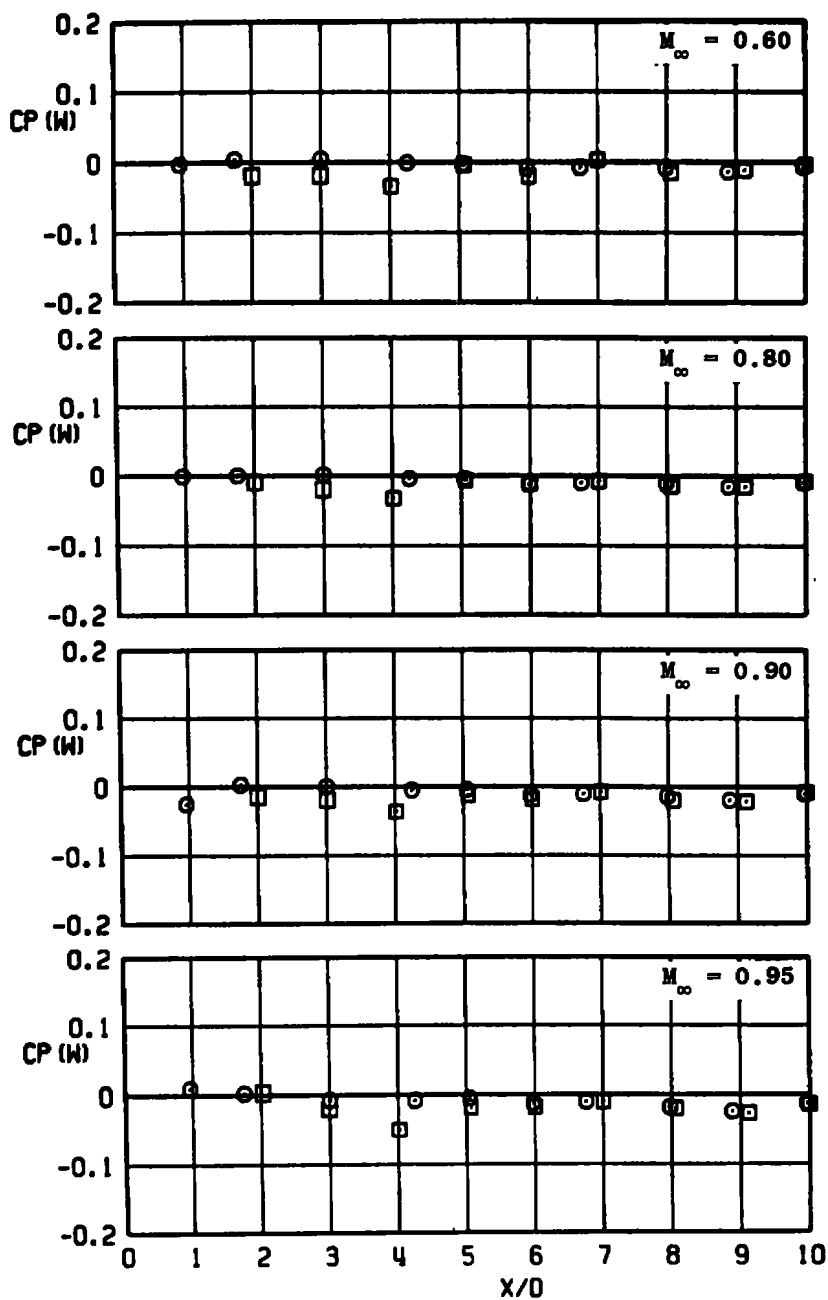
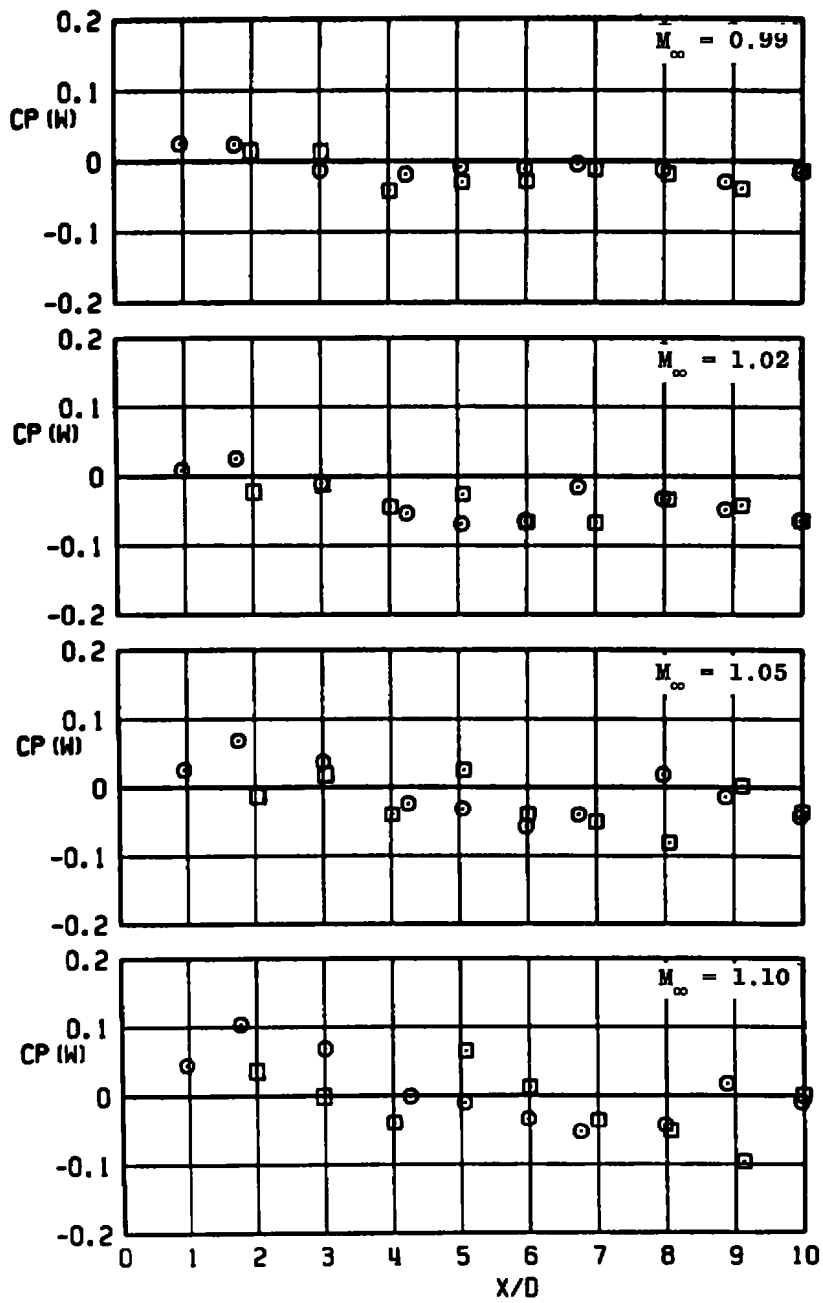
c. $CP(W)$ versus X/D (straight strut, 10-deg boattail, $\phi = 0$)

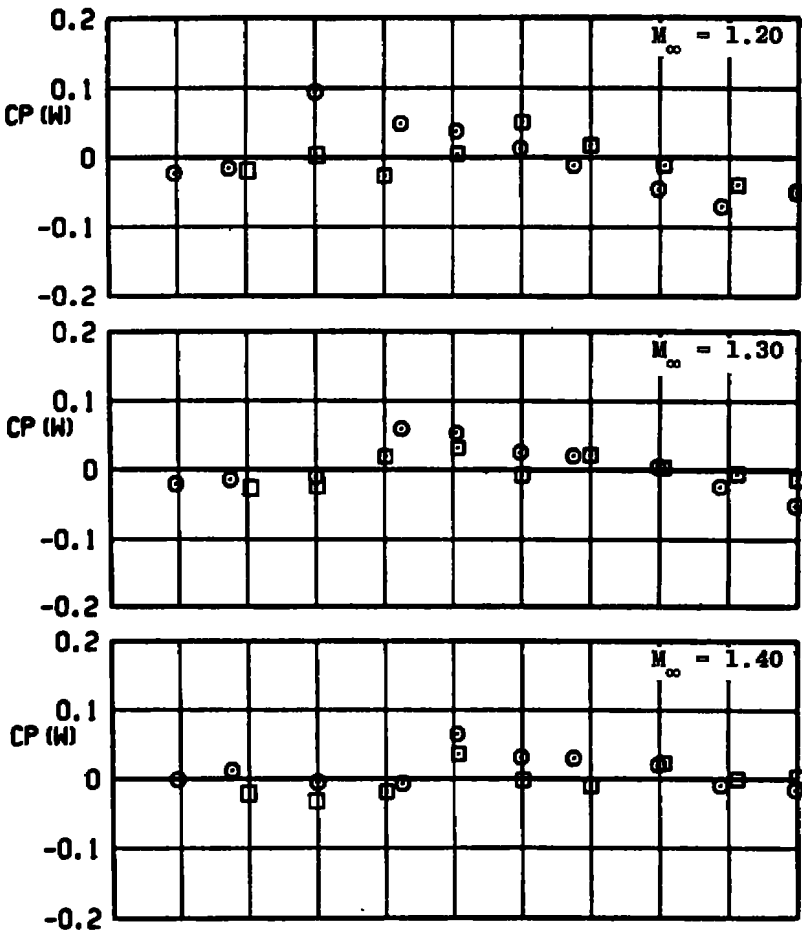
Figure A-4. Continued.

SYM	CONFIG	ℓ , IN.	ϕ , DEG
○	B2-52L1	0.0	0
□	B2-52L3	1.6	0



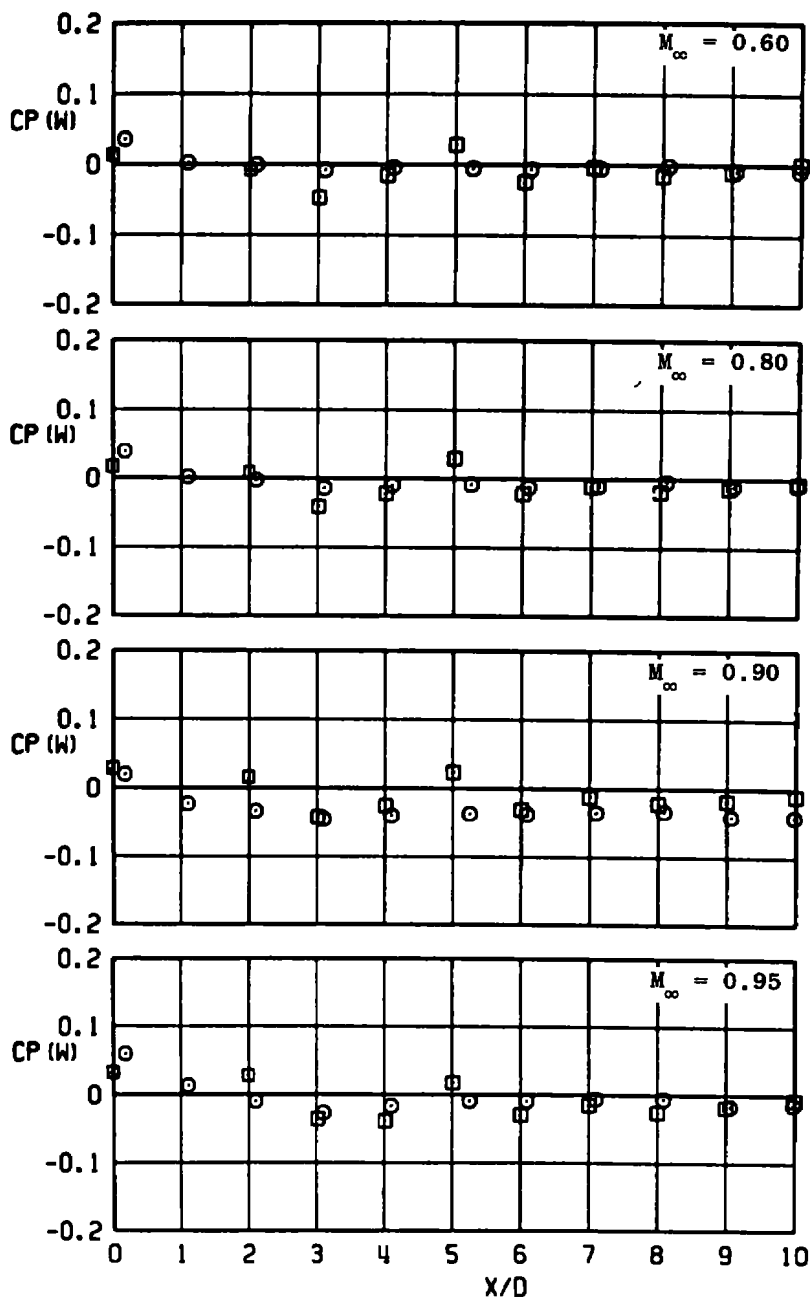
c. Continued
Figure A-4. Continued.

SYM	CONFIG	ℓ , IN.	ϕ , DEG
○	B2-S2L1	0.0	0
□	B2-S2L3	1.6	0



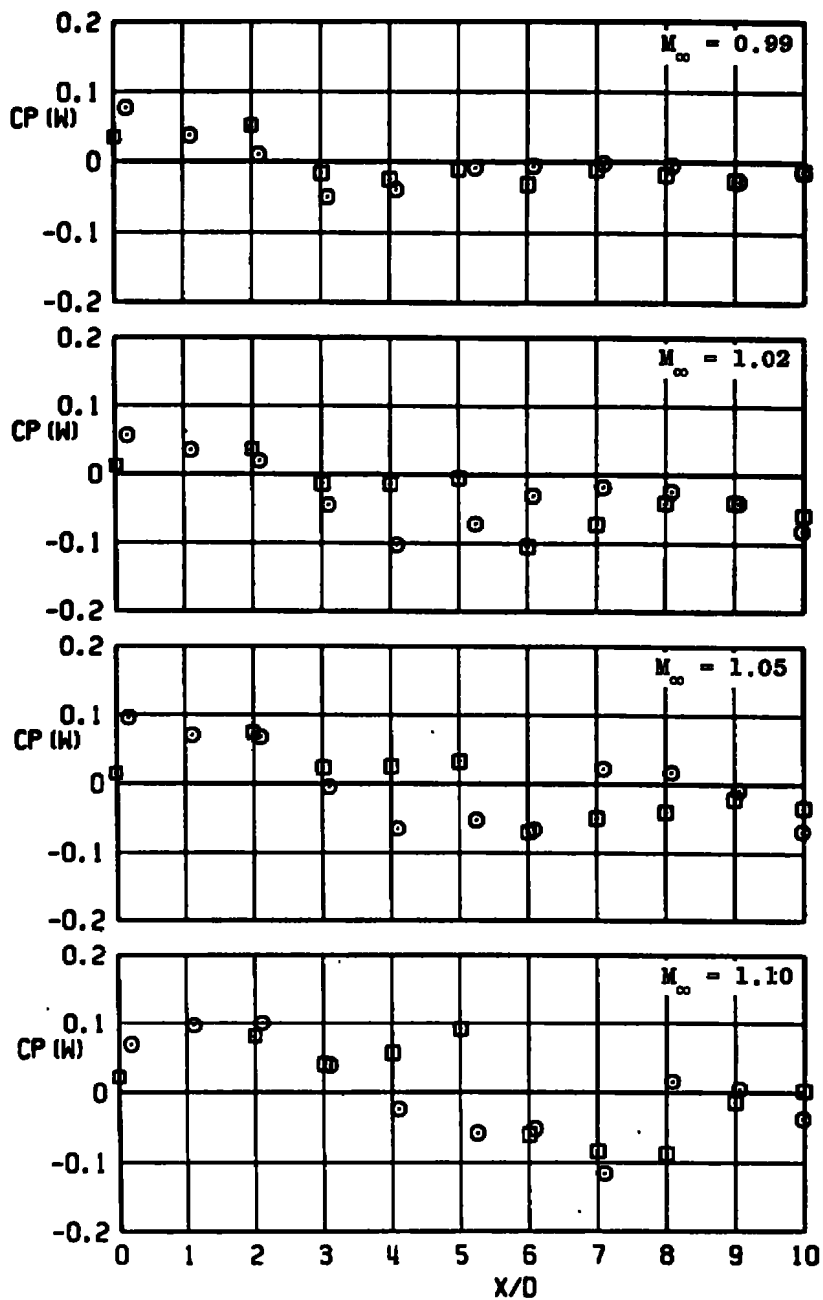
c. Concluded
Figure A-4. Continued.

SYM	CONFIG	l , IN.	ϕ , DEG
○	B2-S2L1	0.0	90
□	B2-S2L3	1.6	90



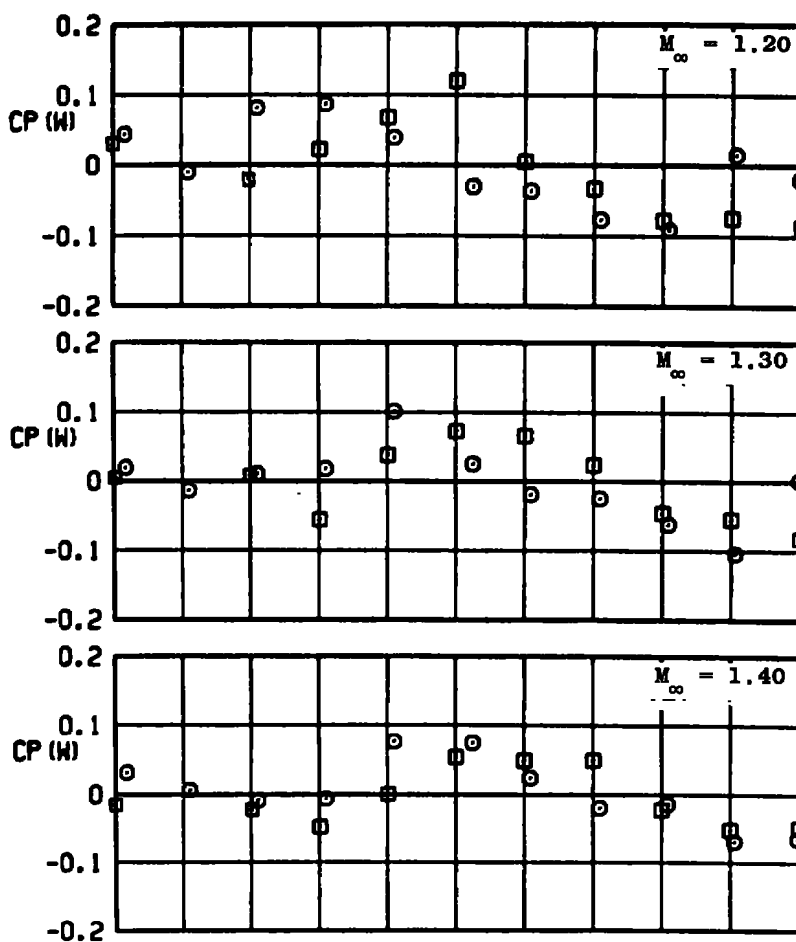
d. CP(W) versus X/D (straight strut, 10-deg boattail, $\phi = 90$ deg)
Figure A-4. Continued.

SYM	CONFIG	l , IN.	ϕ , DEG
○	B2-S2L1	0.0	90
□	B2-S2L3	1.6	90



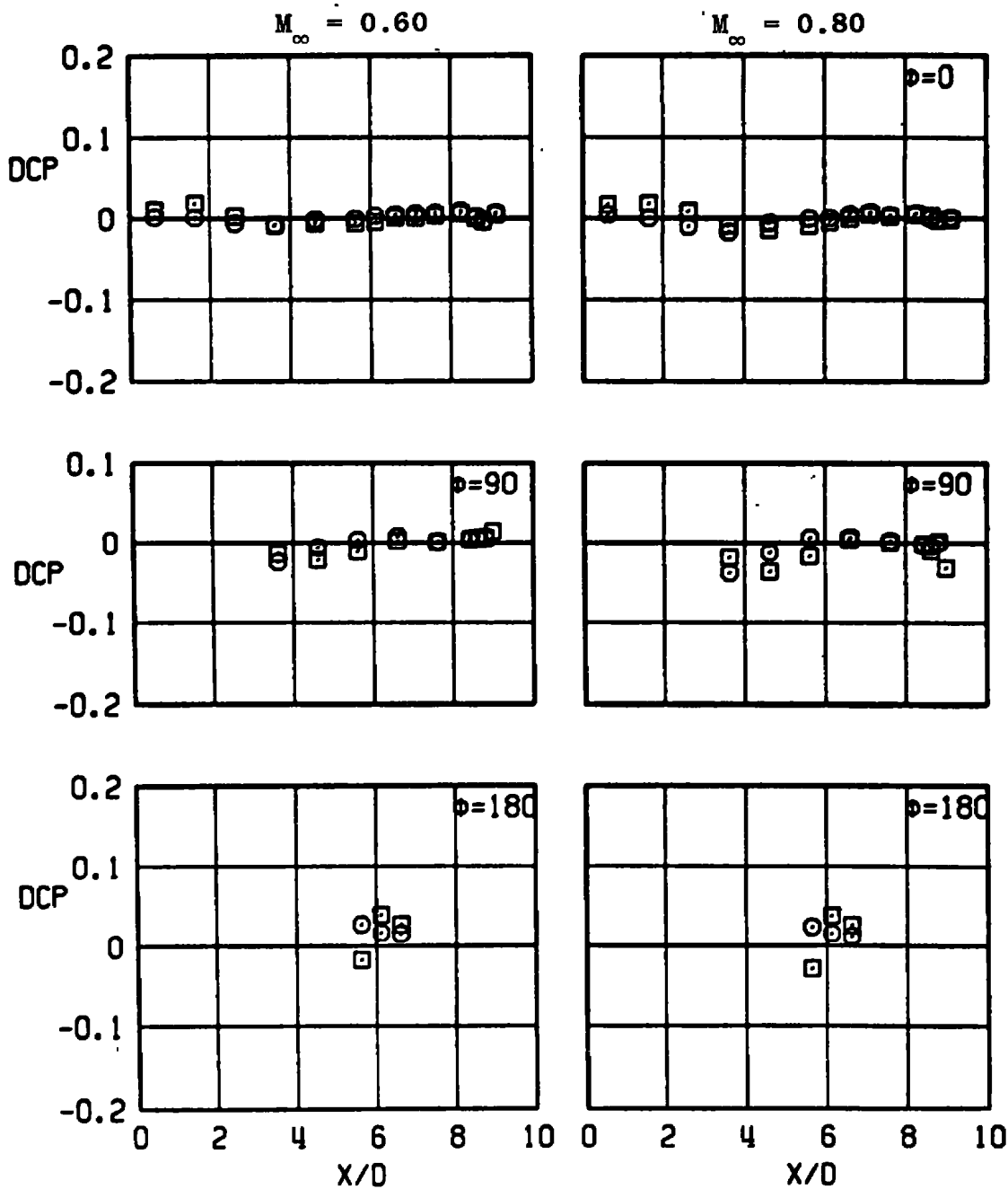
d. Continued
Figure A-4. Continued.

SYM	CONFIG	l , IN.	ϕ , DEG
○	82-S2L1	0.0	90
□	82-S2L3	1.6	90



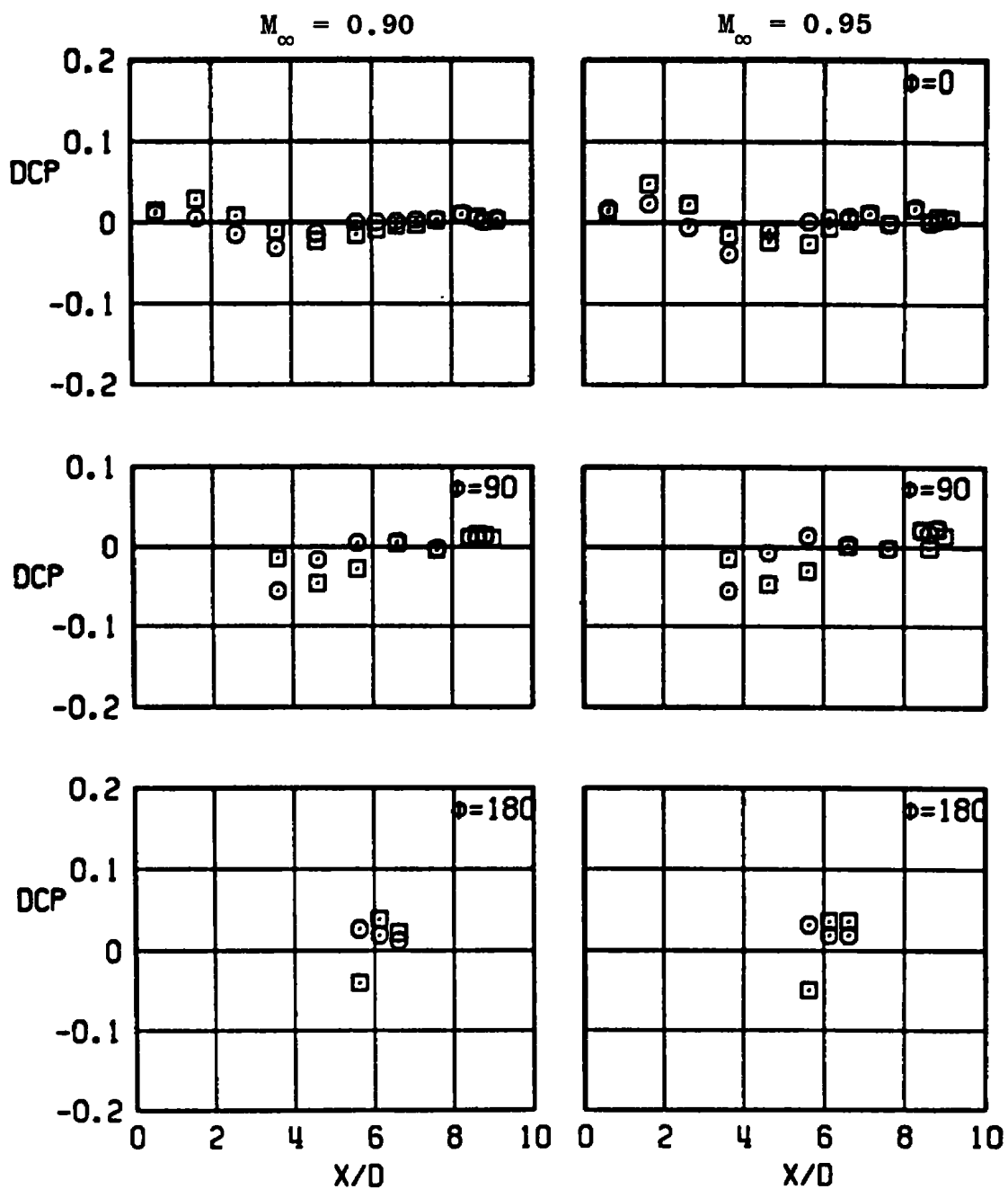
d. Concluded
Figure A-4. Continued.

SYM	CONFIG	l , IN.
○	B1-S3L1	0.0
□	B1-S3L3	1.6



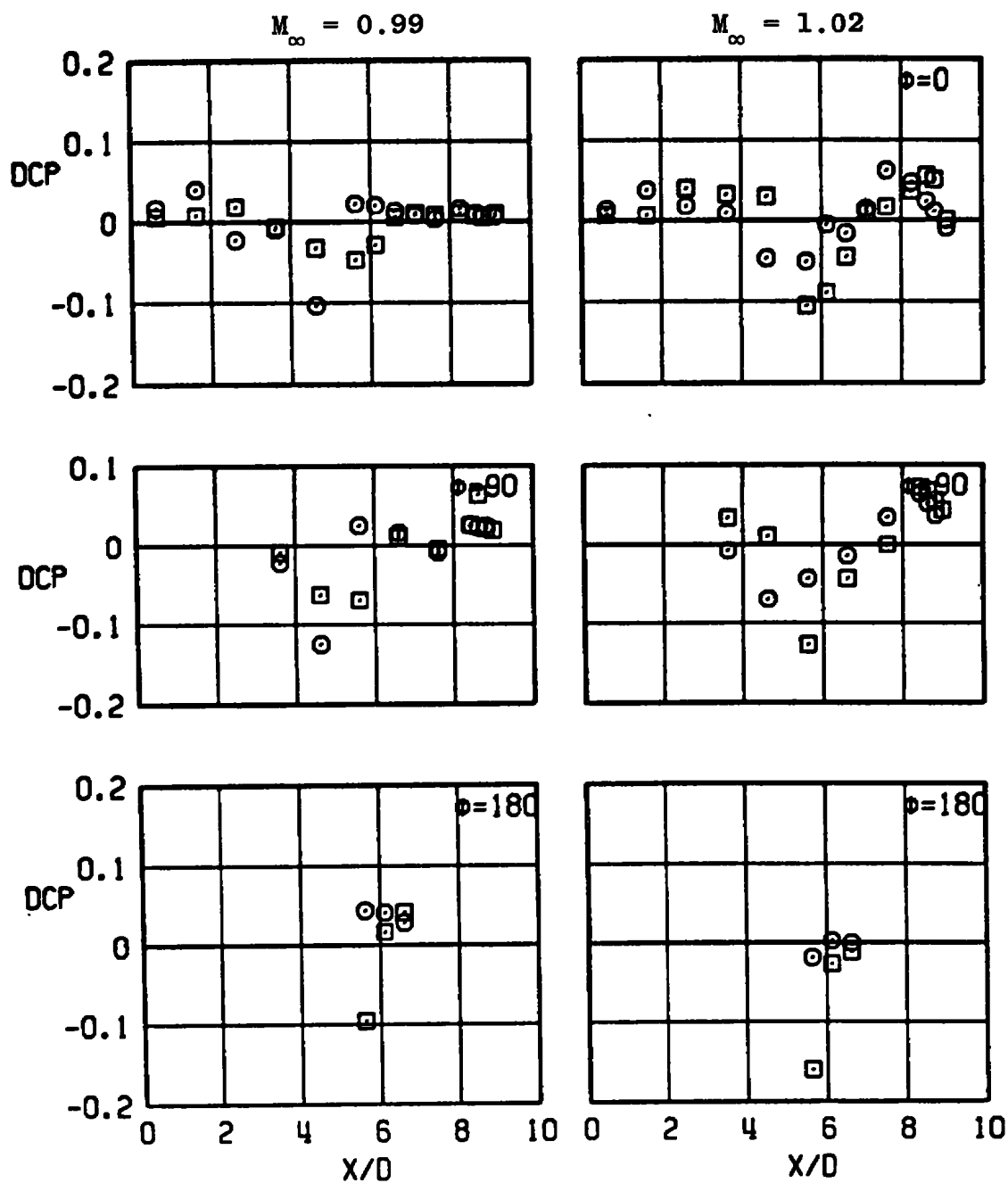
e. DCP versus X/D (30-deg swept strut, cylindrical afterbody)
Figure A-4. Continued.

SYM	CONFIG	l , IN.
○	B1-53L1	0.0
□	B1-53L3	1.6



e. Continued
Figure A-4. Continued.

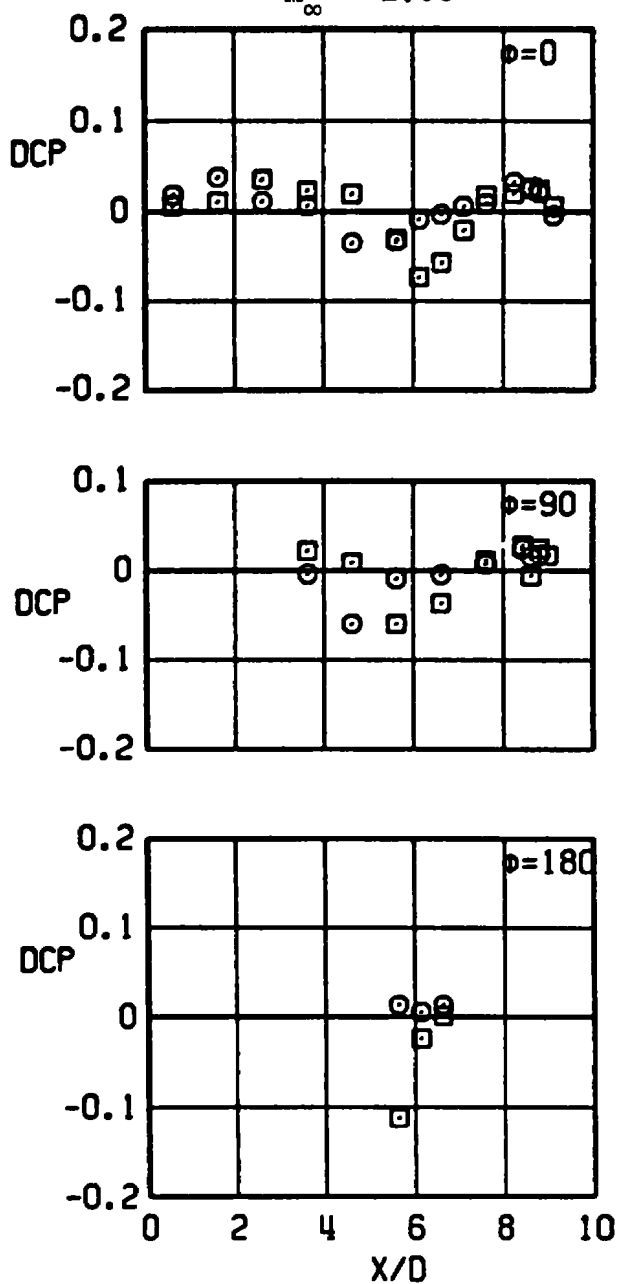
SYM	CONFIG	l , IN.
○	B1-S3L1	0.0
□	B1-S3L3	1.6



e. Continued
Figure A-4. Continued.

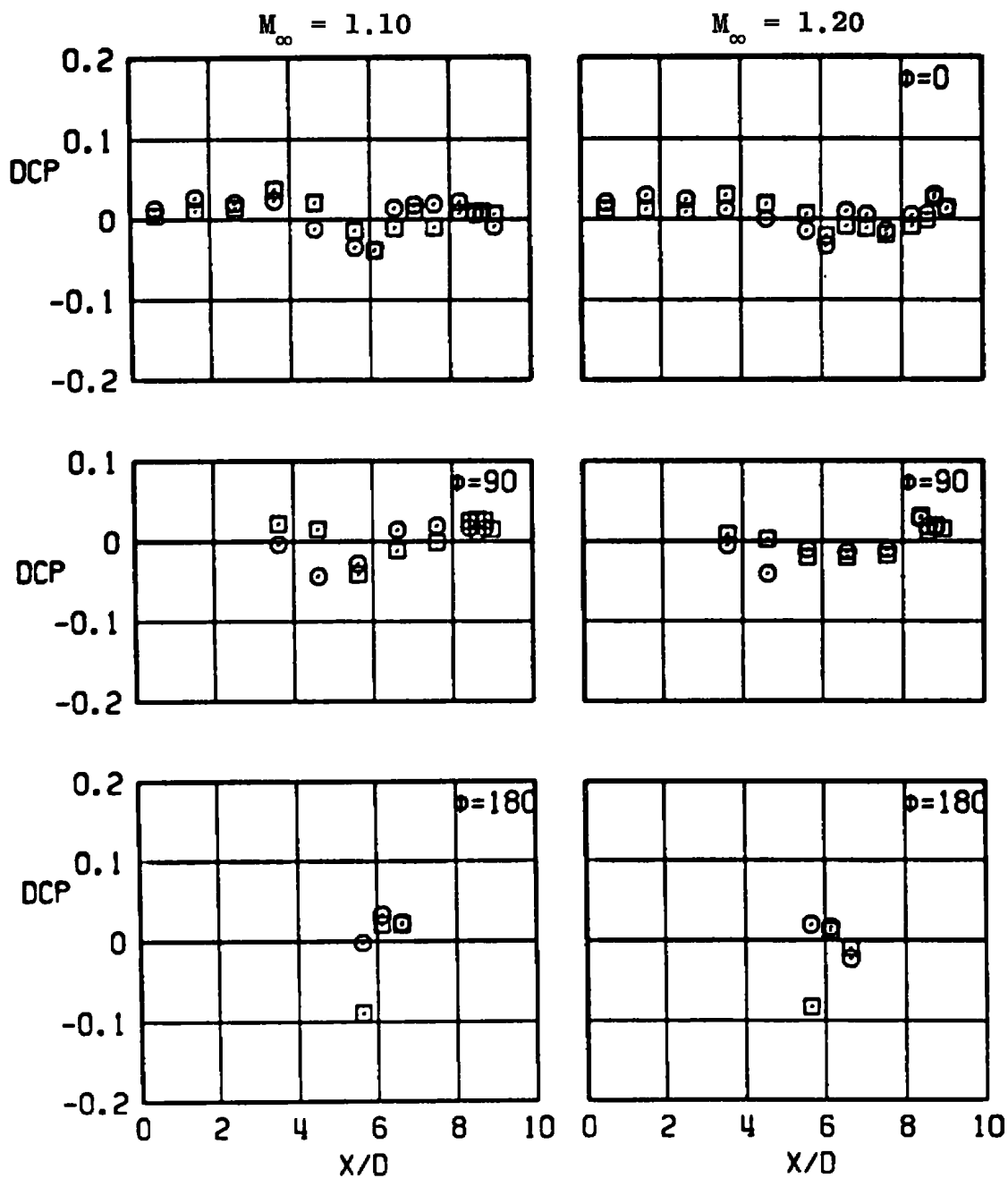
SYM	CONFIG	l , IN.
○	B1-S3L1	0.0
□	B1-S3L3	1.6

$$M_{\infty} = 1.05$$



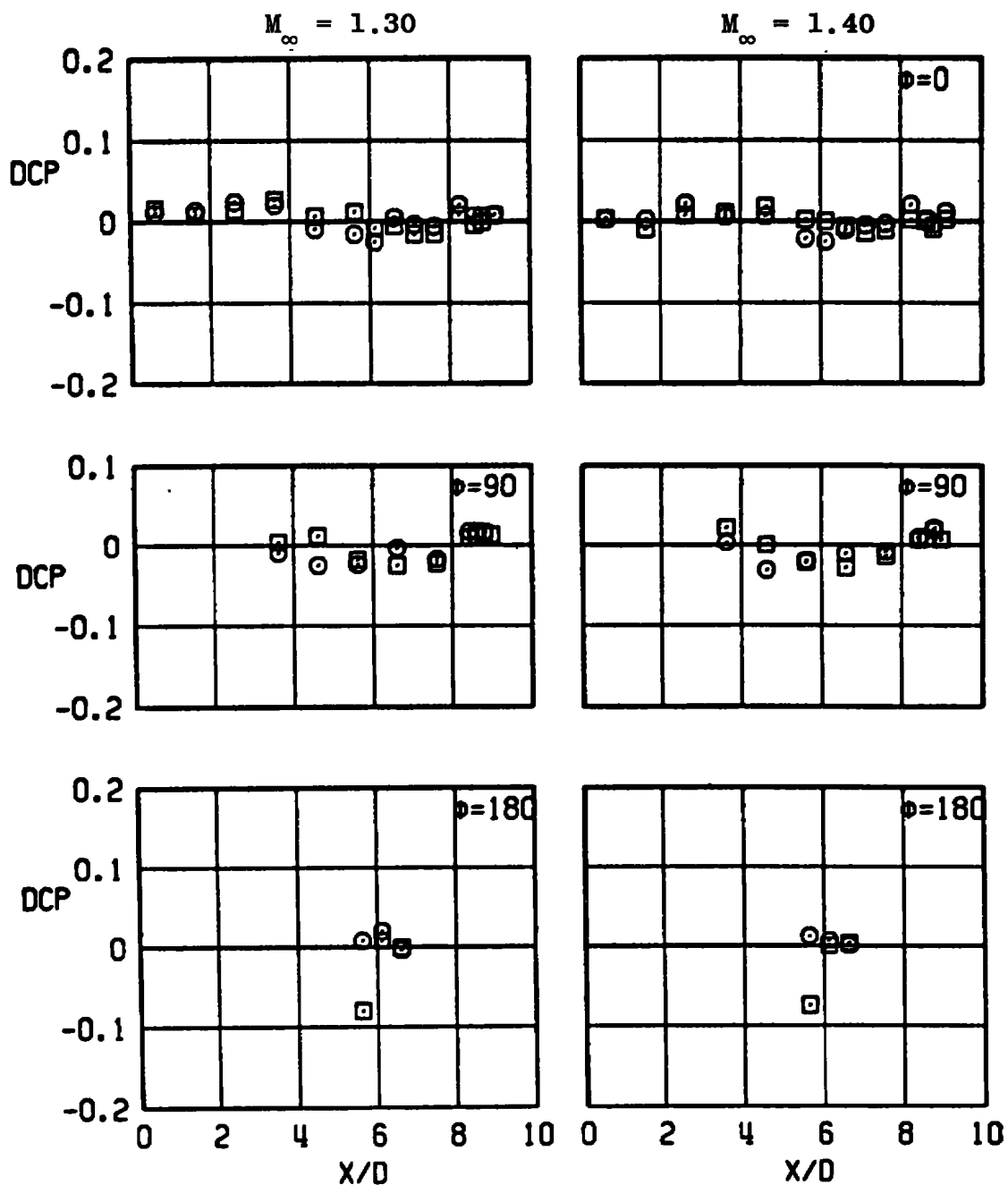
e. Continued
Figure A-4. Continued.

SYM	CONFIG	l , IN.
○	B1-S3L1	0.0
□	B1-S3L3	1.6



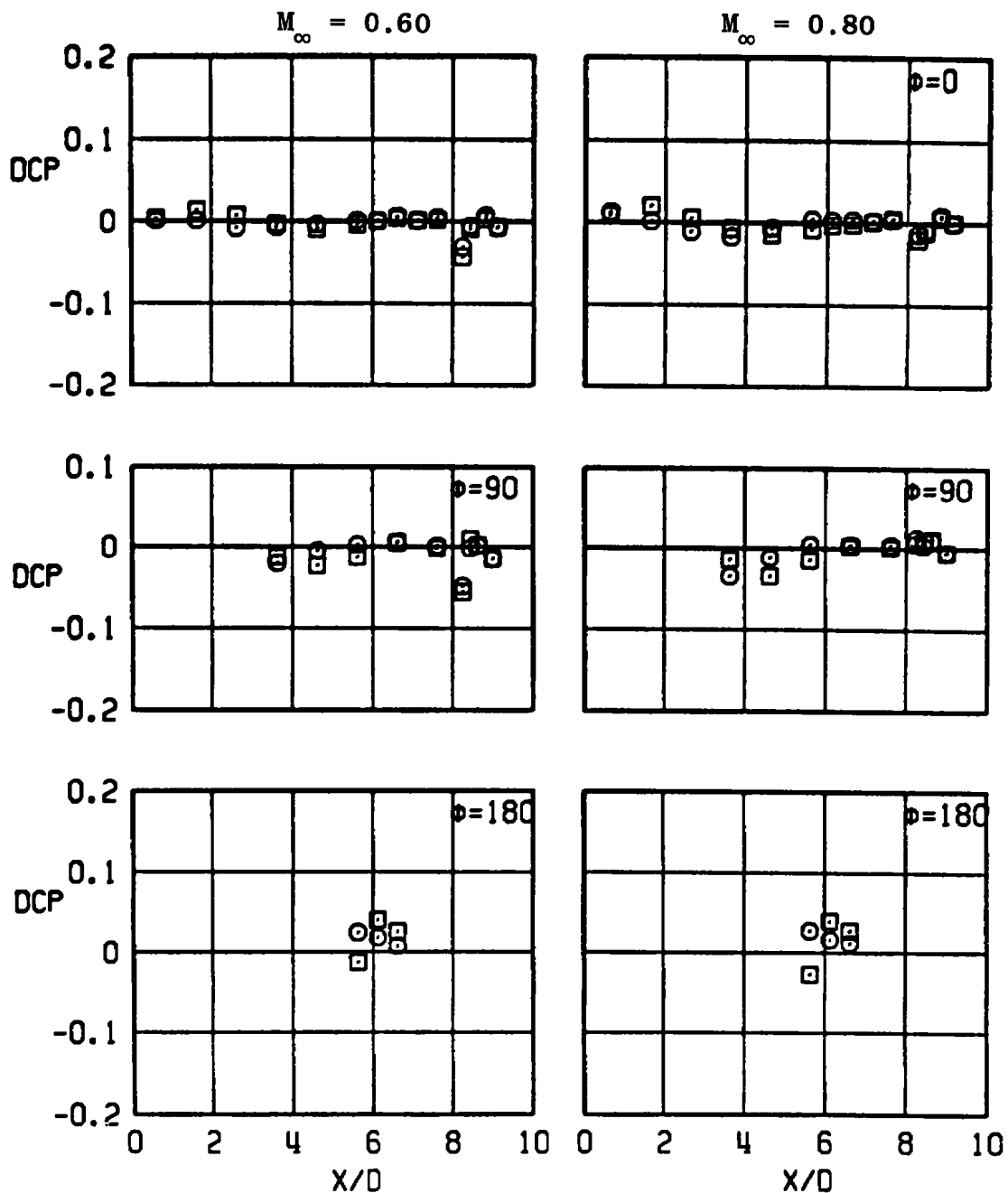
e. Continued
Figure A-4. Continued.

SYM	CONFIG	l , IN.
○	B1-S3L1	0.0
□	B1-S3L3	1.6



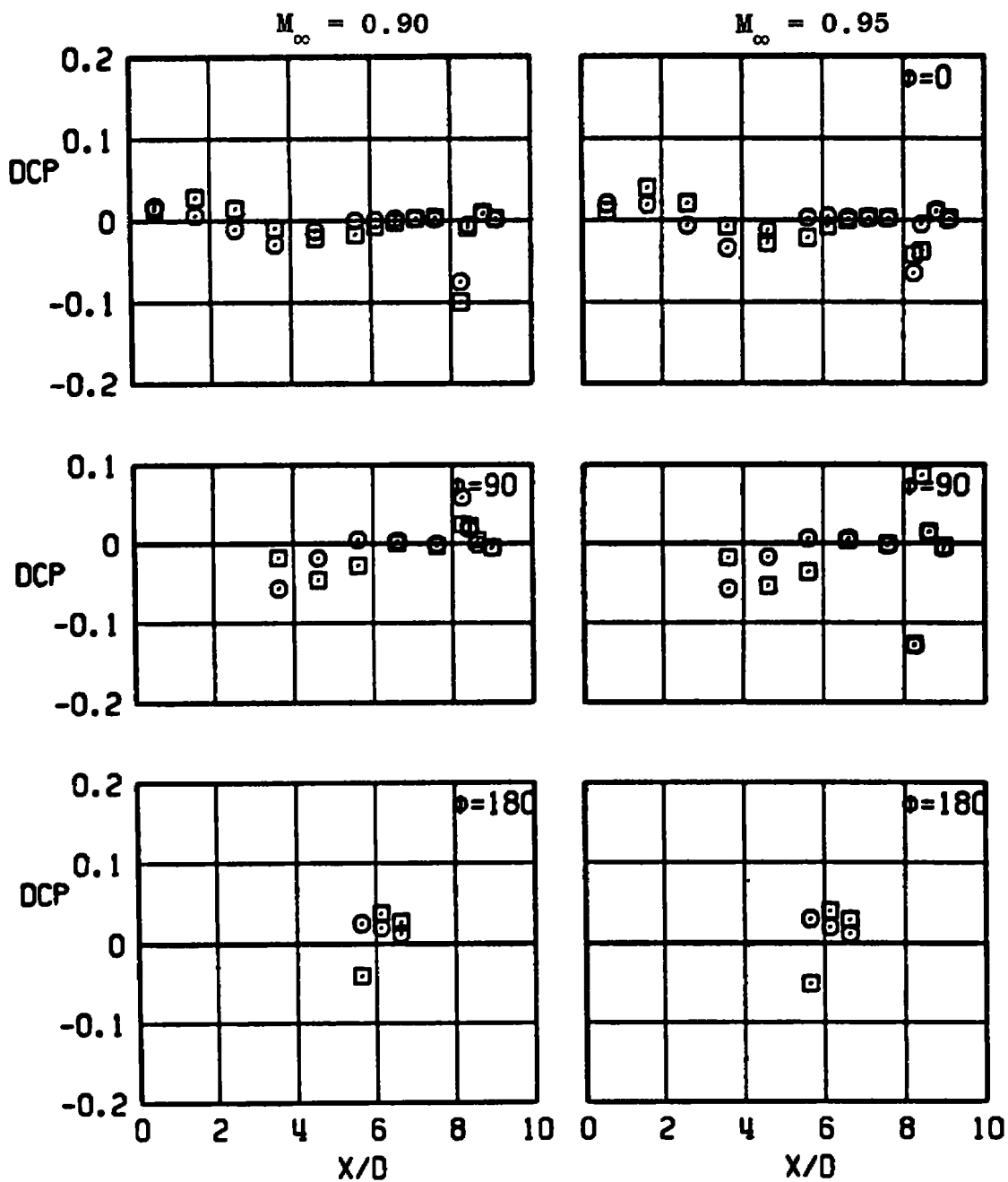
e. Concluded
Figure A-4. Continued.

SYM	CONFIG	l , IN.
○	B2-S3L1	0.0
□	B2-S3L3	1.6



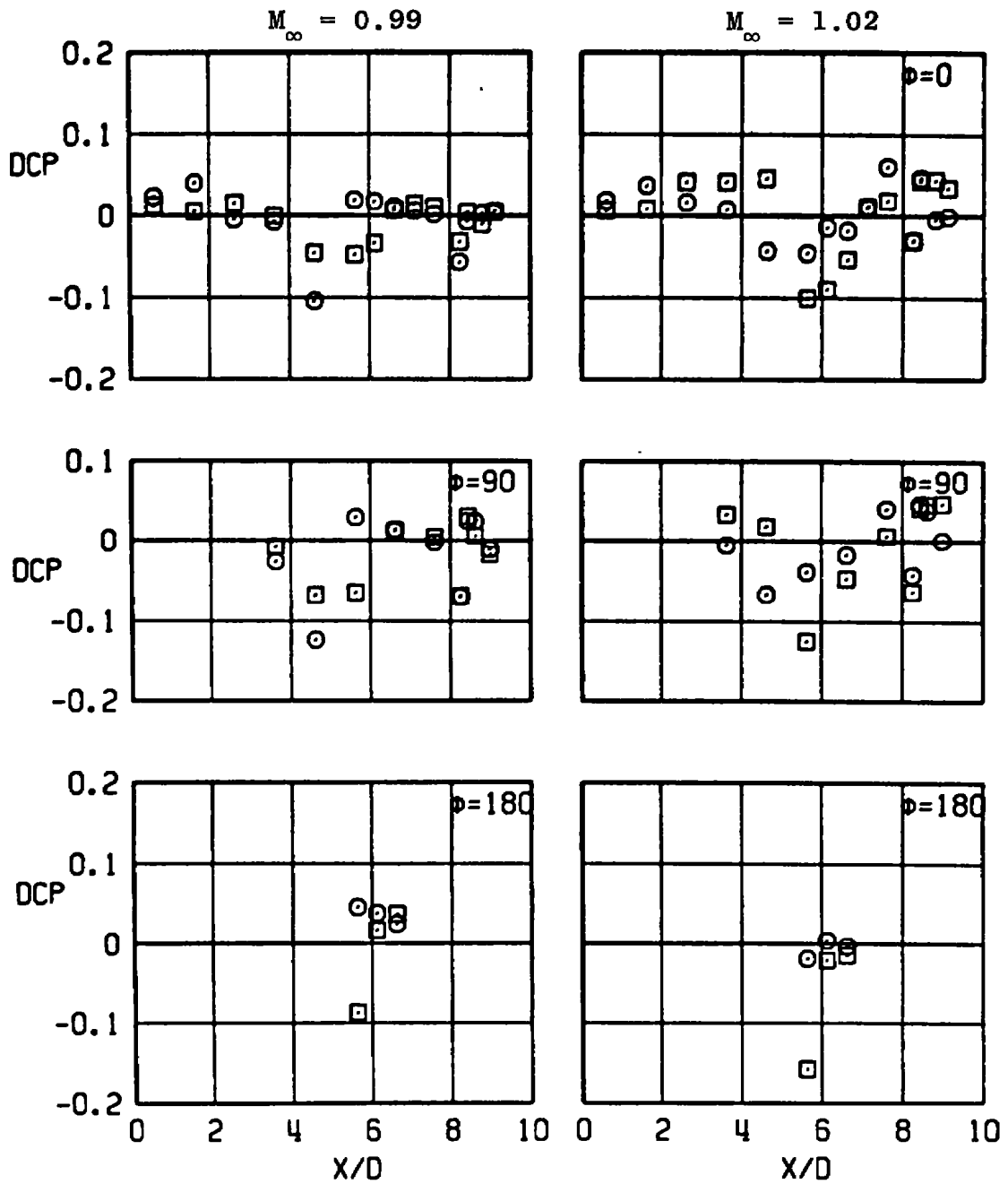
f. DCP versus X/D (30-deg swept strut, 10-deg boattail)
Figure A-4. Continued.

SYM	CONFIG	l , IN.
○	B2-S3L1	0.0
□	B2-S3L3	1.6

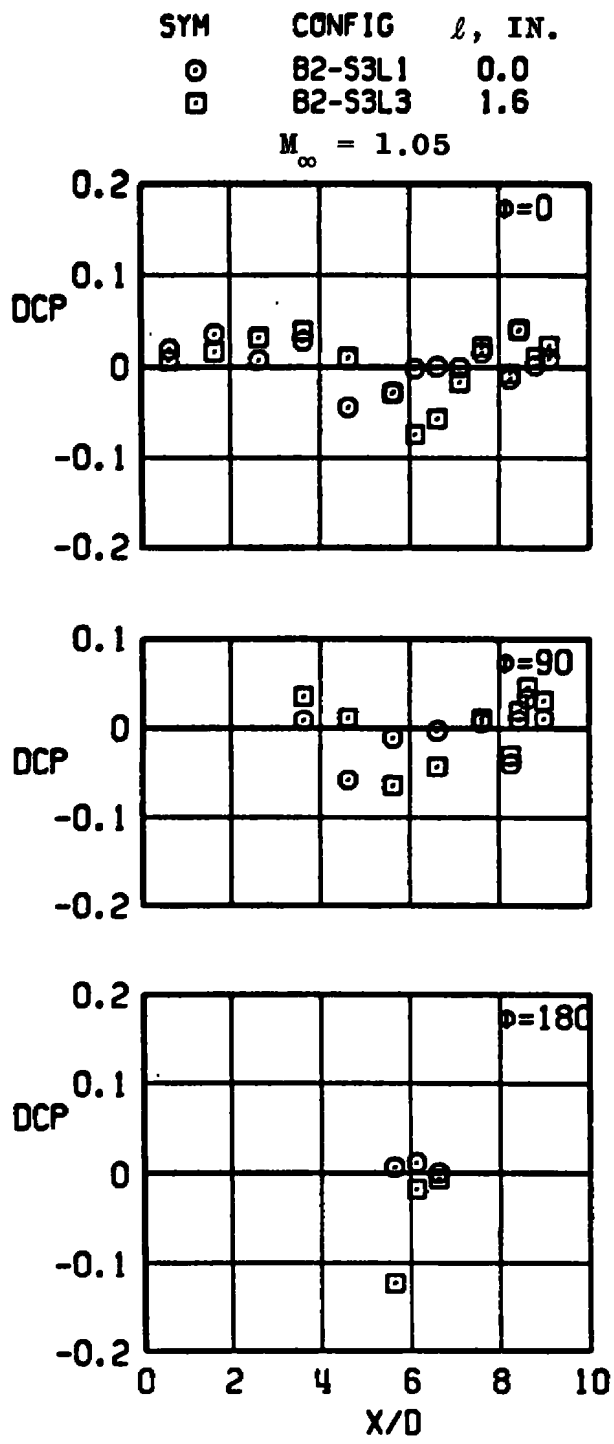


f. Continued
Figure A-4. Continued.

SYM	CONFIG	ℓ , IN.
○	B2-S3L1	0.0
□	B2-S3L3	1.6

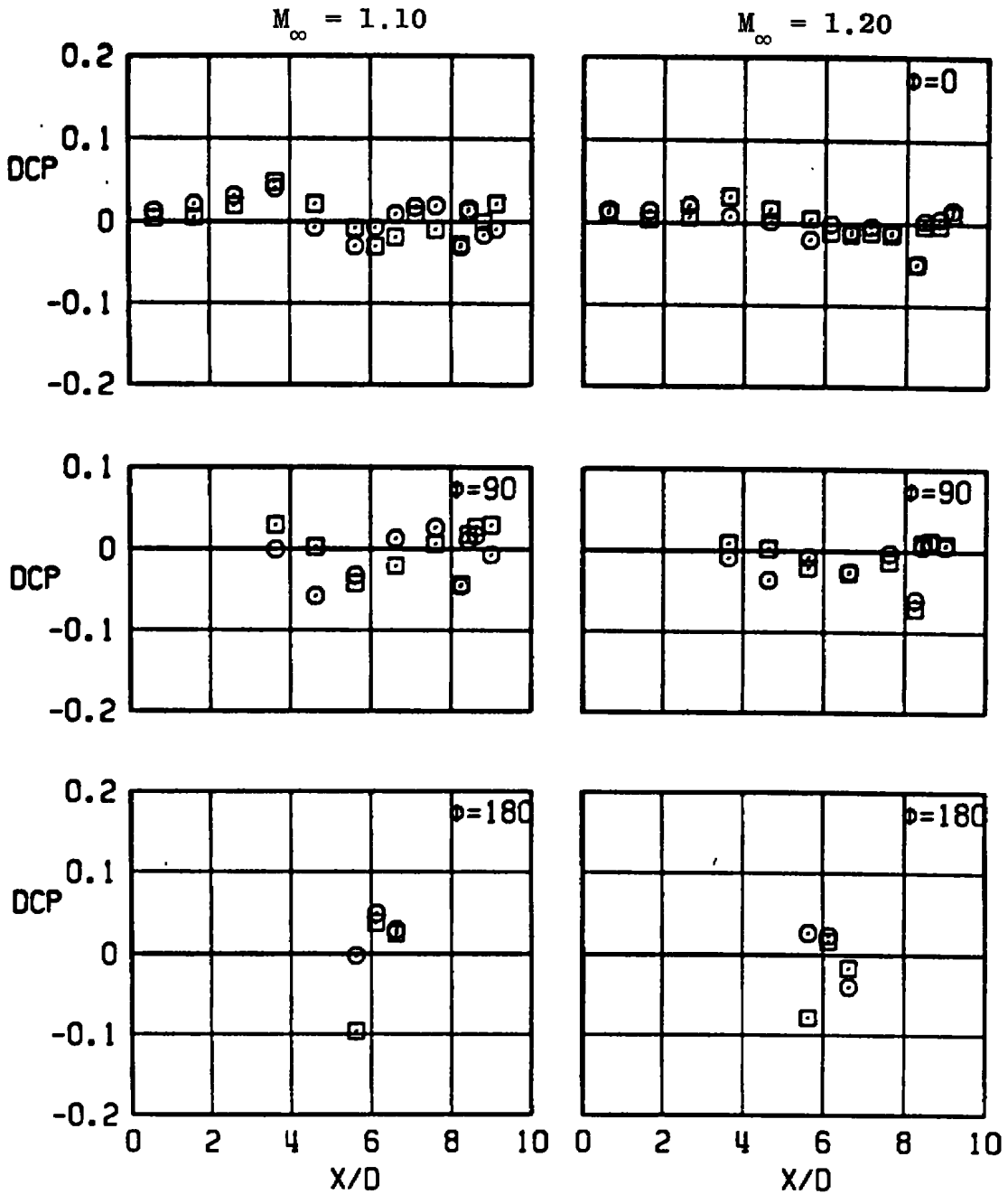


f. Continued
Figure A-4. Continued.



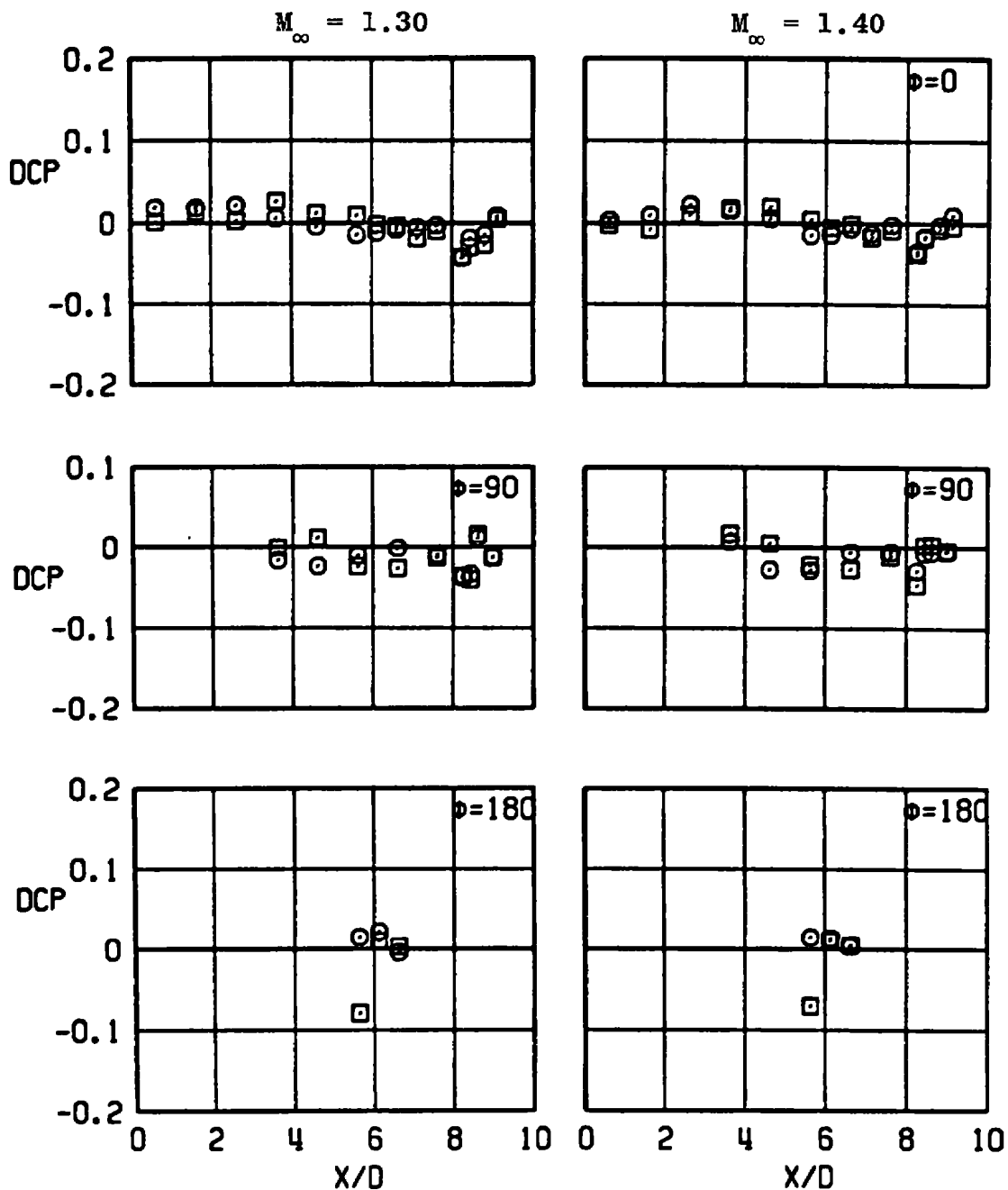
f. Continued
Figure A-4. Continued.

SYM	CONFIG	ℓ , IN.
○	B2-S3L1	0.0
□	B2-S3L3	1.6



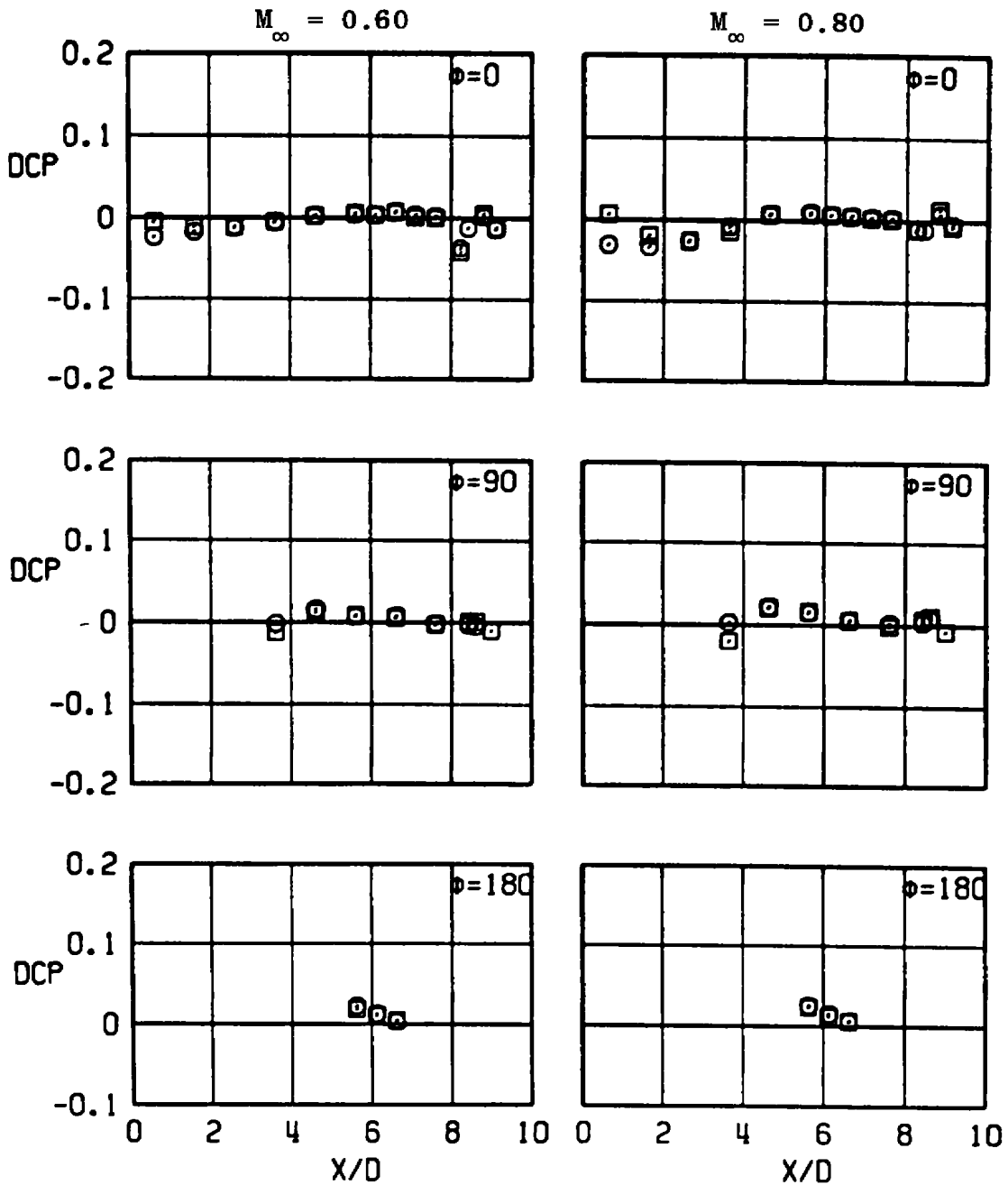
f. Continued
Figure A-4. Continued.

SYM	CONFIG	ℓ , IN.
○	B2-S3L1	0.0
□	B2-S3L3	1.6



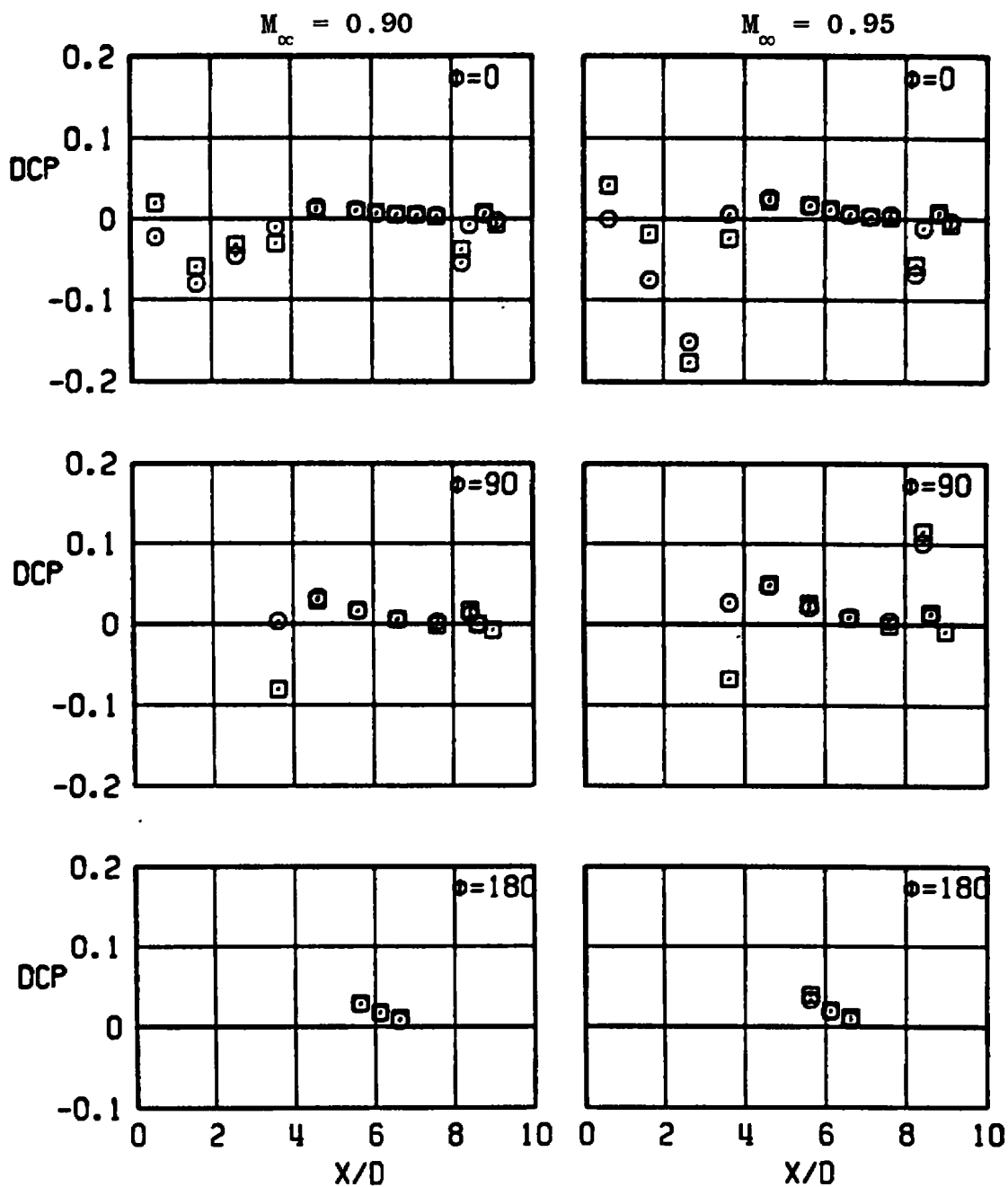
f. Concluded
Figure A-4. Concluded.

SYM	CONFIG	ℓ , IN.
○	B2-S2L1	0.0
□	B2-S1L2	0.8



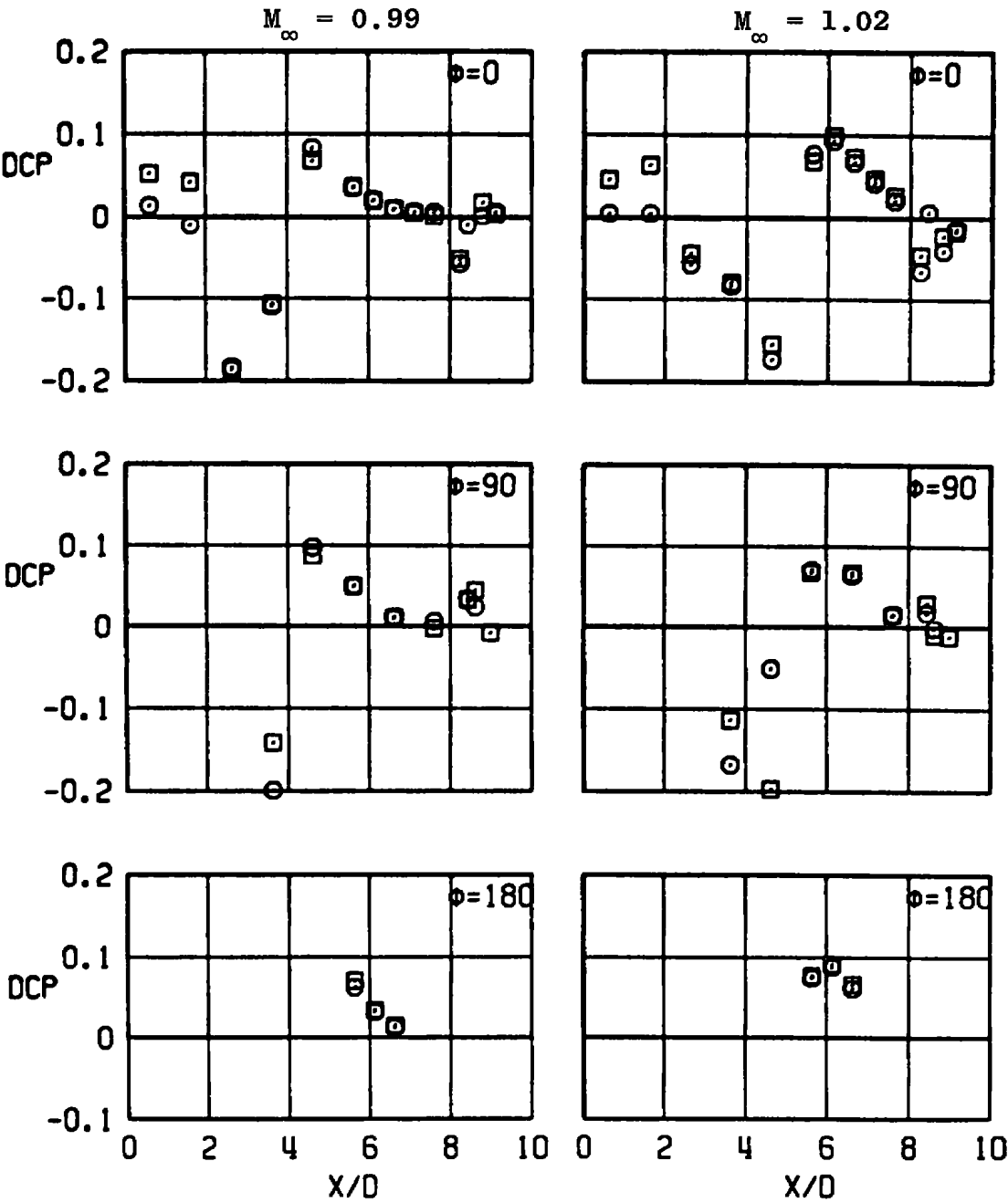
a. DCP versus X/D (straight strut, 10-deg boattail)
 Figure A-5. Effect of trailing-edge location.

SYM	CONFIG	l , IN.
○	B2-S2L1	0.0
□	B2-S1L2	0.8

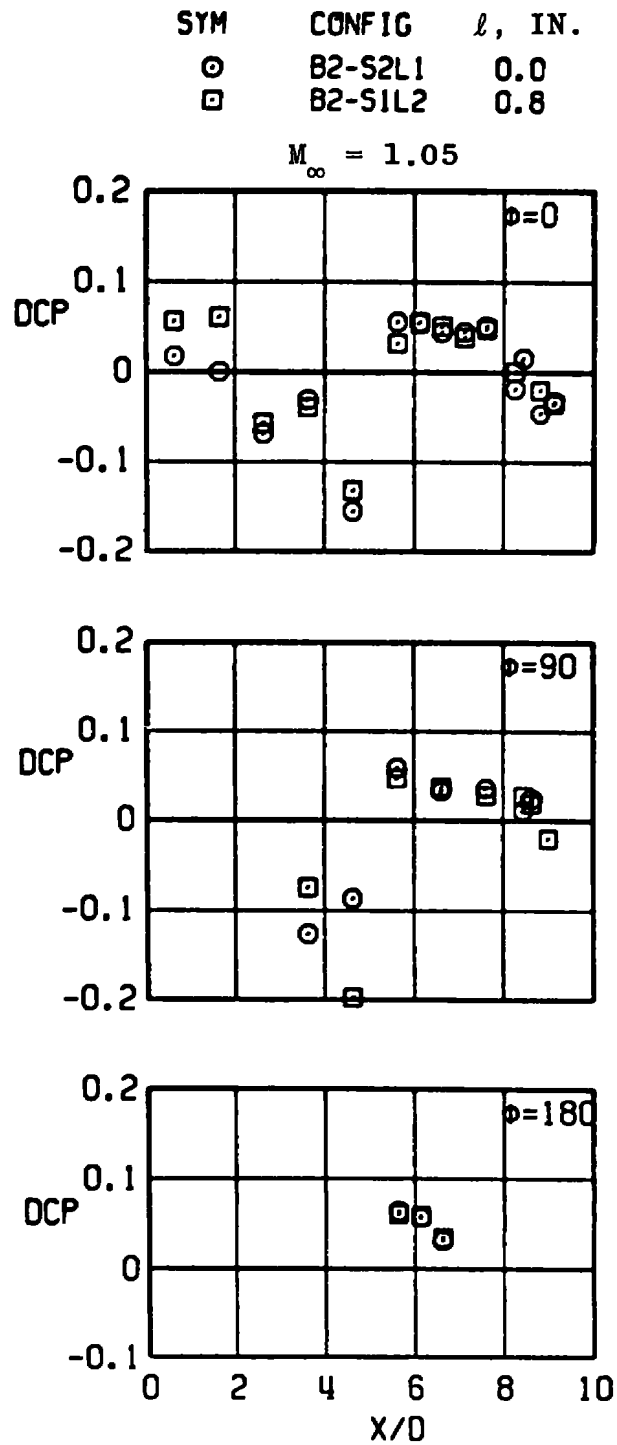


a. Continued
Figure A-5. Continued.

SYM	CONFIG	l , IN.
○	B2-S2L1	0.0
□	B2-S1L2	0.8

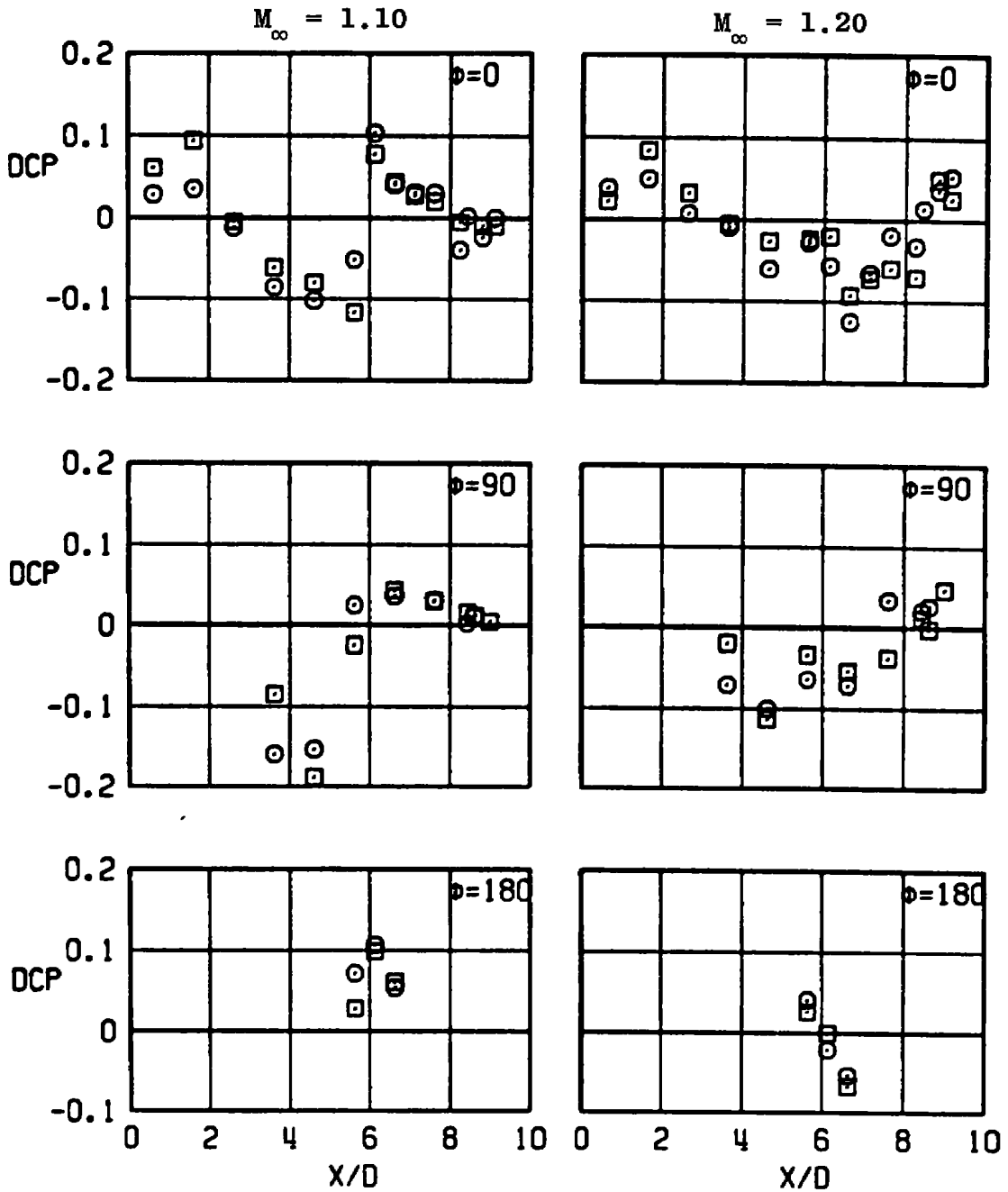


a. Continued
Figure A-5. Continued.



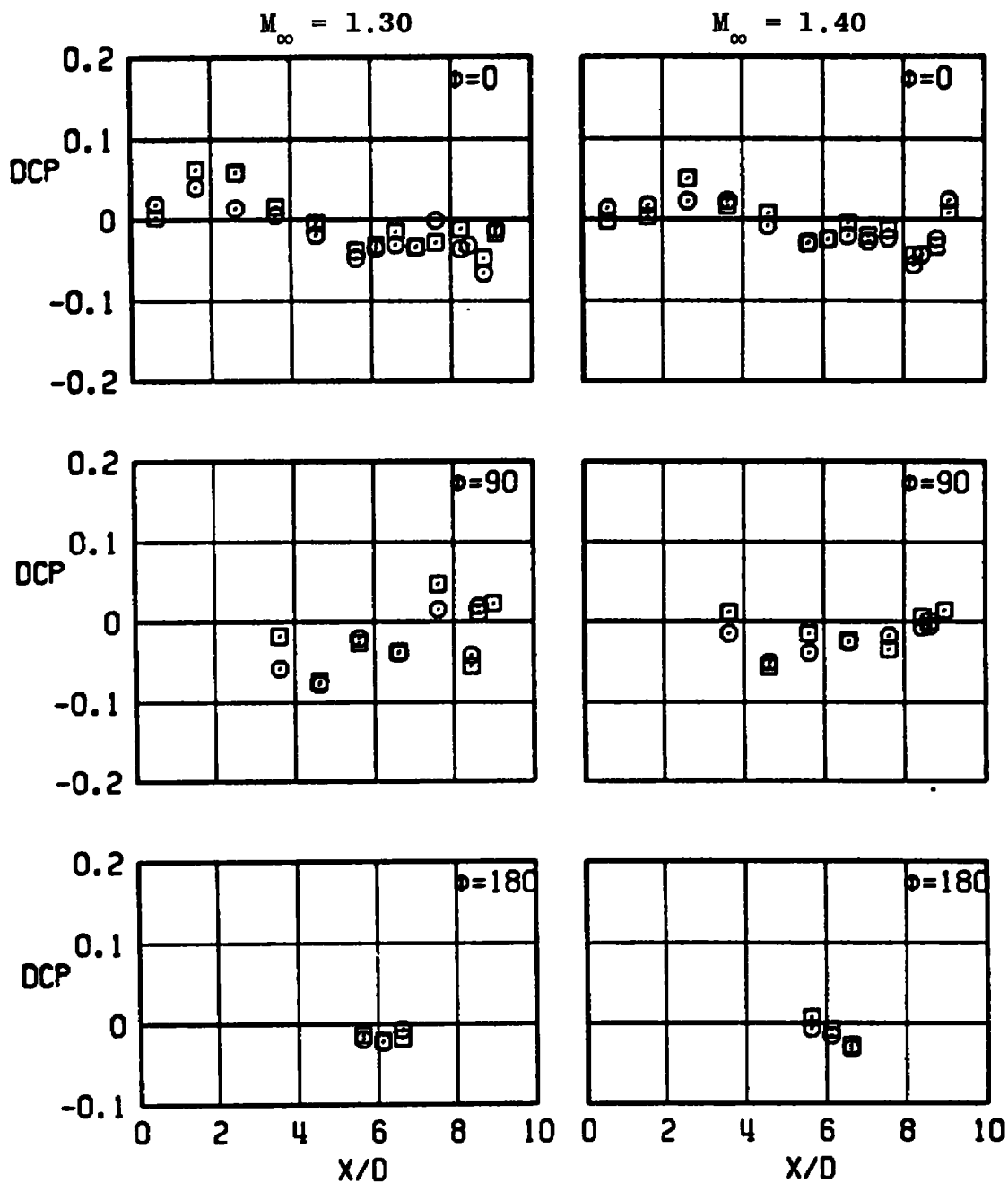
a. Continued
Figure A-5. Continued.

SYM	CONFIG	ℓ , IN.
○	B2-S2L1	0.0
□	B2-S1L2	0.8



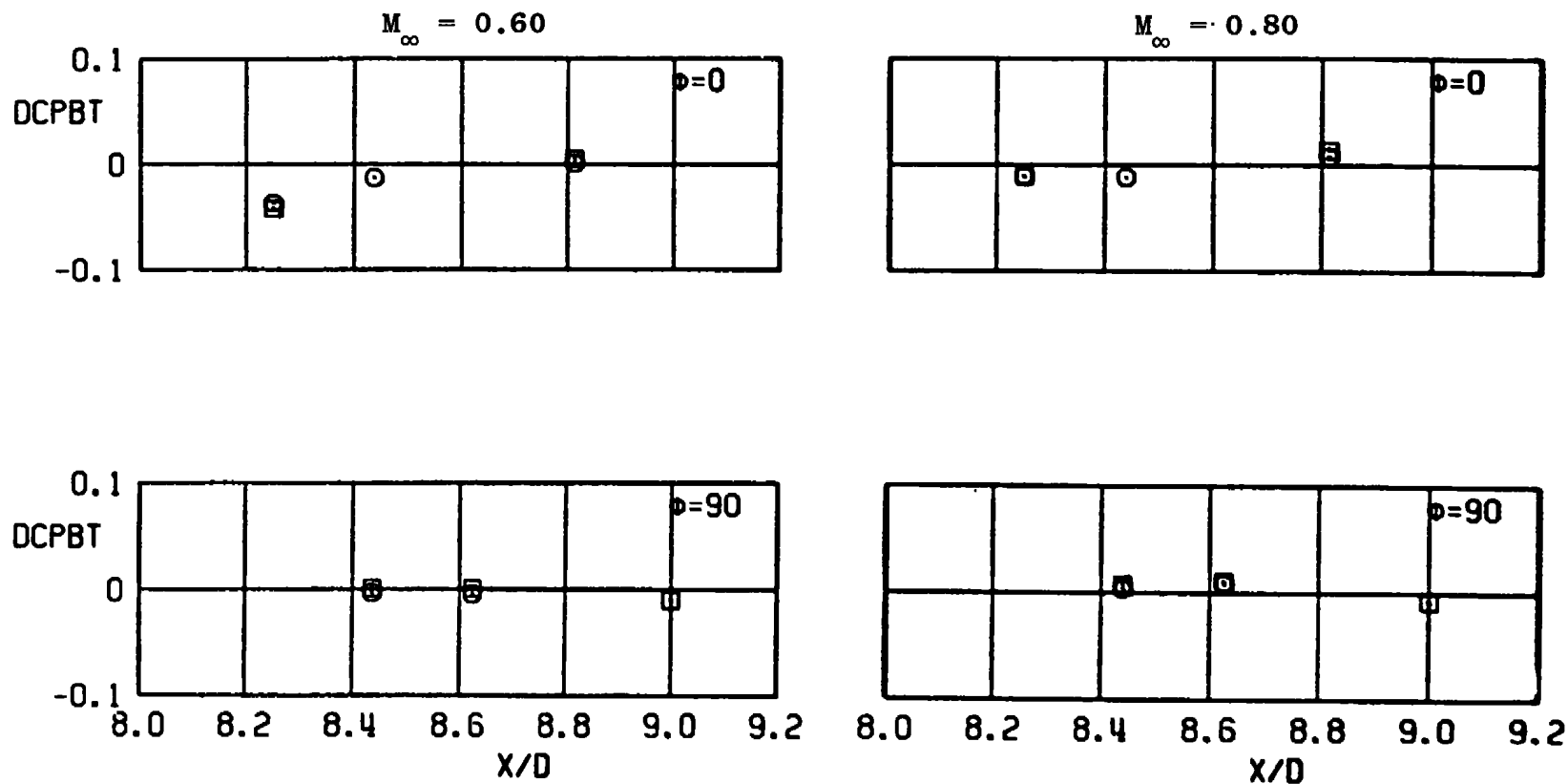
a. Continued
Figure A-5. Continued.

SYM	CONFIG	l , IN.
○	B2-S2L1	0.0
□	B2-S1L2	0.8



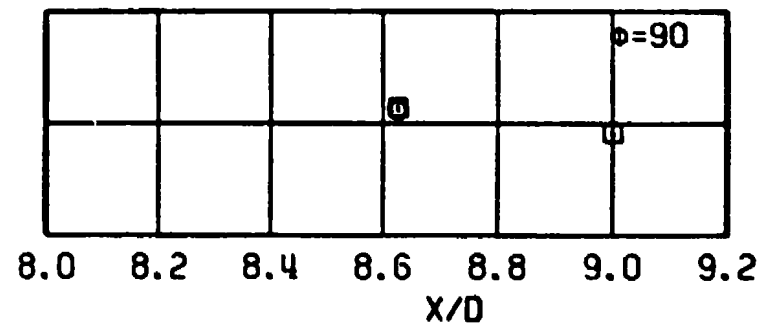
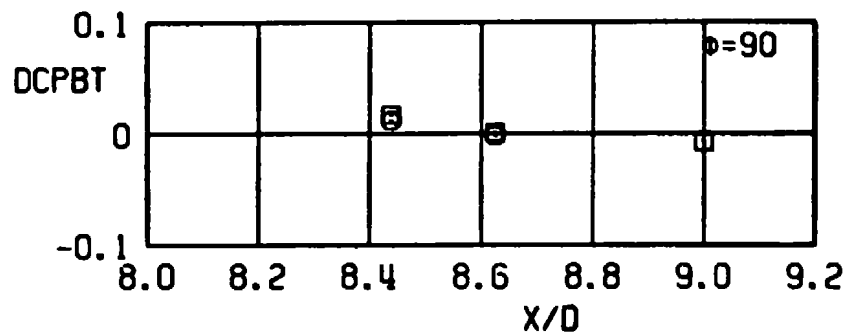
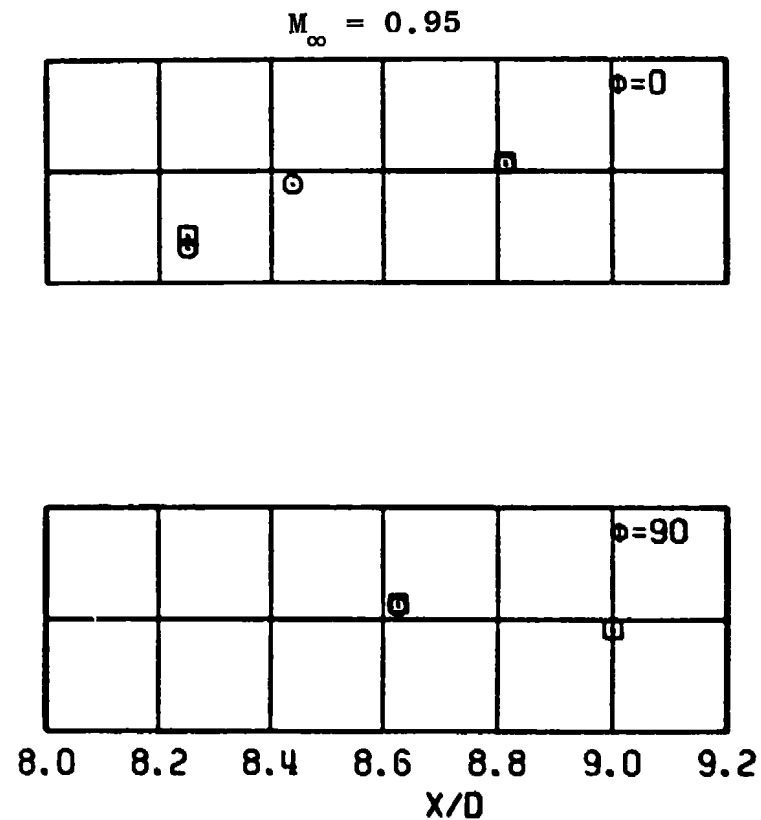
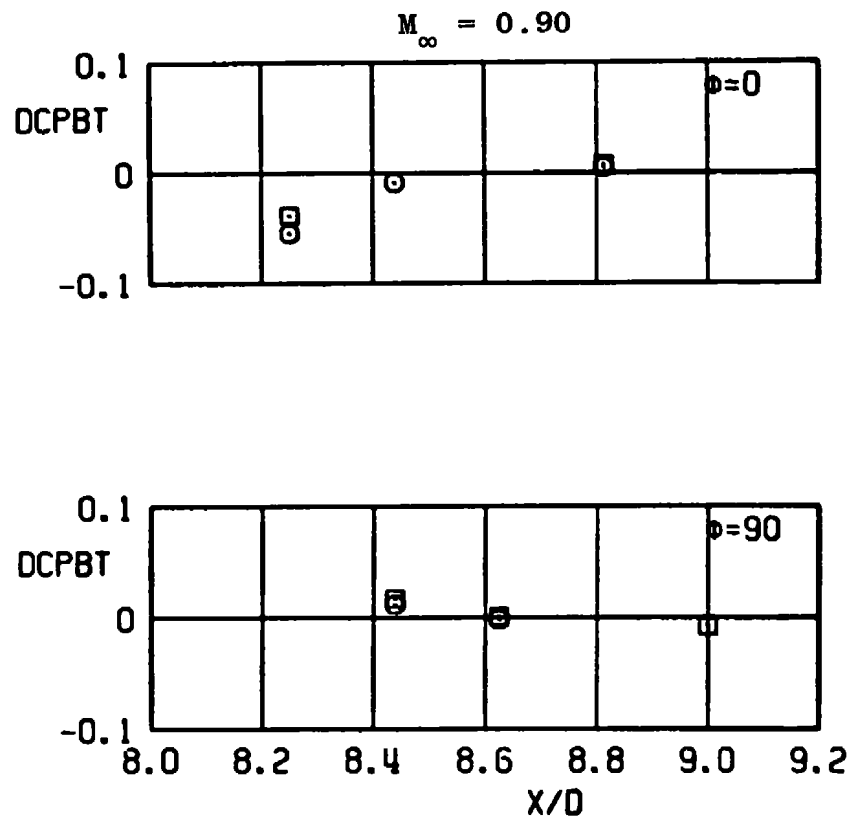
a. Concluded
Figure A-5. Continued.

SYM	CONFIG	l , IN.
○	B2-S2L1	0.0
□	B2-S1L2	



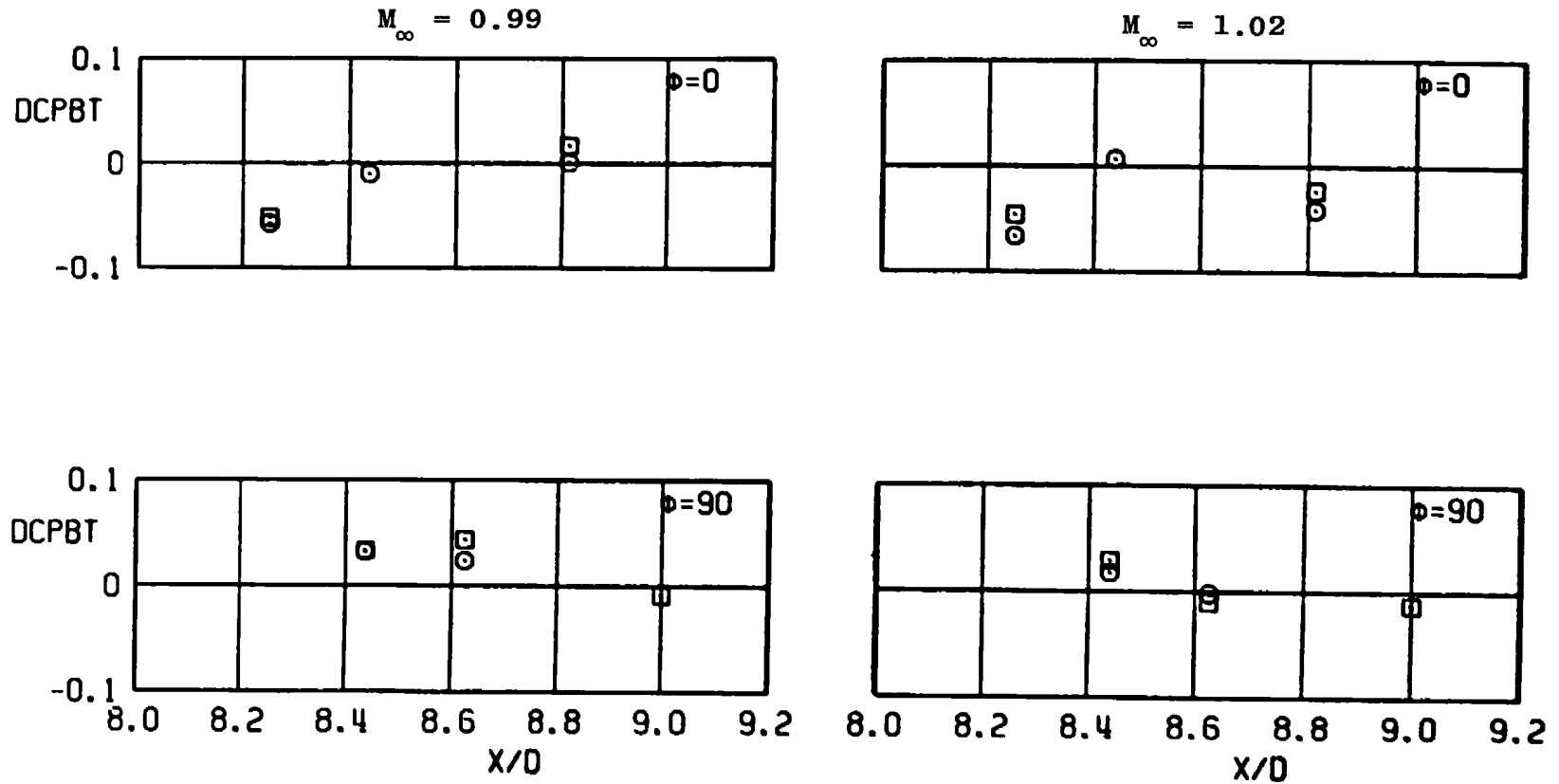
b. DCPBT versus X/D (straight strut, 10-deg boattail)
Figure A-5. Continued.

SYM	CONFIG	l , IN.
○	B2-S2L1	0.0
□	B2-S1L2	0.8



b. Continued
Figure A-5. Continued.

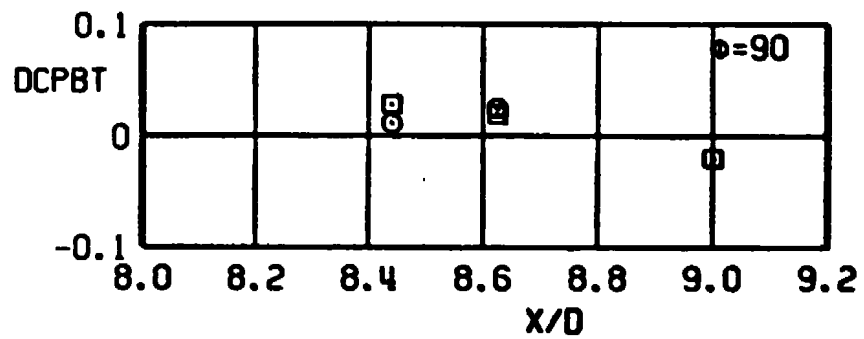
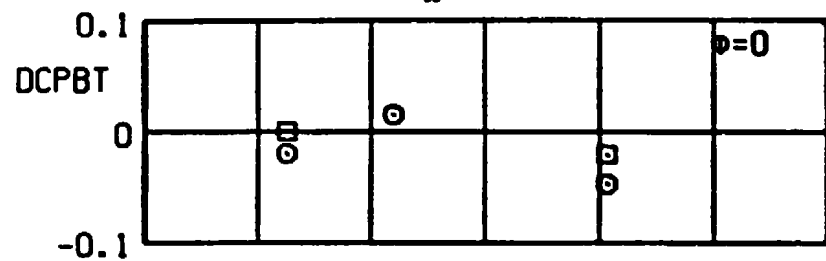
SYM	CONFIG	l , IN.
○	B2-S2L1	0.0
□	B2-S1L2	0.8



b. Continued
Figure A-5. Continued.

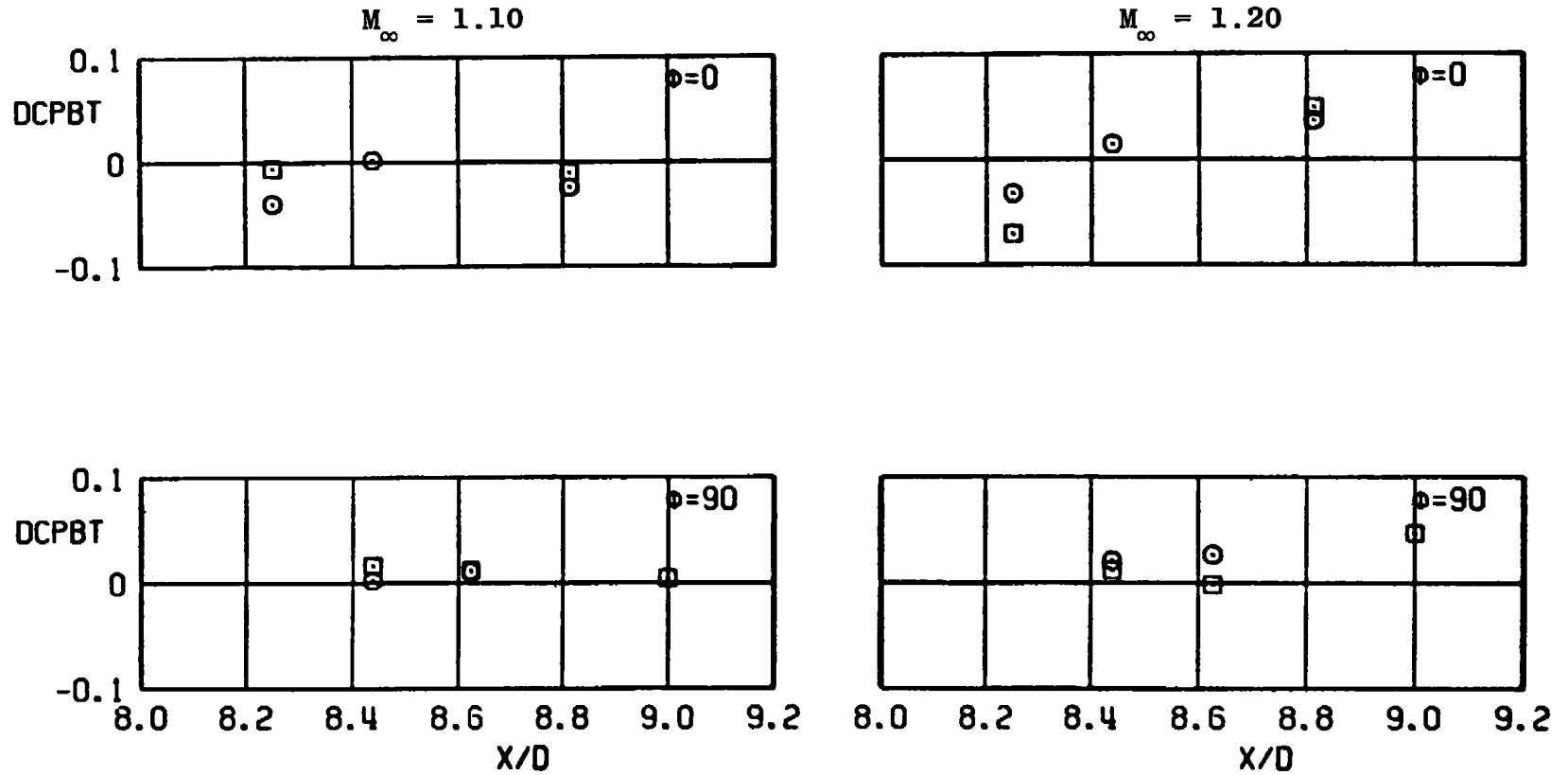
SYM	CONFIG	ℓ , IN.
○	B2-S2L1	0.0
□	B2-S1L2	0.8

$$M_{\infty} = 1.05$$



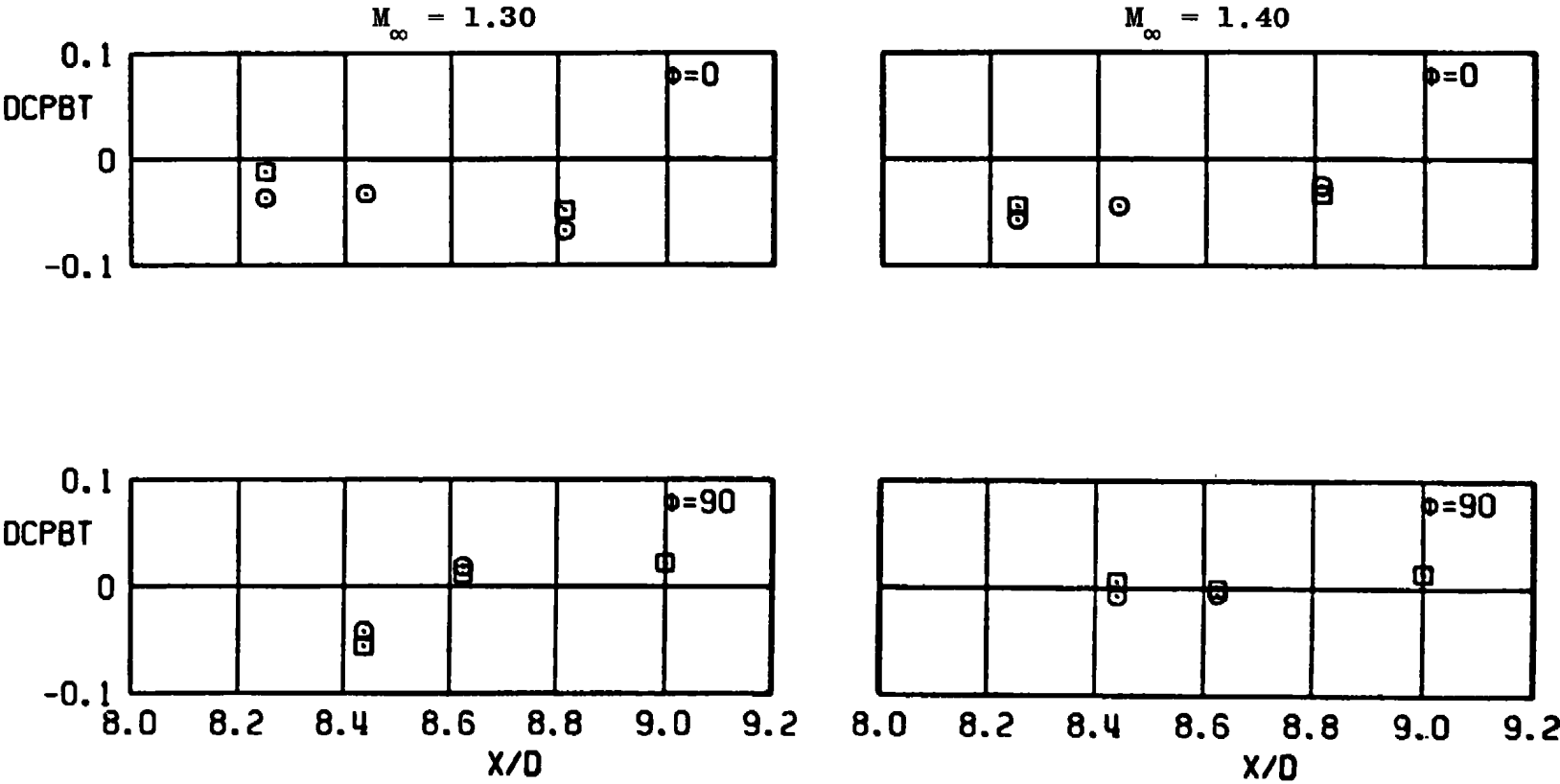
b. Continued
Figure A-5. Continued.

SYM	CONFIG	ℓ , IN.
○	B2-S2L1	0.0
□	B2-S1L2	0.8



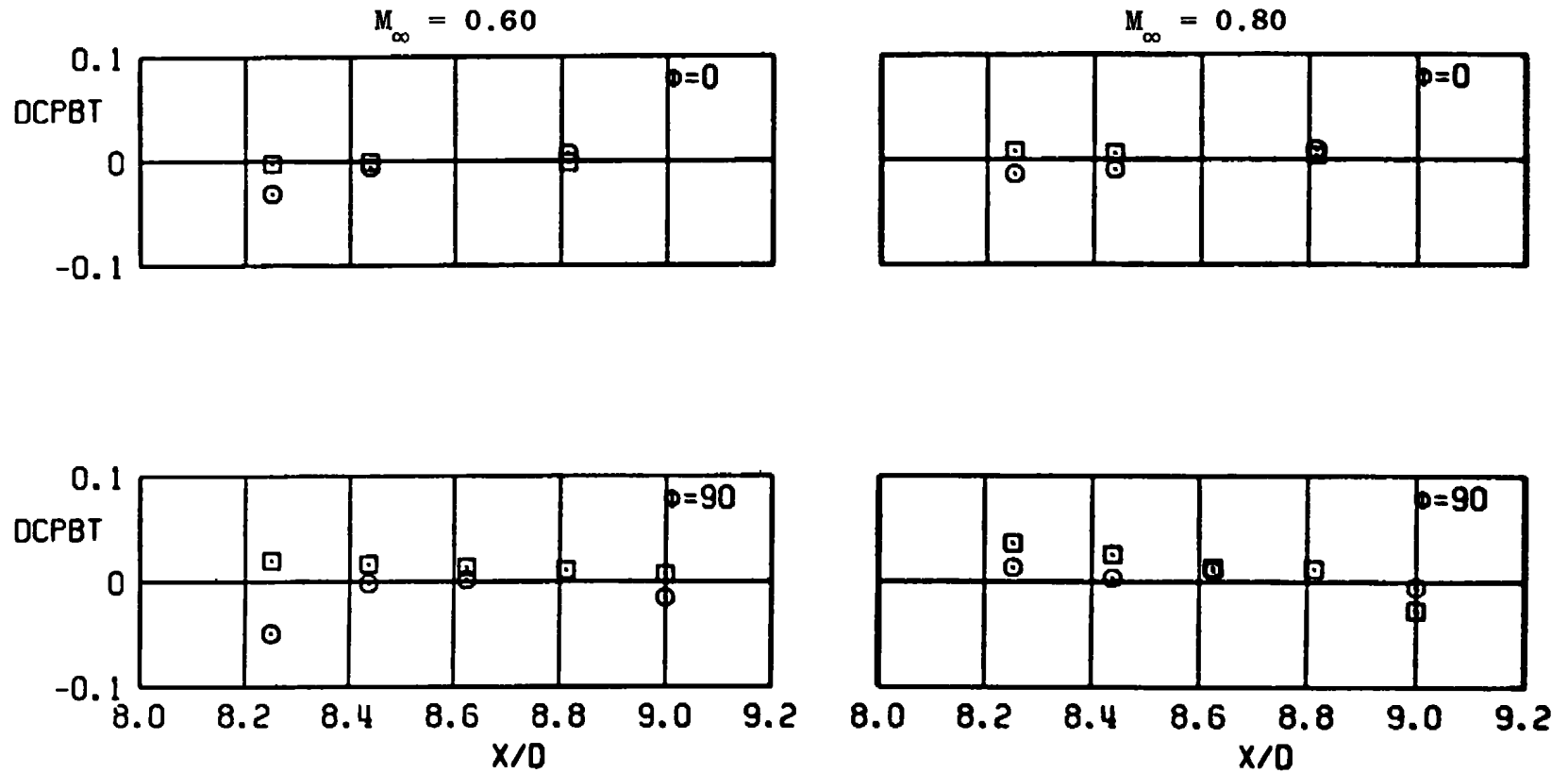
b. Continued
Figure A-5. Continued.

SYM	CONFIG	l , IN.
⊙	B2-S2L1	0.0
⊠	B2-S1L2	0.8



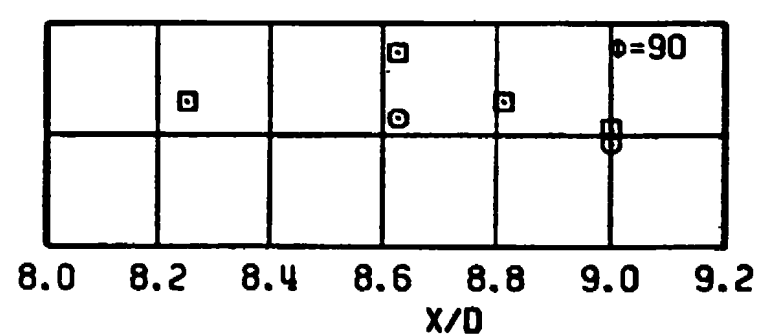
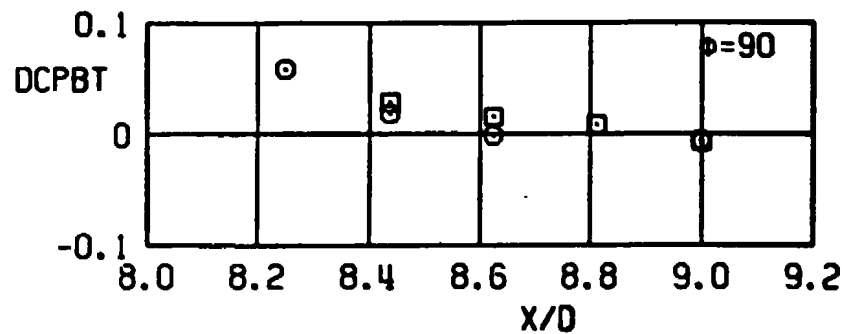
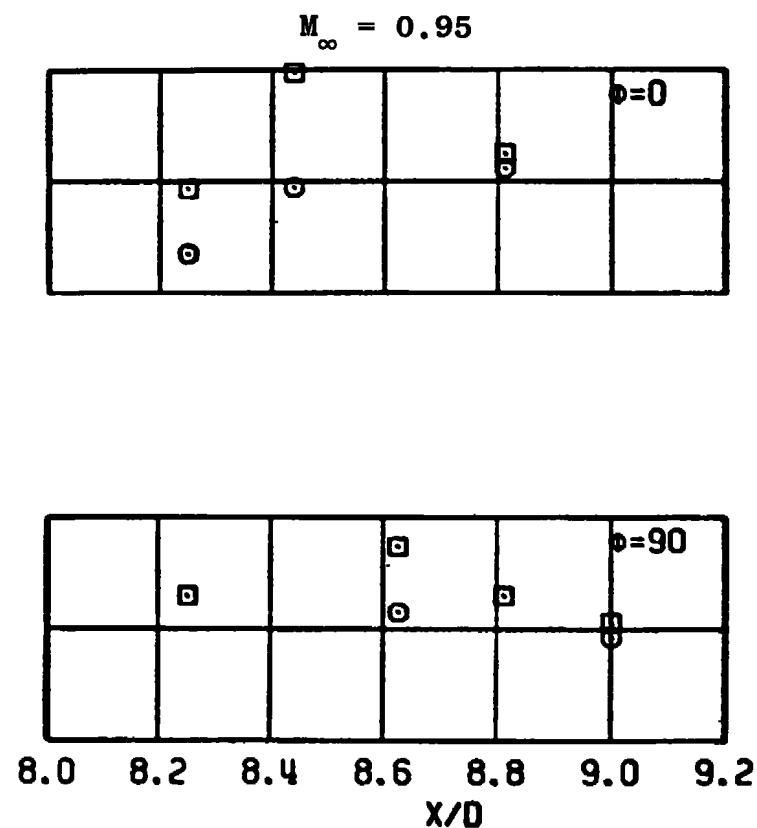
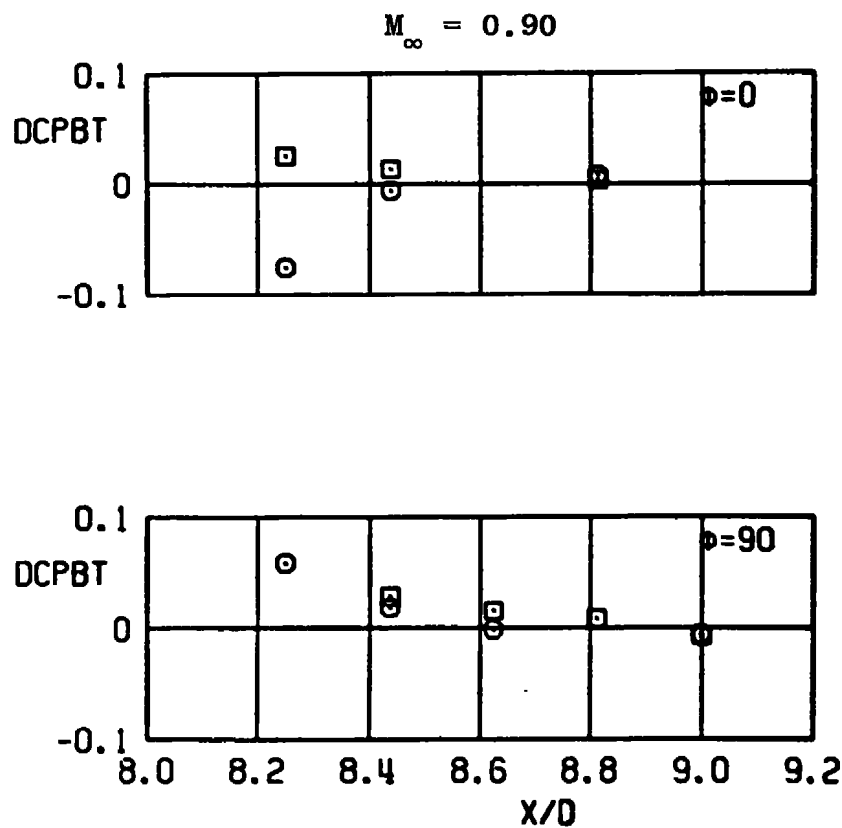
b. Concluded
Figure A-5. Continued.

SYM
 ○ B2-S3L1
 □ B2-S4L1



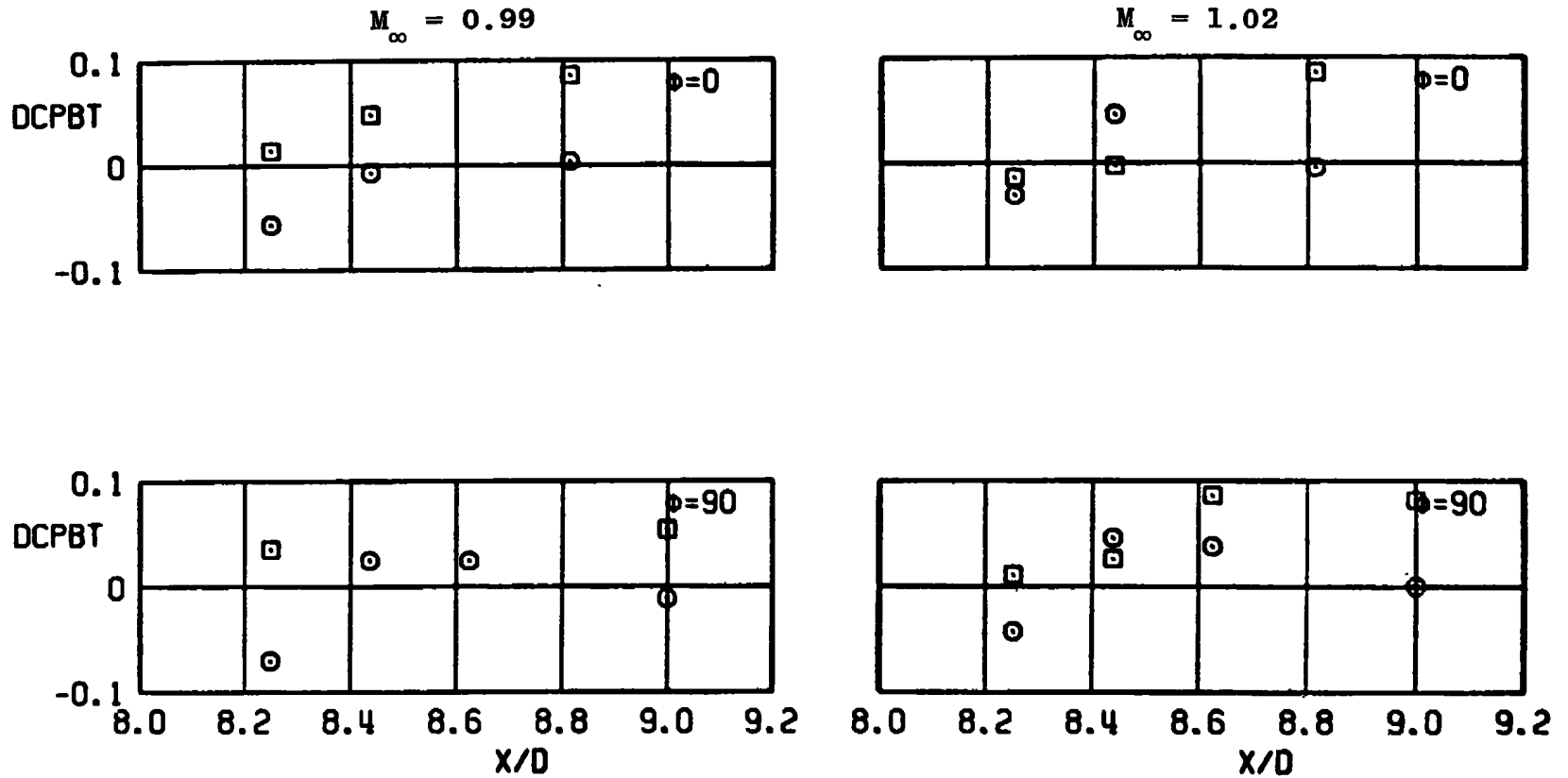
c. DCPBT versus X/D (30-deg swept strut, 10-deg boattail)
 Figure A-5. Continued.

SYM	CONFIG
○	B2-S3L1
□	B2-S4L1

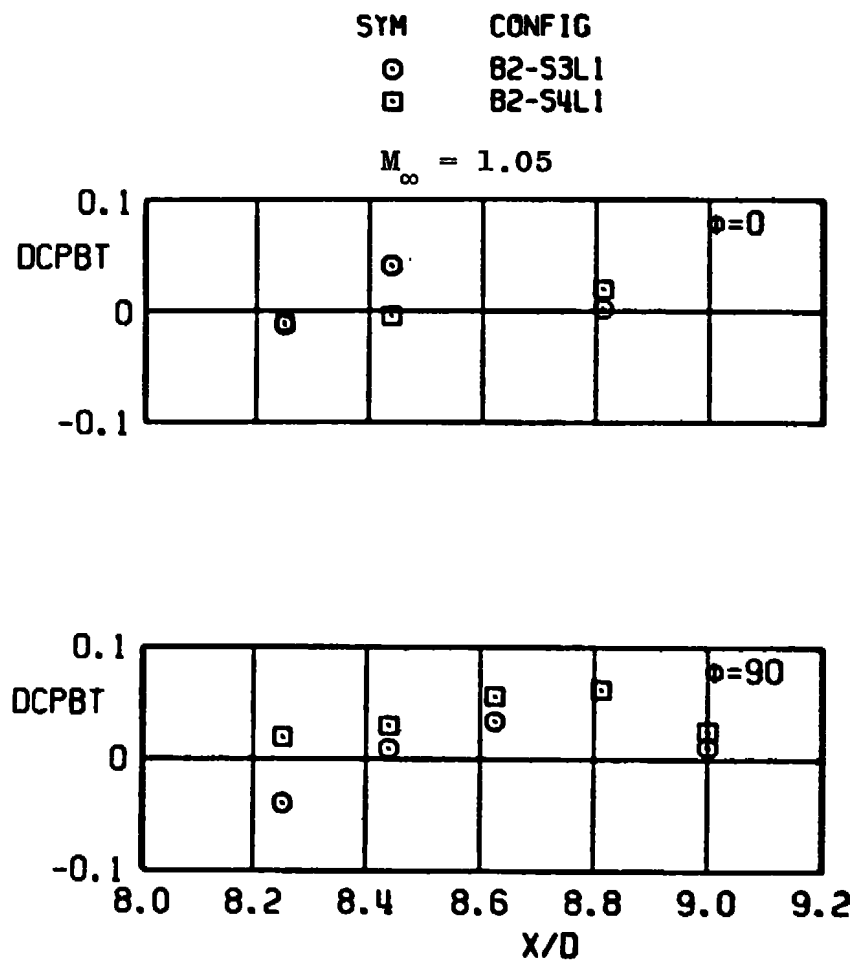


c. Continued
Figure A-5. Continued.

SYM
 ○ B2-S3L1
 □ B2-S4L1

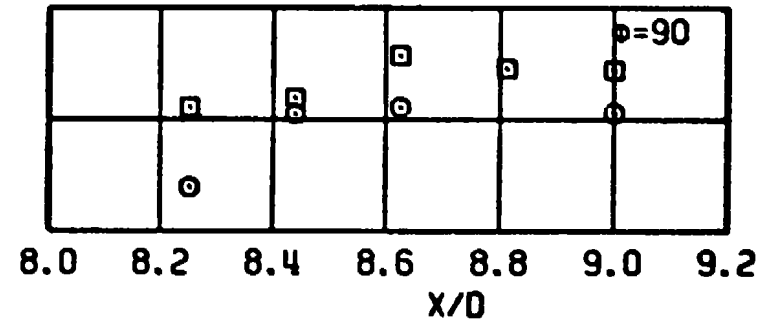
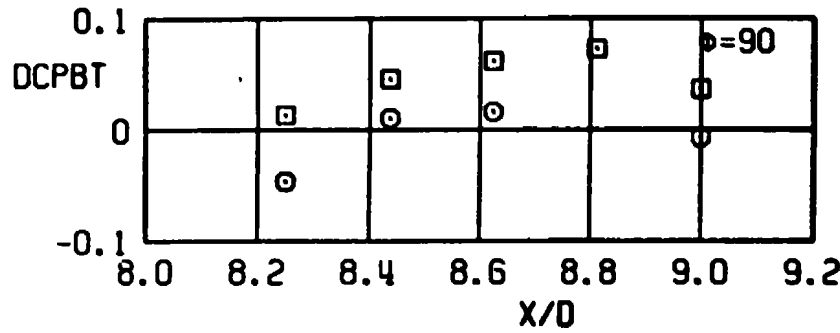
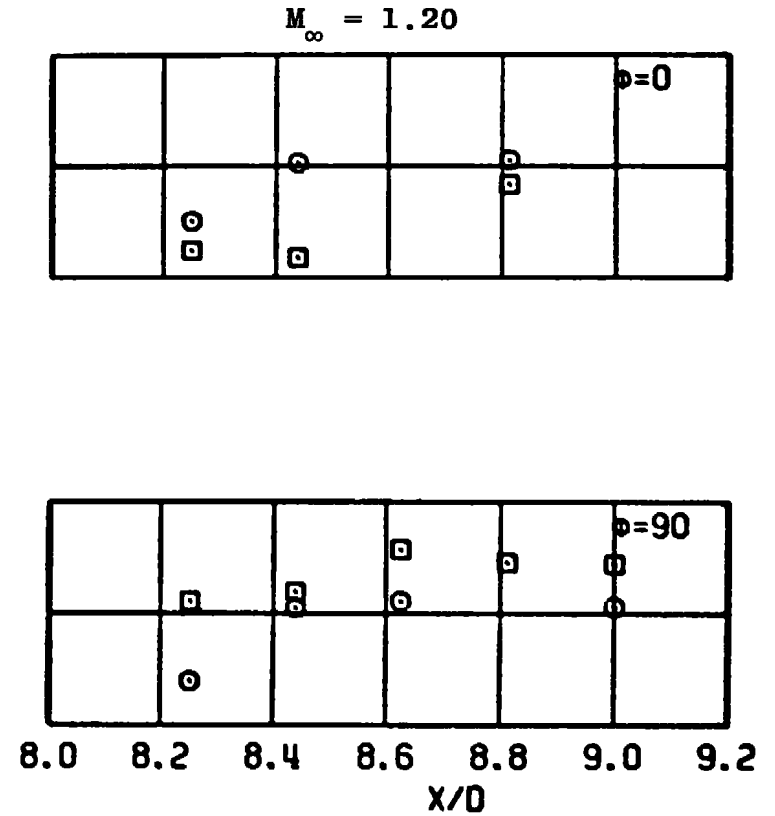
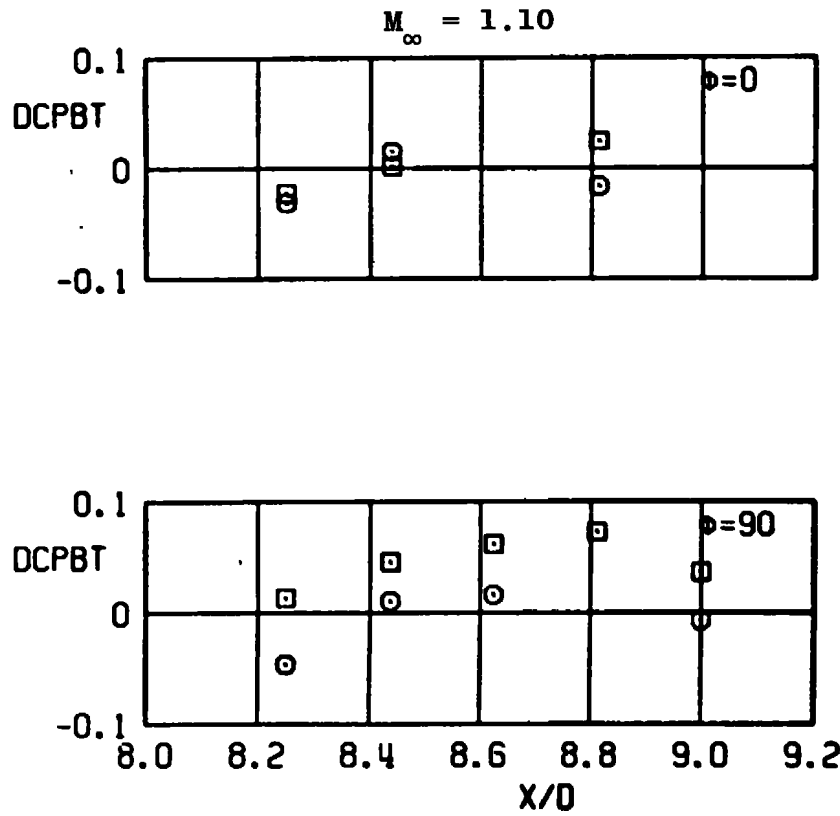


c. Continued
 Figure A-5. Continued.



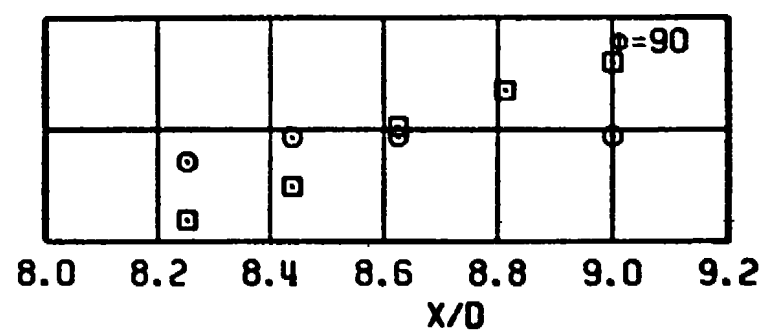
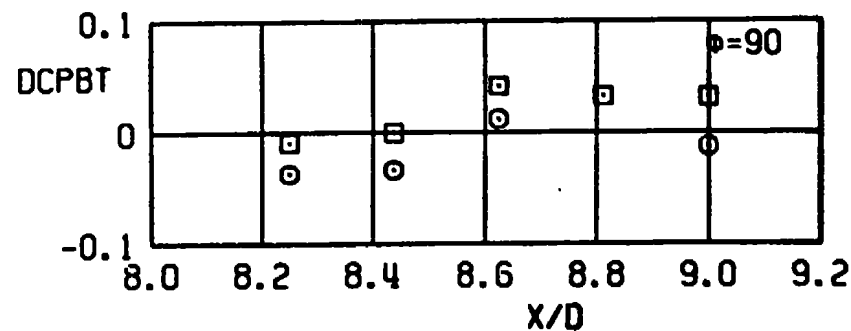
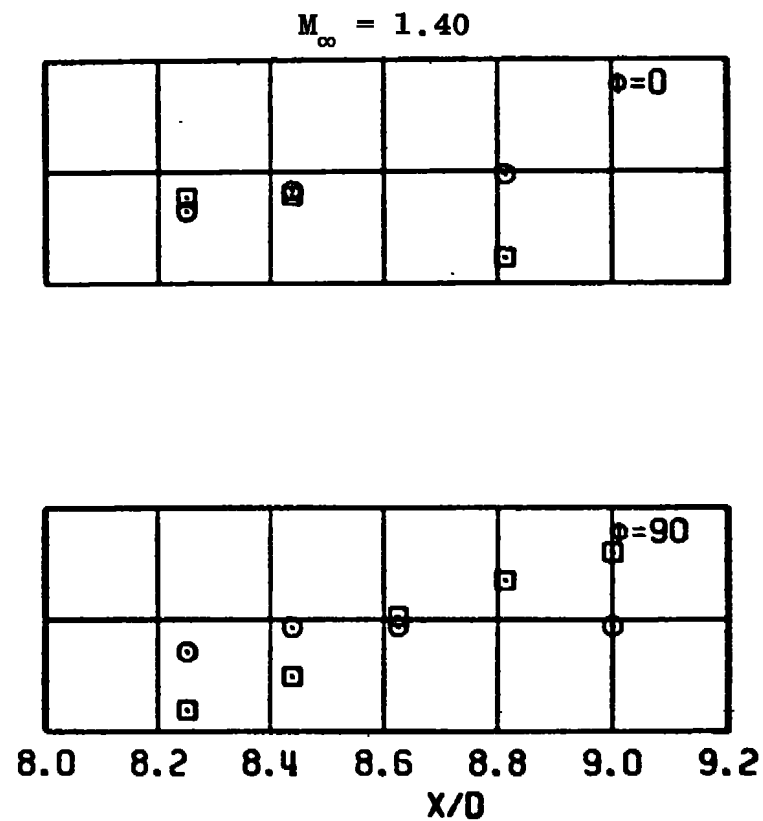
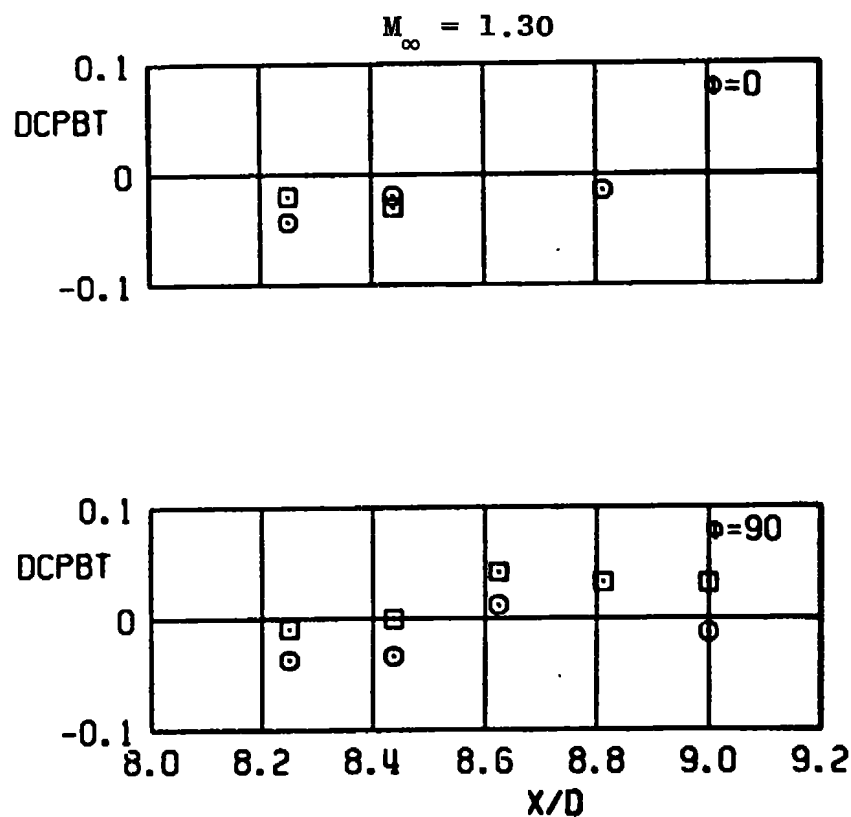
c. Continued
 Figure A-5. Continued.

SYM CONFIG
 ○ B2-S3L1
 □ B2-S4L1



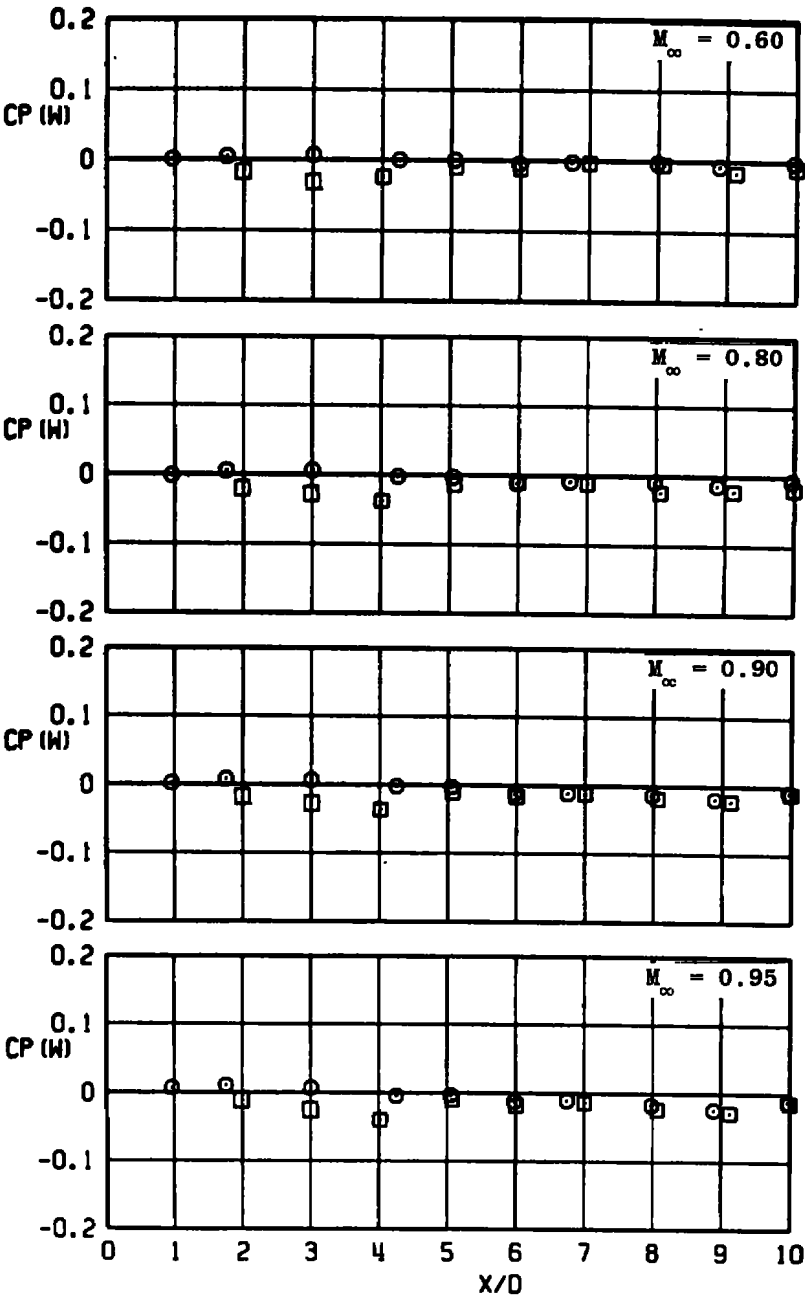
c. Continued
 Figure A-5. Continued.

SYM CONFIG
 ○ B2-S3L1
 □ B2-S4L1



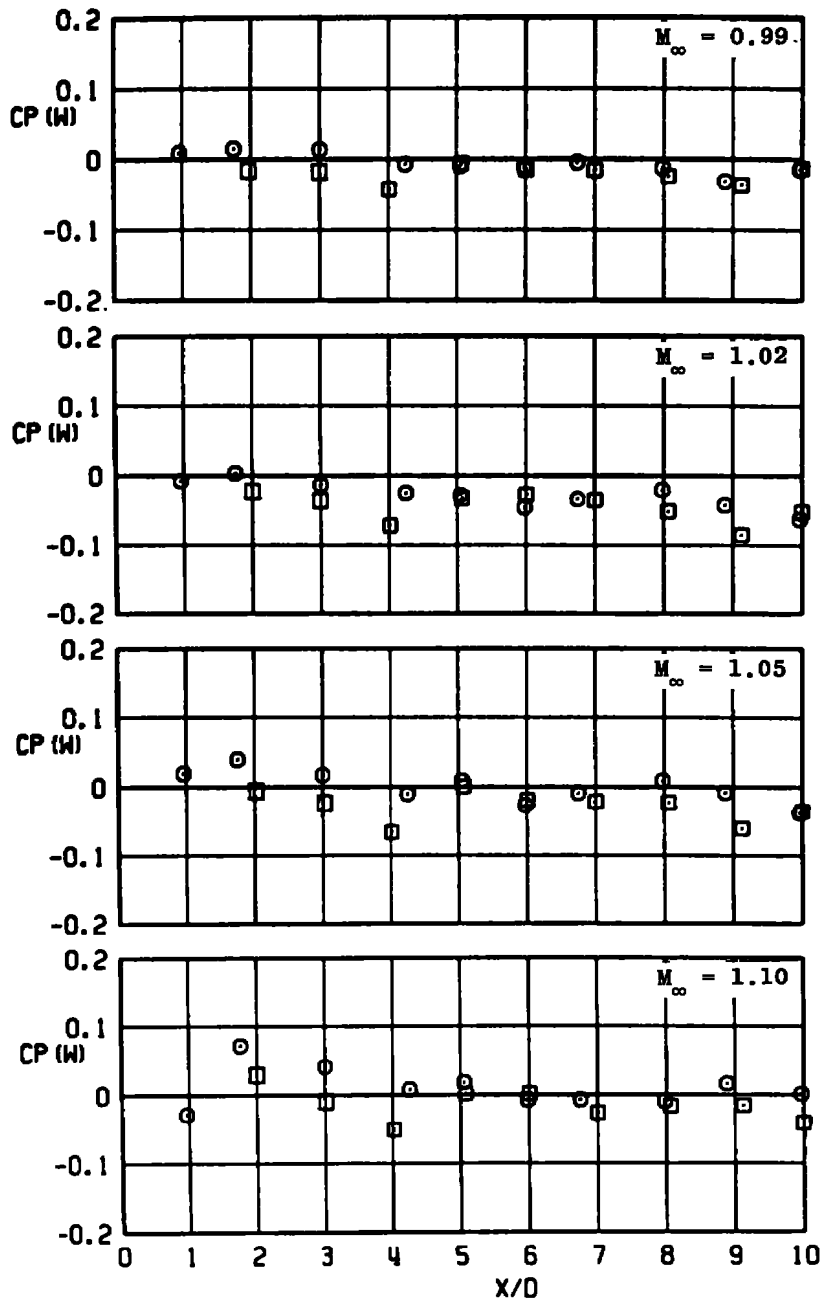
c. Concluded
 Figure A-5. Continued.

SYM	CONFIG	ϕ , DEG
○	B2-S3L1	0
□	B2-S4L1	0



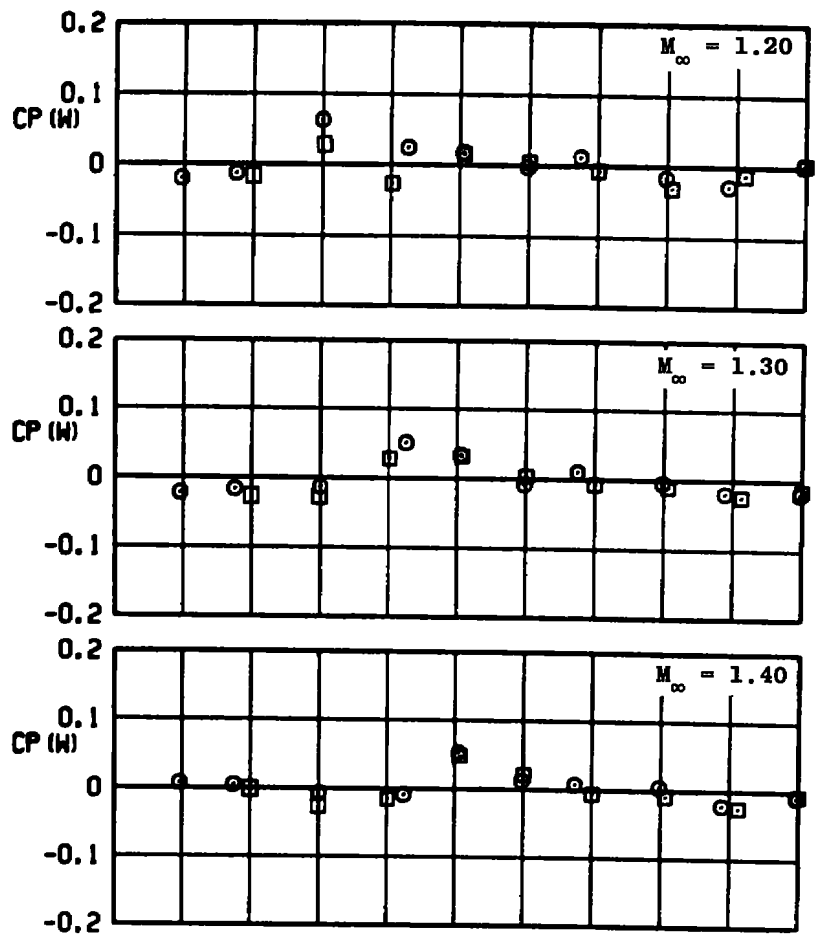
d. $CP(W)$ versus X/D (30-deg swept strut, 10-deg boattail, $\phi = 0$)
Figure A-5. Continued.

SYM	CONFIG	ϕ , DEG
○	B2-S3L1	0
□	B2-S4L1	0



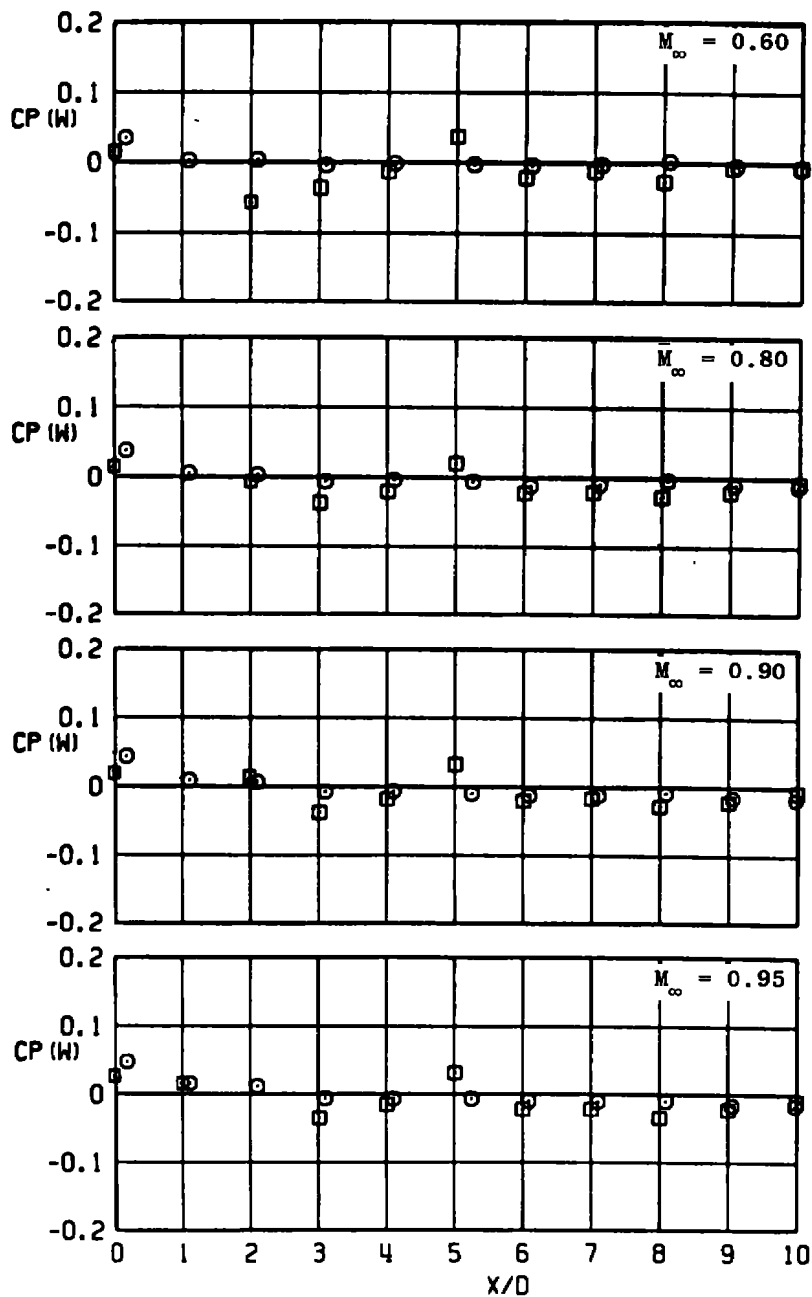
d. Continued
Figure A-5. Continued.

SYM	CONFIG	ϕ , DEG
○	B2-S3L1	0
□	B2-S4L1	0



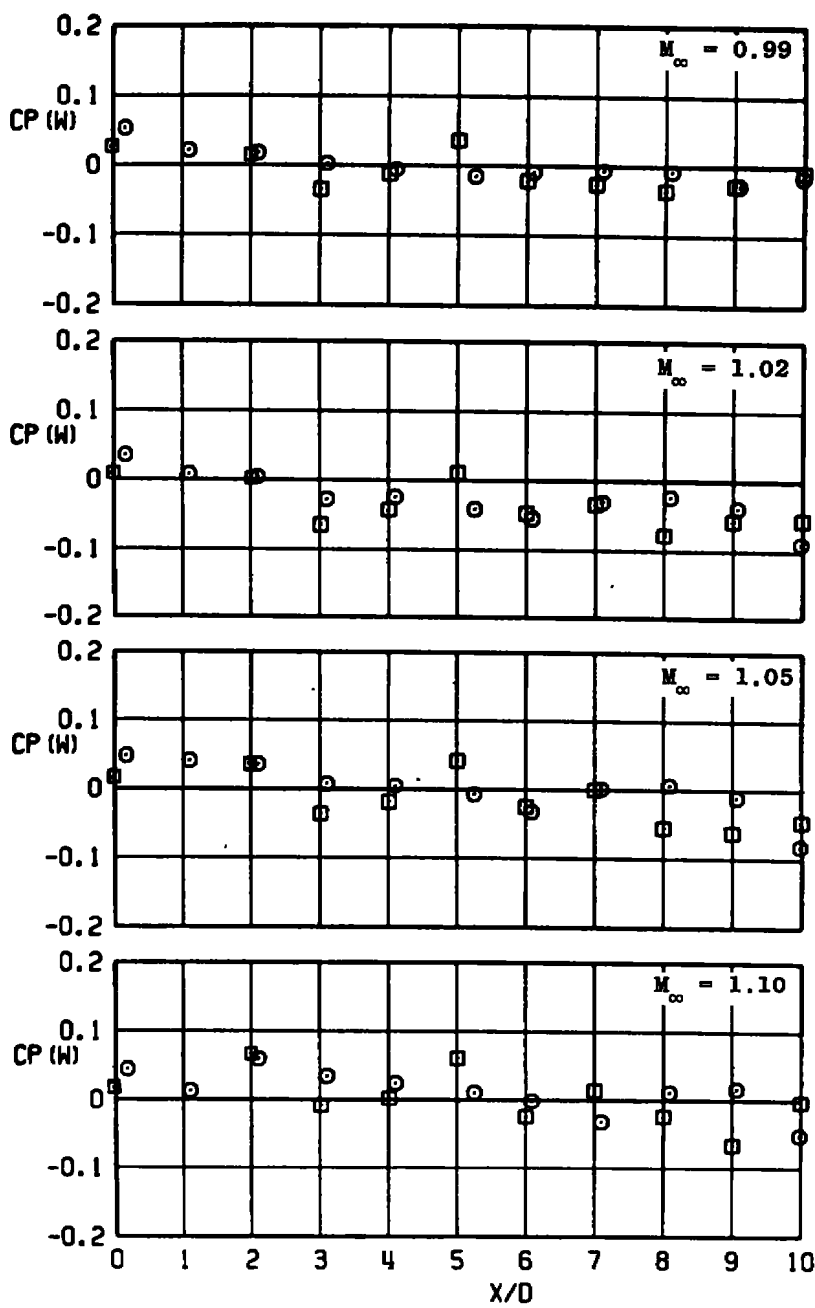
d. Concluded
Figure A-5. Continued.

SYM	CONFIG	ϕ , DEG
○	B2-S3L1	90
□	B2-S4L1	90



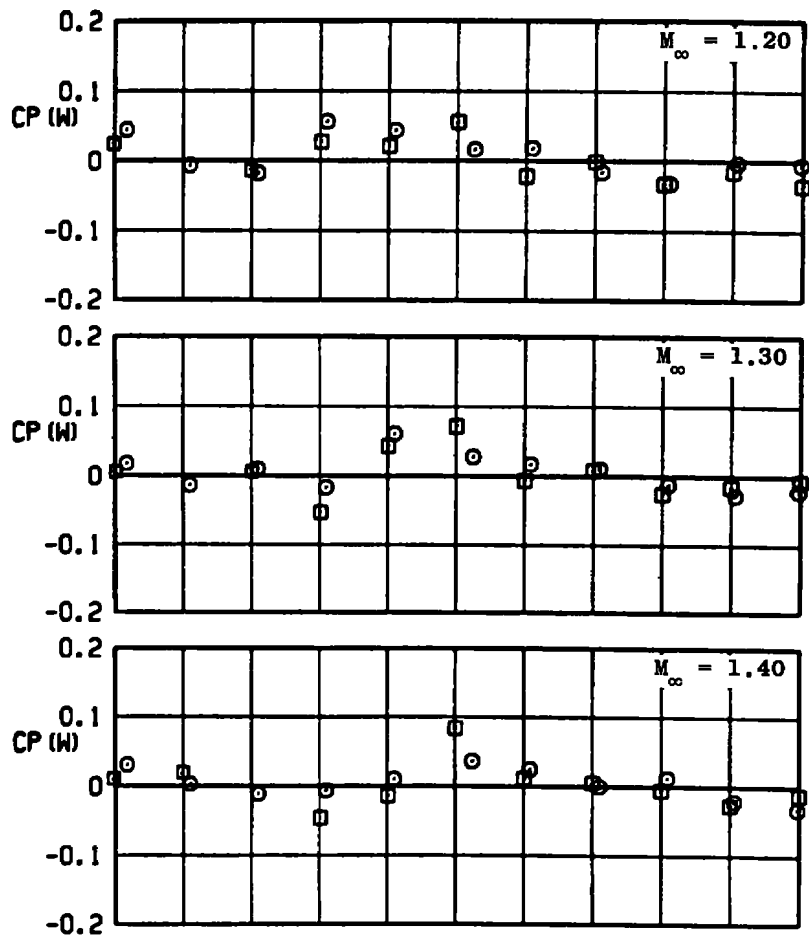
e. $CP(W)$ versus X/D (30-deg swept strut, 10-deg boattail, $\phi = 90$ deg)
Figure A-5. Continued.

SYM	CONFIG	ϕ , DEG
○	B2-S3L1	90
□	B2-S4L1	90



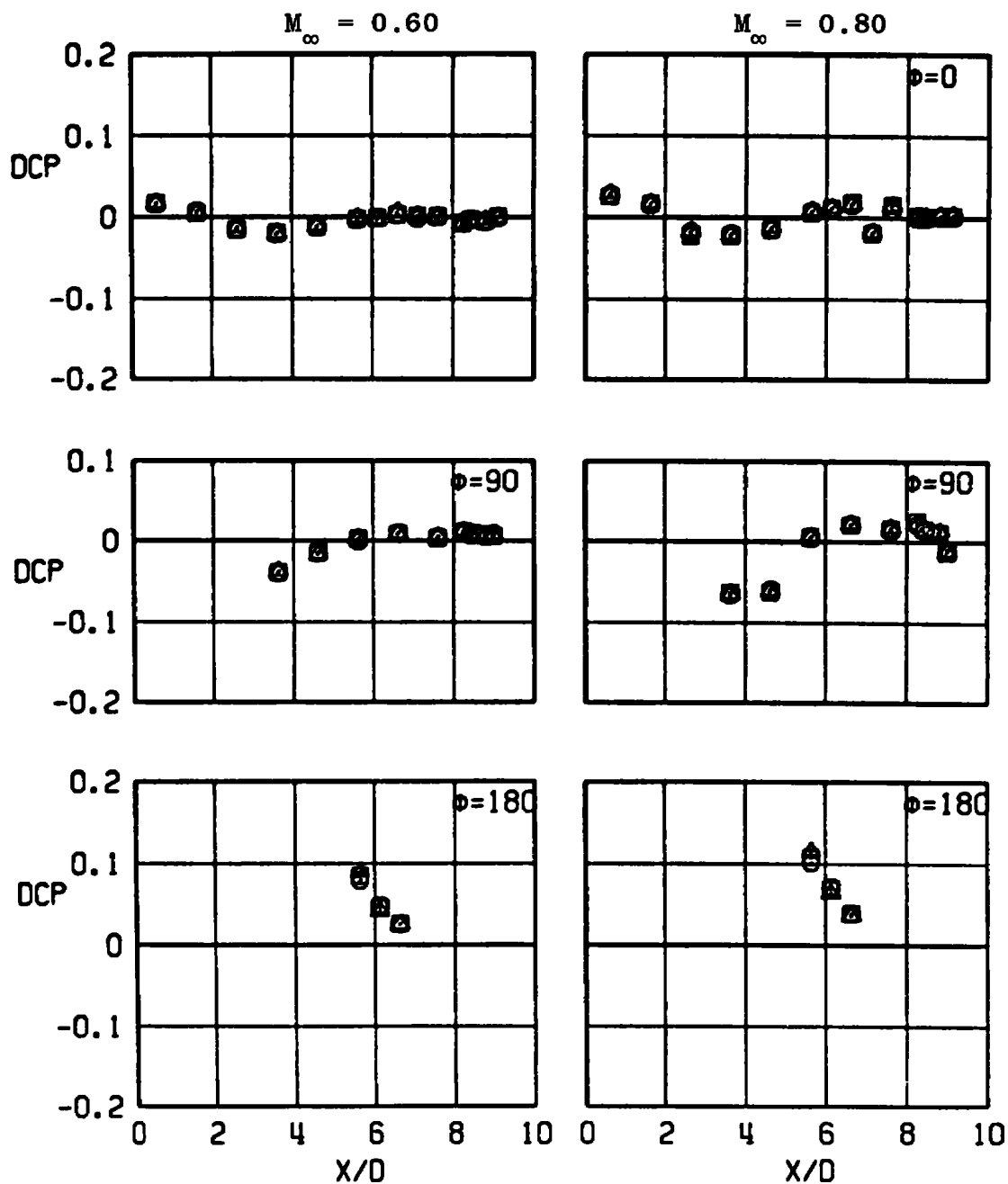
e. Continued
Figure A-5. Continued.

SYM	CONFIG	ϕ , DEG
○	B2-S3L1	90
□	B2-S4L1	90

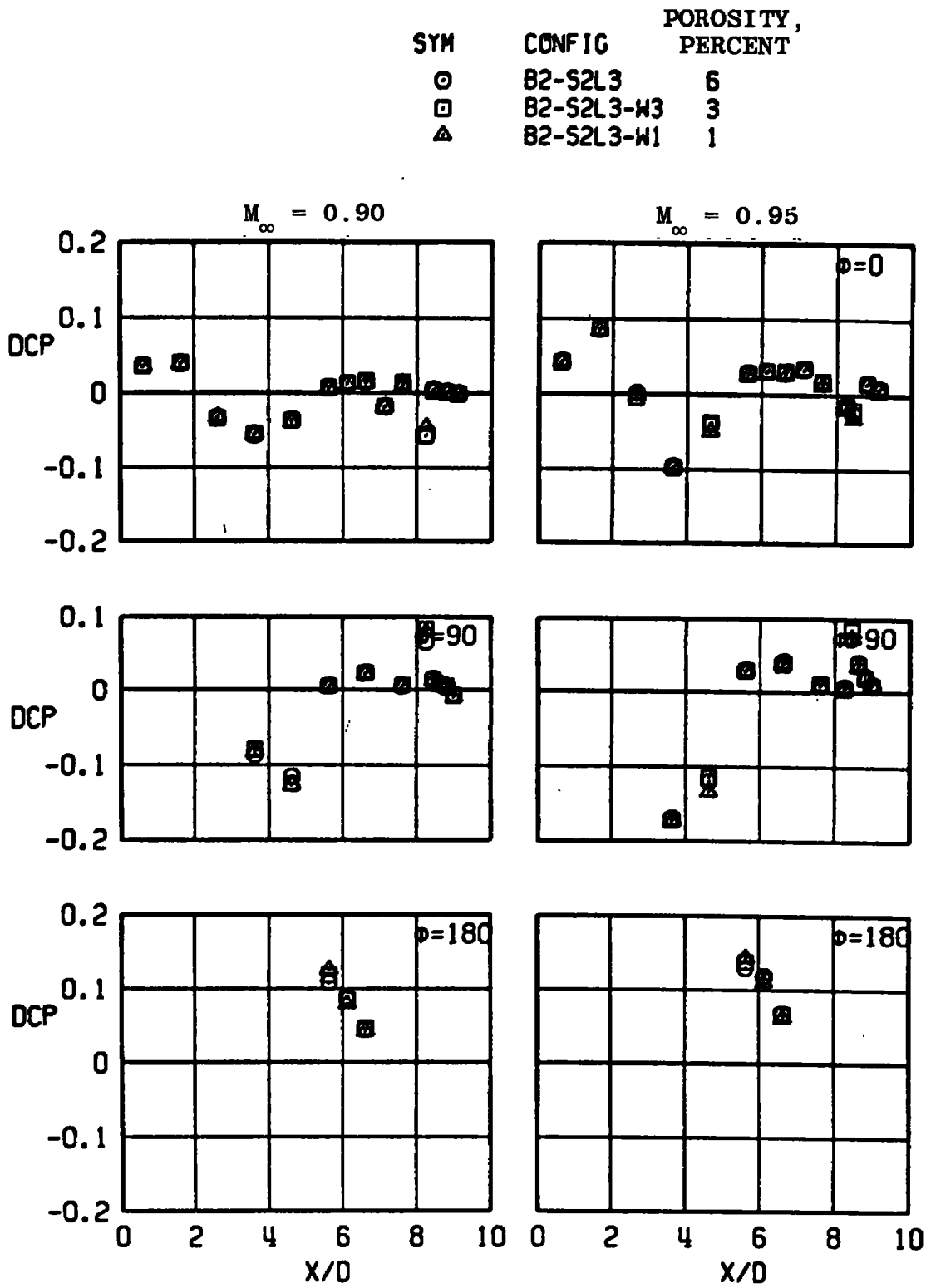


e. Concluded
Figure A-5. Concluded.

SYM	CONFIG	POROSITY, PERCENT
○	B2-S2L3	6
□	B2-S2L3-W3	3
△	B2-S2L3-W1	1

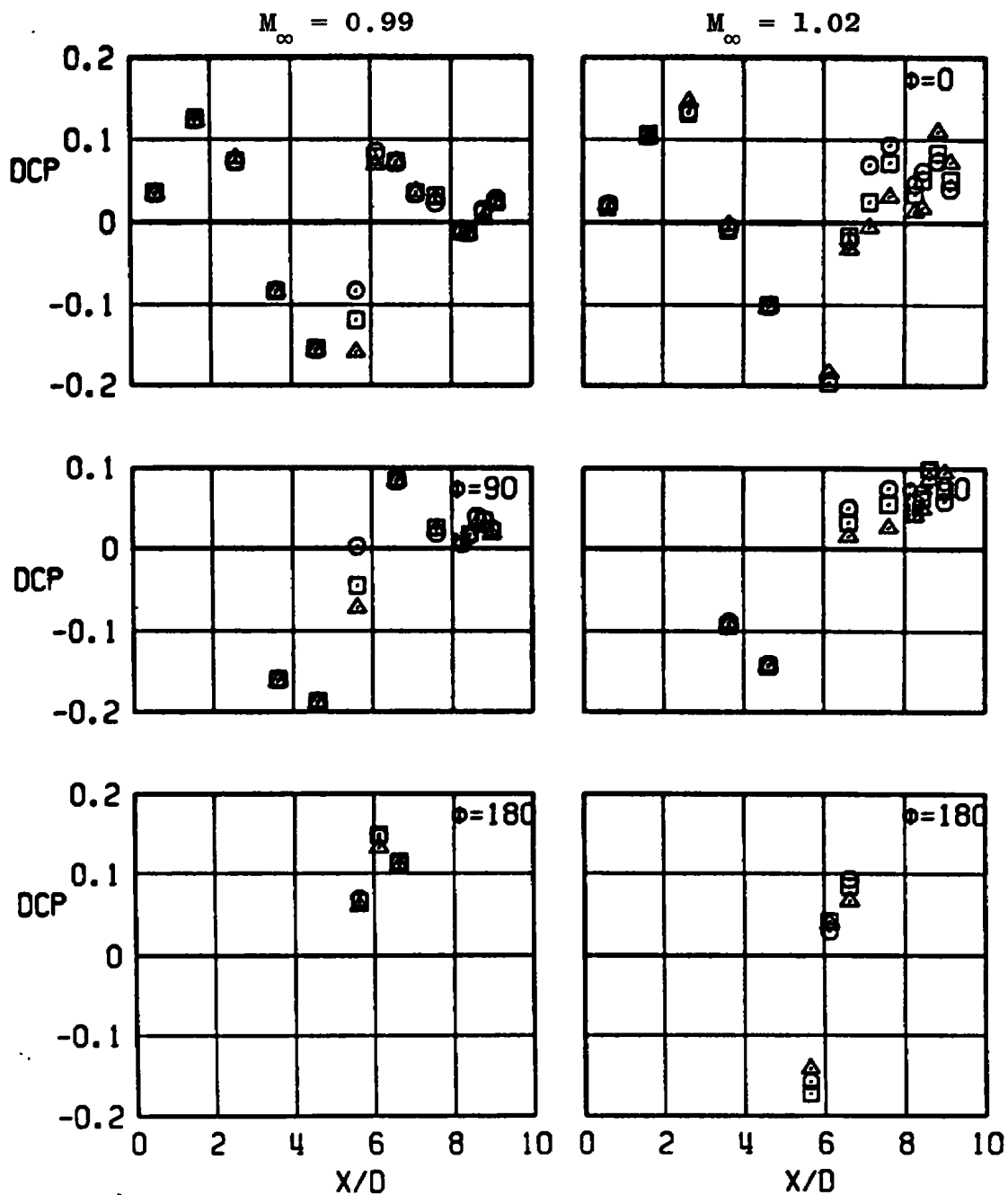


a. DCP versus X/D (straight strut, 10-deg boattail)
Figure A-6. Effect of tunnel wall porosity.



a. Continued
Figure A-6. Continued.

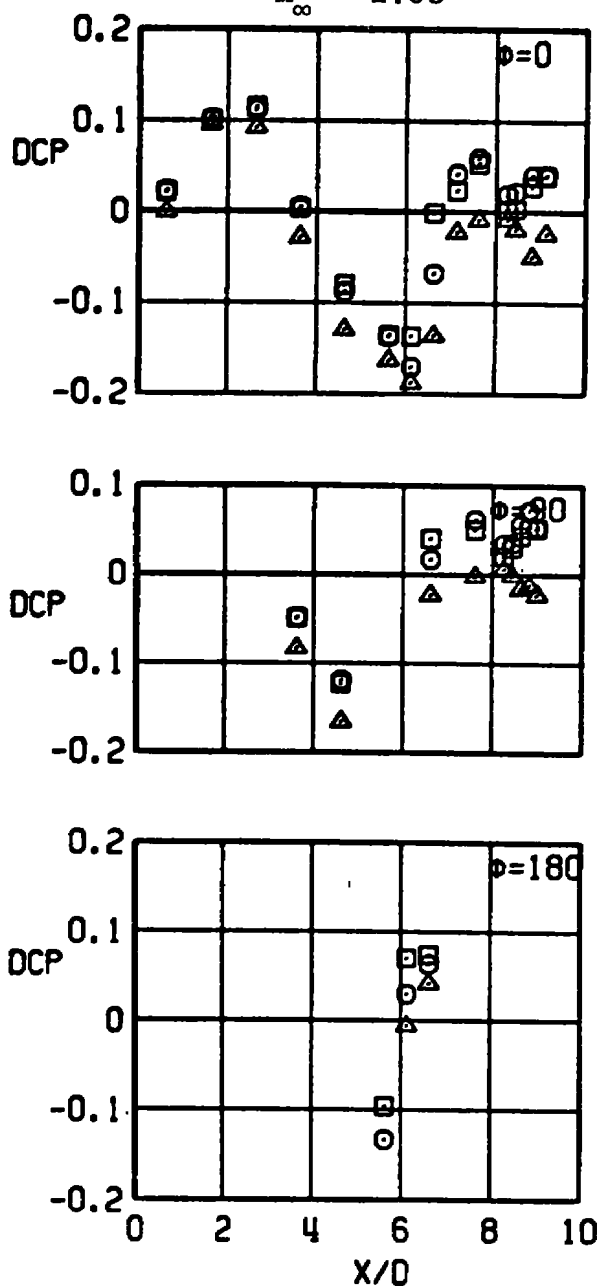
SYM	CONFIG	POROSITY, PERCENT
○	B2-S2L3	6
□	B2-S2L3-W3	3
△	B2-S2L3-W1	1



a. Continued
Figure A-6. Continued.

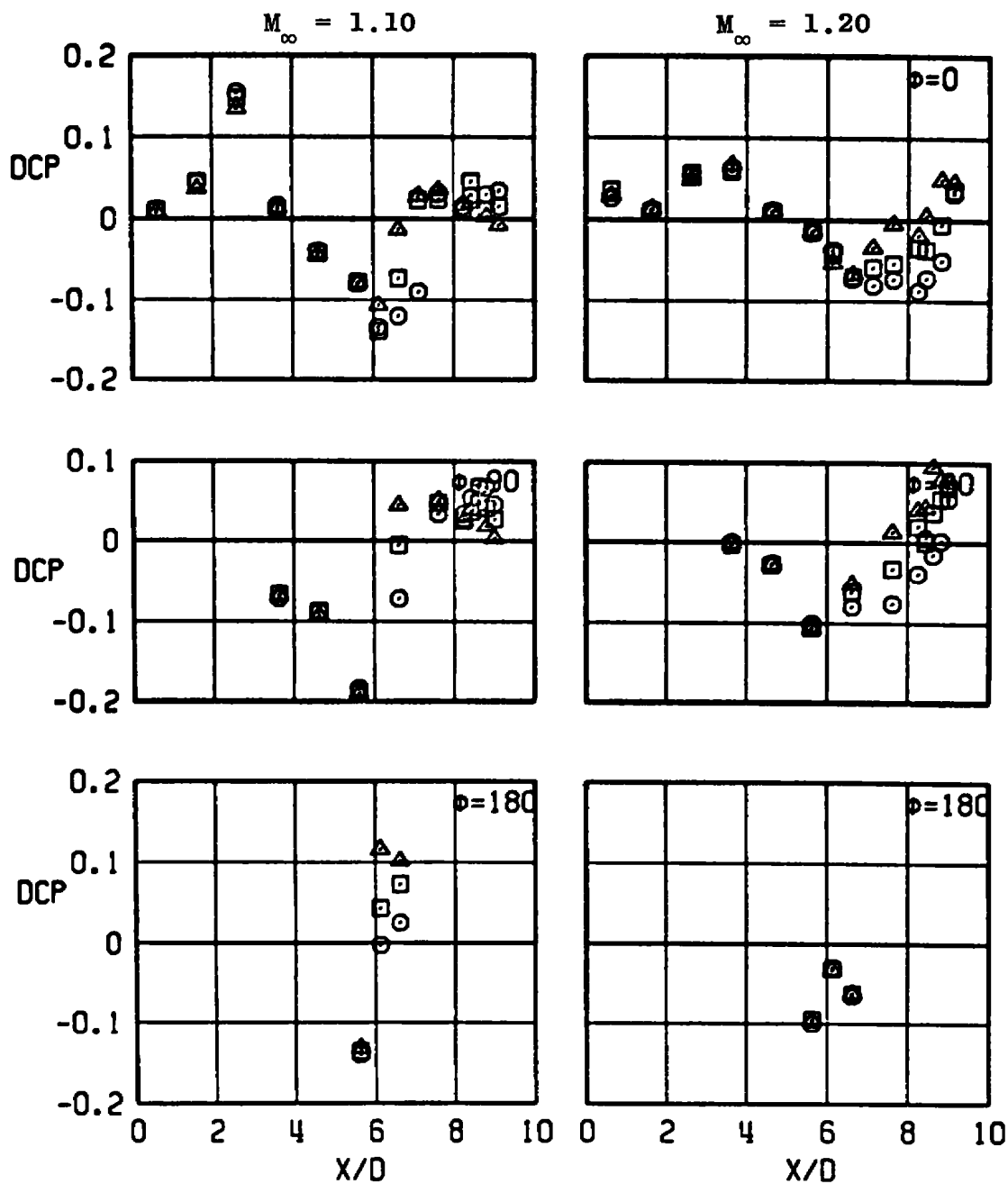
SYM	CONFIG	POROSITY, PERCENT
○	B2-S2L3	6
□	B2-S2L3-W3	3
△	B2-S2L3-W1	1

$$M_{\infty} = 1.05$$

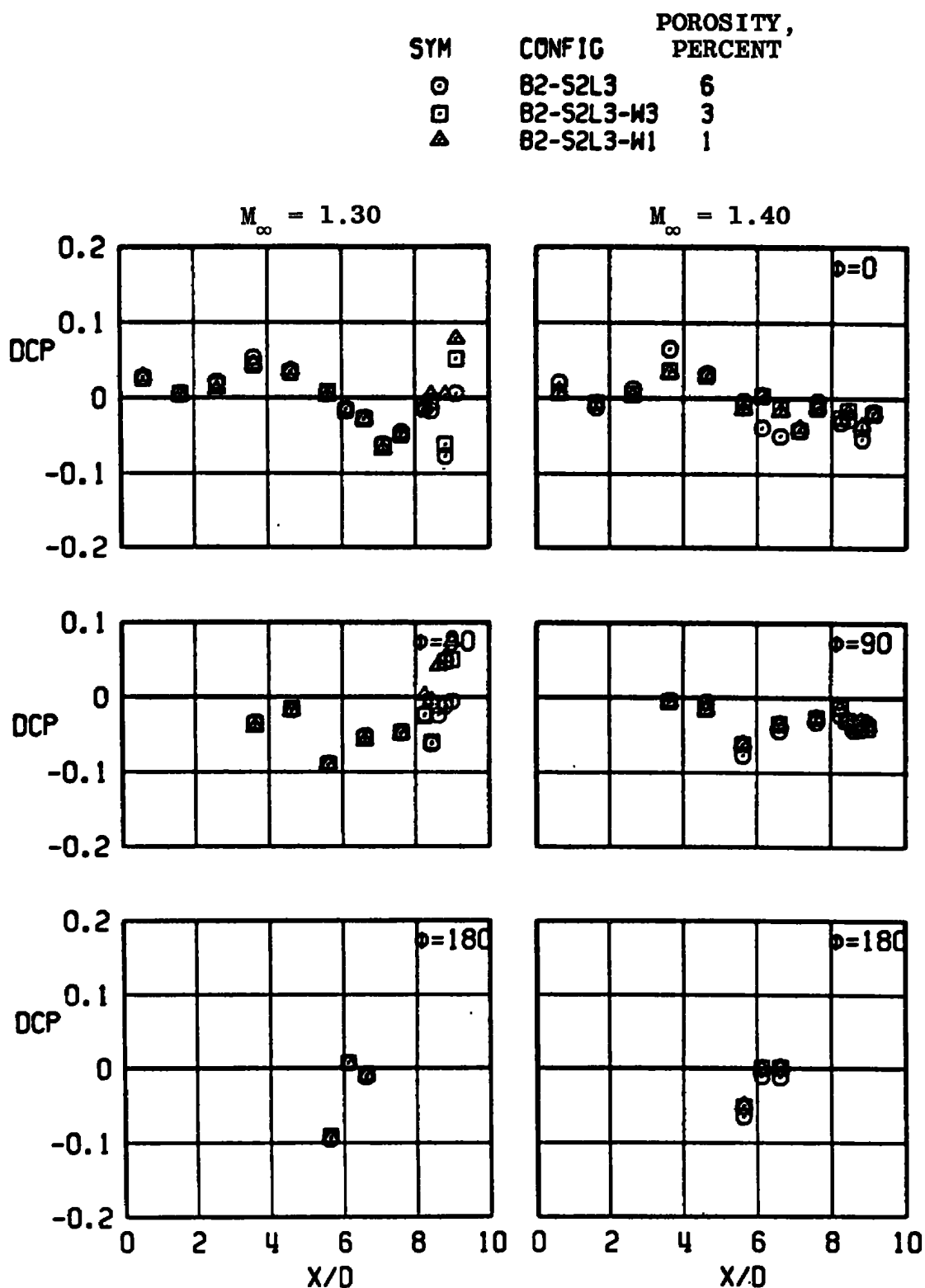


a. Continued
Figure A-6. Continued.

SYM	CONFIG	POROSITY, PERCENT
○	B2-S2L3	6
□	B2-S2L3-W3	3
△	B2-S2L3-W1	1

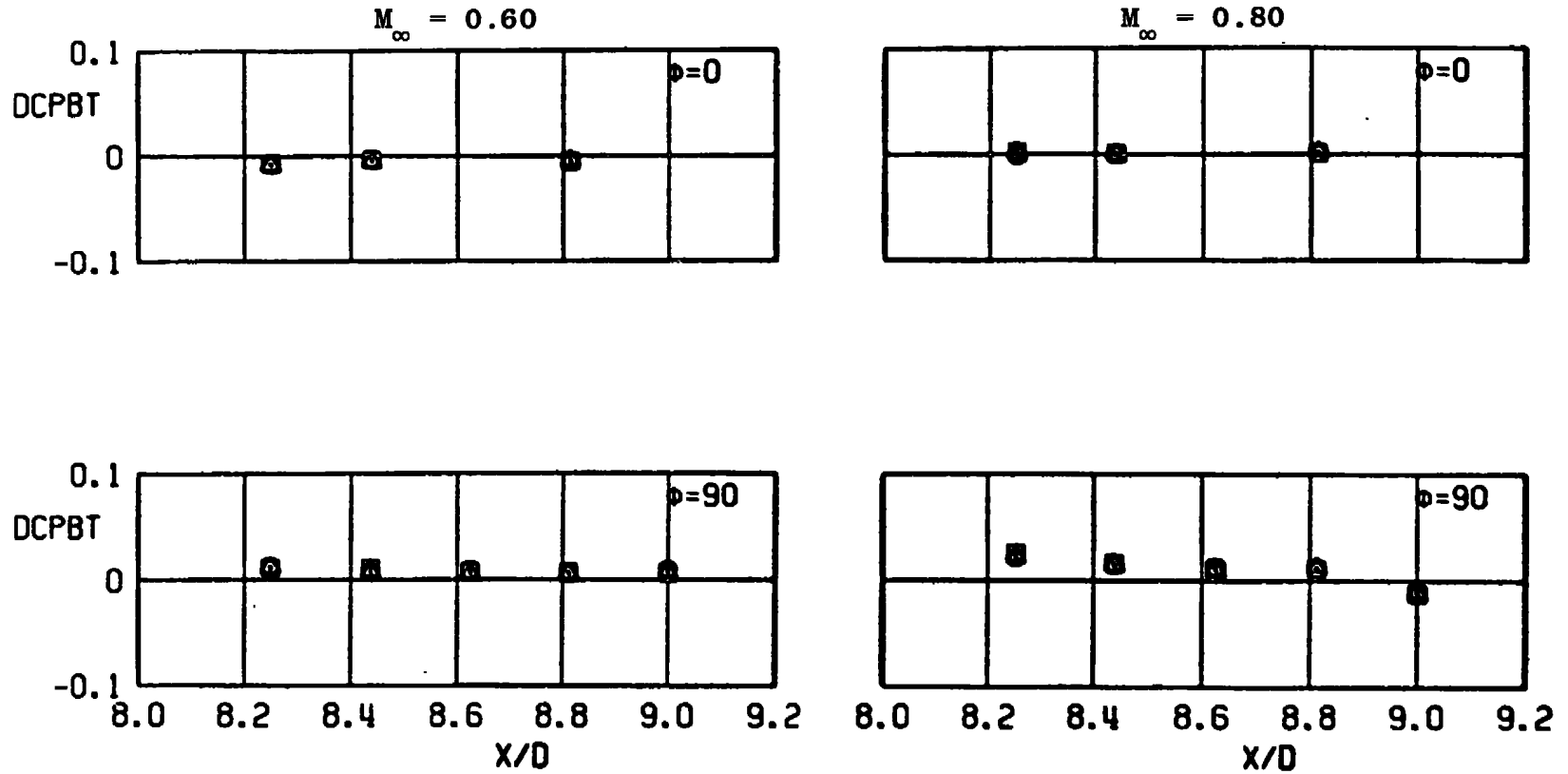


a. Continued
Figure A-6. Continued.



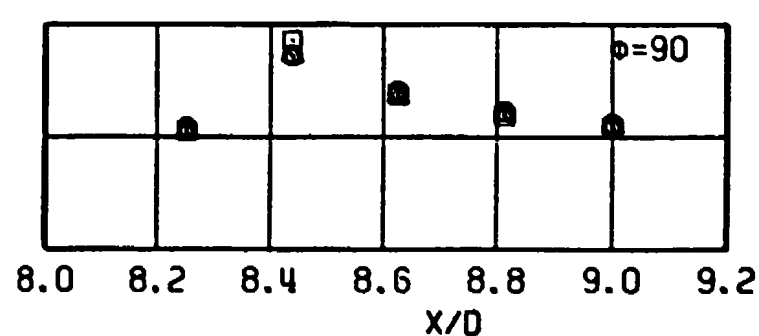
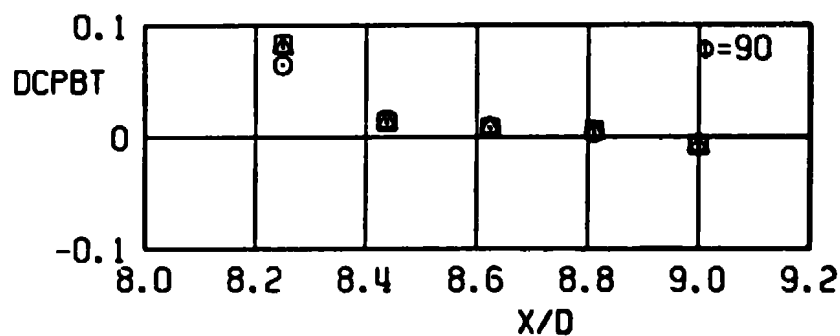
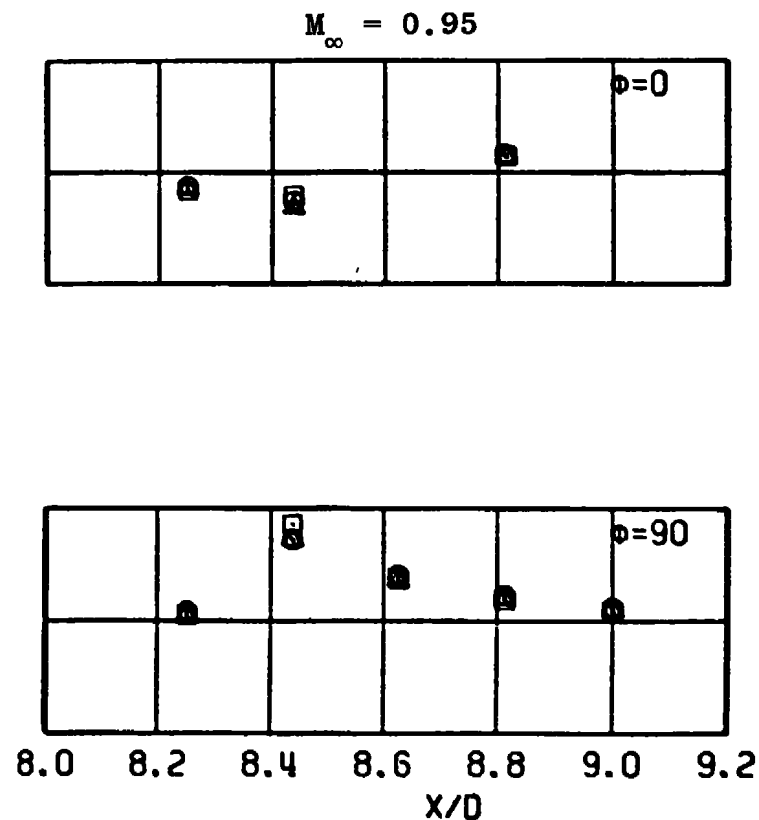
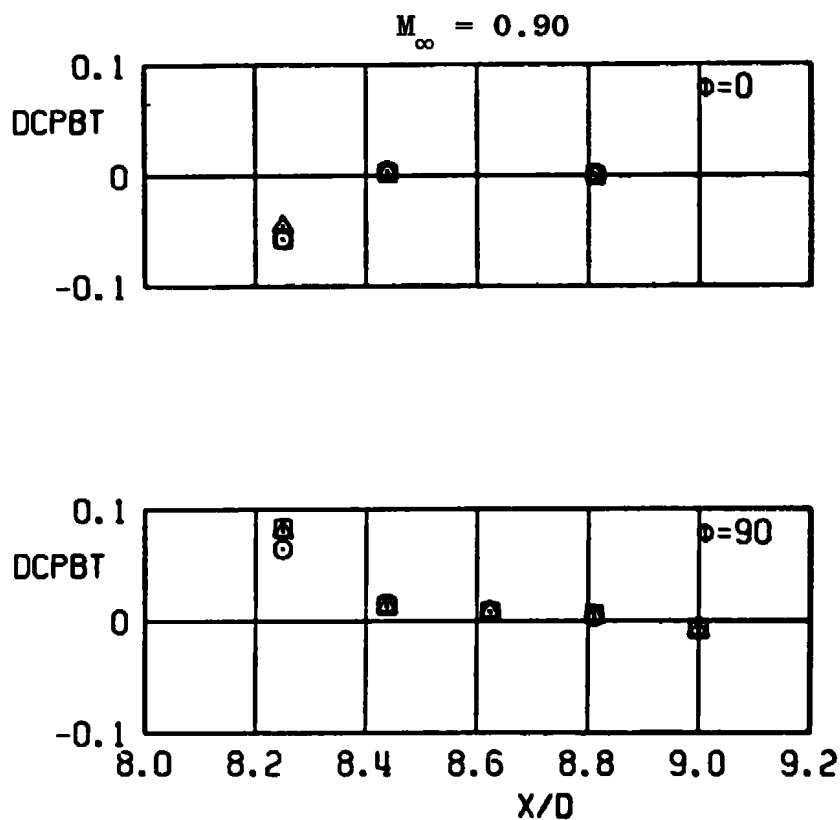
a. Concluded
Figure A-6. Continued.

SYM	CONFIG	POROSITY, PERCENT
⊙	B2-S2L3	6
⊠	B2-S2L3-W3	3
△	B2-S2L3-W1	1



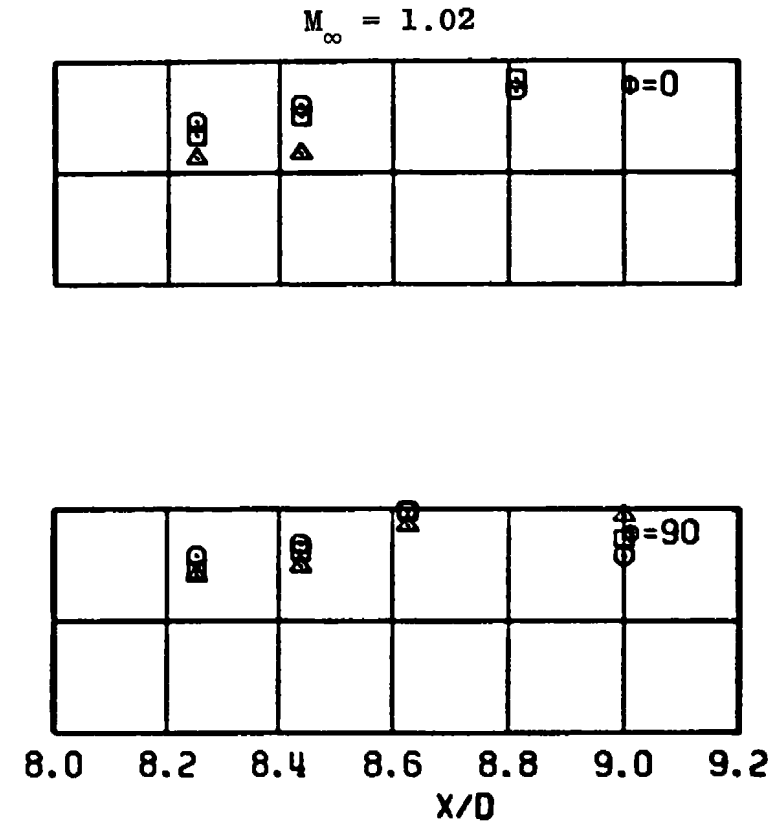
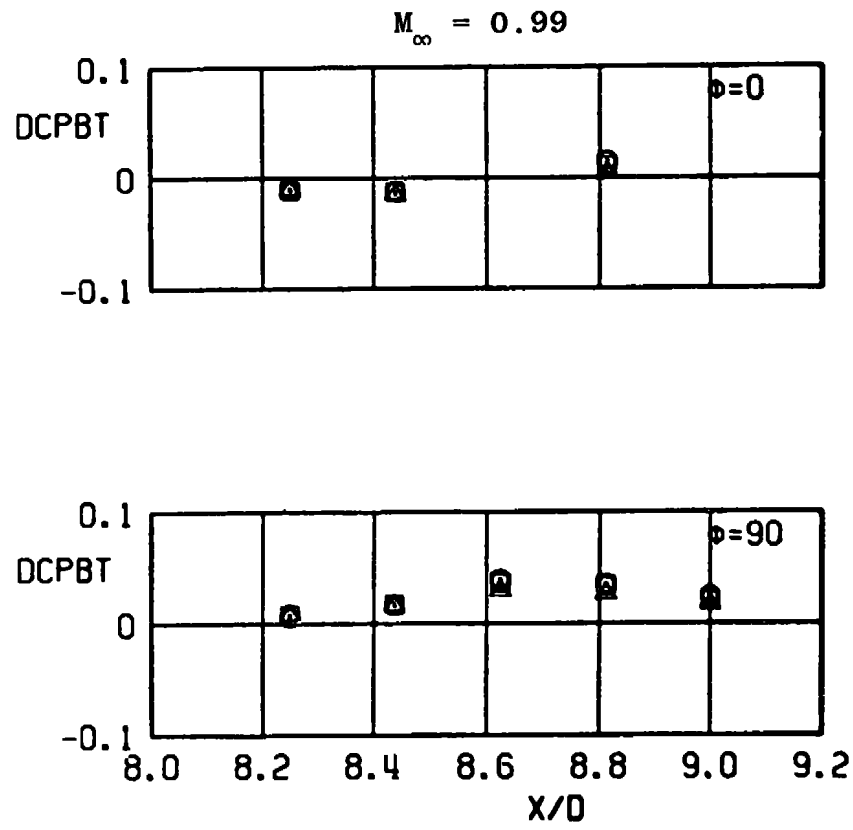
b. DCPBT versus X/D (straight strut, 10-deg boattail)
Figure A-6. Continued.

SYM	CONFIG	POROSITY, PERCENT
○	B2-S2L3	6
□	B2-S2L3-W3	3
△	B2-S2L3-W1	1

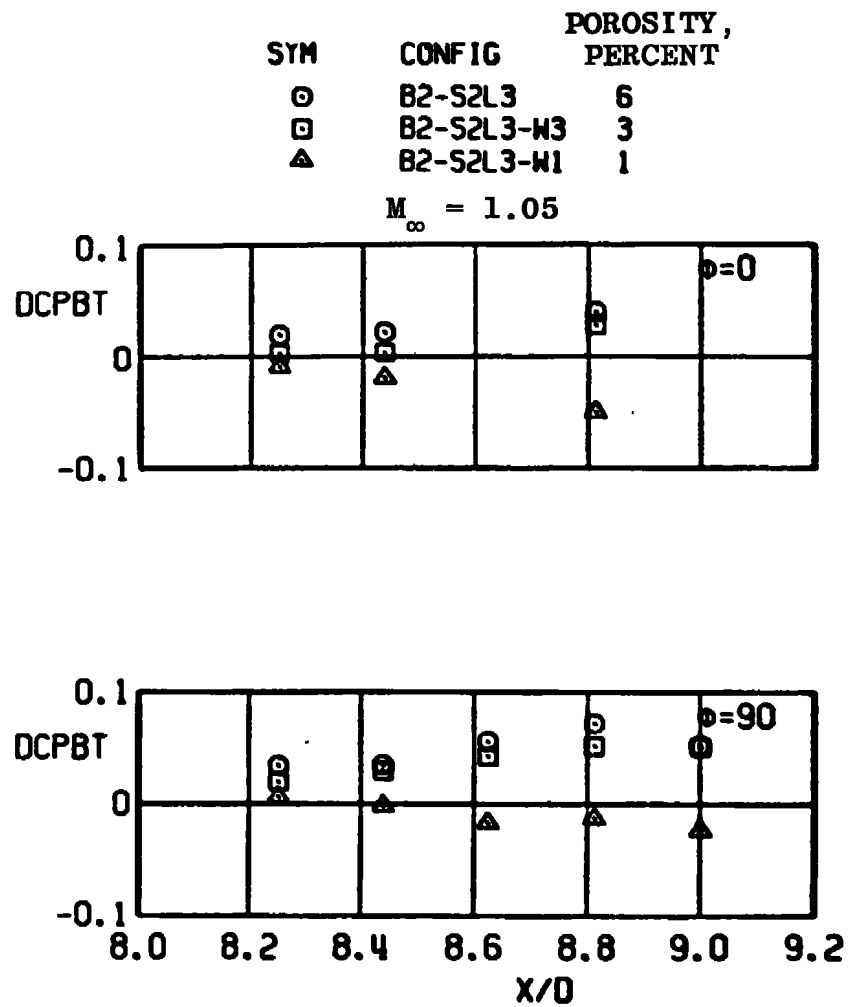


b. Continued
Figure A-6. Continued.

SYM	CONFIG	POROSITY, PERCENT
○	B2-S2L3	6
□	B2-S2L3-W3	3
△	B2-S2L3-W1	1

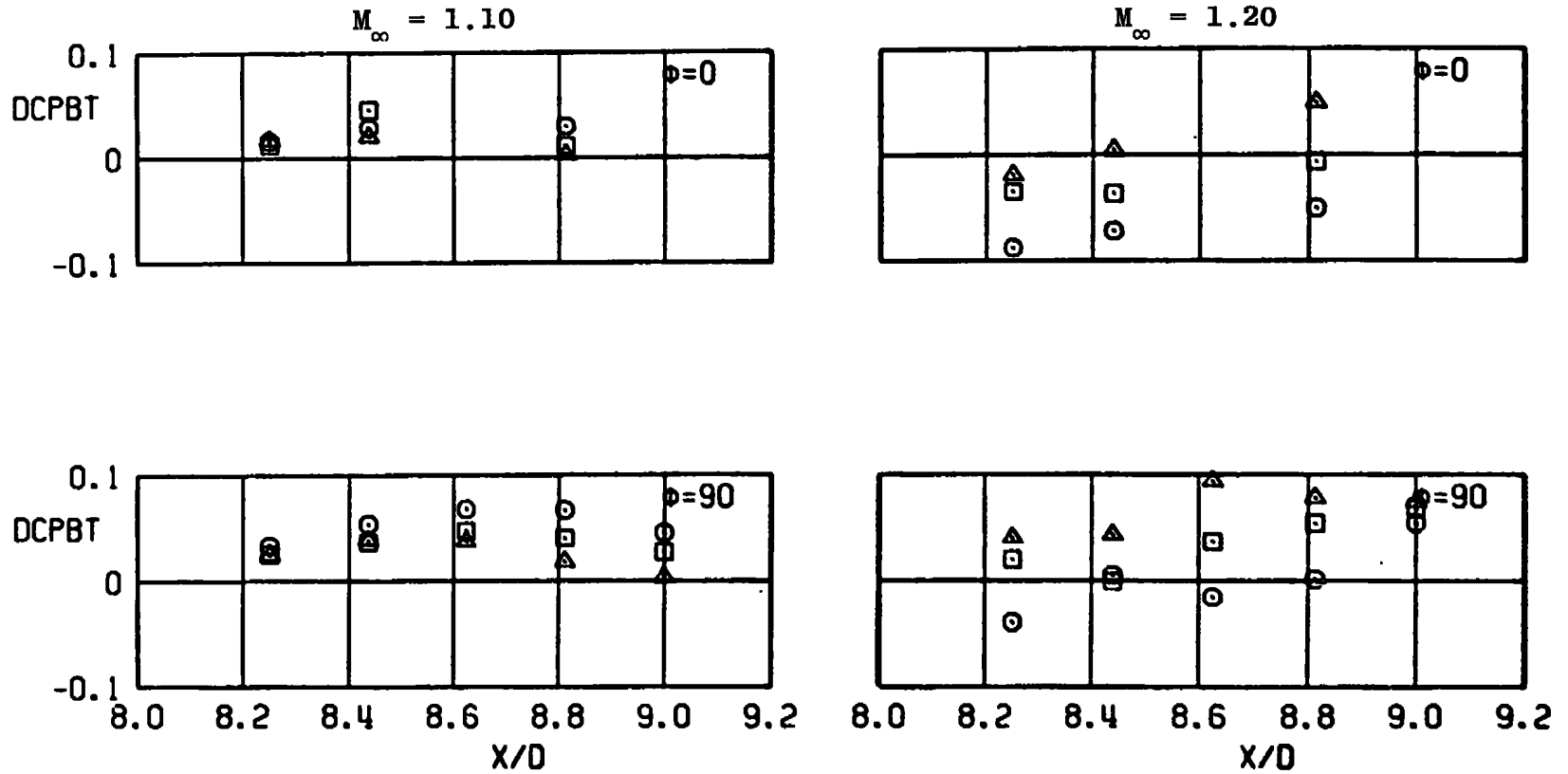


b. Continued
Figure A-6. Continued.



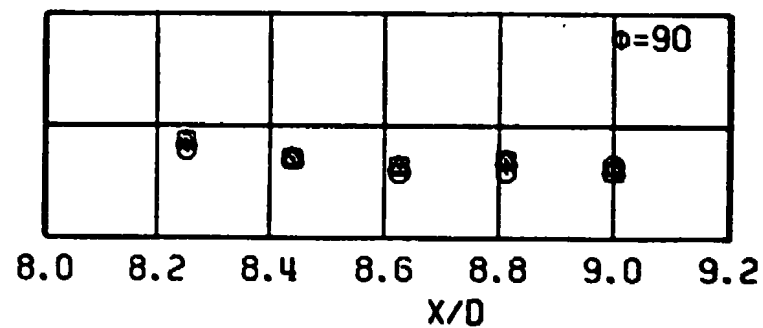
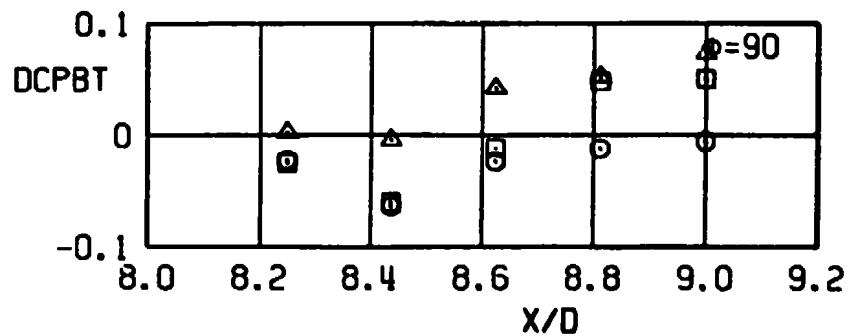
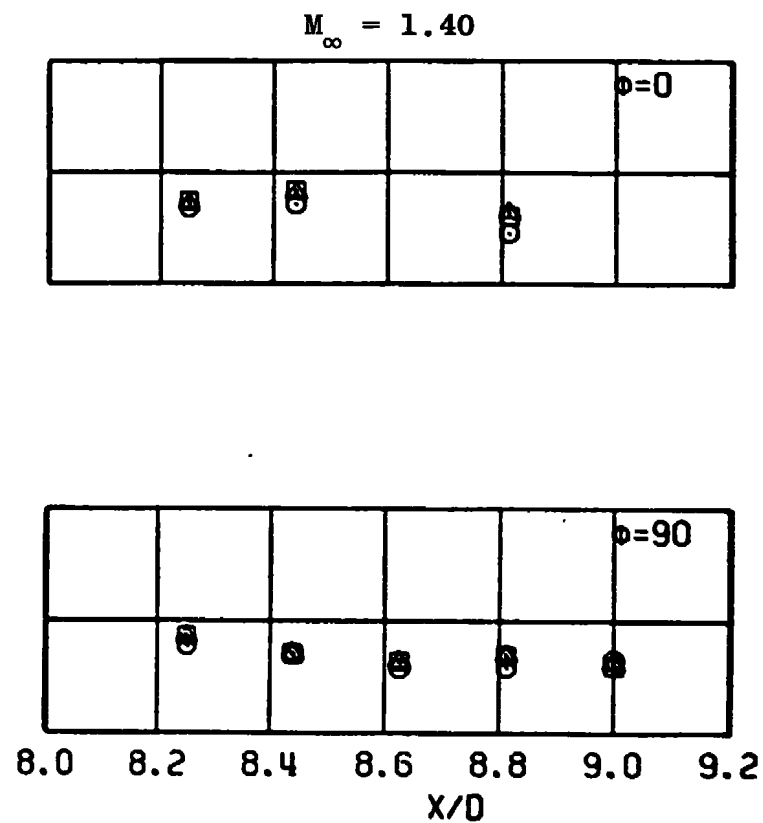
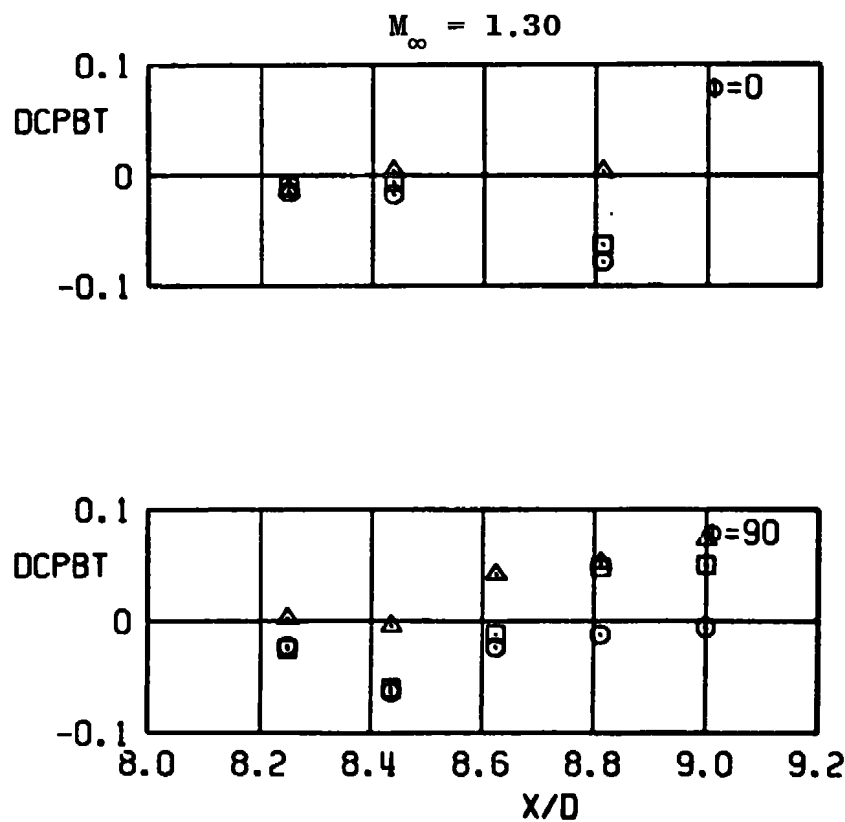
b. Continued
Figure A-6. Continued.

SYM	CONFIG	POROSITY, PERCENT
○	B2-S2L3	6
□	B2-S2L3-W3	3
△	B2-S2L3-W1	1



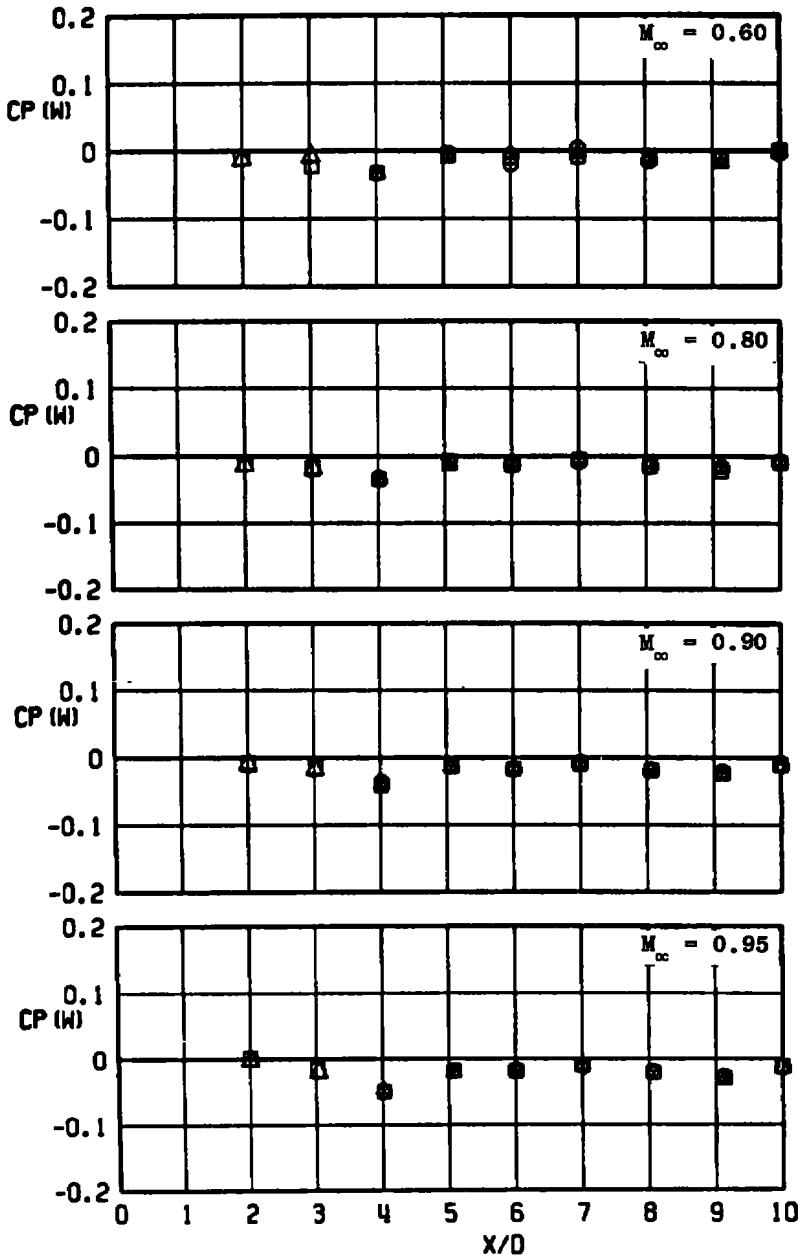
b. Continued
Figure A-6. Continued.

SYM	CONFIG	POROSITY, PERCENT
○	B2-S2L3	6
□	B2-S2L3-W3	3
△	B2-S2L3-W1	1



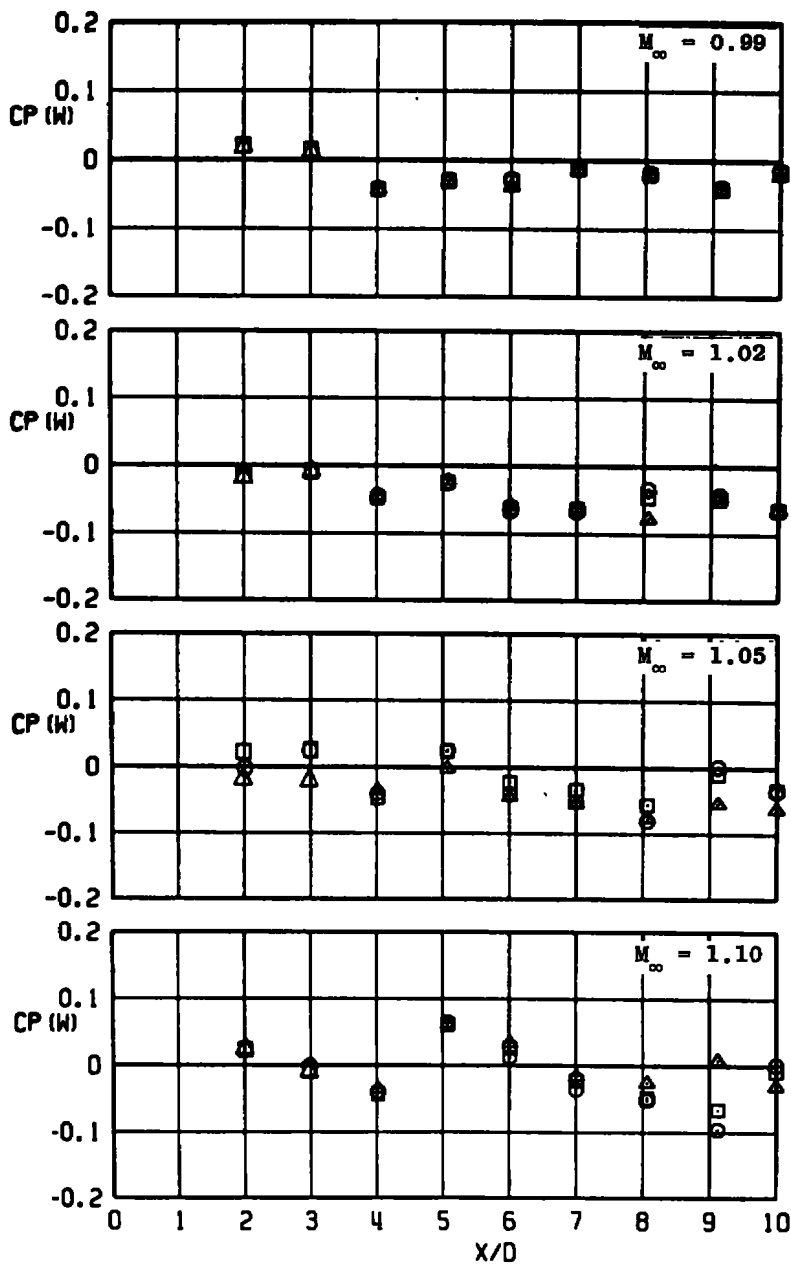
b. Concluded
Figure A-6. Continued.

SYM	CONFIG	POROSITY, PERCENT	ϕ , DEG
○	B2-S2L3	6	0
□	B2-S2L3-W3	3	0
△	B2-S2L3-W1	1	0



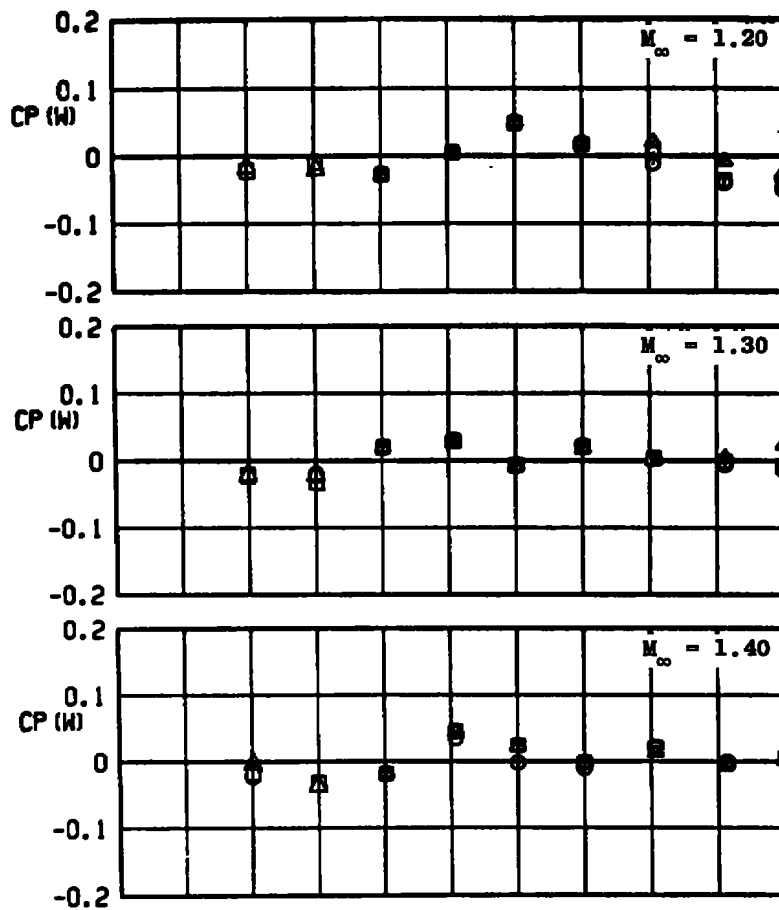
c. $CP(W)$ versus X/D (straight strut, 10-deg boattail, $\phi = 0$)
Figure A-6. Continued.

SYM	CONFIG	POROSITY, PERCENT	ϕ , DEG
⊙	B2-S2L3	6	0
□	B2-S2L3-W3	3	0
△	B2-S2L3-W1	1	0



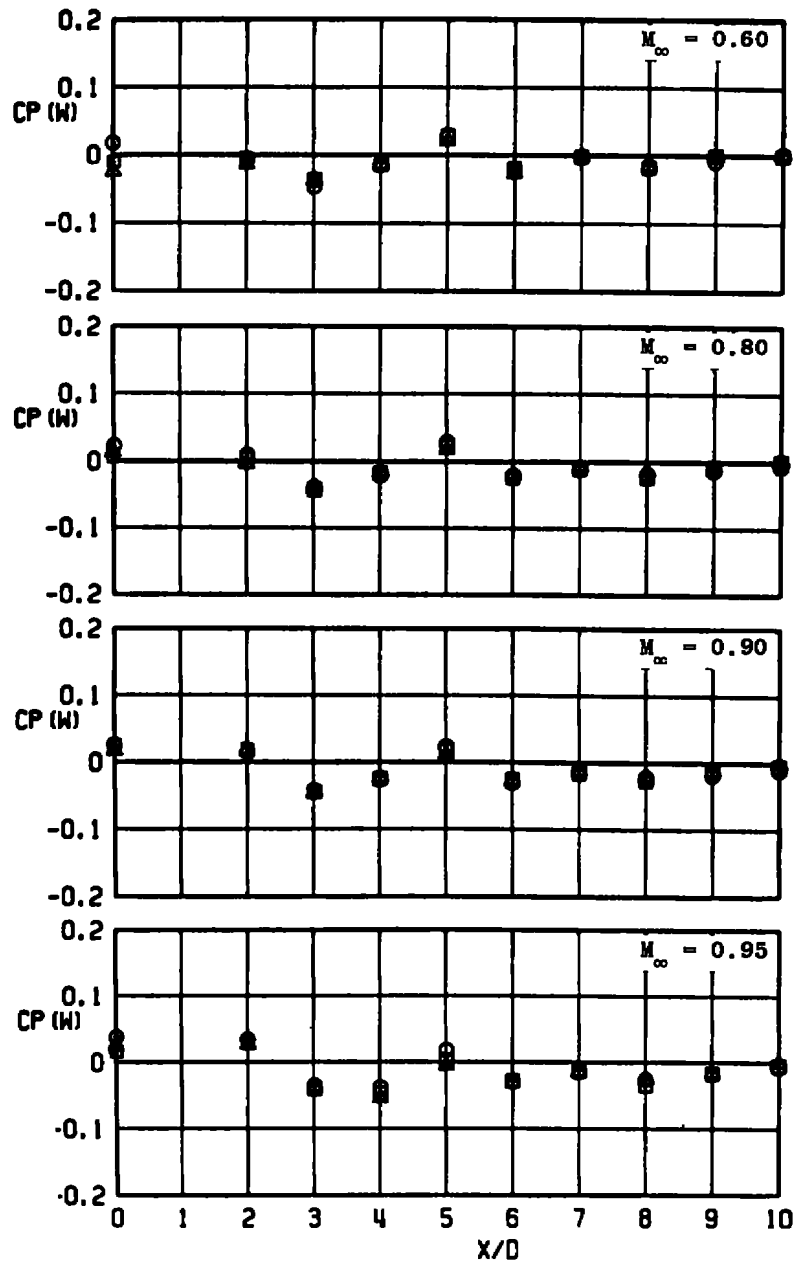
c. Continued
Figure A-6. Continued.

SYM	CONFIG	POROSITY, PERCENT	ϕ , DEG
○	82-S2L3	6	0
□	82-S2L3-W3	3	0
▲	82-S2L3-W1	1	0

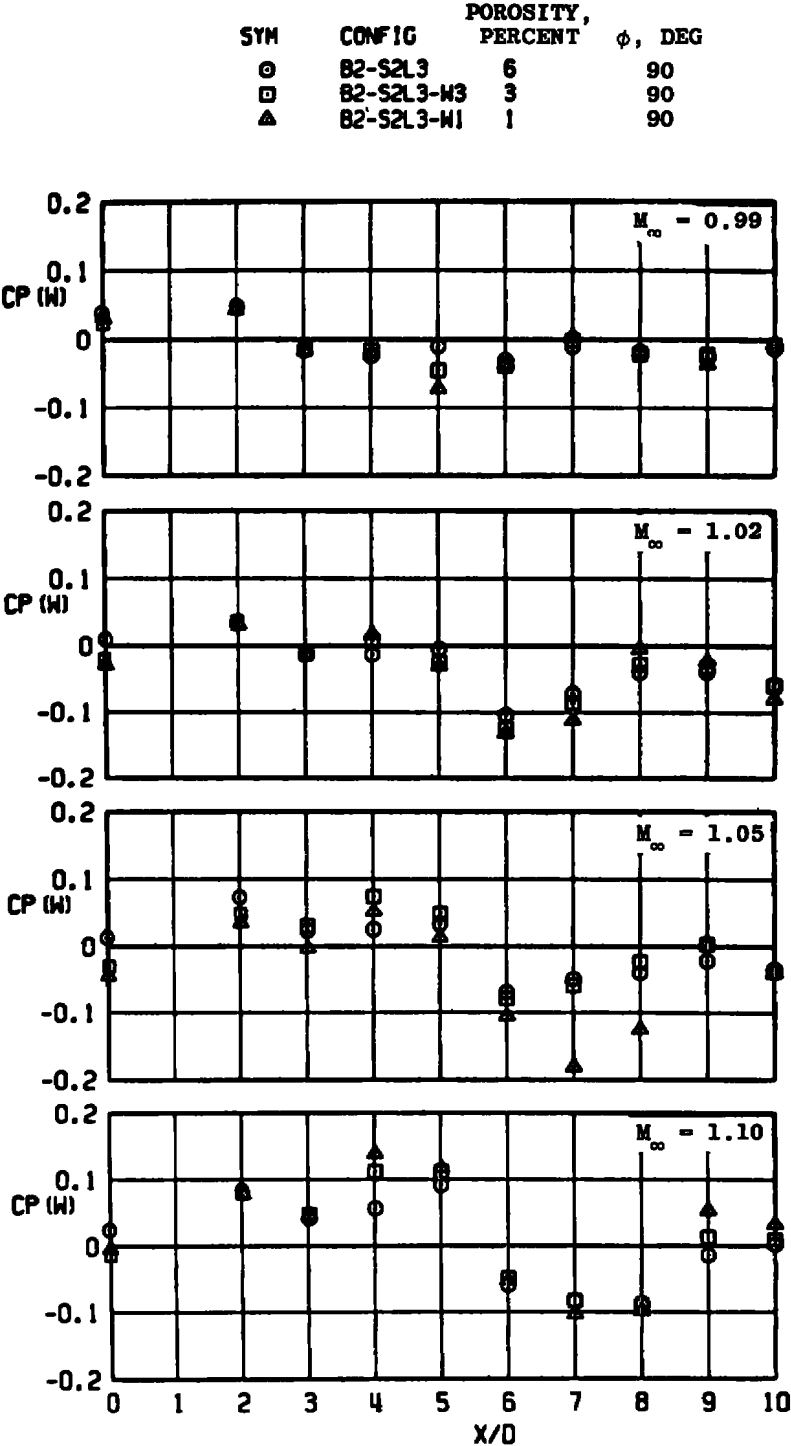


c. Concluded
Figure A-6. Continued.

SYM	CONFIG	POROSITY, PERCENT	ϕ , DEG
○	B2-S2L3	6	90
□	B2-S2L3-W3	3	90
△	B2-S2L3-W1	1	90

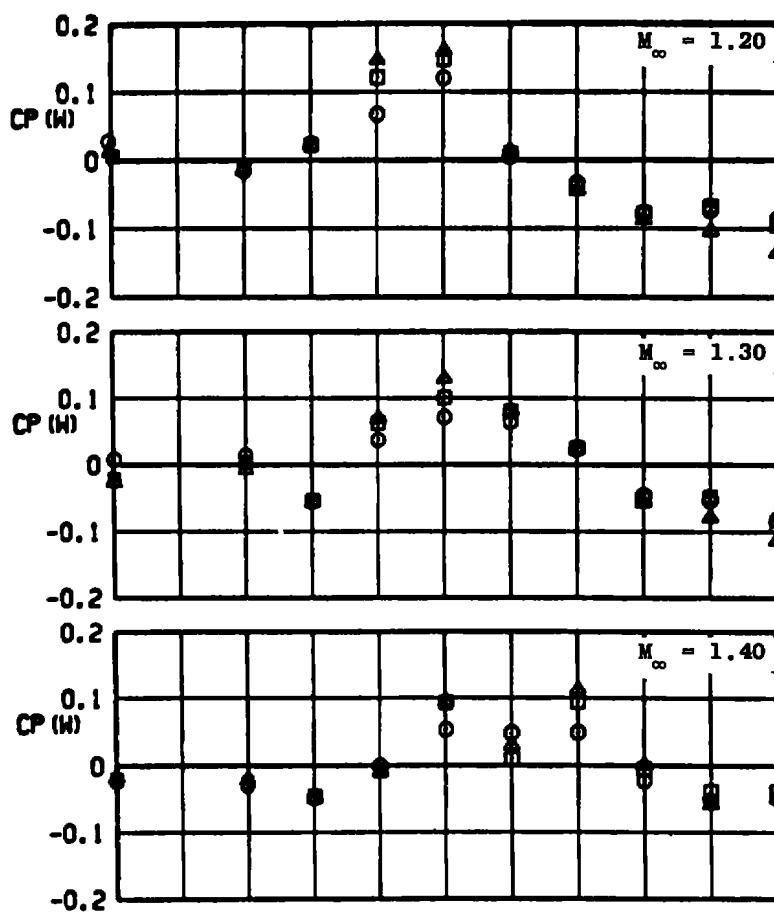


d. $CP(W)$ versus X/D (straight strut, 10-deg boattail, $\phi = 90$ deg)
Figure A-6. Continued.



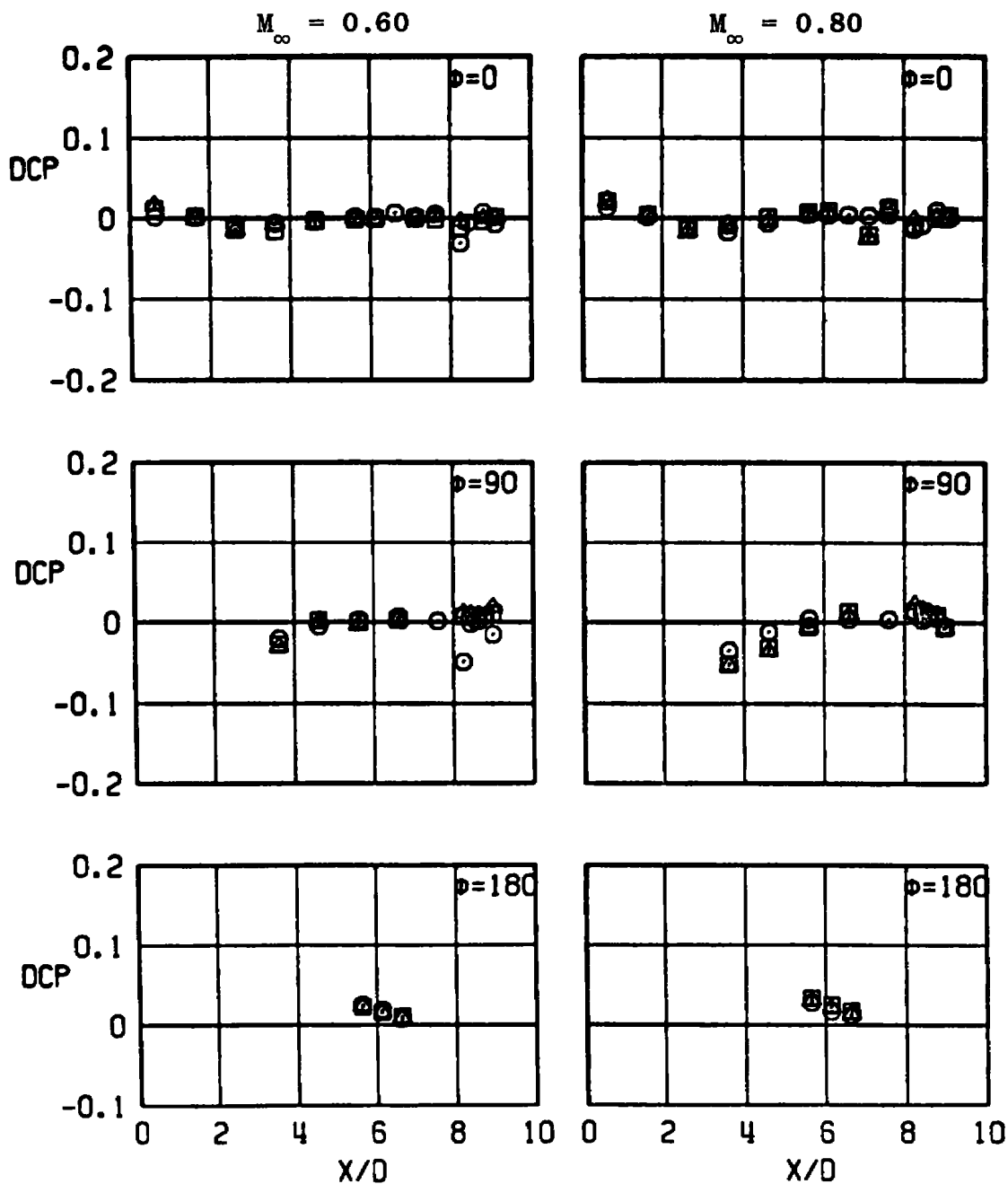
d. Continued
Figure A-6. Continued.

SYM	CONFIG	POROSITY, PERCENT	ϕ , DEG
○	B2-S2L3	6	90
□	B2-S2L3-W3	3	90
▲	B2-S2L3-W1	1	90



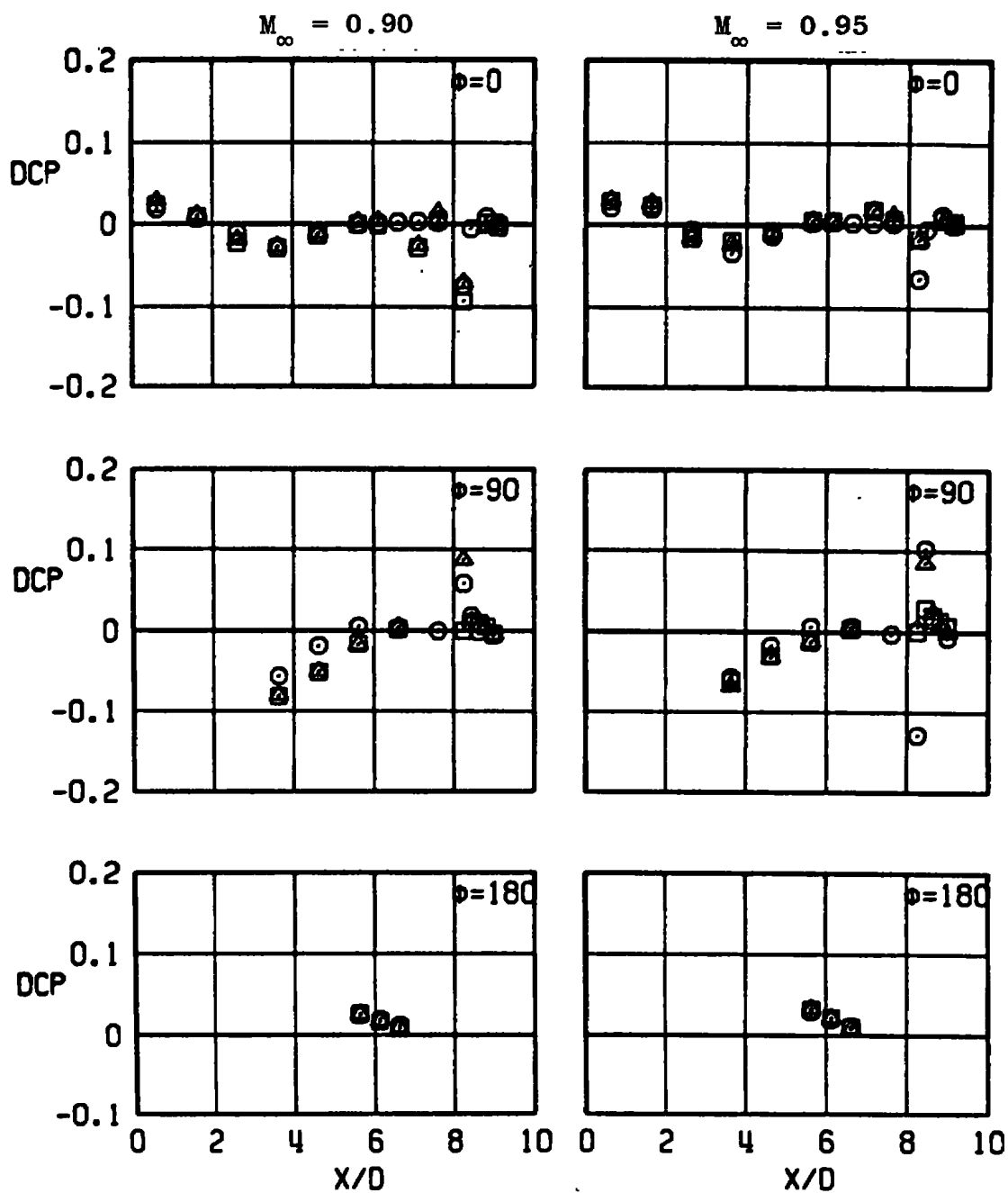
d. Concluded
Figure A-6. Continued.

SYM	CONFIG	POROSITY, PERCENT
○	B2-S3L1	6
□	B2-S3L1-W3	3
△	B2-S3L1-W1	1



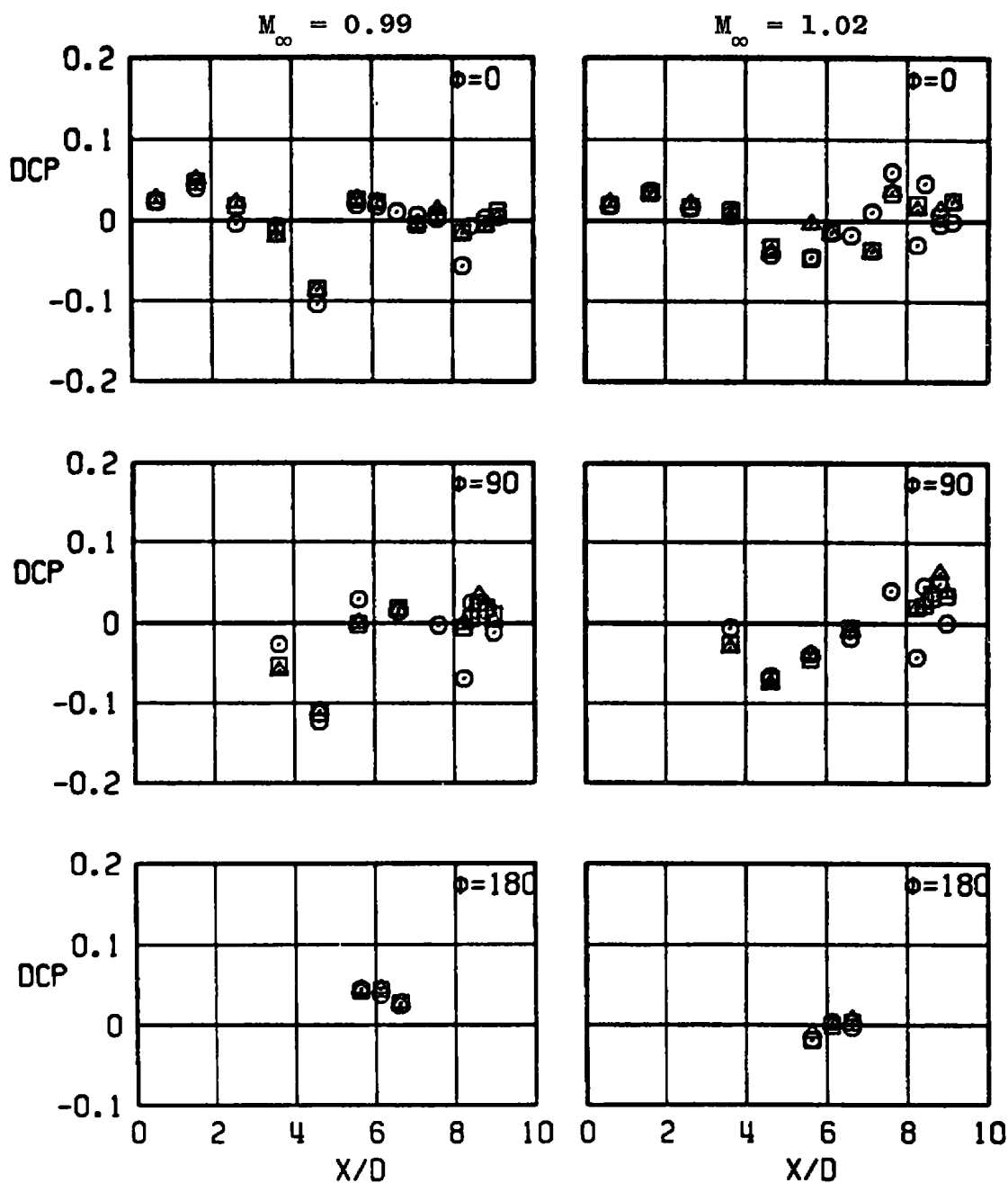
e. DCP versus X/D (30-deg swept strut, 10-deg boattail)
Figure A-6. Continued.

SYM	CONFIG	POROSITY, PERCENT
○	B2-S3L1	6
□	B2-S3L1-W3	3
△	B2-S3L1-W1	1

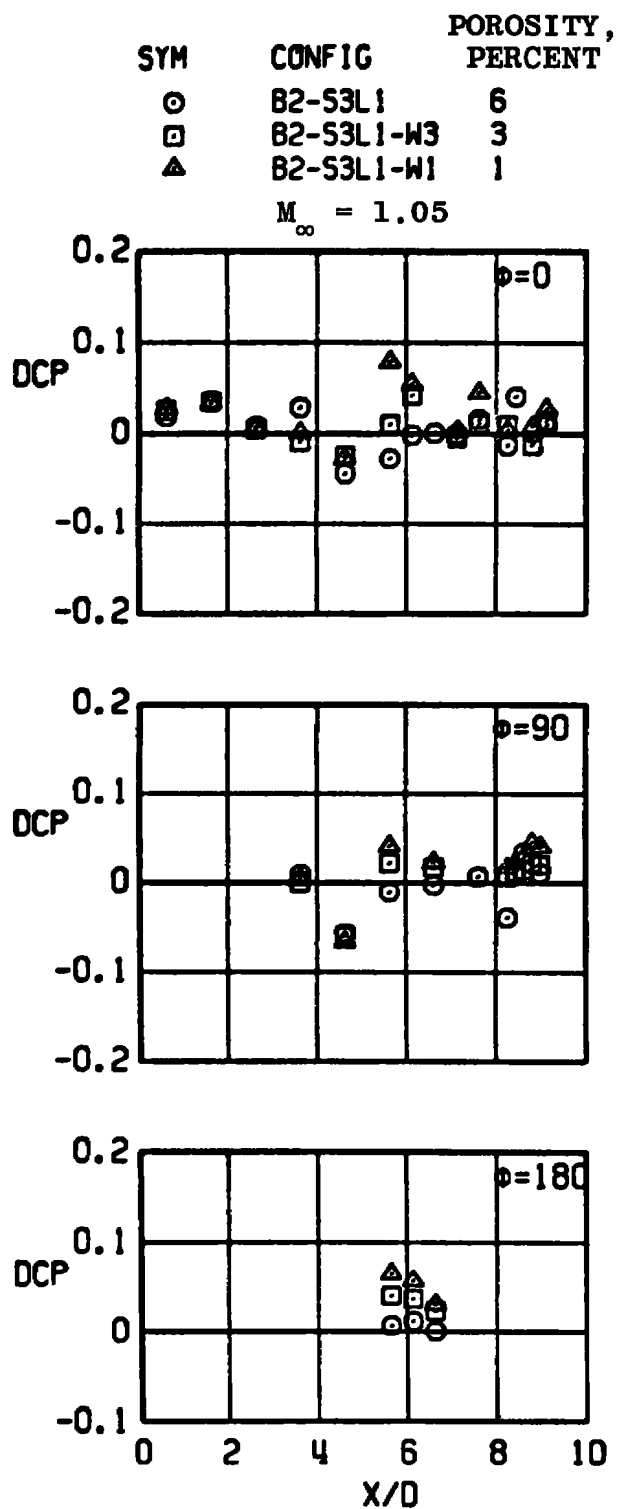


e. Continued
Figure A-6. Continued.

SYM	CONFIG	POROSITY, PERCENT
○	B2-S3L1	6
□	B2-S3L1-W3	3
△	B2-S3L1-W1	1

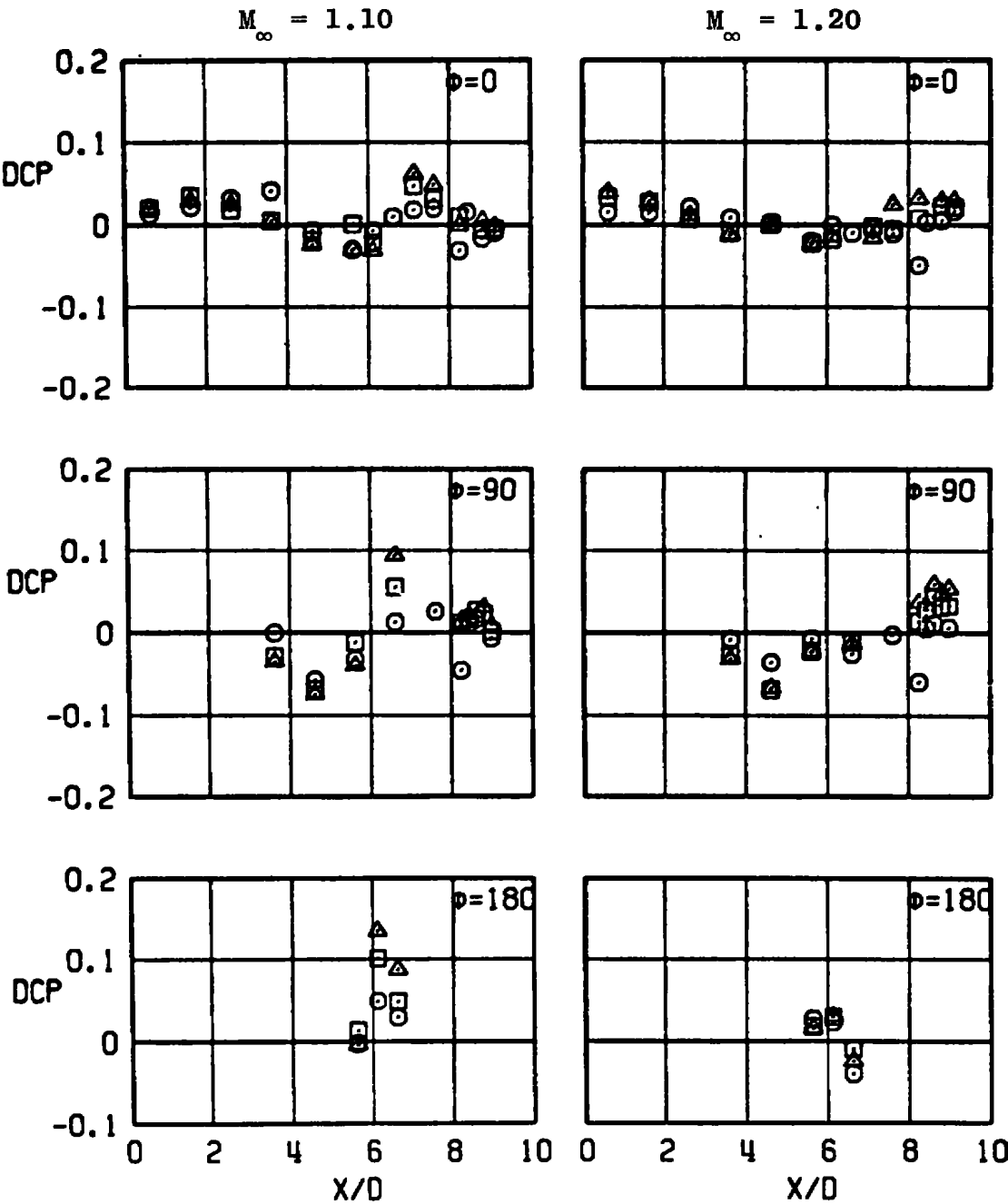


e. Continued
Figure A-6. Continued.

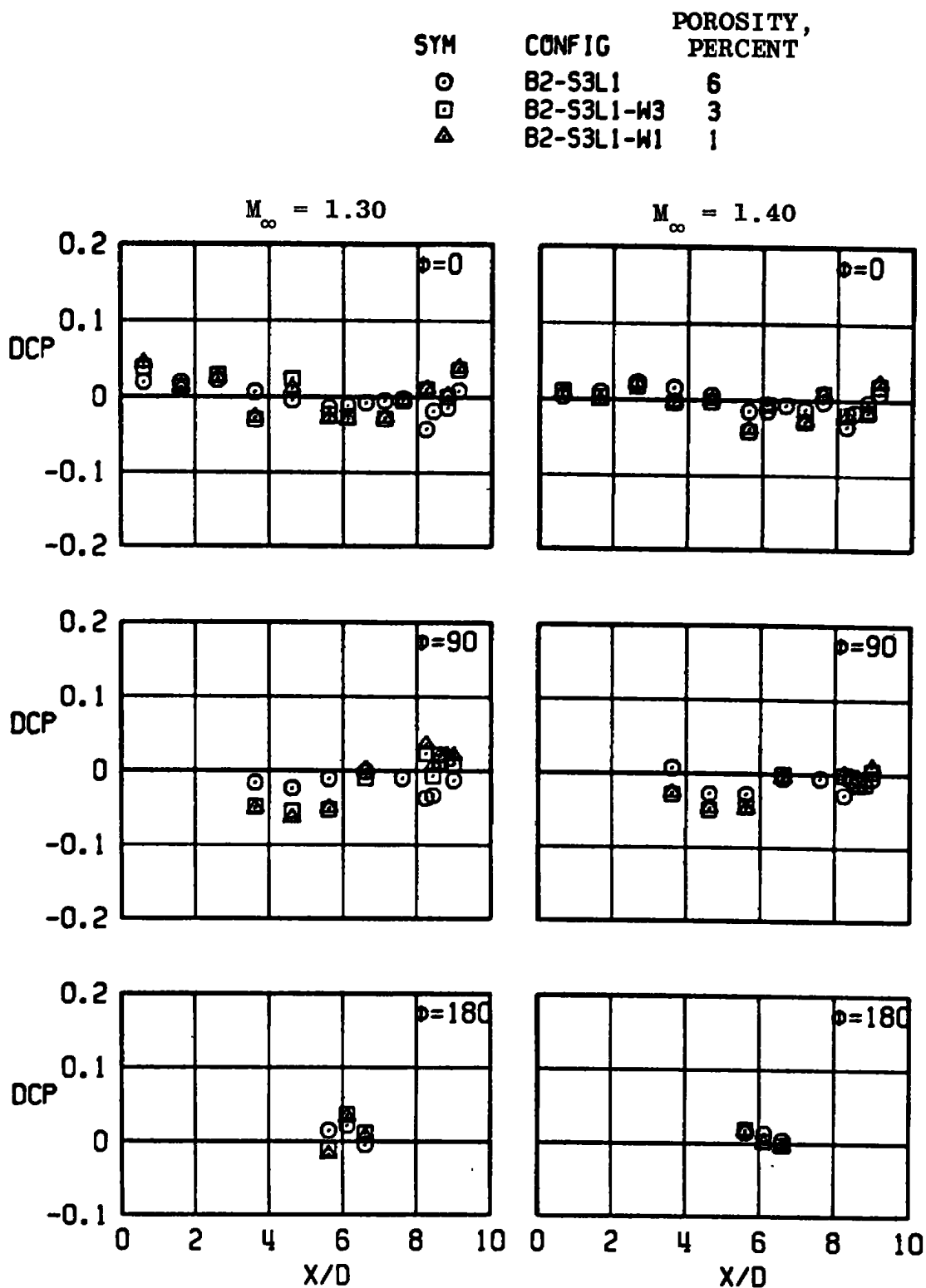


e. Continued
Figure A-6. Continued.

SYM	CONFIG	POROSITY, PERCENT
○	B2-S3L1	6
□	B2-S3L1-W3	3
△	B2-S3L1-W1	1

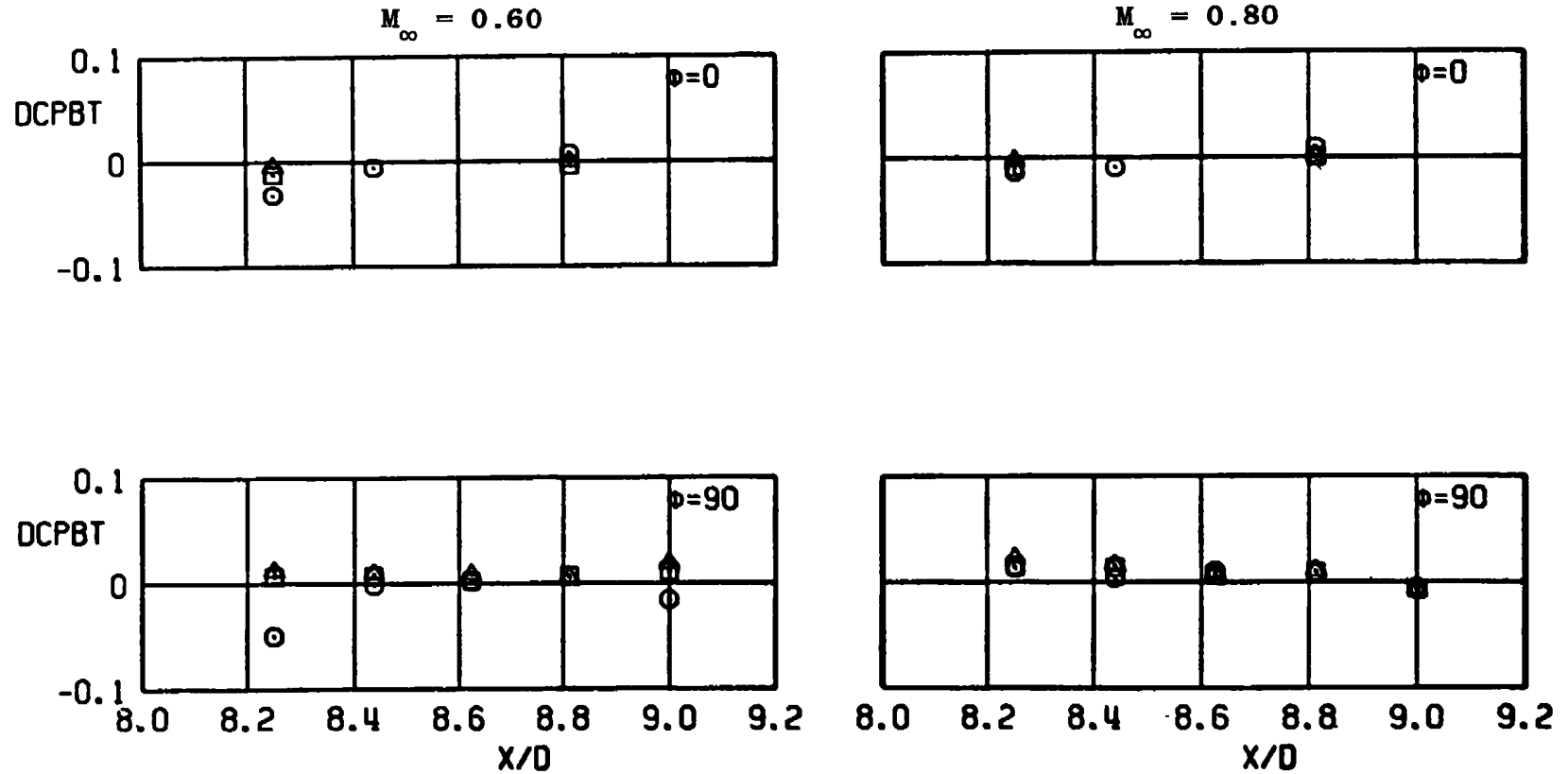


e. Continued
Figure A-6. Continued.



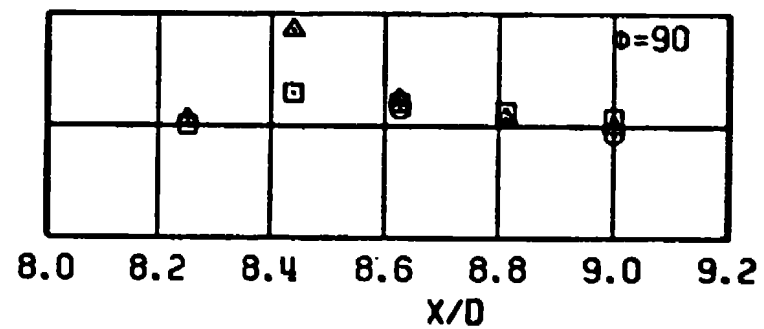
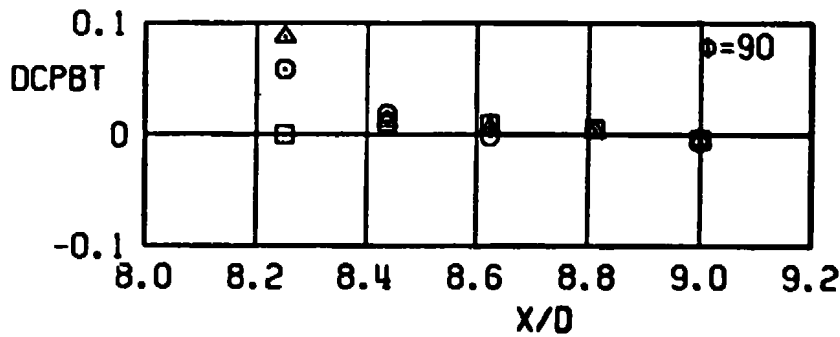
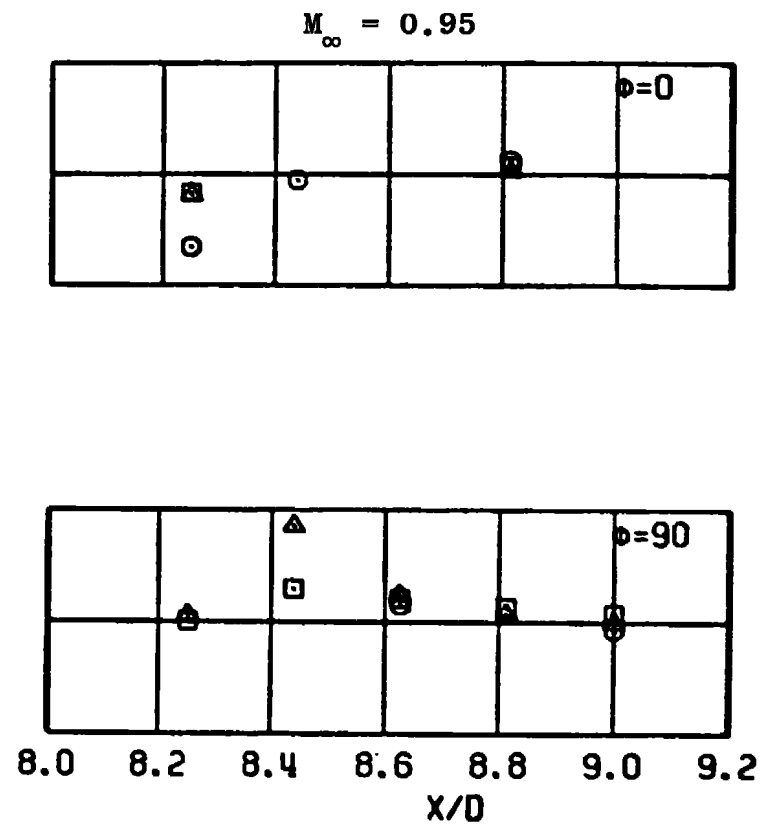
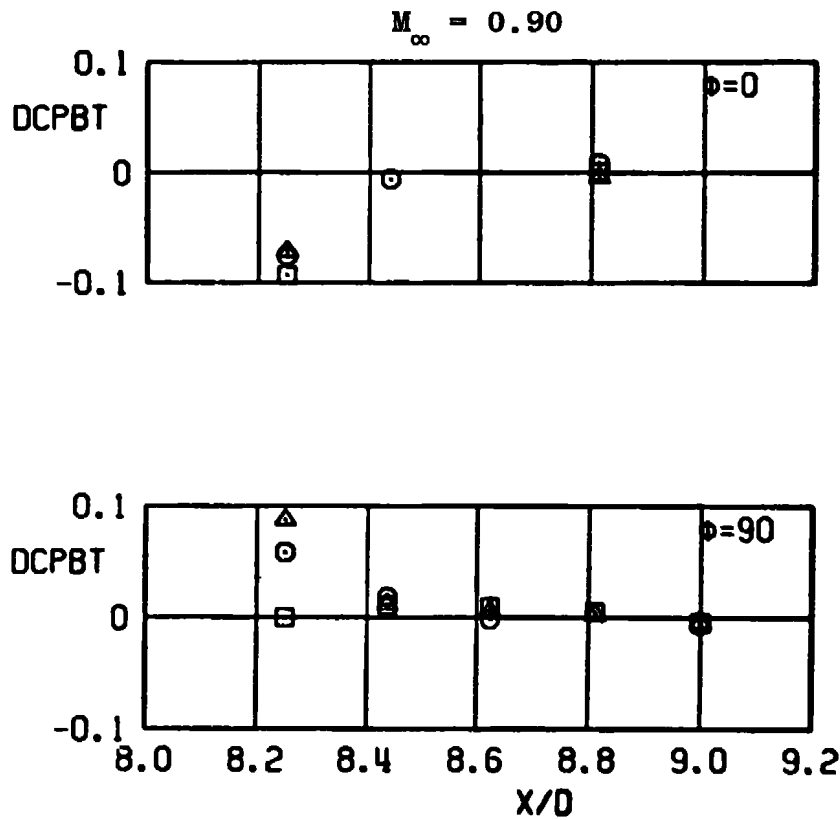
e. Concluded
Figure A-6. Continued.

SYM	CONFIG	POROSITY, PERCENT
○	B2-S3L1	6
□	B2-S3L1-W3	3
△	B2-S3L1-W1	1



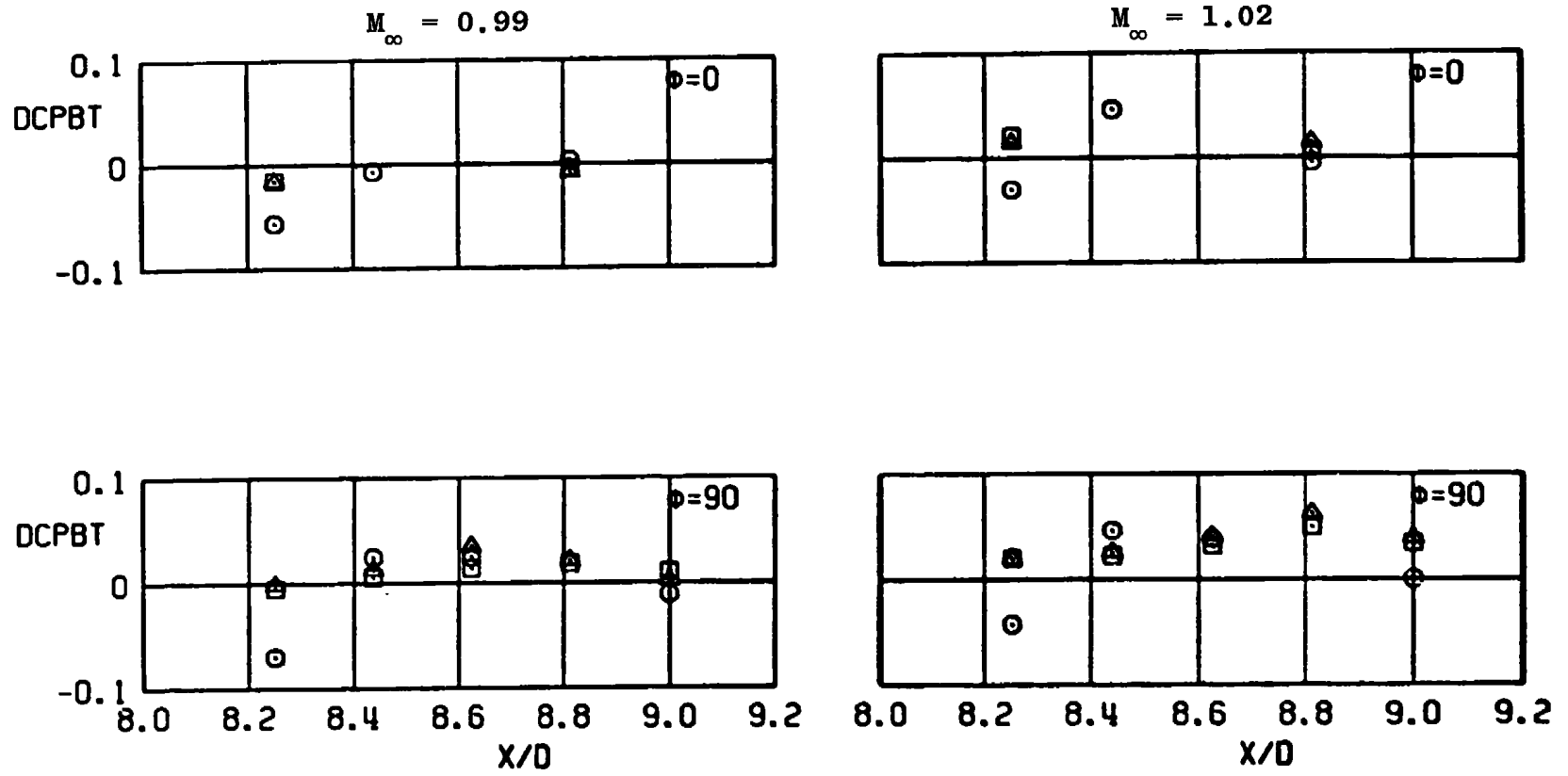
f. DCPBT versus X/D (30-deg swept strut, 10-deg boattail)
Figure A-6. Continued.

SYM	CONFIG	POROSITY, PERCENT
○	B2-53L1	6
□	B2-53L1-W3	3
△	B2-53L1-W1	1

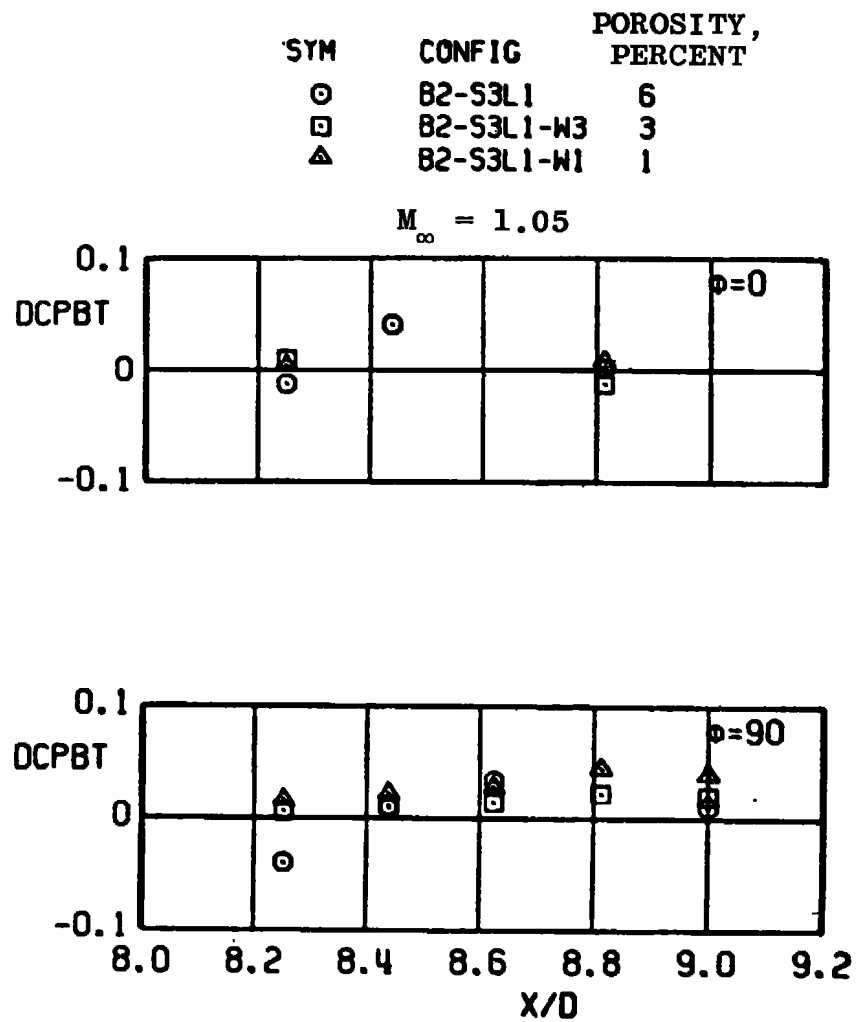


f. Continued
Figure A-6. Continued.

SYM	CONFIG	POROSITY, PERCENT
○	B2-S3L1	6
□	B2-S3L1-W3	3
△	B2-S3L1-W1	1

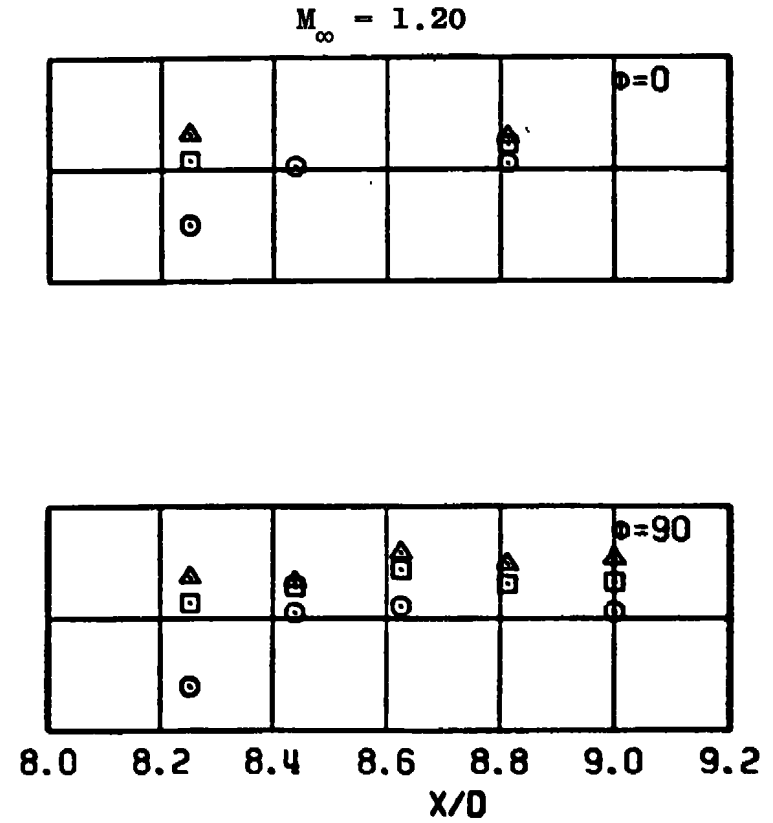
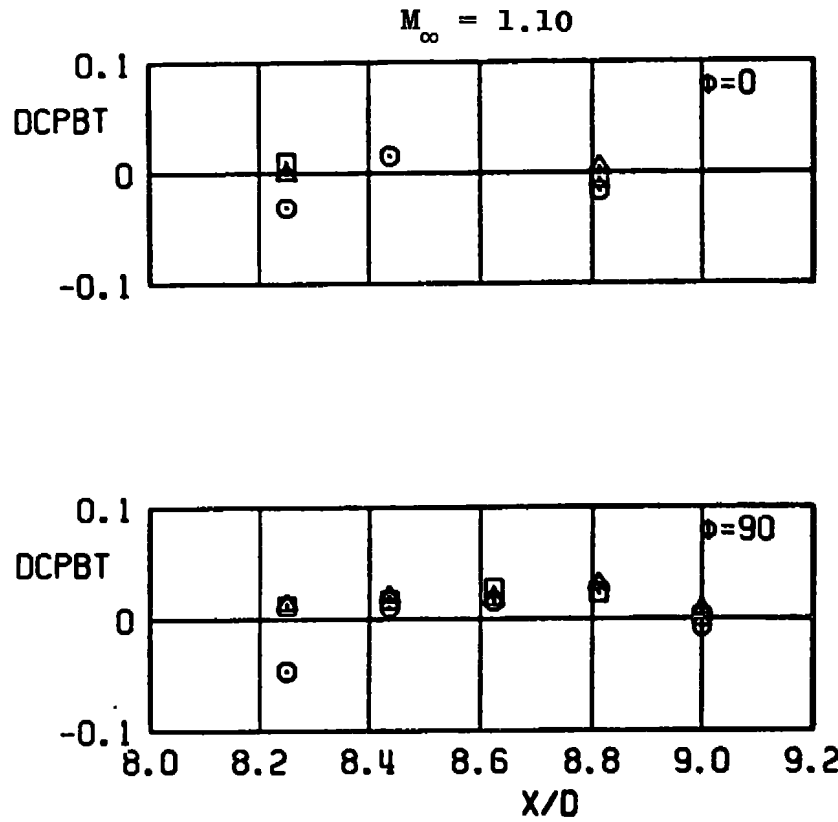


f. Continued
Figure A-6. Continued.



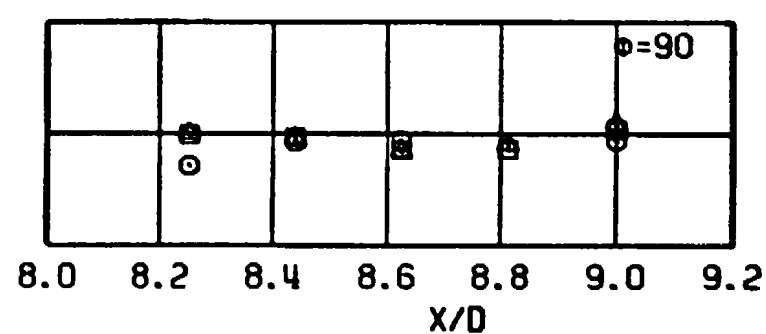
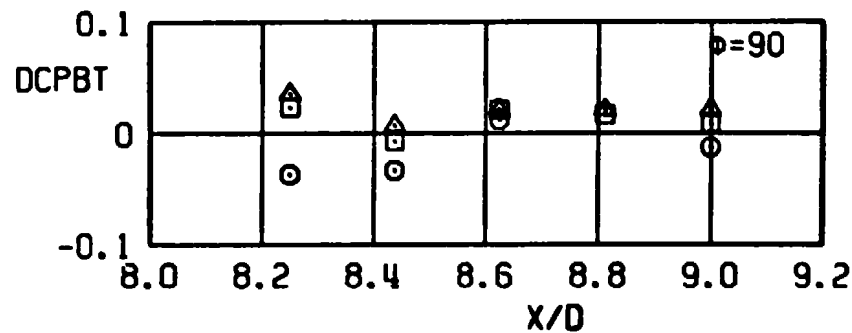
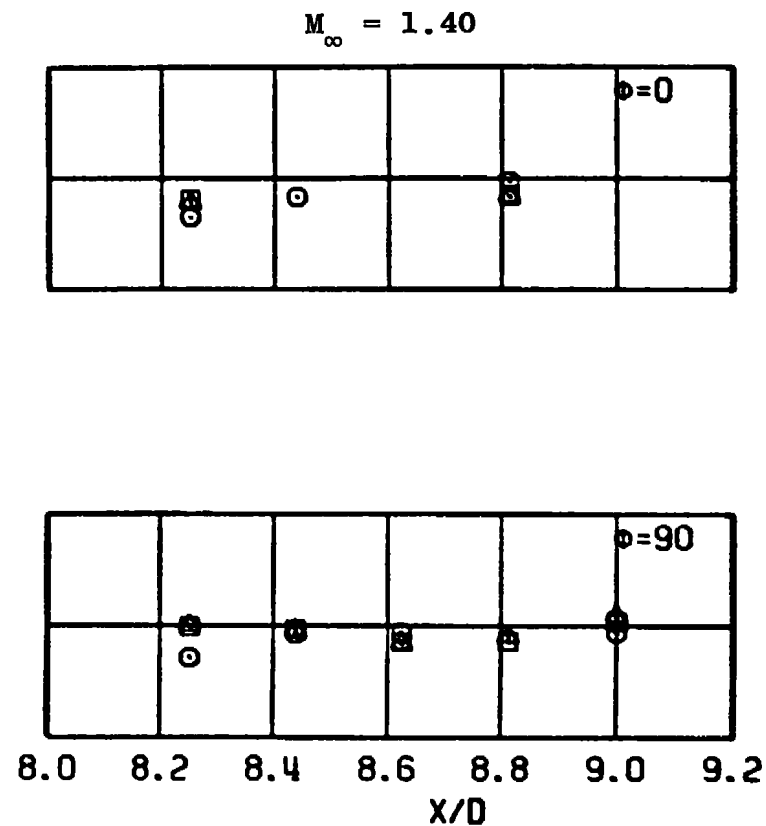
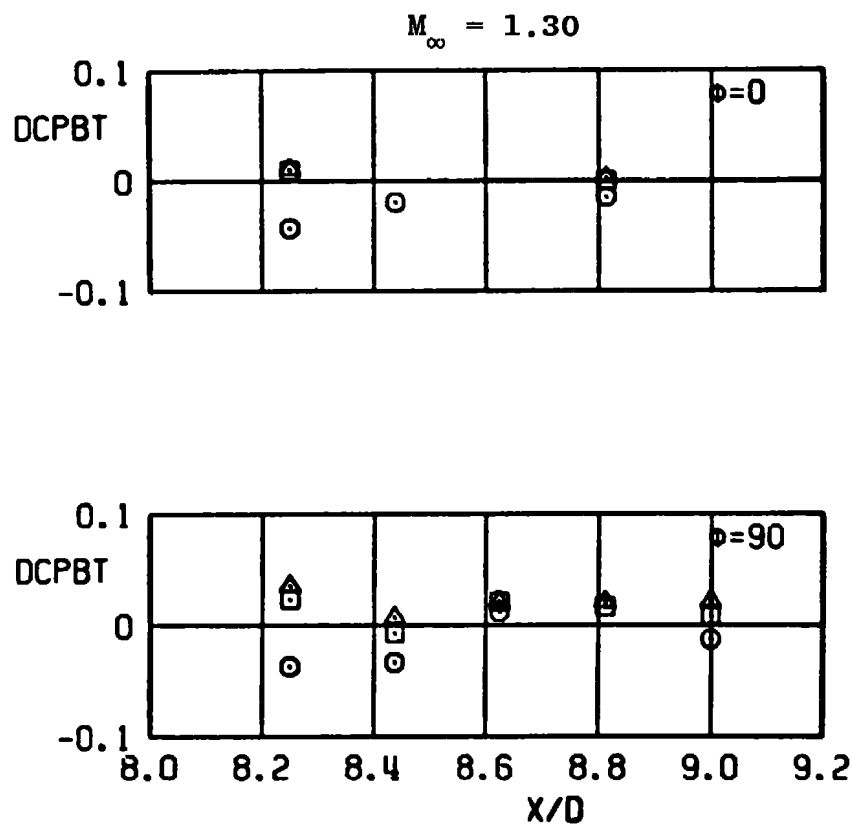
f. Continued
Figure A-6. Continued.

SYM	CONFIG	POROSITY, PERCENT
○	B2-S3L1	6
□	B2-S3L1-W3	3
△	B2-S3L1-W1	1



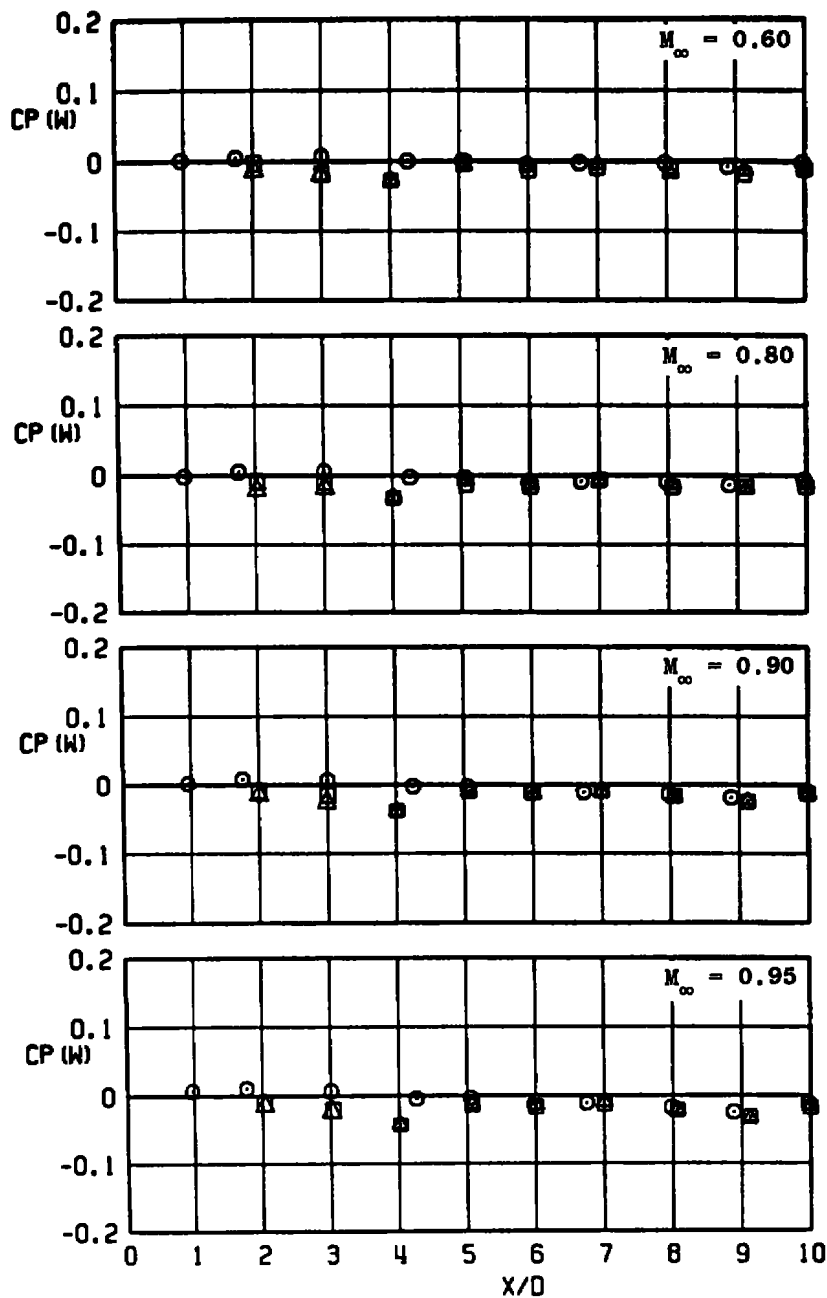
f. Continued
Figure A-6. Continued.

SYM	CONFIG	POROSITY, PERCENT
○	B2-S3L1	6
□	B2-S3L1-W3	3
△	B2-S3L1-W1	1



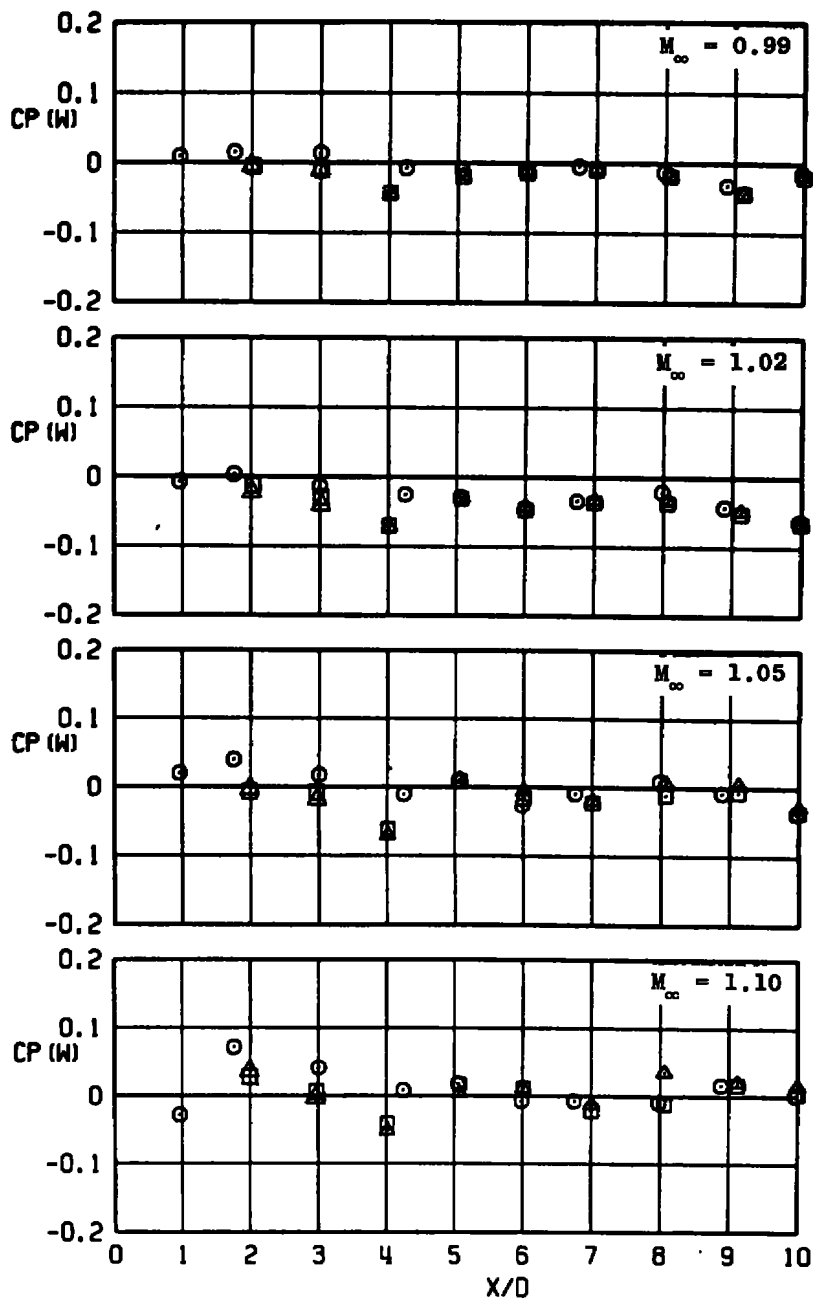
f. Concluded
Figure A-6. Continued.

SYM	CONFIG	POROSITY, PERCENT	ϕ , DEG
○	B2-S3L1	6	0
□	B2-S3L1-W3	3	0
△	B2-S3L1-W1	1	0



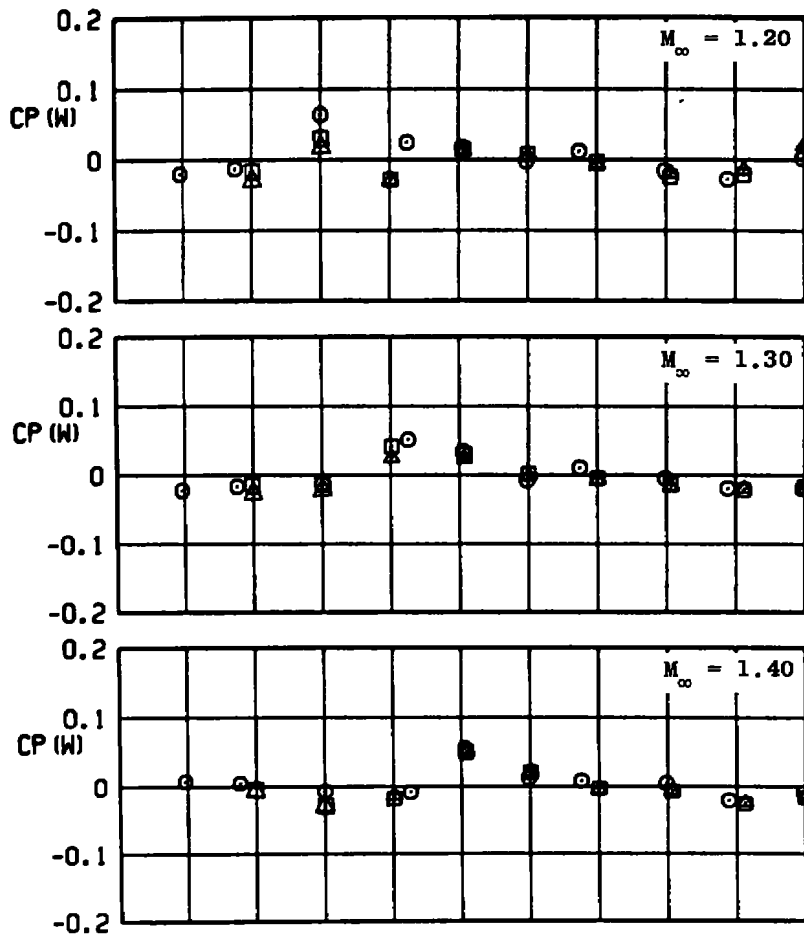
g. $CP(W)$ versus X/D (30-deg swept strut, 10-deg boattail, $\phi = 0$)
Figure A-6. Continued.

SYM	CONFIG	POROSITY, PERCENT	ϕ , DEG
○	82-S3L1	6	0
□	82-S3L1-W3	3	0
△	82-S3L1-W1	1	0



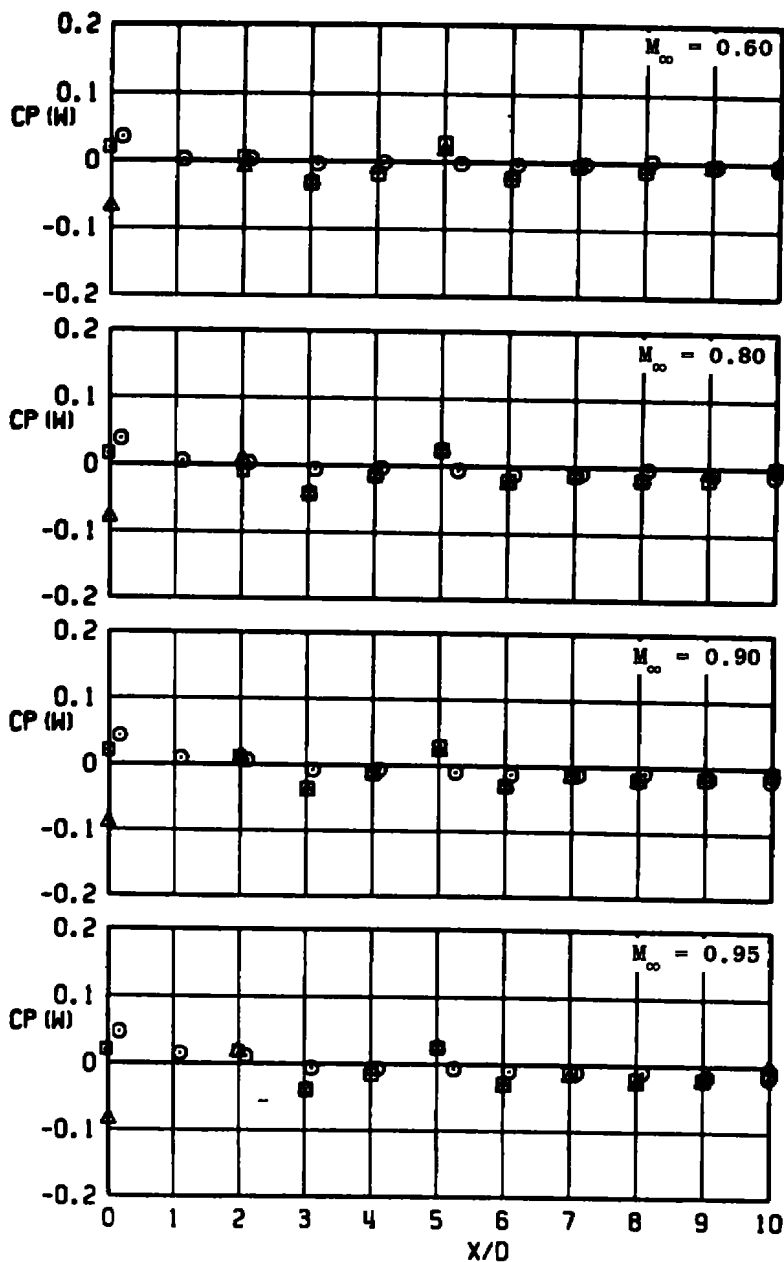
g. Continued
Figure A-6. Continued.

SYM	CONFIG	POROSITY, PERCENT	ϕ , DEG
○	B2-S3L1	6	0
□	B2-S3L1-W3	3	0
△	B2-S3L1-W1	1	0



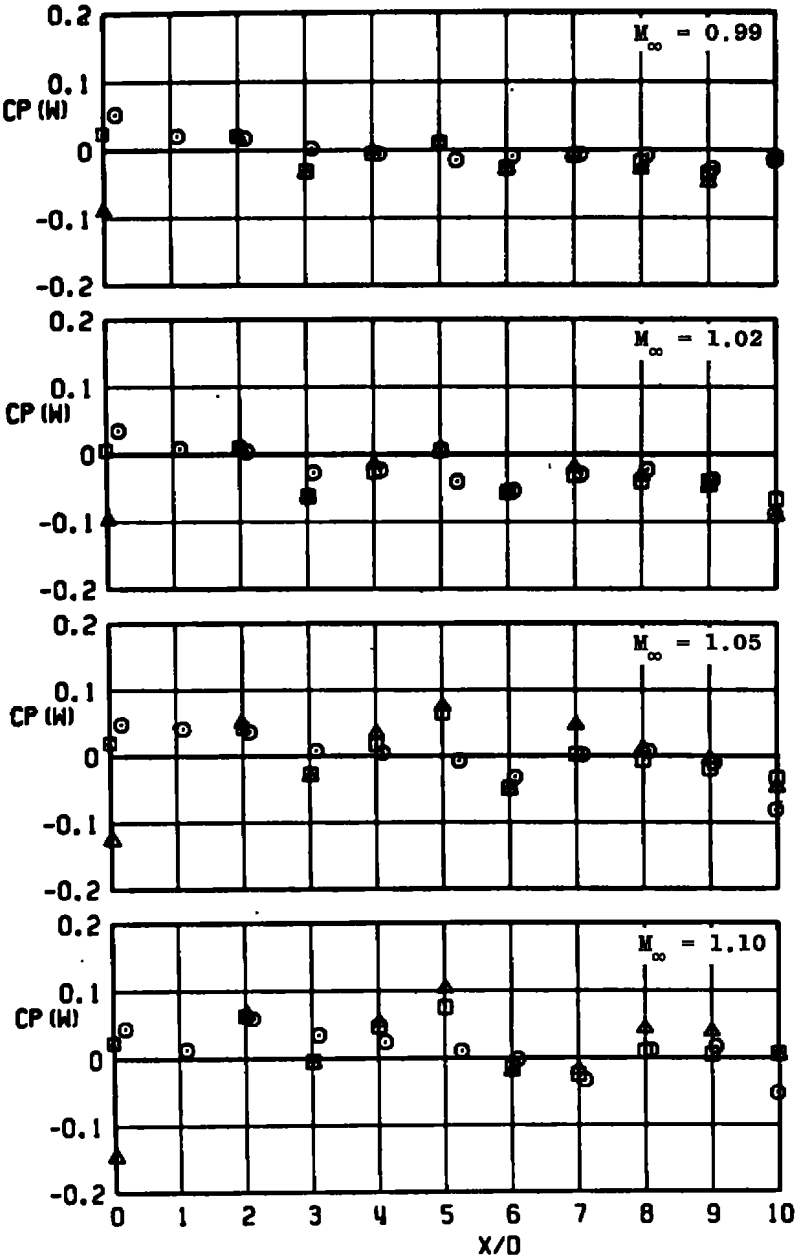
g. Concluded
Figure A-6. Continued.

SYM	CONFIG	POROSITY, PERCENT	ϕ , DEG
○	B2-S3L1	6	90
□	B2-S3L1-W3	3	90
▲	B2-S3L1-W1	1	90



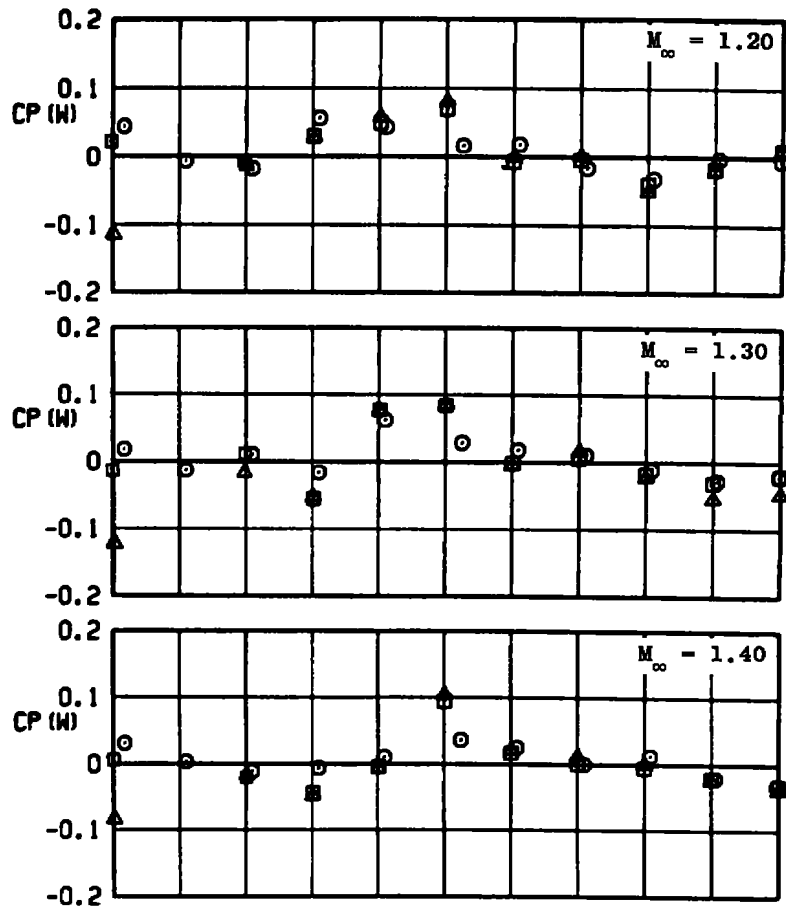
h. $CP(W)$ versus X/D (30-deg swept strut, 10-deg boattail, $\phi = 90$ deg)
Figure A-6. Continued.

SYM	CONFIG	POROSITY, PERCENT	ϕ , DEG
○	B2-53L1	6	90
□	B2-53L1-W3	3	90
▲	B2-53L1-W1	1	90



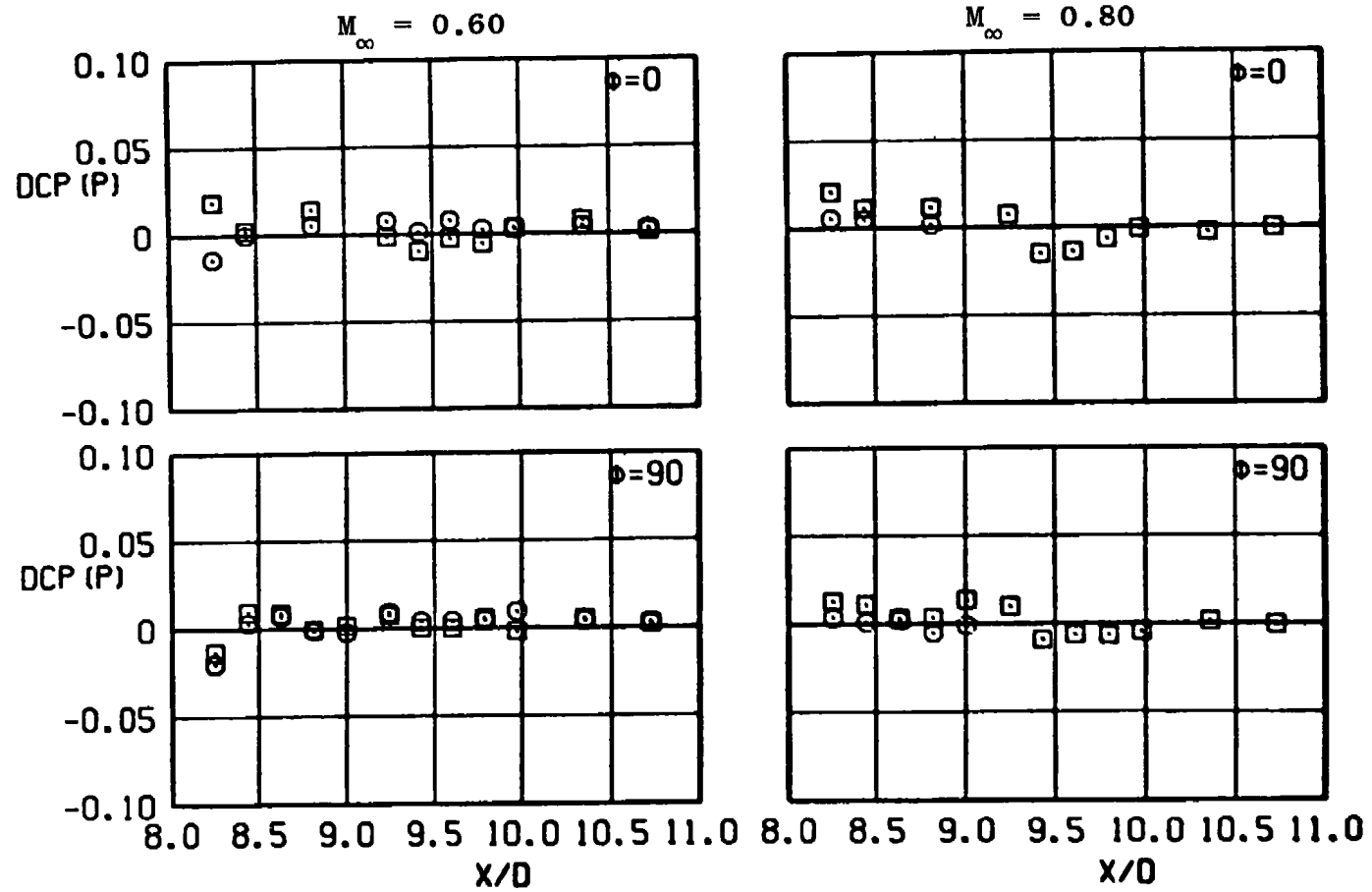
h.. Continued
Figure A-6. Continued.

SYM	CONFIG	POROSITY, PERCENT	ϕ , DEG
○	B2-S3L1	6	90
□	B2-S3L1-W3	3	90
△	B2-S3L1-W1	1	90



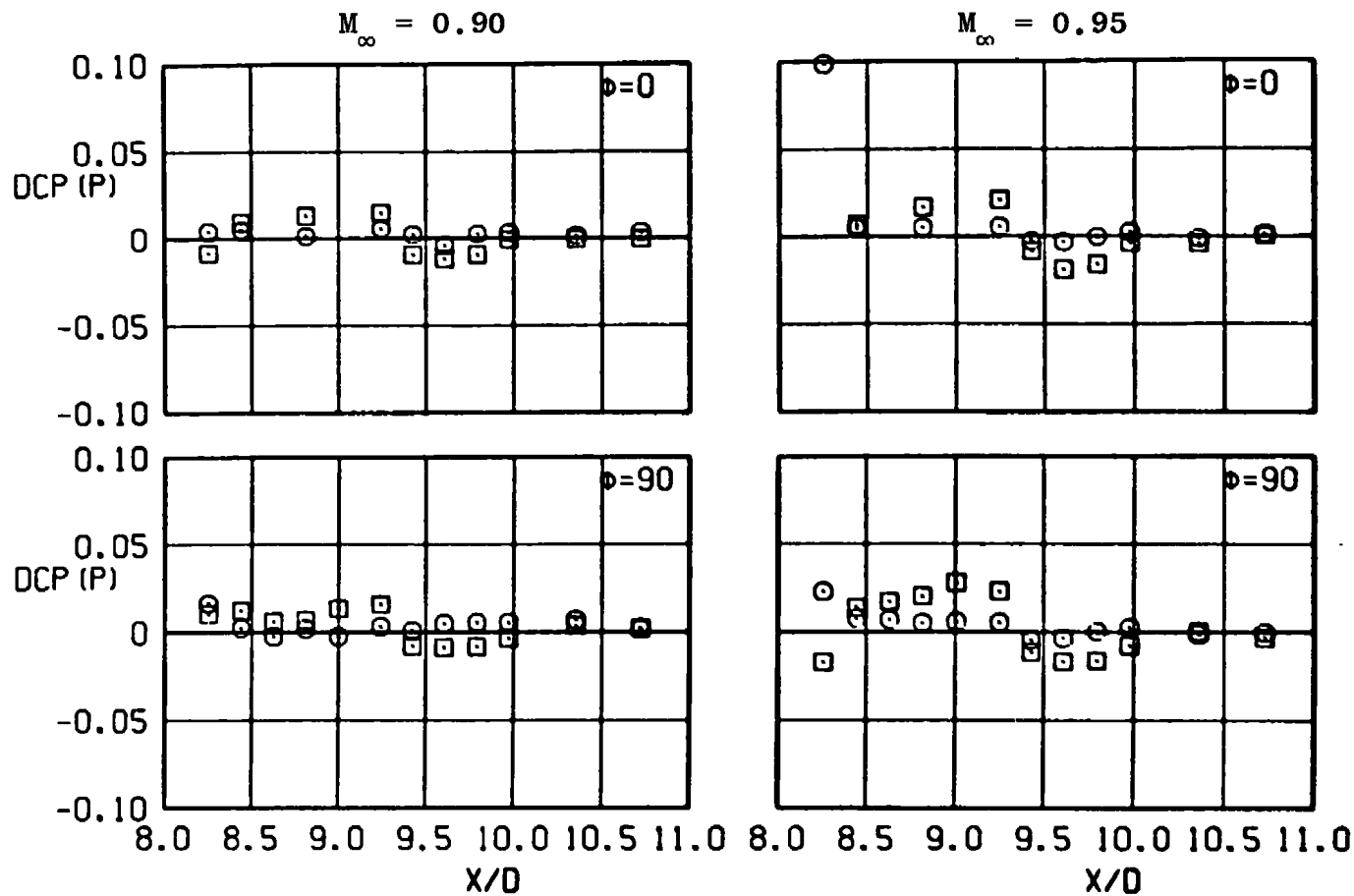
h. Concluded
Figure A-6. Concluded.

SYM	CONFIG	Λ , DEG
○	B2-S2L1-P	0
□	B2-S3L1-P	45



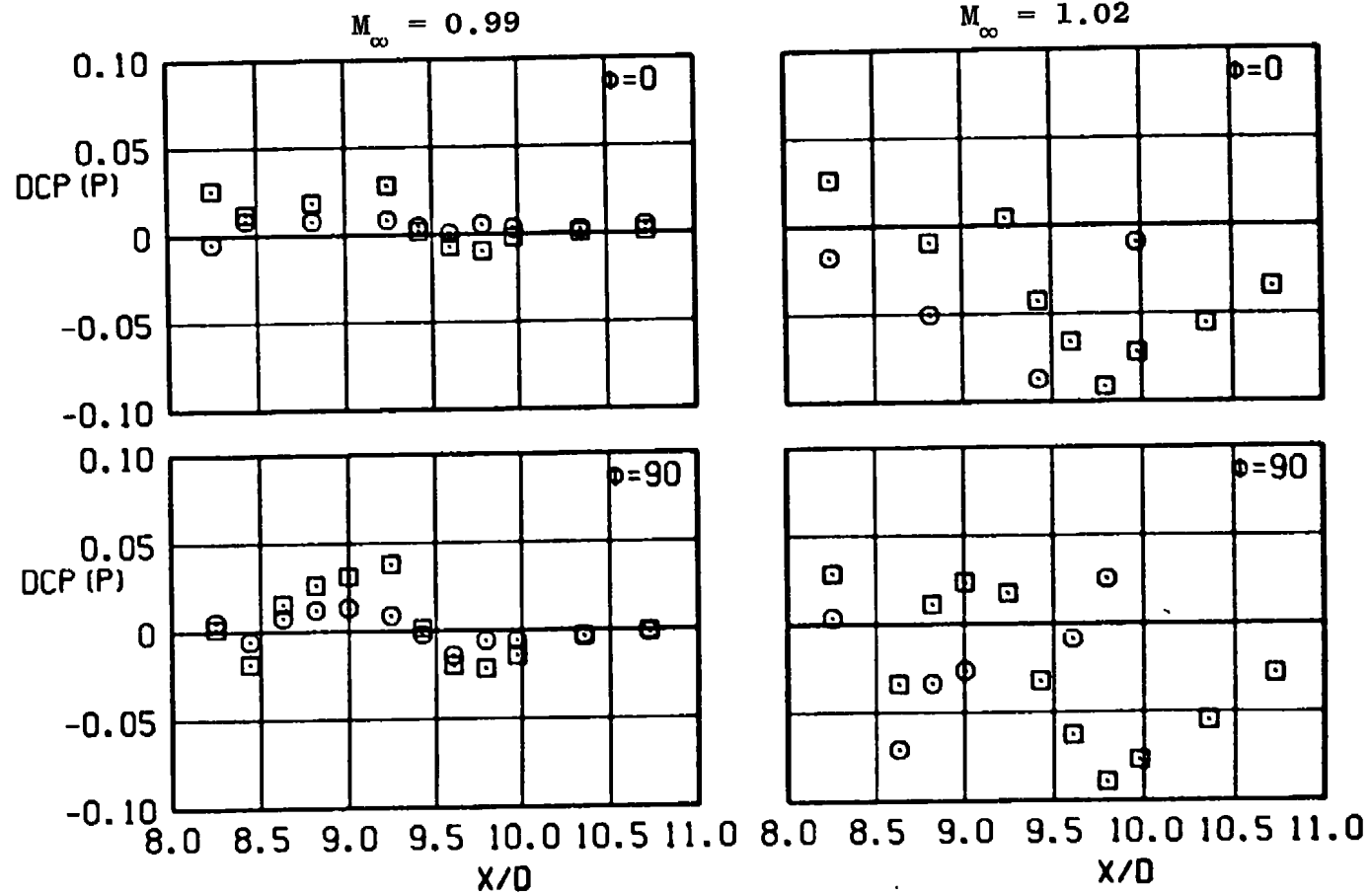
a. DCP(P) versus X/D (with varying strut sweep angle)
 Figure A-7. Effect of simulated jet plume.

SYM	CONFIG	Λ , DEG
○	B2-S2L1-P	0
□	B2-S3L1-P	

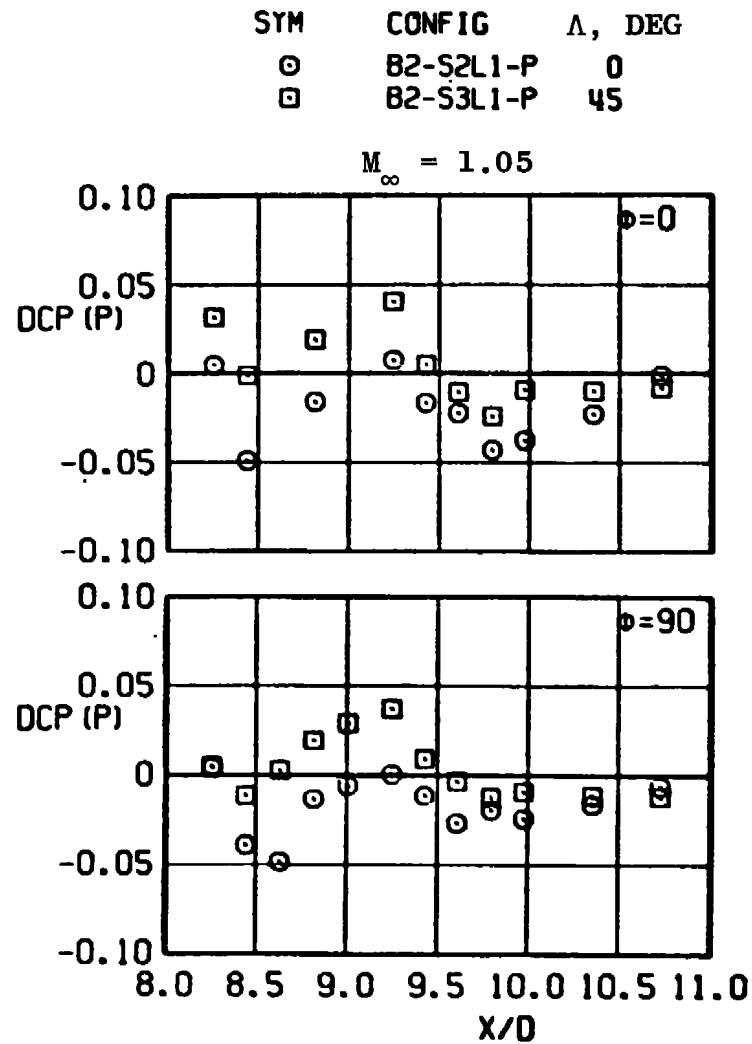


a. Continued
Figure A-7. Continued.

SYM	CONFIG	Λ , DEG
○	B2-S2L1-P	0
□	B2-S3L1-P	45

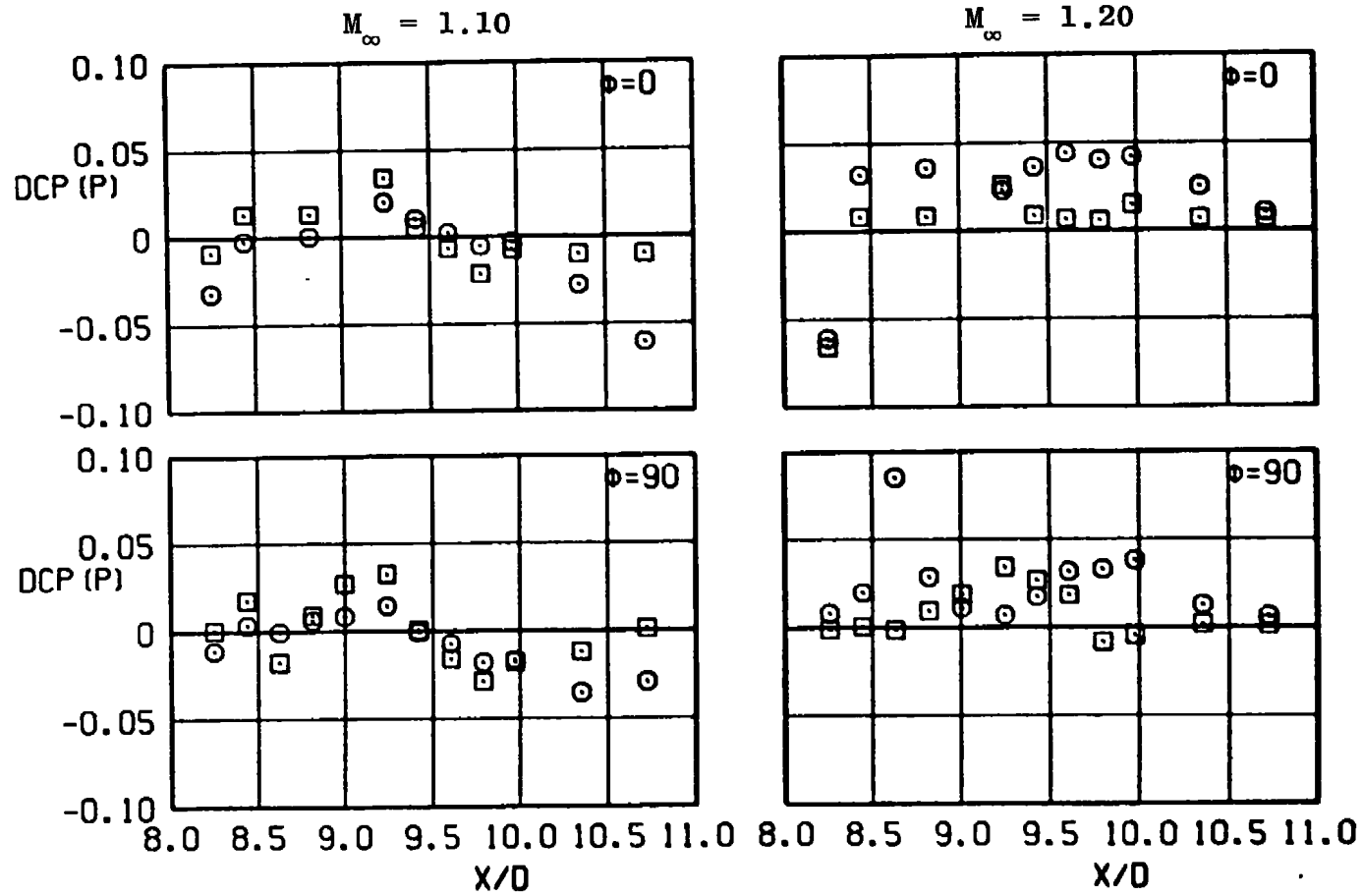


a. Continued
Figure A-7. Continued.



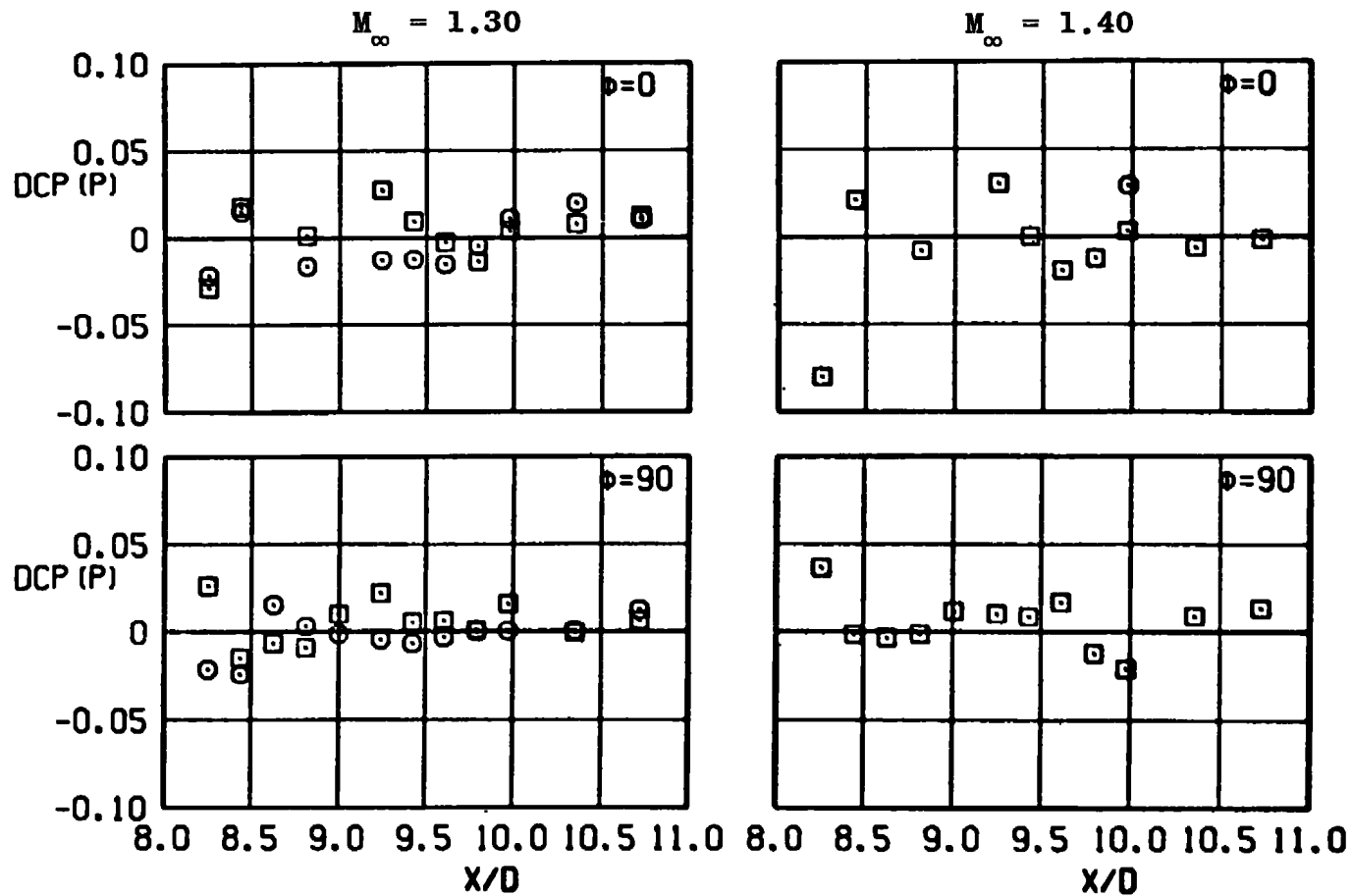
a. Continued
Figure A-7. Continued.

SYM	CONFIG	Λ , DEG
○	B2-S2L1-P	0
□	B2-S3L1-P	



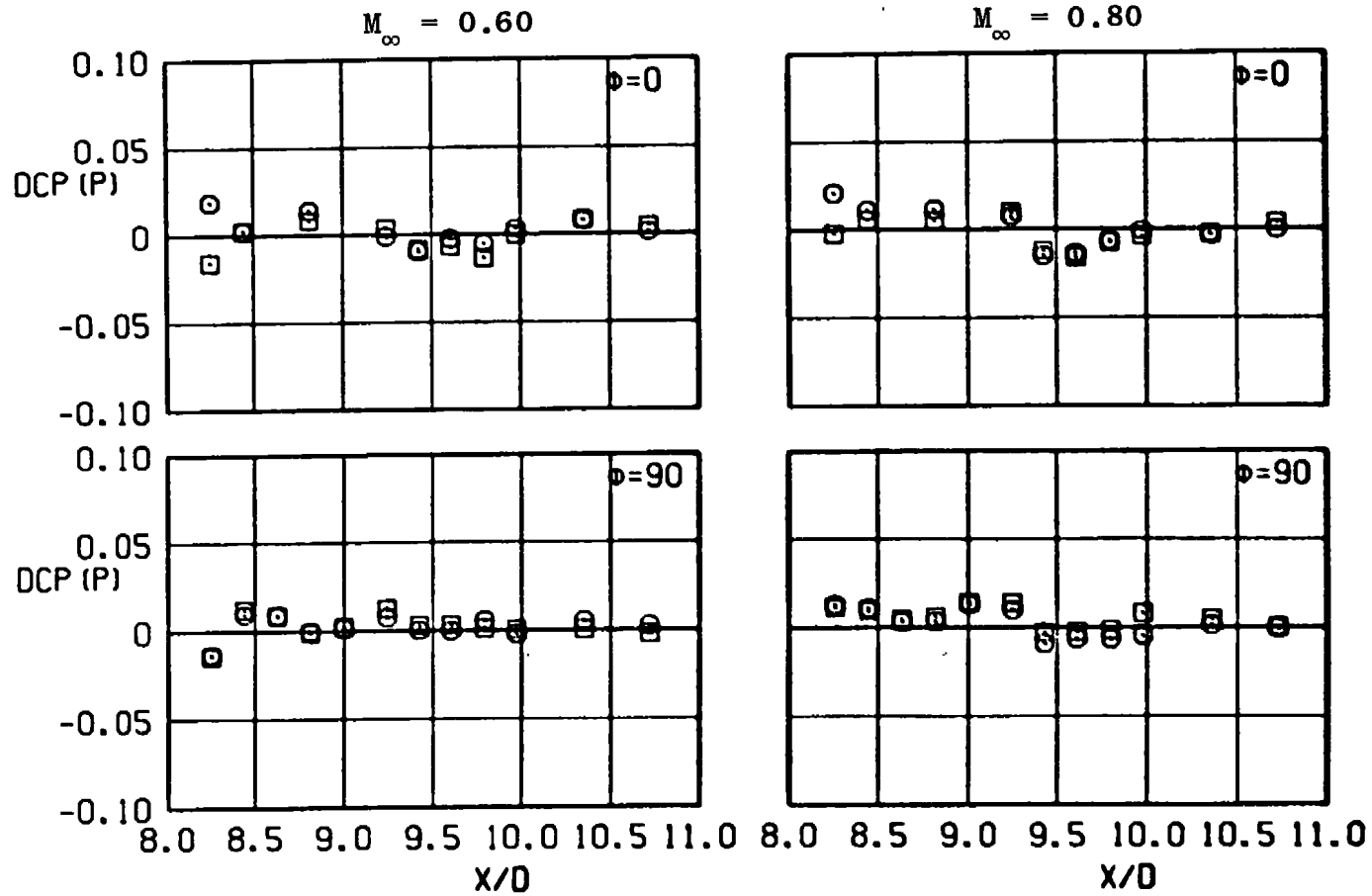
a. Continued
Figure A-7. Continued.

SYM	CONFIG	Λ , DEG
○	B2-S2L1-P	0
□	B2-S3L1-P	



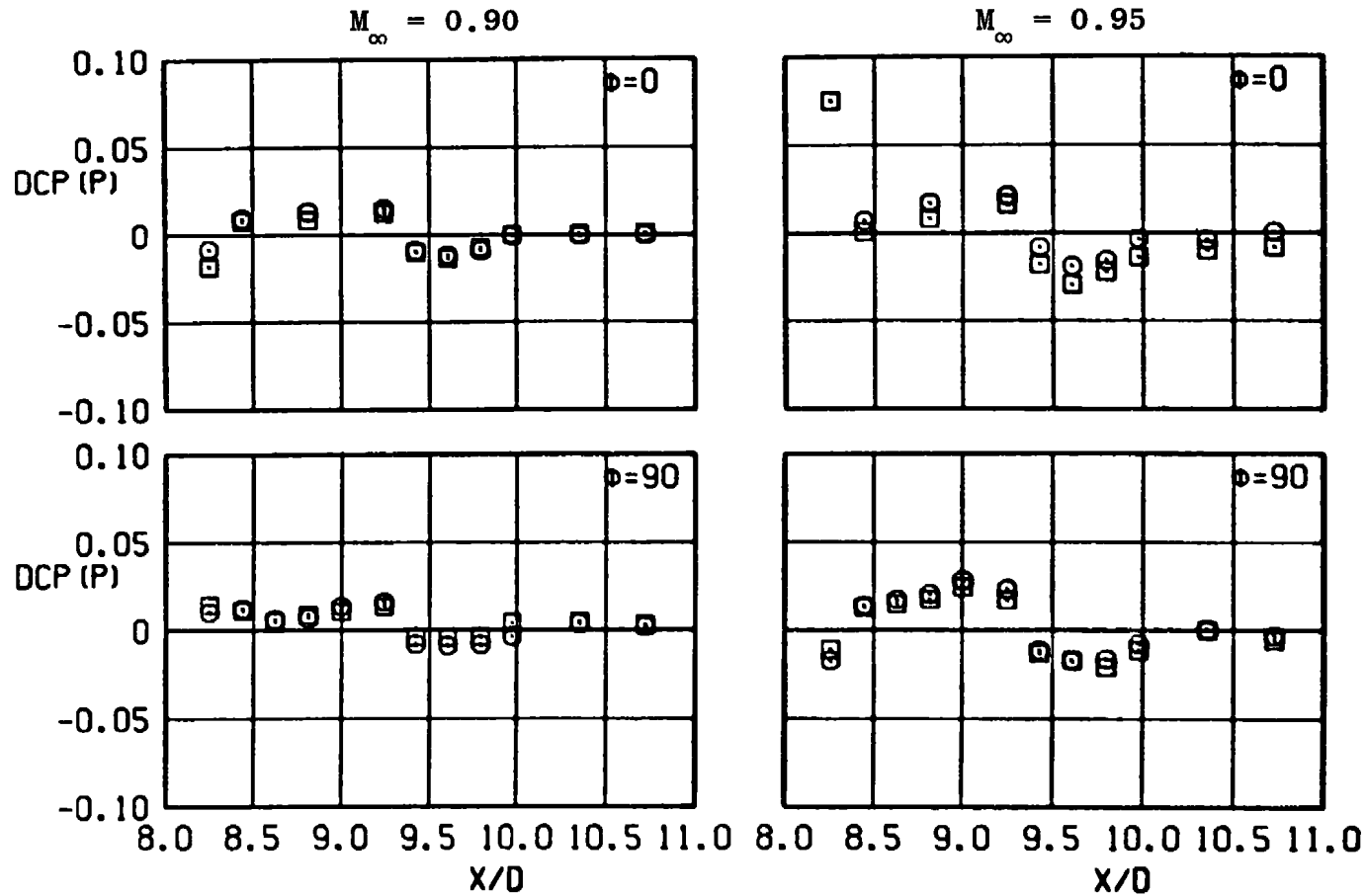
a. Concluded
Figure A-7. Continued.

SYM	CONFIG	ℓ , IN.
○	82-S3L1-P	0.0
□	82-S3L3-P	1.6



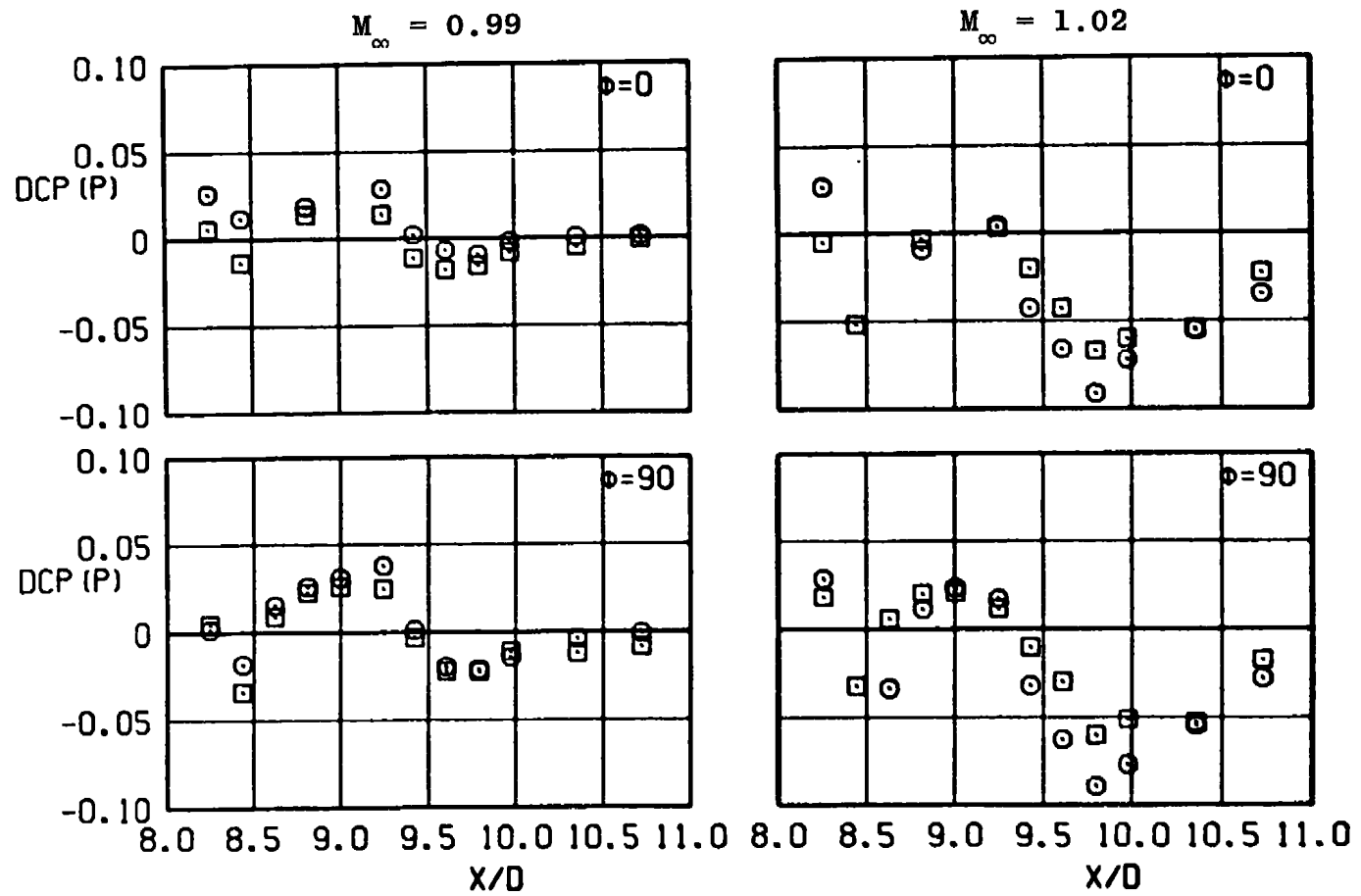
b. DCP(P) versus X/D (30-deg swept strut wity varying position)
Figure A-7. Continued.

SYM	CONFIG	l , IN.
○	B2-S3L1-P	0.0
□	B2-S3L3-P	1.6

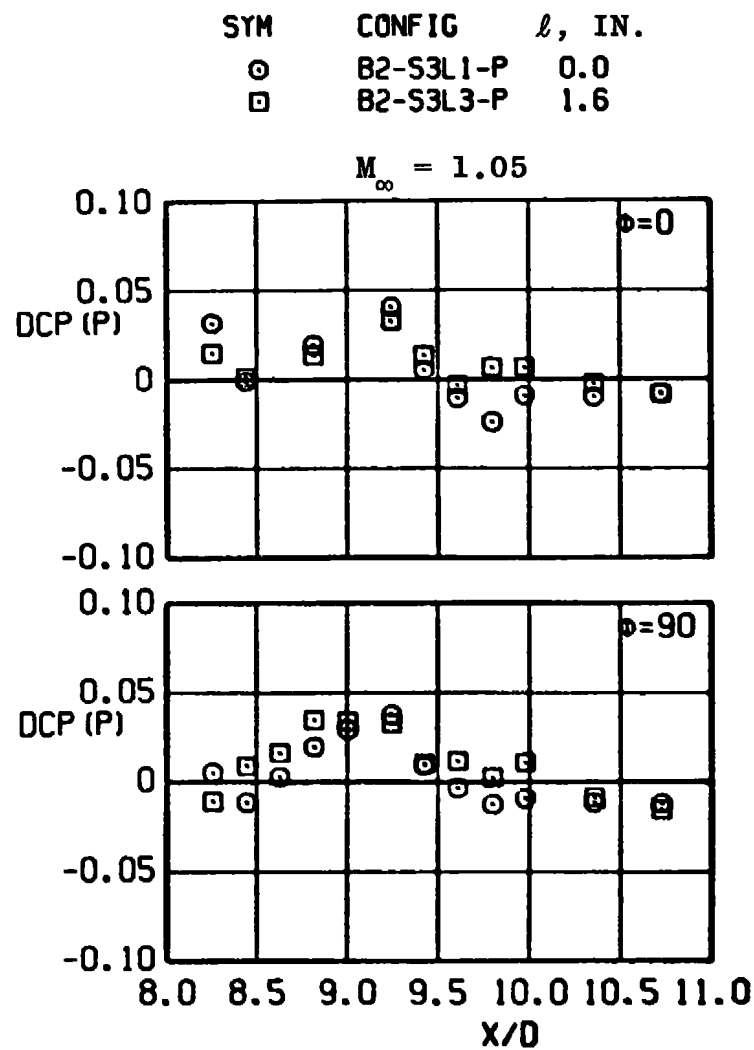


b. Continued
Figure A-7. Continued.

SYM	CONFIG	ℓ , IN.
○	B2-S3L1-P	0.0
□	B2-S3L3-P	1.6

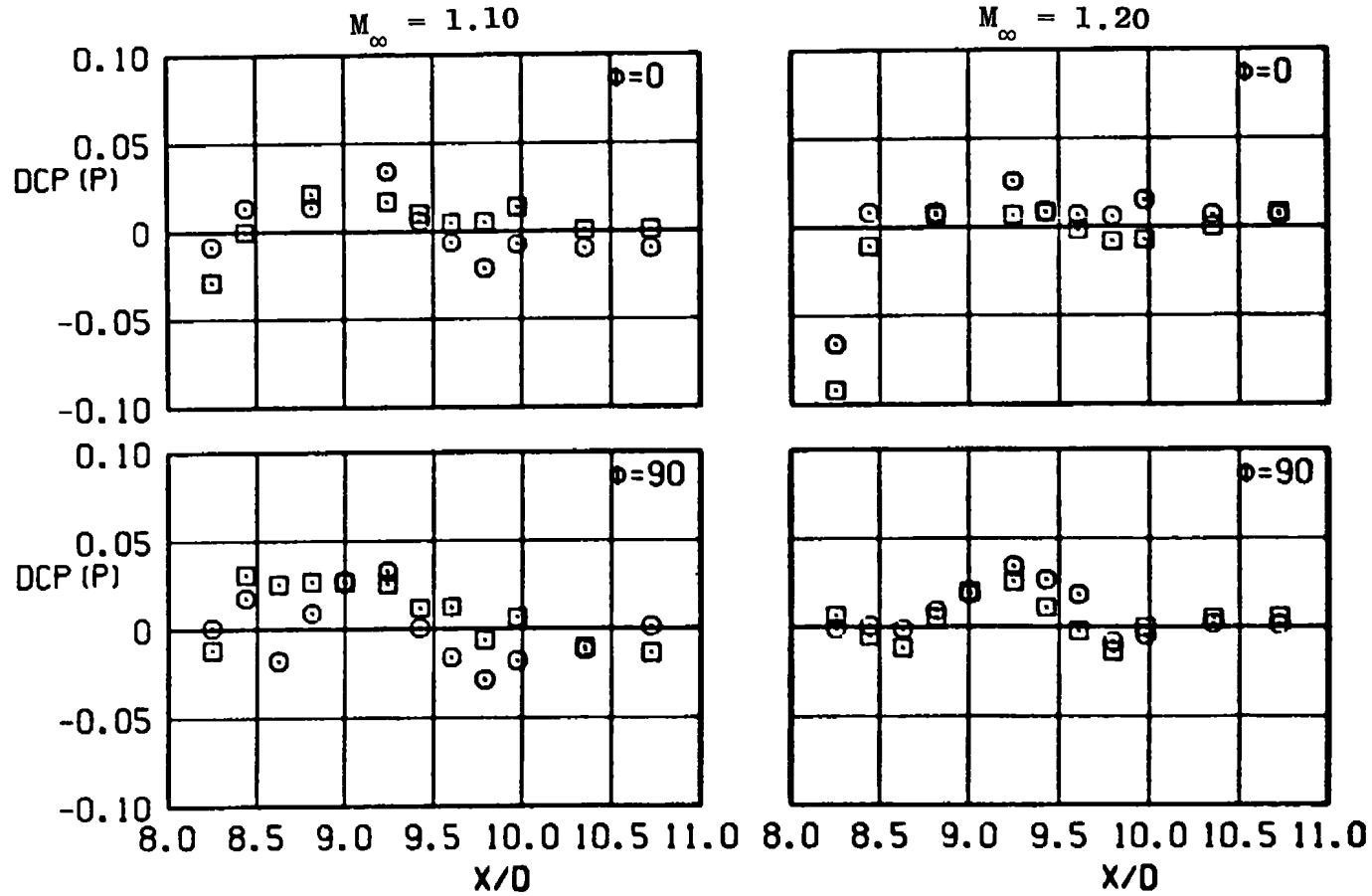


b. Continued
Figure A-7. Continued.



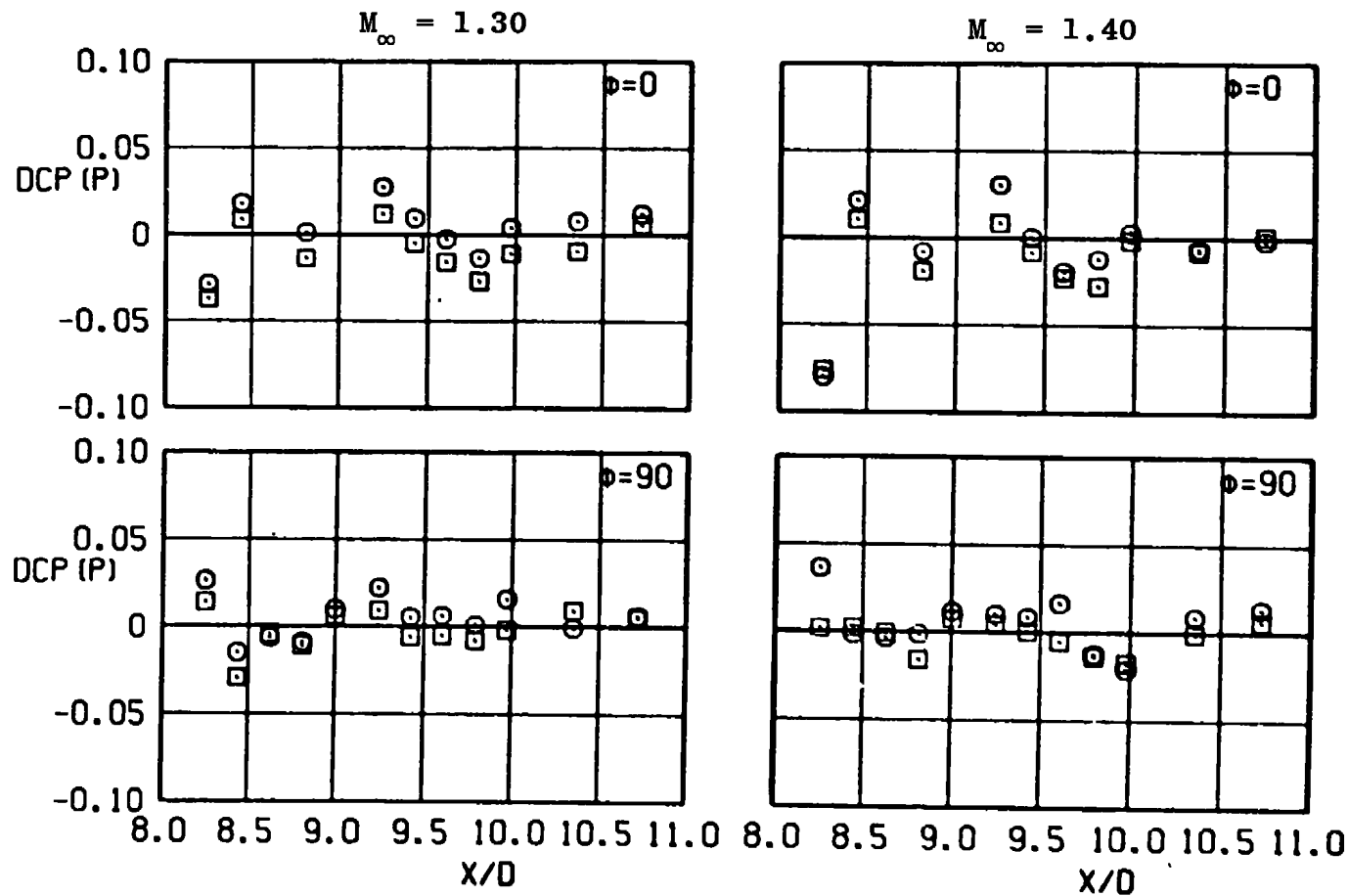
b. Continued
Figure A-7. Continued.

SYM	CONFIG	ℓ , IN.
○	B2-S3L1-P	0.0
□	B2-S3L3-P	1.6



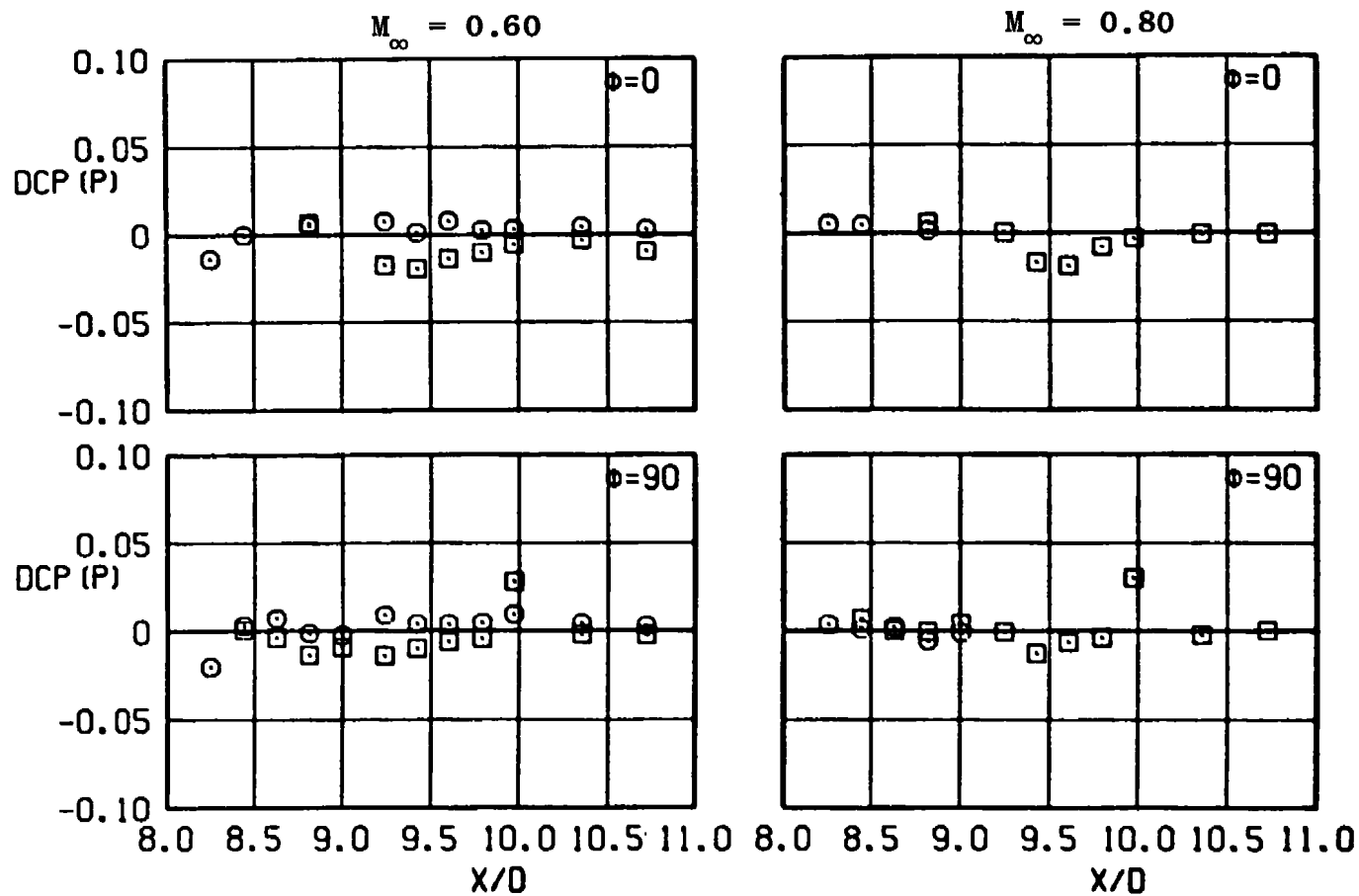
b. Continued
Figure A-7. Continued.

SYM	CONFIG	ℓ , IN.
○	B2-S3L1-P	0.0
□	B2-S3L3-P	1.6

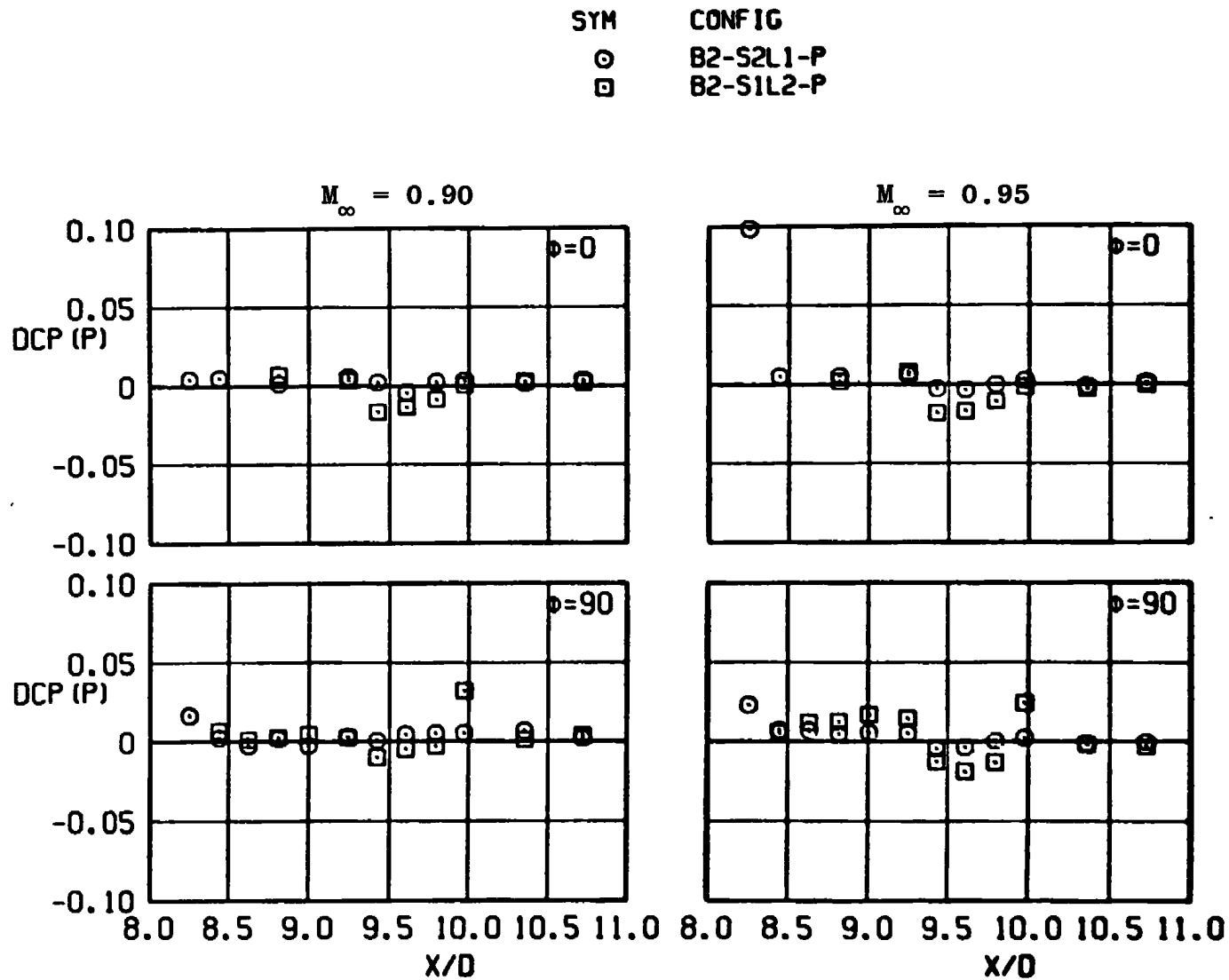


b. Concluded
Figure A-7. Continued.

SYM	CONFIG
○	B2-S2L1-P
□	B2-S1L2-P

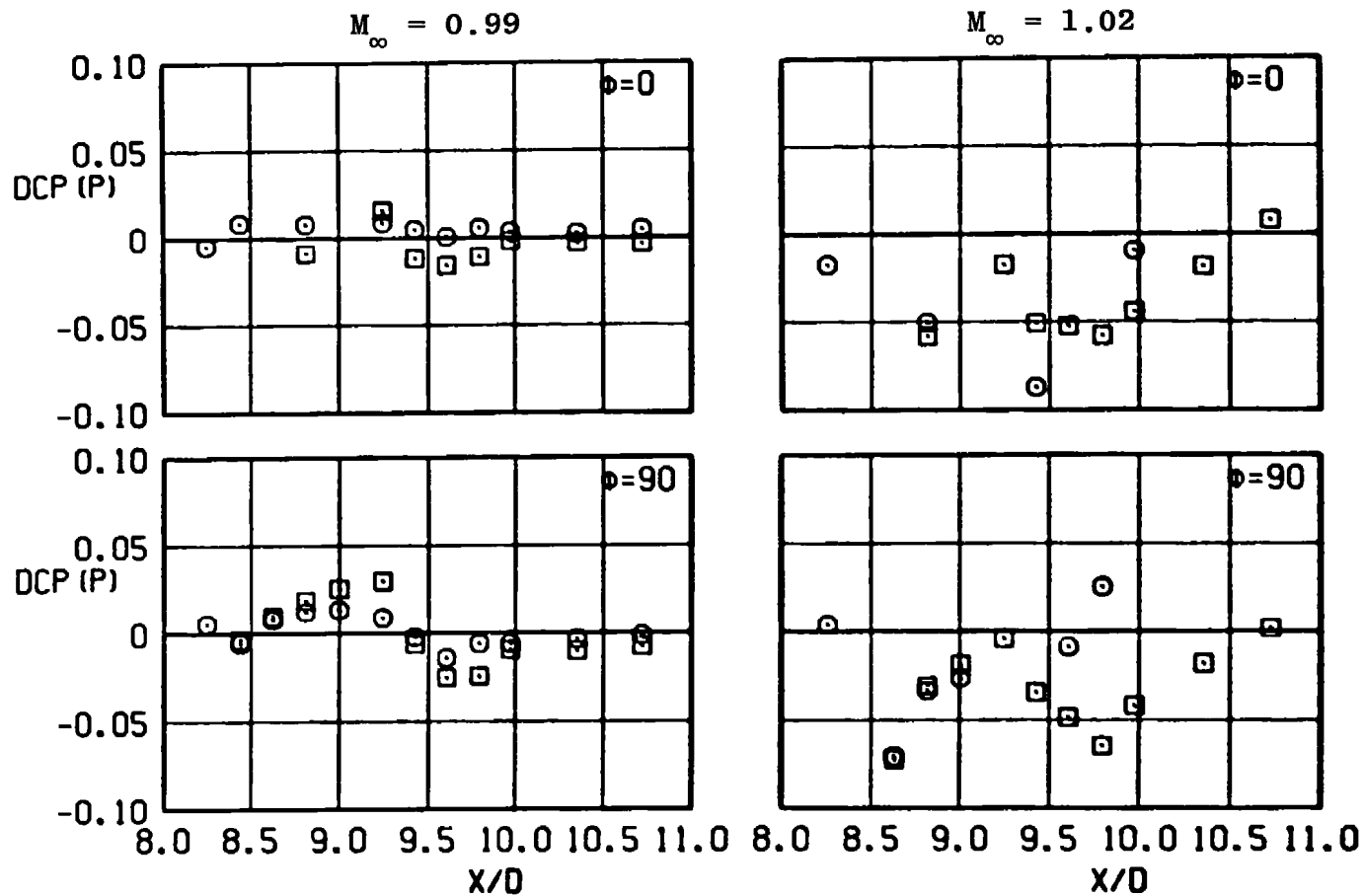


c. DCP(P) versus X/D (straight strut with varying chord)
Figure A-7. Continued.

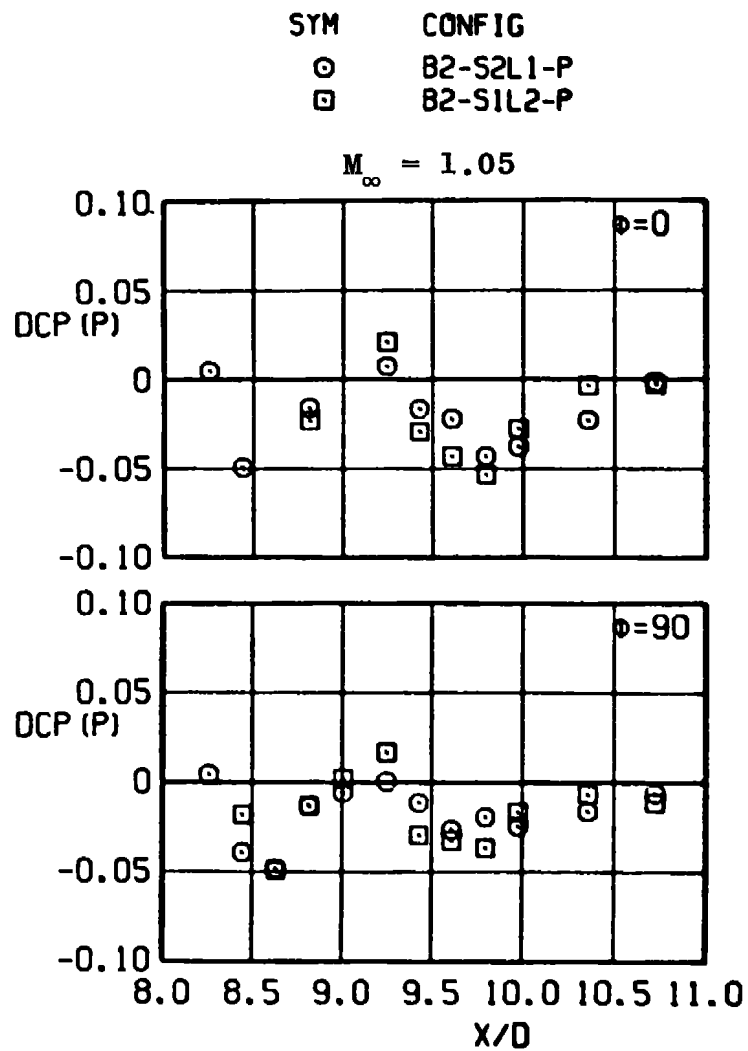


c. Continued
Figure A-7. Continued.

SYM	CONFIG
○	B2-S2L1-P
□	B2-S1L2-P

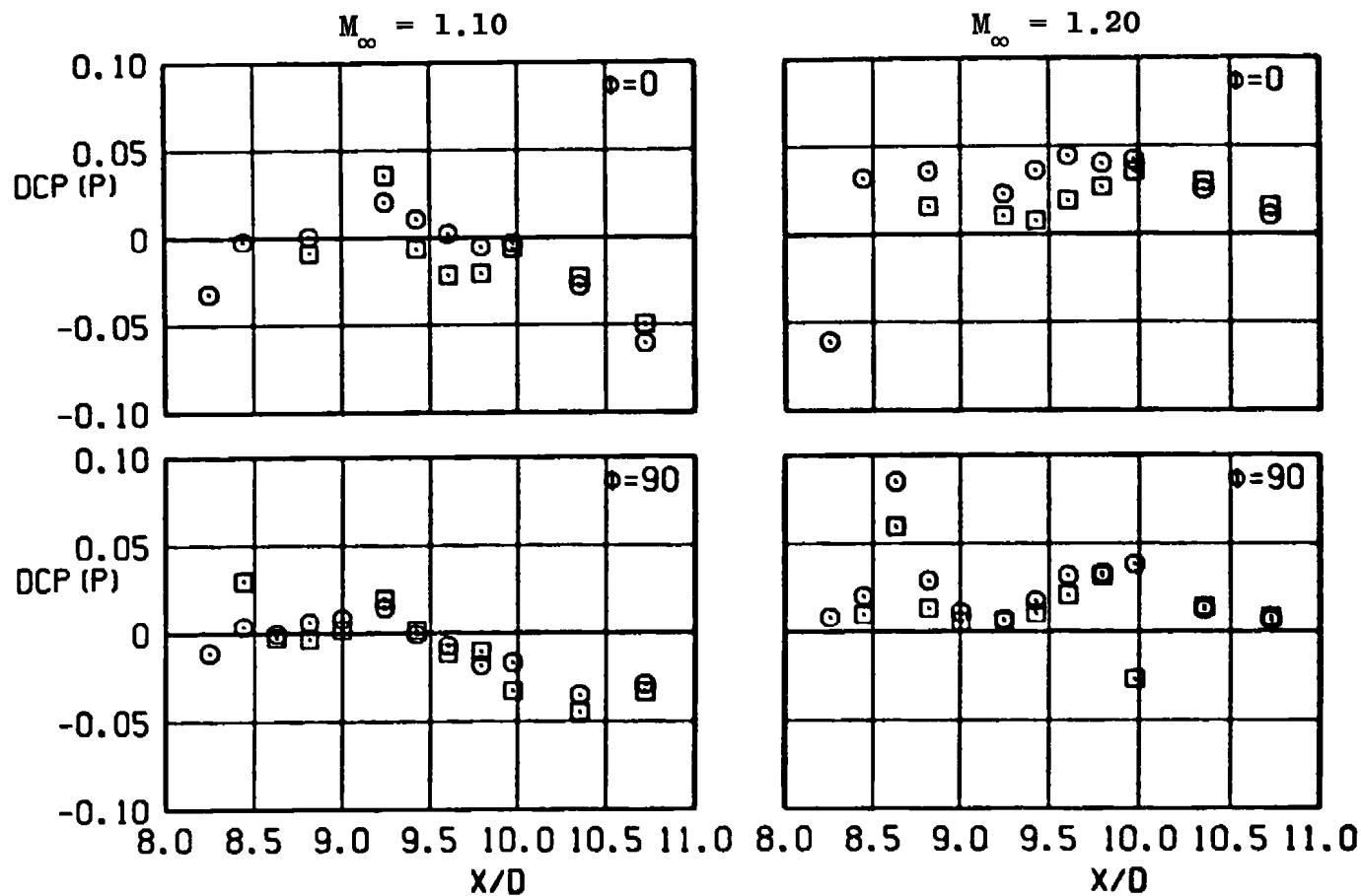


c. Continued
Figure A-7. Continued.

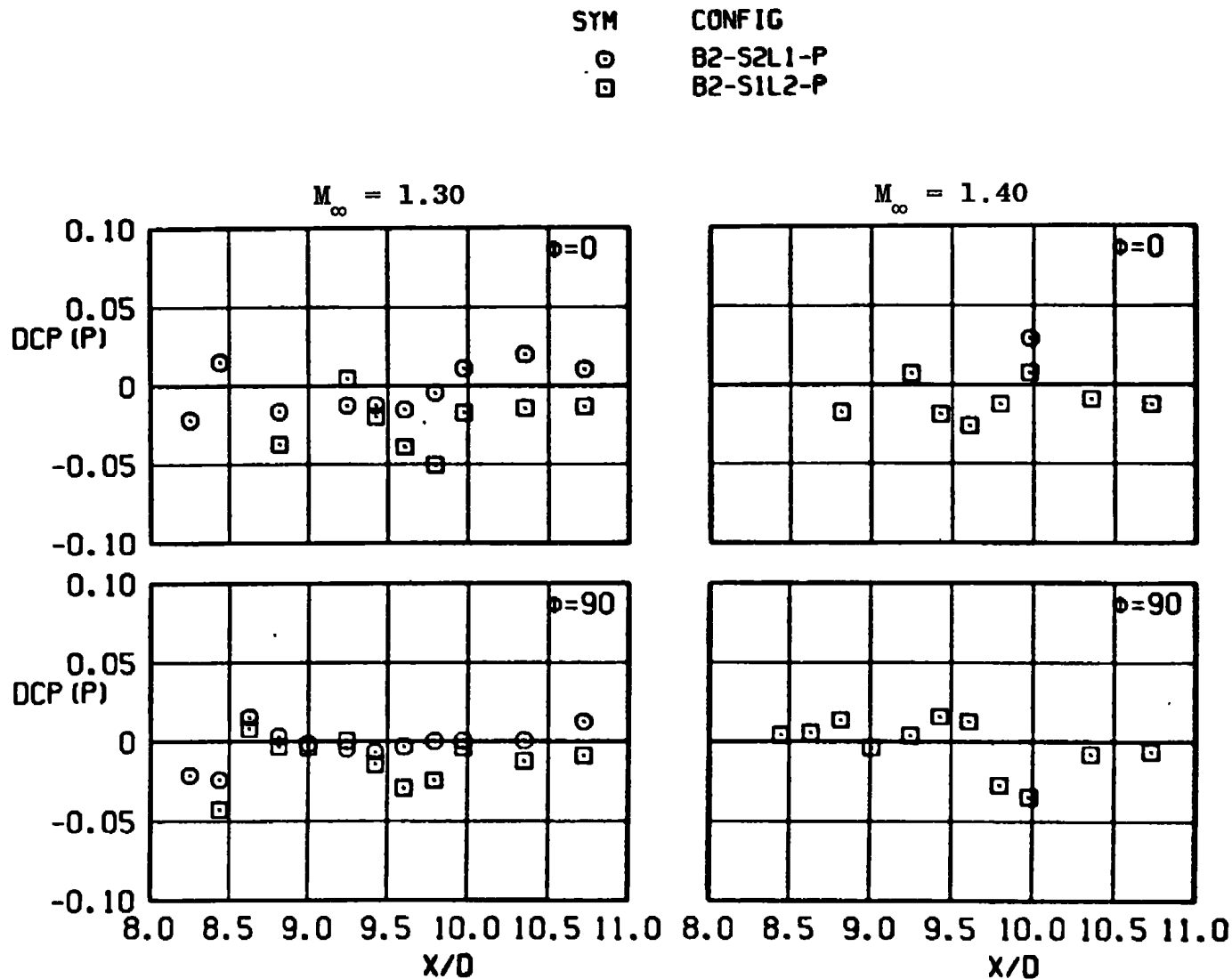


c. Continued
 Figure A-7. Continued.

SYM	CONFIG
○	B2-S2L1-P
□	B2-S1L2-P



c. Continued
Figure A-7. Continued.



c. Concluded
Figure A-7. Concluded.

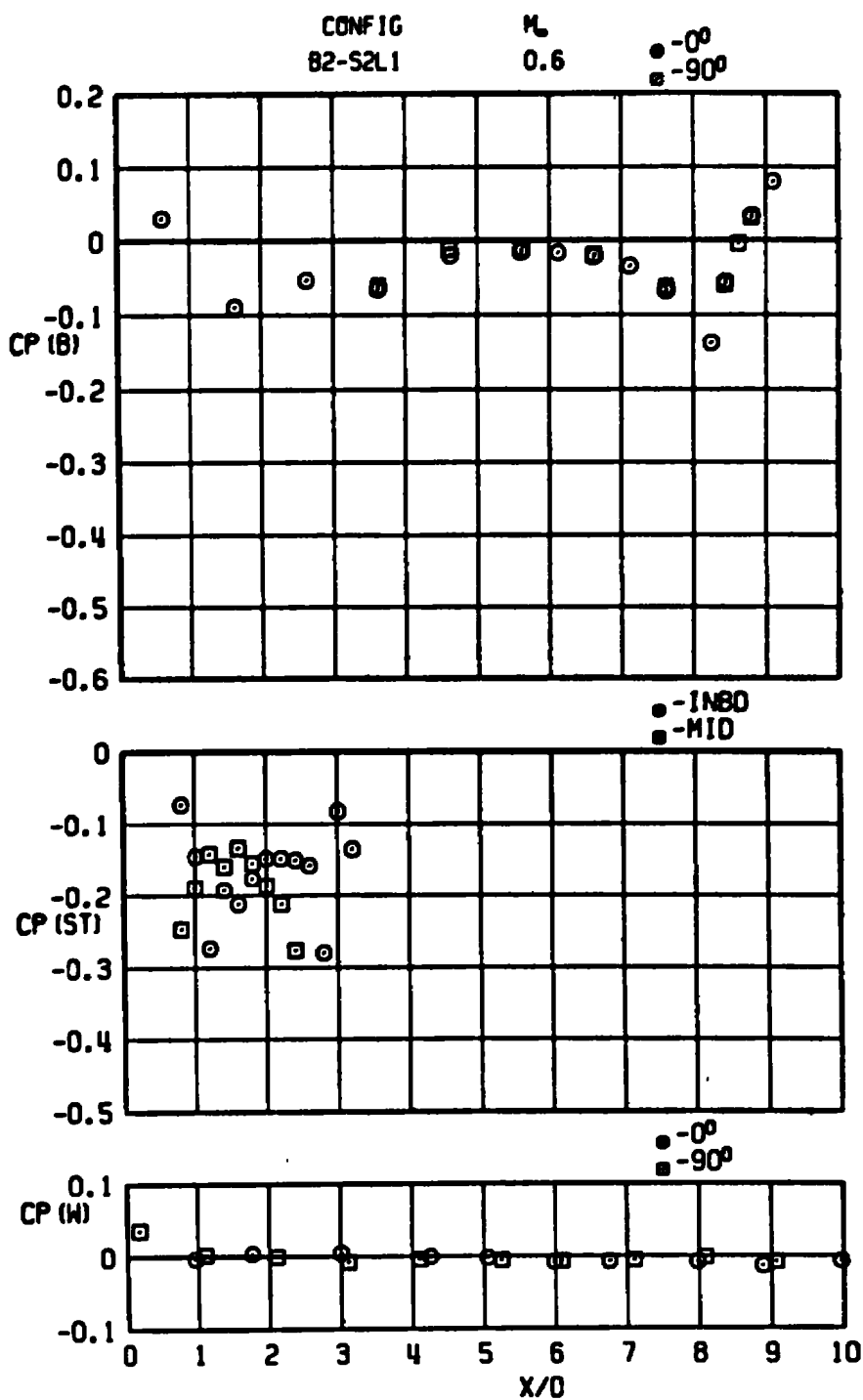
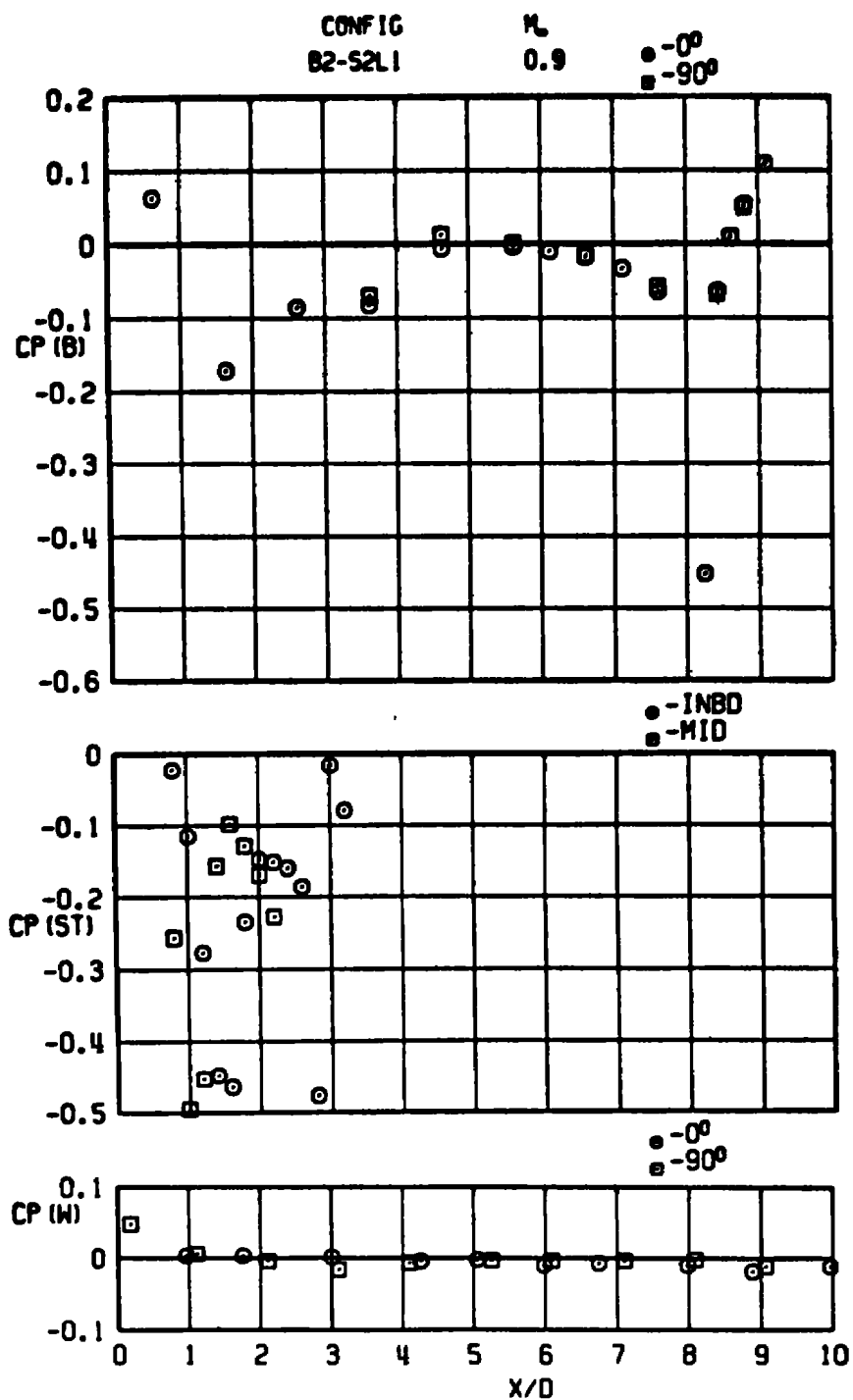
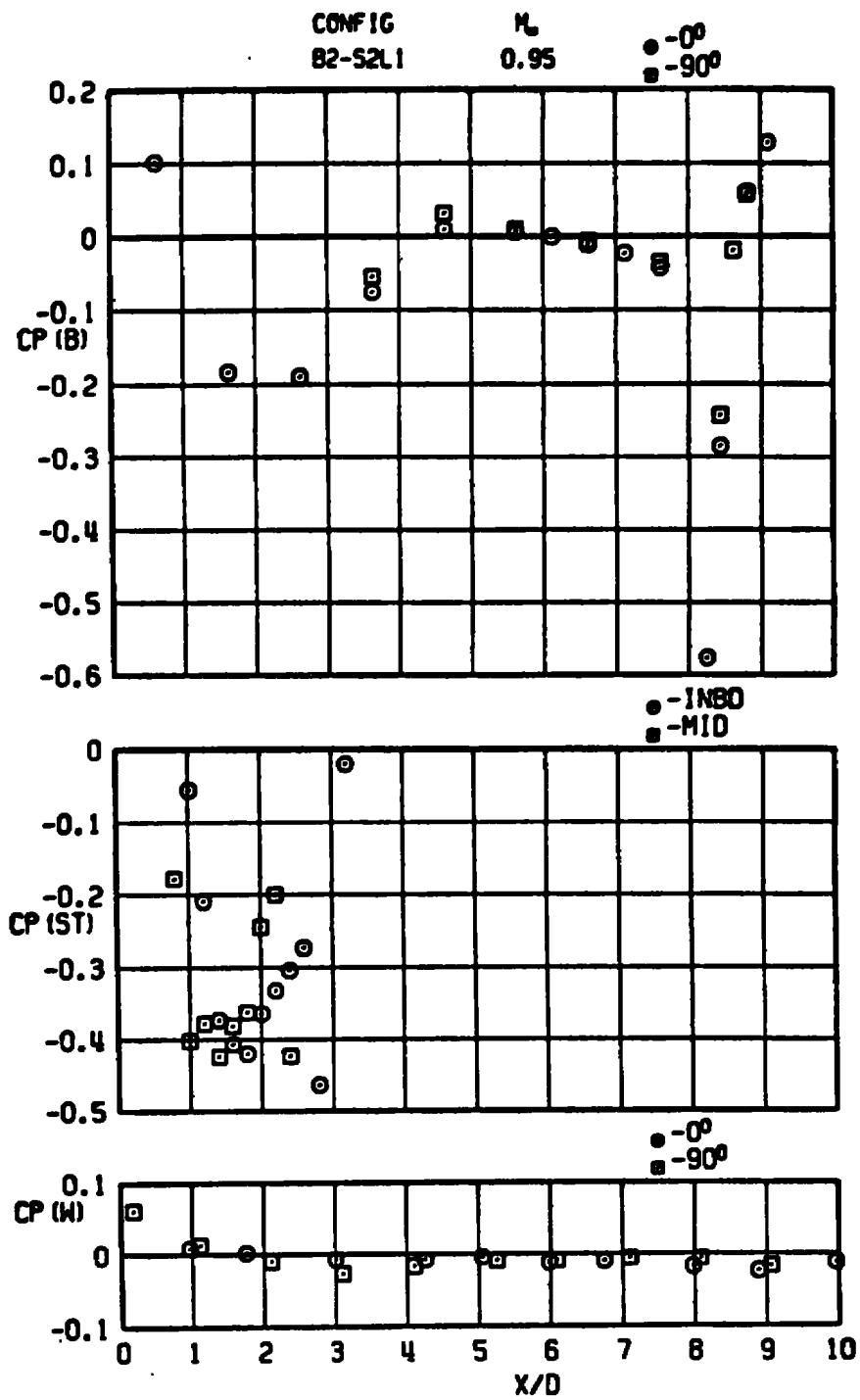
a. Straight strut, $\ell = 0$ (B2-S2L1)

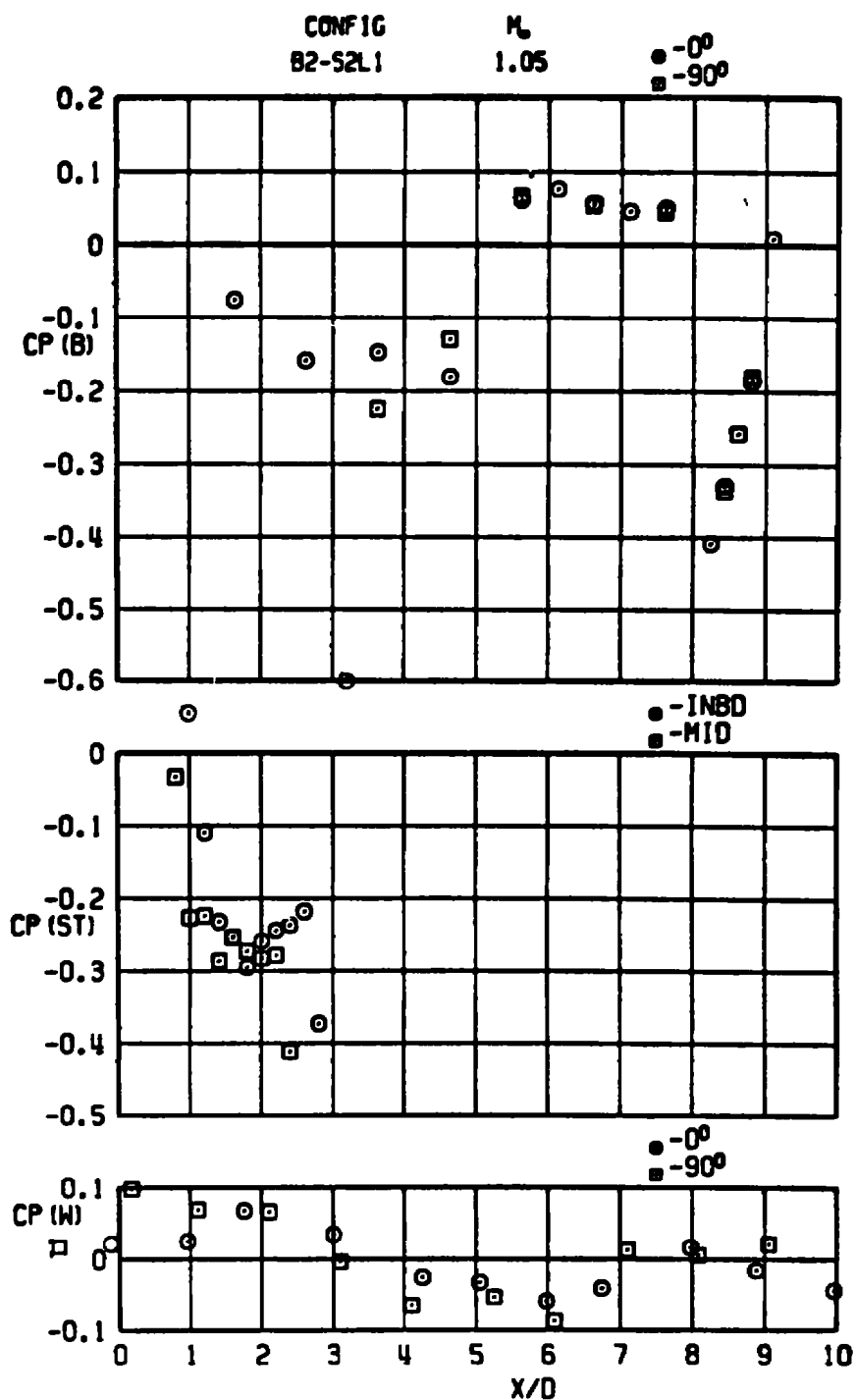
Figure A-8. Pressure coefficient distribution on model body, strut, and tunnel wall.



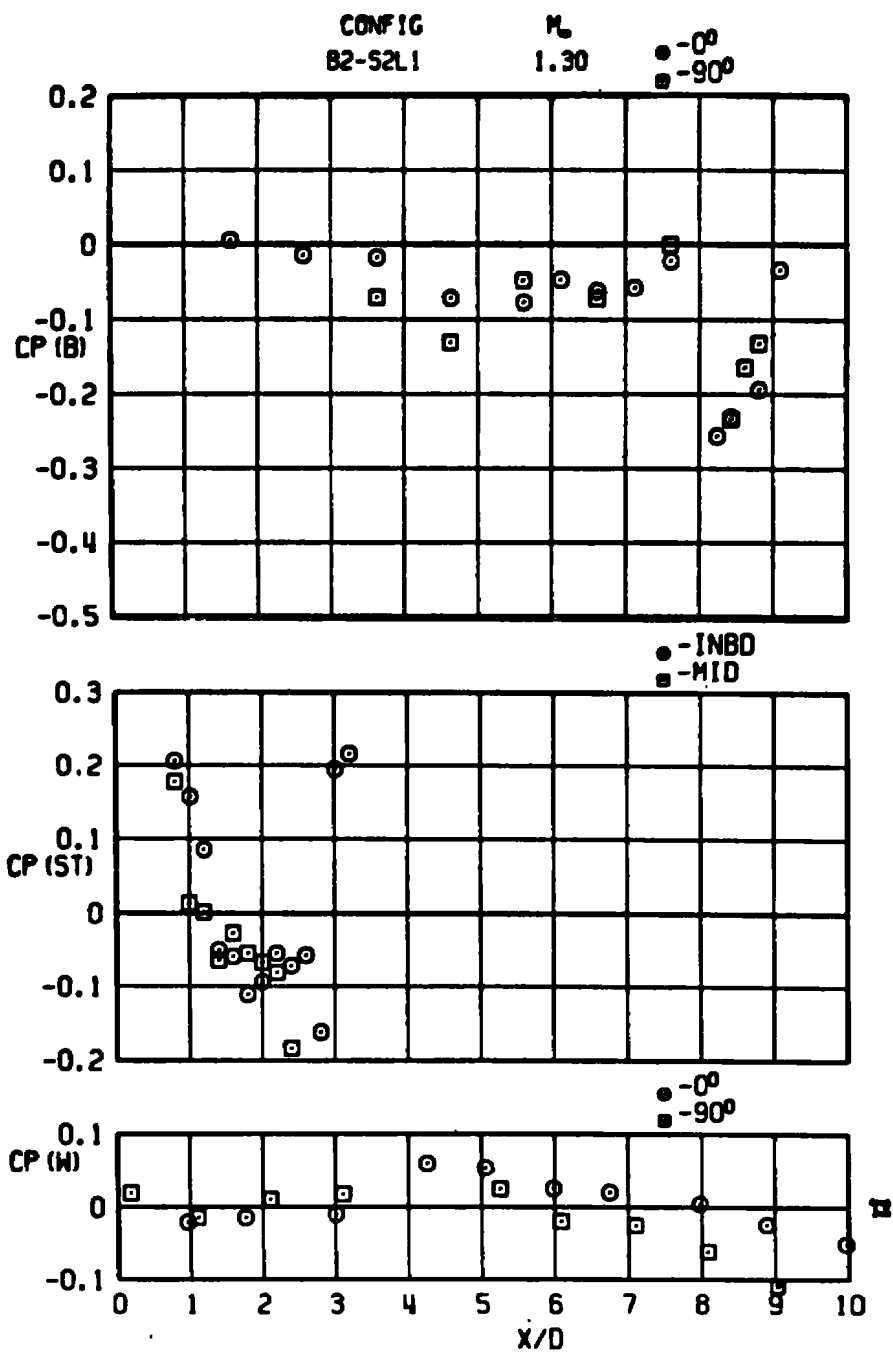
a. Continued
Figure A-8. Continued.



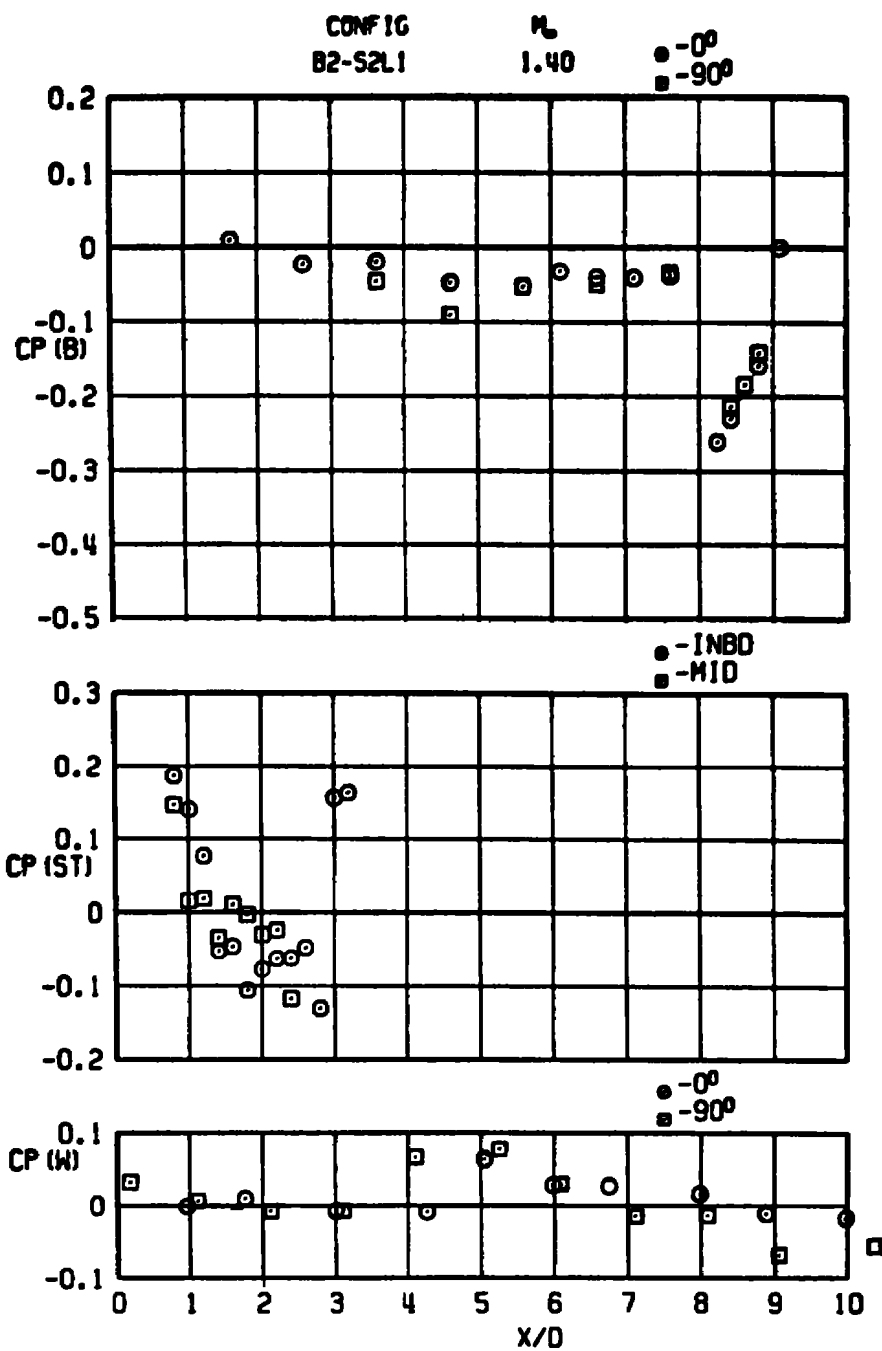
a. Continued
Figure A-8. Continued.



a. Continued
Figure A-8. Continued.



a. Continued
Figure A-8. Continued.



a. Concluded
Figure A-8. Continued.

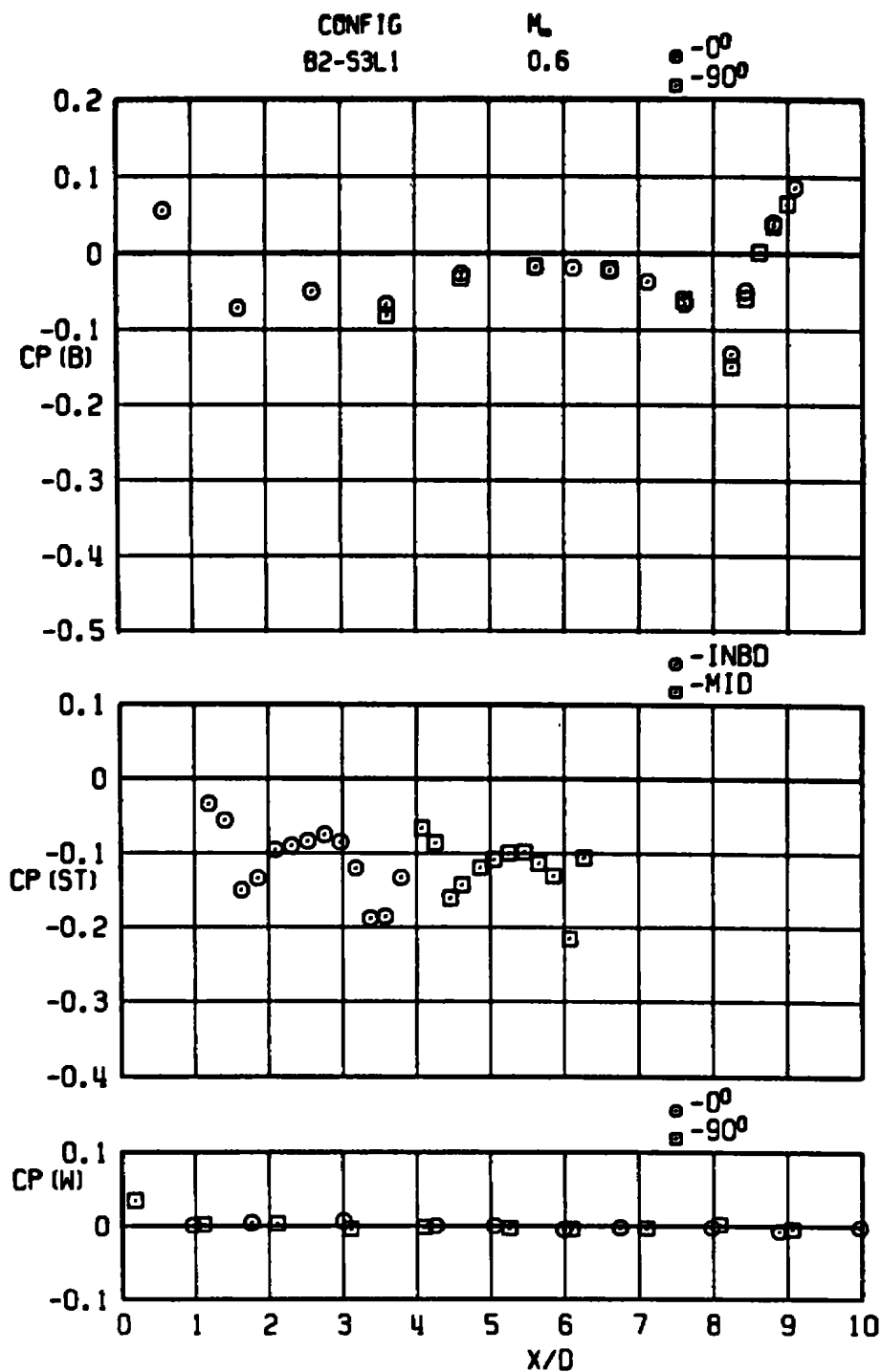
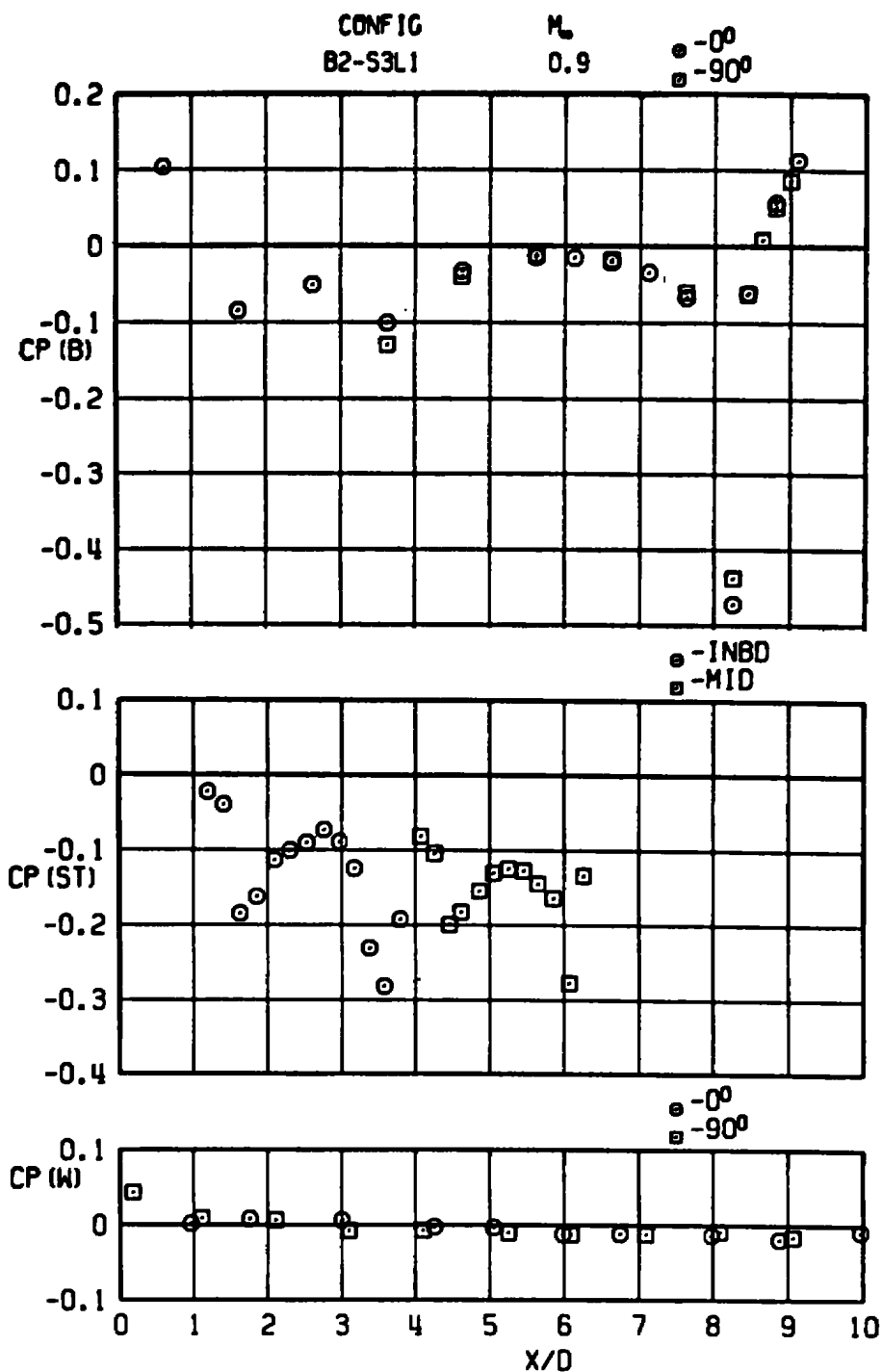
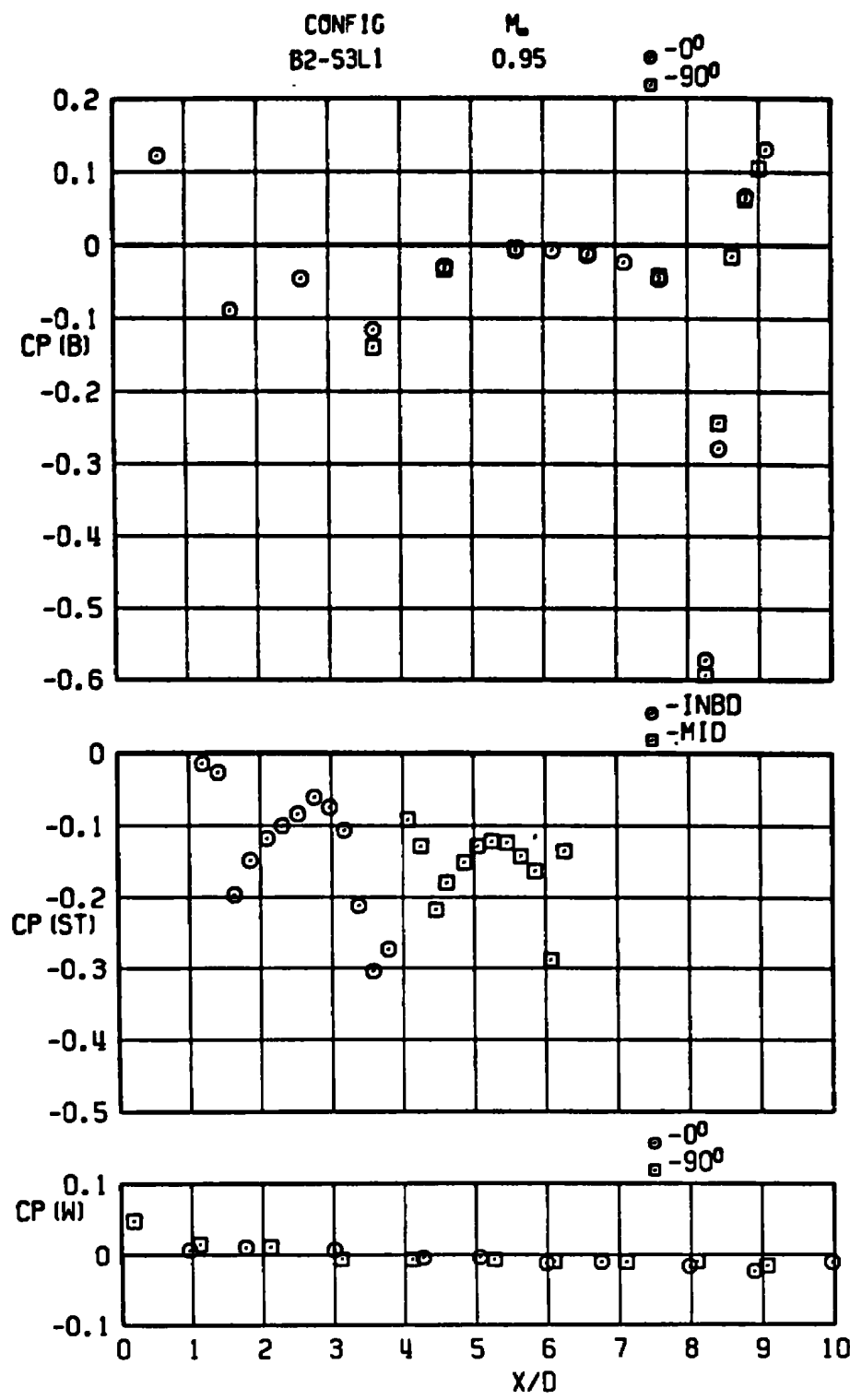
b. Swept strut configuration, $\ell = 0$ (B2-S3L1)

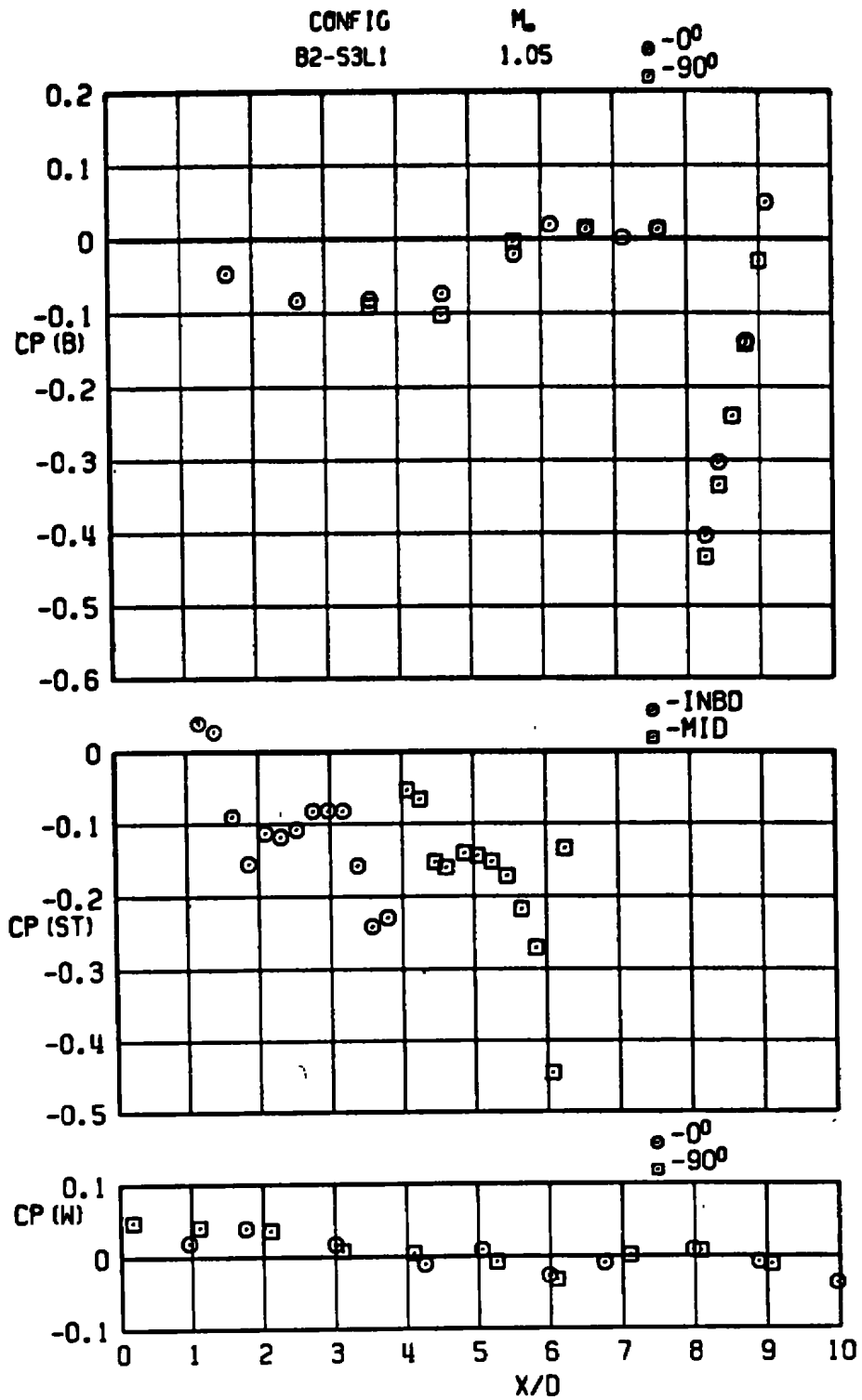
Figure A-8. Continued.



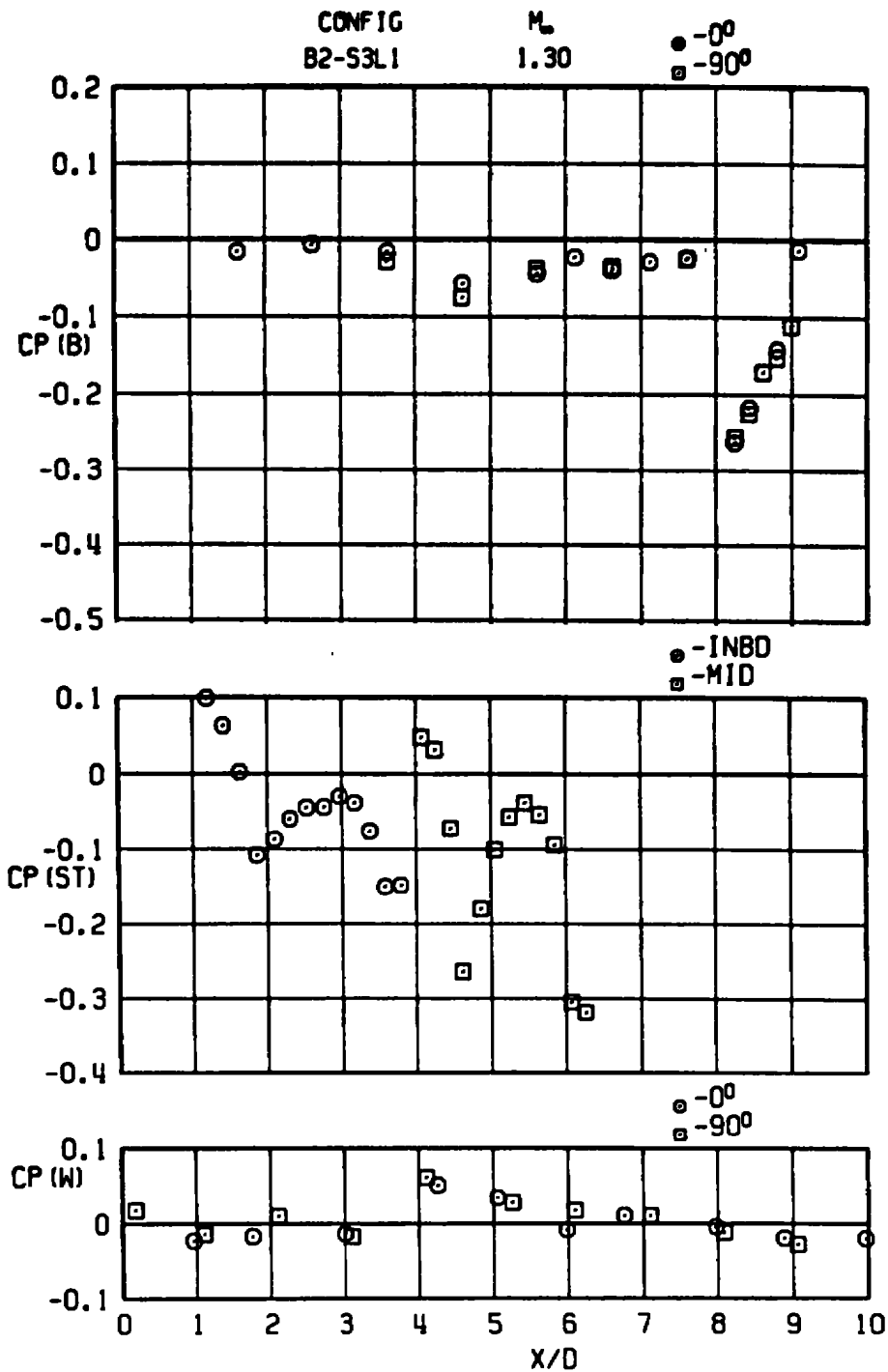
b. Continued
Figure A-8. Continued.



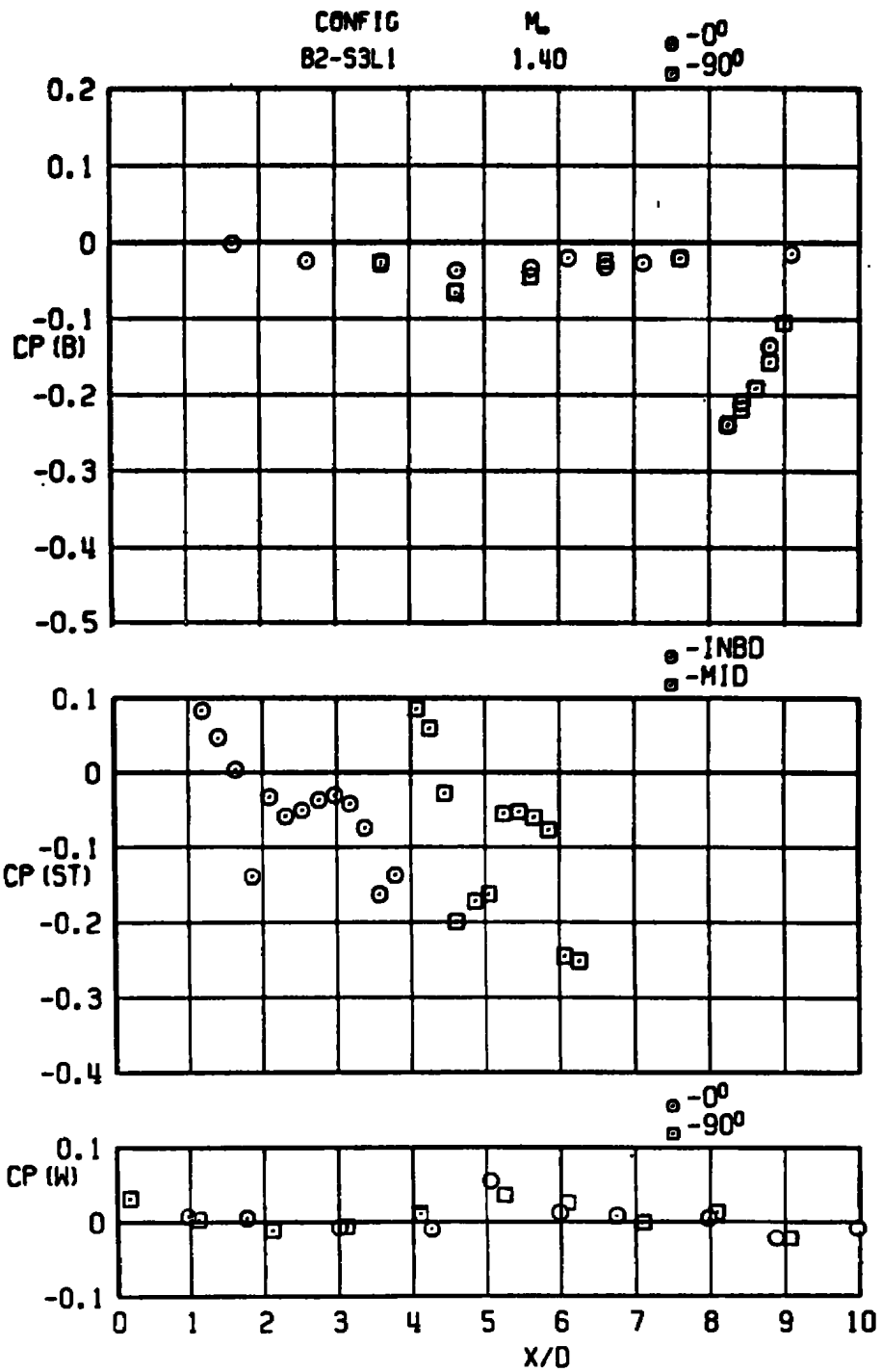
b. Continued
Figure A-8. Continued.



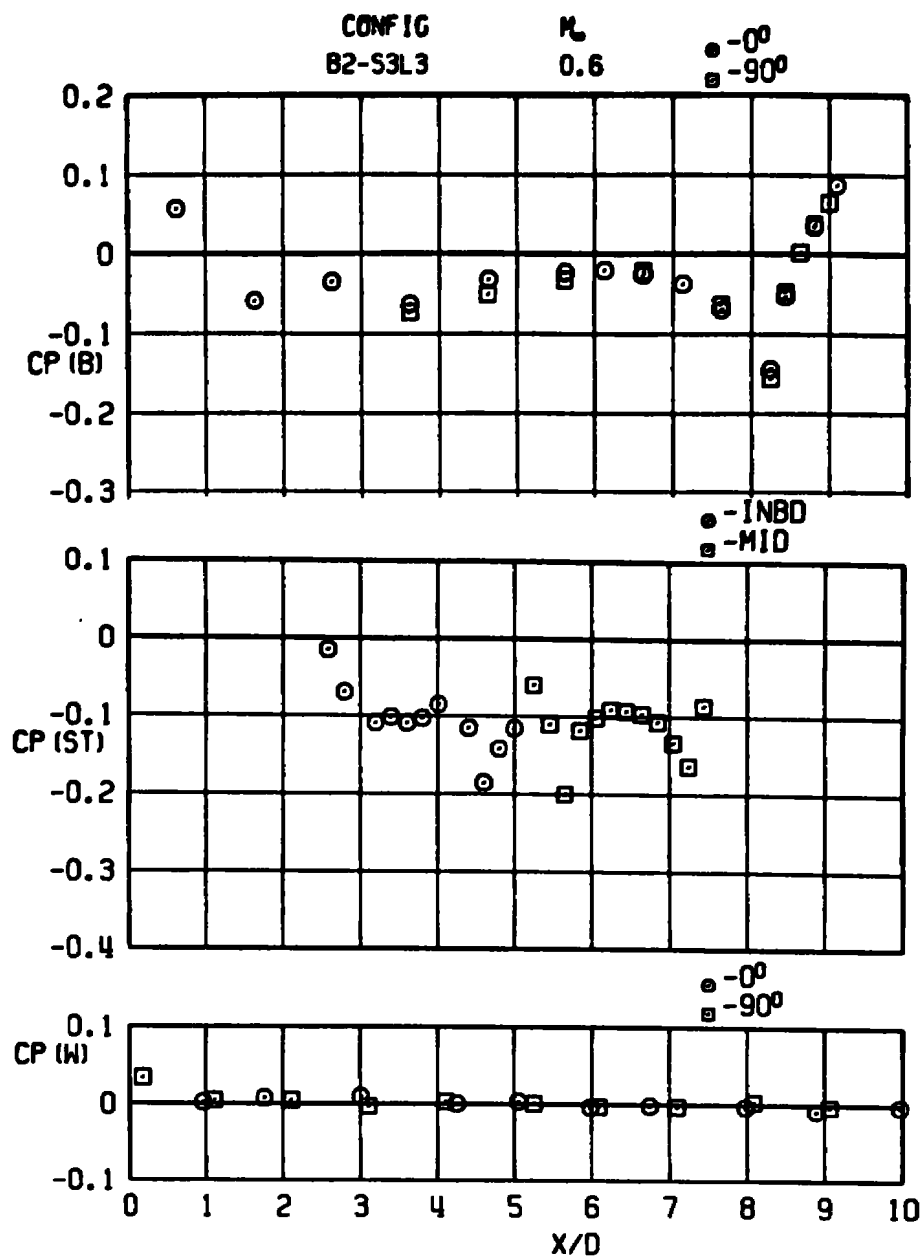
b. Continued
Figure A-8. Continued.



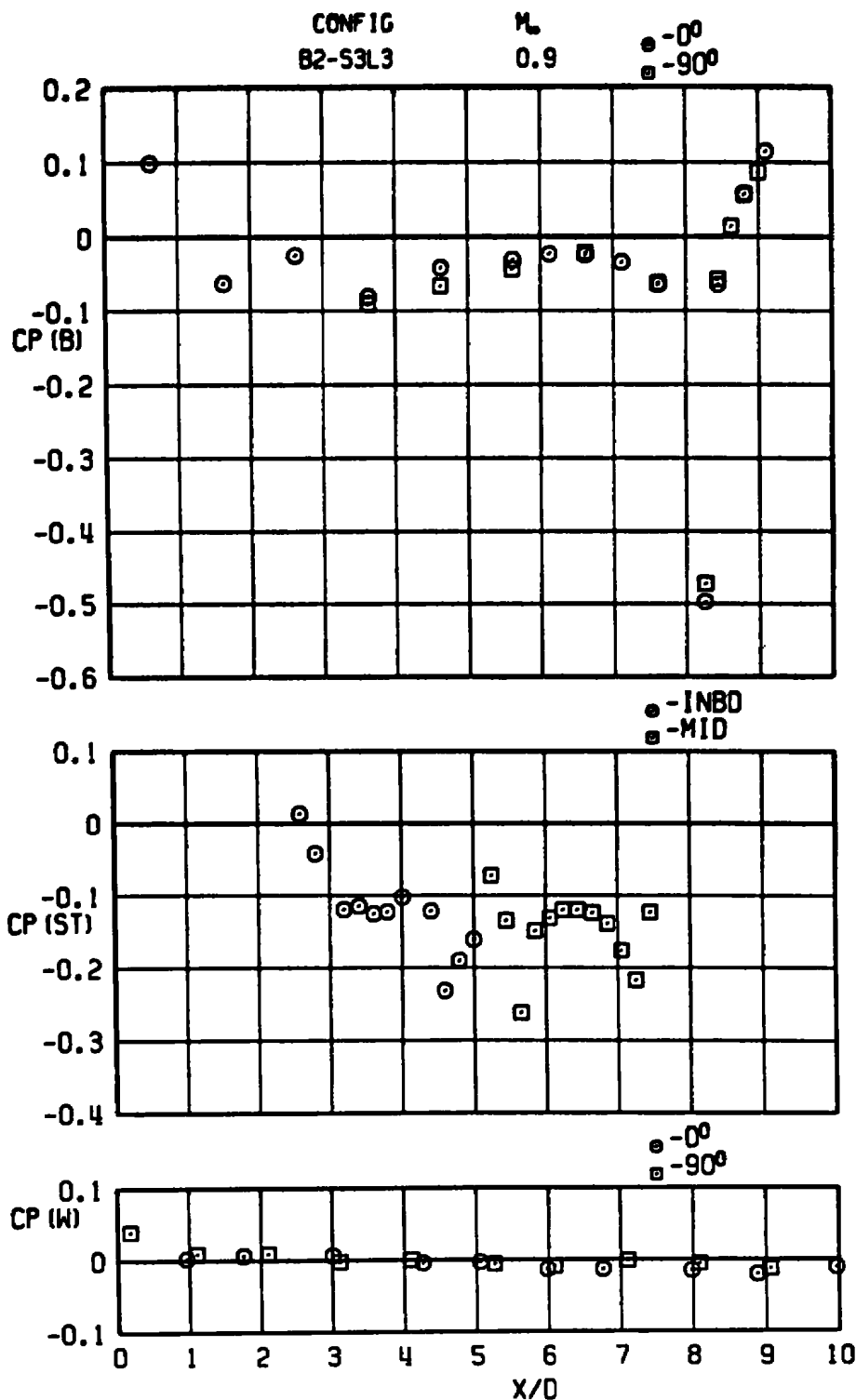
b. Continued
Figure A-8. Continued.



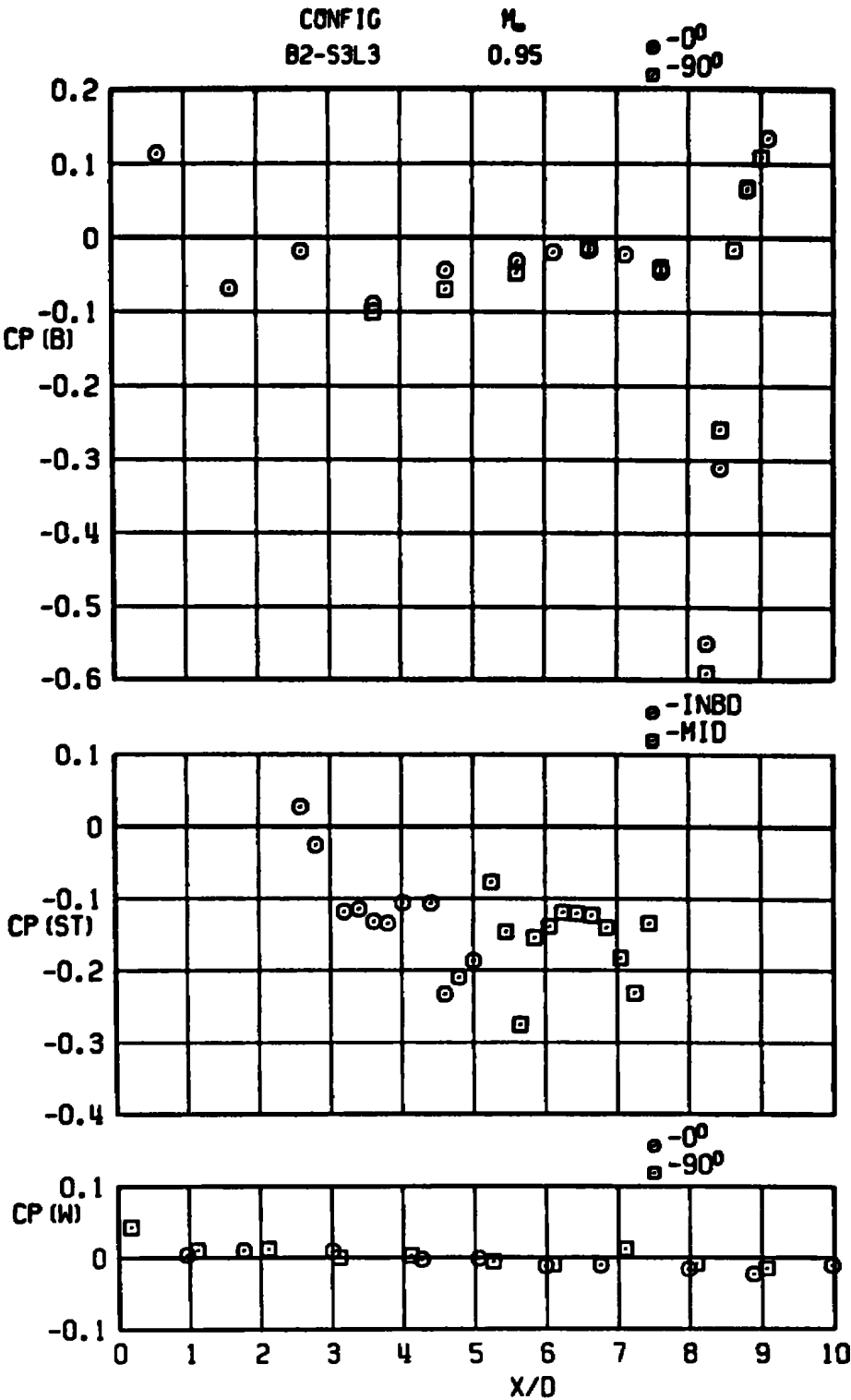
b. Concluded
Figure A-8. Continued.



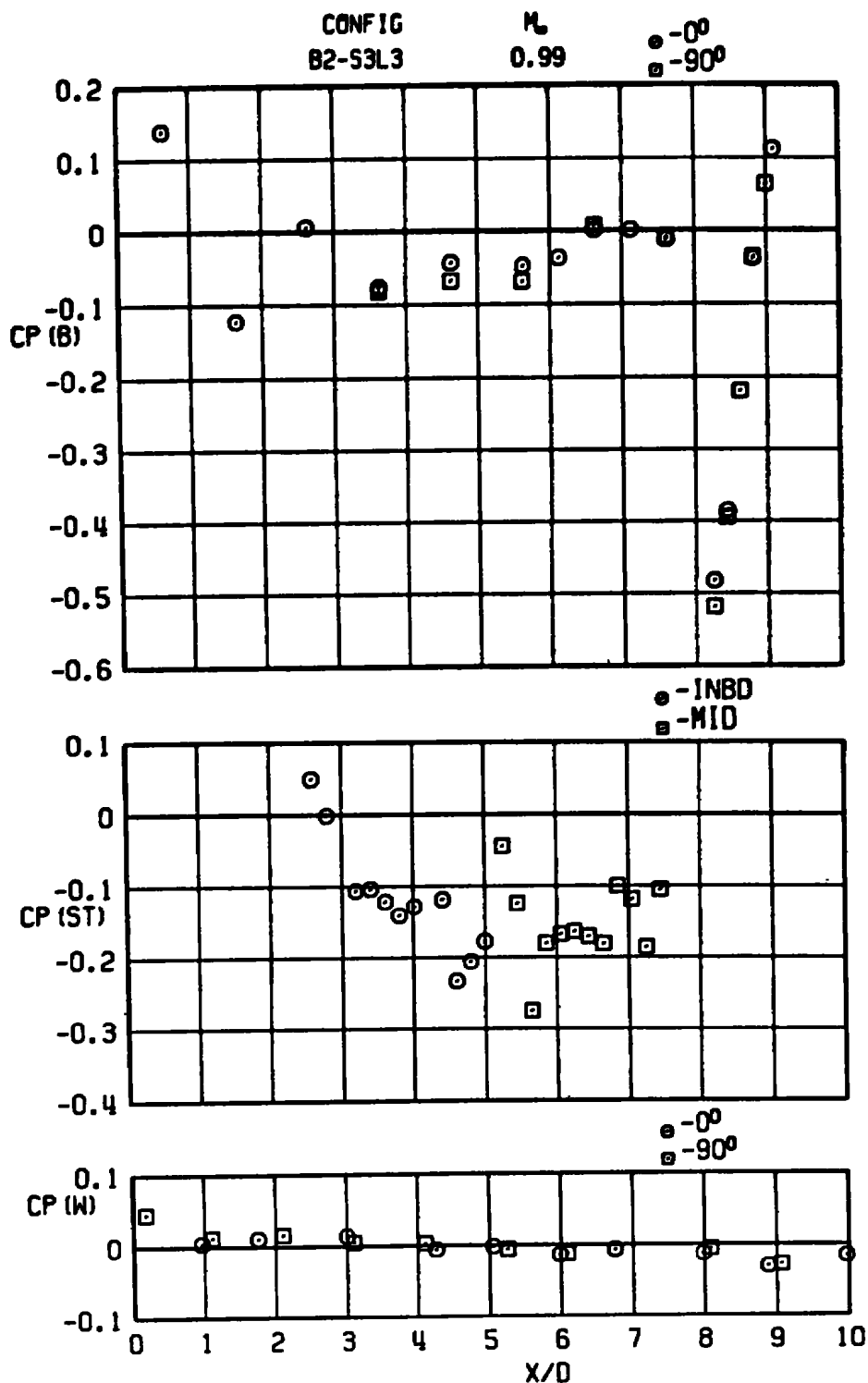
c. Swept strut configuration, $\ell = 1.6$ in. (B2-S3L3)
Figure A-8. Continued.



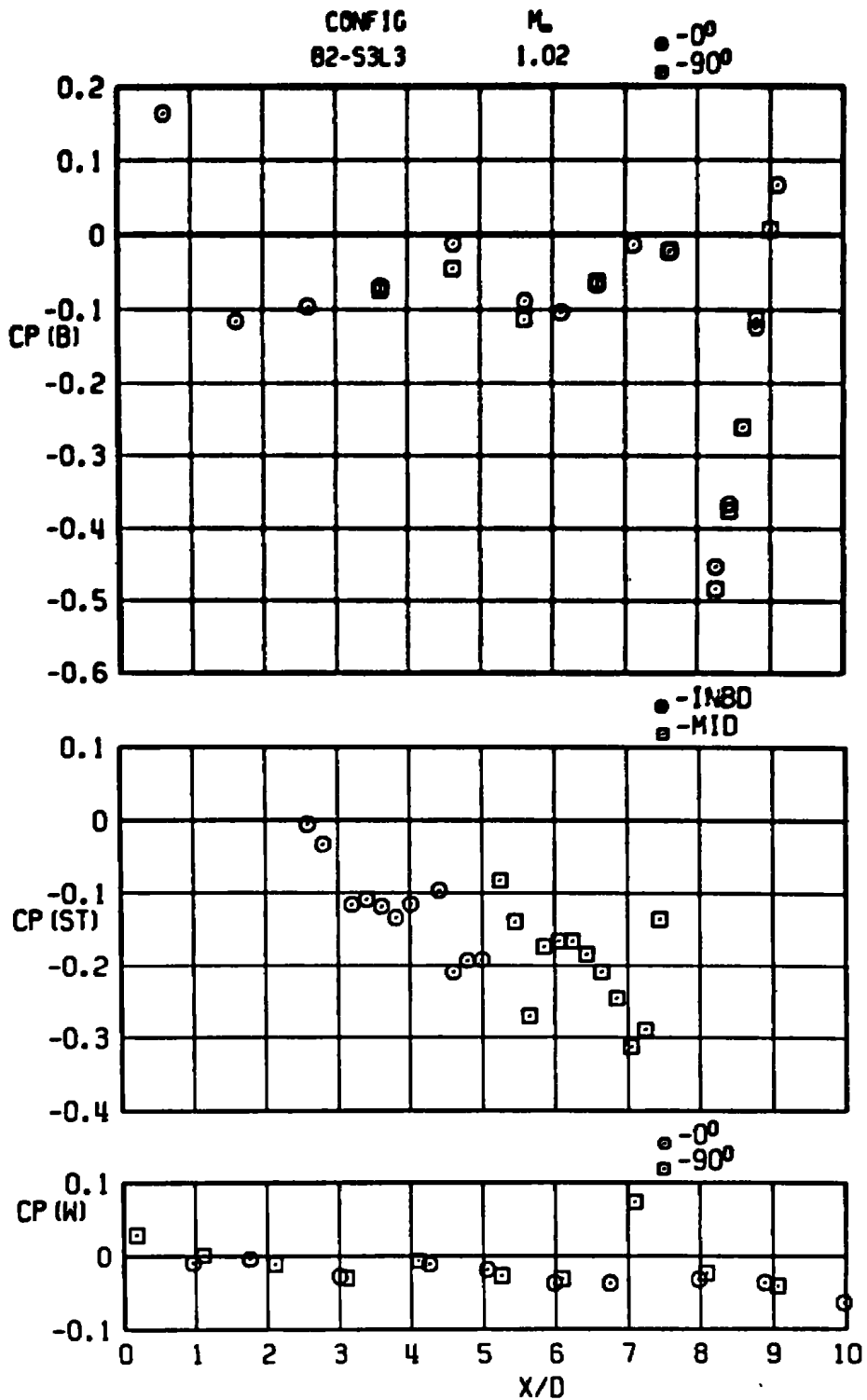
c. Continued
Figure A-8. Continued.



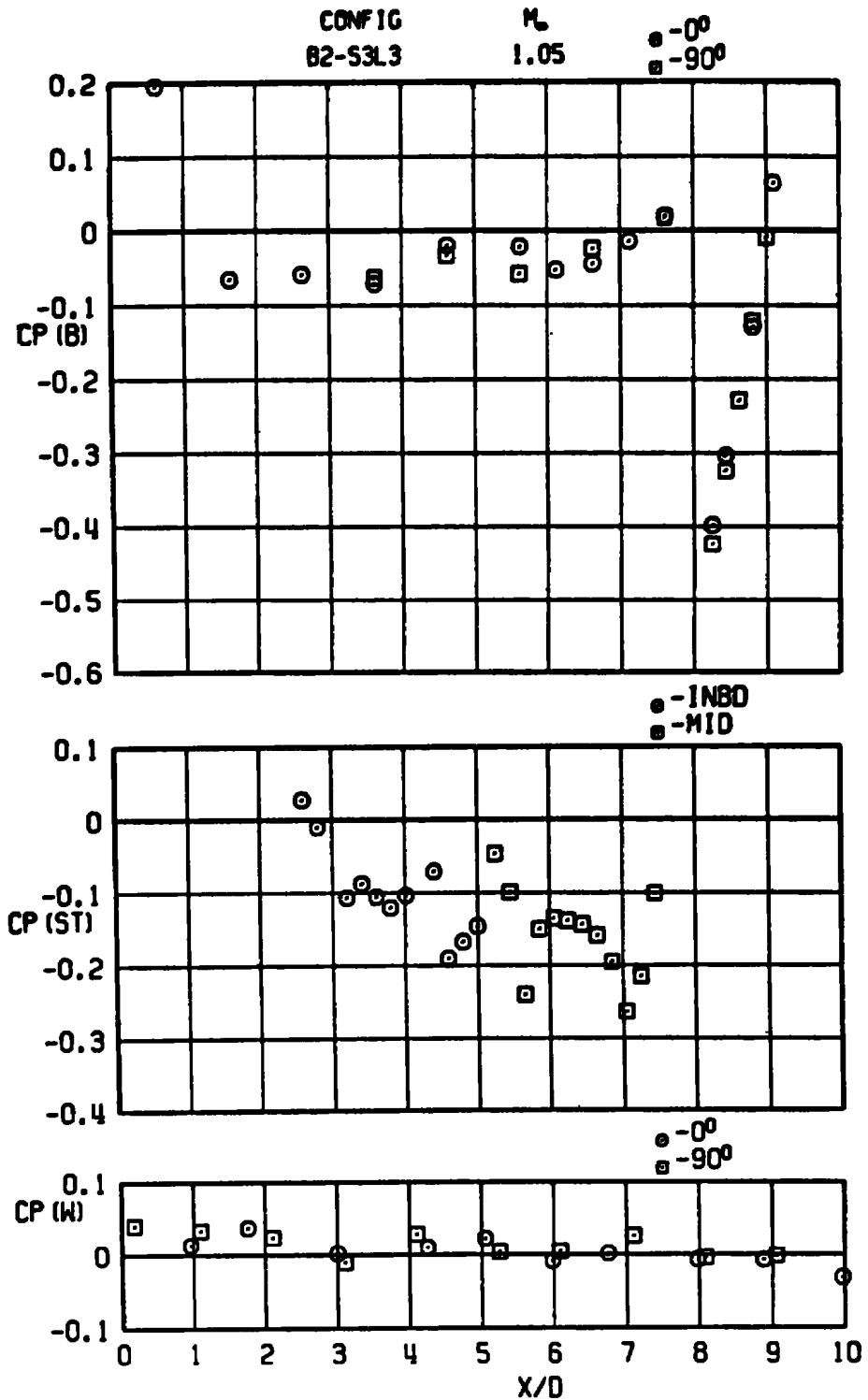
c. Continued
Figure A-8. Continued.



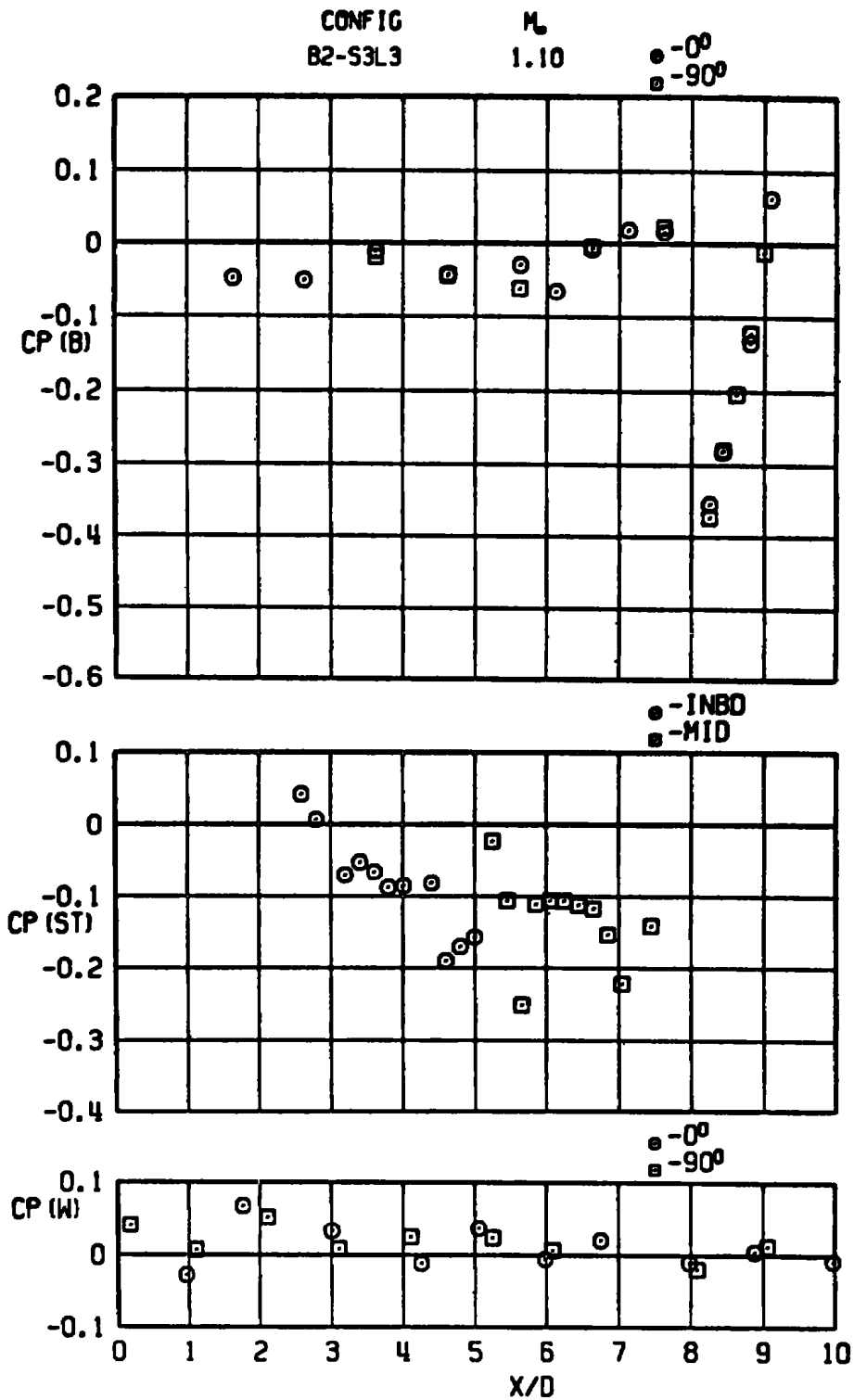
c. Continued
Figure A-8. Continued.



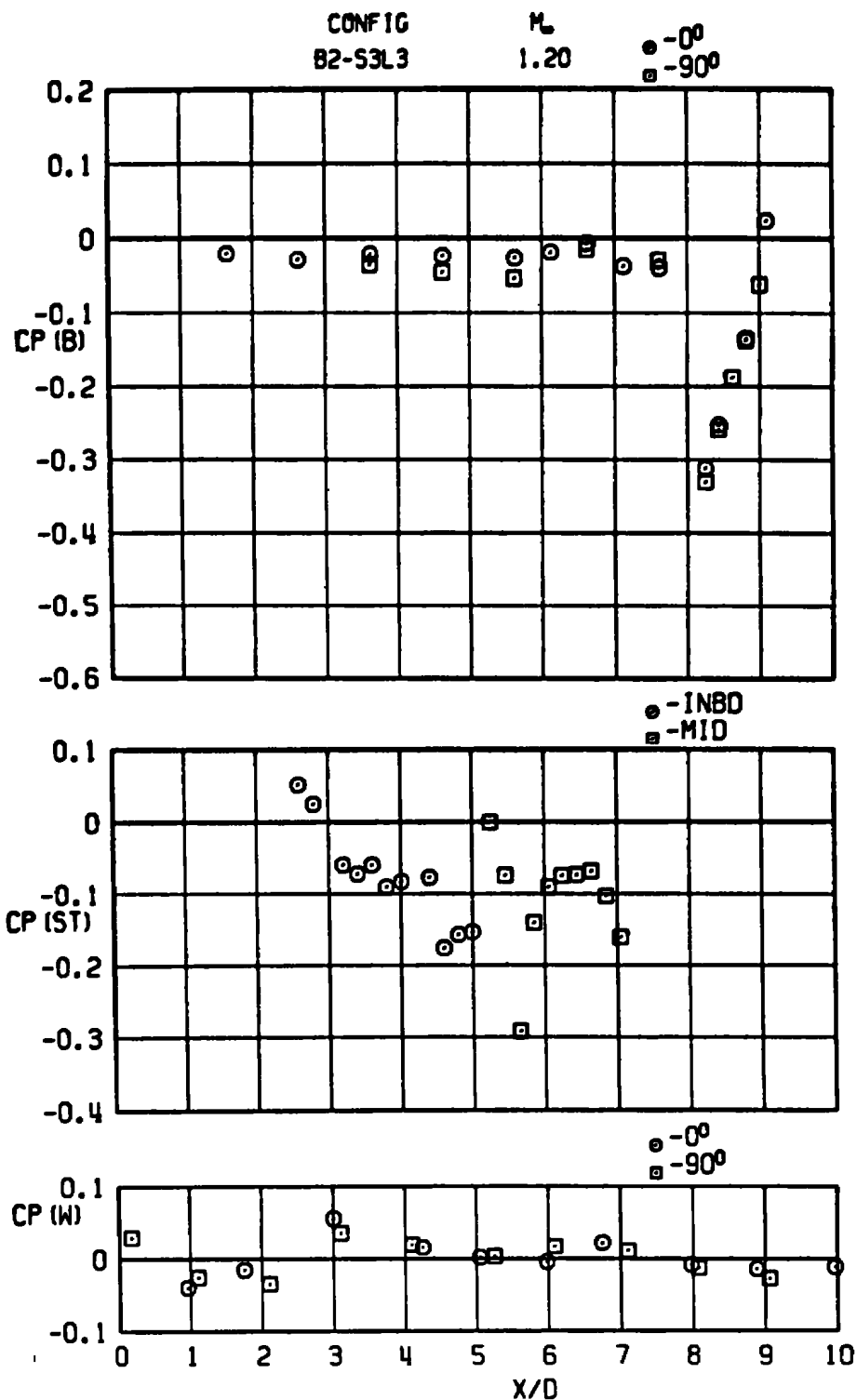
c. Continued
Figure A-8. Continued.



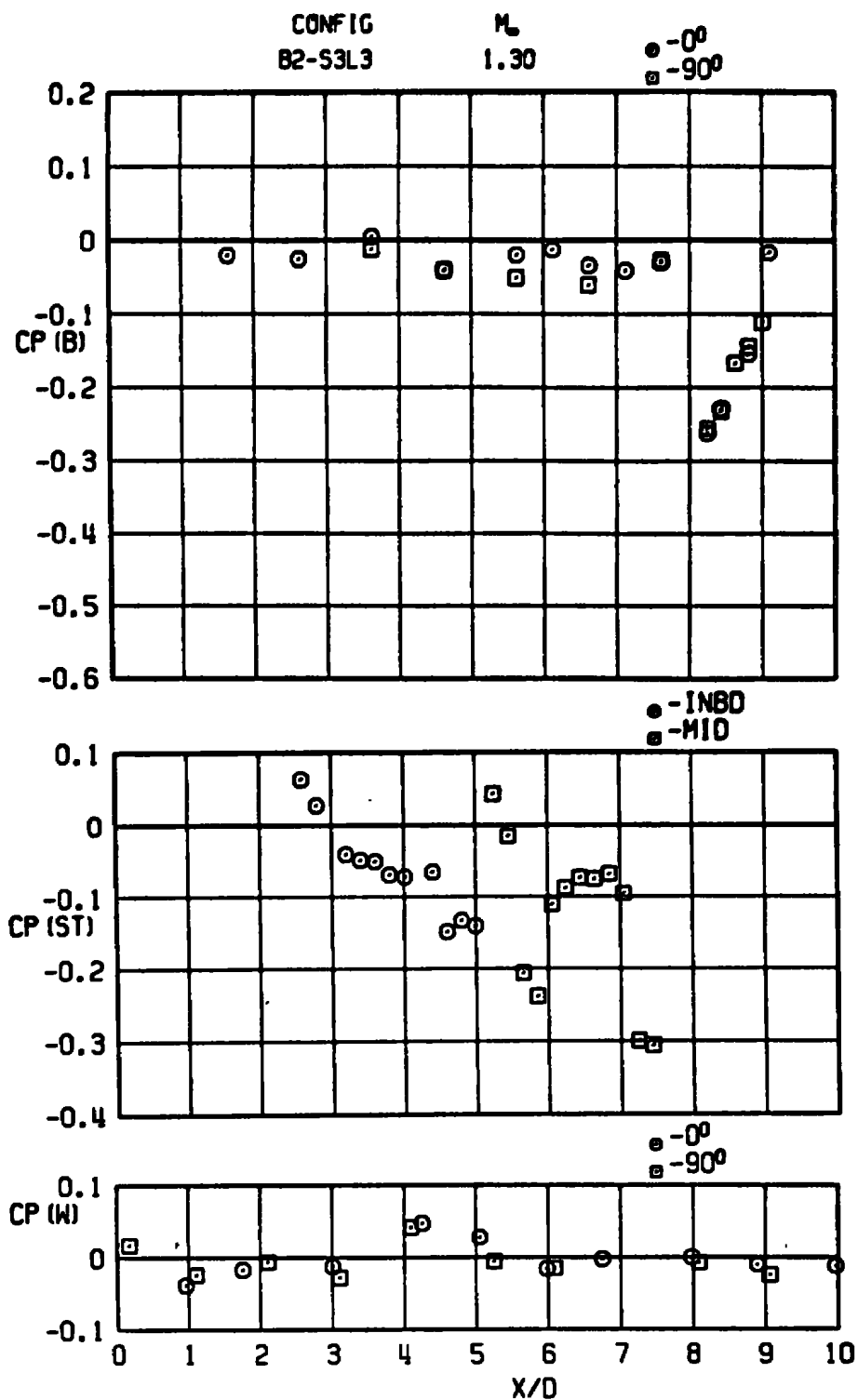
c. Continued
Figure A-8. Continued.



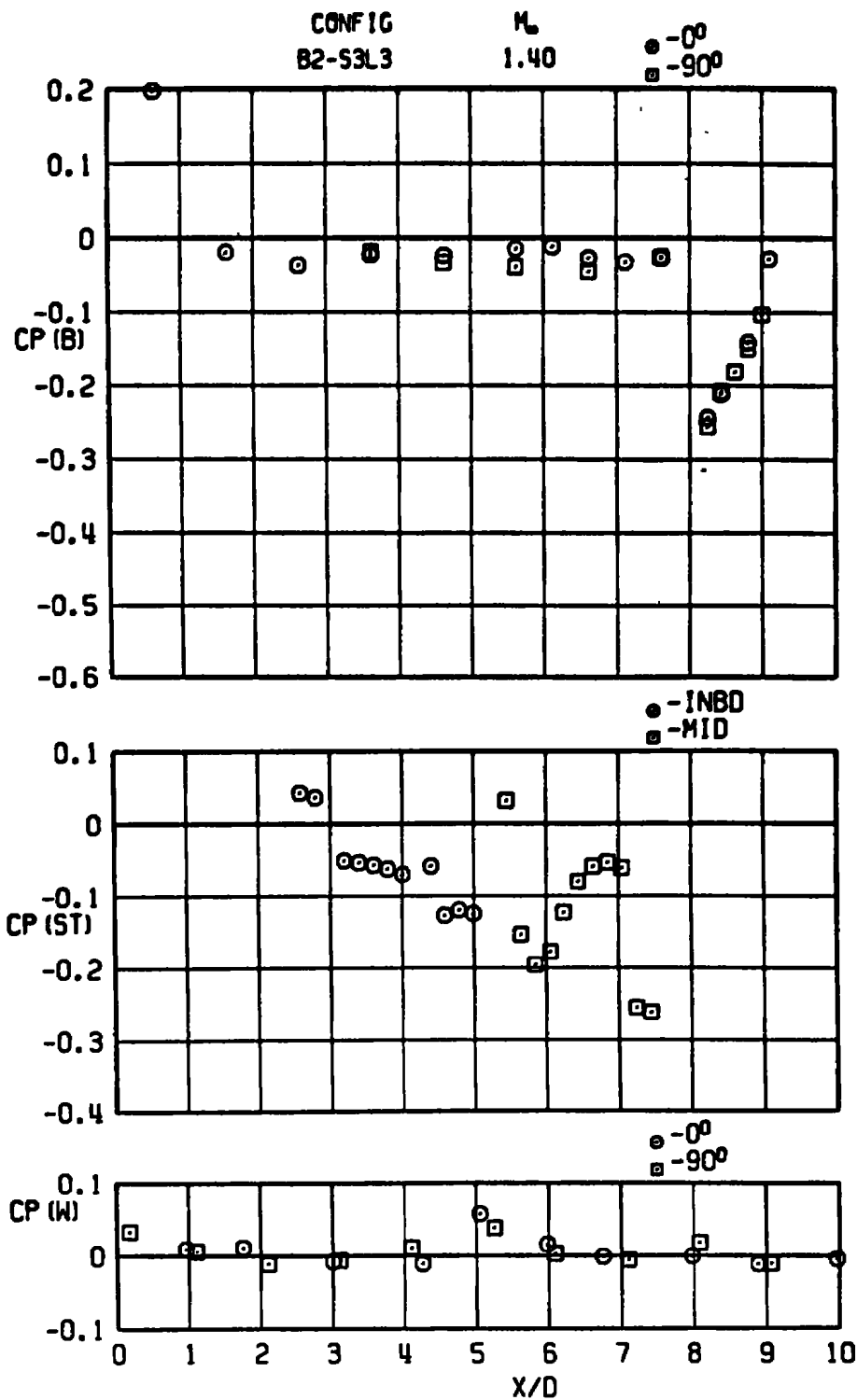
c. Continued
Figure A-8. Continued.



c. Continued
Figure A-8. Continued.



c. Continued
Figure A-8. Continued.



c. Concluded
Figure A-8. Concluded.

NOMENCLATURE

C	Strut chord length, in.
CP	Pressure coefficient, $(p-p_{\infty})/q_{\infty}$
CP _{baseline}	Pressure coefficient on sting-mounted body (no strut)
CPB	Average base pressure coefficient, $(p_b-p_{\infty})/q_{\infty}$
CP(B)	Pressure coefficient on cylindrical body
CPBT	Pressure coefficient on boattail
CP(P)	Pressure coefficient on boattail and simulated plume surfaces
CP(W)	Pressure coefficient on tunnel wall
ΔCPW	Change in pressure coefficient on tunnel wall
D	Model maximum diameter, 1.0 in.
DCP	Interference static pressure coefficient increment, $CP/CP_{baseline}$
DCPB	Interference average base pressure coefficient increment
DCPBT	Interference boattail pressure coefficient increment
INBD	Inboard location of static pressure measurement on strut
L	Body length, in.
ℓ	Distance from model nose station to strut leading edge at strut-body interface, in.
ℓ _F	Distance from model base station to beginning of sting-flare surface, in.
MID	Midlocation of static pressure measurement on strut
M _L	Local Mach number
M _∞	Free-stream Mach number
p	Local static pressure, psfa

p_b	Average base pressure, psfa
p_∞	Free-stream static pressure, psfa
q_∞	Free-stream dynamic pressure, psfa
Re/ft	Unit Reynolds number
SLE	Location of strut leading-edge shock reflection on tunnel wall
SM	Location of model nose shock reflection on tunnel wall
STE	Location of strut trailing-edge shock reflection on tunnel wall
T_t	Total temperature, °F
t	Strut thickness, in.
X	Axial distance from model nose station, in.
θ_{BT}	Nozzle afterbody boattail angle, deg (see Fig. 3)
θ_{LE}	Strut leading-edge wedge angle, deg
θ_{TE}	Strut trailing-edge wedge angle, deg
Λ	Strut support sweep angle, deg (see Fig. 4)
ϕ	Circumferential location of surface pressure orifices, deg (see Fig. 3)